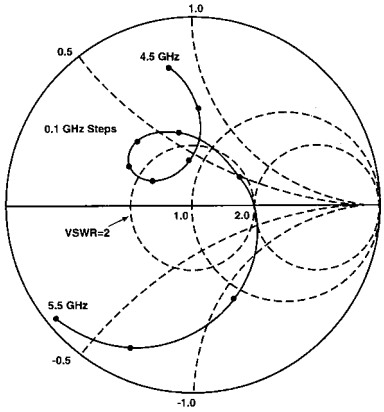

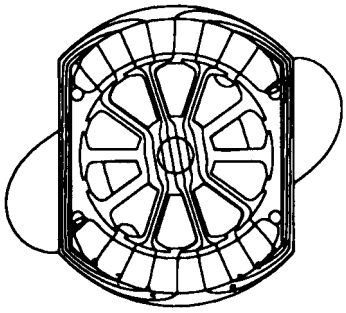

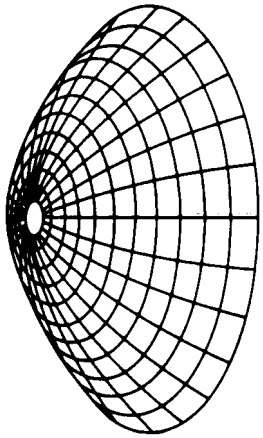

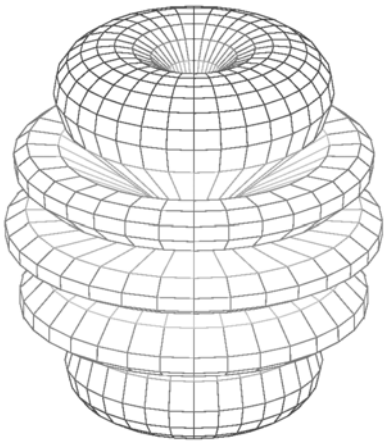

Applied Computational Electromagnetics Society Journal

Special Issue on
Phased and Adaptive
Array Antennas

Guest Editor
Deb Chatterjee

November 2006
Vol. 21 No. 3
ISSN 1054-4887

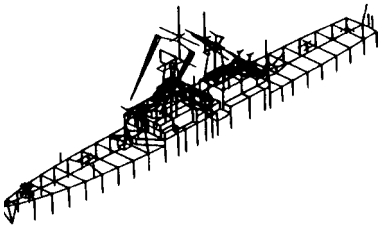

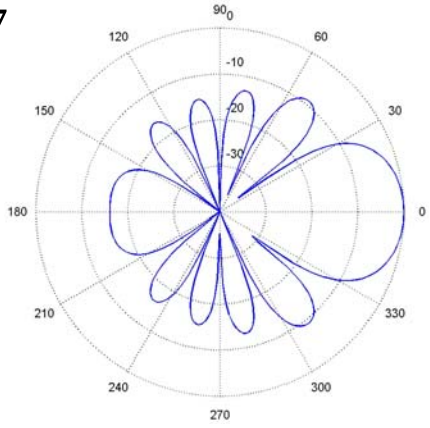

GENERAL PURPOSE AND SCOPE: The Applied Computational Electromagnetics Society ***(ACES)*** Journal hereinafter known as the ***ACES Journal*** is devoted to the exchange of information in computational electromagnetics, to the advancement of the state-of-the art, and the promotion of related technical activities. A primary objective of the information exchange is the elimination of the need to "re-invent the wheel" to solve a previously-solved computational problem in electrical engineering, physics, or related fields of study. The technical activities promoted by this publication include code validation, performance analysis, and input/output standardization; code or technique optimization and error minimization; innovations in solution technique or in data input/output; identification of new applications for electromagnetics modeling codes and techniques; integration of computational electromagnetics techniques with new computer architectures; and correlation of computational parameters with physical mechanisms.

SUBMISSIONS: The ***ACES Journal*** welcomes original, previously unpublished papers, relating to applied computational electromagnetics. Typical papers will represent the computational electromagnetics aspects of research in electrical engineering, physics, or related disciplines. However, papers which represent research in applied computational electromagnetics itself are equally acceptable.

Manuscripts are to be submitted through the upload system of ***ACES*** web site http://aces.ee.olemiss.edu See "Information for Authors" on inside of back cover and at ***ACES*** web site. For additional information contact the Editor-in-Chief:

Dr. Atef Elsherbeni
Department of Electrical Engineering
The University of Mississippi
University, MS 386377 USA
Phone: 662-915-5382 Fax: 662-915-7231
Email: atef@olemis.edu

SUBSCRIPTIONS: All members of the Applied Computational Electromagnetics Society who have paid their subscription fees are entitled to receive the ***ACES Journal*** with a minimum of three issues per calendar year and are entitled to download any published journal article available at http://aces.ee.olemiss.edu.

Back issues, when available, are $15 each. Subscriptions to ***ACES*** are through the web site. Orders for back issues of the ***ACES Journal*** and changes of addresses should be sent directly to ***ACES*** Executive Officer:

Dr. Richard W. Adler
ECE Department, Code ECAB
Naval Postgraduate School
833 Dyer Road, Room 437
Monterey, CA 93943-5121 USA
Fax: 831-649-0300
Email: *rwa@attglobal.net*

Allow four week's advance notice for change of address. Claims for missing issues will not be honored because of insufficient notice or address change or loss in mail unless the Executive Officer is notified within 60 days for USA and Canadian subscribers or 90 days for subscribers in other countries, from the last day of the month of publication. For information regarding reprints of individual papers or other materials, see "Information for Authors".

LIABILITY. Neither ***ACES***, nor the ***ACES Journal*** editors, are responsible for any consequence of misinformation or claims, express or implied, in any published material in an ***ACES Journal*** issue. This also applies to advertising, for which only camera-ready copies are accepted. Authors are responsible for information contained in their papers. If any material submitted for publication includes material that has already been published elsewhere, it is the author's responsibility to obtain written permission to reproduce such material.

APPLIED COMPUTATIONAL ELECTROMAGNETICS SOCIETY JOURNAL

Special Issue on
Phased and Adaptive Array Antennas

Guest Editor
Deb Chatterjee

November 2006
Vol. 21 No. 3

ISSN 1054-4887

The ACES Journal is abstracted in INSPEC, in Engineering Index, and in DTIC.

The first, fourth, and sixth illustrations on the front cover have been obtained from the Department of Electrical Engineering at the University of Mississippi.

The third and fifth illustrations on the front cover have been obtained from Lawrence Livermore National Laboratory.

The second illustration on the front cover has been obtained from FLUX2D software, CEDRAT S.S. France, MAGSOFT Corporation, New York.

Guest Editorial

ACES Invited Special Issue on *Phased and Adaptive Array Antennas*

This *invited* special issue of the Applied Computational Electromagnetics Society (ACES) Journal on *Phased and Adaptive Array Antennas* aims to capture information on a broad spectrum of the various aspects involved in array radiating systems and their applications. Recent advances in this area can be found in [1]-[3]. The earlier special issue [4] on a closely similar topic served as a guide in preparing for this ACES special issue. The information gleaned from these sources resulted in a widening of the scope of this special issue than was originally planned. For enhanced impact, it appeared appropriate to solicit contributions from leading researchers in the antennas and computational electromagnetics (CEM) areas. To that end, in quite a few cases, the topic of the invited contribution was suggested to the individual authors. All invited papers were peer-reviewed per standard guidelines.

In all there are twenty papers co-authored or authored by leading researchers from various countries. They represent a wide range of topics on phased and adaptive arrays. Specifically, papers on characteristic basis functions, genetic algorithms, ship-board arrays, conformal arrays, phased arrays for biomedical applications, multiple-beam phased arrays, array mutual coupling compensation, power-divider network, etc., appear here and provide useful information on both modeling and practical applications of phased and adaptive arrays. The valuable contribution of the authors and their patience is gratefully acknowledged.

In the course of assembling the special issue, special thanks go to Prof. Atef Elsherbeni (editor-in-chief) and Prof. Alexander Yakovlev (associate editor-in-chief) of ACES Journal, University of Mississippi (Ole Miss). The encouragement from Dr. W. Ross-Stone, editor-in-chief, *IEEE Antennas and Propagation Magazine*, is deeply appreciated. It is a pleasure to acknowledge the extensive editorial help from Mr. Mohamed Al Sharkawy (Ole Miss), in the final stages. At University of Missouri Kansas City (UMKC), Mr. Naresh Vijaya Yalamanchili had painstakingly retyped some of the manuscripts for this invited special issue. Thanks to all of them for their continued encouragement and timely help. Without their active support this endeavor would not have come to fruition.

The final judgment on the quality of this invited special issue rests on the reader. It is hoped that the reader shall find the contents in these papers of continuing value. Any drawback or other errors is the sole responsibility of the guest editor.

References

[1] Arun K. Bhattacharyya, *Phased Array Antennas: Floquet Analysis, Synthesis, BFNs, and Active Array Systems*. Hoboken, NJ, USA: John-Wiley & Sons, Inc., 2006.

[2] L. Josefsson and P. Persson, *Conformal Array Antenna: Theory and Design*. Hoboken, NJ, USA: Wiley-Interscience, 2006.

[3] L. C. Godara**,** *Smart Antennas***.** Boca Raton, FL, USA: CRC Press, 2004.

[4] R. J. Mailloux (ed.)**,** Special Issue on *Phased Arrays*, IEEE Transactions on Antennas and Propagation, vol. 47, no. 3, March 1999.

Deb Chatterjee is an associate professor of Electrical and Computer Engineering, with the Computer Science and Electrical Engineering (CSEE) Department at University of Missouri Kansas City (UMKC), where he joined as a faculty in August 1999. He obtained his M.A.Sc. and Ph.D. degrees in Electrical and Computer Engineering and Electrical Engineering, from Concordia University, Montreal, Canada and University of Kansas, Lawrence, Kansas, respectively. His current research interests are in phased arrays, high-frequency scattering and propagation, miniature, ultra-wideband microstrip antennas. He has served as a reviewer of technical articles for *IEEE Transactions on Antennas and Propagation*, *IEEE Antennas and Wireless Propagation Letters*, *Radio Science*, and the *Applied Computational Electromagnetics Society* (ACES) *Journal*. Currently he serves as an associate editor for *International Journal of Antennas and Propagation* (IJAP). Dr. Chatterjee has published 35 articles in peer-reviewed journals and conference proceedings, and has taught courses in the area of electromagnetics and antennas at undergraduate and graduate levels. He is a member of the IEEE Antennas and Propagation and the Applied Computational Electromagnetics Societies.

THE APPLIED COMPUTATIONAL ELECTROMAGNETICS SOCIETY

JOURNAL

Vol. 21 No. 3 November 2006

TABLE OF CONTENTS

A Hybrid Framework for Antenna/Platform Analysis

(*Invited Paper*)

R. J. Burkholder, P. H. Pathak, K. Sertel,
R. J. Marhefka, and J. L. Volakis
The Ohio State University Dept. of Electrical and Computer Eng.
ElectroScience Lab, 1320 Kinnear Road, Columbus, OH 43212

R. W. Kindt
Naval Research Laboratories, Radar Division
4555 Overlook Ave. SW, Washington, D.C. 20375

***Abstract*–** Hybrid combinations of numerical and asymptotic methods are utilized to evaluate in-situ antenna performance, and coupling to other systems on a shared platform such as a ship topside. This paper describes a combination of the finite element-boundary (FE-BI) method with ray techniques for evaluating antenna patterns in the presence of complex platforms. Specifically, a very complex array antenna may be modeled with FE-BI, and interfaced to the platform via the use of equivalent currents. For the case considered here, the FE-BI is accelerated with the array decomposition fast multipole method (AD-FMM) so that large arrays may be considered. A novel discrete Fourier transform method is also introduced to provide a greatly reduced representation of the fields over a planar array aperture and the uniform theory of diffraction (UTD) along with iterative physical optics (IPO) are used to characterize the platform. To tie it all together, a matrix framework is formulated to iteratively increment the higher order interactions between antennas and platform.

I. INTRODUCTION

The Ohio State University ElectroScience Laboratory (OSU-ESL) has a long history of studying the performance of antennas mounted on realistic platforms [1,2]. Prior to using numerical methods, these studies were carried out experimentally, and later also by using ray methods such as the uniform geometrical theory of diffraction (UTD) [3]. Today's availability of numerical methods and their success to accurately model conformal antennas present us with new hybrid tools [4] for modeling realistic antenna structures (and not just simple sources) on complex platforms.

In this article we introduce hybrid techniques for the analysis of electromagnetic (EM) radiation from, and the coupling among, large multiple antenna arrays mounted on a large complex platform, such as a ship (see Figure 1). Other large platforms may include airborne and land vehicles. The antenna-platform problem is challenging because numerical methods require very large computational resources even for the array itself. This is compounded by the presence of the platform and the necessity to account for interactions among multiple antennas. The hybrid approach combining numerical methods for large antenna arrays and high frequency methods for dealing with large platforms appears to be well suited to solve such practical problems in a tractable manner.

In our analysis, the FE-BI along with domain decomposition approach, is used for array analysis [4], whereas the platform is accounted for via high frequency asymptotic methods (see Figure 1). The UTD method [3] is used to model the whole ship at very high frequencies via the UTD-based NEC-Basic Scattering Code (NEC-BSC) [5], which has been extensively used for ship modeling. There are several features of NEC-BSC that make it attractive. Among them are the capability to find ray paths for ship structures efficiently and its CPU scalability as the size increases. In fact, UTD becomes more accurate as the frequency increases. For more arbitrarily shaped CAD models the

iterative physical optics (IPO) method can be more appropriate than NEC-BSC since it can deal with situations for which UTD diffraction coefficients are not currently available [6,7]. IPO has been shown to give good accuracy, and is considerably more efficient than pure numerical

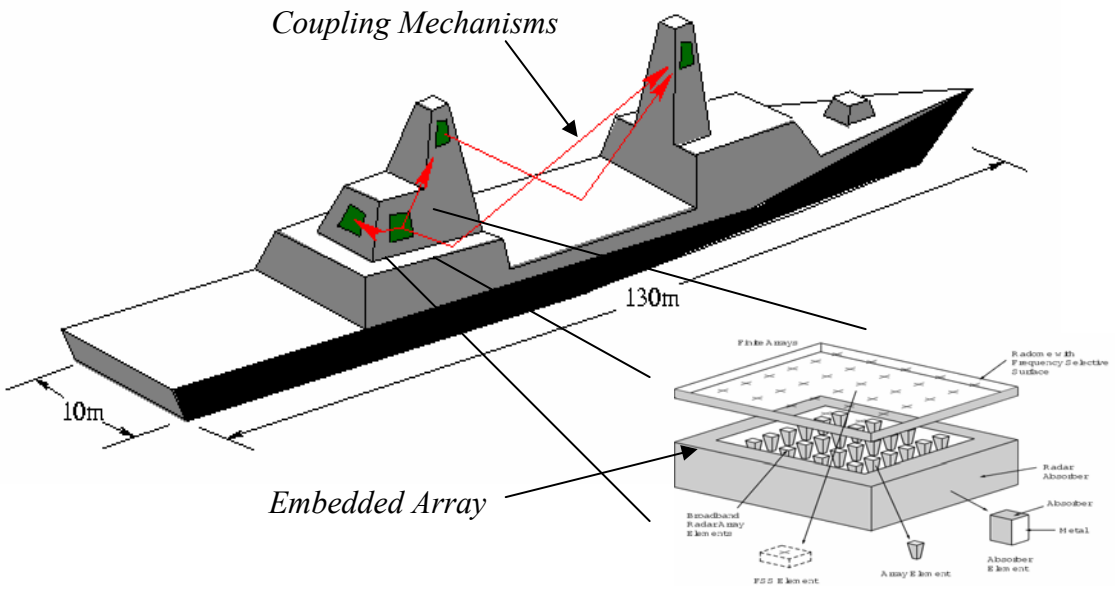

Figure 1: Interactions between antenna arrays on a modern naval vessel.

methods. As such, the IPO serves to bridge the gap between the numerical and the UTD-based approaches.

Central to the proposed hybrid approach is the means of representing the fields over the array apertures in a reduced basis set. This is necessary to efficiently handle the antenna-platform interactions. For this purpose, a novel approach is proposed using a discrete Fourier transform (DFT) representation of the aperture fields which is subsequently truncated to extract the reduced basis set [8]. A more recent approach is to employ a traveling wave (TW) basis set [9] which is even more efficient than the DFT; the latter approach will not be discussed here, but it will be described in detail in a future publication.

The format of this paper is as follows: Section II describes the general formulation for hybridizing the FE-BI method with the high-frequency approaches. Section III gives a brief summary of the accelerated FE-BI method used for analyzing finite array antennas [4], and Section IV describes how high-frequency methods are employed for platform interactions. The integration of the FE-BI method for antennas and the high frequency methods for the platform along with the reduced basis set expansion are described in Section V. Several validation examples are given throughout.

II. GENERAL APPROACH TO HYBRIDIZATION

The main idea of the proposed hybridization approach is to decompose the structure into different domains. These domains are subsequently coupled by iteratively accounting for multiple interactions. Such interactions can be either among array apertures or between an aperture and the array platform ship structure. It is understood that each individual array aperture must be analyzed with rigorous methods. In this case the FE-BI method enhanced with domain decomposition and fast algorithms will be used [4]. Certainly, other analysis methods can be used as they are available.

Let us assume that one of the antennas or substructures can be characterized by a matrix [*Z*]. This matrix can be generated via the method of moments, the finite element method or the FE-BI method. For the latter,

$$[Z]=\begin{bmatrix} E_{vv} & E_{vs} & 0 \\ E_{sv} & E_{ss} & B \\ 0 & P & Q \end{bmatrix} \quad (1)$$

in which E_{vv}, E_{vs}, E_{sv}, E_{ss}, B, P, and Q denote sub-matrices. More specifically, P and Q in (1) are full matrices resulting from the integral operators used to express the fields external to the solution domain, and the remaining sub-matrices are the usual sparse FE matrices for surface and volume unknowns [4].

Regardless of the method used for characterizing a single component of the structure, let us denote the associated matrices for multiple components as $[Z_{11}]$, $[Z_{22}]$, etc. The complete coupling matrix that includes all interactions between the #1 and #2 components or arrays would then be [10],

$$[Z]_{coupled}=\begin{bmatrix} Z_{11} & Z_{12} \\ Z_{21} & Z_{22} \end{bmatrix} \quad (2)$$

where Z_{ij} account for cross-coupling interactions. When Z_{ii} is generated via FE-BI, the coupling matrices have the form,

$$Z_{ij}\Big|_{i\neq j}=\begin{bmatrix} 0 & 0 & 0 \\ 0 & 0 & 0 \\ 0 & P & Q \end{bmatrix} \quad (3)$$

because only the P and Q sub-matrices are needed to "communicate" with outside components.

The identification of (2) allows us to consider matrix partitions and therefore decompose the domain into smaller and more manageable components. Mathematically, we proceed to cast the iterative solution of $[Z]_{complex}\{x\}=\{b\}$ as,

$$\begin{bmatrix} Z_{11} & 0 \\ 0 & Z_{22} \end{bmatrix}\begin{Bmatrix} x_1 \\ x_2 \end{Bmatrix}_{(i+1)}=\begin{Bmatrix} b_1 \\ b_2 \end{Bmatrix}-\begin{bmatrix} 0 & Z_{12} \\ Z_{21} & 0 \end{bmatrix}\begin{Bmatrix} x_1 \\ x_2 \end{Bmatrix}_{(i)}. \quad (4)$$

In this set-up $\{x\}=\{x_1,x_2\}^T$ denotes the unknown quantity in domains #1 and #2, respectively, whereas $\{b\}=\{b_1,b_2\}^T$ is the corresponding excitation vector. Setting $\{x\}_{(0)}=\{0,0\}^T$, (4) can be solved iteratively by updating $\{x\}$ with $\{x\}_{(1)}$, $\{x\}_{(2)}$, etc., until convergence is achieved to within a prescribed error. The above is known as the Jacobi decomposition approach and allows us to initially solve each component/domain independent of the others and therefore avoid large matrices. Moreover, it allows for each domain to be treated with different methods. As an example, the antenna domain can be treated with a rigorous method, whereas the large ship structure can be handled via high-frequency techniques.

Of particular interest is the number of iterations needed for convergence of (4) since the antenna is conformal to the structure. To observe this, we consider the case of a double stacked circular patch mounted on a thick metallic plate as shown in Figure 2. The plate dimensions are 1λ x 1λ x 0.1λ and was modeled via the MLFMM [11,12]. For the double stacked patch the FE-BI was used in conjunction with the iterative algorithm (4) to account for coupling among the plate and the antenna.

The iterative solution process is broken into four major steps. First, the antenna itself is solved in isolation via the FE-BI solver with the metallic plate (platform) absent. In the second step the antenna surface currents are radiated onto the nearby structure. The MLFMM (third step) is then used to compute the scattered fields and surface currents induced on the plate by the antenna. Re-radiating these currents back onto the antenna is the fourth step. The steps begin once again using the updated antenna currents in the FE-BI solver. This process continues to be repeated through several iterations until convergence of the antenna and platform currents is achieved to a given level of accuracy.

To validate the proposed iteration scheme, we first computed the antenna input impedance via a direct FE-BI solution that modeled the entire structure as a single antenna. The resulting value was found to be 89.6724+32.6572i shown by the horizontal lines in Figure 3. Next, we proceeded with the decomposition and iteration. After 20 iterations the input impedance converges to 89.9056+32.9705i. The convergence of the input impedance is shown in Figure 3 as a function of iteration number. The effect of the platform on the input impedance can be seen by the difference between the first iteration and the converged result.

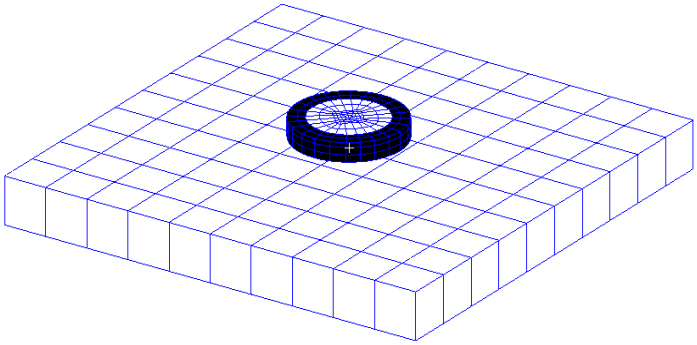

Figure 2: Probe-fed circular stacked patch antenna over a PEC platform. Platform dimensions are 1λ x 1λ x 0.1λ.

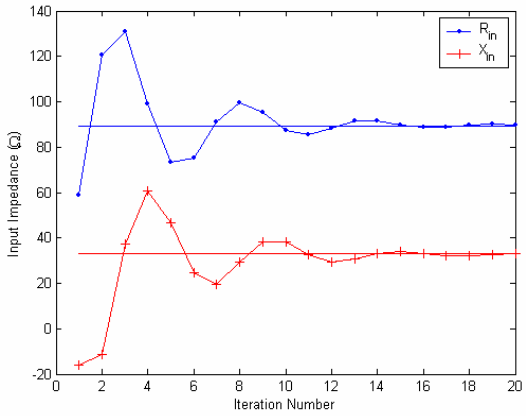

Figure 3: Iterative convergence of the input impedance.

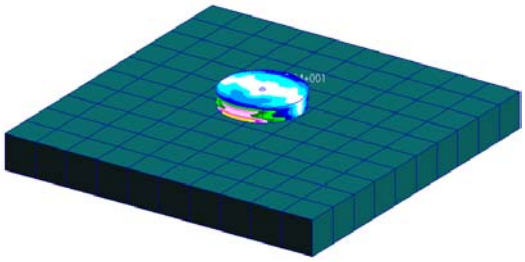

(a) Full FE-BI solution.

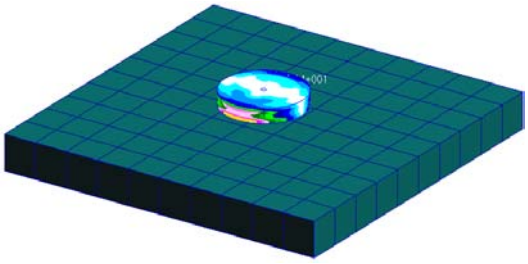

(b) Iterative solution.

Figure 4: Electric fields within the patch antenna.

The difference between converged solutions for the antenna and the platform can also be observed in the following figures. Figures 4 (a) and (b) show the fields within the patch antenna. As seen, the converged results are almost identical to the full FE-BI solution. The surface currents induced on the platform are given in Figure 5. They also agree well with the full FE-BI solution. Excellent agreement between the full and iterative methods is demonstrated in Figure 6 for the radiation pattern of the antenna on the platform.

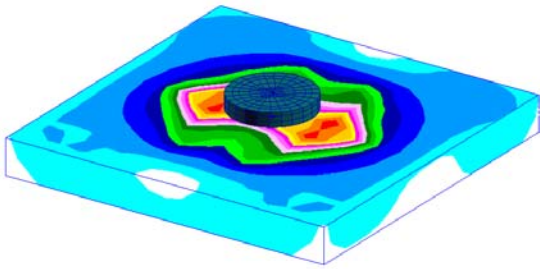

(a) Full FE-BI solution.

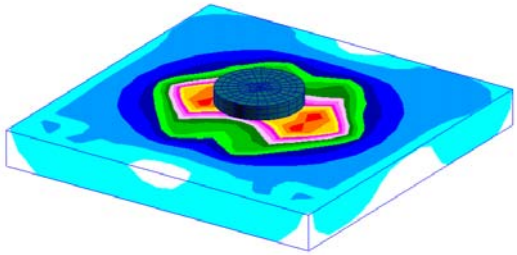

(b) Iterative solution.

Figure 5: Induced surface electric currents on the platform.

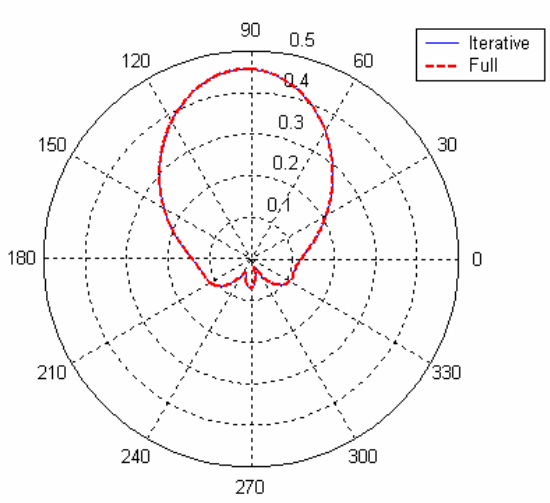

Figure 6: In-situ radiation pattern of the patch antenna.

III. RIGOROUS ANALYSIS OF ANTENNA ARRAYS USING FE-BI

This section summarizes the finite element-boundary integral (FE-BI) method for the rigorous analysis of antenna array structures. It can generate a numerical solution for an antenna array on a complex platform, provided the available computational resources can handle the composite problem (for example, the circular patch antenna on a metallic plate as in Section 2). For larger platforms the FE-BI method may be used in the hybrid scheme described in the last section, wherein the FE-BI method generates the antenna solutions characterized by the matrices Z_{ii} in (2) and (4).

The FE-BI method is useful for modeling complex structures for which an approximate or analytical representation of the structure's electromagnetic properties is not attainable. As expected, FE-BI is able to handle nearly any combination of material properties and arbitrary geometric shapes, making it an ideal tool to analyze complicated antenna structures [13]. However, rigorous analysis tools have practical limits as well. FE-BI and integral equation methods can consume vast amounts of computational resources for electrically large problems. Rather than resort to approximate methods that may not be accurate enough, it is often necessary to introduce special algorithms that alleviate the computational burden of rigorous methods such as FE-BI. Here we examine a powerful decomposition approach that exploits translational symmetry of the array environment, thereby allowing the use of FE-BI for rigorous analysis of array structures without prohibitive storage requirements. This version of FE-BI, known as the Array Decomposition-Fast Multipole Method (AD-FMM), was most recently considered in [14]. It is briefly described here.

Consider a linear array of n identical antenna elements on a regular grid. Each array element is enclosed in an identical rectangular box. A finite element expansion is used for the fields within the box, and a boundary integral is used on the surface to couple the element to other elements and to the external region. Each boundary integral is discretized using m unique current coefficients. The complete impedance matrix $[Z]$ for the array system is of size $N=(mn)^2$, consisting of n^2 blocks of size m^2. (A finite element matrix describes the interactions within each box, but this matrix is generally much smaller than the boundary integral matrices, and is the same matrix for all the array elements.) In an array of identical elements, with a fixed spacing between elements (and hence translational symmetry), this system will have a block-Toeplitz property, i.e., the matrix block Z_{pq} is the same as Z_{p-q}. Hence, of the original $(mn)^2$ terms in the $[Z]$ matrix, it is only necessary to store $m^2(2n-1)$ of them without loss of information. The reduced storage format of the impedance matrix takes the form

$$[Z]_{Toeplitz} = \{Z_{1-n} \quad Z_{2-n} \quad \cdots \quad Z_{-1} \quad Z_0 \quad Z_1 \quad \cdots \quad Z_{n-2} \quad Z_{n-1}\}. \tag{5}$$

This block-Toeplitz property is the first major component of the AD-FMM algorithm, and it generates a pronounced reduction in storage. In fact, we may stop here and employ the fast Fourier transform (FFT) in the iterative solution of the system matrix as done in [4]. However, we can achieve an even greater reduction in the storage as described next.

The fast multipole method (FMM) is used to factorize the non-adjacent block matrices in (5). If $|p-q|>1$, the pqth block may be written in the factorized form,

$$Z_{p-q} \approx U T_{p-q} V \tag{6}$$

where V is the "disaggregation matrix," T_{p-q} is the "translation matrix," and U is the "reaggregation matrix." V contains the far-field radiation pattern coefficients of each of the boundary integral basis functions for a given array element, computed in k directions on the unit sphere. U contains the testing of each boundary integral basis function with a plane wave incident from each of the k far-field directions. The k plane wave directions are chosen to be the same as the k far-field directions, so the elements of U are actually the complex conjugates of the elements of V (provided that Galarkin testing is used in the boundary integral). The translation matrix T_{p-q} is derived from a multipole expansion of the free space Green's function [15]. The accuracy of (6) depends on the truncation of the multipole series, which determines the minimum number of far-field directions k.

The utility of the FMM comes from the fact that T_{p-q} is diagonal and is found analytically. In the AD-FMM approach where identical equally spaced array elements are used, T_{p-q} is also Toeplitz. Therefore, only $2n$-1 translation matrices need to be stored, each with k entries. The U and V matrices are of size km, but they are the same for all the identical array elements. We remark that k is typically of the same order as m, so the storage requirement for U and V is of order m^2. Likewise, the total storage requirement for all T_{p-q} is $m(2n$-1). Lastly, we must also store the full self matrix Z_0 and the nearest-neighbor matrices Z_{-1} and Z_1 because FMM is only applicable to separated blocks with $|p-q|>1$. This storage requirement is $3m^2$. Therefore, the total storage requirement for the AD-FMM is of order $m^2+mn=m^2+N$. If $N >> m$ the storage is O*(N)*. Of course, there is also a required storage of O(N) for the unknown vector coefficients.

The above AD-FMM storage requirements extend to arrays that are periodic in two or three dimensions. The method may also be applied to the interaction of multiple array structures sharing common dimensions or periodicity. This approach to array analysis has been applied numerous times very successfully, with some advanced applications considered in [4,14]. Figure 7 shows a 10 x 40 slot array conformally mounted on a cylindrical platform structure. The table gives the storage requirements and matrix fill times as the size of the problem increases. As seen, the AD-FMM is compared with the array decomposition method (ADM) of [4], and the MLFMM. The AD-FMM matrix storage and fill time does not change as the number of unknowns increases from 15 thousand to nearly 7 million!

IV. INTERACTION WITH PLATFORM

The basis expansion of the aperture fields for each antenna via the boundary integral provides a set of equivalent sources/receivers existing in the presence of the platform structure. The interactions between the sources/receivers of any two antennas are represented by the matrices Z_{12} and Z_{21} in (2) and (4) which incorporate the effects of the platform. Evaluating these interactions amounts to computing the matrix-vector product (MVP) in (4),

$$\text{MVP} = \begin{bmatrix} 0 & Z_{12} \\ Z_{21} & 0 \end{bmatrix} \begin{Bmatrix} x_1 \\ x_2 \end{Bmatrix}. \tag{7}$$

For moderately large platforms, the MVP can be computed with the multi-level fast multipole method (MLFMM) which furnishes an efficient full-wave solution to the integral equation of the platform [11,12]. The MLFMM requires a sampling density on the order of 100 surface basis functions per square wavelength. At 1 GHz this translates to a minimum of about 7 million unknowns required to model the ship's topside. Therefore, the platform can become prohibitively large for the MLFMM at frequencies above 1 GHz. However, it is still very useful for communication frequencies below 1 GHz and provides reference solutions for validating the more approximate high-frequency asymptotic methods.

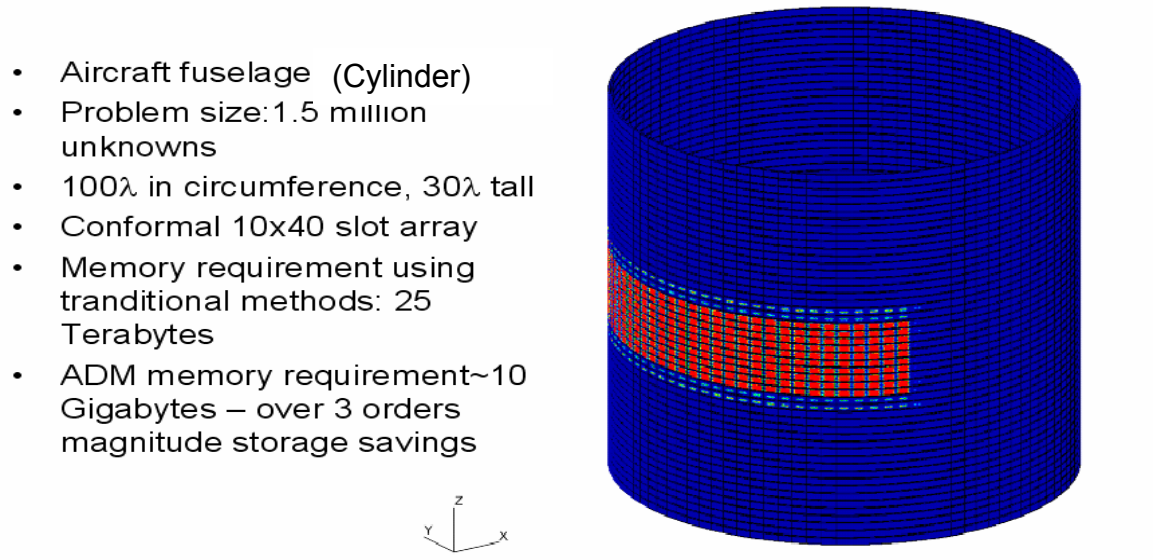

Figure 7: Conformal slot array on a cylinder**.**

For higher frequencies, the iterative physical optics (IPO) method incorporates high-frequency asymptotic principles to solve the platform integral equation more approximately [7,16]. The IPO refines the first-order PO currents by iterating the magnetic field integral equation (MFIE), thereby including multi bounce and multi-diffraction effects. The brute force numerical evaluation of the MFIE at N test points is an $O(N^2)$ computation, but the numerical sampling density of IPO is only on the order of 4 to 16 points per square wavelength. It also uses a simple shadowing rule to determine if any two points "see" each other. This greatly reduces the number of point-to-point computations [17]. Our IPO analysis has also been accelerated with the fast far-field approximation [18] to further reduce the computational complexity down to $O(N^{3/2})$ as described in [17]. These factors produce a highly efficient code for analyzing electrically large multi-bounce structures with a good degree of accuracy. Furthermore, IPO may be applied directly to CAD geometries because no ray tracing is involved.

Figure 8 displays a validation of the induced currents on a generic ship excited by a vertical dipole mounted above the forward mast. The frequency is 200 MHz and the Ohio State University (OSU) MLFMM code [12] with 290,000 unknowns was used for reference. (OSU-MLFMM took 4.5 hours to run on a 6 CPU Itanium 2 cluster.) However, the OSU-IPO code required only 60,000 unknowns for the same problem, and took 8 minutes on a Pentium III PC workstation. The induced currents are in good agreement, although the IPO currents do not show as much resolution because of the coarser sampling density. The far-field pattern of the dipole in the presence of the ship is also shown. As seen, the agreement between the full wave result (OSU-MLFMM) and IPO is excellent in the upper half-space.

The advantage of IPO is demonstrated in Figure 9 and shows the induced currents on a DDG-52 cruiser model excited by an 11-by-11 array radiating at 1 GHz. The 11-by-11 array was placed at one of the locations of the SPY-1 phased array. Here, the IPO method required 270,000 unknowns, but ran in a reasonable amount of time on a low-end PC workstation. For comparison, the MLFMM would require around 5 million unknowns and need to be run on a supercomputer. The gain pattern of the array in free space and in presence of the ship is also shown.

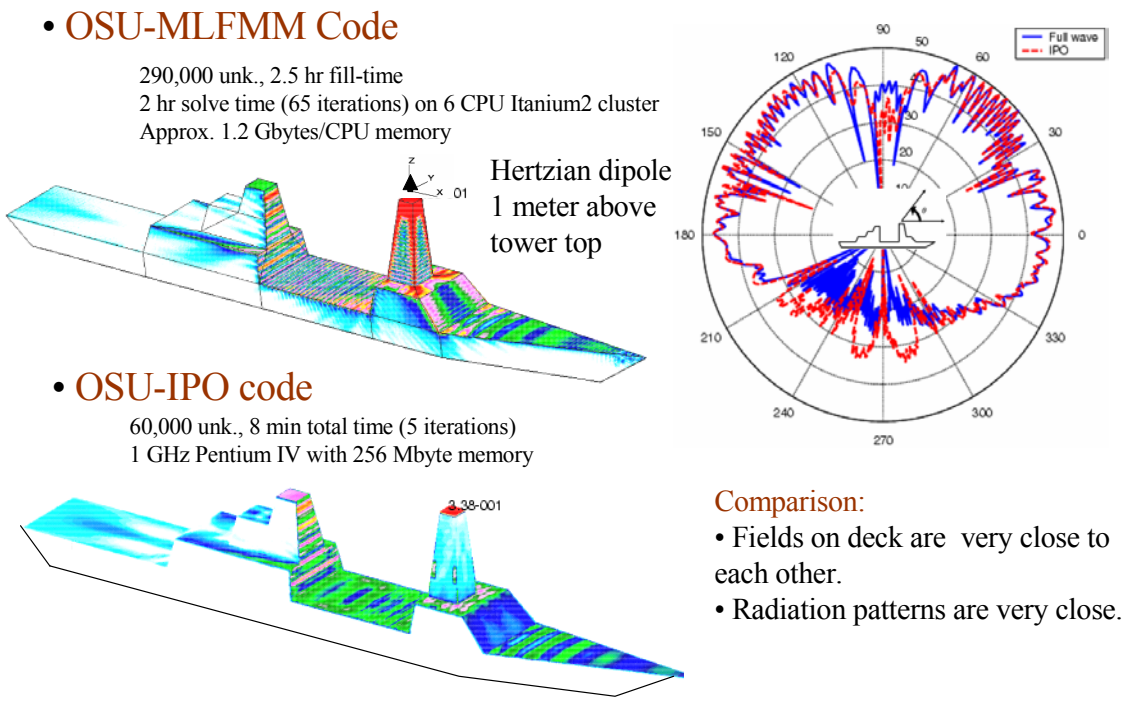

Figure 8: Validation of OSU-IPO method with the OSU-MLFMM code for a vertical dipole above the forward mast of a generic ship model. Frequency is at 200 MHz.

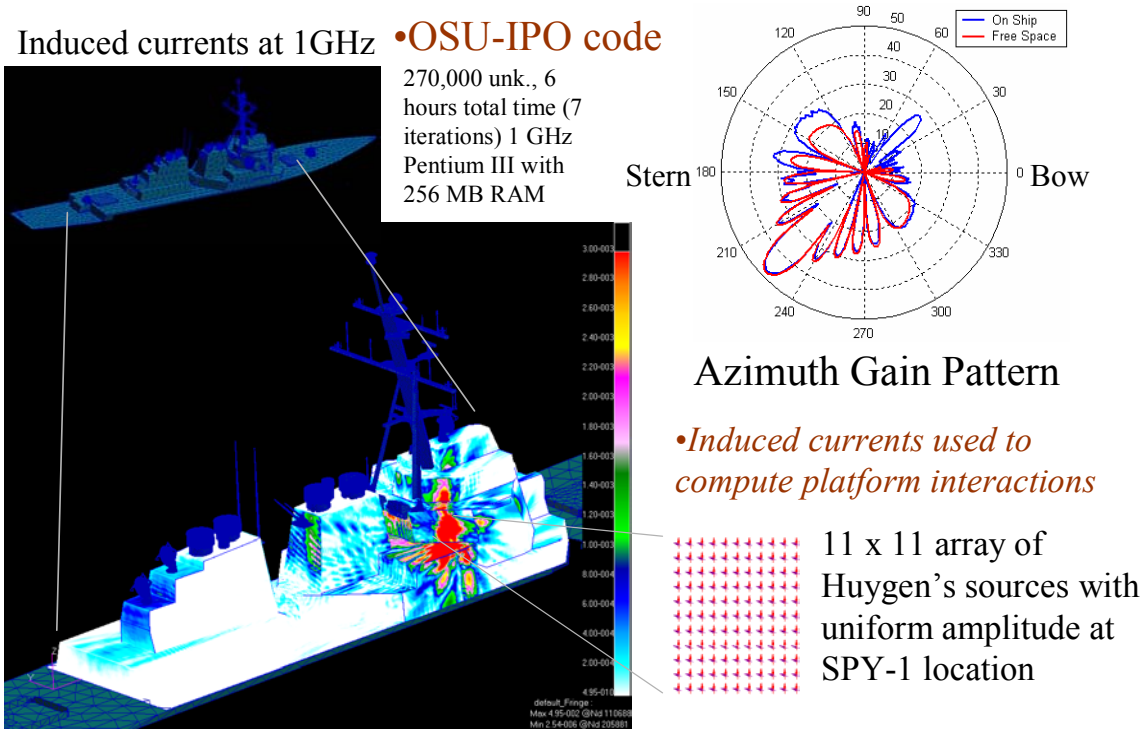

Figure 9: Induced currents on the DDG-52 cruiser model excited by an 11x11 array radiating at 1 GHz.

At this point, we can state that the OSU-IPO code may be used to model ship topsides for frequencies of up to about 4 GHz without resorting to supercomputers. Work is also in progress to implement the asymptotic phasefront extraction (APEx) technique [19] to extend the method of moments (MoM) to as high or higher frequencies as IPO by incorporating frequency-scalable basis functions [20].

At even higher frequencies it becomes necessary to employ the uniform geometrical theory of diffraction (UTD) ray method to account for the platform effects. Thus, the Ohio State University Basic Scattering Code (OSU-BSC) [5] (which employs UTD) is utilized here for evaluating the relevant dominant UTD ray field interactions as described below. It is also possible to employ UTD to describe the fields radiated locally from the arrays themselves. This is necessary to transform the boundary integral basis functions into ray fields that can propagate throughout the platform environment.

Demonstration of Hybrid MoM/UTD Method

In the discussion below, an example involving the EM wave interactions between apertures/arrays with their ship platform is provided using a hybrid method of moments (MoM)/UTD approach. As noted above, such a hybrid approach is useful at high frequencies for which the ship platform becomes electrically very large and a full MoM or FE-BI analysis, as well as the IPO, tend to become intractable.

This example deals with the coupling between two conformal slot arrays on the same face, or different faces, of a large perfectly conducting ship tower model as shown in Figure 10. The array current distribution for a given excitation is found via the numerical MoM solution to the governing array integral equation for the unknown currents. (The current distribution could also have been computed by FE-BI, but the slot array is simple enough to use the ordinary MoM.) The UTD is then used for computing the interaction of array currents with the ship structure.

In a broader sense, one may state that the ship Green's function forms the kernel of the integral equation governing the boundary integrals in (1)-(4). In general, there is no analytical closed form expression for the ship/platform Green's function except at high frequencies where it can be approximated in closed form by the UTD. The UTD can model almost all of the electrically large ship structure except for those portions with electrically small features, or with electrically large features for which the UTD diffraction coefficients are presently not available. For the more complex antenna array configurations that are recessed in the ship platform, the procedure is slightly modified and requires a separate array code (such as the AD-FMM code) to provide the fields in the equivalent aperture formed by such arrays.

As seen in Figure 10, array A is transmitting, whereas arrays B and C are both receiving. The UTD ray coupling, or the dominant rays for the UTD Green's function pertaining to the tower over a ground plane are also illustrated in Figure 10(a). The slot array geometry is shown in Figure 10(b).

The only unknowns in the numerical MoM solution are those associated with the slot aperture electric fields (because the UTD Green's function for the tower accounts for the rest of that structure with the slots now closed by conducting surfaces). The slots are fed by a waveguide and are all identical, and sufficiently short and narrow so that a usual dominant vector mode function (emulating the waveguide mode) can be assumed for each slot-electric field. The UTD is applied by considering each slot as a weighted point source from which rays may be traced [21]. These UTD fields are then employed within the MoM solution in a self consistent manner for both transmitting and receiving arrays [22]. However, the receiving and transmitting arrays can also be considered separately, and then coupled numerically in an iterative fashion using (4).

Figure 11(a) shows the coupling to array B with array A transmitting and array C absent, whereas Figure 11(b) shows the coupling to Array C with B absent. The slots of A are excited uniformly and phased to radiate broadside. We also note that the slots are oriented horizontally in Figure 11(a) and vertically in Figure 11(b). Taking into account the different color scales in the figures, it is clear that the co-planar coupling is much higher than the "around the corner" coupling, as expected.

This UTD-based Green's function for the tower incorporated within the integral equation MoM solution of Figure 11 can be extended to

include not only the interaction of the arrays in the presence of the tower, but also in the presence of the entire ship structure. The rays for the UTD ship Green's function (in contrast to the dominant UTD rays for just the tower only) are shown in Figure 12(a). The UTD coupling between a slot on one face of the ship tower and another slot on the same or different face is plotted as a function of separation distance in Figure 12(b).

We next proceed to introduce large aperture basis functions for modeling the array in conjunction with the UTD or IPO.

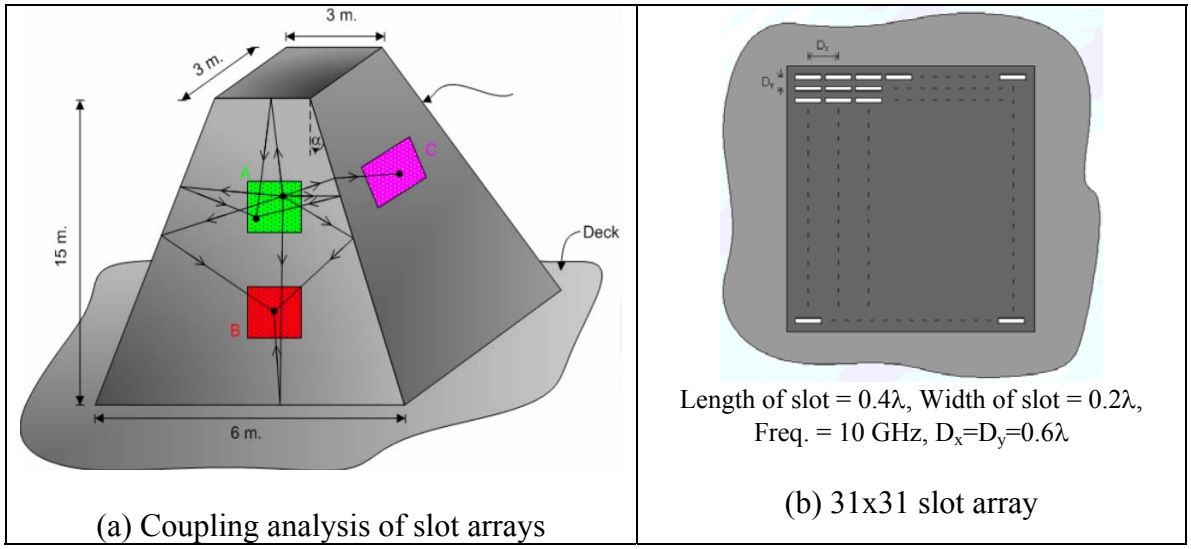

Figure 10: Dominant ray interactions between the excited 31x31 slot array A and the 31x31 receiving slot arrays B and C, respectively.

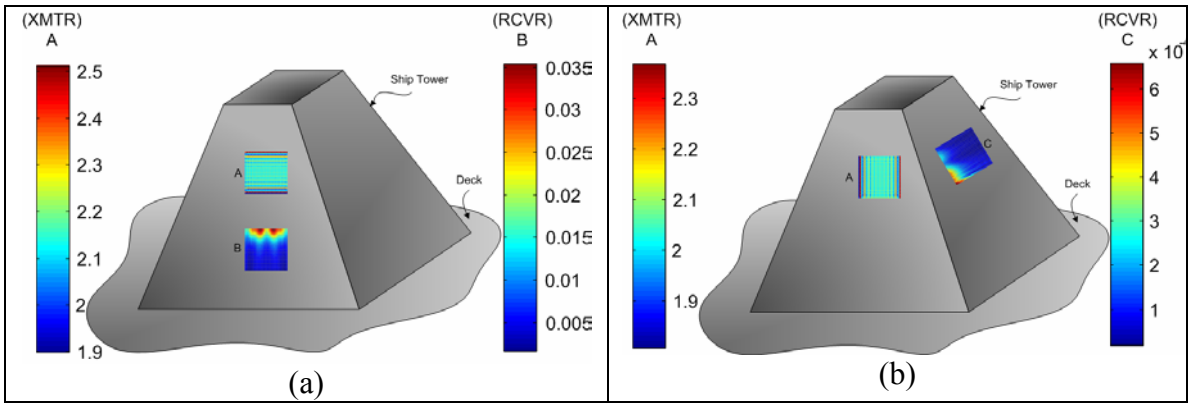

Figure 11: The array distribution on the transmitting slot array A and the receiving slot arrays B and C, respectively.

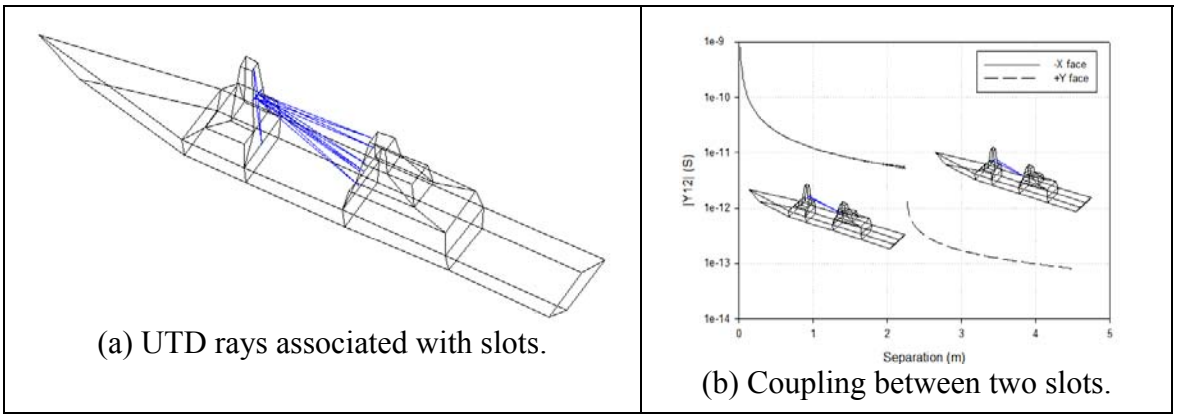

(a) UTD rays associated with slots.

(b) Coupling between two slots.

Figure 12: UTD analysis of coupling between two slots on ship tower. Blue lines on ship are UTD rays.

V. TRUNCATED DFT ARRAY APERTURE BASIS FUNCTIONS

In the boundary integral approach to interfacing an array antenna with the external platform, the number of conventional sub-sectional basis functions on the interface can be quite large. Therefore, the dense interaction matrices $Z_{ij}\big|_{i\neq j}$ in (2) and (4) can be extremely large and the computation of the MVP in (7) very CPU intensive. Further, to apply/integrate the standard FE/BI (with no basis reduction) with IPO or UTD each element or weighted source must be treated individually, making the implementation rather cumbersome and highly inefficient since each elemental source launches its own UTD rays [21]. That is, since rays are traced from all the point sources of the transmitting antenna to all of the points on the receiving antenna, N array elements on each aperture implies O(N^2) rays need to be traced. Considering the time it takes to track a single ray through a complex platform environment, tracking this many rays may not be tractable for complex structures (ships or aircraft).

A simple approach for reducing the number of source points is based on the generalized ray expansion (GRE) depicted in Figure 13. The GRE subdivides an aperture into a set of smaller sub-apertures (not antenna elements) [23]. Rays are then launched from the phase center of each sub-aperture and weighted according to the composite far-field pattern of all the point sources included within the sub-aperture. The rays are subsequently traced to each of the sub-aperture phase centers of the receiving array and weighted by the receiving sub-aperture pattern. For example, if there are M sub-apertures in each array, then O(M^2) rays need be traced. (M is chosen to be as small as possible under the restriction that all nearby scattering structures and antennas are in the far-field of each sub-aperture.) Typically, each sub-aperture may be on the order of 2-5 wavelengths and could contain 400-2500 small basis functions.

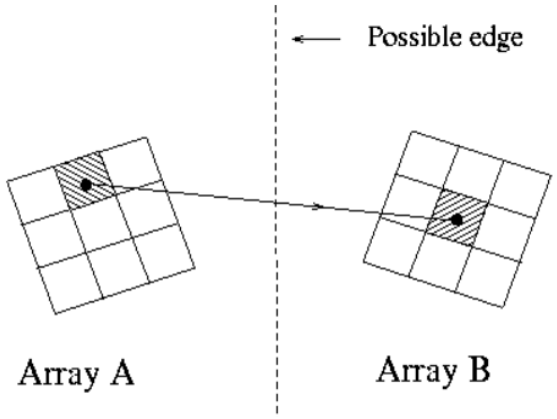

Figure 13: Generalized ray expansion for sub-aperture interactions.

A more sophisticated approach is to employ a discrete Fourier transform (DFT) representation for the fields across the large array aperture. This representation has been shown to provide the same information more compactly when properly truncated [8,24]. Such a truncated DFT which retains only relatively few significant terms may be shown to be very efficient for representing the aperture fields. Rules have also been established to select the significant DFT components (usually 20% or so of the total discrete number of elements

or samples in the aperture). Figure 14 shows a realistic 31 x 31 slot array current distribution and the corresponding DFT spectrum for a uniform excitation. The truncated DFT keeps a certain number of terms in the bands around the l=0 and k=0 spectral lines, where the DFT spectrum is most concentrated. The radiated array field (AF) is plotted in the near zone along the diagonal direction 300λ above the array. As can be seen from this figure, the truncated DFT (with 20% significant terms) is very accurate and agrees well with the exact solution (DFT with all N terms). In some cases it may be necessary to include a small additional set (about 25 more DFT components) within a narrow (5x5) sliding spectral window centered about the DFT component closest to the observation direction [22]. The sliding window correction is shown in the array field results of Figure 14.

As the above example shows, the actual spatially sampled array aperture fields can vary rapidly over the aperture, especially near the finite array edges. The more compact DFT set has the advantage of having large basis functions that are uniform in amplitude with linear phase. It has been shown recently that each DFT basis over a large array generates an efficient closed form UTD ray field representation for the entire array radiation at once [22]. These DFT based UTD rays emanate from certain flash points on the array boundary and one interior point, as shown in Figure 15. Four edge rays are analogous to UTD edge diffraction, four corner rays are analogous to UTD vertex diffraction, and one interior ray is analogous to the geometrical optics ray. Thus the DFT also provides a simple physical picture for the formation of the near and far fields using only a handful of UTD rays that reach an observer in the external region. Futhermore, *the number of UTD*

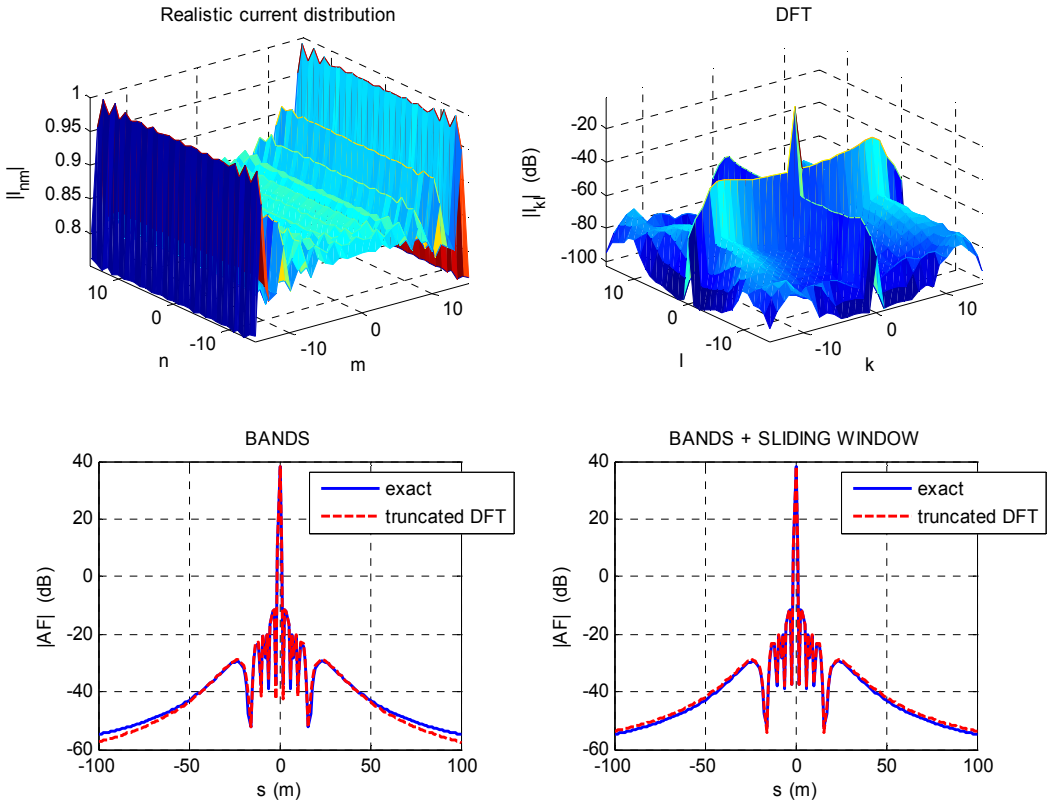

Figure 14: Array distribution for a uniformly excited array including mutual coupling effects, and its DFT spectrum. A sliding window technique is introduced to improve the accuracy from truncating the DFT spectrum.

rays from each significant DFT component stays the same even if the physical dimensions of the array are made larger!

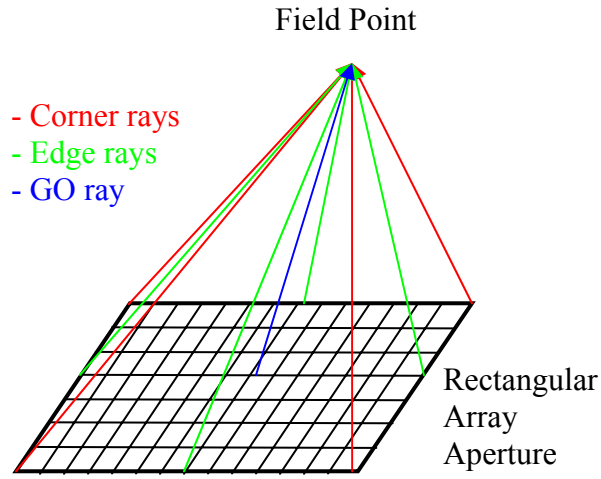

Figure 15: Analogous UTD rays emanating from a rectangular array.

These DFT based UTD rays may emanate from flash points on one array to all the appropriate and corresponding flash points on another array boundary. Some of these ray interactions are shown in Figure 16 for two arrays that are co-planar or on adjacent faces of a ship tower.

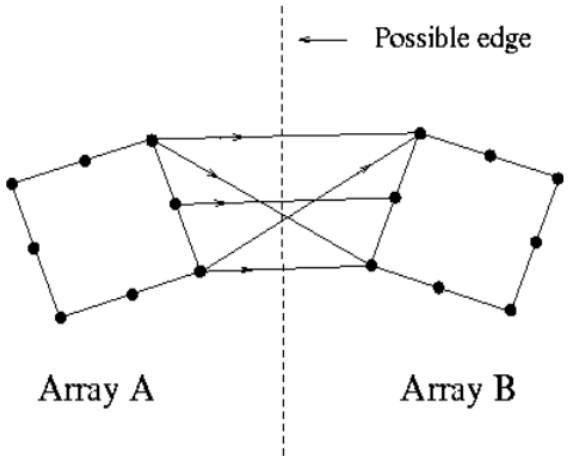

Figure 16: Only a few UTD ray flash points on the boundary array A interact with those of array B to describe the entire coupling of array A to array B via the DFT representation.

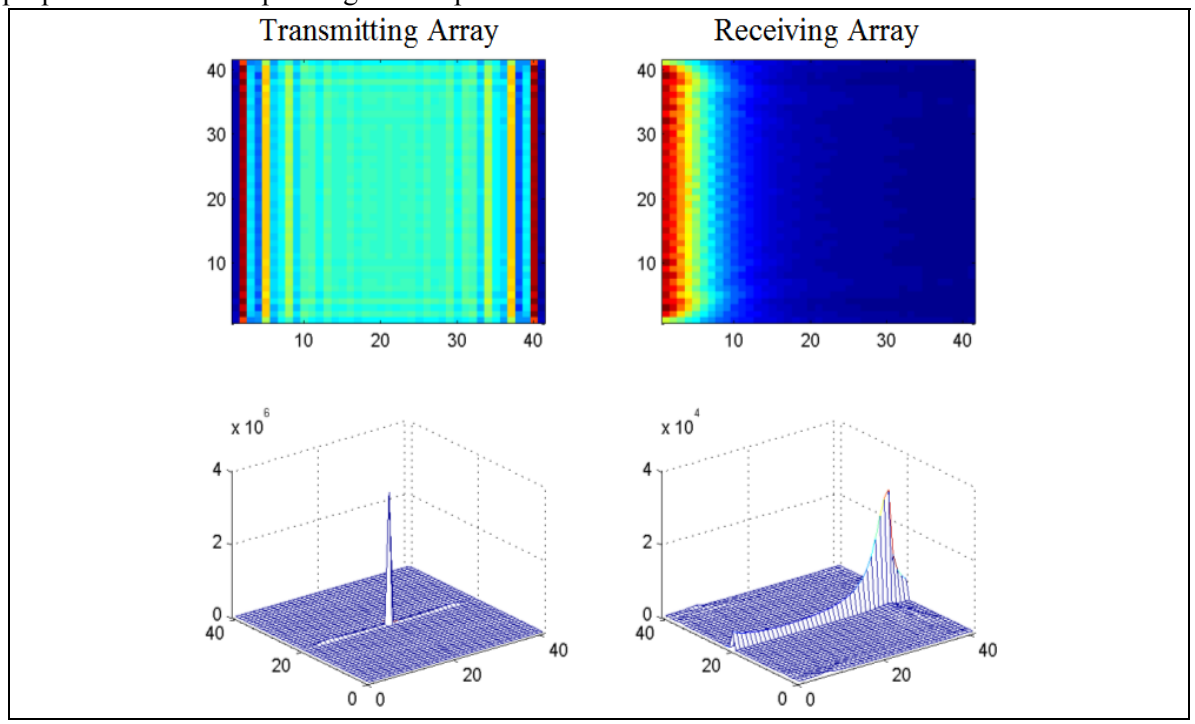

Figure 17: Transmitting and receiving array distributions in the top figures when the transmitting array is uniformly excited. The corresponding DFT spectra for the transmitting and receiving apertures are shown at the bottom. The left hand side top and bottom figures are for the transmitting array and the right hand side is for the receiving case (The color scale for the receiver is scaled by a factor of 100).

It is evident from the above figures that the DFT spectrum is highly localized; i.e., the significant DFT components are highly peaked in a small portion of the entire DFT space. Thus the computational complexity of this method for array aperture to aperture coupling is of O*(PQ)* where *P* is the number of significant DFT terms retained for the transmitting array, and *Q* is the corresponding number for the receiving array. Since *P* and *Q* are expected to be significantly less than the number of discrete aperture samples *N*, this method has the potential to be very efficient. It is shown in Figure 17 that the DFT spectra of a transmitting slot array (as in Figure 10(b)) and that of the receiving slot array (also as in Figure 10(b)) are quite compact when both arrays lie on the same ground plane. It is therefore expected that the coupling between the arrays may be calculated quite efficiently using the proposed approach.

More recently, the DFT approach has been generalized in the context of the traveling wave (TW) expansion that is even more efficient than the DFT approach [9]. However, due to space limitations, this new TW basis will not be described here; it will form the subject of a future publication.

VI. SUMMARY REMARKS

A general matrix formulation has been presented to decouple the antenna analysis from the platform by virtue of the natural domain decomposition feature of the FE-BI method. The interactions between the antenna and platform, and other antennas, are computed via high-frequency asymptotic methods interfaced to the antenna via the boundary integral. The latter is implemented in the context of the AD-FMM for very large arrays with very low memory requirements. For coupling among the arrays, the DFT approach provides a reduced representation of the aperture fields so that far fewer rays need to be traced between array apertures and their complex platforms.

Full-size ships and realistic shipboard array antennas can now be analyzed with this hybrid methodology. For example, a hybrid calculation of the radiation pattern of a stacked circular patch array mounted conformally on a 737 fuselage is illustrated in Figure 18. This calculation used a hybrid combination of the FE-BI for modeling the actual array + DFT-UTD for modeling the array aperture + UTD for the local cylindrical fuselage simulation [25]. Details of such a hybrid approach for a realistic conformal airborne antenna array analysis will be described in a separate publication.

REFERENCES

[1] W. D. Burnside, M. C. Gilreath, R. J. Marhefka and C. L. Yu, "A study of KC-135 aircraft antenna patterns," *IEEE Trans. Antennas and Propagation,* Vol. 23, No. 3, pp. 309-316, May 1975.

[2] J. J. Kim and W. D. Burnside, "Simulation and Analysis of Antennas Radiating in a Complex Environment," *IEEE Trans. Antennas and Propagation,* Vol. 34, No. 4, pp. 554-563, April 1986.

[3] W. D. Burnside and R. J. Marhefka, "Antennas on Aircraft, Ships, or any Large Complex Environment," Chapter 20 in *Antenna Handbook: Theory, Application and Design*, eds. Y. T. Lo and S. W. Lee, Van Nostrand Reinhold, Inc., New York, 1988.

[4] R. W. Kindt, K. Sertel, E. Topsakal and J. L. Volakis, "Array decomposition method for the accurate analysis of finite arrays," *IEEE Trans. Antennas Propagat.*, Vol. 51, No. 6, pp. 1364-1372, June 2003.

[5] R. J. Marhefka, "Numerical Electromagnetic Code—Basic Scattering Code (NEC-BSC Version 4.2), User's Manual," The Ohio State University ElectroScience Lab Technical Report, June 2000.

[6] F. Obelleiro, J. L. Rodriguez, and R. J. Burkholder, "An Iterative Physical Optics Approach for Analyzing the Electromagnetic Scattering by Large Open-Ended Cavities," *IEEE Trans. Antennas Propagat*., Vol. 43, No. 4, pp. 356-361, April 1995.

[7] F. Obelleiro, J. M. Taboada, J. L. Rodriguez, and J. M. Bertolo, "HEMCUVI: A Software Package for the Electromagnetic Analysis and Design of Radiating Systems On Board Real Platforms," *IEEE Antennas and Propagation Magazine,* Vol. 44, No. 5, pp. 44-61, Oct. 2002.

[8] P. Janpugdee, P. H. Pathak, P. Mahachoklertwattana and R. J. Burkholder, "An Accelerated DFT-MoM for the Analysis of Large Finite Periodic Antenna Arrays,"

IEEE Trans. on Antennas and Propagation, Vol. 54, No. 1, pp. 279-283, Jan. 2006.

[9] P. Janpugdee, P. H. Pathak and R. J. Burkholder, "A new traveling wave expansion for the UTD analysis of the collective radiation from large finite planar arrays," *IEEE Antennas and Propagation Society/URSI Symposium, Washington*, D.C., 3-8 July *2005*.

[10] M. Carr and J. L. Volakis, "Domain Decomposition by Iterative Field Bouncing," *IEEE APS/URSI Intl. Symp. Digest*, Vol. 3, pp. 298-301, 16-21 June 2002.

[11] J. M. Song, C. C. Lu and W. C. Chew, "Multilevel fast multipole algorithm for electromagnetic scattering by large complex objects," *IEEE Trans. on Antennas and Propagation,* Vol. 45, No. 10, pp. 1488-1493, Oct. 1997

[12] K. Sertel and J. L. Volakis, "Multilevel fast multipole method solution of volume integral equations using parametric geometry modeling," *IEEE Trans. Antennas Propagat.*, Vol. 52, No. 7, pp. 1686-1692, July 2004.

[13] J. L. Volakis, A. Chatterjee and L. C. Kempel, *Finite Element Method for Electromagnetics*, IEEE Press, New York, 1998.

[14] R. W. Kindt and J. L. Volakis, "Array Decomposition-Fast Multipole Method for finite array analysis," *Radio Science*, vol. 39, no. 216, April 2004.

[15] R. Coifman, V. Rohklin and S. Wandzura, "The Fast Multipole Method for the Wave Equation: A Pedestrian Prescription," *IEEE Antennas and Propag. Mag*., Vol. 35, No. 3, June 1993.

[16] P. H. Pathak and R. J. Burkholder, "High Frequency Scattering," Section 1.5.2 in *Scattering: Scattering and Inverse Scattering in Pure and Applied Science*, pp. 245-276, eds E. R. Pike and P. Sabatier, Academic Press, Ltd., London, 2002.

[17] R. J. Burkholder, "A fast and rapidly convergent iterative physical optics algorithm for computing the RCS of open-ended cavities," *Journal of the Applied Computational Electromagnetics Society,* Vol. 16, No. 1, 2001.

[18] C. C. Lu and W. C. Chew, "Fast far-field approximation for calculating the RCS of large objects," *Microwave and Opt. Tech. Letters,* Vol. 8, No. 5, pp. 238-241, 5 Apr., 1995.

[19] D.-H. Kwon, R. J. Burkholder and P. H. Pathak, "Efficient Method of Moments (MoM) Formulation for Large PEC Electromagnetic Scattering Problems using Asymptotic Phasefront Extraction," *IEEE Trans. Antennas Propagat*., Vol. 49, No. 4, pp. 583-591, April 2001.

[20] R. J. Burkholder, P. H. Pathak, C. Tokgoz and C. J. Reddy, "Frequency-Scalable Basis Functions for the Iterative Physical Optics Method," *Annual Meeting of the Electromagnetic Code Consortium* Seattle, WA, 17-21 May 2004,.

[21] T. Ozdemir, M. W. Nurnberger, J. L. Volakis, R. Kipp and J. Berrie, "A Hybridization of Finite-Element and High-Frequency Methods for Pattern Prediction for Antennas on Aircraft Structures," *IEEE Antennas and Propagation Mag*., Vol. 38, No. 3, June 1996.

[22] K. Tap, T. Lertwiriyaprapa, P. H. Pathak and K. Sertel, "A hybrid MoM-UTD analysis of the coupling between large multiple arrays on a large platform," *IEEE Antennas and Propagation Society/URSI Symposium*, Washington, D.C., 3-8 July 2005.

[23] R. J. Burkholder, R.-C. Chou and P. H. Pathak, "Two ray-shooting methods for computing the EM scattering by large open-ended cavities," *Computer Physics Communications – Thematic Issue on Computational Electromagnetics*, Vol. 68, Nos. 1-3, pp. 353-365, Nov. 1991.

[24] P. Janpugdee, P. Pathak, P. Nepa, O. Civi & H-T. Chou, "Ray Analysis of the Radiation from a Large Finite Array of Antennas on a Grounded Material Slab," *USNC/URSI National Radio Science Meeting, Boston, Mass*., 8-13 July 2001.

[25] R. W. Kindt, P. Janpugdee, P. H. Pathak and J. L. Volakis, "Analysis of Large Finite Arrays Integrated into Curved Platforms," *IEEE Antennas and Propagation Society/URSI Symposium*, Washington, D.C., 3-8 July 2005.

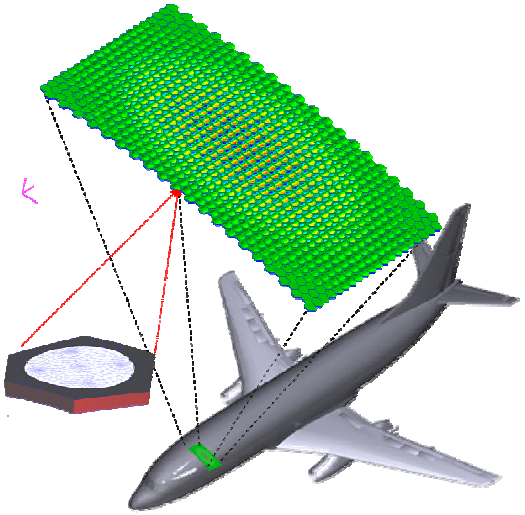

(a) X-band conformal array.

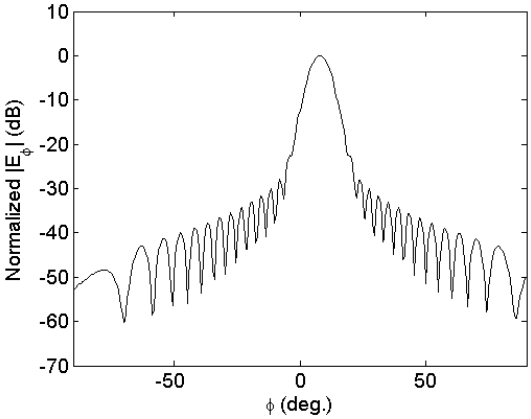

(b) Co-pol.

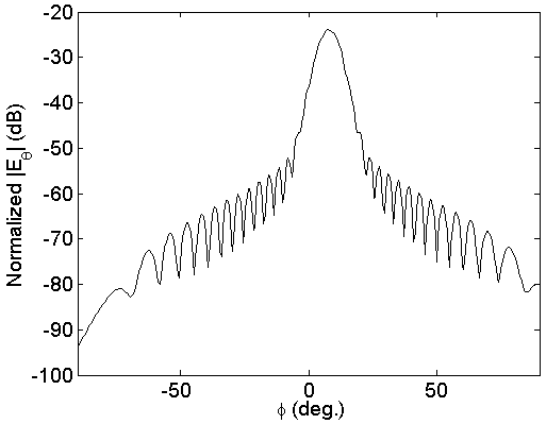

(c) Cross-pol.

Figure 18: Preliminary hybrid calculation of the radiation pattern at 9.5 GHz. of a cavity backed, stacked circular patch array mounted conformally on a 737 aircraft fuselage. Fuselage diameter = 12 ft.; 20×20×2 (=800) array elements; 2×10^5 unknowns; 470 MB memory; 6 mins fill time; 20 sec solve time; 30 dB Taylor distribution on array.

Robert J. Burkholder received the B.S., M.S., and Ph.D. degrees in electrical engineering from The Ohio State University, Columbus, in 1984, 1985, and 1989, respectively.

Since 1989, he has been with The Ohio State University ElectroScience Lab, where he currently is a Senior Research Scientist and Adjunct Professor. Dr. Burkholder has contributed extensively to the EM analysis of large cavities, such as jet inlets/exhausts, and the scattering from targets over a rough sea surface. He is currently working on the more general problem of EM radiation, propagation and scattering in realistically complex environments. His research specialties are high-frequency asymptotic techniques and their hybrid combination with numerical techniques for solving large-scale electromagnetic radiation and scattering problems.

Dr. Burkholder is an elected Fellow of the IEEE, a member of the Applied Computational Electromagnetics Society, a member of the American Geophysical Union, and an elected Full Member of URSI Commission B. He served as an Associate Editor for IEEE Transactions on Antennas and Propagation from 1994 to 1999, and is currently an Associate Editor for *IEEE Antennas and Wireless Propagation Letters*.

Rick W. Kindt received the B.S.E. degree in 1998, the M.S.E. degree in 2000, and the Ph.D. degree in 2004, all in electrical engineering from the University of Michigan, Ann Arbor. His research specialty is the numerical modeling of large, quasi-periodic structures, such as finite antenna arrays. In 2004 and 2005 he was a Postdoctoral Research Associate at the Ohio State University ElectroScience Lab. He is currently employed at the Naval Research Labs, Radar Division, Washington, D.C.

Prabhakar H. Pathak received his Ph.D degree from the Ohio State University, Columbus, Ohio, USA, in 1973, where he is currently a Professor. His main area of research is in the development of uniform asymptotic theories (frequency and time domain) and hybrid methods for the analysis of large electromagnetic antenna and scattering problems of engineering interest. He is one of the major contributors to the development of the uniform geometrical theory of diffraction (UTD). He has also analyzed the scattering from large inlet cavities via hybrid ray and modal/numerical methods. Recently he has developed new fast asymptotic/hybrid methods which provide physical insights into the radiation mechanisms, for the analysis/design of modern satellite antennas such as large reflector systems and large phased arrays. Professor Pathak has presented many short courses and invited lectures both in the U.S. and abroad. He was invited to serve as an IEEE Distinguished Lecturer from 1991 through 1993. He also served as the chair of the IEEE Antennas and Propagation Distinguished Lecturer Program during 1999-2005. Prior to 1993, he served as an Associate Editor of the IEEE Transactions on Antennas and Propagation for two consecutive terms. He received the 1996 Schelkunoff best paper award from the IEEE (Institute of Electrical and Electronics Engineers) Transactions on Antennas and Propagation. He received the George Sinclair award in 1996 for his research contributions to the O.S.U. ElectroScience Laboratory. In July 2000, Prof. Pathak was awarded the IEEE Third Millennium Medal from the Antennas and Propagation Society. He was elected an IEEE Fellow in 1986, and is an elected member of US Commission B of the International Union of Radio Science (URSI).

Kubilay Sertel was born on June 27, 1973, in Tekirdag, Turkey. He received the B.S. degree from Middle East Technical University, Ankara, Turkey in 1995, the M.S. degree from Bilkent University, Ankara, Turkey in 1997, and the Ph.D. degree from the Electrical Engineering and Computer Science Department at the University of Michigan, Ann Arbor, MI in 2003, respectively.

He is currently a Senior Research Associate at the ElectroScience Laboratory at the Ohio State University. His research areas include electromagnetic theory, computational electromagnetics, volume-surface integral equations and hybrid methods, fast and efficient methods for large-scale electromagnetics problems and parallel implementations of fast algorithms.

Ronald J. Marhefka received the B.S.E.E. degree from Ohio University, Athens, in 1969, and the M.Sc. and Ph.D. degrees in electrical engineering from The Ohio State University, Columbus, in 1971 and 1976, respectively. Since 1969, he has been with The Ohio State University ElectroScience Laboratory where he is currently a Senior Research Scientist and Adjunct Professor.

His research interests are in the areas of developing and applying high frequency asymptotic solutions such as the Uniform Geometrical Theory of Diffraction, hybrid solutions, and other scattering techniques. He has applied these methods to numerous practical antenna and scattering problems, including airborne, spacecraft and shipboard antenna analysis and radar cross section prediction. He is the author of two user oriented computer codes, the NEC - Basic Scattering Code and one dealing with radar cross section. The codes are being used in over 300 government, industrial, and university laboratories in the U. S. and 15 countries. In addition, he is the co-author with John Kraus on the textbook *Antennas, Ed. 3*, McGraw-Hill, 2002.

He was a co-author on papers that won the *IEEE Transactions on Antennas and Propagation* Best Application Paper Award in 1976 and the R. W. P. King Paper Award in 1976. He received the IEEE Third Millennium Medal in 2000. In addition, he was the recipient of the Applied Computational Electromagnetics Society's 1993 Technical Achievement Award. Dr. Marhefka is a Fellow of IEEE and has been elected to Tau Beta Pi, Eta Kappa Nu, Phi Kappa Phi, Sigma Xi, and Commission B of URSI. He has served as an officer of the local IEEE Antenna and Propagation and Microwave Theory and Techniques Societies during 1977-1980. He served as Associate Editor of the *IEEE Transactions on Antennas and Propagation* from 1988-1992 and was Editor from 1992-1995. He was elected a member of ADCOM in 1996, Vice President in 1997, and President in 1998. He was co-chair of the Technical Program Committee for the 2003 IEEE APS/URSI Symposium. In addition, he has chaired the AP-S Publications Committee, from 1996-2003. He also is an Associate Editor of the *Applied Computational Electromagnetics Society Journal*.

John L. Volakis was born on May 13, 1956 in Chios, Greece and immigrated to the U.S.A. in 1973. He obtained his B.E. Degree, summa cum laude, in 1978 from Youngstown State Univ., Youngstown, Ohio, the M.Sc. in 1979 from the Ohio State Univ., Columbus, Ohio and the Ph.D. degree in 1982, also from the Ohio State Univ.

From 1982-1984 he was with Rockwell International, Aircraft Division (now Boeing Phantom Works), Lakewood, CA and during

1978-1982 he was a Graduate Research Associate at the Ohio State University ElectroScience Laboratory. From January 2003 he is the Roy and Lois Chope Chair Professor of Engineering at the Ohio State University, Columbus, Ohio and also serves as the Director of the ElectroScience Laboratory (with ~$7.5M in research funding). Prior to moving to the Ohio State Univ, he was a Professor in the Electrical Engineering and Computer Science Dept. at the University of Michigan, Ann Arbor, MI. (1984-2003). He also served as the Director of the Radiation Laboratory from 1998 to 2000. His primary research deals with computational methods, electromagnetic compatibility and interference, design of new RF materials, multi-physics engineering and bioelectromagnetics. Dr. Volakis is listed by ISI among the top 250 most referenced authors (2004, 2005).

Dr. Volakis served as an Associate Editor of the *IEEE Transactions on Antennas and Propagation* from 1988-1992, and as an Associate Editor of Radio Science from 1994-97. He chaired the 1993 IEEE Antennas and Propagation Society Symposium and Radio Science Meeting, and co-chaired the same Symposium in 2003. Dr. Volakis was a member of the AdCom for the IEEE Antennas and Propagation Society from 1995 to 1998 and served as the 2004 President of the IEEE Antennas and Propagation Society. He also serves as an associate editor for the *J. Electromagnetic Waves and Applications,* the *IEEE Antennas and Propagation Society Magazine*, and the URSI Bulletin. He is a Fellow of the IEEE, and a member of Sigma Xi, Tau Beta Pi, Phi Kappa Phi, and Commission B of URSI. He is also listed in several Who's Who directories, including Who's Who in America.

Low SAR Phased Antenna Array for Mobile Handsets

(*Invited Paper*)

J. Moustafa, N. J. McEwan, R. A. Abd-Alhameed and P. S. Excell
j.moustafa@bradford.ac.uk, nmcewan@Filtronic.com, r.a.a.abd@bradford.ac.uk, p.s.excell@bradford.ac.uk
Mobile and satellite Communications Research Centre, Bradford University, Bradford, BD7 1DP, UK

***Abstract*—**A two-element phased antenna array for a mobile handset is investigated using the Finite Difference Time Domain (FDTD) method. The array is designed to provide a spatial minimum in SAR in the near field zone inside the human head. The optimisation algorithms to obtain the minimum peak specific absorption rate (SAR) and minimum total absorbed power are addressed. It is found that these criteria are not seriously conflicting. The effects of the head-array spacing on the optimum array feeding voltages and the reduction in SAR are discussed. The results are compared with those from a normal single element handset, showing that the overall efficiency and azimuth coverage are improved and that peak specific absorption rate in the head can be reduced by at least 8 dB.

***Key words*—**Phased antenna array, Finite Difference Time Domain (FDTD), Specific Absorption Rate (SAR).

I. INTRODUCTION

It has been shown experimentally and theoretically [1-3] that a handset antenna can be designed to direct the radiated power away from the head. Obviously, the simple approach would be to design a simple two-monopole element array for a cardioid pattern with a far-field null in the direction of the head [4, 5].

This paper extends the work in [4, 5] by using the Finite Difference Time Domain (FDTD) method, and by treating a wide range of head-antenna spacings. The FDTD method confers some advantages over the previously used integral-equation representation [4, 5] in allowing more investigations of the effect of the array when the head juxtaposed with the handset. It also gives information on the effect of the head on the steering voltages required for feeding. The array considered is for a personal communications handset working at frequencies near 2 GHz. It is designed to provide a spatial null in the near field zone within the human head, which is treated as a lossy dielectric sphere for initial studies.

It will be seen that the overall efficiency and azimuth coverage are improved and the peak specific absorption rate in the head can be reduced by at least 8 dB, as compared with a conventional single monopole element handset.

II. ARRAY CONCEPT

It was found previously that the most promising handset antennas were those with the radiating element shielded in some way from the user's head, and having extension in the direction normal to the head surface [4-6]. The most encouraging result was that the reduction of absorption in the user's head could be accompanied by an improvement in the radiated power level at almost all azimuth angles.

The typical structure needed to achieve this was a reflecting plate or shield interposed between a cylindrical radiator and the head. Other examples, not fundamentally different in principle, are the microstrip patch radiator and PIFA where the ground plane resembles the reflecting plate. Both of these cases could be viewed as a form of array in which the shield or the ground plane constitutes the second element and is parasitically excited.

Thus, it is clear that these structures may not realise all the potential advantage of an array, because the ratio of excitations in the driven element and the parasite is incidental and not under the complete control of the designer. However, the reflector plate is a structure with extension in two dimensions. This has too many degrees of freedom, and it is not clear how the currents in such an extended structure could be controlled by the designer [7]. To make the problem easier to analyse, the second element in the array needs to be simplified to one whose excitation is described by just one parameter and is controllable by choosing the voltage or current at a single port or terminal pair.

It was shown by McEwan et al [7-9], that the most sensitive regions of the head could be selectively protected using the proposed two element array. Space averaged exposure could be reduced at the time as improving the azimuthal coverage. Referring to earliest papers [1, 9-11], the scattering of an EM wave incident on a sphere was solved by expanding the incident, internal and scattered waves as a series of spherical waves.

III. PRACTICAL HANDSETS

The results obtained by [8, 9] using ideal dipoles were encouraging, but the antenna is not very realistic. It is clear that the elements individually need not produce linear polarisations at any point inside the head, nor do their polarisations have to be identical. It would be expected from the geometry that they actually

produce polarisation ellipses with a fairly high axial ratio and the longest axis roughly parallel to the dipoles.

In a practical handset, the two elements of the phased array would work in the presence of the set's ground plane. This means that, when each element is excited in turn, the currents produced are physically separate on the monopole elements, but to a large extent spatially coincident (though not of identical configuration) on the common ground plane against which they are both excited. Furthermore, there must be currents flowing transversely to the board plane, because the elements are separated along the normal to that plane. A realistic practical model is a complete metallic box with two monopoles mounted on its top.

IV. SOFTWARE STRUCTURES

Earlier work [4] using only the MoM encountered difficulties in the memory requirements. The results obtained were fairly good but could only exploit an extremely coarse representation of the head. The hybrid technique of MoM and FDTD [5] is excellent when there is no physical contact between the handset and the head. The present work uses only the FDTD method [12]: this is suitable for this particular situation where the handset is in direct contact with the head. The antenna geometry proposed here (see Figure 1) makes the method applicable since only straight monopoles are to be modelled. The method is augmented by the thin wire code that takes account of the monopole wire radius and enables prediction of the admittance matrix of the antenna for optimisation purposes. The method will find currents and fields throughout a structure when it is excited by specified voltage sources at arbitrary points. An additional piece of software was written to optimise the excitation of the array. This has two very important features: (a) It does not require repeated field solving to optimise the excitation of the array. (b) It solves rigorously the problem of optimising the array to minimise either the total power absorbed in the head or the worst point value of SAR occurring in the head.

V. LINEARLY POLARISED PHASED ARRAY ANTENNA

The near field (E_{total}) produced from linearly polarised phased array at any chosen point in the desired region should be made to be equal or very close to zero. This is obtained by a proper choice of the complex feed voltage source ratio R_v of the second array element relative to the first. The problem obviously requires that the phases of field components are included in the field solution, while normal SAR calculations only require the magnitude of the electric field. Since the problem is linear, a free space null can be obtained by summation thus:

$$E_{total} = E_1 + R_v E_2 = 0 \qquad (1)$$

where E_1 and E_2 are the induced near fields at the worst case SAR location for each element when they are excited separately with unit voltages of the same phase. If E_1 and E_2 are proportional to each other, i.e. the two elements are producing the same polarisation at the point in question, then the R_v magnitude and phase required to satisfy equation (1) are given as follows:

$$|R_v| = |E_1/E_2| \qquad (2)$$

$$\theta = \phi_{E_1} - \phi_{E_2} + 180^\circ \qquad (3)$$

where θ, φ_{E1}, φ_{E2} are the phases of R_v, E_1 and E_2 respectively, and need to be calculated accurately to place the appropriate null at the point in the head that would otherwise be a hot spot.

These expressions for the required voltage ratio R_v between the two array elements are only appropriate for cases where the two elements produce the same polarisation, at the spatial point where nulling is to be performed. In practice, the only case where this obviously the holds is where the polarisations are approximately linear and in the same direction.

The case of non-identical and noticeably elliptical polarisations applies for any realistic two-element phased array on the top of a handset. In this case much more elaborate optimisation procedures are required to obtain an accurate value of R_v for minimising the power absorbed or the maximum SAR inside the user's head. These procedures that were developed to optimise the more complex phased antenna arrays are now described. Throughout the remaining discussion, we use the notation SAR_{max} to denote the peak SAR (with or without a stated volume averaging) in the head, regardless of where it occurs. The total power absorbed in the head will be denoted P_{abs} .

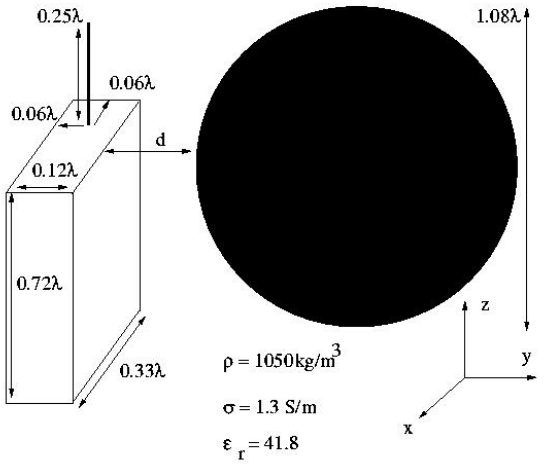

(a)

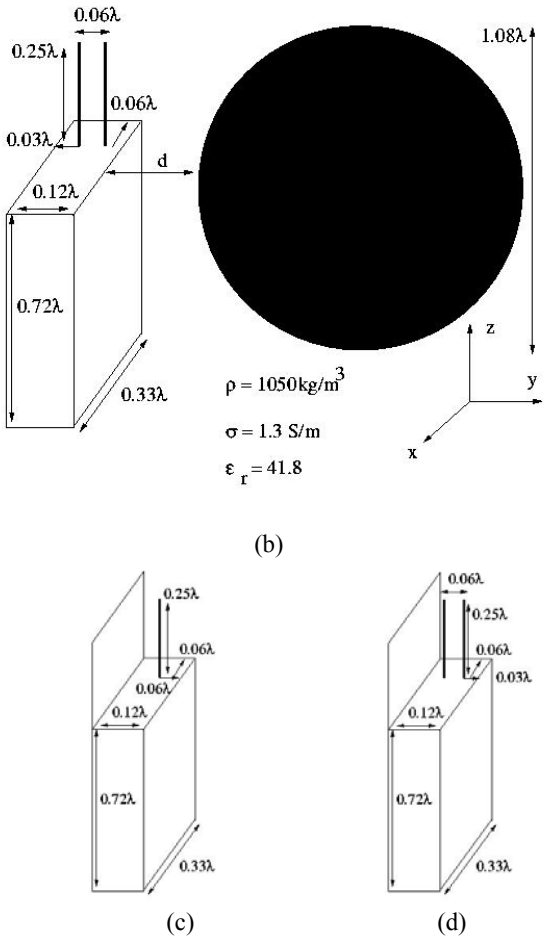

Fig. 1. (Top two) the basic structure of the mobile handset next to a spherical head with the following antenna configurations; (a) single monopole; (b) two-element array. (Bottom) wire grid models for different innovative geometries: (c) single monopole with reflector sheet; (d) two element array with reflector.

VI. SAR OPTIMISATION PROCEDURE

The complex excitation voltages of the array can be optimised to minimise at least three different quantities:

(1) The SAR at a selected fixed point in the head;
(2) P_{abs};
(3) SAR_{max}, i.e. its peak local value anywhere in the head.

The first kind of optimisation would be appropriate if it is believed that some particular small anatomical structure in the head is the most sensitive to a thermal or athermal hazard. In the present state of biological knowledge there is probably little basis for choosing any such structure, except possibly the central structures in the brain at which SAR is already greatly reduced by intervening tissue. Optimisation (3) would be appropriate if there is an athermal or thermal hazard for all tissues and it rises rapidly above some threshold value of SAR. An optimisation of type (2) could be useful if there is a probabilistic risk of, for example, abnormal cells being produced throughout the entire brain, and this probability is a nearly linear function of local SAR. It is beyond the scope of the present work to throw any light on these biological aspects. Instead, results will be presented for optimisations of both types (2) and (3), which are probably the most useful.

All the optimisations assume that a numerical solution of the fields inside the head are available at the outset. The type (1) optimisation can be easily performed analytically as follows. Let E_1 , E_2 be evaluated at a fixed cell in the head where the SAR is to be minimised. Since the electromagnetic responses are linear, the fields induced in the head due to the feeding of both antennas can be expressed using the voltage ratio as $V_1(E_1+R_vE_2)$ where V_1 is the excitation voltage of element 1. The problem of minimising SAR with respect to R_v is equivalent to minimising $|E_{total}|^2$ where E_{total} is the resultant electric field produced from the array. $|E_{total}|^2$ can be written as $|V_1|^2 f$ where f depends only on R_v Hence:

$$f = (E_1 + R_v E_2) \bullet (E_1 + R_v E_2)^* \tag{4}$$

$$f = |E_1|^2 + |R_v|^2 |E_2|^2 + \mathrm{R_v}^* E_1 \bullet E_2^* + R_v E_1^* \bullet E_2 . \tag{5}$$

Let $R_v = me^{j\theta}$ and $E_1 \bullet E_2^* = \mathrm{ke}^{\mathrm{j}\phi}$ then:

$$f(m,\theta) = |E_1|^2 + m^2 |E_2|^2 + 2km\cos(\phi - \theta) \tag{6}$$

where '•' represents vector dot product. Changing R_v for a fixed value of $|V_1|$ causes a change in the total power transmitted from the array. In practical operation with appropriate impedance matching, the value of $|V_1|$ would make the total power transmitted by the array equal to its design value. Hence R_v should be optimised on the assumption that constant total power P_{rad} emerges from the array feed terminals, although some of this is subsequently absorbed in the user. It is shown below that P_{rad} can be expressed in the form:

$$P_{\mathrm{rad}} = |V_1|\, g(m,\theta) \tag{7}$$

where the function g also depends on the admittance matrix of the array, as modified by the interaction with the user. It is now clear that the optimisation problem is that of minimising f while keeping g constant, or equivalently of minimising the ratio f /g. The required R_v can thus be found analytically as the solution of the simultaneous conditions:

$$\frac{\partial}{\partial m}\left[\frac{f(m,\theta)}{g(m,\theta)}\right] = 0, \qquad \frac{\partial}{\partial \theta}\left[\frac{f(m,\theta)}{g(m,\theta)}\right] = 0. \tag{8}$$

An optimisation of type (2) can be performed by a similar method, if the differentiation is performed on the sum of SAR over all cells. The type (3) optimisation cannot be performed easily by differentiation because the cell location at which SAR_{max} occurs may change as the value of R_v is varied.

A numerical algorithm has therefore been developed which performs the type (3) optimisation without

making any assumptions about the initial location of the worst cell or how its position might change with changes in R_v. It is easy to also include in this algorithm the type (2) optimisation by a "brute force" rather than a differentiation method.

The final SAR optimisation algorithm for any two-element phased antenna array is illustrated in Fig. 2 and can be explained as follows:

1. The FDTD computation was initially run twice, with each element in turn excited with a terminal voltage of 1V rms and zero phase, while the other element was short circuited. For each case, the complex electric field vector at the centre of each cubical cell of the head model was stored in an array. (i.e $3N$ complex field values, where N is the number of cubic cells in the head model used).
2. From each FDTD run the current at the base of each element is computed, so that the $[Y]$ (admittance) matrix of the two antenna ports, as modified by the head proximity effect, is then known.
3. The assessment of the reduction in RF absorption was made on the assumption that P_t (the total power leaving the handset) remained constant with a value of 1 Watt, with the head present, and as the excitation is varied. The variable design parameter was again taken as the complex ratio of the element excitation voltages $R_v = V_2/V_1$. The total power P_t leaving the handset using RMS values of voltages is given by:

$$P_t = \mathrm{Re}\ (V_1 I_1^* + V_2 I_2^*). \tag{9}$$

Since $\mathrm{Re}(XY^*) = \mathrm{Re}(X^*Y)$, then P_t can be written as:

$$P_t = \mathrm{Re}\left[\begin{bmatrix} V_1^* & V_2^* \end{bmatrix} \begin{bmatrix} Y_{11} & Y_{12} \\ Y_{21} & Y_{22} \end{bmatrix} \begin{bmatrix} V_1 \\ V_2 \end{bmatrix}\right]. \tag{10}$$

Arbitrarily taking $|V_1|$ as unity, this leads to:

$$P_t = \mathrm{Re}[Y_{11} + Y_{12}R_V + Y_{21}R_v^* + Y_{22}|R_V|^2] \tag{11}$$

where Y_{ij} (i=1,2, j=1,2) are the admittance matrix elements of the two-port antenna.

4. Once a value of R_v has been set, which is done in the outer loop of the program, then the electric field inside each cell in the head can be found as $(E_1 + R_v E_2)$, and the inner loop of the program is used to compute both the maximum SAR and the summation of SAR over all cells. Results are divided by P_t, calculated from (11) to impose the condition that the total power leaving the handset is 1 watt.

Figure 2 shows the form of the program that was used for minimisation of P_{abs}. The innermost loop is performing a summation of SAR over all cells. In the alternative form for optimising SAR_{max}, the inner loop simply updates the highest value of SAR that has yet been found. The outer loop locates the optimum value of R_v in both cases. It also outputs a data file defining P_{abs} or SAR_{max} as a function of R_v, which is used to generate plots for visual inspection.

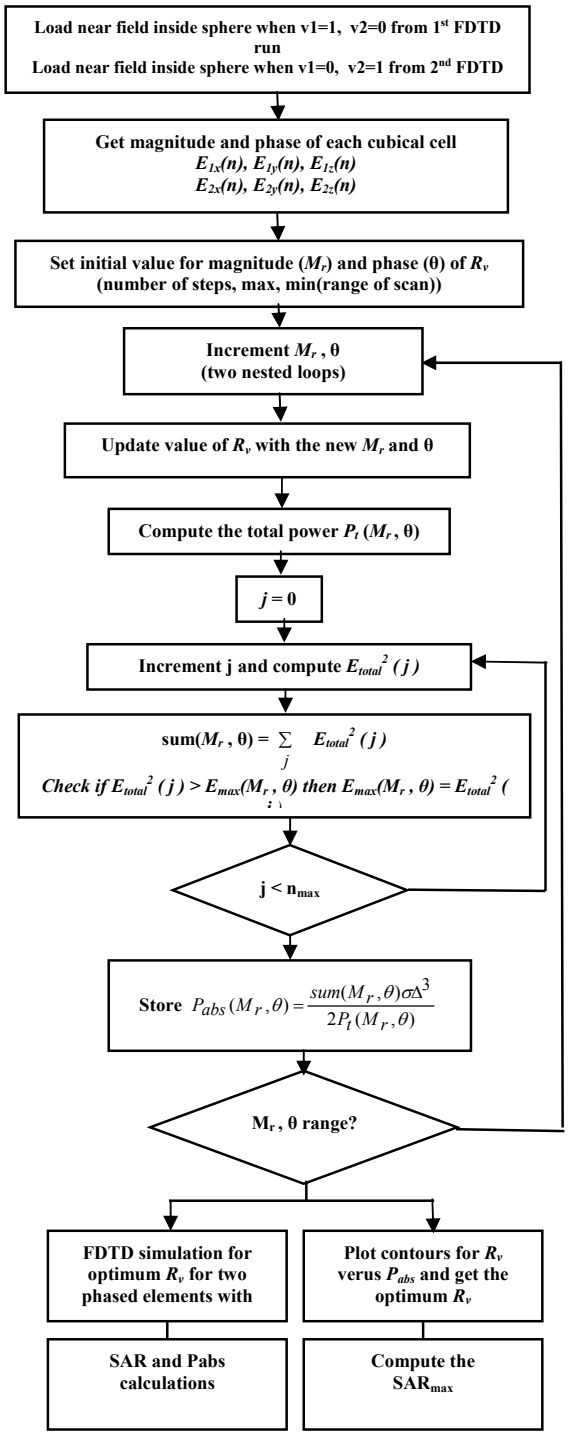

Fig. 2. Flow chart of implementation of SAR optimisation algorithm.

VII. HANDSET AND HEAD MODELS

The handset and head models used are shown in Fig. 1. The quarter wavelength monopoles were chosen to be of radius 0.0045λ, where λ is the free-space wavelength at 1.8 GHz. For defining R_v, element number 1 is taken as the one further from the head. The box size adopted was 0.12λ × 0.333λ × 0.72λ and the

head was approximated by small cubes, each with a side of 0.015λ, forming a discretised approximation to a sphere. The sphere was assigned homogeneous dielectric properties representing the average values for the human head: a relative permittivity and conductivity of 41.8 S/m and 1.3 S/m respectively, for a working frequency of 1.8 GHz. The cell size was chosen to be 2.5 mm. Although the FDTD method can handle an inhomogeneous head of more realistic shape, the simple model was considered sufficiently accurate for evaluating the array performance [13,14]. The problem space size of the FDTD method was 85 × 101 × 107 cells with an additional 6-cell layer for the Perfectly Matched Layer (PML). Several configurations of monopoles attached to, and driven against, this box were modelled, including conventional single monopoles for comparison. The effect of including a reflecting plate with a single monopole and the two-element array was also investigated; these geometries are as shown in Fig. 1(c, d).

As the array spacing is only 0.06λ, it has to operate with very strong mutual coupling between its elements. The computed Y matrix at 1.8 GHz, with the head model present, is $Y_{11} = 0.0053 - j0.020$, $Y_{22} = 0.0125 - j0.024$, $Y_{21} = -0.00056 + j0.024$. The mutual effects are automatically included in the above optimisation procedure for R_v. They are critical in the design of the practical power splitter which must also include impedance matching, but they prove quite straightforward to allow for.

VIII. ANALYSIS OF THE NUMERICAL RESULTS

The single monopole antenna, single monopole antenna with reflector, two-element array, and two element array with reflector, have been investigated and the results compared with some available data [5,7,9]. Tables 1 and 2 present the performance of the above antennas. Table 1 shows the maximum unaveraged SAR in any FDTD cell, when the excitation ratio R_v is optimised for minimum SAR_{max} in column (c), or optimised for minimum $P_{abs,tot.}$ in column (d). Since the electromagnetic problem is linear, any absorbed power can be expressed as a fraction of the transmitted power and hence for example an SAR can be expressed in kg^{-1}. The figure given is thus the actual W/kg when the transmitted power is 1 Watt. This avoids the confusion caused by authors basing published SAR figures on different assumed values of transmitted power.

It is found from Table 1 that the reductions in the maximum SAR for the monopole with reflector, two element array, and two element array with reflector, as compared with a single λ/4 monopole, are -8.2 dB, -10.3 dB, and -15.4 dB, respectively when the head is juxtaposed with the handset (0 cm distance). As the separation distance between the head and the handset is increased to 2 cm, the reductions become -4.4 dB, -7.7 dB, and -7.8 dB, respectively. These values have been compared with some other published figures found for similar structures using MoM [4,7,9] and hybrid method [5], and for 2 cm distance only. Using MoM, the predicted reduction for the two element array and the two element array with reflector, with respect to a single monopole element, are –6.3 dB and –7.9 dB, while the predicted reduction using the hybrid method for the two element array is –8.3 dB. It is seen that the results of FDTD are close to those from other methods. Note that in Tables 1 and 2, the excitation ratio is re-optimised when the antenna-head separation is changed.

Table 1. The maximum SAR for the monopole with reflector, two element array, and two element array with reflector, as compared with a single λ/4 monopole.

D (cm)	Unaveraged SARmax (kg^{-1})				
	a	b	c	d	e
0.0 cm	68.80	10.38	6.49	7.22	1.99
0.5 cm	23.53	4.37	2.78	2.95	0.99
1.0 cm	11.12	2.82	1.55	1.73	0.97
1.5 cm	6.08	1.89	0.97	1.11	0.79
2.0 cm	3.73	1.37	0.64	0.75	0.62

(a) Monopole, (b) Monopole with reflector, (c) Two element array (optimised to minimise SARmax), (d) Two element array (optimised to minimise total power absorbed), (e) Two element array with reflector (optimised to minimise SARmax).

Table 2. The total power absorbed in the spherical head, normalised to 1W input, obtained by optimising for minimum SAR_{max} and for minimum $P_{abs,tot}$.

D (cm)	Total Power absorbed (milliunits)				
	a	b	c	d	e
0.0 cm	674	304	237.6	216.6	118.5
0.5 cm	446	185.6	153.2	143.6	83.3
1.0 cm	301	148.16	114.4	111.6	79
1.5 cm	241	117.77	87.8	85.8	65.8
2.0 cm	161	94.07	67.95	66.1	54.5

Table 2 shows the total power absorbed in the spherical head, normalised to 1W input, obtained by optimising for minimum SAR_{max} and for minimum P_{abs}. It is immediately apparent from comparing columns c and d in each table that the strategies of optimising SAR_{max} or P_{abs} are not seriously in conflict, as either choice gives a reduction in both quantities that is not far below the optimum. For comparison with some related work [4,5], the total power absorbed in the head, for the case of the two element antenna separated 2 cm from the head, was found here as 6.6% of the radiated power, while for the two element array with reflector it is 5.45%. These figures indicate a low interaction between

Table 3. The maximum SAR for the various cases but averaged over 1g and 10g of head tissue.

	SARmax (Monopole)			SARmax (Monopole with reflector)		
D (cm)	Unaver (kg^{-1})	1gm (kg^{-1})	10 gm (kg^{-1})	Unaver (kg^{-1})	1 gm (kg^{-1})	10 gm (kg^{-1})
0.0cm	68.80	29.11	16.44	10.38	4.59	2.93
0.5cm	23.53	12.70	7.75	4.37	2.50	1.75
1.0cm	11.12	6.42	4.14	2.82	1.74	1.24
1.5cm	6.08	3.67	2.48	1.89	1.21	0.87
2.0cm	3.73	2.35	1.62	1.37	0.85	0.61

	SARmax (Two element array)			SARmax (Two element array with Reflector)		
D (cm)	Unaver (kg^{-1})	1gm (kg^{-1})	10 gm (kg^{-1})	Unaver (kg^{-1})	1 gm (kg^{-1})	10 gm (kg^{-1})
0.0cm	6.49	3.63	2.03	1.99	0.96	0.71
0.5cm	2.78	1.84	1.11	0.99	0.73	0.52
1.0cm	1.55	1.07	0.68	0.97	0.60	0.43
1.5cm	0.97	0.65	0.43	0.79	0.55	0.39
2.0cm	0.64	0.42	0.29	0.62	0.42	0.30

the antenna and the human head, and are comparable with those found by others for other forms of low-interaction antenna. One figure is 5.7% for a printed structure on the back of the handset [3]. Other published figures [4] are 6.2% and 9.2% for a two-element array, and a two-element array with reflector and tilted elements. The latter results have only been given for 2 cm spacing, but compare well with the present figures and were obtained by a different method, namely MoM. Table 3 shows the maximum SAR for the various cases, but averaged over 1g and 10g of head tissue.

Figures 3 and 4 present the variation of the real and imaginary parts of the voltage ratio R_v for the two-element array, corresponding to minimised P_{abs} and minimised SAR_{max}, respectively, for a range of handset-sphere distances. In Figure 3 it is noteworthy that the real part is almost constant and the imaginary part is very close to zero at a distance of 1.5 cm. Thus for this particular case the feed network can be easily implemented using only a simple reactive splitter circuit, a directional coupler or any RF network which approximates to an ideal transformer. This simplification can be achieved at other values of the handset-sphere distance by varying the separation distance between the monopoles or changing the antenna geometry.

Figure 5 shows the variation of the real and imaginary parts of R_v corresponding to minimised SAR_{max}, for a range of handset-sphere distances, for a two element array with reflector. The real part still varies much less than the imaginary, but both parts vary more than in Figure 4. This contrasting behaviour is clearly due to the reflector but does not have an obvious physical explanation.

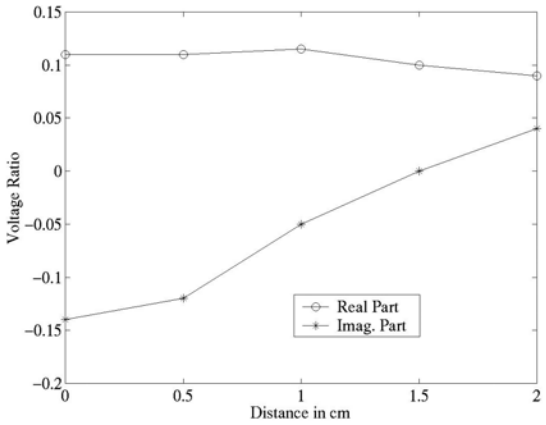

Fig. 3. The voltage ratio vs. distance d for minimised total P_{abs} of two element array.

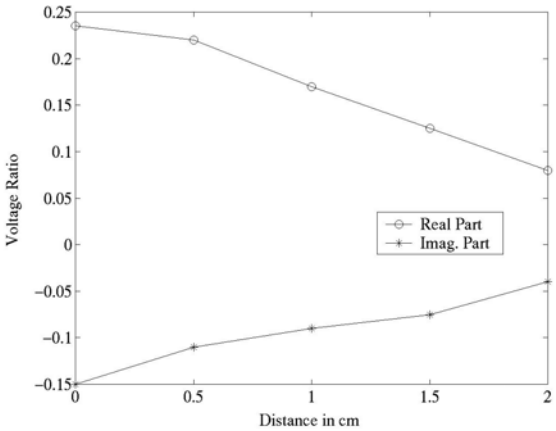

Fig. 4. The voltage ratio vs. distance d for minimised SAR_{max} of two-element array.

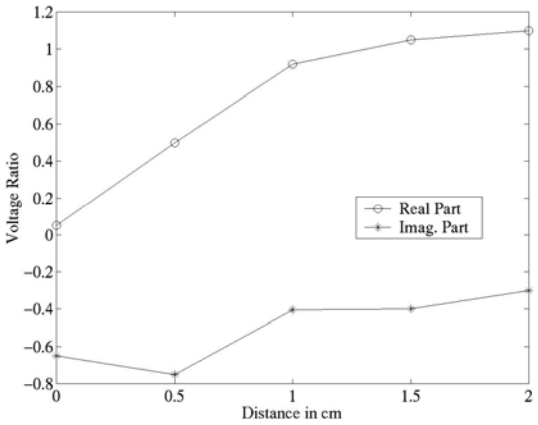

Fig. 5. The voltage ratio versus distance d for minimised SAR_{max} of two-element array with reflector.

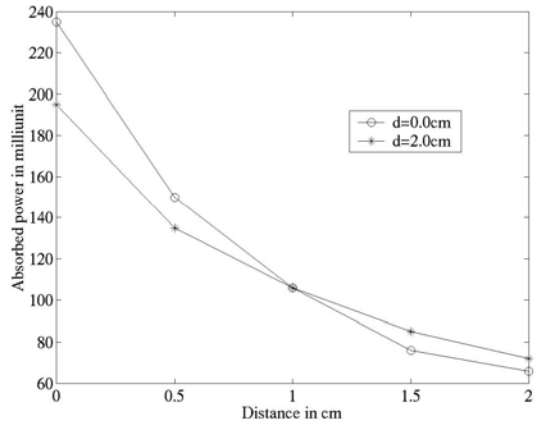

Fig. 6 Total absorbed power versus distance d using fixed voltage ratio for two-element monopole array optimised for d = 0 cm.

It would be practically difficult to change R_v adaptively to remain optimum for a variable head-antenna spacing, but it could be fixed at the optimum value for a particular spacing. The resulting dynamic range of P_{abs} and SAR_{max}, for fixed R_v and varying distances, is presented in Figures 6 and 7 respectively. For both figures, R_v values optimised for SAR_{max} at d = 0 cm and 2 cm are used. Figure 7 suggests that the former would probably be best used in practice as it gives better performance in the most critical (closest approach) condition and it is also seen to give better average performance. Figure 6 indicates that this also gives a near-optimum reduction in P_{abs} and so is probably the best practical choice without deeper knowledge of biological factors.

Figure 8 shows a contour plot of computed P_{abs} as a function of R_v for a two-element array at d=0 cm, and the optimum value can be read here or in Figure 3 as *0.106-j0.146*. Values for d = 0.5, 1, 1.5, and 2 cm have been similarly found as *0.106-j0.106, 0.107+j0.055, 0.09+j0.0*, and *0.0918+j0.0408*, respectively. Corresponding values in Figure 4, optimised for SAR_{max} are noticeably different. The improvement factors for $P_{abs,}$ using ratios optimised for this quantity and at each individual spacing, are 9.79 dB, 9.03 dB, 8.07 dB, 7.38 dB and 6.95 dB respectively. Comparing these factors with those computed using minimised SAR_{max}, the differences are fairly small, so the question of whether peak or integrated SAR is biologically more important is not crucial.

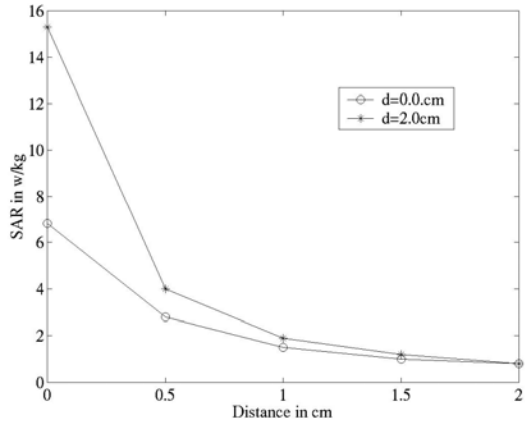

Fig. 7. SAR versus distance d using fixed voltage ratio for two element monopole array optimised for d = 0 cm.

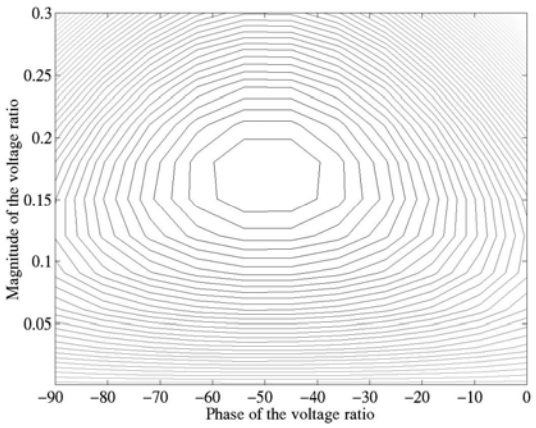

Fig. 8. Total absorbed power contours as a function of the voltage ratio of two element monopole array for d = 0.0 cm (stationary point is a minimum).

Figures 9 and 10 show the computed SAR distribution in dB over two different slices, horizontally and vertically through the spherical head, for four versions of the handset: a. single monopole; b. single monopole with reflector sheet, c. two element array, and d. two element array with reflector sheet, for d = 0 cm. It is important to note the method of normalising these plots, which is to divide values in all plots by the peak value occurring at zero distance for the monopole. Clearly, these Figures show an overall reduction and the

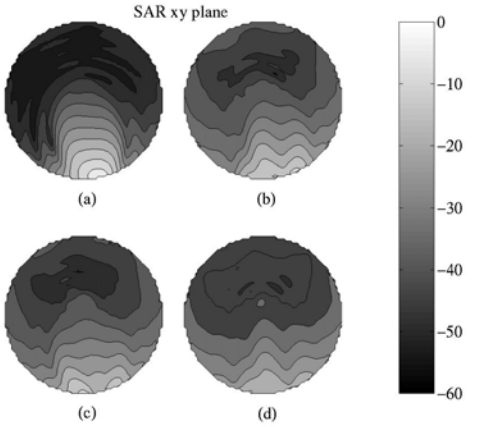

Fig. 9. SAR distributions over a horizontal cut through the sphere, at d = 0.0 cm: (a) single monopole antenna; (b) single monopole antenna with reflector sheet; (c) two element array; (d) two element array with reflector sheet.

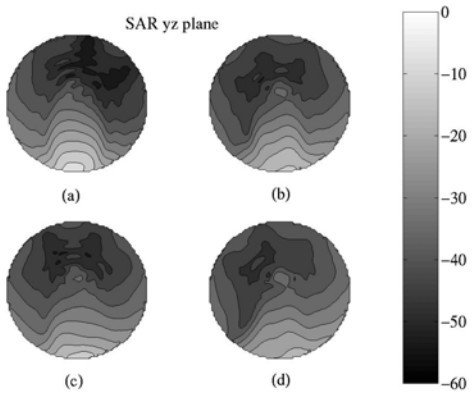

Fig. 10. SAR distributions over a vertical cut through the sphere, at d = 0.0 cm: (a) single monopole antenna; (b) single monopole antenna with reflector sheet; (c) two element array; (d) two element array with reflector sheet.

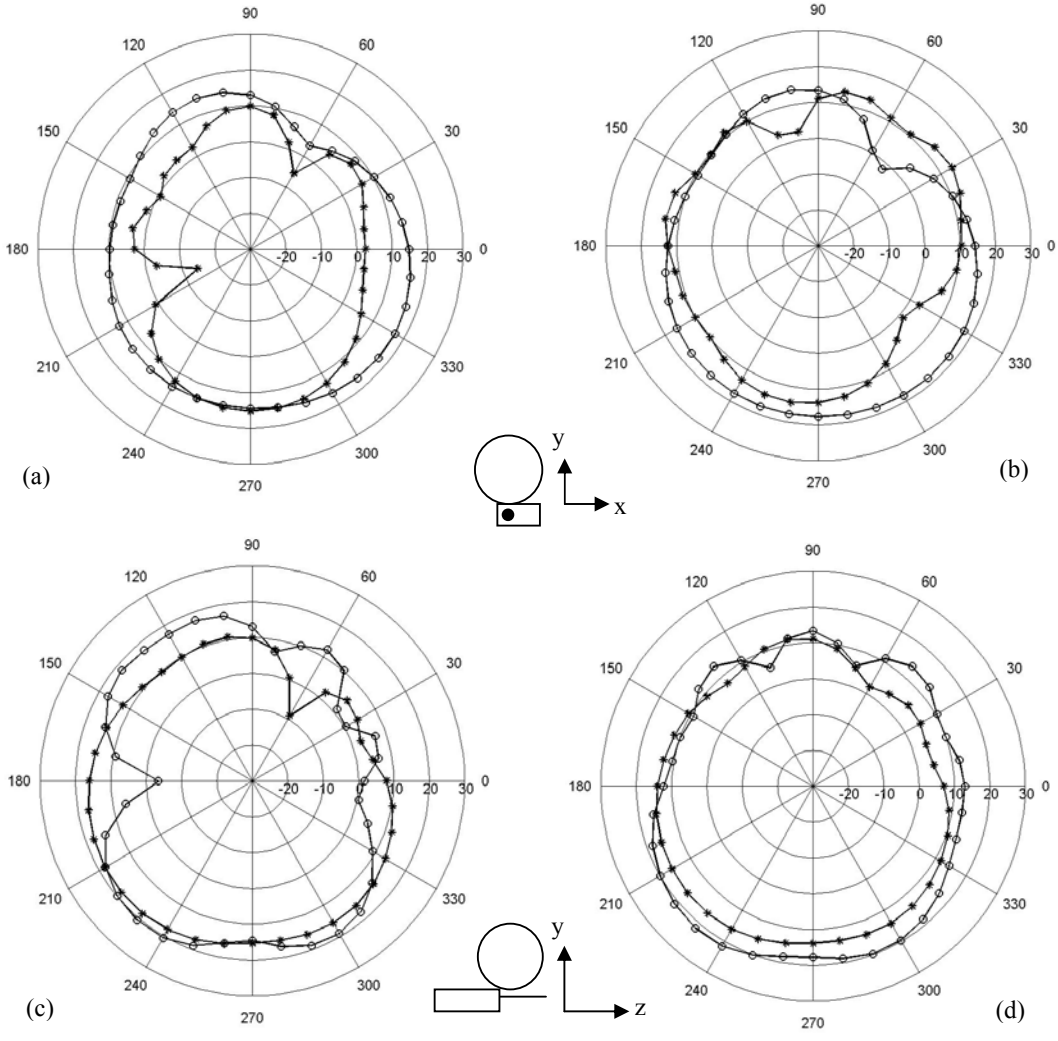

Fig. 11. Far field patterns for two different planes: (a) and (b) horizontal plane (θ =90°) for single monopole and two element array respectively; (c) and (d); vertical plane at ϕ = 90° for single monopole and two-element array, respectively; d = 0.0 cm (E_θ: ooo, E_ϕ: ***).

improvement for the array relative to the monopole when they are at the same distance.

The spatial null in SAR towards the outer surface of the head, when the two element array antenna is used, is clearly seen. Adding a reflector sheet improves results in all cases, but the array without reflector is better than the monopole with reflector (note that the SAR distributions are asymmetric since the antennas are located towards one edge of the handset). The distributions of SAR prove to be quite similar to those obtained using the less realistic model of the antenna as two ideal dipoles [1], despite the considerable structural difference in the antenna. As expected, the realistic handset does show visible asymmetries in the distributions, whereas the dipole model has exact symmetry.

Figure 11 shows the radiated far-field patterns for two different planes and two versions of the handset, namely a single monopole and a two element array optimised for SAR_{max}. The horizontal and vertical plane pattern cuts are displayed at $\theta = 90^0$ and $\phi = 90^0$ respectively. Comparing plots (a) and (b), it is clear that the array has superior performance in terms of the power averaged over azimuth, for the dominant field component (E_θ) or for the power sum of both components, than the single monopole. This is consistent with the reduction of P_{abs} making more power available to be radiated into space.

IX. CONCLUSIONS

This work has demonstrated that a simple phased array handset antenna can be designed to protect the user from radio frequency exposure, and will have additional benefits in terms of improved overall performance. The array can be designed to produce the minimum $P_{abs,}$ the total absorbed power in the head or the smallest $SAR_{max,}$ the local spatial peak in SAR. For

the second criterion, a novel optimisation algorithm was presented which allows for migration of the location of worst SAR as the array excitation is varied. Either approach produces significant reductions in exposure and improvements in the power available for communications with a base station. The voltage ratio found for minimised SAR_{max} at the minimum distance (handset touching the simulated head) is probably the best compromise for minimising both SAR_{max} and Pabs over a wide range of separation distances of the handset from the head. An important conclusion is that the criteria of minimising the total absorbed power or the worst point value of SAR are not seriously in conflict. Optimisation for minimum SAR at another point such as the head centre could also be selected if it were believed to be biologically more sensitive. Almost certainly, more complex arrays could give greater protection, as remains to be investigated.

REFERENCES

[1] R. A. Sadeghzadeh, N. J. McEwan and M. A. Al Sabey, "Approximate modelling of head-antenna interactions using spherical wave expansions," *IEE Int. Conf. on Antennas and Propagation*, Edinburgh, pp. 249-252, 1993.

[2] J. Toftgard, S. N. Hornsleth, and J. B. Anderson, "Effects on portable antennas of the presence of a person," *IEEE Trans. Antennas and Propagation*, vol. AP-41, pp. 739-746, 1993.

[3] H. O. Ruoss, N. Berger, and F. M. Landstorfer, "Optimised slot antennas for hand held mobile telephones," *IEE Int. Conf. on Antennas and Propagation*, Edinburgh, pp. 249-252, 1997.

[4] R. A. Abd-Alhameed, N. J. McEwan, P. S. Excell and E. A. Abdulmula, "A two-element phased array antenna for mobile handsets to reduce the mutual effect with the human head," *IEE Conf. on Antennas and Propagation*, York, pp. 291-4, 1999.

[5] M. A. Mangoud, R. A. Abd-Alhameed, N. J. McEwan, P. S. Excell, and E. A. Abdulmula, "SAR reduction for handset with two element phased array antenna using hybrid MOM/FDTD technique," *Electronics Letters*, vol 35, no. 20, pp. 1693-1694, 1999.

[6] N. J. McEwan, B. A. W. Ibrahim, R. A. Sadeghzadeh, E. A. Abdulmula, and K. A. Qassim, "Pattern Shaping for Handset Antennas," *IEE 9th International Conference on Antennas and Propagation*, IEE Conf. Pub1. no. 407, Eindhoven, pp. 106-110, 4-7 April 1995.

[7] E. A. Abdulmula, "Improved Handset Antennas for Personal Communications at 1.8 GHz," PhD Thesis, University of Bradford, UK, 2000.

[8] R. A. Sadeghzadeh and N. J. McEwan, "Antenna design considerations for personal communications user protection," *IEEE 45th Vehicular Technology Conference*, vol. 2 pp. 844-847, 1995.

[9] E. A. Abdulmula, N. J. McEwan, and R. A. Sadeghzadeh, "Phased Array Antennas for personal communications Handset," High frequency postgraduate student colloquium, University of Leeds, pp.112 -117, 1997.

[10] M. A. Al-Sabey, "Spherical wave expansion for scattering by a sphere at a finite distance from a dipole source," MSc Dissertation, University of Bradford, UK, 1992.

[11] R. A. Sadeghzadeh, N. J. McEwan and M. S. Abrishamian, "Improved modelling of head-antenna interactions using spherical wave expansions," *2nd International Conference on Computation in Electromagnetics*, Nottingham, Uk, IEE Conf. Pub1. 384, pp. 95-98, 12-14 April 1994.

[12] P. S. Excell and R. A. Abd-Alhameed, "Experience of antenna simulation using NEC, FDTD and a novel moment method," *IEE Colloquium on High Frequency Simulation in Practice*, London, pp. 8.1-8.4, 1997.

[13] K. W. Kim and Y. R. Samii, "EM Interactions between handheld antennas and human: anatomical head vs. multi-layered spherical head," *Antennas and Propagation for Wireless Communications, IEEE-APS Conference*, pp. 69-72, 1-4 Nov.1998.

[14] V. F. Perez et al, "Analysis of proposals to reduce SAR levels from GSM Terminals," *IEEE MTT-S Digest*, pp. 2227 – 2230, 2001.

Jinan Moustafa was born in Mosul, Iraq. She received the BEng.(Hons.) degree in Electronic and Electrical engineering and MPhil degree from University of Bradford , UK, in 1995 and 1997 respectively. Her research field for the MPhil degree was in coplanar waveguide based antennas for broadside radiation and circular polarisation. Later as a Research Assistant she was involved in projects on printed antennas and reduction of harmonic radiation from an active microstrip patch antennas. Currently, she is working toward the PhD degree at the University of Bradford. Her main research has been in use of FDTD techniques for simulating the user interaction of mobile telephones employing different phased array and balanced antennas.

Neil J McEwan was born in London, U.K. in 1948. He received the BA degree in mathematics from Cambridge University, U.K. in 1969, and the PhD degree in radio astronomy from Manchester University, U.K. in 1975. Since 1998 he has been a Principal Research Engineer with Filtronic PLC at Shipley, U.K., having previously been Reader in Electromagnetics in the Department of Electronics and Telecommunications, University of Bradford, UK. He has previously worked on microwave propagation in the troposphere, and was involved in propagation experiments using the ATS-6 and European OTS satellites. More recently he has worked on various aspects of active and passive antennas. He spent the year 1987 with Millitech Corporation, MA, as Visiting Research Scientist. Dr McEwan is a member of the Institution of Electrical Engineers.

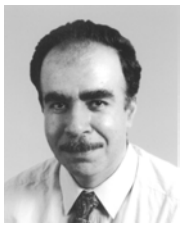

Raed A. Abd-Alhameed was born in Basrah, Iraq in 1959. He received the B.Sc. and M.Sc. degrees from Basrah university, Iraq, in 1982 and 1985 respectively, and the Ph.D. degree from the university of Bradford, UK, in 1997, all in electrical engineering. From 1997 to 1999 he was a Postdoctoral Research Fellow at the university of Bradford, specialisation in computational modelling of electromagnetic field problems, microwave nonlinear circuit simulation, signal processing of preadaption filters in adaptive antenna arrays and simulation of active inductance. From 2000 to 2003 he has been a lecturer in the University of Bradford. Since August 2003 he was appointed as a senior lecturer in applied Electromagnetics in the same University. His current research interests include hybrid electromagnetic computational techniques, antenna design, low SAR antennas for mobile handset, RF mixers and active antennas. Dr Abd-Alhameed is a member of the Institution of Electrical Engineers and Institution of Learning and Teaching for Higher Education.

Peter Excell is Professor of Applied Electromagnetics and Associate Dean for Research in the School of Informatics at the University of Bradford, UK, where he has worked since 1971. He obtained his BSc in Engineering Science from the University of Reading in 1970 and his PhD from the University of Bradford in 1980 for research in electromagnetic hazards. His research interests cover computational electromagnetics, EMC, antenna design, bioelectromagnetics and mobile applications: he has published over 200 papers and he holds three patents. He is a Senior Member of the Institute of Electronics and Electrical Engineers, a Fellow of the Institution of Electrical Engineers and a Chartered Engineer.

Numerical Simulation Approaches for Phased Array Design

(*Invited Paper*)

Levent Sevgi
Doğuş University, Electronics and Communication Engineering Department,
Zeamet Sok. No. 21, Acıbadem / Kadıköy, 34722 Istanbul - Turkey

Abstract **-** This paper reviews the two well-known numerical simulation techniques that are widely used in antenna modeling; the finite-difference time-domain (FDTD) and the Method of Moments (MoM). The packages FDANT (prepared in Fortran language by using FDTD) and NEC2 (public domain code for the MoM) are used to model various types of antenna arrays, their advantages/disadvantages are discussed on characteristic design examples, and they are calibrated one against the other. Also, a simple Matlab package (ANTEN_GUI) for the visualization of radiation patterns, beam forming and beam steering capabilities of user-designed planar arrays of isotropic radiators (which can be used to test the above mentioned packages and as an educational tool, in e.g., antennas and propagation lectures) is introduced[1].

Keywords – Computational electromagnetics, antenna simulation, phased arrays, isotropic radiators, radiation pattern, high frequency radars, ground screen, MATLAB, FDTD, MoM, NEC, three-dimensional graphics, visualization.

I. INTRODUCTION

Recent years have witnessed a lot of research activities focused on the topics of antennas and arrays. For example, smart (intelligent) antennas have started to be used widely to enhance the performance of cellular radio systems. Switched or adaptive beam forming techniques, antenna diversity in combination with enhanced digital signal processing, etc., increase signal quality and channel capacity significantly in comparison with standard antenna configurations. The demand of low cost, small size, but extremely effective smart antennas in both military and commercial Markets make antenna engineers attractive. On the other hand an antenna engineer is required to be more sophisticated, and should be equipped with the theory and practice on a wide range of antennas from basic to state-of-the-art.

[1]ANTEN_GUI, FDANT and their source codes can be downloaded from http://www3.dogus.edu.tr/lsevgi

An antenna engineer must have strong analytical background and be well-equipped with computer tools and signal processing algorithms. For example, a log-periodic array of monopoles erected over the ground beneath which exist a complicated ground screen design as shown in Fig. 1 requires understanding of high level electromagnetics (EM), ground effects, array design, beam forming, etc. ([1-5] are good examples of classical antenna books), as well as strong numerical computational background together with model validation, software verification and code calibration capabilities.

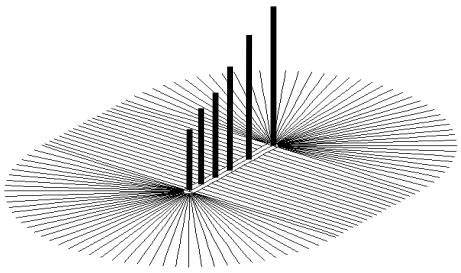

Figure 1. A transmitting antenna array of vertical monopoles for a long-range HF surface wave radar erected above a specially-designed ground screen layout.

One aim of this paper is to review powerful time domain (TD) and frequency domain (FD) numerical antenna simulation tools. Another aim is to supply sample packages, together with the source codes, so that the reader may enjoy running, testing, doing comparisons, as well as developing new modules for the other calculations that are not included in the packages. Although the perspectives of a code developer and a user are quite different the antenna engineer should be well-equipped in terms of both. Since a developer leaves only a small set of tuning parameters that will be supplied by the user, an antenna engineer should develop his/her own codes in order to have maximum flexibility and capability in numerical designs and simulations.

Numerical simulation approaches have long been applied to the design and/or investigation of various types of antennas, from wire arrays to microstrip patches. There are many FD and TD handy simulation tools that are widely used by antenna engineers. The pioneering one is the Numerical Electromagnetic Code (NEC) which is based on the Method of Moments [6] and has many versions. They have been in use for more than a few decades [7]. The public domain simulator NEC2 can easily be downloaded from many internet sites [8], or can easily be purchased with a price less than a few hundred dollars [9] (mostly, the price goes to the supplied graphical user interfaces).

An FDTD based TD simulator FDANT is designed to investigate (although not restricted to) wire antenna arrays of 1D and 2D in free-space and their beam steering capability [10]. FDANT contains almost every major routines, FDTD iterations, PML blocks, NTFF routine, power routines, etc. to direct interested users towards building his/her own antenna simulator, by just adding a specifically designed GUI. The user may also make modifications in source codes of FDANT to simulate other complex antenna structures.

FDTD discretizes Maxwell's equations directly in TD by replacing partial derivatives with their finite difference approximations. Since Maxwell's equations models TD EM wave scattering (i.e., it is an *initial-value problem*) boundary conditions must be satisfied artificially during the simulations. Moreover, since far fields are of interest in order to calculate antenna radiation patterns, this can not be done directly with a *finite-volume* FDTD method; therefore a near-to-far-field (NTFF) transformation is a must in this case. On the other hand, MoM is an FD method and first requires derivation of the Green's function of the problem at hand (i.e., it is a *boundary-value problem*). Then, segmentation is used and a set of equations is formed for the *N*-segment geometry to calculate surface currents induced by the incident/excitation fields. While the physical size of the problem is critical in FDTD simulations, the most critical parameter in MoM is the number of segments.

II. SIMULATION APPROACHES

Three simulation packages have been outlined in this Section. First, beam forming capability of various planar arrays of isotropic radiators is investigated analytically. A simple, but effective and educating Matlab package – ANTEN_GUI – is introduced [11]. Then the public NEC2 package is reviewed shortly. Finally, the TD FDTD-based simulator FDANT is discussed briefly.

2.1 A Matlab package: Anten_GUI based on analytical formulations

The radiation pattern of a group of isotropic radiators is determined by the type of individual elements, their location, spacing, orientation, excitation amplitudes and phases. In general, the total electric field (which is known as the array factor) of an *N*-element array located at (x_i, y_i, z_i) $(i = 1,...,N)$ and at a far field point along (θ, φ) direction (under $\exp(-j\omega t)$ assumption) is

$$E(\theta,\phi) = \sum_{i=1}^{N} I_i \, e^{j\psi_i(\theta,\phi)} \tag{1}$$

where I_i is the complex current for the i[th] element [12]. The phase contribution ψ_i is at the far field point from the i[th] radiator with respect to the origin. For the planar arrays located at xz-plane the array factor can be expressed as:

$$E(\theta,\phi) = \sum_{i=1}^{N} I_i \, \exp\left(jkr_i \sin\theta \cos(\phi_i - \phi)\right) . \tag{2}$$

This expression corresponds to the pattern of arbitrarily-located, isotropic, equi-amplitude, non-phased radiators when $I_i = 1.0$. The main beam of an array can be steered electronically by varying the phases of the currents applied to the array elements. Equation 2 takes on the form of

$$E(\theta,\phi) = \sum_{i=1}^{N} I_i \times \exp\left\{jkr_i\left[\sin\theta\cos(\phi_i - \phi) - \sin\theta_0 \cos(\phi_i - \phi_0)\right]\right\} \tag{3}$$

if the beam angle is specified as (θ_0, ϕ_0). This means each element is phased accordingly to direct the beam of the array along (θ_0, φ_0) direction. It reduces to (2) when $\theta_0 = 0^\circ$, therefore it represents "no-phasing". The default θ_0 value is zero in the GUI and should be kept as it is if one does NOT want to phase elements.

Extra line phasing capability can be added to change front-to-back (FBR) characteristics in the planar array option. The user may change the phase angle Δβ of the lined-up radiators and observe how FBR improves or gets worse. In this case complex currents I_i in (3) is replaced with I_{in} as

$$I_i \to I_{in} = \sum_{n=1}^{M} I_i \exp\left\{j(n-1)\Delta\beta\right\}. \tag{4}$$

For an *N*×*M* planar array, if for example, a phase of Δβ=*30*° is selected, then the phases of the second row (*M=2*) lag *30*° the phases of the first row (*M=1*), the phases of the third row (*M=3*) lag 3*0*° the phases of the

second row (*M=2*), and *60°* the phases of the first row (*M=1*), etc.

The Matlab-based antenna package ANTEN_GUI has been prepared for the visualization of radiation characteristics of planar arrays of isotropic radiators (see Fig. 2) [11,12]. The package allows the user to choose different types of arrays with a number of user-selected and located isotropic radiators. The default array type is *arbitrary*. Once the number of radiators (*N*), maximum radius (in meters) of the polar region where the radiators will be located, and the operating frequency (in MHz) are specified, the user may proceed to locate the radiators one by one after pressing the "*Locate Radiators*" button. The coordinates of the located radiators are also displayed in the list-box at the bottom.

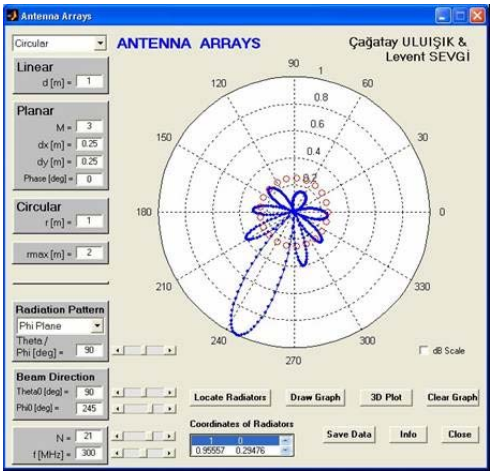

Figure 2. The ANTEN_GUI front panel that shows the radiation pattern of a 21-element circular array located on the xy-plane ((f=300 MHz, the radius is r= 0.5 m (λ/2), elements are phased in a way that the beam points θ_0=90º, φ_0=245°).

By clicking the mouse the user may design any kind of an array, but the package also locates the radiators automatically when one of the other types of the arrays is selected and required parameters are supplied (see Fig. 3). If the array type is set to *linear*, *N*-elements are located on the y-axis symmetrically, with an inter-element distance of *d*. If it is planar, *N*×*M* elements are located on *xy*-plane. In this case, *N* and *M* are the number of the elements along y- and x-directions, respectively. The distances between the radiators along *x*- and *y*-directions are *dx* and *dy*, respectively. If the circular array type is selected, *N*-elements are located symmetrically on a circle whose center is at the origin and radius is *r*.

After locating the radiators the user may visualize a 2D radiation pattern at the selected plane by pressing the "*Draw Graph*" button. The 2D radiation pattern plane to be displayed is specified by the *Theta/Phi Plane* popup menu and *Theta/Phi value* box. If the *θ-plane* is selected (vertical pattern) the angle θ varies between [0°, 360°] at a fixed φ value (specified by the *Theta/Phi* box). If the *φ-plane* is selected, the angle φ varies between [0°, 360°] at a fixed *θ*-value specified by the user; the radiation pattern in this case is called "horizontal". All the 2D radiation patterns are plotted with an angular resolution of Δθ=Δφ=*1°*.

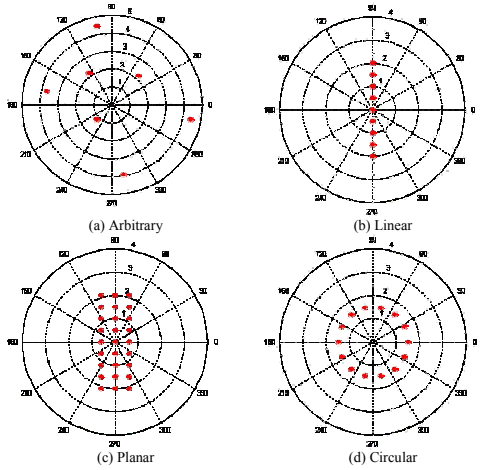

Figure 3. Different geometrical configurations of planar arrays of isotropic radiators that can automatically be located once the number of radiators is chosen, (a) arbitrary, (b) linear, (c) planar, and (d) circular arrays.

Fig. 2 shows the radiation pattern of an arbitrarily-located 7-element array. The user selects the radiation pattern plane and the beam direction from the front panel (on the bottom-left). In this example, the pattern belongs to φ-plane (i.e., on the *xy*-plane) since *θ=90°*. The beam angles are selected to be *θ=90º* and φ=*245°*. In Fig. 4, horizontal radiation pattern (*θ=90º*) of a planar array of *5×1* (i.e. a 5-element linear array) is shown as an example. Here, frequency is *300 MHz*, beam angles are θ_0=*90º* and φ_0=*90°*, and inter-element distance is 0.4 m (0.4λ).

ANTEN_GUI also has a 3D radiation pattern plotting capability. The approach [13] (in *dB* scale with a *30 dB* margin along each axis) is based on normalization of the radius of the unit sphere for each observation angle (θ_i, φ_i) in 3D Cartesian coordinates according to the radiation intensity calculated from (3). The angular resolution for the 3D plots is set to be Δθ=Δφ=*2.5°*

which means the calculations are repeated at *151×151=22,801 vertices*.

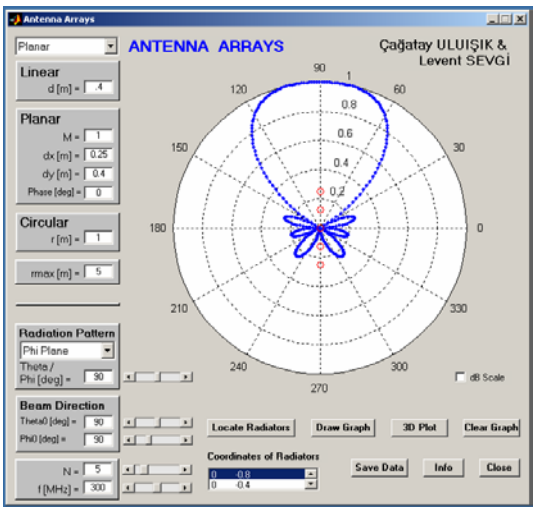

Figure 4. The H-plane (horizontal) 2D radiation pattern of a 5-element linear array (f=300 MHz, inter-element distance is d=0.5 m (d=λ/2), beam angles are θ_0=90º and φ_0=0°).

The 3D radiation pattern of the array given in Fig. 4 is plotted in Fig. 5 as an example.

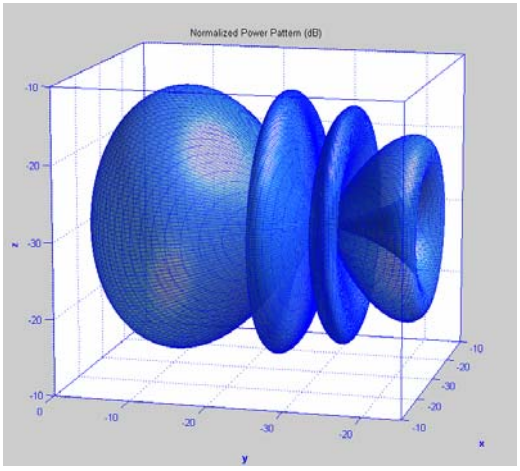

Figure 5. The 3D radiation pattern of the same 5-element linear array (f=300 MHz, inter-element distance is d=0.5 m (d=λ/2), beam angles are θ_0=90º and φ_0=0°).

Another exciting feature of ANTEN_GUI is that the user can use sliding bars to change *N, f,* θ_0, φ_0. For instance, by pressing the sliding bar of the frequency continuously, the user can increase or decrease the frequency, see the corresponding radiation pattern immediately, and may easily understand the effect of frequency change on the radiation pattern. The package also allows the user to save the radiation pattern data (field intensity vs. angle) to a file named *Arraypattern.dat*. The first column of this file corresponds to *361* observation angle values (in *radians*), and the corresponding array factors are in the second column.

Any 2D array may be designed by the user and its radiation characteristics can be investigated. Beam forming capabilities for different locations, number of radiators, as well as for operating frequencies can be visualized. The package may be used as an educational tool in many undergraduate antenna lectures. It may also be used to validate and verify the FDTD and MoM packages described below. Moreover, the reader may add novel features to the supplied source codes, such as a module for the formation of 3D (volume) arrays which is straightforward.

2.2 NEC2 package based on FD Method of Moments (MoM) technique

The NEC is an outgrowth of a program developed in the 1970s, called the Antenna Modeling Program (AMP). It has been developed at the Lawrence Livermore Laboratory, Livermore, California, under the sponsorship of the Naval Ocean Systems Center and the Air Force Weapons Laboratory [7]. There are at least 4 versions of NEC, with NEC2 emerging in 1981 and NEC4 appearing in 1992. NEC2 is the highest version of the code under public domain. NEC4 remains proprietary with the Lawrence Livermore National Laboratory (as far as the author's knowledge,) and the University of California. It requires a separate license for use.

NEC in all its forms is a computer code for the analysis of the EM response of antennas and other metal structures that uses MoM techniques. It is a numerical solution to integral equations for the currents induced on a metallic structure by sources or incident fields. The approach has no theoretical limit and may be used for very large arrays or for the very fine subdivision of smaller arrays. Any geometry (e.g., a loop antenna, helical antenna, a monopole over a rectangular PEC box, an array over the ground with complex ground screen layout, a radio antenna on a car, a radar antenna beneath an aircraft, etc.,) can be modeled with NEC as long as their mesh representation can be built, which is the most difficult (and time-consuming) part in NEC simulations.

It should be noted that all the radiating elements of the antenna structure must be in a volume bounded by the

near-field criteria; otherwise the presented patterns become invalid.

2.3 The FDTD-based antenna simulations and FDANT package

FDTD technique [14] depends on the solution of Maxwell's equations directly in time domain, where the physical geometry is divided into small (mostly rectangular or cubical, but non-orthogonal in general) cells. Both time and spatial partial derivatives are handled with finite- (central-) difference approximation and the solution is obtained with a marching scheme in iterative form. The characteristics of the medium are defined by three parameters; permittivity, conductivity and permeability, and three electric and three magnetic field components are calculated at different locations of each cell.

The FDTD has almost become a standard tool for antenna simulations for the last decade or so (see, e.g., [15-17] for our studies). The addition of powerful absorbing boundary simulators (such as perfectly matched layers, PML), and near-to-far field transformation (NTTF) either in FD or TD, has made it possible to simulate almost any kind of complex structure's radiation characteristics. An example [17] is given in Fig. 6 and the radiation and beam steering capabilities are presented in Fig. 7.

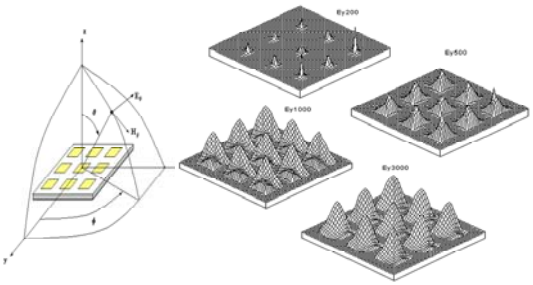

Figure 6. A 3×3 microstrip patch array designed to form a main beam of 35º at 1.8 GHz and near-field transient behaviors at different time instants (FDTD parameters: $\Delta x=\Delta y=2.758$ mm, $\Delta z=0.250$ mm, w=5.516 mm=20×Δx, h=1 mm=4×Δz, $\varepsilon_r=2.2$, a=18×Δ, $b_y=5\times\Delta$, $b_x=7\times\Delta$).

In Fig. 6, a *3×3 coax-fed microstrip* patch array (which is designed to form a main beam of 35º at 1.8 GHz) is illustrated. Near field values at different time instants calculated inside the FDTD volume are also plotted in the figure. The FDTD parameters of this simulation are as follows: $\Delta x=\Delta y=2.758$ mm, $\Delta z=0.250$ mm, w=5.516 mm=20×Δx, h=1 mm=4×Δz, $\varepsilon_r=2.2$, a=18×Δ, $b_y=5\times\Delta$, $b_x=7\times\Delta$. The radiation patterns in Fig. 7 are at 1.8 GHz, left: $\phi=0^o$, right: $\phi=90^0$. The first row corresponds to feeding without time delay (i.e., without phasing in FD). The second row corresponds to feeding with delays of 0.094 ns which points the main beam towards $\theta=\pm 20^\circ$, respectively.

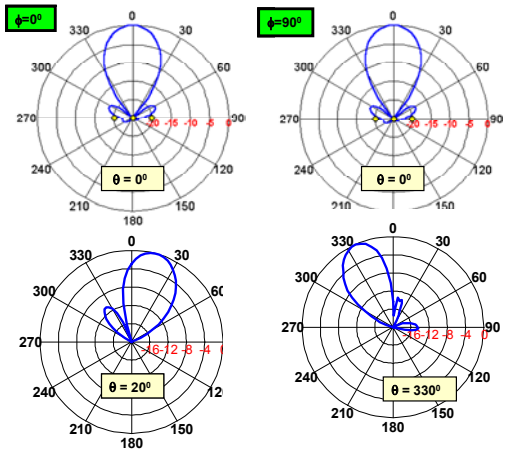

Figure 7. Radiation patterns at 1.8 GHz, left: $\phi=0^o$, right: $\phi=90^0$. First row: feeding without time delay (i.e., without phasing in frequency domain). Second row: feeding with delays of 0.094 ns which points the main beam towards$\theta=\pm 20°$, respectively.

FDANT is supplied in [10] and can be used for antenna analysis. Its structure is given in Fig. 8. It first reads user defined parameters from the input file ANT.INP. Transient analysis is done within FDTD computation space for short-pulse excitations, and TD output data is stored in three different files. SOURCE.dat contains time vs. source amplitude to allow the user to see the excitation signal in TD. AN-NEAR.dat has near field E_z values in two columns; time in [ns] and E_z in [V/m]. Finally, AN-FAR.dat has TD far field data along the number of chosen directions, obtained via NTFF transformation directly in TD.

FDANT is prepared to investigate vertical or horizontal radiation patterns for a 2D array of maximum 2 by 6 elements (but, the size of the array may be changed by the user). The array is located longitudinally along y-direction (see Fig. 9). The elements are half-wavelength, vertical, center-fed dipoles. Inter-element distance along y-direction is "*d*" and supplied by the user. Inter-element distance along x-direction is automatically set as "*d/2*". The lengths of the dipoles are set as "*d/4*". The excitation is a short pulse of modulated Gaussian function. The modulation signal and bandwidth is determined automatically to include frequencies for the first few resonances. The user may decide which row to excite; both, front row or back

row. These are all given by the user in the input file ANT.INP explained in Table 1.

Table 1. The ANT.INP and required parameters.

Row	Parameter
1	# of elements in X [1-2], # of elements in Y [1-6]
2	Inter-element distance along Y [m]
3	Excitation (0: Both rows, 1: Front Row, 2: Back Row)
4	Delay [sec]
5	Observation point for near fields (Obsx, Obsy, Obsz)
6	Pattern Plane [1-0] (1: Vertical Pattern, 2: Horizontal Pattern)
7	Angle [deg] PHI (for Vertical Pattern), Theta (for Horizontal Pattern)

In ANT.INP file, fourth line is reserved for time delay to allow the antenna array to steer its beam in azimuth. The calculation of this delay for an array to steer φ degrees from antenna bore-sight (from x-direction) is given in Fig. 9. Since the array is in free-space velocity of light (c) and inter-element distance (d) are used to calculate the delay (τ). This is the delay of the second element with respect to the first one. The third, fourth, etc. elements have delays of "2τ", "3τ", etc., respectively.

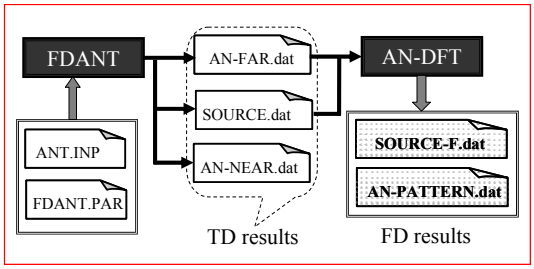

Figure 8. The flow chart of the FDTD-based antenna simulator FDANT. The package calculates radiation patterns of a given array by using broadband (pulse) excitation, near-field EM simulation inside the FDTD volume terminated by powerful perfectly matched layer (PML) blocks, near-to-far-field transformation directly in time domain, and finally by applying off-line DFT all around on a chosen radiation plane.

When the simulation is run, it first requires selection of (vertical or horizontal plane) radiation pattern. Then, angular resolution is supplied. If for example, horizontal plane radiation pattern is selected with 2° resolution, NTFF transformation is applied at 181 assumed directions (with 2° angular separation) inside the TD loop (although they are same, calculations at 0° and 360° are performed separately, only for graphical illustrations). The results are written to the output file AN-FAR.DAT. There are four columns in this file: These are the angle, time, E_θ and E_φ. If the number of time steps and angle are NSTOP and 181, respectively, then the number of lines will be NSTOP+200 for each angle with a total of 181×(NSTOP+200).

It should be noted that, extrapolated TD far fields are stored in a time array, and dimension of this array must be grater than the number of simulation time steps, NSTOP. This is due to TD far field extrapolation as explained in [10]. Here, 100 time cells are reserved for this transformation in front, and at the back of the array. This is why the total simulation time will be NSTOP+200.

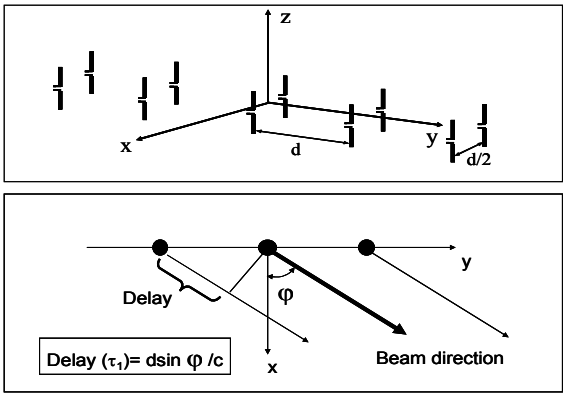

Figure 9. The location and parameters of the 2×5 of vertical, center-fed wire array; inter-element distance (along x-direction) is d/2, but inter-array distance (along y-direction) is d. The beam direction and the excitation delay to obtain this direction is also shown.

The user may select to use a short pulse or a single frequency sinusoidal excitation in TD simulations. Choosing a short-pulse, results in a broad band response with a single TD run. FDTD based simulation yields broad band response in time domain. Radiation patterns at multiple frequencies are computed by the Fortran program AN_DFT (it should be noted that source codes FDANT.FOR, FDANT.PAR and AN-DFT.FOR are also included, therefore any user who is familiar with the classical FDTD method can directly go into the codes and do the analysis of their own structures).

III. DESIGN EXAMPLES

Characteristic antenna structures are presented in this Section to discuss capabilities of the FDANT and NEC2 packages. Since FDANT uses 3D FDTD volume and NTFF transformation routine any kind of antenna structure can be simulated with this package. The only restriction is the computer memory and the speed,

therefore the larger the structure (or the higher the number of elements in the array) the higher the requirement for large memory and high-speed. With today's regular PC (e.g., with 1 GB RAM Memory) a cubical volume of $250\times250\times250$ (nearly 20 million cell volume) (i.e., $25\lambda\times25\lambda\times25\lambda$ volume with $\lambda/10$ rough discretization at the highest frequency) can be handled in a few minutes (with a 4-GHz-CPU speed).

NEC2 uses the coordinates of the antennas in 3D Cartesian coordinate system and represents wires with small pieces called *segments* (roughly with maximum segment lengths of $\lambda/10$). Any length of an array may be located as long as long as the number of segments is less than the number that can be handled via the PC at hand (e.g., less than ten thousand segments). An *N-segment* system is represented a linear system of equations with *N*-unknowns (i.e., segment currents) and *N*-equations. The MoM is a semi-analytical method which requires the Green's function of the problem at hand [6].

One should be aware of the assumptions and approximations made in and the limitations of the packages at hand. FDANT is based on discretization of 4D Maxwell's equations from very beginning; therefore it may be accepted as a reference solution (as long as parameters are chosen accordingly). On the other hand, NEC2 does not take the diffraction (secondary) effects into account.

Finally it should be remembered that FDANT simulates near EM transient fields in TD and then gives the radiation patterns in FD via the application of off-line DFT. NEC2 simulates far field interference effects of elements along a chosen direction in FD and yields the radiation pattern. Although time-consuming multi-frequency responses can be obtained via a single FDANT simulation, while NEC2 requires repeat ion of the calculations for every frequency.

3.1 Wire and loop (resonant) arrays (FDANT vs. NEC2)

Arrays of wire antennas in free-space are basic structures that can easily be handled via both FDANT and NEC2 packages. Two typical comparisons between FDANT and NEC2 are given in Figs. 10 and 11.

Very good agreement between results of the two methods is clearly seen in the plots. This should be expected because the structures are rectangular and contain no curvature, therefore discretization error is minimal. Note that the array can not steer beams beyond $\varphi=\pm45°$ as clearly observed in the figures. The beams formed in these figures are forward/backward symmetric with zero FBR. To direct energy forward the two corresponding elements in x-direction must be an end-fire property. At 250 MHz (i.e., inter-element distance along x is $\lambda/4$ and inter-array distance along y is $\lambda/2$) this may be satisfied by giving extra delay of $d/2c$ in FDANT (90° phase lag in NEC2). Fig. 12 shows the horizontal patterns for this scenario.

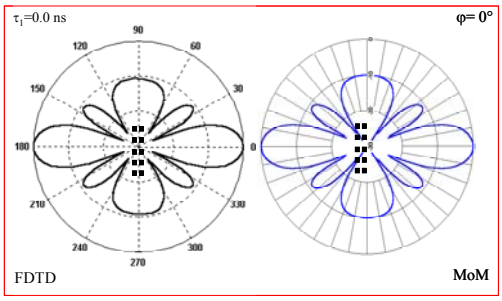

Figure 10. A sample radiation pattern of the 2×5 array on the xy-plane (f=250 MHz, d=λ/2, τ_1=0 s, θ= 90°,φ= 0°), left: FDTD, right: MoM (NEC2).

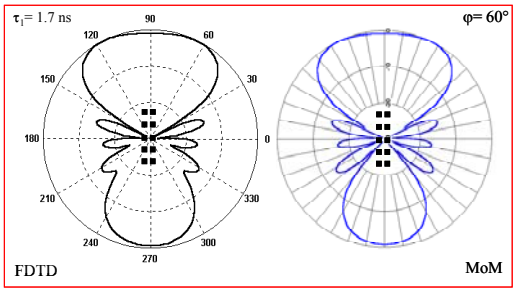

Figure 11. A sample radiation pattern of the 2×5 array on the xy-plane (f=250 MHz, d=λ/2, τ_1= 1.7 s, θ= 90°,φ= 60°), left: FDTD, right: MoM (NEC2).

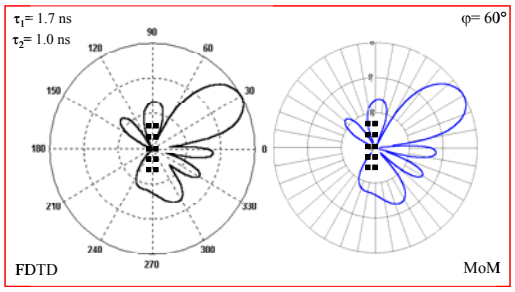

Figure 12. A sample radiation pattern of the 2×5 array on the xy-plane (f=250 MHz, d=λ/2, τ_1=1.7 s, τ_2= 1.0 s, θ= 90°,φ= 60°, 90° between the first and second rows), left: FDTD, right: MoM (NEC2).

Another structure used in FDANT and NEC2

comparisons is a 2×10 square loop array. Loop antennas form another antenna type, which features simplicity, low cost and versatility. In Fig. 13, the array is given. Each square loop is 0.25 m^2. By using 4 wires, 40 segments for each square loop, the array is modeled with a total of 800 segments in NEC simulator. With the same discretization ($\Delta x=\Delta y=\Delta z=2.5$ cm) the array needs an FDTD space of 50×230×50. At 300 MHz, the array correspond to loops with $\lambda/4$ sides and $\lambda/2$ inter-element separation. The simulated radiation patterns and steered beams obtained via both NEC and FDTD simulators are also given in the figure, where vertical field components are plotted.

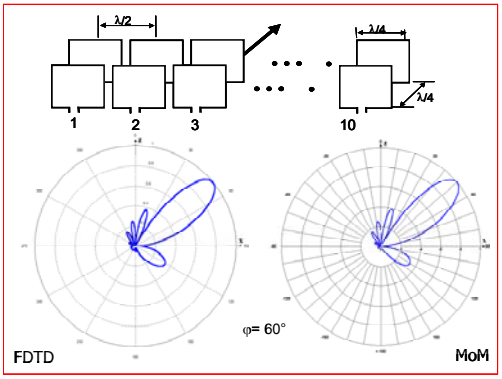

Figure 13. Another sample array of 2×10 rectangular wire antennas on the yz-plane (f=250 MHz, d=λ/2, τ_1= 1.7 s, θ= 90°,φ= 40°), left: FDTD, right: MoM (NEC2).

3.2 HFSWR arrays (NEC2)

High frequency surface wave radars (HFSWR) have become attractive systems for wide area (up to 500 km in range and 120° in azimuth) all-weather, continuous surveillance. HFSWR receive array is one typical example that belongs to large-system, complicated arrays. The array must be located near the sea, parallel to the shore line, have high and equal array gain over the entire surveillance area with minimum sensitivity to signals arriving from other directions (especially from ionosphere). Operating at the lower end of the HF band requires that the receive array occupies a significant shoreline area, with the aperture of the array inversely proportional to frequency. For example, at 3 MHz, a 5° azimuth beamwidth requires an array aperture of approximately 800 m - 1 km. Moreover, the receive array should direct its power towards the ocean surface, with high FBR, so that it neither interfere land based other systems, nor is interfered by them. To satisfy all these requirements first elements (i.e., channels) of the array shall be designed to

- form a maximum radiation along the channel axis with as much azimuth coverage as possible (typically 100° - 120°),
- give as high gain as possible (at least 2-3 dB)
- give as much FBR ratio as possible (at least 12-15 dB),
- give as deep over-head null as possible (at least 25-30dB).

To satisfy these requirements, three different structures (i.e., *quadlet*, *triplet* and *doublet*) are investigated as array channels [18]. In quadlet, four elements are spaced approximately quarter-wavelength apart and are phased to form an end-fire channel. Similarly, three and two elements are used in triplets and doublets, respectively. A short monopole is used as a channel radiator and a 16-radial ground screen layout is used underneath. Fig. 14 pictures the top view of the designs of these channels, where radials of different elements in a channel are connected to each other when intersect.

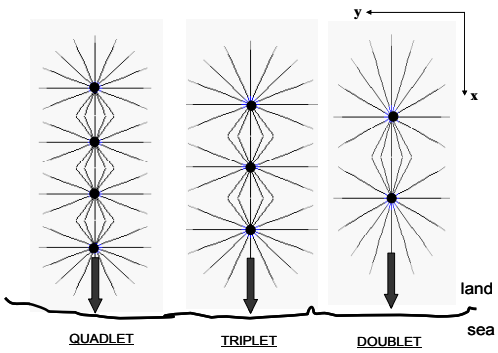

Figure 14. Top view of three different array elements of the HFSWR receiver; doublet, triplet and quadlet, located on the shore of the site, looking towards the sea. The array elements should satisfy high FBR. A ground screen (of 16-element radials) lowers the ground losses.

The channels are optimized for the frequency band of 3 MHz - 6 MHz. The parameters of the channels are listed in Table 2. Ground is assumed to be POOR (σ_g=0.003 S/m and ε_g =4.0). Parameters for the ocean are assumed to be ε_r=80.0, σ=5.0 S/m in NEC calculations, where EM shooting towards ocean surface is simulated. The difference between erecting the antennas over POOR ground or PEC surface may result in a reduction of gain by up to 15 dB. Beside this loss, there is also an extra near field propagation path loss because of the POOR ground.

Table 3 lists vertical electrical field strength and path loss at 1 km away from a 1 kW vertical radiator. It is

clear that, at 1 km distance; propagation loss over POOR ground may be 10-15 dB higher than the propagation loss over ocean surface. Therefore, together with the reduction in antenna gain, there may be a total of 30 dB extra loss just because the antenna elements are erected over POOR ground. A typical solution to overcome this problem is to use ground screen [19].

Table 2. HFSWR Receive array channel parameters.

Parameter	Value	
Antenna height	9.22	[m]
Element spacing	19.0	[m]
Element wire radius	0.15	[m]
Number of radials	16	
Radial wire lengths	19.0	[m]
Radial wire radius	0.001	[m]
Incremental increase in cable length	19.0	[m]
Phase velocity in electrical cable	0.84×c	[m/s]

Table 3. Field strength and path loss values of a vertical radiator with 1 kW transmitter power at 1 km distance (d=1 km, ε_g =15.0, f=3 MHz).

Conductivity [S/m]	Field Strength [dBμV/m]	Path Loss [dB]
0.0001	95.2	56.3
0.001	96.6	55.0
0.01	106.4	45.1
0.1	109.3	42.2
1.0	109.5	42.0
5.0	109.5	42.0

The channel elements discussed here are all bottom fed. The feeder cable losses are represented by voltage drops. The loss of the cable is given as 0.55 dB/100 ft at 10 MHz, therefore 0.5 dB/100 ft cable loss is taken into account within the band of 3 MHz - 6 MHz. For 19.0 m cable length voltage drop corresponds to 5 V. Therefore, elemental feeding voltages are taken as:

Quadlet: *100 V, 95 V, 90 V and 85 V*
Triplet: *100 V, 95 V and 90 V*
Doublet: *100 V and 95 V.*

Vertical and horizontal radiation patterns obtained via NEC2 simulations are given in Figs. 15 and 16. Here, the channels are located along x-axis. Vertical radiation patterns in Fig. 15 are obtained at xz-plane ($\varphi=0°$, $-90°<\theta<90°$).

On top comparisons of the three proposed channels is given at 4.5 MHz, at the bottom vertical patterns of the quadlet with and without ground screen (16-radial design) at 3.5 MHz. As shown in the figure almost 12-13 dB improvement is obtained in the channel gain when radials are used. However, employment of a ground screen can be seen to have had a negative effect on direct overhead nulling. The surface-wave coupling effect (for the array 50 m away from the shore line) is also plotted (see the dotted line).

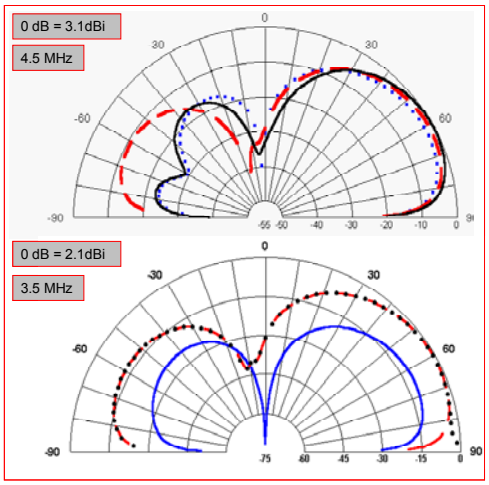

Figure 15. NEC2 simulated vertical radiation patterns of the array elements shown in Fig. 14; (Top) comparisons among the channels (f =4.5 MHz, φ=0°, 0 dB corresponds to 3.1 dBi). Dots: doublet, Dashed: triplet, Solid: quadlet. (Bottom) quadlet with and without radials, solid: without radials, dashed: with radials, dots: surface-wave coupling at 50 m away from the shore line (f= 3.5 MHz, φ=0°, 0 dB corresponds to 2.1 dBi). More than 30 dB overhead null is satisfied.

Horizontal radiation patterns in Fig. 16, comparing the three proposed channels at left, and the quadlet with and without radials at right) are plotted 5° above xy-plane (θ=85°, 0°<φ<360°). As observed in Figs. 15 and 16, quadlet, triplet and doublet as receive array channel elements have similar channel gain and FBR at this frequency. On the other hand, vertical and horizontal back lobe shapes and overhead nulling effects are quite different.

One HFSWR receive array is designed as a 24-channel array by using quadlets [18]. Inter-channel distances are taken as 31 m. With these parameters, a rectangular area of 57 m × 713 m is required only for the 4×24 monopoles. With ground screen and a security fence this area may be as large as 100 m × 1000 m. The connections between channels are done via underground cables and their lengths are very important since they introduce signal attenuation and phase distortion. Horizontal radiation patterns and electronic beam forming are simulated and illustrated in Fig. 17

for different beam pointing angles. Here, patterns with beam angles 0°, 15°, 55° towards right and -15°, -30° and -60° towards left are plotted. As observed in the figure, for the 0° beam the array has nearly 5° beam width, 30 dB FBR and more than 20 dB side lobe suppression. These performance parameters are almost satisfied for the beams within ± 45°. Acceptable values are obtained when the beam is within ± 45°. On the other hand, unwanted strong side lobes appear when the beam angle is higher than ± 45° (see the 55° and - 60° beams in the figure).

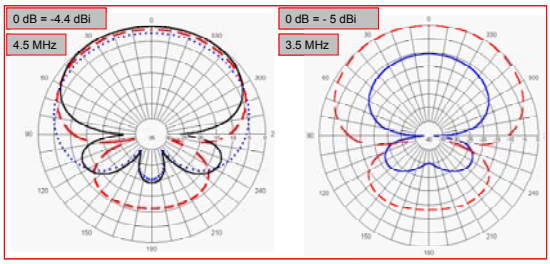

Figure 16. NEC2 simulated horizontal radiation patterns of the array elements shown in Fig. 14; (left) comparisons among the three channels (f = 4.5 MHz, θ=90°, 0 dB corresponds to – 4.4 dBi). Dots: doublet, Dashed: triplet, Solid: quadlet, (right) quadlet with and without ground screen layout, solid: without radials, dashed: with radials (f= 3.5 MHz, θ=90°, 0 dB corresponds to - 5 dBi). The front beam characteristics of the array elements do not change significantly.

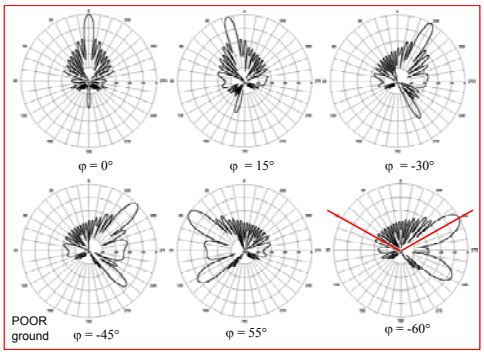

Figure 17. NEC2 simulated horizontal radiation patterns of the 4×24 element monopole array designed for the HFSWR receiver with beam steering capabilities (f= 3.5 MHz, θ=90°).

HFSWR is an all-whether, continuous system, and very often one or more channels fail to operate. The operator should know what happens when one or more channels are not working properly. This is simulated in NEC2 and typical results are plotted in Fig. 18. In the 24-channel array, the channels are numbered 1 to 24 from left to right. The blanked channels are (left) 7-9-10, (right) 11-12-13 in the figure. The thin and thick lines correspond to 24-channel beam forming with and without blanked channels, respectively.

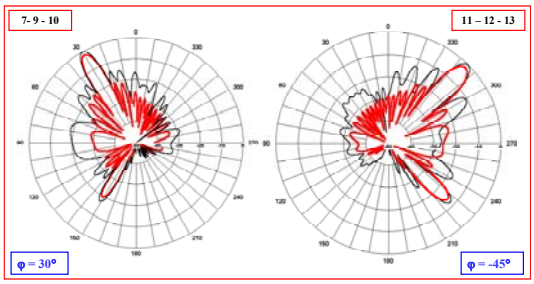

Figure 18. NEC2 simulated channel failure effects of the 4×24 element monopole array designed for the HFSWR receiver (f= 3.5 MHz, θ=90°), The top numbers represent the failed channels.

It should be noted that NEC2 does not model diffraction; thus attention must be paid in interpreting its numerical results. Differences above 30 – 35 dB may be practically meaningless because of the diffraction. The example presented in this subsection may also be simulated via the FDTD simulator, but it requires an NTFF transformation module for a two-layer volume (the one supplied in FDANT is designed for free-space).

IV. CONCLUSIONS AND DISCUSSIONS

Three different packages are reviewed in this paper. A simple user-friendly antenna array package ANTEN_GUI prepared with Matlab 6.5, the well-known, public domain NEC2 package, and the FDTD-based FDANT package are presented together with some practical array examples that illustrate their capabilities and inefficiencies. Characteristic designs are also given for mutual comparisons.

Roughly speaking, a few tens of millions of cells may be simulated in FDTD in the order of minutes (much less than an hour) with today's regular PC (e.g., 512 MB RAM 1-2 GHz CPU speed), and most of the time is used for NTFF process (there is at least an order of magnitude difference between the FDTD simulation and NTFF transformation). MoM-based calculations may also be performed in the same PC with similar computation time if the number of segments is less than 2300-2500. Some other critical parameters and comparisons are given in Table 4.

It should be noted that there are highly impressive commercial antenna packages that have been widely used in industry, which may be listed through a quick

internet search. Although it is very handy to use these packages as antenna engineers for design purposes, people should never forget to practice with their own codes if they do research. It may be claimed that practicing with in-house prepared codes first shall also increase performances while using commercial codes.

Table 4. Performance comparisons; FDTD vs. NEC

EVALUATION PARAMETER	FDAND (FDTD)	NEC2 (MoM)
Full wave solution	Accounts for major wave phenomena	Diffraction effects can not be handled
Analytical derivation	Not required	Requires derivation of Green's function
Critical parameter	Cell size & time step (discretization)	Segment in terms of wavelength
Assumptions	Everything is constant inside a cell	Current is constant along the segment
Capability	Broad class of EM problems (antennas, propagation, RCS, EMC, EMI, etc.)	Certain class of antenna and RCS problems
Stability	May be instable (iterative open-form representation)	Always stable (closed-form representation)
Convergence	Not a problem (as long as stability condition is satisfied)	May be a problem (depending on segmentation)
Computation time	Increases parallel to the # cells	Increases parallel to the # segments
RAM Memory	Huge; increases parallel to the # of cells	Medium; increases parallel to the # segments)
Problem structure	Good for every kind of media	Good for only metallic structures
Geometry error	Should fit into the coordinate system	No restriction (but elements must be inside the coupling region)
Broadband evaluation	Can be obtained with a single-run	Indirectly, requires multi-runs
Beam forming / steering	Controlled via time delay in excitation	Controlled via element phasing

REFERENCES

[1] E. Jordan and K. G. Balmain, *Electromagnetic Waves and Radiating Systems*, Prentice-Hall, Englewood Cliffs, NJ 1950.

[2] J. D. Kraus, *Antennas*, 2nd Ed., MacGraw-Hill Book Co., NY 1988.

[3] C. A. Balanis, *Antenna Theory - Analysis & Design*, 2nd Ed., John Wiley and Sons, Inc., NY 1997.

[4] R. E. Collins, *Antennas and Radiowave Propagation,* MacGraw-Hill Book Co., NY 1985.

[5] W. L. Stutzman and G. A. Thiele, *Antenna Theory and Design, 2nd Ed.,* John Wiley and Sons, Inc., NY 1998.

[6] R. F. Harrington, *Field Computation by Moment Methods*, New York, The Macmillan Co., 1968.

[7] G. J. Burke and A. J. Poggio, "Numerical Electromagnetic Code-Method of Moments, Part I: Program Description, Theory," Technical Document, 116, Naval Electronics System Command (ELEX 3041), July 1977.

[8] Visit http://members.home.net/nec2/ and http://www.emlib.jpl.nasa.gov.

[9] Visit http://www.nittany-scientific.com or http://www.poynting.co.za .

[10] L. Sevgi, *Complex Electromagnetic Problems and Numerical Simulation Approaches*, IEEE Press – John Wiley and Sons, NY 2003.

[11] L. Sevgi and Ç. Uluışık, "A Matlab-based Visualization Package for Planar Arrays of Isotropic Radiators," *IEEE Antennas and Propagation Magazine*, Feb 2005.

[12] B. R. Mahafza and A. Z. Elsherbeni, *MATLAB Simulations for Radar Systems Design*, Chapman and Hall/CRC Press, 2003.

[13] J. C. Bregains, F. Ares, and E. Moreno, "Visualizing the 3D Polar Power Patterns and Excitations of Planar Arrays with MATLAB," *IEEE Antennas and Propagation Magazine*, Vol.46, No.2, pp.108–112, Apr 2004.

[14] K. S. Yee, "Numerical solution of initial boundary value problems involving Maxwell's equations," *IEEE Transactions on Antennas and Propagat*, Vol.14, No.3, pp.302-307, May 1966.

[15] L. Sevgi and S. Paker, "FDTD Based RCS Calculations and Antenna Simulations," *AEU, International J. of Electronics and Commun.*, Vol.52, No.2, pp.65-75, Mar 1998.

[16] L. Sevgi, "HF Wire Antenna Array Design via FDTD and MoM Techniques," *IEEE Canadian Conference on Electrical and Computer Engineering*, May 9-12, 1999, Alberta, Canada.

[17] G. Cakir and L. Sevgi, "Design, simulation and test of a low-cost microstrip patch antenna arrays for the wireless communication," Special issue of

ELEKTRIK, Turkish J. of Electrical Engineering and Computer Sciences, Vol. 13, No.1, pp.93-104, 2005.

[18] L. Sevgi, A. M. Ponsford, and H.C. Chan, "An Integrated Maritime Surveillance System Based on Surface Wave HF Radars, Part I – Theoretical Background and Numerical Simulations," *IEEE Antennas and Propagation Magazine*, Vol.43, No. 4, pp. 28-43, Aug 2001.

[19] A. M. Ponsford, L. Sevgi, and H.C. Chan, "An Integrated Maritime Surveillance System Based on Surface Wave HF Radars, Part II – Operational Status and System Performance," *IEEE Antennas and Propagation Magazine*, Vol.43., No.5, pp.52-63, Oct 2001.

Levent Sevgi was born in Akhisar, Turkey in 1958. He received his B.S., M.S. and Ph.D. degrees in EE from Istanbul Technical University (ITU) in 1982, 1984 and 1990, respectively. In 1987, he was awarded a fellowship that allowed him to work with Prof. L. B. Felsen at Weber Research Institute/New York Polytechnic University York for two years. His work at the Polytechnic concerned the propagation phenomena in non-homogeneous open and closed waveguides. He became assistant (ITU), associate (ITU) and full professor (Doğuş University) in 1991, 1996 and 2002, respectively.

He was with the Center for Defense Studies, ITUV-SAM for the Long Horizon Project – Integrated Maritime Surveillance System – studies of the Turkish Navy during 1993-1997. He was with the Scientific Research Group of Raytheon Systems Canada from Sep 1998 till Jun 1999 for surface wave HF Radar based Integrated Maritime Surveillance System trials. By invitation, he joined TUBITAK-MRC, Information Technologies Research Institute as the Chair of Electronic Systems Department and spent two years from Jun 1999 till Aug 2000. He was also with ITUV-SAM for Vessel Traffic System installation for Turkish Straits during 2000 - 2002. Since Feb 2002, he has been with ECE Department of Engineering Faculty of Doğuş University in Istanbul.

His research study has focused on propagation in complex environments, analytical and numerical methods in electromagnetics, EMC/EMI modeling and measurement, radar systems, surface wave HF radars, radar cross section modeling and bio-electromagnetics. He is a senior member of IEEE and a member of Turkish Chamber of Electrical Engineers (EMO).

He is the author or co-author of more than 100 journal and international conference papers, 6 books (1 in English, 5 in Turkish), and 2 book chapter.

Modeling Large Phased Array Antennas Using the Finite Difference Time Domain Method and the Characteristic Basis Function Approach

(*Invited Paper*)

Nader Farahat*, Raj Mittra, and Neng-Tien Huang****
*Polytechnic University of Puerto Rico
P.O. box 192017 San Juan, PR 00919
**The Pennsylvania State University, 319 EE East
University Park, PA, 16802, USA

***Abstract*–**In this paper we describe an approach for solving large phased array problems, using the Characteristic Basis Function Method (CBFM) in conjunction with the Finite Difference Time Domain (FDTD) technique. The method is especially tailored for solving large arrays that may be covered with Frequency Selective Surfaces (FSSs). Several illustrative examples are provided and the results are validated for a number of test cases. This is accomplished by comparing the results derived by using the proposed technique with those obtained via a direct simulation of the entire array on a PC cluster. Of course, the direct problem places a heavy demand on the computer resources, especially as the problem size becomes large. In contrast to the direct method, the increases in the simulation time and the burden on the computer memory are incrementally small in the present approach, as the problem size is increased from moderate to large.

I. INTRODUCTION

Numerical modeling of large but finite phased array antennas is a challenging problem because it places a heavy burden on the computer resources, especially when the array element is complex, and the antenna operates in a close proximity of an FSS radome whose period is not commensurate with that of the array. The array element is typically a microstrip patch, a Vivaldi or a waveguide, and the antenna may be covered by an FSS radome, whose elements may be patches, slots, cross-dipoles, etc., typically different from those of the array. Accurate prediction of the performance of such complex antenna systems is a very challenging problem indeed.

The Finite Difference Time Domain (FDTD) [1] method has proven to be a robust technique for modeling a wide variety of electromagnetic systems. In addition to its versatility and ability to handle complex geometries, it has the added advantage of being able to obtain the response of a device over a wide band of frequencies from a single run. Although the parallelization of the FDTD enables us to solve large problems using distributed processing, it is still desirable to reduce the solve time and memory requirements, whenever possible. Recently, the Characteristic Basis Function Method (CBFM) has been proposed as a technique for fast and accurate modeling of large structures both for scattering and radiation problems, and has been tailored for both the Method of Moments (MoM) and the FDTD [2-5]. The CBFM utilized in this work is based on the localization of the fields by using certain types of excitations to generate a set of basis functions with which to synthesize the solution to the original problems.

In this paper we extend the application of the CBFM to the problem of analyzing large phased array antennas, taking into account of the inter-element mutual coupling, which is often ignored in approximate methods—such as the pattern multiplication technique—in order to render the problem manageable. The validation is carried out by comparing the CBFM-based results with those obtained by using the parallel version of the FDTD (PFDTD) on a cluster. It should be mentioned that the use of the CBFM allows one to solve much larger problems than would be possible by using the direct method, at little or no extra cost beyond that needed to solve of a moderate-size problem, which can be conveniently handled by using the PFDTD code, because of its manageable size. In addition, we show how the discrete phase progression of antenna elements which is modeled in the FDTD has a significant effect on the accuracy of the resulting far-field patterns.

II. THE CBFM TECHNIQUE

To further explain the underlying concepts of the CBFM for arrays, we start with an example of a 21 by 21 rectangular waveguide array, shown symbolically in Fig. 1.

Fig. 1. Illustration of 21 × 21 rectangular waveguides. The picture symbolically shows the TE_{10} mode excitation in each waveguide.

Each element of the array is excited in a TE_{10} mode. The entire array is simulated by using the FDTD method and the electric field distribution at the frequency of operation in the aperture of the waveguides are derived (see Fig. 2 that shows the co-polar components). We observe that the distribution of the fields at the edges and corners differs from those in the center region. Hence, we note that the inherent assumption in the pattern multiplication approach, namely that all the elements are identical, is not really valid. Next, we investigate the case where only the center element of the same array is excited. We see from Fig. 3 that the effect of the inter-element mutual coupling is extended up to a few neighboring elements and is relatively strong in the E-plane (vertical direction) as compared to the H-plane (horizontal direction). Next, we argue that in the center region the field distribution only shifts in space (Fig. 4) as we move the location of the excitation source. We refer to these aperture distributions as the CBFs. We note that for the center region, the CBFs are relatively invariant to the location of the excitation source. Hence, we can bypass a considerable amount of computation involved in the generation of the CBFs by taking advantage of this feature. We can also use the localization approach to generate the CBFs for the edge and corner regions, and can reduce the computation time for these CBFs again by avoiding the duplicate calculations.

Once the CBFs have been constructed, we can synthesize the aperture field of the array via superposition, as shown in Fig. 5.

Assuming that the array is mounted in a metallic frame, we can assume that the fields external to the array vanish in the plane of the array. We can then perform a near-to-far-field transformation to compute the pattern of the array. If we make the further assumption that the

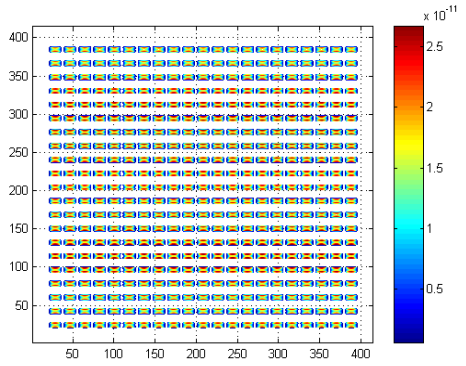

Fig. 2. Distribution of the co-polar component of the electric field in the opening of the 21 × 21 rectangular waveguides.

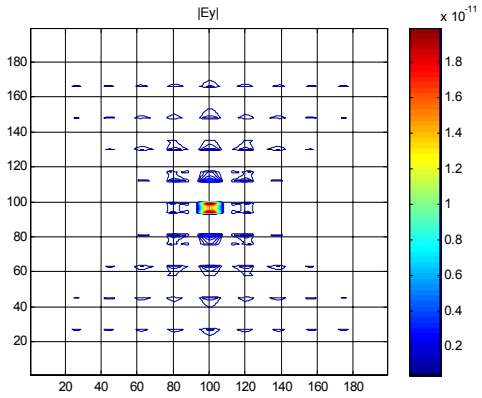

Fig. 3. Distribution of the co-polar component of the electric field in the opening of the 9 × 9 rectangular waveguides when only the center element is excited.

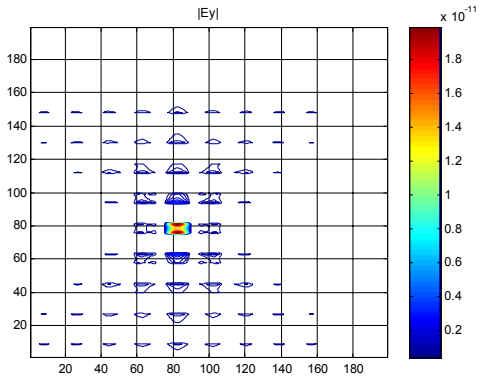

Fig. 4. Distribution of the co-polar component of the electric field in the opening of the 9 × 9 rectangular waveguides when only the next to the center element is excited.

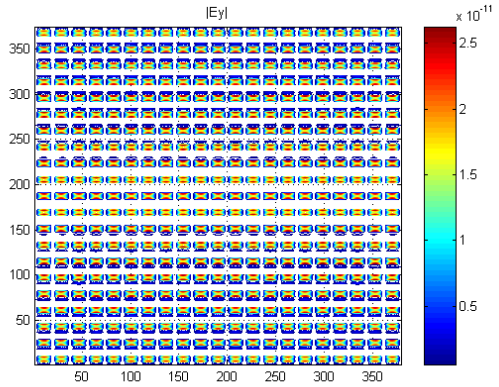

Fig. 5. Distribution of the co-polar component of the electric field in the opening of the 21 × 21 rectangular waveguides reconstructed after proper shift and superposition.

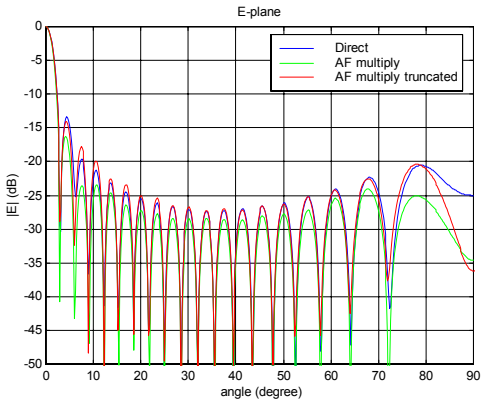

Fig. 6. E-plane far-field pattern of the 21 × 21 waveguide array obtained by using different techniques.

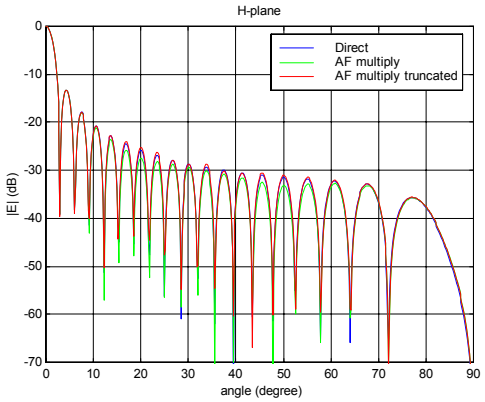

Fig. 7. H-plane far-field pattern of the 21 × 21 waveguide array obtained by using different techniques.

behavior of the aperture fields remains relatively unchanged when we move the source from one waveguide to another, even when we are close to edge, or a corner, we can construct the aperture field by simply shifting, superposing and, finally, truncating the synthesized aperture fields to within the interior of the metallic frame. The above procedure can be implemented equally well in the spectral domain by superposition of the spectral transforms of CBFs. However, at the end, it becomes necessary to perform a convolution of the resultant with a window function, which is equivalent to truncating the fields in the region external to the array aperture in the spatial domain approach. We have found that the first approach (spatial domain) is simpler to implement than its counterpart in the spectral domain.

Next, we present in Figs. 6 and 7 the far-field patterns, for the E- and H-planes, respectively, derived by using the different techniques. We see that the effect of mutual coupling is insignificant in the H-plane and that the pattern multiplication, though approximate, yields results with reasonably good accuracy in this plane. This is consistent with the results shown in Figs. 3 and 4, in which the coupling in the horizontal plane is seen to be weak. However, the pattern multiplication approach is no longer accurate in the E-plane, and the improvement in accuracy in the CBFM results over the pattern multiplication method is evident in this plane.

We now summarize the CBFM as applied to the large but finite array problems. We begin in this method with the modeling of a moderate-size array, which is only large enough to capture the mutual coupling effects associated with the excited element. Once we have derived this aperture field, we can generate the results for the larger sizes of the array by shifting, superposing and truncating the above aperture field. We mention, once again, that an extrapolation of the solution from a moderate to a large-size array only requires a trivial amount of additional computational effort and memory usage, and the accuracy of the results improves as well. These are unique and very desirable features of the CBFM, not readily found in other approaches.

III. BEAM SCANNING CASE

We now go on to show in this section that the method, described above, can be used for beam scanning as well. The only modification needed is the addition of appropriate phase shift to the CBFs to account for the progressive phase shift introduced in the array elements to enable the array to scan. To illustrate the application of the CBFM to this case, we consider the example of a 9 x 9 array of waveguides and use the procedure for synthesizing the aperture field to obtain the results for a 21 x 21 array with 60 degree progressive phase shift of the elements along the H-plane, which corresponds to an 11 degree scan. The aperture field synthesis is accomplished by simulating the 9 x 9 array when only the center region

is excited, followed by aperture translation, introduction of the phase progression, superposition, truncation, etc., and, finally, the near-to-far-field transformation. Figure 8 shows the comparison of the CBFM results with that obtained by using the direct simulation of array 21 x 21 by FDTD, in which the progressive "time delay" has been added in the excitation of the elements corresponding to the 60 degree progressive phase at the frequency of interest.

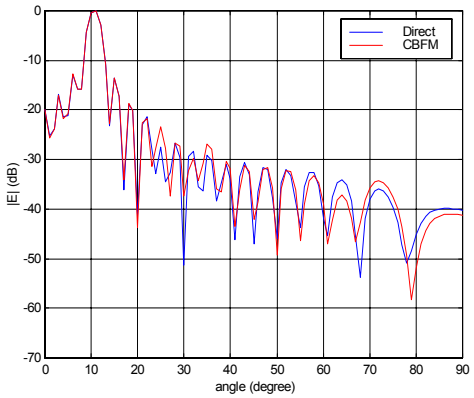

Fig. 8. H-plane far-field pattern of 21 × 21 rectangular waveguides (H-plane 60 degree progressive phase).

The difference between the direct solution and the CBFM result is evident in this case. A close examination of the source of the error reveals that it is the discretization in the time delays introduced in the FDTD excitation that is responsible for this error, and this leads us to conclude that we need to enforce the time delay more precisely in the direct method to obtain the results with the desired accuracy. To mitigate the phase error problem, we need to deliberately decrease the time step to a value smaller than that dictated by the Courant condition from stability considerations. We illustrate this fact by referring to Fig. 9, which shows the linear phase taper introduced in the FDTD simulation along the 21 elements in the H-plane (Fig 9). Next, in Fig. 10, we plot the deviation from the ideal linear phase for two cases: (i) Courant-based time-step; (ii) one-half of Courant-based time-step. We observe that decreasing the time step has the effect of reducing the error in phase shift from 10 to 4 degrees, and the resulting improvement in the corresponding the patterns is evident from Fig. 11. Figure 12 shows that the phase shift error can be further reduced by choosing smaller time steps and, as expected, this helps reduce the deviation of the pattern from the expected exponential decrease of the side lobes (see Fig. 13).

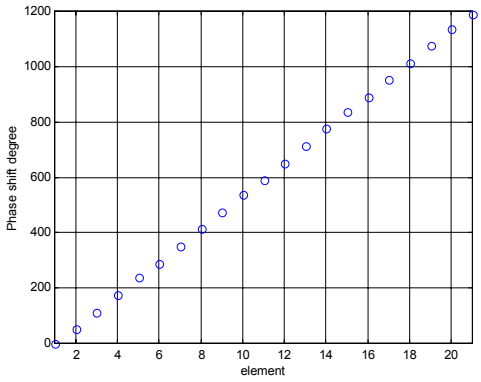

Fig. 9. Linear phase taper introduced in the FDTD simulation.

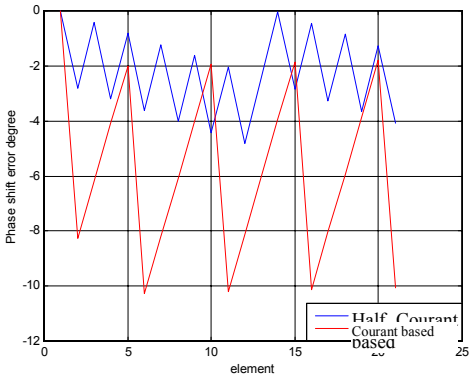

Fig. 10. Reduction of the phase errors when the time step is shortened by a factor of two from that of the Courant condition.

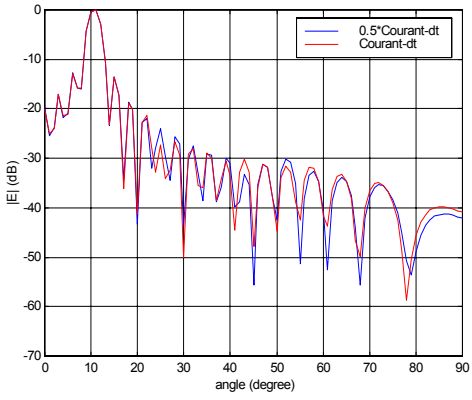

Fig. 11. Change in the Pattern with the reduction in the time step.

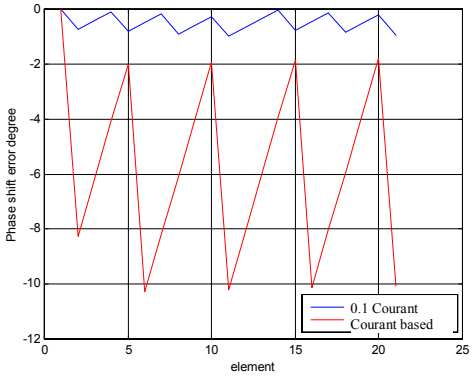

Fig. 12. Further reduction of the phase error when the time step is 0.1 of Courant condition.

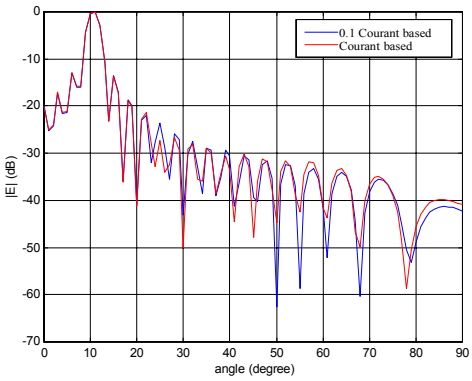

Fig. 13. Comparison between the patterns with time delay equal to 0.1 Courant condition and that obtained by using CBFM.

It is worthwhile mentioning here that it is not necessary to significantly reduce the time step--which leads to a long simulation time--if we are only interested in modeling the array single frequency at a time. This is because we can always find an adjusted time-step, which is not much smaller than the Courant-based time-step, whose integral multiple equals the required time delay, and whose use essentially eliminates the phase errors. For instance, in the previous example, we can choose a time step that equals 0.9432 of the Courant time-step so its integral multiple is exactly equal to the time delay. The maximum error between the elements then reduces to levels below a few thousandth of a degree as shown in Fig. 14, and the pattern (see Fig. 15) is identical to that obtained by using a time-step equal to a tenth of the Courant-based time step. Note that, with this modification in the direct FDTD solution, we again obtain an excellent agreement (see Fig. 16) between it and the CBFM, albeit for a fixed frequency. (The time step has to be reset as the frequency is changed in order to maintain the accuracy of the direct solution).

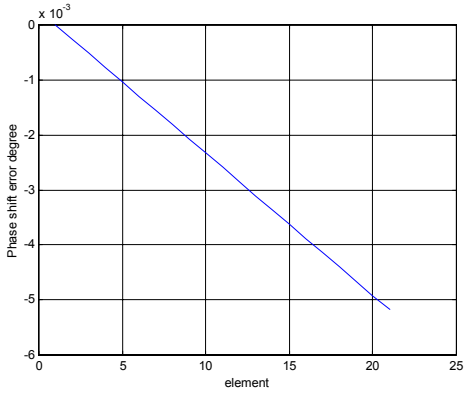

Fig. 14. Phase error for the time step of 0.9432 of Courant condition.

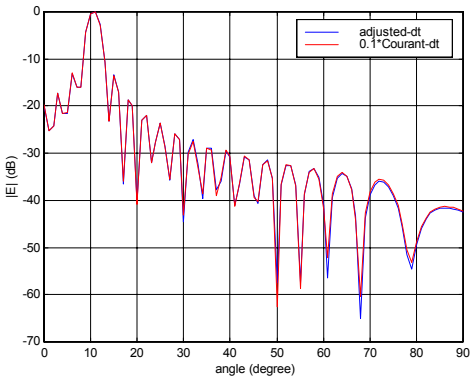

Fig. 15. Comparison between the patterns with time steps equal to 0.9432 and 0.1 Courant condition.

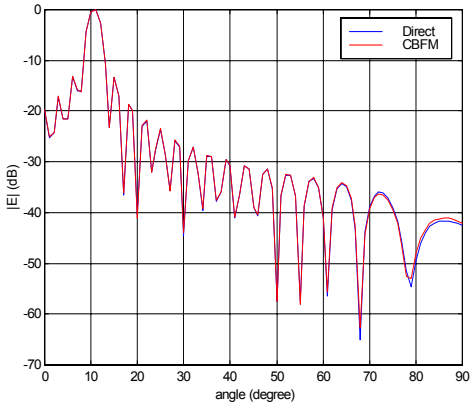

Fig. 16. Comparison between the direct H-plane pattern employing 0.9432 Courant for the time step and that generated by CBFM.

On the basis of the above study, we conclude that one has to be careful while generating the direct solution during the process of validating the CBFM result to ensure that the former is sufficiently accurate.

Of course, we realize that the above phase error problem would not exist if we were to carry out the simulation in the frequency rather than in the time domain.

Earlier we had mentioned that the CBFM technique does not suffer from the phase error because the phase shifts are introduced directly and precisely in the aperture. However there is an exception to the above statement that we should bring to the attention of the reader. The phase error may also exist in the CBFM analysis, unless the time delay is adjusted to minimize or eliminate it, when we derive the aperture basis functions by exciting a cluster of elements in the array, rather than a single one. As detailed in the next section, this type of excitation is employed, for instance, when we are modeling composite arrays, comprising of phased array antennas covered with FSS radomes, whose periods are dissimilar. For this configuration, we excite a macro-unit cell of the antenna-radome composite to generate the basis functions, and we introduce a progressive time delay for the scan case within this macro-cell. We reiterate that this error does not exist for the case of single element excitation and, more importantly, when we extend the results from a moderate array to a larger one using the CBFM, since it carries out the phase shifting artificially, independent of the FDTD simulation.

IV. COMPOSITE ARRAYS

For the last example, we apply the CBFM to a composite array structure, comprised of phased array antenna covered by an FSS radome, depicted symbolically in Fig. 17. It shows a waveguide array covered by a loop-type FSS radome, and we note that the periodicities of the two are not the same.

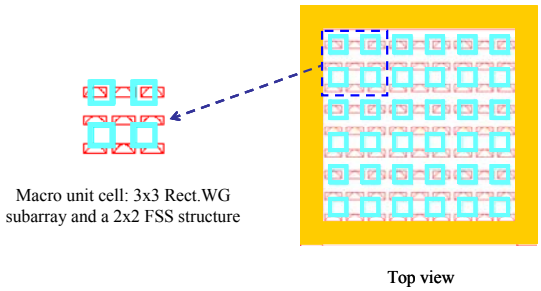

Fig. 17. Illustration of the 3 x 3 array of waveguide-with-FSS macrocell.

To tackle this problem using the CBFM, we define a macro-unit containing 3 x 3 waveguide array, covered by the 2 x 2 loop array. To implement the CBFM for this problem, we again simulate a moderate-size array of 3 x 3 macro-unit cells, and then use the result of this simulation to synthesize the aperture distribution of a larger array comprising of 441 waveguides. In the simulation of the 3 x 3 macro-unit cells we have to excite the waveguides of the center macro-unit cell in the progressive time delay in order to scan 11 degrees along the H-plane. As explained in the previous section, to achieve the required accuracy we need to adjust the time step such that an integral multiple of this step exactly equals the required time delay for the corresponding beam scan at the frequency of interest. Once again, to validate the CBFM result, we carry out a direct simulation of the entire array using a parallel FDTD code running on a cluster of computers. Similar to the previous example, we adjust the time step for the required time delay. The comparison between the two results, shown in Fig. 18, demonstrates that the CBFM results are quite accurate. We reiterate, once again, the fact that the extension to larger arrays merely requires a post-processing of the data obtained previously, and does not require additional simulation that can be time-consuming. Fig. 19 verifies the above statement and shows that the patterns obtained by CBFM and direct simulation for a 3969 waveguide array are in good agreement with each other. It goes without saying that direct simulation is very expensive to obtain for this large problem, as it requires sizable computational resources in terms of CPU time and memory. On the other hand, the CBFM can handle arbitrarily large arrays with little difficulty, and with only a slight increase in the computational burden.

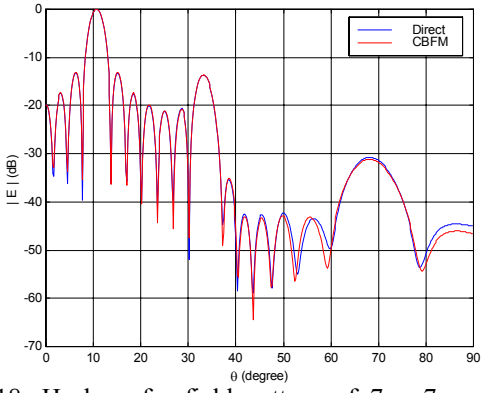

Fig. 18. H-plane far field pattern of 7 x 7 array of waveguide-with-FSS macrocell (441 waveguide elements).

We close this section with one final comment on the slight differences between the direct and CBFM results for wide angles that are present in the pattern plots appearing in both Figs. 18 and 19. Our experience shows that, for large problems being simulated directly, it becomes necessary to extend the size of the computational domain in the vertical direction in order to reduce the spurious reflections from the top surface of the perfectly matched layer (PML) boundary that

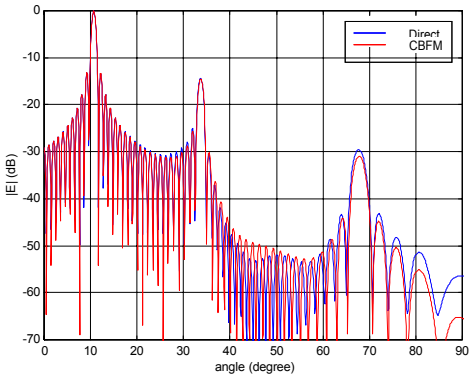

Fig. 19. H-plane far field pattern of 21 x 21 array of waveguide-with-FSS macrocell (3969 waveguide elements).

introduce errors at wide scan angles. Obviously, moving the PML boundary further away increases the problem size even more in the direct simulation case, and often renders the problem unmanageable. However, we note that the levels of these spurious reflections from the PML boundaries are much lower in the CBFM, since the simulation is carried out for a much smaller geometry than in the direct simulation. In fact, we have found that, for large problems, the CBFM results can be more accurate than the direct solution, especially at wide angles.

V. CONCLUSION

In this paper we have presented a novel approach, based on the Characteristic Basis Function Method (CBFM), for solving large phased array problems that may be covered with an FSS radome. A key feature of the method is that it builds on the solution of a moderate-size problem, which is manageable in terms of CPU memory and time, to construct the solution of a much larger problem, with little extra computational effort. Numerous representative examples have been included in the paper to validate the proposed approach, both for phased arrays and array-radome composites. Although not discussed in this paper, the CBFM has been useful for solving large-body scattering problems as well, including radar targets and antennas mounted on complex platforms.

References

[1] Yee, K. S. "Numerical solution of initial boundary value problems involving Maxwell's equation in isotropic media," *IEEE Trans. Antennas and Propagation*, Vol. 14, 1966, pp. 302-307.

[2] R. Mittra, "A Proposed New Paradigm for Solving Scattering Problems Involving Electrically Large Objects using the Characteristic Basis Functions Method," *Proceedings of the International Conference on Electromagnetics in Advanced Applications (ICEAA)* 2003, Turin, Italy, pp. 621-624, Sep. 2003.

[3] R. Mittra, "Solution of Large Array and Radome Problems using the Characteristic Basis Function Approach," *IEEE Antennas & Propagation Society International Symposium/URSI*, Columbus, Ohio, June 2003.

[4] H. E. AbdEl-Raouf, R. Mittra, and J.-F. Ma, "Solving Very Large EM Problems (109 DoFs or Greater) Using the MPI-CBFDTD Method," *IEEE International Symposium on Antennas and Propagation and USNC/URSI National Radio Science Meeting* (AP-S'05), July 3-8, 2005.

[5] T. Su, L. Ma, N. Farahat, and R. Mittra, "Modeling of a Large Slotted Waveguide Phased Array Using the FDTD and Characteristic Basis Function (CBF) Approaches," URSI'03, June 22-27, 2003.

Nader Farahat is Associate Professor in the Electrical Engineering Department of Polytechnic University of Puerto Rico. He is also adjunct research associate at the Pennsylvania State University.

Neng-Tien Huang recently completed his Ph.D. program in Electrical Engineering at the Pennsylvania State University, and is currently serving as an intern at Intelligent Automation Incorporated (IAI) in Rockville, Maryland.

Raj Mittra is Professor in the Electrical Engineering department of the Pennsylvania State University and the Director of the Electromagnetic Communication Laboratory. He is also the President of RM Associates, which is a consulting organization that provides services to industrial and governmental organizations, both in the U. S. and abroad.

Direction of Arrival Estimation in a Multipath Environment: an Overview and a New Contribution

(*Invited Paper*)

Ebrahim M. Al-Ardi, Raed M. Shubair, and Mohammed E. Al-Mualla

Etisalat College of Engineering,
P.O.Box: 980, Sharjah, United Arab Emirates
Tel: +971 6 5611333, Fax: +971 6 5611789
E-mail: {rshubair, almualla}@ece.ac.ae

***Abstract* —** This paper proposes a new computationally efficient algorithm for direction-of-arrival (DOA) estimation in a multipath environment using a uniform linear array (ULA) of equispaced sensors. The paper starts by presenting a comprehensive overview of the classical MUSIC algorithm used for DOA estimation of uncorrelated signals. The effect of different factors related to the signal environment as well as the sensor array is investigated. The concept of spatial smoothing required in the case of correlated signals encountered in multipath propagation environments is then discussed. This then leads to the development of a new computationally efficient DOA estimation algorithm that is proposed for a multipath environment with unknown correlated signals. The algorithm comprises two stages: a first stage for discriminating uncorrelated signals, and a second stage for resolving the directions of arrival of correlated signals using covariance differencing and iterative spatial smoothing. Simulation results show that the proposed algorithm operates at a much lower computational cost compared to standard methods. The proposed algorithm also offers a hardware saving by reducing the number of sensors required to detect a given number of signals.

I. INTRODUCTION

The area of signal processing using sensor arrays to estimate the directions of radio signals has drawn considerable interest in recent years. This is due to the opportunities that this area offers in satisfying the increasing demand of wireless communication networks for higher capacity, larger coverage areas, and lower interference effects. Direction-of-Arrival (DOA) estimation methods based on eigen value evaluation of the signal covariance matrix are known to have high-resolution capabilities and yield accurate estimates [1]. The MUltiple SIgnal Classification (MUSIC) algorithm, proposed by Schmidt [2, 3], is an example of these methods that gained most of the research interest since it uses an accurate data model with a sensor array of arbitrary form. Section II of this paper highlights the concept of adaptive antenna arrays, or what is known as smart antennas, and the benefits that they offer for wireless communication systems. Section III demonstrates the sensor array geometry and the signal model used to develop the DOA estimation algorithm. Detection of radio signals incident on a uniform linear array (ULA) of equi-spaced sensors using the MUSIC algorithm is illustrated in Section IV. This section also provides a performance evaluation of MUSIC by studying the effect of changing parameters related to the signal environment, as well as the sensor array. Section V explains the concept of using spatial smoothing for the detection of correlated signals encountered in practical multipath propagation environments. Performance evaluation of classical spatial smoothing methods is also presented. Finally, Section VI proposes a new technique for DOA estimation in a multipath environment based on covariance differencing and iterative spatial smoothing. It is shown that the proposed technique offers noticeable advantages including lower computational time and reduced array size.

II. ADAPTIVE ANTENNA ARRAYS: CONCEPT AND BENEFITS

A block diagram of a typical adaptive (or smart) antenna array system is illustrated in Fig. 1. The system consists of an array of fixed set of elements (or sensors) that are connected to a signal processing unit. This unit contains Direction Finding (DF), or what is known as Direction of Arrival (DOA) estimation, algorithms to estimate the directions of the signals coming from the mobile users. The signal processing unit then adjusts the weights of a beamforming network in order to maximize the array output towards intended users and minimize it towards interferers [4]. This paper focuses on the DOA part of the system.

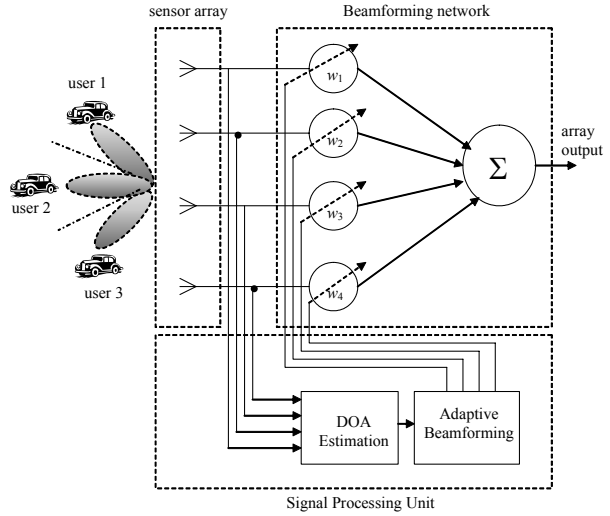

Fig. 1. Block diagram of an adaptive antenna array system.

The use of adaptive antenna arrays in mobile communication networks brings a number of benefits as summarized in what follows.

A. Extended Coverage

The *range extension factor* (REF) that an *N*-element adaptive antenna array offers is given by [5]:

$$\mathrm{REF} = \frac{r_{array}}{r_{conv}} = N^{\frac{1}{\alpha}}, \tag{1}$$

where α is an exponent modeling the path loss, and r_{conv} and r_{array} are the ranges covered by the conventional antenna (with single element) and the antenna array, respectively. The *extended area coverage factor* (ECF) that an adaptive antenna array provides is then calculated as [5]:

$$\mathrm{ECF} = \left(\frac{r_{array}}{r_{conv}} \right)^2 . \tag{2}$$

The inverse of the ECF represents the reduction factor in the number of base stations required to cover the same area that is covered by a single antenna. Fig. 2 demonstrates the improvement gained in coverage area when deploying adaptive antenna arrays in the base stations for different path loss values. It can be seen from Fig. 2 that the coverage area can be almost doubled, compared with conventional single antenna base stations, if an antenna array of six elements is used with α=5, or an antenna array of three elements is used with α=3. More examples that demonstrate the improvement in the coverage range of wireless systems can be found in [6–8].

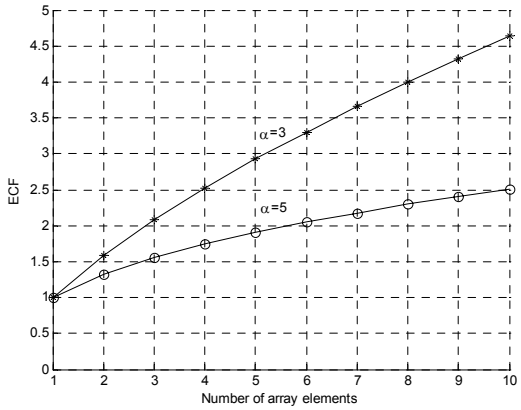

Fig. 2. Improvement of coverage range using adaptive antenna arrays.

B. Reduced Transmission Power

The *array gain G* that is achieved by an *N*-element adaptive antenna array is expressed as [5]:

$$G = 10 \log_{10} N . \tag{3}$$

This gain leads to a reduction in the transmission power of the base station. If the required base station reception sensitivity is kept the same, then the power requirement of the base station with *N*-element array is reduced to N^{-1} and, correspondingly, the required output power of the power amplifier of the base station can be reduced to N^{-2} [5]. Fig. 3 illustrates the reduction in the transmission power of the base station as the number of elements of the antenna array is increased.

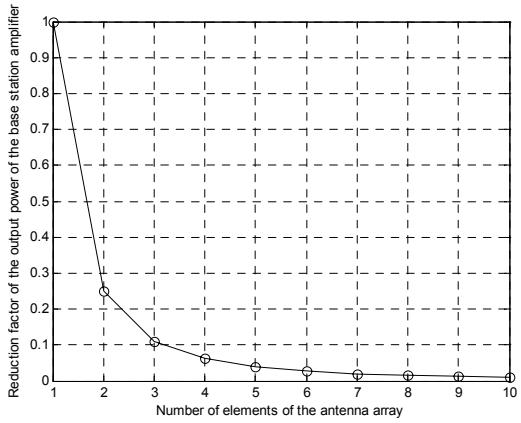

Fig. 3. Reduction in transmission power at the base station using adaptive antenna arrays.

C. Improved Signal Quality

The additional gain offered by adaptive antenna arrays leads to better output *SINR* (signal to interference ratio).

For an antenna array of N elements with a number of interferers smaller than N–1, the output *SINR* in a single propagation environment (i.e., without multipath fading) can be evaluated as [9]:

$$SINR_{out}\,(\mathrm{dB}) = 10\log_{10} N + SNR_{in}\,(\mathrm{dB})\,, \qquad (4)$$

where SNR_{in} represents the input *SNR* in dB. Fig. 4 shows the improvement in the output *SINR* value for different values of SNR_{in} using antenna arrays of different sizes. It is clearly seen from Fig. 4 that higher $SINR_{out}$ is achieved as more elements are used in the sensor array.

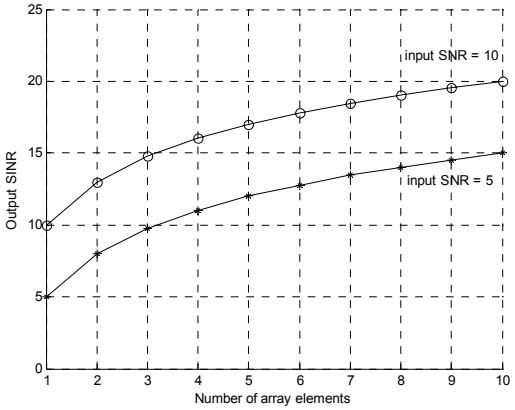

Fig. 4. Improvement of output *SINR* using adaptive antenna arrays.

D. Improved System Capacity

Mitigating the effect of interference is another major capability of adaptive antenna arrays. With conventional antennas, a small portion of the transmitted power is actually received by the intended users while most of the transmitted power is considered to be a source of interference for other users. The radiation pattern of an antenna array is determined by positions of the array elements as well as the amplitude and phase of their feeding currents [10]. By adjusting these parameters, the radiation pattern of the antenna array can be optimized such that the main beams are formulated at the directions of the intended users and null-patterns are placed at the directions of the interferers. Reducing the effect of interference in GSM networks, as an example, allows the reduction of the frequency reuse patterns and this, consequently, leads to an increase in the system capacity. Examples that demonstrate the capacity improvement gained by using adaptive antenna arrays can be found in [11–13].

E. Introduction of New Services

Due to the high signal quality and increased system capacity offered by adaptive antenna arrays, a wide range of applications can be introduced to 3G and future 4G wireless networks including location-based services. When using adaptive antenna arrays, the network will have access to spatial information of users. This information can be used to estimate the positions of users much more accurately compared to the methods used in existing networks. Positioning can be used in services such as emergency calls and location specific billing [14].

III. PROBLEM FORMULATION

A. Sensor Array Geometry

An antenna array consists of a set of elements (or sensors) that are spatially distributed at known locations with reference to a common fixed point [15]. The array sensors can be fashioned into different geometries such as linear, circular, semi-circular and planer arrays. In this paper, the case of a linear sensor array is considered where the centres of the sensors are aligned along the same axis. If the linear array sensors are spaced at equal distances, then the array is known as a uniform (or equispaced) linear array (ULA), which is the type considered in this paper.

B. Array Signal Model

Fig. 5 demonstrates an equispaced linear array of N omni-directional sensors, with spacing d, used to receive M narrowband signals $s_m(t)$ incident with azimuth angles of arrival θ_m, $1 \le m \le M$. The N-dimensional received data vector $\mathbf{u}$ at time t is given by:

$$\mathbf{u}(t) = \sum_{m=1}^{M} \mathbf{a}(\theta_m)s_m(t) + \mathbf{n}(t) = \mathbf{A}(\theta)\mathbf{s}(t) + \mathbf{n}(t)\,, \qquad (5)$$

where $\mathbf{n}$ is a noise vector modeled as temporally white and zero-mean complex Gaussian process, and $\mathbf{a}(\theta_m)$ is the array response (or steering) vector, corresponding to the DOA of the m^{th} signal, and is defined as:

$$\mathbf{a}(\theta_m) = \begin{bmatrix} 1 & e^{-j\varphi_m} & e^{-j2\varphi_m} & e^{-j(N-1)\varphi_m} \end{bmatrix}^T, \qquad (6)$$

where ^{T} is the transpose operator, and φ represents the electrical phase shift from element to element along the sensor array [16], and is expressed as:

$$\varphi_m = 2\pi\left(\frac{d}{\lambda}\right)\sin(\theta_m)\,, \qquad (7)$$

where λ is the wavelength of the incident signals. The combination of all possible steering vectors forms the array manifold matrix $\mathbf{A}$.

As seen from equation (5), the intersection of the source waveforms (i.e., signals) with one or more of the steering vectors of matrix $\mathbf{A}$ builds up the signal model. The array manifold can be a multi-dimensional matrix if other signal characteristics such as the elevation angle of incidence and the signals distance from the sensor array are considered. However, for simplicity, this

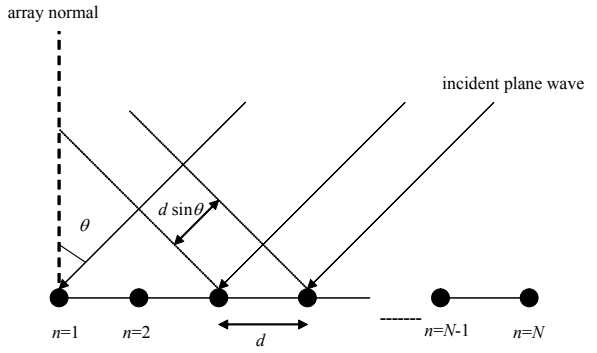

Fig. 5. Equispaced linear array of *N* sensors.

paper considers the case of one-dimensional array manifold (i.e., a function of the azimuth angle of incidence only).

Physical array calibration is very important to adjust the array response to the incident signals. Inaccuracies in the array response (or steering) vectors lead to a decrease in the accuracy of the DOA estimation process [17]. A basic form of array calibration is carried out such that the array manifold is measured by rotating the antenna array relative to a fixed signal source under controlled multipath conditions.

IV. DETECTION OF UNCORRELATED SIGNALS: THE MUSIC ALGORITHM

A. Theory

The MUltiple SIgnal Classification (MUSIC) algorithm was first introduced by Schmidt [2, 3]. The algorithm starts by applying temporal averaging over *K* snapshots (or samples) taken from the signals incident on the sensor array. This averaging process leads to forming a spatial correlation (or covariance) matrix **R** defined as:

$$\mathbf{R} = \frac{1}{K}\sum_{t=1}^{K}\mathbf{u}(t)\,\mathbf{u}(t)^{H}\,, \tag{8}$$

where ^{H} denotes the Hermitian operator. Substituting $\mathbf{u}(t)$ from (5) into (8) results in:

$$\mathbf{R} = \frac{1}{K}\sum_{t=1}^{K}\mathbf{A}(\theta)\mathbf{s}(t)\,\mathbf{s}(t)^{H}\,\mathbf{A}(\theta)^{H} + \mathbf{n}(t)\,\mathbf{n}(t)^{H}\,, \tag{9}$$

$$\mathbf{R} = \mathbf{A}\,\mathbf{R}_{ss}\,\mathbf{A}^{H} + \sigma_n^2\mathbf{I}\,, \tag{10}$$

where $\mathbf{R}_{ss}$ is the signal covariance matrix, σ_n^2 is the noise variance and **I** is an identity matrix of size $N\times N$. Since matrix **A** contains the linearly-independent steering vectors, and the signal covariance matrix $\mathbf{R}_{ss}$ is non-singular as long as the incident signals are uncorrelated, then this implies that *N–M* of the eigen values of the covariance matrix **R** are equal to σ_n^2. The eigen values of matrix **R** are the values $\{\gamma_1\ \gamma_2\ \ldots\ \gamma_N\}$ such that:

$$\left|\mathbf{R} - \gamma_i\mathbf{I}\right| = 0\,. \tag{11}$$

The basic idea behind the MUSIC algorithm is that the eigen vectors corresponding to the smallest *N–M* eigen values form the noise subspace, and are also orthogonal to the steering vectors that make up matrix **A**. The eigen vector associated with a particular eigen value γ_i is the vector $\mathbf{q}_i$ that satisfies the following equation:

$$(\mathbf{R} - \gamma_i\mathbf{I})\,\mathbf{q}_i = 0\,. \tag{12}$$

Therefore, by exploiting the orthogonality between the steering vectors making matrix **A** and the noise subspace, the MUSIC angular or spatial spectrum is defined as:

$$P(\theta) = \frac{1}{\mathbf{a}(\theta)^{H}\,\mathbf{V}_{\mathrm{n}}\mathbf{V}_{\mathrm{n}}^{H}\,\mathbf{a}(\theta)}\,, \tag{13}$$

where $\mathbf{V}_{\mathrm{n}}$ is the matrix of eigen vectors corresponding to the noise subspace of matrix **R**. Orthogonality between **a** and $\mathbf{V}_{\mathrm{n}}$ will minimize the denominator and hence will give rise to peaks in the MUSIC spectrum. Those peaks correspond to the directions of arrival of the signals impinging on the sensor array. The standard MUSIC algorithm has a high computational load and storage requirements due to the exhaustive search through all possible steering vectors to estimate the direction of arrivals. Thus, other versions of MUSIC as well as other DOA estimation algorithms have been introduced in [20–25] to reduce the computational load and storage requirements.

B. Results and Discussion

The effect of changing different parameters on the performance of MUSIC is investigated in this section of the paper. Some of these parameters are related to the size of the sensor array in terms of the number of sensors forming the array and the physical separation between them. Other parameters are related to the signal environment. These parameters include the number of incident signals, their angular separation, number of samples taken as well as the *SNR* (signal to noise ratio).

B.1. Sensor Array Parameters

The performance of MUSIC improves as more elements are used in the sensor array especially in the case of closely spaced incident signals. This is demonstrated in Fig. 6 which shows the improvement when the number of elements of a sensor array, used to detect 2 signals incident at angles $+10^{o}$ and -10^{o}, is increased from *N*=3 to *N*=6 elements. This improvement is seen in the form of sharper spectral peaks at the directions of the detected signals.

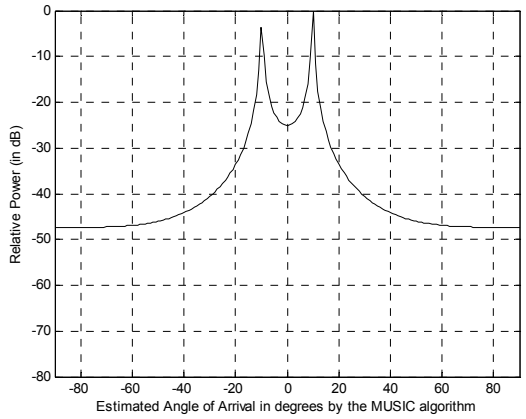

(a) N=3

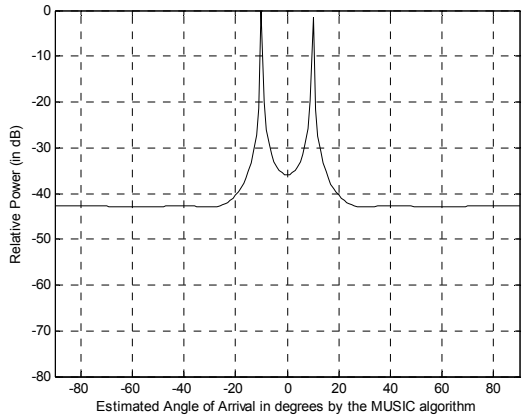

(b) N=6

Fig. 6. Effect of increasing the number of elements of the sensor array on the MUSIC spectrum (d=0.5λ, SNR=10 dB and K=100).

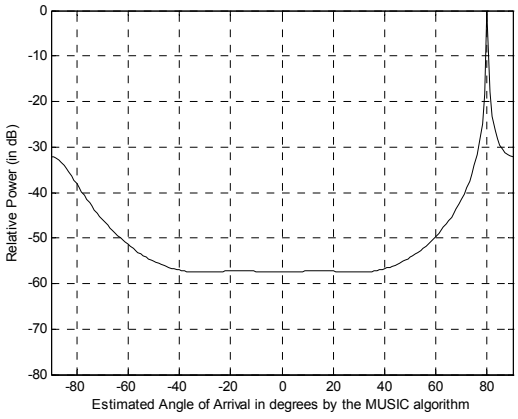

(a) d=0.5λ

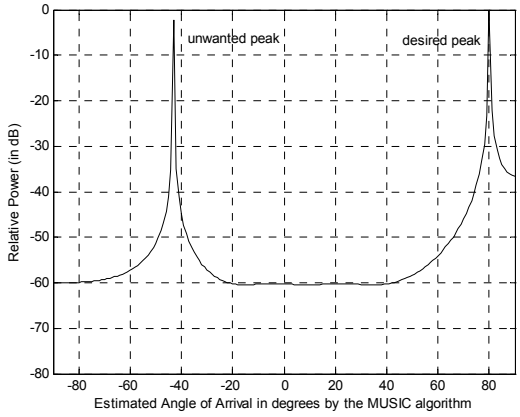

(b) d=0.6λ

Fig. 7. Effect of increasing the spacing of elements of the sensor array on the MUSIC spectrum (SNR=10 dB and K=100).

The effect of changing the spacing between the elements of the sensor array was also investigated for a sensor array of two elements used to detect one signal incident at an angle θ=80^o. It was observed that MUSIC is capable of detecting an incident signal successfully, without generating unwanted peaks in the angular spectrum, as long as the element spacing does not exceed 0.5λ, as evident from Fig. 7(a). However, using larger values for the element spacing results in unwanted peaks appearing in the MUSIC spectrums, as evident from Fig. 7(b). A further study of the reason behind this degradation in performance is presented in [26]. Since most of the DOA estimation algorithms ignore the effect of mutual coupling between the elements of the sensor array, an element spacing of 0.5λ is recommended. It is to be noted that the existence of mutual coupling [27–30] has to be taken into consideration when designing the physical antenna array elements with spacing less than 0.5λ.

B.2. Signal Environment Parameters

Experimental results show that the performance of MUSIC degrades as more signals are incident on the sensor array. This is illustrated in Fig. 8 which shows the degradation of the MUSIC spectral peaks as the number of signals incident on a six-element sensor array increases from M=2 to M=5. To overcome this, the number of elements of the sensor array must be increased [18, 19].

The spatial correlation between the incident signals, in terms of their angular separation, was also investigated. It was found that MUSIC produces sharper peaks, with a lower noise floor, as the angular separation between the incident signals increases. Fig. 9 demonstrates the improvement in the performance of MUSIC when the

angular separation between two signals incident on a sensor array of three elements is increased from 10^o to 60^o.

Moreover, it was found that the performance of MUSIC improves as more snapshots (or sapmples) are taken from the incident signals as illustrated in Fig. 10.

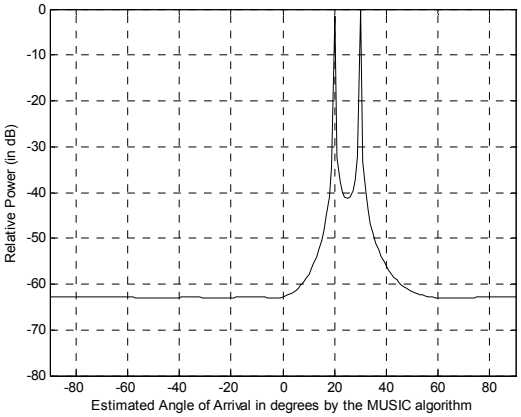

(a) Angles of arrival = $+20^o$, and $+30^o$

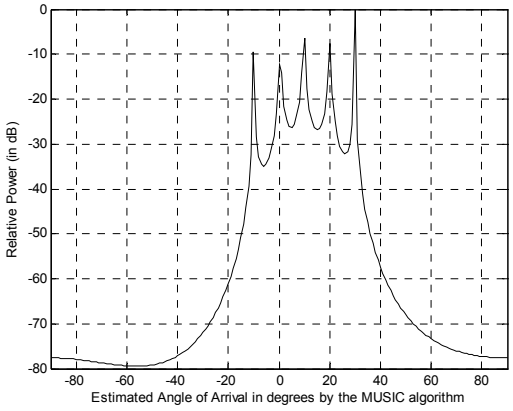

(b) Angles of arrival = -10^o, 0^o, $+10^o$, $+20^o$, and $+30^o$

Fig. 8. Effect of increasing the number of incident signals on the MUSIC spectrum (d=0.5 λ, SNR=20 dB and K=100).

Finally, the effect of SNR has been investigated and results are depicted in Fig. 11. As one would expect, it is clear that sharper peaks are resolved at the directions of the incident signals as the value of the SNR is made larger.

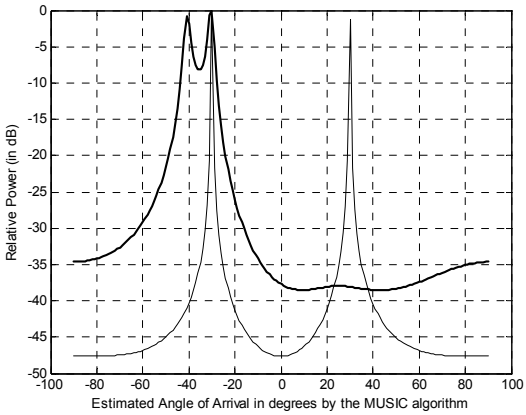

Fig. 9. Effect of increasing the angular separation between the incident signals on the MUSIC spectrum (N=6, d=0.5λ, SNR=10 dB, and K=100).

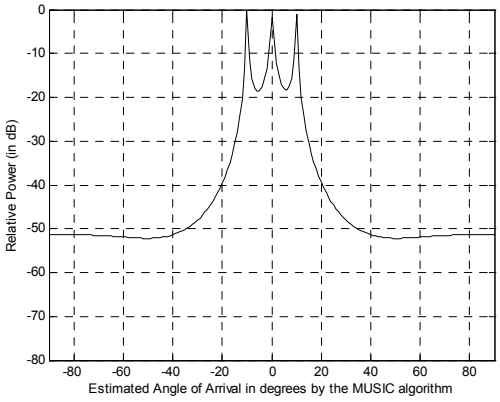

(a) K=10

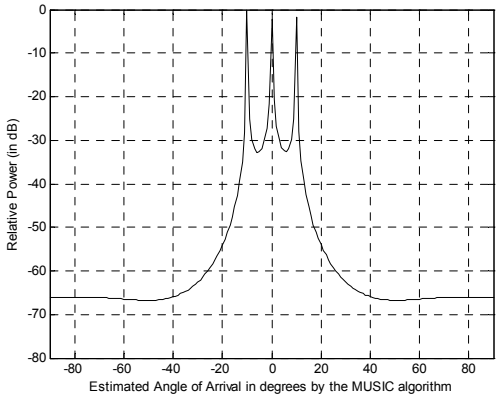

(b) K=100

Fig. 10. Effect of increasing the number of snapshots taken from the incident signals on the MUSIC spectrum (d=0.5λ, SNR=10 dB, N=5, and M=3).

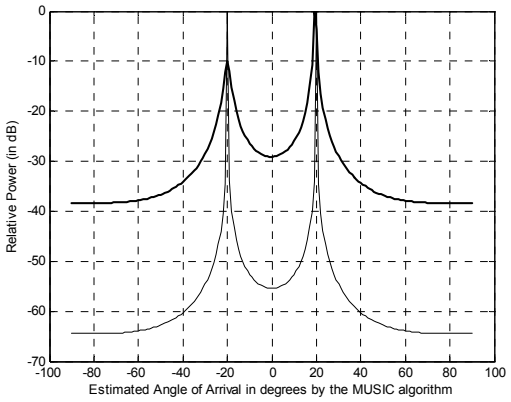

Fig. 11. Effect of increasing the *SNR* value on the MUSIC spectrum (d=0.5λ, K=100, N=3, and M=2).

V. DETECTION OF CORRELATED SIGNALS: SPATIAL SMOOTHING

As mentioned in Section IV, the signal covariance (or correlation) matrix $\mathbf{R}_{ss}$ is a full-rank matrix (i.e., non-singular) as long as the incident signals on the sensor array are uncorrelated, which is the key to the MUSIC eigen values decomposition. However, if the incident signals become highly correlated, which is a realistic assumption in practical radio environments, matrix $\mathbf{R}_{ss}$ will lose its non-singularity property and, consequently, the performance of MUSIC will degrade severely [31]. A technique known as Spatial Smoothing (SS) [32, 33] can be used to remove the correlation between the incident signals by dividing the antenna array into subarrays as described in what follows.

A. Forward Spatial Smoothing (FSS)

The basic idea of this method is to decorrelate the incident signals by dividing the sensor array into overlapping smaller subarrays and introducing phase shifts between them [34]. Fig. 12 demonstrates the FSS method when used to partition an N=6 elements sensor array into L=4 overlapping subarrays, each of size p=3 elements.

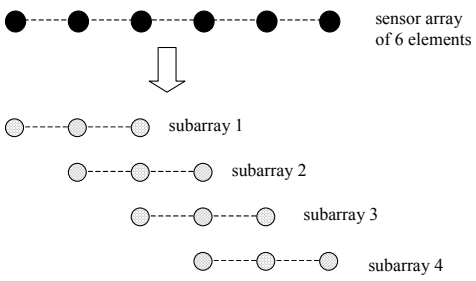

Fig. 12. FSS applied to a six-element sensor array.

The vector of the received signals at the k^{th} forward subarray is expressed as:

$$\mathbf{u}_k^F(t) = \mathbf{A}\,\mathbf{D}^{(k-1)}\mathbf{s}(t) + \mathbf{n}_k(t)\,, \tag{14}$$

where (k–1) denotes the k^{th} power of the diagonal matrix $\mathbf{D}$ given by:

$$\mathbf{D} = \text{diag}\left\{ e^{-j\frac{2\pi}{\lambda}\sin\theta_1}\,,\ \ldots\,,\ e^{-j\frac{2\pi}{\lambda}\sin\theta_M} \right\}. \tag{15}$$

The spatial correlation matrix $\mathbf{R}$ of the sensor array is then defined as the sample mean of the covariance matrices of the forward subarrays:

$$\mathbf{R} = \frac{1}{L}\sum_{k=0}^{L-1}\mathbf{R}_k^F\,. \tag{16}$$

It is to be noted that the division of the sensor array into forward subarrays must satisfy the following conditions [19]:

$$L \geq M \;\Rightarrow\; N - p + 1 \geq M\,, \tag{17}$$

$$N > p > M\,. \tag{18}$$

It can be clearly seen from (18) that $p_{\min}=M_{\max}+1$. By substituting this in (17), the maximum number of correlated signals that can be detected by FSS becomes N/2 compared to N–1 uncorrelated signals that can be detected by conventional MUSIC.

B. Forward/Backward Spatial Smoothing (FBSS)

It has been proven that it is possible to increase the number of detected correlated signals to 2N/3 by using a set of forward and conjugate backward subarrays simultaneously [35]. Fig. 13 illustrates the FBSS method when used to partition an N=6 elements sensor array into L=4 overlapping forward subarrays and L=4 overlapping backward subarrays, each of size p=3 elements. In this method, the vector of the received signals at the k^{th} backward subarray is expressed as:

$$\mathbf{u}_k^B(t) = \mathbf{A}\,\mathbf{D}^{(k-1)}\,cong[\mathbf{D}^{(N-1)}\mathbf{s}(t)] + \mathbf{n}_k(t)\,. \tag{19}$$

The spatial correlation matrix $\mathbf{R}$ of the sensor array is then given by:

$$\mathbf{R} = \frac{\mathbf{R}^F + \mathbf{R}^B}{2}\ \begin{matrix}\text{sensor array}\\ \text{of 6 elements}\end{matrix} \tag{20}$$

where $\mathbf{R}^F$ is the average covariance matrix of the forward subarrays vectors $\mathbf{u}^F$ given by (14) and $\mathbf{R}^B$ is the average covariance matrix of the backward subarrays vectors $\mathbf{u}^B$ given by (19).

C. Results and Discussion

First, the need for using spatial smoothing techniques for the detection of correlated signals is demonstrated. A simple case of two correlated signals which are incident at angles θ= –30° and –60° on an N=5 element

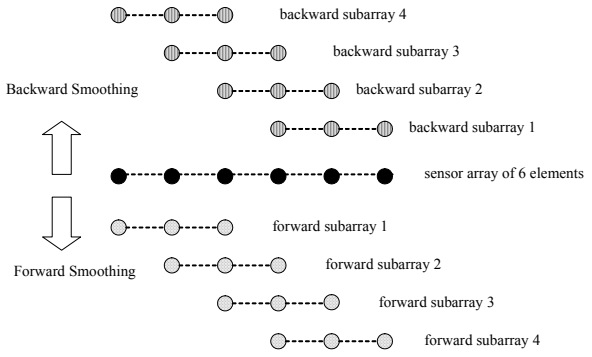

Fig. 13. FBSS applied to a six-element sensor array.

sensor array is considered. Fig. 14 shows that conventional MUSIC fails to detect the two correlated signals as evident from the absence of spectral peaks at the incident angles. These spectral peaks are clearly resolved when FSS-MUSIC is employed with p=3.

Although spatial smoothing techniques can be used to detect correlated signals, the existence of correlation reduces the number of signals that can be detected by the N-elements linear array. As mentioned previously, conventional MUSIC can successfully detect up to N–1 uncorrelated signals while FSS-MUSIC allows the detection of only up to N/2 correlated signals, and FBSS-MUSIC can detect up to 2N/3 correlated signals. Fig. 15 compares the performance of the two spatial smoothing techniques for detecting M=6 correlated signals incident on a linear sensor array comprised of N=9 elements. It can be clearly seen that FSS-MUSIC fails in such a case due to the fact that the number of incident signals is greater than N/2. However, FBSS-MUSIC is able to detect all the incident signals due to the fact that the number of incident signals does not exceed 2N/3.

Moreover, conditions (17) and (18) discussed previously highlight the constraints on the size p and number of subarrays L that should be used in order to ensure successful detection of correlated signals. Fig. 16 demonstrates the failure of FSS-MUSIC in detecting M=3 correlated signals by an antenna array of N=6 elements if the main antenna array is divided into L=2 overlapping subarrays of p=5 elements each. This is simply due to the fact that the number of subarrays L is less than the number of correlated signals M, which violates condition (17). Fig. 16 also demonstrates the success of the same smoothing technique if the main antenna array is divided into L=3 overlapping subarrays of p=4 elements each. Obviously, spatial smoothing works in this case since condition (17) is now satisfied.

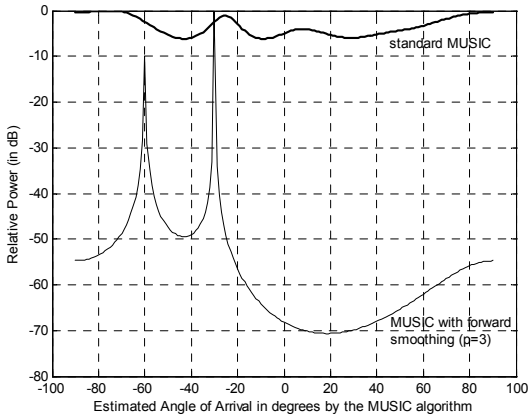

Fig. 14. DOA estimation using conventional MUSIC and FSS-MUSIC (K=100 and SNR=20 dB).

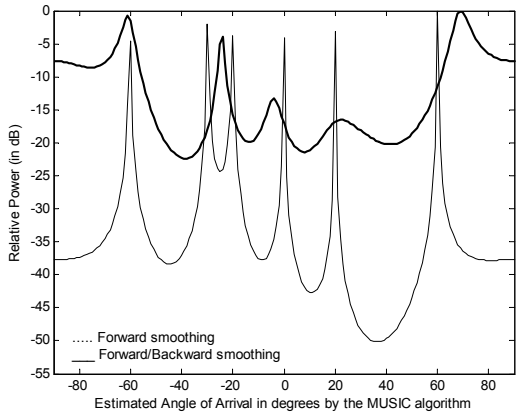

Fig. 15. DOA estimation using FSS-MUSIC and FBSS-MUSIC (θ = –60°, –30°, –20°, 0°, +20°, +60°, and p=7).

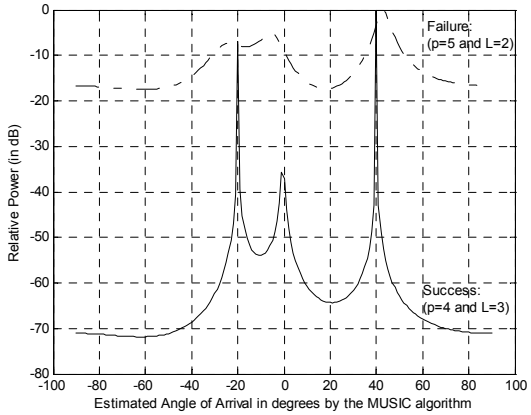

Fig. 16. Performance of FSS-MUSIC for different values of p and L (θ = –20°, 0°, and +40°, K=100, SNR=10 dB).

The size p and hence the number of the subarrays L are the key parameters which determine the computational complexity of spatial smoothing techniques. The acceptable values of these two parameters are determined by the number of correlated signals to be detected. Fig. 17 demonstrates the computational complexity of conventional MUSIC compared to FSS-MUSIC and FBSS-MUSIC when detecting two signals incident on a sensor of N=20 elements. If the two incident signals are uncorrelated, then conventional MUSIC can be used and there is no need to divide the sensor array into overlapping subarrays. However, if the two incident signals become correlated, then spatial smoothing techniques must be used. Fig. 17 shows that dividing the sensor array into larger subarrays reduces the number of subarrays to be processed and hence reduces the computational time. It is also obvious from Fig. 17 that FBSS-MUSIC requires more computational time compared to FSS-MUSIC due to the fact that the smoothing process is carried out in two directions instead of one direction only. Finally, it is to be noted from Fig. 17 that the difference in computational time between the two smoothing techniques reduces when fewer subarrays (i.e., smaller L) are processed.

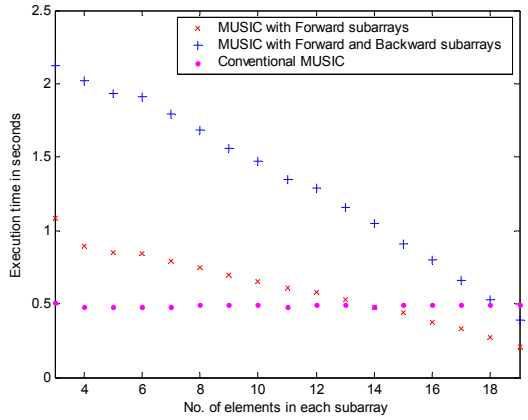

Fig. 17. Computational time of conventional MUSIC and spatial smoothing techniques (K=500, SNR=20 dB).

VI. DOA ESTIMATION IN A MULTIPATH ENVIRONMENT

A. *Standard Methods*

The question that may arise now is: "what is the maximum number of signals that can be detected if some of the incident signals are correlated while others are not?". In this case, conventional MUSIC cannot be used as it fails for detecting even two correlated signals regardless of the number of elements of the sensor array. Hence, spatial smoothing techniques must be used with a minimum number of array sensors equal to $N=2M_c+M_u$ in the case of FSS-MUSIC [19]. Here, M_c is the number of correlated signals and M_u is the number of uncorrelated signals. In the case of FBSS-MUSIC, the minimum number of array sensors becomes $N=(3M_c/2)+M_u$ [19]. In both cases, spatial smoothing should be carried out with respect to $L= M_c$ subarrays, with $p= M_c+1$ elements in each subarray. Fig. 18 illustrates the performance of both, conventional MUSIC and FSS-MUSIC for detecting M_c=2 correlated signals incident at angles –20° and +20°, and M_u=4 uncorrelated signals incident at angles –60°, –40°, +40°, and +60° on a sensor array of N=8 elements. It can be clearly seen from Fig. 18(a) that conventional MUSIC detects only the four uncorrelated signals, whereas in Fig. 18(b) all six signals have been detected using FSS-MUSIC.

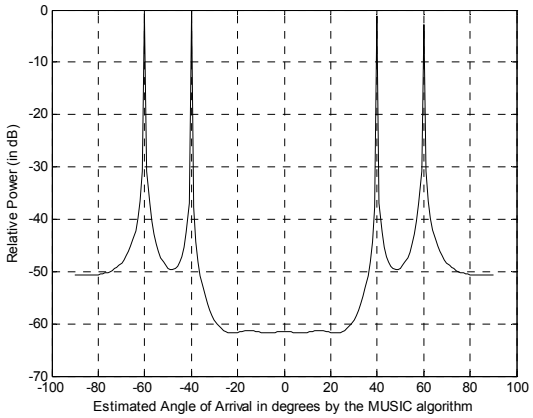

(a) MUSIC detects correlated signals only

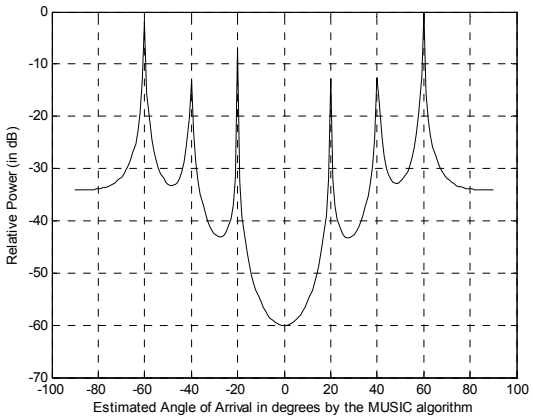

(b) FSS-MUSIC detects correlated and uncorrelated signals

Fig. 18. DOA estimation using conventional MUSIC and FSS-MUSIC in a multipath environment.

B. Proposed Method: Covariance Differencing and Iterative Spatial Smoothing

As highlighted in Section V, the performance of MUSIC shows severe degradation when trying to detect highly correlated signals as encountered in multipath propagation environments. To overcome this, spatial smoothing must be used in conjunction with MUSIC. However, the spatial smoothing process adds computational load to the DOA estimation process as well as reducing the number of signals that can be detected by the sensor array. In this subsection, a computationally efficient high-resolution algorithm, which is based on covariance differencing and iterative spatial smoothing, is proposed. Unlike standard MUSIC, which estimates the DOAs simultaneously, the proposed algorithm estimates them sequentially, in two stages, yet at a much lower computational cost. Fig. 19 shows a flowchart of the proposed method. It comprises two stages through which the uncorrelated and correlated signals are separated and processed independently.

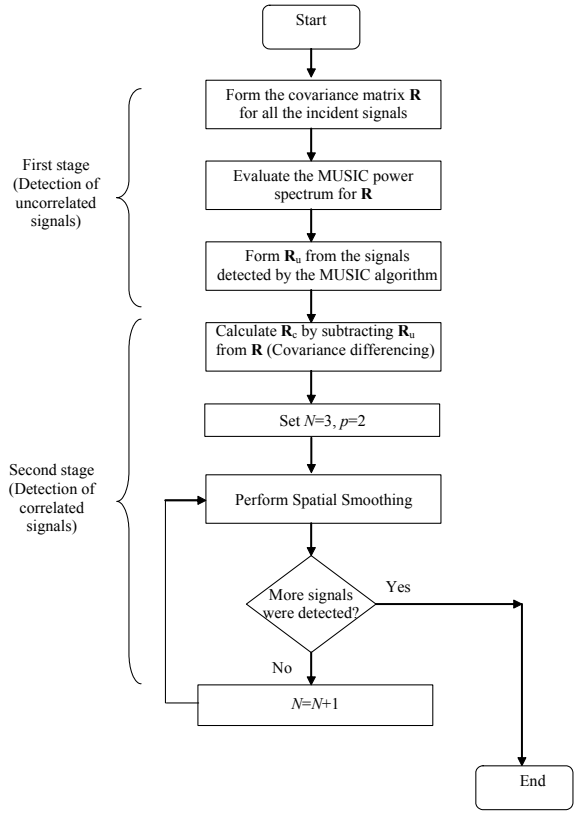

Fig. 19. Flowchart of the proposed algorithm.

In the first stage, standard MUSIC is applied to the overall signal covariance matrix $\mathbf{R}$ of all the incident signals. The DOAs that are resolved in this stage, if any, are used to form a new covariance matrix $\mathbf{R}_u$, corresponding to the uncorrelated signals only. In the second stage, a new covariance matrix $\mathbf{R}_c$, containing information on the correlated signals only is formed by covariance differencing of $\mathbf{R}$ and $\mathbf{R}_u$. Thus:

$$\mathbf{R}_c = \mathbf{R} - \mathbf{R}_u \,. \tag{21}$$

Spatial smoothing is then performed iteratively with respect to the new covariance matrix $\mathbf{R}_c$. In the first iteration of applying spatial smoothing, a sensor array of N=3 elements divided into L=2 overlapping subarrays each of size p=2 elements is used. This arrangement is capable of detecting two correlated signals only. If no peaks appear in the MUSIC angular spectrum, then this indicates that there are more correlated signals embedded in the spectrum of $\mathbf{R}_c$ and that the number of elements used in the sensor array was not sufficient to detect them all. Hence, in the second iteration, the number of elements is increased to N=4 so that the sensor array may be divided into L=3 overlapping subarrays each of size p=2 elements capable of detecting three correlated signals. The iteration process continues until the peaks corresponding to the DOAs for the correlated signals appear in the MUSIC angular spectrum.

The lower computational cost of the proposed method compared to the standard DOA estimation method is due to the fact that spatial smoothing is applied iteratively utilizing smaller sensor arrays and fewer overlapping subarrays. As already mentioned, the standard method with FSS requires the use of $N = 2M_c + M_u$ sensors to successfully detect all incident signals, whereas the proposed method with iterative FSS uses only $N = 2M_c$ sensors when $M_c > M_u$, and $N = M_c + M_u + 1$ sensors when $M_u \geq M_c$. Similarly, the standard method with FBSS requires the use of $N = 3/2\, M_c + M_u$ sensors to successfully detect all incident signals, whereas the proposed method with iterative FBSS uses only $N = M_c + M_u + 1$ sensors for any combination of correlated and uncorrelated signals. Therefore, it can be concluded that the proposed method also offers a hardware saving by reducing the size of the sensor array required to detect a given number of correlated and uncorrelated signals.

C. Results and Discussion

The simulation results shown in this part of the paper are taken for the case of a linear array of sensors equispaced at half the carrier wavelength. Simulations were carried out using an *SNR* value of 20 dB with K=200 snapshots taken from the incident signals. Fig. 20 shows the MUSIC spectrum obtained using the proposed method. The solid line shows that two uncorrelated signals at angles θ=0° and θ=+60° were

successfully detected using the first stage of the proposed method. The dotted line shows the spectrum corresponding to covariance differencing which yields the covariance matrix of the correlated signals, $\mathbf{R}_c$. The dashed line shows that after applying iterative spatial smoothing on $\mathbf{R}_c$, two correlated signals at $\theta = -30^o$ and $\theta = +30^o$ have been successfully detected.

Fig. 21 compares the computational time of the standard and proposed methods with FSS as the number of correlated signals M_c is varied. It can be seen that the proposed method is highly efficient as it offers a saving of up to 75% in computational time, when compared with the standard method. Similarly, Fig. 22 shows this saving if the proposed method is used with iterative FBSS compared to the standard method. A saving of up to 77% in computational time can be seen for this particular example.

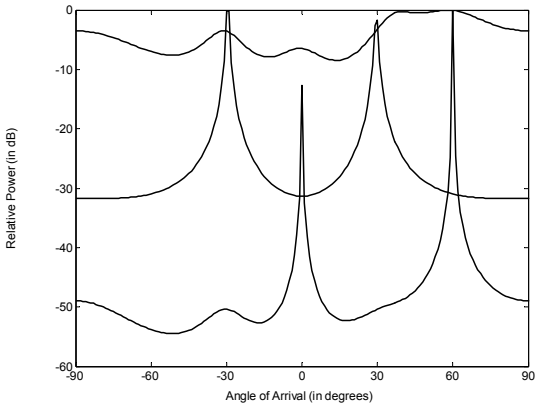

Fig. 20. MUSIC spectrum with two uncorrelated signals at $0^o$and $+60^o$, and two correlated signals at -30^o and $+30^o$.

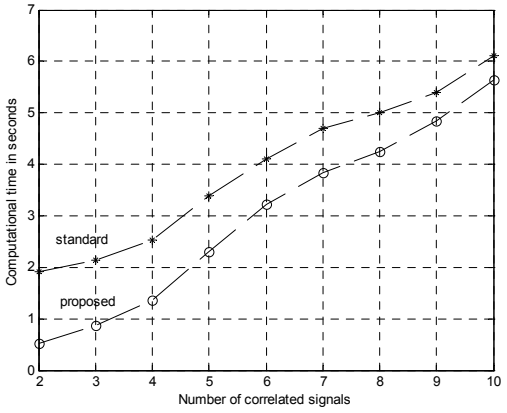

Fig. 21. Computational time of the standard and proposed methods using FSS as the number of correlated signals M_c increases (N=30, K=200, M_u=2).

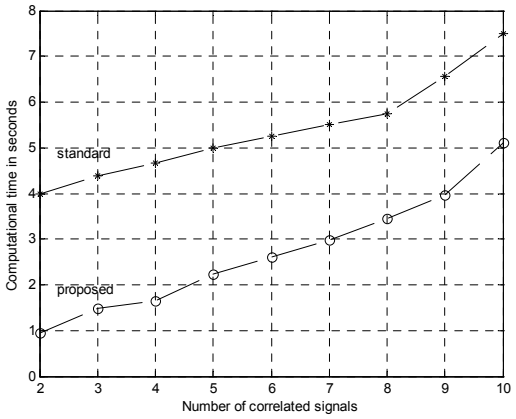

Fig. 22. Computational time of the standard and proposed methods using FBSS as the number of correlated signals M_c increases (N=30, K=200, M_u=2).

Besides the saving in computational time, the proposed method offers also hardware saving in the form of fewer elements in the sensor array, as shown in Table 1.

Table 1. Comparison between the standard and proposed methods in terms of the number of sensor array elements required to detect correlated and uncorrelated signals.

Number of signals		Required Number of elements		
Uncorrelated M_u	*Correlated* M_c	*Standard FSS-MUSIC*	*Proposed*	
			with FSS	*with FBSS*
3	2	7	6	6
3	3	10	7	7
3	4	11	8	8
3	5	13	10	9
3	6	15	12	10
3	7	17	14	11
4	2	8	7	7
4	3	10	8	8
4	4	12	9	9
4	5	14	10	10
4	6	16	12	11
4	7	18	14	12
5	2	9	8	8
5	3	11	9	9
5	4	13	10	10
5	5	15	11	11
5	6	17	12	12
5	7	19	14	13

VII. CONCLUSIONS

The performance of the MUSIC DOA estimation algorithm was investigated for a set of parameters related to the sensor array and signal environment. The performance of MUSIC was shown to improve by using more elements in the sensor array, more samples of the incident signals, as well as an increased *SNR*. Increasing the angular separation between the incident signals also leads to an improvement in the MUSIC power spectrum in the form of sharper peaks at the directions of the detected signals. Extensive simulations demonstrated that an element spacing of $\lambda/2$ results in optimum performance of the sensor array.

The use of spatial smoothing to detect correlated signals was also demonstrated. A comparative study of the performance of two spatial smoothing methods has been carried out. These methods are based on dividing the sensor array into overlapping subarrays which are used to remove the correlation between the incident signals. Each subarray must consist of a number of elements that exceeds the number of correlated signals. It was found that the forward/backward spatial smoothing technique (FBSS) requires more computational time when compared to the forward spatial smoothing (FSS) technique due to the fact that the smoothing process is carried out in two opposite directions instead of one. It is to be noted that the existence of correlation reduces the number of correlated signals that can be detected by the *N*-elements sensors array to $N/2$ in the case of FSS, and to $2N/3$ in the case of FBSS.

A computationally efficient method for DOA estimation in a multipath environment has been proposed. This method is based on covariance differencing and iterative spatial smoothing. Simulation results demonstrated the savings offered in computational time and hardware in comparison with the standard method. This makes the proposed method more suitable for real-time DSP implementations.

REFERENCES

[1] M. Viberg and B. Ottersten, "Sensor Array Processing Based on Subspace Fitting," *IEEE Transactions on Signal Processing*, Vol. 34, No. 5, pp. 1110–1121, 1991.

[2] R. Schmidt, "Multiple Emitter Location and Signal Parameter Estimation," *Proceedings of RADC Spectrum Estimation Workshop*, New York, USA, pp. 243–258, 1979.

[3] R. O. Schmidt, "Multiple Emitter Location and Signal Parameter Estimation," *IEEE Transactions on Antennas and Propagation*, Vol. 34, No. 3, pp. 276–280, 1986.

[4] L. Godara, "Application of Antenna Arrays to Mobile Communications, Part I: Performance Improvement, Feasibility and System Considerations," *IEEE Proceedings,* Vol. 85, No. 7, pp. 1031–1060, 1997.

[5] G. Tsoulos, "Smart Antennas for Mobile Communication Systems," *IEE Electronics and Communication Engineering Journal,* Vol. 11, No. 2, pp. 84–94, 1999.

[6] J. Winters, "Signal Acquisition and Tracking with Adaptive Arrays in the Digital Mobile Radio System IS-45 with Flat Fading," *IEEE Transactions on Vehicular Technology*, November 1993.

[7] J. Liang and A. Paulraj, "On Optimizing Base Station Antenna Array Technology for Coverage Extension in Cellular Radio Networks," *Proceedings of the IEEE 45th Vehicular Technology Conference*, Vol. 1, pp. 866–870, 1995.

[8] R. Cupo, G. Golden, C. Martin, K. Sherman, N. Sollenberger, J. Winters and P. Wolniansky, "A Four-Element Adaptive Antenna Array for IS-136 PCS Base Stations," *Proceedings of the IEEE 46th Vehicular Technology Conference*, pp. 1577–1581, 1996.

[9] X. Tram, "Sub-band Adaptive Array for Mobile Communications with Applications to CDMA Systems," *Ph.D. Thesis*, University of Electro-Communications, Japan, 2003.

[10] Z. Rong, "Simulation of Adaptive Array Algorithms for CDMA Systems," *M.Sc. Thesis*, Virginia Polytechnic Institute and State University, USA, 1996.

[11] A. Naguib, A. Paulraj and T. Kailath, "Capacity Improvement with Base Station Antenna Arrays in Cellular CDMA," *IEEE Transactions on Vehicular Technology*, Vol. 43, No. 3, pp. 691–698, 1994.

[12] J. Liberti and T. Rappaport, "Analytical Results for Capacity Improvements in CDMA," *IEEE Transactions on Vehicular Technology*, Vol. 43, No. 3, pp.680–690, 1994.

[13] J. Fuhl and A. Molisch, "Capacity Enhancement and BER in a Combined SDMA/TDMA System," *Proceedings of the IEEE 46th Vehicular Technology Conference*, pp. 1481–1485, 1996.

[14] P. Lehne and M. Pettersen, "An Overview of Smart Antenna Technology for Mobile Communication Systems," *IEEE Communications Survey,* Vol. 2, No. 4, 1999.

[15] S. Pillai. *Array Signal Processing*. Springer-Verlag, New York, USA, 1989.

[16] K. Al Midfa, "Direction Finding Methods: A Theoretical and Practical Performance Analysis Including the Effect of Polarization Diversity," *Ph.D. Thesis*, Department of Electrical and Electronic Engineering, University of Bristol, UK, 2003.

[17] J. C. Liberti and T. S. Rappaport. *Smart Antennas for Wireless Communications*. Prentice Hall New Jersey, USA, 1999.

[18] E. M. Al Ardi, R. M. Shubair and M. E. Al Mualla, "Performance Evaluation of Direction Finding Algorithms for Adaptive Antenna Arrays," *Proceedings of the IEEE 10th International Conference on Electronics, Circuits and Systems*, Sharjah, UAE, December 14–17, 2003, pp. 735–738.

[19] E. M. Al Ardi, R. M. Shubair and M. E. Al Mualla, "Investigation of High-Resolution DOA Estimation Algorithms for Optimal Performance of Smart Antenna Systems," *Proceedings of the IEE 4th International Conference on 3G Mobile Communication,* London, UK, pp. 310–314, 2003.

[20] A. Barabell, "Improving the Resolution Performance of Eigenstructure-Based Direction Finding Algorithms," *Proceedings of the IEEE International Conference on Acoustics, Speech and Signal Processing-83*, pp. 336–339, 1983.

[21] R. Roy and T. Kailath, "ESPRIT – Estimation of Signal Parameters via Rotational Invariance Techniques," *IEEE Transactions on Acoustics, Speech and Signal Processing*, Vol. 37, No. 7, pp. 984–995, 1986.

[22] M. Haardt and J. Nossek, "Unitary ESPRIT: How to Obtain Increased Estimation Accuracy with a Reduced Computational Burden," *IEEE Transactions on Signal Processing*, Vol. 43, No. 5, pp. 1232–1242, 1995.

[23] F. Taga, "Smart MUSIC Algorithm for DOA Estimation," *IEE Electronics Letters*, Vol. 33, No. 3, pp. 190–191, 1997.

[24] Q. Ren and A. Willis, "Fast Root MUSIC Algorithm," *IEE Electronics Letters*, Vol. 33, No. 6, pp. 450–451, 1997.

[25] I. Kim, G. Park and K. Lee, "Computationally Efficient High Resolution DOA Estimation Algorithm," IEE Electronics Letters, Vol. 37, No. 12, pp. 795–796, 2001.

[26] C. Tan, S. Foo, M. Beach and A. Nix, "Ambiguity in MUSIC and ESPRIT for Direction of Arrival Estimation," *IEE Electronics Letters*, Vol. 38, No. 11, pp. 1598–1600, 2002.

[27] I. Gupta and A. Ksienski, "Effect of Mutual Coupling on the Performance of Adaptive Arrays," *IEEE Transactions on Antennas and Propagation*, Vol. 31, No. 5, pp. 785–791, 1983.

[28] B. Friedlander and A. Weiss, "Direction Finding in the Presence of Mutual Coupling," *IEEE Transactions on Antennas and Propagation*, Vol. 39, No. 3, pp. 273–284, 1991.

[29] H. Steyskal and J. Herd, "Mutual Coupling Compensation in Small Array Antennas," *IEEE Transactions on Antennas and Propagation*, Vol. 38, No. 12, pp. 1971–1975, 1995.

[30] D. Vargas, R. Cuerdo and M. Perez, "Mutual Coupling Effects Correction in Microstrip Arrays for Direction of Arrival (DOA) Estimation," *Proceedings of IEE Microwave, Antennas and Propagation*, Vol. 149, No.2, 2002.

[31] S. Swales, "Spectrum Efficient Cellular Base Station Antenna Architectures," *Ph.D. Thesis*, Department of Electrical and Electronic Engineering, University of Bristol, UK, 1990.

[32] T. Moon and W. Stirling. *Mathematical Methods and Algorithms for Signal Processing*. Prentice Hall, New Jersey, USA, 1999.

[33] D. Johnson and D. Dudgeon. *Array Signal Processing: Concepts and Techniques*. Prentice Hall, New Jersey, USA, 1993.

[34] T. Shan, M. Wax and T. Kailath, "Spatial Smoothing for Direction of Arrival Estimation of Coherent Signals," *IEEE Transactions on Acoustics, Speech and Signal Processing*, Vol. 33, No. 4, pp. 806–811, 1985.

[35] S. Pillai and B. Kwon, "Forward/Backward Spatial Smoothing Techniques for Coherent Signal Identification," *IEEE Transactions on Acoustics, Speech and Signal Processing*, Vol. 37, No. 1, pp. 8–15, 1989.

Ebrahim M. Al-Ardi received his B.Eng. (Honours) degree in Communication Engineering from Etisalat College of Engineering, United Arab Emirates (UAE) in 1999. Since then, he has been with the Emirates Telecommunications Corporation (Etisalat), UAE, where he is currently a Senior Engineer at the Mobile Systems Section. His current responsibilities include quality control and performance monitoring of the nationwide GSM, GPRS and UMTS networks. Moreover, he is currently pursuing his postgraduate studies at Etisalat College of Engineering towards an M.Sc. by Research degree. His research is focused on new smart antenna techniques for broadband wireless access.

Raed M. Shubair received his B.Sc. degree from Kuwait University, Kuwait, in 1989 and his Ph.D. degree from the University of Waterloo, Canada, in 1993, both in Electrical Engineering. From February 1993 to August 1993 he was a Postdoctoral Fellow at the Department of Electrical & Computer Engineering, University of Waterloo, Canada. In September 1993 he joined Etisalat College of Engineering, United Arab Emirates (UAE), where he is currently an Associate Professor at the Communication Engineering Department. His current research interests include space-time signal processing, smart antennas and MIMO systems, as well as electromagnetic modeling of RF and microwave circuits for wireless communications. Dr. Shubair has authored over 60 papers in technical journals and international conferences. He is a Senior Member of the IEEE, Member of the Applied Computational Society (ACES), and Member of the Electromagnetics Academy. He organized and chaired a number of technical sessions in IEEE conferences and is a Reviewer for IEEE Transactions on Antennas & Propagation, IEEE Antennas & Wireless Propagation Letters, IEEE Transactions on Signal Processing, as well as the Applied Computational Electromagnetics Journal. Dr. Shubair is listed in Who's Who in Electromagnetics.

Mohammed E. Al-Mualla received the B. Eng. (Honours) degree in Communication Engineering from Etisalat College of Engineering, United Arab Emirates (UAE), in 1995, the M.Sc. degree in Communication Systems and Signal Processing in 1997, and the Ph.D. degree in Electrical and Electronics Engineering in 2000, both from the University of Bristol, United Kingdom. Since December 2000, Dr. Al-Mualla has been with Etisalat College of Engineering, UAE, where he leads the Multimedia Communication and Signal Processing (MCSP) research group. His current research interests include smart antennas, multimedia communication, image/video processing and coding, and multimedia copyright management. Dr. Al-Mualla has published widely in refereed technical journals and international conferences and is the first author of the book "Video Coding for Mobile Communications", Signal Processing and Its Applications Series, Academic Press, March 2002. He is a Member of both the IEE and the IEEE. He was a member of the organizing and technical program committees of the 10th IEEE International Conference on Electronics, Circuits, and Systems (ICECS2003). He is a reviewer for a number of international conferences and technical journals including the IEEE Transactions on Circuits and Systems for Video Technology, the IEE Proceedings on Vision, Image & Signal Processing, and the IEE Electronic Letters.

Polarization Isolation Characteristics Between Two Center-Feed Single-Layer Waveguide Arrays Arranged Side-by-Side

(Invited Paper)

Yasuhiro Tsunemitsu[1, 2], Jiro Hirokawa[1], Makoto Ando[1], Yohei Miura[2], Yasuhiro Kazama[2], and Naohisa Goto[3].

[1] Dept. of Electrical and Electronic Engineering, Tokyo Institute of Technology, 2-12-1-S3-19, O-okayama, Meguro-ku, Tokyo, 152-8552, JAPAN
tsunemitsu@antenna.ee.titech.ac.jp, jiro@antenna.ee.titech.ac.jp, mando@antenna.ee.titech.ac.jp
[2]Japan Radio Co., Ltd., 1-1, Shimorenjaku 5 chome, Mitaka-shi, Tokyo, 181-8510, JAPAN
tsunemitsu.yasuhiro@jrc.co.jp, miura.yohei@jrc.co.jp, kazama.yasuhiro@jrc.co.jp
[3]Dept. of Electronics and Systems, Takushoku University, 815-1, Tatemachi, Hachioji-shi, Tokyo, 193-0985, JAPAN n.goto@m.ieice.org

Abstract - The near field coupling between two large alternating-phase fed single-layer waveguide arrays arranged side-by-side is analyzed by the Finite Element Method (FEM) (HFSS). First, the overall reflection as well as the radiation pattern from the array (320 slots and 18.4 λ x 14.9 λ) is analyzed, and excellent agreement with measurements is observed. Next, the isolation between two arrays is computed, and remarkable polarization isolations of more than 80 dB are predicted. The isolation is verified by measurements. The influence of the relative arrangement of the arrays upon the isolation is discussed.

I. INTRODUCTION

Millimeter-wave applications [1] have been highlighted and intensively developed for high-speed and broadband communication due to their extensive frequency resources. To overcome serious attenuations due to rain, snow, etc., relatively short-range FWA (Fixed Wireless Access) systems in the 26GHz band are in commercial use in Japan [2] where extremely small size and low-cost wireless terminals have been realized. Single-layer slotted waveguide arrays [3] are one of the key components in this system since they have a high gain of about 32dBi, high efficiency of more than 70%, and mass producible structures. One difficulty, however, of this antenna is the relatively narrow bandwidth due to its traveling wave operation. Polarization re-use is attractive and effective for mitigating this difficulty since linear polarized slot arrays have inherently high XPD and the polarization purity does not deteriorate greatly in short range propagation.

This paper demonstrates the feasibility of a challenging system where frequency is fully re-used by the use of polarization isolation only [4]. An FWA system with this concept is presented in Figure 1. Figure 2 presents two center-feed single-layer slotted waveguide arrays with orthogonal polarization in exactly the same frequency band for transmission and reception. In order to completely reuse the frequency two times [5, 6], approximately 100dB of transmission-reception isolation is required. A preliminary scenario is to realize this isolation by the combination of an antenna isolation of 50dB and a cross-polarization compensating algorithm circuit of 50dB. The latter dispenses with the diplexer, and the use of Microwave Integrated Circuits realizes the miniaturization and economization of equipment. This paper assesses and verifies the isolation between two pairs of arrays in orthogonal polarization by simulation using Ansoft HFSS™ (High-Frequency Structure Simulator) and measurement.

We prepared two center-feed single-layer waveguide arrays [7] which have boresight beams as shown in Figure 2. The arrays are arranged side-by-side in the same plane: one is for transmitting and the other is for receiving in the FWA system. Isolation of about 80 dB is observed in both measurement and simulation.

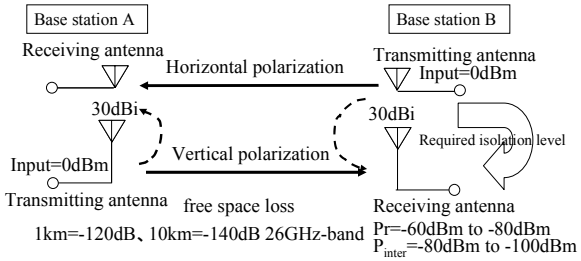

Figure 1. Dual polarization wireless system for two-times frequency reuse.

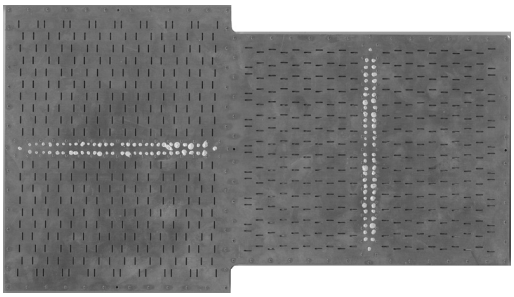

(a) Transmitting antenna (b) Receiving antenna

Figure 2. Orthogonally polarized slot arrays in side-by-side arrangement.

II. CONFIGURATION AND SIMULATION MODEL FOR AN ARRAY

Figure 3(a) shows the structure of a center-feed single-layer waveguide array. The unique structure of the alternating-phase fed array consists of two parts: a slotted plate and a base plate with corrugations screwed to each other, which dispenses with the need for perfect electrical contact. Slots are cut in the broad wall of the rectangular waveguide [8-10]. This structure has a cross-junction power divider [11-16] at the center of the array as shown in Figure 3(b) and has a stable boresight main beam. Heretofore, a beam tilting technique was used for suppression of reflection from the slot array at the antenna input [17]. This time, reflection canceling walls are introduced to suppress reflections from each radiating slot [18-20] as shown in Figure 3(c). In the FWA system, two center-feed single-layer waveguide arrays with the same structure are placed orthogonally as shown in Figure 2. Since the main beams of both antennas radiate in the same boresight direction, transmitting and receiving antennas can be installed in the same plane, and, hence, be unified.

This structure has the manufacturing advantage that it can be dug from only one side of the slotted aperture. Figure 4 shows the simulated model of this antenna. The antenna size is 14.9 λ (176mm) x 18.4 λ (218mm) at the design frequency 25.3GHz. We simulated this model using HFSS. The simulation computer's specifications are given in Table 1, and the parameters used in the HFSS simulation are presented in Table 2. HFSS's adaptive mesh generation is used [21].

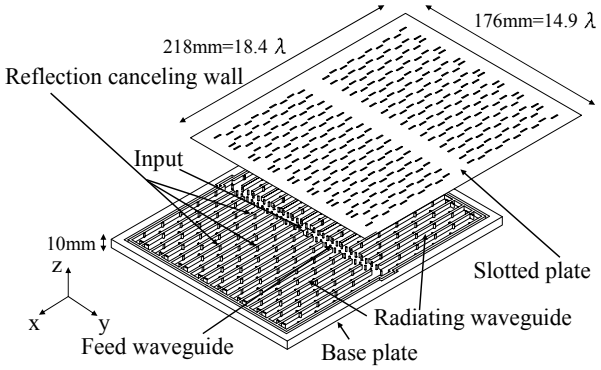

(a) Full array

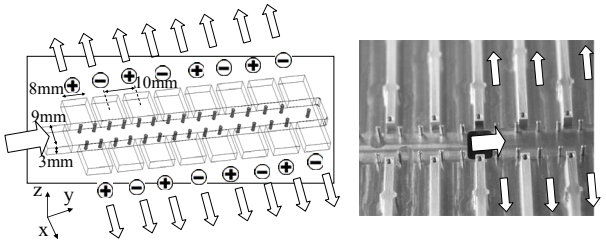

(b) A multiple-way power divider consisting of series of cross-junctions.

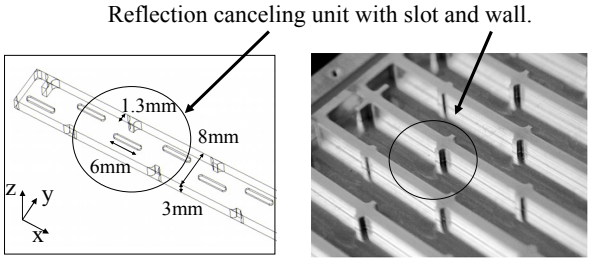

(c) Reflection canceling unit consisting of slot and wall.

Figure 3. A center-feed alternating-phase fed single-layer waveguide array.

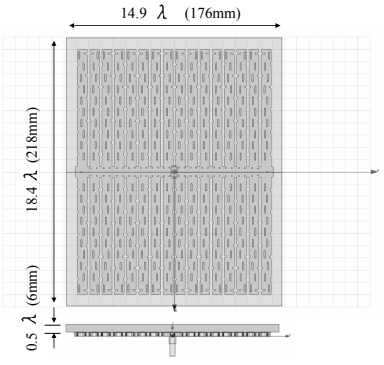

Figure 4. Full model of center–feed single layer waveguide array (10*32=320slots) for simulation.

Table 1. Personal computer specification.

CPU	Xeon 3.6GHz
Memory	16GB
HDD	500GB × 2
OS	Windows XP 64bit Edition
HFSS	Version 10

Table 2. Parameters used in HFSS simulation.

Model	Figure 4	Figure 9 h=0, d=0	Figure 9 h=1, d=0
Pass Number	12	10	10
Tetrahedra	829154	1104685	1084560
Delta S	0.0024275	0.0070885	0.0088132
Real Time	28h20m03s	37h23m31s	33h06m39s
Memory	14GB	14GB	14GB
Matrix	4953196	6541060	6421842

III. REFLECTION AND RADIATION PATTERNS OF AN ARRAY

In order to evaluate and understand the slot coupling in the array, the analysis model of an external half space is discussed. In the design of the slots of the prototype array, a linear array model with an infinite ground plane, called "isolated waveguide model", is considered and the mutual coupling effects between slots in adjacent radiating waveguides are neglected. The full structure simulation adopts the more realistic model as shown in Figure 5 (a) where the actual mutual coupling between slots in the adjacent waveguides via the half space is considered. The alternating-phase fed array is unique in that the adjacent waveguide is fed 180 degrees out-of-phase, and, if it is large enough, the external half space is well approximated by conducting metal walls that extend from the narrow walls as shown in Figure 5 (b). Figure 6 shows the calculated and measured overall reflection characteristics of this antenna. The measurements are predicted well by the simulation for model (a), though the array structure is very large and computationally heavy. As is expected from the principle of the design, the simulated result for model (b) with the metal walls also agrees with the measurements as well as the full model in (a). From the practical design point of view, the results suggest that the slot design for the reflection and the illumination control in a single radiating waveguide may be conducted by use of the linear array model with the conducting walls in (b) instead of the full array model in (a) [22]. In Figures 7 and 8 are presented the radiation patterns. The calculated and measured radiation patterns are almost identical.

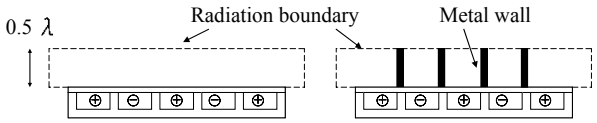

(a) Free space (b) Metal wall

Figure 5. Simplified design/analysis model of external half-space above the array aperture.

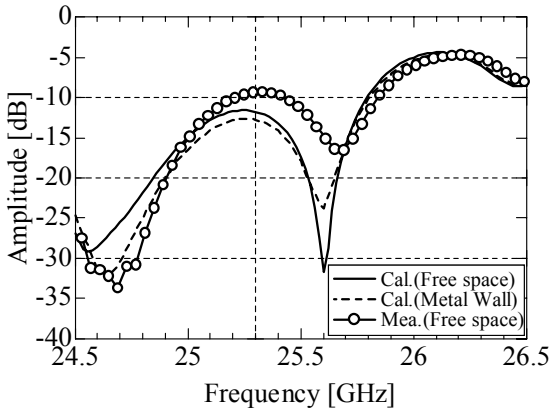

Figure 6. Overall reflection characteristics.

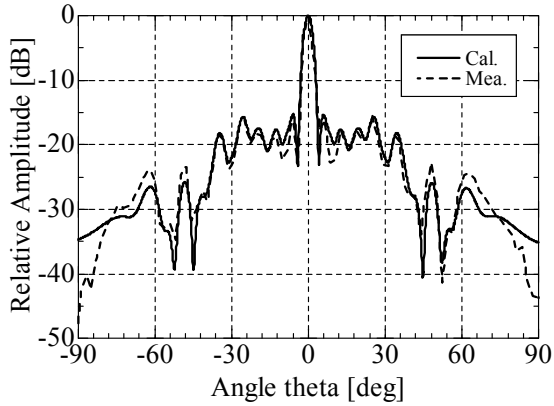

Figure 7. H-plane radiation pattern at 25.3GHz.

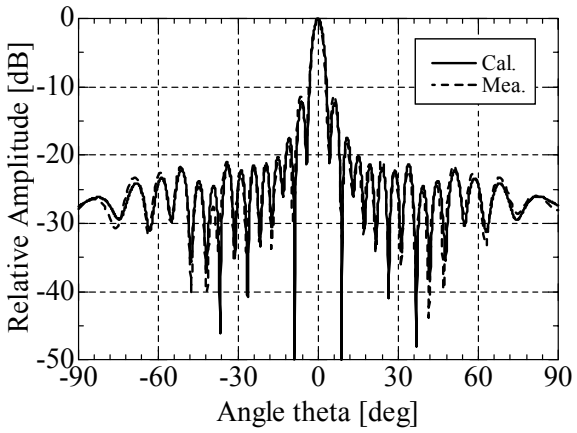

Figure 8. E-plane radiation pattern at 25.3GHz.

IV. ISOLATION CHARACTERISTICS OF ORTHOGONALLY POLARIZED PAIR ARRAYS ARRANGED SIDE-BY-SIDE

Two center-feed waveguide arrays are combined side-by-side as shown in Figure 2. This antenna has a gain of more than 30 dBi. Figure 9 shows the simulated model of this antenna. The antenna size is 18.4 λ (218mm) x 33.3 λ (394mm) at the design frequency 25.3GHz. We simulated this model using HFSS, and the parameters used in the HFSS simulation are presented in Table 2. Figure 10 shows the mesh on the slotted plate, and Figure 11 presents the calculated S-parameters. Isolation (S21 and S12) between the ports of the two antennas is more than 80dB at 25.3GHz. This value is very promising for the dual polarization wireless systems proposed in Fig. 1. Figure 12 compares the measured data with the simulated data and the results support the above proposal.

Next, the degradation of polarization isolation due to the offset in the arrangement in the pair is discussed. The second array is offset with the distance h as shown in Figure 9. The simulated and measured isolations for h=1 λ is also included in Fig.12 and are in reasonable agreement with each other. The polarization isolation is about 60-70dB and is degraded by about 10-20 dB.

The effects of arrangement are now discussed in more detail. We prepared two center-feed single-layer waveguide arrays which have the same structure. We measured the isolation for different values of distance d (= 0, 1, 2, 3 λ) and position h (= 0, 1, 2, 3 λ) as shown in Fig.13. In Figure 14, the measured isolation results are summarized as functions of d and h. The results indicate a serious degradation of isolation due to increasing h but an improvement in isolation due to increasing d. In order to confirm these general results qualitatively, we conducted a series of simulations. Figure 15 shows the full size arrays used in the simulation; isolation is evaluated for variety of distances d (= 0, 1, 2, 3 λ) and positions h (= 0, 1, 2, 3 λ).
Figure 16 shows the results of isolation between two arrays at 25.3GHz. If the distance d is increased, the isolation improves, but, if the position h is increased, isolation degrades. Almost the same tendency as in Figure 14 is observed. This phenomenon can be summarized as follows. The residual cross polarization coupling between two arrays is effectively cancelled out at the receiving antenna output resulting in remarkably high isolation, due to the symmetrical structure and arrangement of the paired arrays.

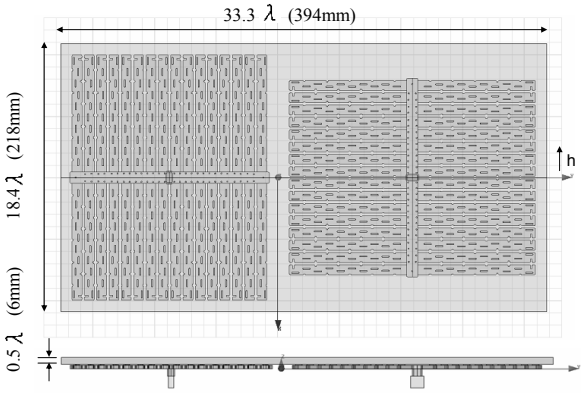

(a) Transmitting antenna (b) Receiving antenna

Figure 9. Simulation model of orthogonally polarized pair arrays in symmetrical arrangement.

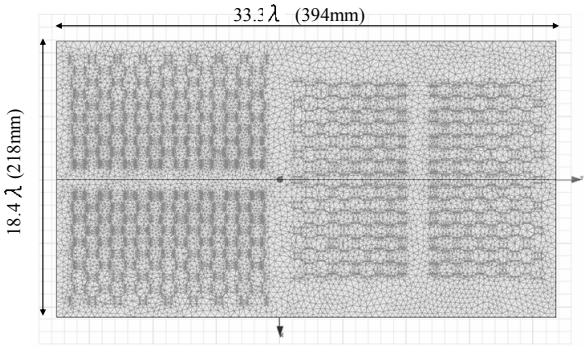

(a) Transmitting antenna (b) Receiving antenna

Figure 10. Mesh on the slotted plate (HFSS).

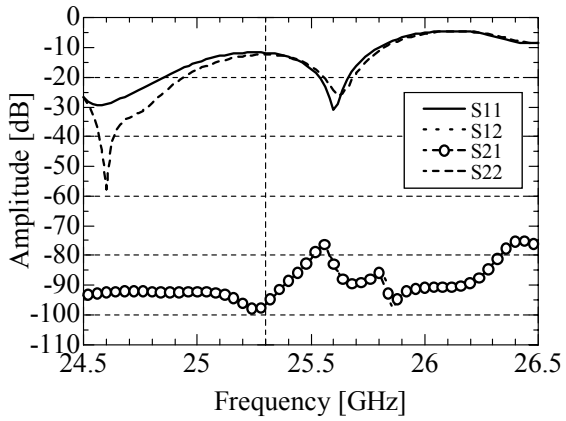

Figure 11. Simulation results of reflection and isolation characteristics between two center-feed waveguide arrays.

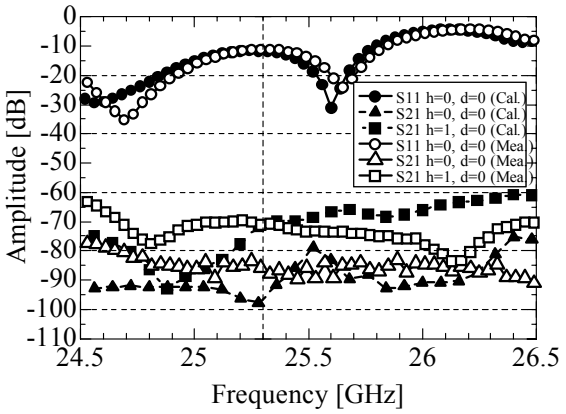

Figure 12. Measured results of reflection and isolation characteristics between two center-feed waveguide arrays.

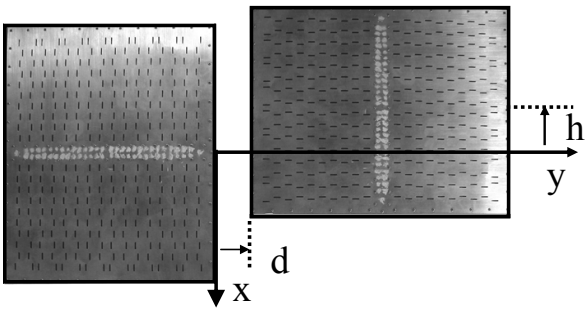

(a) Transmitting antenna (b) Receiving antenna

Figure 13. Isolation between two trial manufactured antennas arranged with distance d and position h.

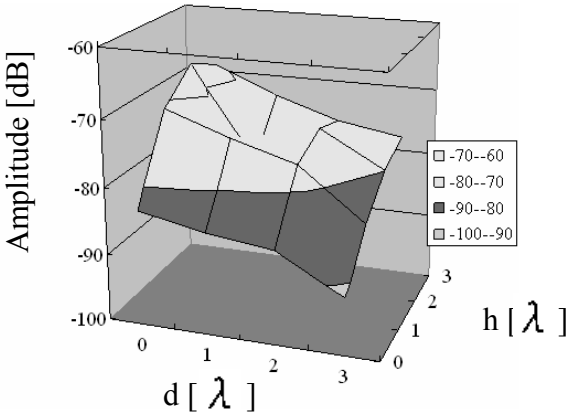

Figure 14. Position dependence of isolation at 25.3GHz (Measured).

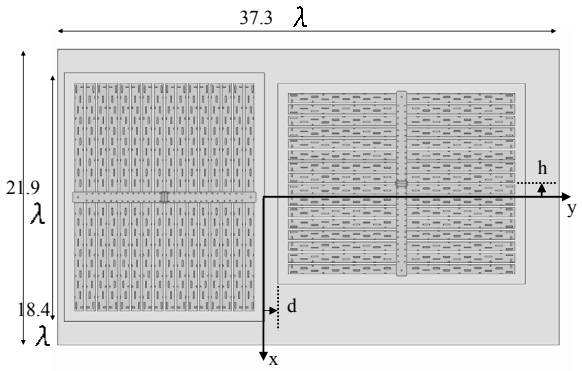

(a) Transmitting antenna (b) Receiving antenna

Figure 15. Full array model for simulation of position dependence of isolation.

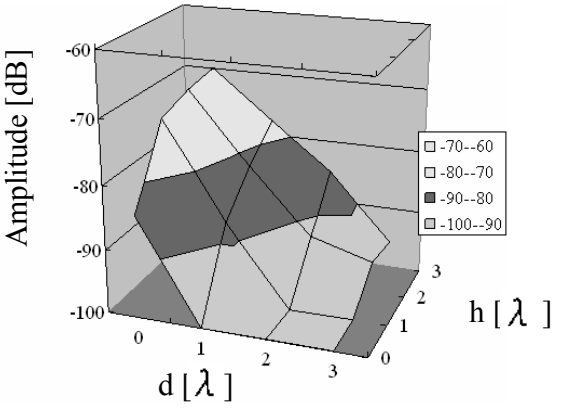

Figure 16. Position dependence of isolation between two arrays at 25.3GHz (Calculated).

V. CONCLUSION

We discussed the coupling characteristics of two center-feed alternating-phase fed single-layer waveguide arrays. Large-size arrays were analyzed by using HFSS. The total size of the problem is 320 x 2 = 640 slots and 37.3 λ x21,9 λ .Results of simulation and measurements exhibit good agreement. More than 80 dB of isolation is achieved by the symmetrical and tight arrangement. The symmetry of the arrangement as well as the structure is the key for high isolation. These results provide the basis for the application of slot arrays to dual polarization wireless systems. Also, the effectiveness of performance simulation of large scale arrays in terms of polarization isolation and reflection indicates a promising design tool in antenna engineering.

ACKNOWLEDGMENT

This study is partly supported by the Strategic Information and Communications R&D Promotion Programme (SCOPE) in the Japan Ministry of Internal Affairs and Communications.

REFERENCES

[1] K. Sakakibara, J. Hirokawa, M. Ando and N. Goto, "Single-Layer Slotted Waveguide Arrays for Millimeter Wave Applications," IEICE Trans. Commun., vol. E79-B, no.12, pp.1765-1772, Dec.1996.

[2] 26GHz FWA http://www.jrc.co.jp/eng/product/26g_fwa/index.html

[3] N.Goto, "A waveguide-fed printed antenna," IEICE Technical Report, AP89-3, Apr. 1989.

[4] Y. Tsunemitsu, Y. Miura, Y. Kazama, S. H. Park, J. Hirokawa and M. Ando, "Polarization Isolation between Two High-gain Slotted Waveguide Arrays Arranged Side-by-side," IEICE General Conv., B-1-210, Sept. 2003.

[5] Y. Tsunemitsu, Y. Miura, Y. Kazama, S. H. Park, J. Hirokawa, M. Ando and N. Goto, "Polarization Isolation between Center Feed Waveguide Arrays Arranged Side-by-side," IEICE General Conv., B-1-172, Mar. 2004.

[6] Y. Tsunemitsu, Y. Miura, Y. Kazama, S. H. Park, J. Hirokawa, M. Ando and N. Goto, "Polarization Isolation between Two Center-Feed Single-Layer Waveguide Arrays Arranged Side-by-side," IEEE AP-S Int. Symp. Dig., vol.3, pp. 2380-2383, June. 2004.

[7] SeHyun Park, Yasuhiro Tsunemitsu, Jiro Hirokawa, Makoto Ando, "Center Feed Single Layer Slotted Waveguide Array," IEEE Trans. Antennas Propag., vol. 54, no5, pp. 1474-1480, May 2006.

[8] R. S. Elliott and L.A. Kurtz, "The Design of Small Slot Arrays," IEEE Trans. Antennas Propagat., vol. AP-26, pp.214-219, 1978.

[9] K. Mahadevan, H. A. Auda, C. E. Smith, "Analysis and Design of Planar Waveguide Slot Arrays Using Scattering Matrix Approach", ACES JOURNAL., vol.13, no.3, NOV. 1998.

[10] R. C. Johnson and H. Jasik, "Antenna Engineering Handbook," McGraw-Hill, Chap.9, 1993.

[11] SeHyun Park, Jiro Hirokawa and Makoto Ando, "Single-Layer Cross-Junction Power Divider for the Center Feed in Slotted Waveguide Arrays," IEICE General Conv., B-1-167, Sept. 2001.

[12] SeHyun Park, Jiro Hirokawa and Makoto Ando, "Single-layer cross-junction power divider for the center feed in slotted waveguide arrays," IEICE Tech. Rep., EMCJ2001, vol.101, No.392, 143-147.

[13] S. H. Park, J. Hirokawa and M. Ando, "Planar Cross-Junction for the Center Feed in Single-Layer Slotted Waveguide Arrays," 2002 IEEE AP-S Int. Symp. San Antonio, Texas, Dig., vol.3, pp. 416-419, June. 2002.

[14] SeHyun Park, Jiro Hirokawa and Makoto Ando, "A Planar Cross-Junction Power Divider for the Center Feed in Single-Layer Slotted Waveguide Arrays," IEICE Trans. Commun., vol. E85-B, no.11, pp.2476-2481, Nov.2002.

[15] S. H. Park, J. Hirokawa and M. Ando, "Design of a Center-Feed Multiple-Way Circuit for a Single-Layer Waveguide Array," IEICE General Conv., B-1-87, March. 2003.

[16] S. H. Park, J. Hirokawa and M. Ando, "Design of a Multiple-Way Power Divider for Center feed Single Layer Waveguide Arrays," 2003 IEEE AP-S Int. Symp. Dig., vol.2, pp. 1165-1168, June. 2003.

[17] R.E.Collin and F.J.Zucker, "Antenna Theory," part 1, Sec.14.8, McGraw-Hill, 1969.

[18] S. H. Park, J. Hirokawa and M. Ando, "Analysis of a waveguide slot and a reflection-canceling inductive wall," 2003 IEEE Topical Conference on Wireless Communication Technology, Hawaii, s23p08, Oct. 2003.

[19] S. H. Park, J. Hirokawa and M. Ando, "Simple Analysis of a Slot and a Reflection-Canceling Post in a Rectangular Waveguide Using only the Axial Uniform Currents on the Post Surface," IEICE Trans. Commun., vol.E86-B, no.8, pp.2482-2487, Aug. 2003.

[20] S. H. Park, J. Hirokawa and M. Ando, "Analysis of a Waveguide Slot with a Reflection-Canceling Post," IEICE Tech. Rep., AP2002, vol. 102, No.232, 31-36.

[21] Ansoft Corporation, "Ansoft HFSS manual," 2004.

[22] Y. Tsunemitsu, S. H. Park, J. Hirokawa, M. Ando, Y. Miura, Y. Kazama and N. Goto, "Reflection

Characteristics of Center-Feed Single-Layer Waveguide Arrays," IEICE Trans. Commun., vol. E88-B, no.6, pp.2313-2319, June.2005.

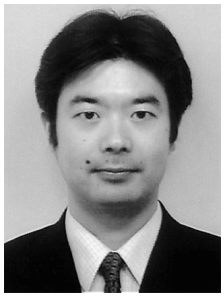

Yasuhiro Tsunemitsu was born in Kanagawa, Japan, on September 1, 1976. He received the B.S. degree in electrical engineering from Takushoku University, Tokyo, Japan in 2000 and the M.S. degree in electrical and electronic engineering from Yokohama National University, Yokohama, Japan in 2002. He works at Japan Radio Co., Ltd. He is currently studying for the D.E. degree at Tokyo Institute of Technology, Tokyo, Japan. His current research interests are in slotted waveguide array antennas. He is a member of IEICE Japan, ACES, and IEEE.

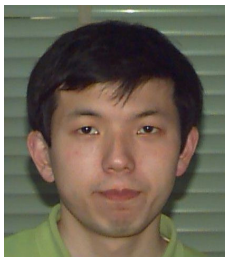

Jiro Hirokawa was born in Tokyo, Japan, on May 8, 1965. He received the B.S., M.S., and D.E. degrees in electrical and electronic engineering from Tokyo Institute of Technology (Tokyo Tech.), Tokyo, Japan, in 1988, 1990, and 1994, respectively. He was a Research Associate from 1990 to 1996, and is currently an Associate Professor at Tokyo Tech. From 1994 to 1995, he was with the antenna group at Chalmers University of Technology, Gothenburg, Sweden, as a Postdoctoral Fellow, on leave from Tokyo Tech. His research area has been in analyzes of slotted waveguide array antennas.
Dr. Hirokawa is a Member of the Institute of Electronics, Information and Communication Engineers (IEICE), Japan. He received an IEEE AP-S Tokyo Chapter Young Engineer Award in 1991, a Young Engineer Award from IEICE in 1996, a Tokyo Tech. Award for Challenging Research in 2003, and a Young Scientist Award from the Minister of Education, Cultures, Sports, Science and Technology of Japan in 2005.

Makoto Ando was born in Hokkaido, Japan, on February 16, 1952. He received the B.S., M.S., and D.E. degrees in electrical engineering from Tokyo Institute of Technology, Tokyo, Japan, in 1974, 1976, and 1979, respectively. From 1979 to 1983, he was with Yokosuka Electrical Communication Laboratory, NTT, and was engaged in development of antennas for satellite communication. He was a Research Associate with Tokyo Institute of Technology from 1983 to 1985, and is currently a Professor. His main interests have been high-frequency diffraction theory such as physical optics and geometrical theory of diffraction. His research also covers the design of reflector antennas and waveguide planar arrays for DBS and VSAT. His latest interest includes the design of high-gain millimeter-wave antennas. Dr. Ando is a Member of the Institution of Electrical Engineers (IEE) London, U.K., and the Institute of Electronics, Information and Communication Engineers (IEICE), Japan. He has been a Member of the Scientific Council for the Antenna Centre of Excellence (ACE) in EU's Sixth Framework Programme for research a network of excellence since 2004. He received the Young Engineers Award of the Institute of Electronics, Information and Communication Engineers (IEICE), Japan, in 1981, the Fifth Telecom Systems Award in 1990, the Eighth Inoue Prize for Science in 1992, the Achievement Award and the Paper Award from IEICE Japan in 1993, and the Meritorious Award on Radio, the Minister of Public Management, Home Affairs, Posts and Telecommunications in 2004. He has been the Vice-Chair and Chair of Commission B of the International Union of Radio Science (URSI), for 1999 to 2002 and 2002 to 2005, respectively. He is the Chairman of the Board of Association of Radio Industries and Businesses (ARIB) in 2004. He served as the Chairman of the Technical Program Committee of the International Symposium on Antennas and Propagation (ISAP) in 2000, the Technical Program Co-Chair for the 2003 IEEE Topical Conference on Wireless Communication Technology, the Vice-Chair of ISAP 2004, the Chair of 2004 URSI International Symposium on Electromagnetic Theory, and the Co-Chair of 2005 IEEE ACES International Conference on Wireless Communications and Applied Computational Electromagnetics. He is the Chair of the IEICE Electronic Society's Technical Group of Electromagnetic Theory for 2004 to 2005 and the IEICE Communication Society's Technical Group of Antennas and Propagation for 2005 to 2007. He is a Member of the Administrative Committee of the IEEE Antennas and Propagation Society for 2004 to 2006. He served as the Guest Editor-in-Chief of the Special Issue on Innovation in Antennas and Propagation for Expanding Radio Systems in IEICE Transactions on Communications in 2001 and the Special Issue on Wave Technologies for Wireless and Optical Communications in IEICE Transactions on Electronics in 2004. He has also been appointed Guest Editor-in-Chief for several special issues in Radio Science and IEICE Transactions on Electronics to appear in 2005.

Yohei Miura was born in Tokyo, Japan, on November 19, 1976. He received the B.S. and M.S. degrees in electrical engineering from Takushoku University, Tokyo, Japan in 1999 and 2001. He joined Japan Radio Co., Ltd., Mitaka, Japan in 2001. He is engaged in the development of FWA antennas.

Yasuhiro Kazama received the B.E. and M.S. degrees from Hosei University, in 1976 and 1978 and Ph. D. degree in electrical engineering from Chiba Institute of Technology, in 1999, respectively. He has been with Japan Radio Co., Ltd. (JRC), Mitaka, Japan in 1980. Since then, he has been engaged in the research and development of communications antennas, including Satellite, Mobile, and Fixed communications antennas. Currently, he is General Manager in Research & Development Center, Laboratory, JRC. Dr. Kazama is a member of the IEEE.

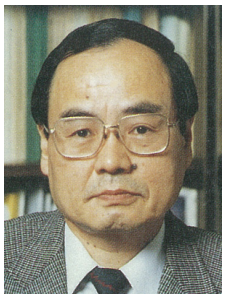

Naohisa Goto was born in Utsunomiya, Japan, on June 8, 1935. He received the B.S., M.S. and D.E. degrees from Tokyo Institute of Technology, Tokyo, Japan, all in electrical engineering, in 1959, 1961 and 1964, respectively. From 1966 to 1968 he was an Associate Professor at the Training Institute for Engineering Teachers, Tokyo Institute of Technology. From 1968 to 1975 he was an Associate Professor at Chiba University, Chiba, Japan. From 1975 to 1980 he was an Associate Professor and from 1980 to 1996 he was a Professor at Tokyo Institute of Technology. He has been a Professor at Takushoku University since 1996. He has been engaged in research and development of array antennas. He has developed a planar slotted waveguide array called “Radial line slot antenna”, “Single-layered waveguide slot antenna” and a ring patch antenna for dual frequency use called “Self-diplexing antenna”. He received the Medal with Purple Ribbon in 2000.

Radiation by a Linear Array of Half-Width Leaky-Wave Antennas

(*Invited Paper*)

Daniel Killips[1], Joshua Radcliffe[2], Leo Kempel[1], and Stephen Schneider[2]
[1] Department of Electrical and Computer Engineering, Michigan State University, East Lansing, MI 48824-1226 (Corresponding author: kempel@msu.edu).
[2] Sensors Directorate, Air Force Research Laboratory, Wright-Patterson AFB, OH 45433

Abstract—Leaky-wave antennas are interesting apertures for a variety of applications due to their low profile and wide bandwidth. They are inherently traveling wave antennas, and hence are best suited for end-fire applications. A new type of leaky-wave antenna, the half-width leaky-wave antenna (HWLW), has been recently investigated and found to have similar radiation properties as its full-width leaky-wave (FWLW) counterpart, but only requiring half the transverse dimension. In addition, the feeding mechanism for a HWLW antenna is considerably simplified compared to the FWLW antenna. This paper discusses arraying these antennas to provide both increased gain and scanning capability. It will be seen that arraying HWLW antennas is more complex than its narrowband counterpart, the patch antenna.

Index Terms—microstrip, leaky-wave, transverse resonance, traveling wave antenna, wide bandwidth, array.

I. INTRODUCTION

MICROSTRIP leaky-wave antennas have both low profile and wide bandwidth features. The thickness of a microstrip leaky-wave antenna is no greater than that of the common patch antenna albeit with substantially more bandwidth. Leaky-wave antennas have been extensively studied by Oliner [1], Menzel [2], Lee [3], and Lin [4-6] among others. The radiating mode for all of these cases is the EH_1 mode, e.g. the first higher-order mode. One of the major issues with operating a microstrip antenna in the first leaky-wave mode involves preferential excitation of that mode (as compared to the fundamental, non-radiating EH_0 mode). Menzel [2] utilized a periodic array of slots to suppress the fundamental mode while Lin *et al.* [4] utilized a more complex two-port feeding structure. All of the antennas examined in these previous papers were full-width leaky-wave (FWLW) microstrip antennas.

An alternative is the half-width leaky-wave (HWLW) antenna extensively studied by Thiele *et al*. [7-9]. This antenna is formed by placing a shorting ridge, between the microstrip and ground, along one long edge of the antenna. The other long edge will support a magnetic current wall that is responsible for radiation. Full-width microstrip leaky-wave antenna arrays have been extensively studied [10-11]. For HWLW antennas, due to the relatively strong coupling between the array elements via the leaky-wave mode, it is useful to utilize full-wave computational electromagnetics (CEM) solvers rather than to rely on traditional antenna array theory that neglects coupling. Since the HWLW antenna occupies half the surface area of a conventional FWLW antenna, the potential for closer spacing between antenna elements is attractive for array design.

The HWLW antenna by itself has a major advantage over the FWLW antenna, relatively simple feed and loading. One of the major challenges of the FWLW antenna is suppression of the EH_0 mode. Clearly, if the antenna is operated at a frequency above the cut-off frequency for both the EH_0 and EH_1 modes, then both modes can be excited. Previous papers have discussed various methods for suppressing the lower-order mode in preference to the leaky-wave mode [2, 4-6, 11]. For the HWLW antenna, due to the presence of the shorting wall along one long edge, the lower order mode is automatically suppressed. The driving point impedance can be approximated using an open waveguide model [6] along with estimated wavenumbers using the Transverse Resonance Method [3]. Using this information, both the feed location and the location of a lumped load can be estimated. The purpose of the lumped load is to suppress the backward traveling wave that will exist if no load is used.

In this present paper, the radiation properties of an array of HWLW antennas are examined using a finite element-boundary integral (FE-BI) model. The antenna feeds, loads, and geometrical features will be modeled within the context of the FE-BI model. In addition, since this is a full-wave model, the coupling between elements attributed to the leaky-wave mode will be included. Radiation properties will be examined using the model.

MICROSTRIP LEAKY-WAVE ANTENNAS

A. Leaky-wave Antenna Theory

The fundamental mode of a microstrip line, the so-called EH_0 mode, is not a radiating mode (hence the popularity

of microstrip transmission lines). The electric and magnetic fields for this mode are shown in Figure 1. Radiation from such a structure can be represented by two long magnetic current walls (for the FWLW antenna) separated the width of the microstrip. Since these current sources are out-of-phase, the co-polarized radiated field in a plane bisecting the width of the antenna is identically zero. Therefore, as an end-fire antenna, such a microstrip is unsuitable.

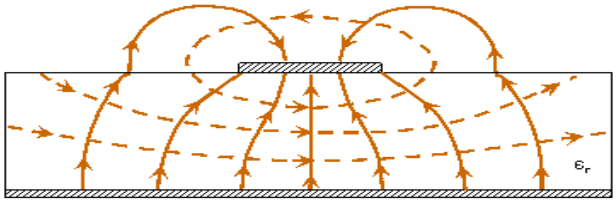

Figure 1. Field diagram for the EH_0 mode (E-field = solid, H-field = dashed).

Rather, higher-order modes must be preferentially excited to realize a radiating traveling wave structure. The first higher-order mode, the EH_1 mode, is one such radiating mode. This mode (shown in Figure 2) exhibits electric field odd symmetry about the axial centerline of the

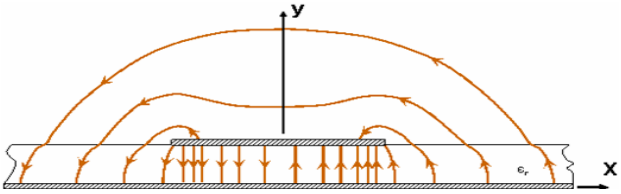

Figure 2. E-field diagram for the EH_1 mode.

antenna as compared to the even symmetry of the EH_0 mode. The radiating magnetic currents are now in-phase and hence radiate along the axis of the antenna.

The current on either wall can be represented as

$$\mathbf{M}(x,y,z) = \pm\hat{z}A_{\pm}e^{-\left(\frac{\alpha(z,f)}{k_0}\right)k_0 z}e^{-j\left(\frac{\beta(z,f)}{k_0}\right)k_0 z} \quad (1)$$

where the attenuation term $\alpha(z,f)$ and the propagation term $\beta(z,f)$ are in general a function of both position and frequency, k_0 is the free-space wavenumber, and the wave coefficients $(A_{\pm})$ are associated with the two magnetic wall currents at $x = \pm w/2$ where w is the width of the full-width microstrip. The attenuation and propagation terms for an axially invariant structure can be determined using the Transverse Resonance Method (TRM) [3]. Once the propagation parameters are known, the driving point impedance for a semi-infinite line can be estimated using an open waveguide model, viz. [5-6][1] as

$$Z_w = 8Z_0\sin^2\left(\frac{\pi y}{w_{eff}}\right)\frac{k_0 h}{k w_{eff}}\sqrt{\frac{\mu_r}{\varepsilon_r}}. \quad (2)$$

The input impedance for a finite, loaded leaky-wave antenna can be estimated using the impedance transformation

$$Z_{in} = Z_w\left[\frac{Z_L + Z_w\tanh(\gamma L)}{Z_w + Z_L\tanh(\gamma L)}\right] \quad (3)$$

where Z_L is the load impedance (for this paper, $Z_L = 50\Omega$) and $\gamma = jk = j(\beta - j\alpha)$.

In (2), the effective microstrip width is given by Wheeler's approximation [12]

$$w_{eff} = h\left\{\frac{w}{h} + \frac{2}{\pi}\ln\left[2\pi e\left(\frac{w}{2h} + 0.92\right)\right]\right\}. \quad (4)$$

Use of (2)-(4), with the propagation parameters provided by TRM, allows determination of the appropriate feed and load locations along the width of the strip.

Assuming a single radiating current of the type represented in (1), hence a leaky-wave antenna that is perfectly terminated but aligned parallel to the x-axis and centered on the origin, the radiated electric field in the far-zone (with the spherical wave assumed and suppressed) is given by

$$\mathbf{E}(\theta,\phi) \sim \frac{k_0 I_0}{4\pi L}\frac{\sinh\left(\chi L/2\right)}{\left(\chi L/2\right)}\left[\hat{\theta}\sin\phi + \hat{\phi}\cos\theta\cos\phi\right] \quad (5)$$

where $\chi = jk_0\left[\sin\theta\cos\phi - k/k_0\right]$ and I_0 is the strength of the current. If a linear array of uniformly spaced, with a separation of d, similar elements is aligned along the y-axis, the array factor will be given by

$$AF = \sum_{m=-M}^{M} e^{jk_0(md)\sin\theta\sin\phi}. \quad (6)$$

Obviously, use of (5) and (6) assumes no coupling between array elements.

B. Example: Leaky-wave Antenna on Duroid

As an example, consider a leaky-wave antenna printed on Duroid 5870 (31 mils thick, $\varepsilon_r = 2.33$, $\tan\delta = 0.0005$). The full-width strip width is 15 mm while the half-width strip width is 7.5 mm. The strip is taken to be 190 mm long for the simulations and measurements and it is infinite for the

[3] There is a typographical error in the expression in [6] where the sine function should be squared as shown in (2). The expression is correct in [5].

TRM analysis. The propagation terms, as determined using the transverse resonance method, are shown in Figure 3. Traditionally, the leaky-wave region of operation is defined between the frequency such that $\alpha = \beta$ to the frequency such that $\beta = k_0$; hence, for the example presented, approximately from 6 GHz to 8 GHz. Using this information, along with (2) and (3), the driving point impedance for a 190 mm realization of the antenna is shown in Figure 4 where the feed point is taken at the transverse midpoint of the HWLW antenna and a 50Ω lumped load is also placed along the midline of the antenna at the opposite end from the feed.

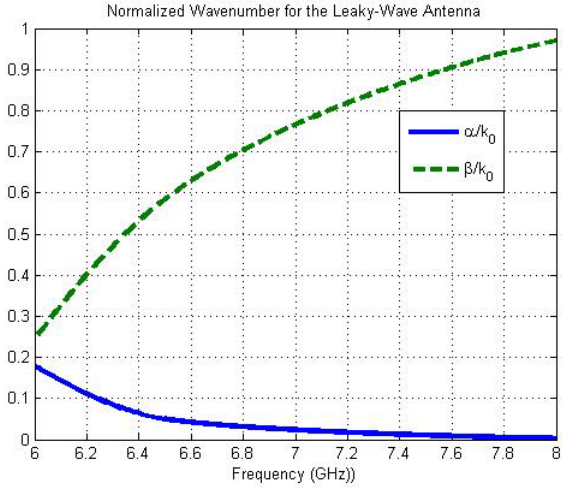

Figure 3. Normalized attenuation and phase constant for a leaky-wave antenna.

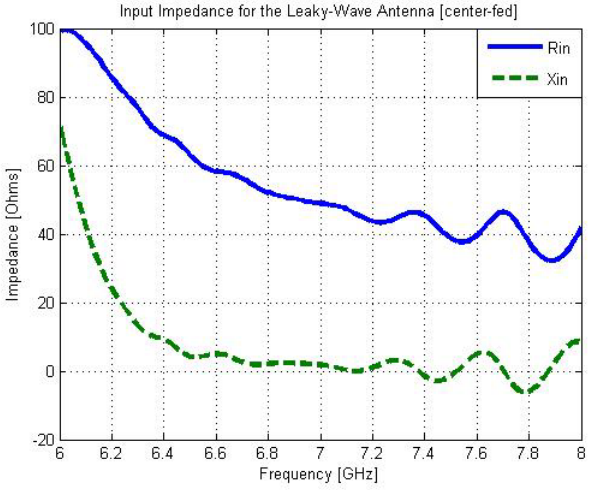

Figure 4. Input impedance at the center of the half-width strip width for this leaky-wave antenna.

As can be seen, the impedance seen at the input port of the antenna is dispersive and hence a perfect match to a 50Ω line is not possible across the entire operational bandwidth. In addition, as noted in [10,11], the traveling wave fields guided by a microstrip structure couple rather strongly to the leaky-waves emanating from neighboring microstrips causing deviation from theoretical predictions for both the wavenumber, driving point impedance, and consequently, the radiated field. Hence, use of a full-wave computational method is desirable for designing leaky-wave arrays.

II. FINITE ELEMENT-BOUNDARY INTEGRAL MODEL

The hybrid finite element-boundary integral (FE-BI) method is widely understood to be an accurate and efficient method for modeling planar, microstrip apertures. The assumed geometry is a cavity-backed aperture recessed within an infinite metallic plane. The FE-BI formulation is an integro-differential equation representing a weak enforcement of the relevant boundary conditions applied to the vector wave equation. This FE-BI expression is given as

$$\int_V \left[(\nabla \times \mathbf{W}_i)\cdot \overline{\overline{\mu}}_r^{-1}\cdot(\nabla \times \mathbf{E}^{int}) - k_0^2 \mathbf{W}_i \cdot \overline{\overline{\varepsilon}}_r \cdot \mathbf{E}^{int}\right] dV + k_0^2 \int_S\int_S \mathbf{W}_i \cdot \left[\hat{z}\times \overline{\overline{G}}_{e2}\times \hat{z}\right]\cdot \mathbf{E}^{int}\, dS'dS = -jk_0 Z_0 \int_V \mathbf{W}_i \cdot \mathbf{J}^{imp}\, dV \tag{7}$$

where $\mathbf{W}_i$ is a vector testing function, $\overline{\overline{G}}_{e2}$ is the half-space dyadic Green's function, and $\mathbf{J}^{imp}$ is an impressed current used to represent the antenna feed. The material in the computational volume, e.g. the antenna cavity, is represented by the relative permittivity tensor $\left(\overline{\overline{\varepsilon}}_r\right)$ and the relative inverse permeability tensor $\left(\overline{\overline{\mu}}_r^{-1}\right)$. The FE-BI formulation is reduced to a linear system via Galerkin's procedure resulting in the following linear system

$$\left[Y_{ij}^{FE}\right]\{E_j\} + k_0^2 \begin{bmatrix} Y^{BI} & 0 \\ 0 & 0 \end{bmatrix} \begin{Bmatrix} E_j^S \\ E_j^V \end{Bmatrix} = \{f_i^{int}\}. \tag{8}$$

In this, the unknown coefficients associated with the expansion functions $(\mathbf{W}_j)$ are represented by (E_j). For the unknown coefficients, (E_j^S) represents unknowns associated with the surface while (E_j^V) represent unknowns not associated with the surface. This system can efficiently be solved, both in terms of memory consumption and wallclock time, using an iterative solver such as the biconjugate gradient method [14].

By utilizing a fast Fourier transform (FFT) method to accelerate the computation of matrix-vector products in an iterative solution of the FE-BI linear system, simulation of a large antenna is feasible within practical design time limits. Hence, brick elements were used to

discretize the computational volume [13]. The shorted side of the HWLW antenna is modeled using an infinitesimally thin perfectly conducting wall running from one end of the strip to the other end. The lumped loads were modeled as infinitesimally thin loads placed along the shorted edge of the half-width antenna. The feeds are modeled likewise as infinitesimally thin probe feeds placed along the shorted edge of the antenna opposite the loads on the mid-line of the antenna.

In addition, the computer program was parallelized using OpenMP [15] and run on a dual-core AMD 64-bit system with a total of four cores per node. The program has also been used on an SGI Altix 3700 Bx2 using 64-bit Itanium processors [16]. The primary routine that was parallelized was the iterative matrix solvers (the biconjugate gradient and transpose-free QMR algorithms are implemented) and fast Fourier transforms. For this work, the BiCG algorithm [14] was used.

III. COMPUTED DATA FOR A FIVE ELEMENT LINEAR ARRAY

To validate the computational model discussed above, an experiment was conducted in a compact anechoic chamber using a single HWLW antenna. The shorting wall in the half-width antenna was approximated using shorting pins that were 5 mm apart running the length of the antenna strip. The ports were attached to an HP-8510 vector network analyzer. A representative radiation pattern, comparing computed and measured data, is shown in Figure 6.

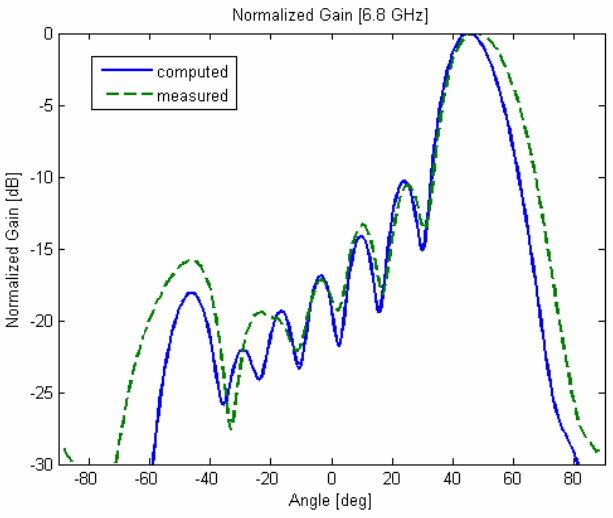

Figure 6. Comparison of computed and measured radiation patterns from a half-width, leaky-wave antenna at 6.8 GHz.

The agreement is reasonably good considering that the shorting wall was not solid, the FE-BI model used a probe feed, and the actual groundplane was finite while the modeled one was infinite.

Next, the FE-BI model was used to determine the impact of leaky-wave coupling on the fields supported by adjacent microstrip elements. Figure 7 illustrates a representative coupling between a driven element (the lower one in the figure) and an unfed element that is terminated on both ends of the antenna with 50Ω loads and 1.95 cm (center-to-center) away from the lower element. The simulation was conducted with a single cavity containing both the driven element and the passive element. In this manner, coupling between elements can occur via substrate, across the surface of the aperture, and via space-wave mechanisms. For an aperture where each element is contained within individual cavities, coupling via the substrate is suppressed. Since this is assumed to be the dominant mechanism, since the EH_1 mode is a leaky-wave mode, this geometrical arrangement is appropriate.

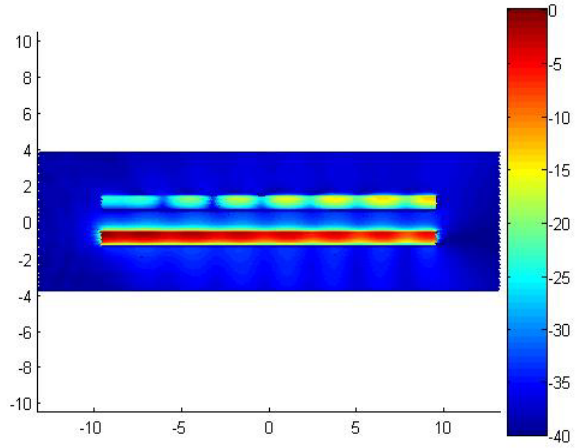

Figure 7. Normal fields in cavity for driven lower element and passive upper element.

It is clear that the leaky-wave from the driven lower element is coupled into the upper element. Notice that the fields in the upper element are strongest in the end of the element opposite the driving-point in the lower element; a phenomena expected from leaky-wave coupling since the driven leaky-wave will have a directional component from left to right in the figure. To assess the impact of this coupled field to the radiating current (and hence the fidelity of the radiation pattern to predictions based on a single traveling wave), the coupling ratio was determined for various separations. The coupling ratio is defined as the ratio of the maximum field strength in the region of the passive antenna to the maximum field strength in the region of the driven element. Hence, it is a measure of how strong one leaky-wave couples, and hence corrupts, the leaky-wave propagating in another microstrip. As a

function of the center-to-center separation distance, the coupling between these elements at 7 GHz is given in the Figure 8. As can be seen, the coupling remains fairly strong even out to a distance of 6.45 cm. For 7 GHz, the free-space wavelength is 4.29 cm and hence a separation of 6.45 cm would result in grating lobes. This result enforces the assumption made previously that to accurately assess the radiation properties of a leaky-wave array, either the rather complex formulation presented in [11] or a full-wave model such as the FE-BI method must be used.

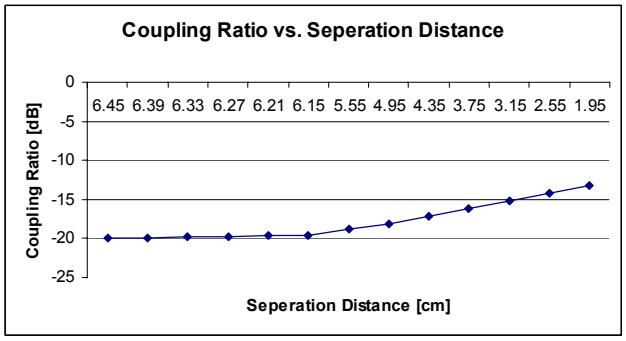

Figure 8. Coupling ratio between elements vs. separation distance.

A five-element array was simulated using the FE-BI model and having a separation of 1.2 cm between elements (e.g. less than 1/3rd of the free-space wavelength to avoid grating lobes). The theoretically predicted radiation patterns based on (5) and (6) – e.g. the normalized radiation intensity [17] – is shown in Figures 9 and 10 for a uniformly illuminated array.

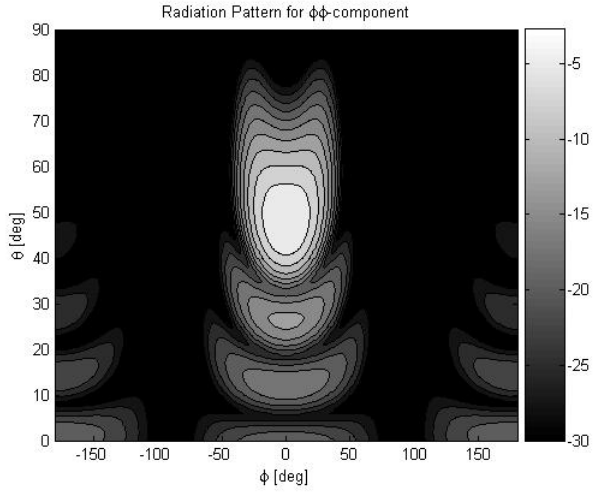

Figure 9. Theoretical ϕ-ϕ radiation pattern for a uniformly illuminated array.

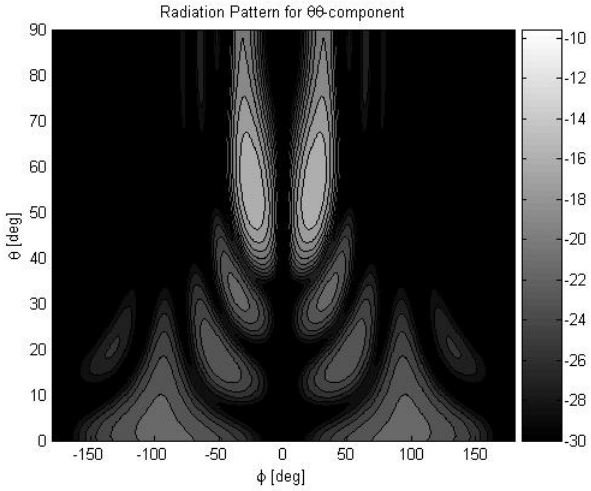

Figure 10. Theoretical θ-θ radiation pattern for a uniformly illuminated array.

The corresponding patterns as computed by the FE-BI model are shown in Figures 11 and 12, respectively.

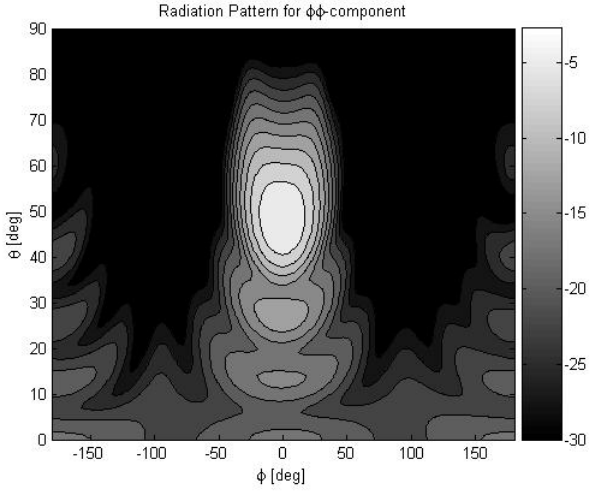

Figure 11. Numerical ϕ-ϕ radiation pattern for a uniformly illuminated array.

For all of the contour plots, each contour represents 3 dB of change. As seen by comparing Figure 9 to Figure 11 and Figure 10 to Figure 12, the agreement is quite good with the exception of the somewhat diffused sidelobes for the numerically computed results. The reason is presumably due to the leaky-wave coupling that is neglected in the theoretical results.

Another example is the same array; however, the main beam is now steered 30 degrees from the array axis normal. The theoretical results are shown in Figures 13 and 14 and the numerical results are shown in Figures 15 and 16, respectively.

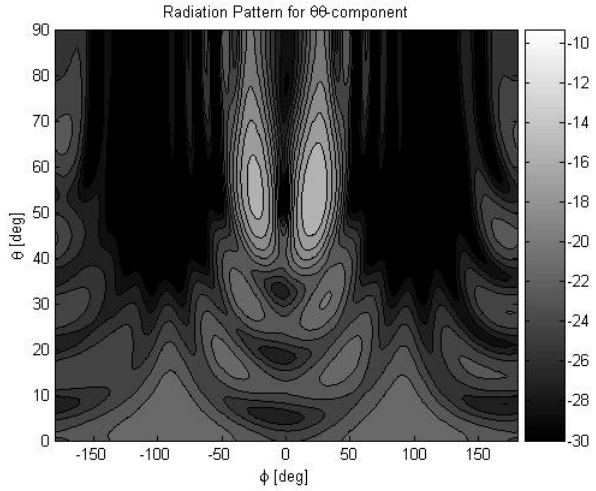

Figure 12. Numerical θ-θ radiation pattern for a uniformly illuminated array.

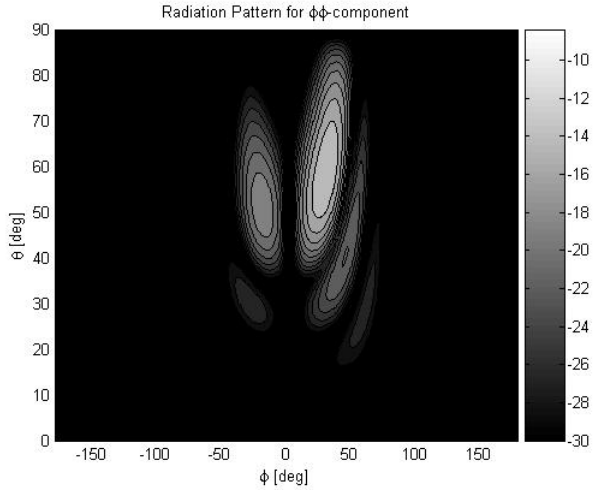

Figure 13. Theoretical ϕ-ϕ radiation pattern for an array steered 30 degrees off the x-axis.

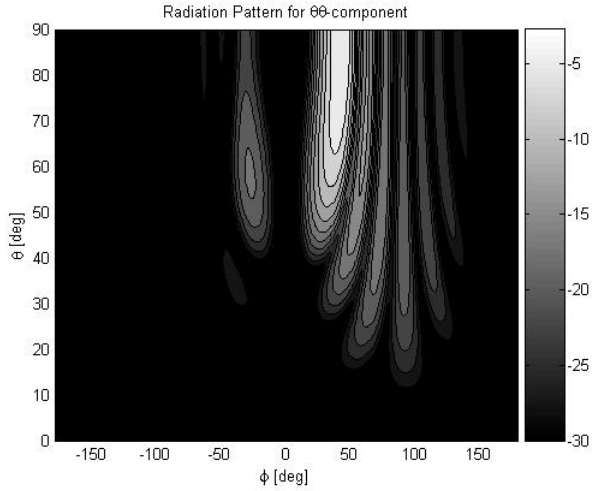

Figure 14. Theoretical θ-θ radiation pattern for an array steered 30 degrees off the x-axis.

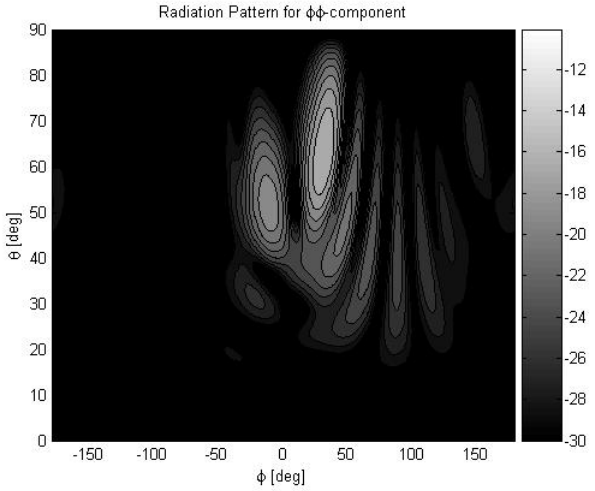

Figure 15. Numerical ϕ-ϕ radiation pattern for an array steered 30 degrees off the x-axis.

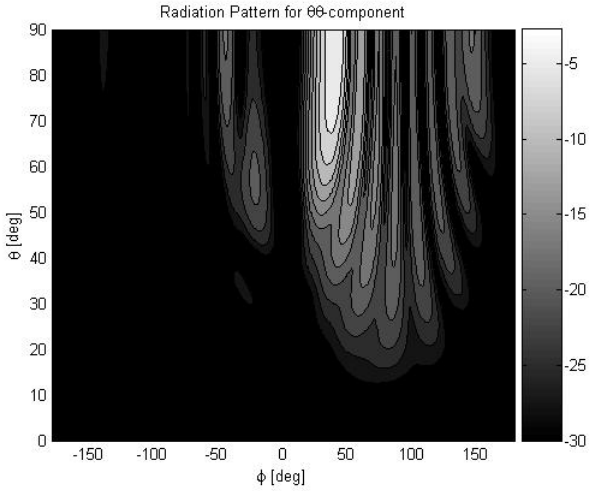

Figure 16. Numerical θ-θ radiation pattern for an array steered 30 degrees off the x-axis.

Again, the agreement between the theoretical and numerical results is quite good with the exception of higher sidelobes for the numerical results.

IV. Conclusions

Microstrip leaky-wave antennas offer an attractive end-fire aperture that is thin and easy to manufacture. The half-width leaky-wave antennas investigated herein have a particularly simplified feed structure compared to the more traditional full-width leaky-wave antennas. An array of these antennas was investigated using a hybrid finite element-boundary integral method. Strong coupling between adjacent elements was observed and quantified. Nevertheless, the radiation patterns between the theoretical and numerical results agreed quite well except for the sidelobes. It is assumed that the leaky-wave coupling between elements perturbs the radiating magnetic current for each element causing changes in the

sidelobes. Hence, for applications requiring tight sidelobe control, use of a full-wave analysis method is essential.

ACKNOWLEDGEMENTS

LCK would like to thank the Michigan State University High Performance Computing Center for providing computational support to this research and AFOSR under grant F-496-2002-10196 for partial support of this research.

REFERENCES

[1] A. Oliner, "Leakage from Higher Modes on Microstrip Line with Applications to Antennas", *Radio Science*, 22, pp. 907-912, Nov. 1987.

[2] W. Menzel, "A New Traveling-Wave Antenna in Microstrip," *Archiv fur Elektronik und Ubertragungstechnik (AEU),* Band 33, Heft 4:137-140, April 1979.

[3] K.S. Lee, "Microstrip Line Leaky Wave Antenna," Ph.D. Dissertation, Polytechnic University, June 1986.

[4] Y-D Lin, J-W Sheen, and C-K. C. Tzuang, "Analysis and design of feeding structures for microstrip leaky wave antennas," *IEEE Trans. Microwave Theory Tech*., 44, pp. 1540-1547, Sept. 1996.

[5] J-W Sheen, W. Hong, and Y-D Lin, "Wide band tapered microstrip leaky-wave antenna," *Proc. 30th European Microwave Conf.*, 2, pp. 234-237, 2000.

[6] W. Hong, T-L Chen, C-Y Chang, J-W Sheen, and Y-D Lin, "Broadband tapered microstrip leaky-wave antenna," *IEEE Trans. Antennas Propagat*., 51, pp. 1922-1928, Aug. 2003.

[7] J. S. Radcliffe, G. A. Theile, and G. Zelinski, "A microstrip leaky wave antenna and its properties," *26th AMTA Symp*., St. Mountain, GA, Oct. 2440.

[8] G. M. Zelinski, M. L. Hastriter, M. J. Havrilla, J. S. Radcliffe, A. J. Terzuoli, and G. A. Thiele, "FDTD analysis of a new leaky traveling wave antenna," *2005 IEEE/ACES Intl. Conf*., Honolulu, Hawaii, Apr. 2005.

[9] L. Kempel, S. Schneider, T. Kastle, and G. Theile, "Comparison of two termination schemed for a half-width leaky-wave antenna," URSI National Radio Science Mtg., Washington DC, July 2005.

[10] P. Baccarelli, P. Burghignoli, F. Frezza, A. Alli, and P. Lampariello, "The nature of the end-of-scanning region in printed-circuit arrays of leaky-wave antennas," *IEEE Ant. Wirless Propagat. Ltrs*., 1, pp. 60-63, 2002.

[11] P. Baccarelli, P. Burghignoli, F. Frezza, A. Alli, and P. Lampariello, "Novel modal properties and relevant scanning behaviors of phased arrays of microstrip leaky-wave antennas," *IEEE Trans. Antennas Propagat*., 51, pp. 3228-3238, Dec. 2003.

[12] H. A. Wheeler, "Transmission line properties of parallel strips separated by a dielectric sheet," *IEEE Trans. Microwave Theory Tech*., 13, pp. 172-185, 1965.

[13] J. L. Volakis, A. Chatterjee, and L. C. Kempel, *Finite Element Methods for Electromagnetics*, IEEE Press: Piscataway, N.J., 1998.

[14] C. F. Smith, A. F. Peterson, R. Mittra, "The biconjugate gradient method for electromagnetic scattering," *IEEE Trans. Antennas Propagat*., 38, pp. 938-940, June 1990.

[15] H. F. Jordan and G. Alaghband, *Fundamentals of Parallel Processing,* Prentice Hall: Upper Saddle River, NJ, 2003.

[16] MSU High Performance Computing Center, http://www.hpc.msu.edu.

[17] C.A. Balanis, *Antenna Theory: Analysis and Design*, 3rd Ed., Chapter 14, Wiley: New York, 2005.

Daniel S. Killips was born in Bay City, MI, in May 1979. He earned his B.S.E.E. at Michigan State University in 2002 as well as the M.S.E.E. in 2004. Currently he is completing his Ph.D. at Michigan State University and anticipates graduating by May 2007.

His primary research interests include electromagnetic material characterization and design. Throughout his research, Daniel has presented at such conferences as Antennas and Propagation Symposium as well as Antennas and Measurements Techniques Association. He is a member of Eta Kappa Nu, and a student member to IEEE.

Joshua S. Radcliffe received a B.S.E.E. from Cedarville University in 2002 and an M.S.E.E from the University of Dayton in 2005. He has 3 years experience as an electronics engineer working in applied Radio Frequency Aperture Technology for the Sensors Directorate of the Air Force Research Laboratory at Wright-Patterson AFB, Ohio. Mr. Radcliffe has authored four publications and coauthored five others. Mr. Radcliffe is a member of IEEE and the Antenna Measurement Techniques Association (AMTA).

Leo C. Kempel was born in Akron, OH, in October 1965. He earned his B.S.E.E. at the University of Cincinnati in 1989 as well as the M.S.E.E. and Ph.D. degrees at the University of Michigan in 1990 and 1994, respectively.

After a brief Post-Doctoral appointment at the University of Michigan, Dr. Kempel joined Mission Research Corporation in 1994 as a Senior Research Engineer. He led several projects involving the design of conformal antennas, computational electromagnetics, scattering analysis, and high power/ultrawideband microwaves. He joined Michigan State University in 1998. Prof. Kempel's current research interests include computational electromagnetics, conformal antennas, microwave/millimeter wave materials, mixed-signal electromagnetic interference techniques, and measurement techniques. Prof. Kempel has been awarded a CAREER award by the National Science Foundation and the Teacher-Scholar award by Michigan State University in 2002. He also received the MSU College of Engineering's Withrow Distinguished Scholar (Junior Faculty) Award in 2001. He served as an IPA with the Air Force Research Laboratory's Sensors Directorate from 2004-2005 and is currently on a new IPA appointment with AFRL. He is the inaugural director of the Michigan State University High Performance Computing Center.

Dr. Kempel served as the technical chairperson for the 2001 Applied Computational Electromagnetics Society (ACES) Conference and technical co-chair for the Finite Element Workshop held in Chios, GREECE in 2002. He is a member of the Antennas and Propagation Society's Administrative Committee and was a member of the ACES Board of Directors (2003-2006). He is an Associate Editor for the *IEEE Transactions on Antennas and Propagation*. He is an active reviewer for several IEEE publications as well as T-AP, JEWA and Radio Science. He co-authored *The Finite Element Method for Electromagnetics* published by IEEE Press. Dr. Kempel is a member of Tau Beta Pi, Eta Kappa Nu, and Commission B of URSI.

Stephen W. Schneider received his B.S.E.E. degree from Arizona State University in 1985 and the MS and Ph.D. degree from the Ohio State University in 1988 and 1992, respectively. He has over 20 years of experience in the area of applied electromagnetics. From 1985 to 1992, Dr. Schneider was employed at the Ohio State University ElectroScience Laboratory where he was involved in the analysis, design and measurement of periodic surfaces for frequency selective surfaces and phased arrays. Since 1992, Dr. Schneider has been a civilian researcher at Wright-Patterson AFB OH, where he is currently a Principal Engineer performing research and development in Applied Radio Frequency Aperture Technology for the Sensors Directorate of the Air Force Research Laboratory. He is responsible for creating and leading multidisciplinary teams and is a technical consultant on numerous Air Force, Joint Service, and other Federal research initiatives. He is an active, dedicated mentor to a large number of AFRL junior workforce professionals. Dr. Schneider is the Past President of the Antenna Measurement Techniques Association (AMTA) and was also the Technical Coordinator for that association's annual meeting from 2002-2004. He is a member of Tau Beta Pi and Eta Kappa Nu, a member of AMTA and the Association of Old Crows (AOC), and a Senior Member of the IEEE.

Macro-Scale Basis Functions for the Method of Moment Analysis of Large Periodic Microstrip Arrays

(*Invited paper*)

A. Cucini and S. Maci
Dipartimento di Ingegneria dell'Informazione, University of Siena, Via Roma 56, 53100 Siena, Italy
E-mail: cucini@dii.unisi.it, macis@dii.unisi.it

Abstract – This paper presents a hybrid numerical-asymptotic technique for the analysis of large periodic microstrip arrays. In the solution of a typical array problem, both macro-scale and element-scale spatial variations of the electromagnetic quantities are encountered. For large periodic arrays, the truncated periodicity induces a macro-scale behavior that is weakly dependent on the radiating elements themselves, but strongly dependent on the array periodicity and phasing. To incorporate this global phenomena, appropriate macro-scale functions are used in the framework of a method of moment solution. These macro-functions are associated to Floquet wave induced diffracted waves and guided waves, excited at the array boundary. The properties of these functions are discussed here. The technique is applied to the simple but significant case of printed dipole array, in order to demonstrate the effectiveness of the approach.

I. INTRODUCTION

Modelling large periodic array antennas involves critical issues relevant to the intrinsic multi-scale features of these structures. Macro-scale spatial variations coexist with element-scale variations which require much-smaller than wavelength discretization. These latter are due to element shape, and are responsible of quasi-static interactions which often dominate the frequency response of the antenna input impedance. On the other side, macro-scale variations are strongly dependent on the periodicity of the array and on the phasing of the excitation. Aim of this paper is to highlight such basic macro-scale phenomena and to incorporate them, as array-domain basis functions, into a full-wave method of moment (MoM) analysis of the entire structure. In order to simplify the treatment, we will refer to simple configurations constituted by finite periodic arrays of printed dipoles on a grounded dielectric slab.

The approach based on the MoM solution of integral equations is largely used for array problems. It is well known, however, that conventional formulations are severely limited by the problem size. Large and very-large arrays are often treated using the approximation of infinite periodic structure [1], [2]. Under this hypothesis, the electromagnetic analysis is reduced to that of a single periodic cell, by representing the Green's function of the infinite array as a summation of Floquet waves (FWs). This approach, although computationally very efficient, cannot be rigorously applied when the array has a finite extension, since FWs do not constitute a complete basis. The truncation effects are particularly relevant for elements near the array edge and, for wide scan angles, even for elements at the center of the array. Moreover, in the case of arrays printed on a stratified dielectric media or with a dielectric cover, the array truncation may excite guided waves (either surface waves (SWs) or leaky waves (LWs)) that cannot be predicted through the analysis of the infinite periodic array. These guided waves cause large oscillations of the current amplitude over the array and are responsible of scan-blindness effects in phased array antennas [3]. The presence of SWs can be detected also in finite free-space dipole arrays, when the array operates below the resonance and the inter-element spacing is smaller than half of a wavelength [4].

On the other side, a brute force application of the MoM to the finite array leads indeed to large, dense and sometimes ill-conditioned matrices, with a consequent huge memory occupation and CPU

1054-4887 ' 2006 ACES

time. In order to overcome these problems, synthetic [5] or characteristic [6] basis functions have been recently proposed. These basis functions are defined from the solution of small-size numerically-tractable problems, and then used in the MoM solution of the large problem. This allows one to incorporate the small- and intermediate-scale features of the structure, while maintaining a reduced number of unknowns.

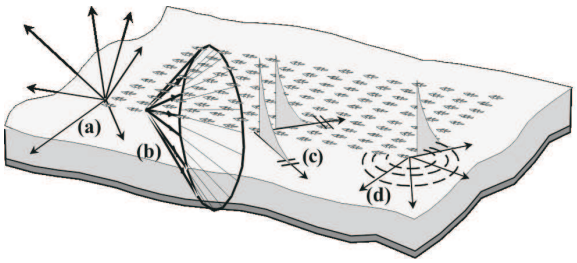

Fig. 1. Waves excited by Floquet waves at a finite array of linearly phased elementary dipoles printed on a grounded dielectric slab: (a) spherical vertex-excited (space) diffracted wave, (b) conical edge-excited (space) diffracted wave, (c) planar edge-excited surface wave, (d) cylindrical vertex-excited surface wave.

In this paper, the use of problem-matched macro-scale basis functions is proposed, to obtain a compression of the MoM matrix, provided that a suitable integral equation is derived in order to isolate the edge-induced phenomenology. The basic principles of this technique have been introduced in [8]-[10] for free-space arrays, such as dipole or slot arrays as well as open-ended waveguide arrays, and it is extended here to arrays composed of planar radiating elements printed on or embedded in dielectric stratifications.

The definition of macro-scale functions is based on a high-frequency analysis of the radiation and scattering by truncated periodic arrays. The frequency-domain phenomenology of wave excitation in truncated periodic arrays has been extensively analyzed in a series of recent papers dealing with semi-infinite and sectoral arrays in free space [11]-[13] and in stratified media [14]. The various species of diffracted and guided waves excited in a truncated periodic array are illustrated in Fig. 1, referring to a finite array of elementary electric dipoles on a infinite grounded dielectric slab. Each periodicity-induced FW excites conical and spherical space diffracted waves emanating from array edges and corners, respectively. These wave contributions are also present when the array is in free-space. In addition, plane and cylindrical guided waves (which can be either SWs or LWs) are excited at edges and corners of the array. The direction of propagation of edge-induced diffracted and guided waves is such as to match the phase velocity of the dominant FW along the edge. As we will see next, while for elementary dipoles the SW/LW wavenumber is dictated by the multilayered dielectric environment [14], for actual finite-size patches the SW/LW wavenumber is influenced also by the presence of the periodic metallization, and its calculation cannot leave apart the solution of the dispersion equation.

The paper is organized as follows. Sec. III summarizes the formulation that allows to separate the different features of the array: the original integral equation (IE) is decomposed into two equations, one relevant to the infinite periodic problem, and one relevant to the truncation-induced current. The infinite periodic array IE is solved in Sec. IV by using a conventional spectral-domain FW approach. Then Sec. V presents the solution of the integral equation associated to the truncation effects. Particular emphasis is given to the identification and construction of the array-domain basis function, which allows for a numerically efficient and physically appealing solution. Numerical results are presented in Sec. VI to show the accuracy of the method as compared with a conventional element-by-element technique. Finally, some concluding remarks are traced in Sec. VII.

II. INTEGRAL EQUATIONS FORMULATION

The geometry of a finite rectangular periodic array of printed dipoles is shown in Fig. 2. The array is composed by x-oriented dipoles, with length L and width W ($W \ll L$), arranged on a rectangular grid, with spatial periodicity denoted by d_x and d_y. The grounded dielectric slab has thickness h and relative permittivity ε_r. The array excitation may be provided by an incident plane wave (Fig. 2a) or by delta-gap sources (Fig. 2b), with uniform amplitude and linear phase $e^{-j\mathbf{k}_0\cdot\mathbf{r}}$, where an $e^{j\omega t}$ time dependence has been assumed and

suppressed. In the previous expression, $\mathbf{r} = x\hat{x} + y\hat{y}$ is the position vector in an arbitrary point of the array plane, $\mathbf{k}_0 = \gamma_x\hat{x} + \gamma_y\hat{y}$ is the transverse-to-z wavevector component of the excitation field, where $\gamma_x = k\sin\theta_0\cos\phi_0$, $\gamma_y = k\sin\theta_0\sin\phi_0$, $k = \omega\sqrt{\epsilon_o\mu_o}$ is the free-space wavenumber, and (θ_0, φ_0) denote the direction of the scattered/radiated main beam in the conventional spherical coordinate system.

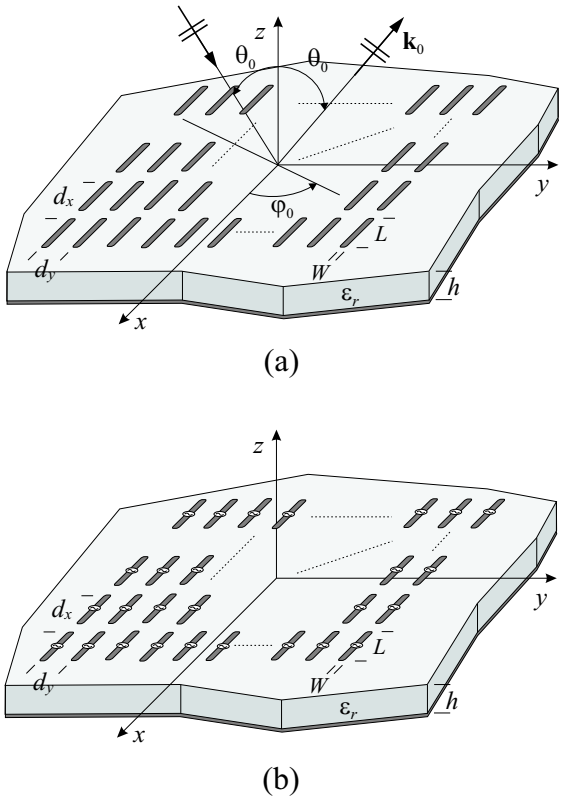

Fig. 2. Finite rectangular planar periodic array of metallic dipoles printed on a grounded dielectric slab. (a) Scattering problem: incident plane-wave excitation; (b) Radiation problem: delta-gap excitation.

An electric current distribution $\mathbf{J}$ is defined on the surface of the printed dipoles. Imposing the vanishing of the total electric field at the perfectly conducting dipoles yields the electric field integral equation (EFIE)

$$\chi_A \mathbf{E}^s_{tan}(\mathbf{J}) = -\chi_A \mathbf{E}^{imp}_{tan} \tag{1}$$

where $\mathbf{E}^s_{tan}(\mathbf{J})$ is the tangential (to the xy-plane) component of the electric field scattered by the unknown current distribution $\mathbf{J}$ and $\mathbf{E}^{imp}_{tan}$ is the impressed tangential electric field. In Eq. (1), A denotes the portion of the xy-plane occupied by the conducting dipoles and χ_A is the characteristic function of A ($\chi_A(\mathbf{r}) = 1$ if $\mathbf{r} \in A$, $\chi_A(\mathbf{r}) = 0$ if $\mathbf{r} \notin A$).

Following the procedure introduced in [7], [8], the unknown electric current is decomposed as

$$\mathbf{J} = \chi_A \mathbf{J}_\infty + \mathbf{J}_f \tag{2}$$

where $\mathbf{J}_\infty$ is the infinite periodic array current, and $\mathbf{J}_f$ denotes the 'fringe' current, i.e. the perturbation current induced by the truncation. We define $\chi_A\mathbf{J}_\infty$ as the Physical Optics (PO) approximation current, where the PO terminology is used with reference to the abrupt truncation (via the function χ_A) of the infinite array current on A. The current $\mathbf{J}_\infty$ is the solution of the EFIE pertinent to the infinite periodic array,

$$\chi_\infty \mathbf{E}^s_{tan}(\mathbf{J}_\infty) = -\chi_\infty \mathbf{E}^{imp}_{tan} \tag{3}$$

where χ_∞ is the characteristic function of the dipole region of the infinite periodic array. Note that the infinite array characteristic function can be written as $\chi_\infty = \chi_A + \chi_{A^*}$, where A^* is the portion of the xy-plane external to the array region A.

By inserting (2) into (1), and successively subtracting (3) from (1), yields the Fringe Integral Equation (FIE)

$$\chi_A \mathbf{E}^s_{tan}(\mathbf{J}_f) = \chi_A \mathbf{E}^s_{tan}(\chi_{A^*}\mathbf{J}_\infty) \tag{4}$$

whose unknown function is the fringe current $\mathbf{J}_f$. The forcing term of Eq.(4), $\chi_A \mathbf{E}^s_{tan}(\chi_{A^*}\mathbf{J}_\infty)$, represents the tangential component of the electric field radiated by the infinite array current truncated on the complementary array region A^*. (Note that this term is known once the infinite array current has been computed.) Thus, the FIE (4) interprets the fringe current $\mathbf{J}_f$ as the perturbation, with respect to the PO approximation, which is necessary to compensate for the absence of radiation from the suppressed current $\chi_{A^*}\mathbf{J}_\infty$, in order to ensure the boundary conditions (1) on A. The total current of the finite array is found, through relationship (2), by the MoM solution of Eq. (3) and (4), with the process described next.

III. INFINITE PERIODIC ARRAY SOLUTION

The first step of the procedure is the MoM solution of the integral equation (3) relevant to the

infinite periodic array. The problem is solved by using a conventional periodic MoM [1]. The current $\mathbf{J}_\infty$ of the infinite periodic array respects the pseudo-periodic property imposed by the Floquet condition

$$\mathbf{J}_\infty(\mathbf{r}) = \mathbf{J}_0(\mathbf{r})e^{-j\mathbf{k}_0\cdot\mathbf{r}} \tag{5}$$

where $\mathbf{J}_0(\mathbf{r})$ is a doubly periodic function with periodicity (d_x, d_y). Thus, the MoM computation of the infinite array current is reduced to that of a single periodic cell, by representing the Green's function kernel as a summation of FWs. The electric current $\mathbf{J}_0$ on the dipole of the reference cell is expanded into a set of basis functions (either entire or sub-domain functions). By applying the Galerkin method, the integral equation (3) is reduced to the algebraic linear system

$$\overline{\overline{Z}}_\infty(\mathbf{k}_0, \omega)\bar{I} = \bar{V}(\mathbf{k}_0, \omega) \tag{6}$$

where, for the sake of convenience, we have explicitated the dependence of the matrix $\overline{\overline{Z}}_\infty$ and of the vector $\bar{V}$ (and consequently of the unknown coefficients vector $\bar{I}$) on the excitation wavevector $\mathbf{k}_0$ and (angular) frequency ω.

IV. FRINGE INTEGRAL EQUATION SOLUTION

The solution of the FIE is expressed in terms of diffracted and guided wave contributions associated to the truncation effects. The unknown fringe current $\mathbf{J}_f$ is expanded using array-domain basis functions, associated to diffracted waves $\mathbf{F}^d_{i,\mu}$ and to guided waves $\mathbf{F}^{GW}_{i,\nu}$,

$$\mathbf{J}_f(\mathbf{r}) \approx \sum_i \left[\sum_\mu a_{i,\mu}\mathbf{F}^d_{i,\mu}(\mathbf{r}) + \sum_\nu b_{i,\nu}\mathbf{F}^{GW}_{i,\nu}(\mathbf{r}) \right] \tag{7}$$

where $a_{i,\mu}$ and $b_{i,\nu}$ are unknown coefficients to be determined through a MoM scheme. In the previous expressions, the first subscript ($i = 1, \ldots, 4$) denotes the edge numbering of the rectangular array, while the second subscript μ (ν) denotes the diffracted (guided) wave. The array-domain basis functions are obtained by multiplication of the element-scale current $\mathbf{J}^d_{i,\mu}$ and $\mathbf{J}^{GW}_{i,\nu}$ with the macro-scale functions $f^d_{i,\mu}$ and $f^{GW}_{i,\nu}$, respectively,

$$\mathbf{F}^d_{i,\mu}(\mathbf{r}) = \sum_{\mathbf{r}_{nm}\in A} \mathbf{J}^d_{i,\mu}(\mathbf{r}-\mathbf{r}_{nm}) f^d_{i,\mu}(\mathbf{r}_{nm}) \tag{8}$$

$$\mathbf{F}^{GW}_{i,\nu}(\mathbf{r}) = \sum_{\mathbf{r}_{nm}\in A} \mathbf{J}^{GW}_{i,\nu}(\mathbf{r}-\mathbf{r}_{nm}) f^{GW}_{i,\nu}(\mathbf{r}_{nm}). \tag{9}$$

Details on the selection and construction of the macro-scale and element-scale functions are given in the following paragraph. It is worth noting that the number of basis functions is completely independent of the number of array elements, thus allowing the numerical analysis of arbitrarily large arrays with the same number of unknowns.

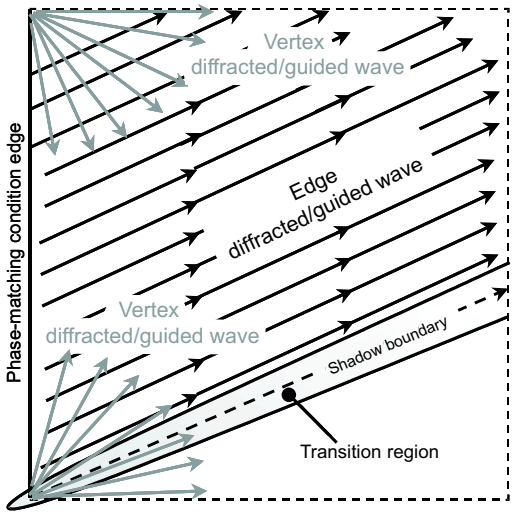

Fig. 3. Ray description of macro-scale diffracted and guided wave basis functions. The macro-scale function includes an edge contribution plus two end-point vertex contributions, ensuring the unform continuity of the current at the shadow boundaries. The propagation constant along the edge is fixed by the excitation according the generalized Fermat condition in (13) and (14).

A. Macro-scale functions: FW-matched diffracted and guided waves

Each macro-scale function $f^d_{i,\mu}$, $f^{GW}_{i,\nu}$ includes an edge contribution plus two end-point vertex contributions, which ensure the uniform continuity to the current (Fig. 3). The edge diffracted waves are cylindrical wave which asymptotically propagate with the speed of light and decay like $\rho_i^{-3/2}$, where ρ_i denotes the distance of the observation point from the i-th edge. The vertex diffracted waves are spherical waves with ray spreading r_i^{-2}, being r_i the distance from the i-th vertex. The exact expression of the FW-induced space diffracted waves

and the relevant phenomenology is given in [8]-[10]. The edge-excited guided waves decay as ρ_i^0 (inhomogeneous plane waves), thus providing the dominant contribution to the fringe current $\mathbf{J}_f$. The propagation constant of the guided waves is dictated by the environment and by the shape and periodicity of the microstrip array elements. The problem of the identification of the guided waves wavenumbers is addressed in the following sub-section. The vertex-excited terms are cylindrical waves originating from the end-point of the edge with ray spreading $r_i^{1/2}$. In this latter case, we approximate the wavenumber with that of the relevant edge term, by using the criterion to compensate for the discontinuities at the shadow boundaries. Actually, the propagation constant of the guided waves excited in the array varies with the azimuthal angle since the 'effective' periodicity of the medium depends on this angle. Nevertheless, it will be shown from the numerical results that this approximation does not affect the accuracy of the method.

B. Identification of FW-matched guided wavenumber

The propagation constant of the guided waves excited in the microstrip array differs from that of the grounded slab modes, since it is affected by the periodic loading effect of the finite-size metallic patches. Indeed, the guided waves excited in the microstrip array can be seen as a periodicity-induced perturbation of those supported by the bare grounded slab structure. The individuation of the propagation constant of the array guided waves is achieved through the solution of a homogeneous resonance equation [15] which is obtained from Eq. (6) by removing the excitation term, namely

$$\overline{\overline{Z}}_\infty(\mathbf{k}^{GW},\omega)\bar{I}=0. \tag{10}$$

For any frequency, this equation admits non-trivial solutions when the matrix determinant vanishes, i.e.,

$$\det[\overline{\overline{Z}}_\infty(\mathbf{k}^{GW},\omega)]=0 \tag{11}$$

where the unknown is the guided-wave complex transverse wavevector

$$\mathbf{k}^{GW}=k_x^{GW}\hat{x}+k_y^{GW}\hat{y} \qquad GW=SW,LW. \tag{12}$$

When the propagation wavenumber is real ($k_{x,y}^{SW}=\beta_{x,y}^{SW}$), the corresponding mode is a bound (non-radiating) SW. When the propagation constant is complex ($k_{x,y}^{LW}=\beta_{x,y}^{LW}-j\alpha_{x,y}^{LW}$), the mode is a (radiating) LW. The elements of the matrix $\overline{\overline{Z}}_\infty$ involve a double summation in the spectral domain over the transverse FW wavenumbers $k_{xp}^{GW}=k_x^{GW}+2\pi p/d_x$ and $k_{yq}^{GW}=k_y^{GW}+2\pi q/d_y$. Different branch choices are possible for the doubly infinite number of spatial harmonics. The branch choice for the wavenumber in the dielectric region $k_{zd,pq}=\sqrt{\varepsilon_r k^2-k_{xp}^2-k_{yq}^2}$ (the superscript GW has been suppressed for simplicity) is arbitrary, since the Green's function is an even function of $k_{zd,pq}$. Each wavenumber in the semi-infinite air region $k_{z,pq}=\sqrt{k^2-k_{xp}^2-k_{yq}^2}$ may be chosen to be proper (negative imaginary part, corresponding to a spatial harmonic that exponentially decays in the z-direction) or improper (positive imaginary part, corresponding to a harmonic exponentially increasing in the z-direction). Since only physical solutions must be retained, the branches are chosen according the rules given next. Before proceeding further, it is worth emphasizing that, since we are looking for edge-excited guided waves, one component of the propagation constant (the one along the edge) is imposed by the phasing of the excitation.

In the SW case, the FW phase-matching condition [14] along the edges of the array imposes

$$\beta_x^{SW}=k_{xp}^{FW} \quad \text{or} \quad \beta_y^{SW}=k_{yq}^{FW} \tag{13}$$

for edges along x or y, respectively, where $k_{xp}^{FW}=\gamma_x+2\pi p/d_x$ and $k_{yq}^{FW}=\gamma_y+2\pi q/d_y$ are the FW transverse wavenumbers. Consequently, the only unknown is the real propagation constant orthogonal to the edge. In this case, all FW harmonics are in the slow-wave region and the proper branch choice is taken.

In the LW case, the phase-matching condition imposes

$$\begin{aligned}\beta_x^{LW}&=k_{xp}^{FW},\ \alpha_x^{LW}=0\\ \beta_y^{SW}&=k_{yq}^{FW},\ \alpha_y^{LW}=0\end{aligned} \tag{14}$$

for edges along x or y, respectively. Note that, since the transverse components of FW wavevectors are real, the LW attenuation constant along the edges is always zero. In this case, the unknowns are the propagation and attenuation constant orthogonal to the edge. For a radiating fast-wave harmonic the physical solution correspond to the proper branch choice when the harmonic is a backward wave (the

group velocity is in opposite direction with respect to the phase velocity), and to the improper one when the harmonic is a forward wave [16].

Finally we note that, since in practical phased array antenna or FSS problems only one FW harmonic is propagating, the couple of indices p, q in (13) and (14) reduces to $p, q = (0, 0)$.

C. Element-scale functions

The element current distribution $\mathbf{J}_{i,\mu/\nu}^{d/GW}(\mathbf{r})$, associated to both diffracted and guided waves, has to be determined, to construct the basis functions (8) and (9).

In the case of guided-wave current, $\mathbf{J}_{i,\nu}^{GW}(\mathbf{r})$ represents the eigenfunction of the homogeneous system (10), which can be computed by setting to unity one element of the vector $\bar{I}$ and then solving for the remaining elements [17].

In the case of diffracted-wave functions, the element current on the dipoles $\mathbf{J}_{i,\mu}^{d}(\mathbf{r})$ is assumed of resonant type, without care on the sub-wavelength details, which are indeed described by the infinite array solution. For more complicated element shapes, synthetic basis functions are generated by solving a periodic array problem with a suitable excitation [18].

V. NUMERICAL RESULTS

In this section, a sample of numerical results is shown to validate the above technique and to highlight some typical truncation effects of finite microstrip arrays. The results obtained with this technique (labelled $\mathrm{T(FW)}^2$) are compared with those from a conventional element-by-element MoM (El.-by-el. MoM) and with the (windowed) infinite array approximation (PO approx.). In all cases, the current on the dipoles is expanded in terms of PWS basis functions.

First, a 41×41 array is considered, with dipole length $L = 0.6$ cm, width $W = 0.1$ cm, and periodicity $d_x = d_y = 0.8$ cm. The dielectric substrate has relative permittivity $\varepsilon_r = 10.2$ and thickness $h = 0.1905$ cm. An incident TM-polarized plane wave is assumed to illuminate the array, with the scattered main beam angles $\theta_0 = 40^o$ and $\varphi_0 = 20^o$. The operating frequency is $f = 7$ GHz. The propagation constants of the guided waves excited at the edges of the array are computed by solving the resonance equation (11). Only one real solution is found, corresponding to a non-radiating SW. Complex roots associated to LWs are neglected due to the high values of the attenuation constant. The propagation constant of the SW excited by the y-oriented edges is given by Eq. (11), with the $k_y^{GW} = k \sin\theta_0 \sin\varphi_0 = 0.22k$, that yields $k_x^{GW} = \beta_x = 1.197k$. For the SW excited by the x-oriented edges, the solution of Eq. (11), with $k_x^{GW} = k \sin\theta_0 \cos\varphi_0 = 0.604k$, gives $k_y^{GW} = \beta_y = 0.920k$. Thus, the transverse propagation constant of the SW supported by the array is $k^{GW} = |\mathbf{k}^{GW}| = 1.217k$ for the mode excited by the y-

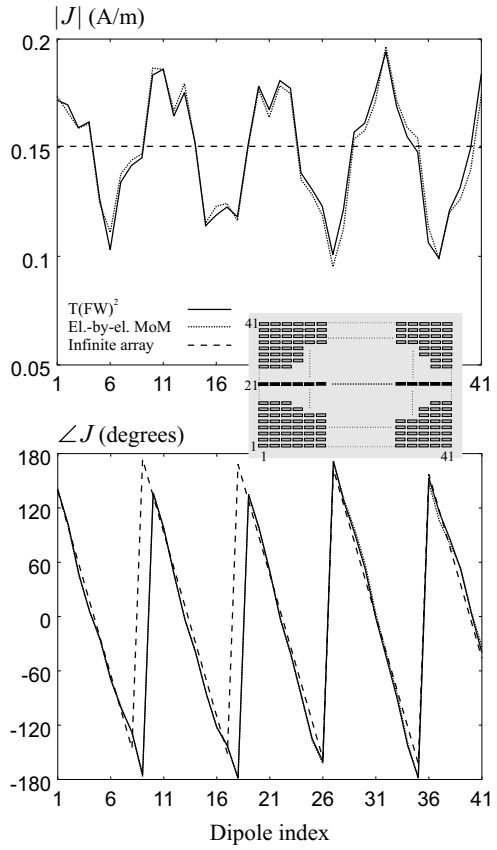

Fig. 4. Magnitude (in A/m) and phase (in degrees) of the surface electric current sampled at the centers of the dipoles on the central row of the array. Results refers to a 41×41 array of dipoles with $L = 0.6$ cm, $W = 0.1$ cm, $d_x = 0.8$ cm, and $d_y = 0.8$ cm. The dielectric substrate has $\varepsilon_r = 10.2$ and $h = 0.1905$ cm. The array is excited by an incident TM-polarized plane wave with $\theta_0 = 40^o$ and $\varphi_0 = 20^o$. The operating frequency is $f = 7$ GHz.

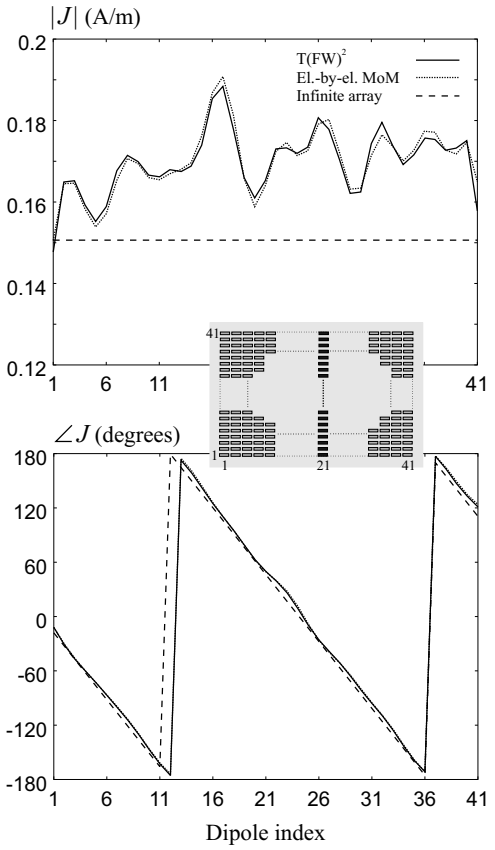

Fig. 5. Magnitude (in A/m) and phase (in degrees) of the surface electric current sampled at the centers of the dipoles on the central row of the array. Results refers to the 41×41 array of dipoles described in the caption of Fig. 4.

oriented edges, and $k^{GW} = |\mathbf{k}^{GW}| = 1.1k$ for the mode excited by the the x-oriented edges. Note that the phase constant of the SWs excited at two orthogonal edges differs each other, due to the anisotropy of the *effective* periodic medium. Figs. 4 and 5 present the electric current (amplitude and phase), sampled at the centers of each dipole, for the dipoles on the central row and on the central column of the array, respectively. An excellent agreement is found between the present technique (solid line) and the reference solution (dotted line). Also the infinite array data (dashed line) are shown in the diagrams, in order to appreciate the influence of the fringe current contributions. In the E-plane (Fig. 4), this influence can be quantified in terms of a large oscillation of the current amplitude around the value of the infinite array level. The normalized far

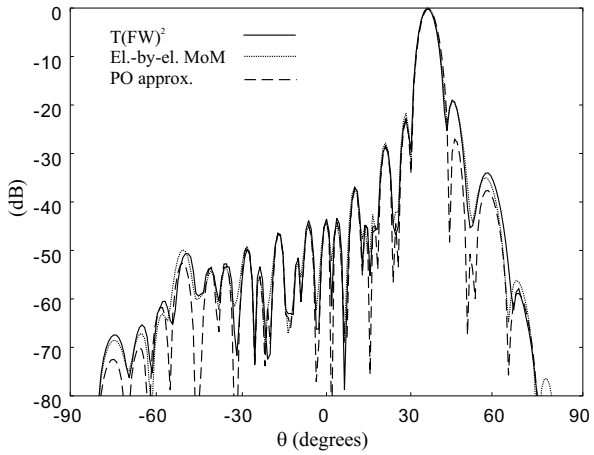

Fig. 6. Normalized far field scattered by the array on the incidence plane. Results refers to the 41×41 array of dipoles described in the caption of Fig. 4.

field scattered by the array on the incidence plane is shown in Fig. 6. It can be noted that the crude PO approximation (dashed line) fails in predicting even the amplitude of the first side lobe.

In the previous case the dominating guided mode was a bound SW. This mode does not radiate directly, but affects the far-field pattern by virtue of the diffraction at the truncation of the array. A change in the nature of the guided wave may happen when the frequency is varied. When one of the spatial harmonics associated to the guided wave enters the visible region, the wave becomes a radiating LW, with a complex propagation constant. To describe this phenomenon and its effects on the array performance, we refer to a 19×19 array of dipoles, with length $L = 0.39$ cm, width $W = 0.01$ cm, and periodicity $d_x = d_y = 0.6$ cm, printed on a dielectric substrate with thickness $h = 0.1$ cm and relative permittivity $\varepsilon_r = 2.55$. The array is illuminated by an incident plane wave from broadside, at frequency $f = 30$ GHz. The diffracted and guided waves excited at the array edges propagate orthogonally to the edges. The dominant TM guided wave is excited at the y-oriented edges of the array (direction of propagation along the dipoles), while it is not excited at the x-oriented edges, due to the polarization mismatch (direction of propagation orthogonal to the dipoles). The solution of the dispersion equation with $k_y^{GW} = 0$, yields the propagation constant of the dominant TM mode of the structure.

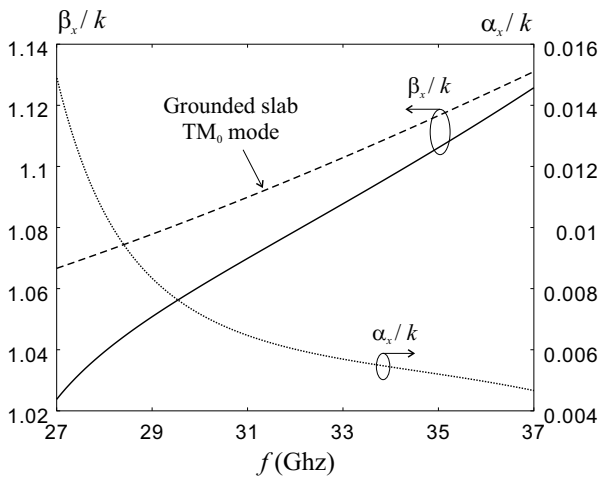

Fig. 7. Normalized phase (solid line) and attenuation (dotted line) constants of the fundamental harmonic $(p, q) = (0, 0)$ of the dominant TM mode versus frequency for the infinite periodic array of printed dipoles, with $L = 0.39$ cm, $W = 0.01$ cm, $d_x = 0.6$ cm, $d_y = 0.6$ cm, $\varepsilon_r = 2.55$, and $h = 0.1$ cm. Propagation along x direction is considered. Also the normalized propagation constant of the dominant TM_0 mode of the grounded dielectric slab is plotted (dashed line).

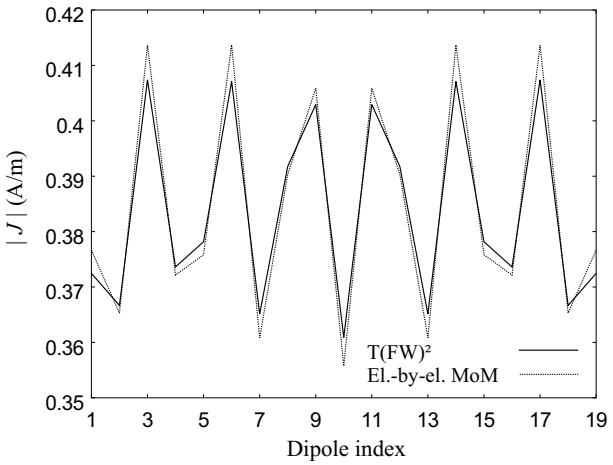

Fig. 8. Magnitude (in A/m) of the surface electric current sampled at the centers of the dipoles on the central row of the array. Results refers to a 19×19 array of dipoles, with $L = 0.39$ cm, $W = 0.01$ cm, $d_x = d_y = 0.6$ cm, $h = 0.1$ cm and $\varepsilon_r = 2.55$. The array is excited by a broadside incident plane wave at frequency $f = 30$ GHz.

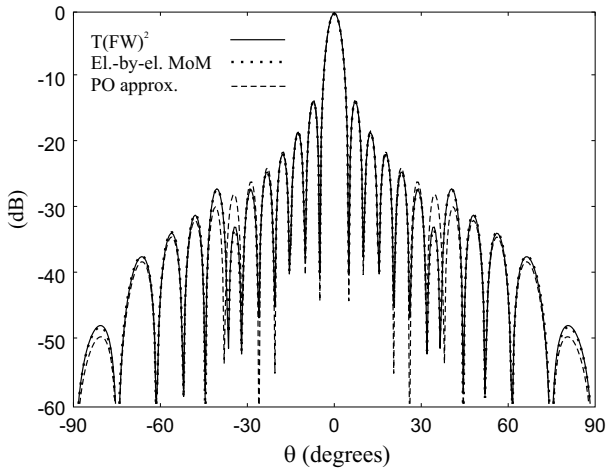

Fig. 9. Normalized magnitude of the θ-component of the electric field scattered by the array on the E-plane, for broadside plane-wave incidence. Results refers to the 19×19 array of dipoles of Fig. 8.

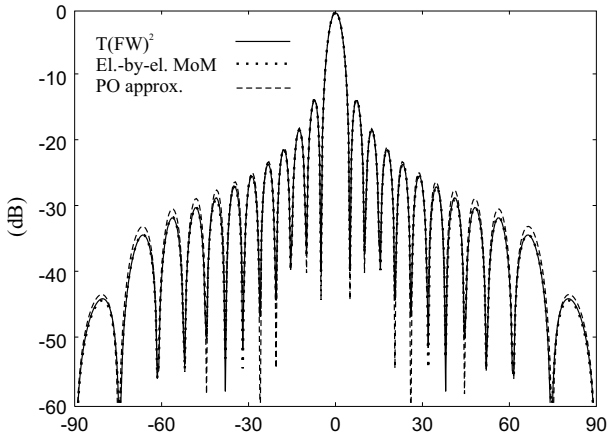

Fig. 10. Normalized magnitude of the ϕ-component of the electric field scattered by the array on the H-plane, for broadside plane-wave incidence. Results refers to the 19×19 array of dipoles of Fig. 8.

The $\beta - f$ diagram in Fig. 7, shows the behavior of the normalized phase and attenuation constants of the fundamental harmonic $(p, q) = (0, 0)$ of the wave in the frequency range $(27 - 37)$ GHz, together with the behavior of the normalized phase constant of the TM_0 surface wave of the grounded bare dielectric slab. At the operating frequency, the value of the propagation constant of the fundamental harmonic is $\beta_{x,00} - j\alpha_x = (1.0607 - j0.0071)k$. The $(p, q) = (-1, 0)$ spatial harmonic of the dominant TM mode is in the $\beta_x < 0$ zone of the fast-wave

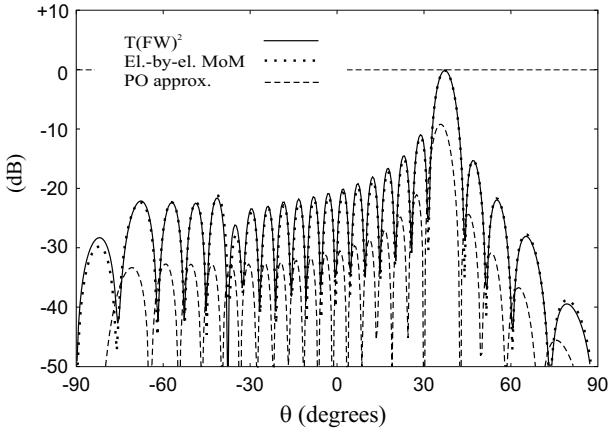

Fig. 11. Normalized magnitude of the θ-component of the electric field scattered by the array on the E-plane, for ($\varphi = 0^o$, $\theta_0 = 36^o$) plane-wave incidence. Results refers to the 19×19 array of dipoles of Fig. 8.

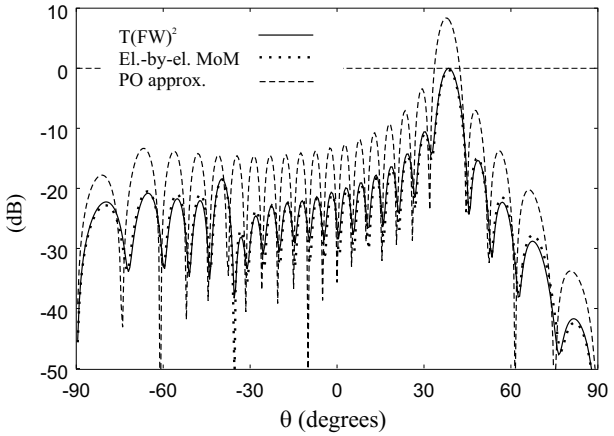

Fig. 12. Normalized magnitude of the θ-component of the electric field scattered by the array on the E-plane, for ($\varphi = 0^o$, $\theta_0 = 38^o$) plane-wave incidence. Results refers to the 19×19 array of dipoles of Fig. 8.

region; thus, representing a backward radiating LW, with the imaginary part of the propagation constant associated to the leakage of power. The direction of maximum radiation of the LW, computed through the relationship $\theta_{LW} \approx \sin^{-1}(\beta^{LW}_{x,-1,0}/k)$, is ± 37.6 degrees.

The results obtained with the present technique (solid line) are compared with the reference element-by-element MoM solution (dotted line). Fig. 8 presents the amplitude of the electric current at the center of the dipoles along the central row of the array. Fig. 9 shows the normalized scattered far field on the E-plane. The dip, noticeable in the far-field pattern around ± 37.6 degrees, is due to the interference between the PO field and the field radiated by the $(p, q) = (-1, 0)$ harmonic of the dominant LW mode excited at the two edges of the array (those orthogonal to the dipoles). In the case of a phased array antenna, this kind of LW is responsible for the scan-blindness phenomenon. Clearly, this effect cannot be predicted by a crude PO approximation (dashed line in Fig. 9), since it neglects the excitation of guided waves. Leaky wave radiation is absent on the H-plane, as shown in the far-field pattern of Fig. 10, due to the fact that the leaky-wave pattern has a null on this plane (analogously to the case of a TM mode excited by a dipole on a grounded dielectric slab). In order to better appreciate the effects of the LW radiation on the scattered field, two additional cases are considered with a plane wave incident along the E-plane ($\varphi = 0^o$) from directions $\theta_0 = 36$ and $\theta_0 = 38$ degrees, that are slightly below and above the LW radiation direction. Far-field results are shown in Fig. 11 and Fig. 12, and are normalized with respect to the maximum of the actual scattered field. In both cases, it is evident how the PO approximation dramatically fails in predicting the correct field. In particular, for incidence at $\theta_0 = 36$ degrees, the PO scattered field maximum is about 9 dB below the actual field maximum. Moreover, the direction of the maximum is shifted of about 1.5 degrees. On the contrary, for incidence at $\theta_0 = 38$ degrees, the PO scattered field maximum is about 8 dB above the actual field maximum, with a shift of 0.5 degrees. These results demonstrate how the infinite array approximation can lead to erroneous results in certain conditions.

VI. CONCLUSIONS

This paper presented a study on the edge effects in large periodic microstrip arrays. The analysis is performed through a hybrid numerical-asymptotic method, which allows to efficiently compute the fringe current excited at the truncation of the array. Based on physical considerations, this fringe current is expanded in terms of array-domain diffracted and guided wave basis functions. The unknown coefficients are found through the numerical solution

of a linear system, where the number of unknowns is completely independent of the number of elements in the array. Thus, this method constitutes an efficient and effective technique to analyze large arrays. Moreover, it provides a deep physical insight into the truncation effects of large periodic microstrip arrays, which can be an aid during the design stage of a practical array. The technique has been applied to the simple case of an array of microstrip dipoles, in order to highlight the fundamental effects. The generalization to more general shapes of the radiating element and to arbitrary stratified dielectric layers can be performed following the criteria furnished in this paper.

REFERENCES

[1] D. M. Pozar and D. H. Shaubert, "Scan blindness in infinite phased arrays of printed dipoles," *IEEE Trans. Antennas Propagat.*, vol. AP-32, no. 6, pp. 602-610, Jun. 1984.

[2] J.-M. Jin and J. L. Volakis, "Electromagnetic scattering by a perfectly conducting patch array on a dielectric slab," *IEEE Trans. Antennas Propagat.*, vol. 38, no. 4, pp. 556-563, Apr. 1990.

[3] G. H. Knittel, A. Hessel, and A. A. Oliner, "Element pattern nulls in phased arrays and their relation to guided waves," *IEEE Proceedings*, vol. 56, no. 11, pp. 1822-1836, Nov. 1968.

[4] D. S. Janning and B. A. Munk, "Effects of surface waves on the currents of truncated periodic arrays," *IEEE Trans. Antennas Propagat.*, vol. 50, no. 9, pp. 1254-1265, Sep. 2002.

[5] P. Pirinoli, L. Matekovits, G. Vecchi, F. Vapiana, and M. Orefice, "Synthetic functions: multiscale MoM analysis of arrays," *Proceedings of the 2003 IEEE Antennas Propagat. Society Symposium*, vol. 4, pp. 799-802, Columbus, 22-27 June 2003.

[6] J. Yeo and R. Mittra, "Numerically efficient analysis of microstrip antennas using the characteristic basis function method (CBFM)," *Proceedings of the 2003 IEEE Antennas Propagat. Society Symposium*, vol. 4, pp. 85-88, Columbus, 22-27 June 2003.

[7] A. Neto, S. Maci, G. Vecchi, and M. Sabbadini, "A truncated Floquet wave diffraction method for the full-wave analysis of large phased arrays, Part I: Basic principles and 2D case," *IEEE Trans. Antennas Propagat.*, vol. 48, no. 4, pp. 594-600, Apr. 2000.

[8] A. Neto, S. Maci, G. Vecchi, and M. Sabbadini, "A truncated Floquet wave diffraction method for the full-wave analysis of large phased arrays, Part II: generalization to the 3D case," *IEEE Trans. Antennas Propagat.*, vol. 48, no. 4, pp. 601-610, Apr. 2000.

[9] A. Cucini, M. Albani, and S. Maci, "Truncated Floquet wave full-wave ($\mathrm{T(FW)^2}$) analysis of large periodic arrays of rectangular waveguides," *IEEE Trans. Antennas Propagat.*, vol. 51, no. 6, pp. 1373-1385, Jun. 2003.

[10] A. Cucini, M. Albani, and S. Maci, "Truncated Floquet wave full-wave analysis of large phased arrays of open-ended waveguides with non-uniform amplitude excitation," *IEEE Trans. Antennas Propagat.*, vol. 51, no. 6, pp. 1386-1394, Jun. 2003.

[11] F. Capolino, M. Albani, S. Maci, and L. B. Felsen, "Frequency domain Green's function for a planar periodic semi-infinite phased array. Part I: Truncated Floquet wave formulation," *IEEE Trans. Antennas Propagat.*, vol. 48, no. 1, pp. 67-74, Jan. 2000.

[12] F. Capolino, M. Albani, S. Maci, and L. B. Felsen, "Frequency domain Green's function for a planar periodic semi-infinite phased array. Part II: Diffracted wave phenomenology," *IEEE Trans. Antennas Propagat.*, vol. 48, no. 1, pp. 75-85, Jan. 2000.

[13] F. Capolino, S. Maci, and L. B. Felsen, "Asymptotic high-frequency Green's function for a planar phased sectoral array of dipoles," *Wave Motion,*, vol. 34, no. 3, pp. 263-279, Sep. 2001.

[14] A. Polemi, A. Toccafondi, and S. Maci, "High-frequency Green's function for a semi-infinite array of electric dipoles on a grounded slab. Part I: Formulation," *IEEE Trans. Antennas Propagat.*, vol. 50, no. 12, pp. 1667-1677, Dec. 2001.

[15] H.-Y. D. Yang, K. Reonghee, and D. R. Jackson, "Design considerations for modeless integrated circuit substrates using planar periodic patches," *IEEE Trans. Microwave Theory Tech.*, vol. 48, no. 12, pp. 2233-2239, Dec. 2000.

[16] P. Lampariello, F. Frezza, and A. A. Oliner, "The transition region between bound-wave and leaky-wave ranges for a partially dielectric-

loaded open guiding structure," *IEEE Trans. Microwave Theory Tech.*, vol. 38, no. 12, pp. 1831-1836, Dec. 1990.

[17] J. L. Blanchard, E. H. Newman, M. E. Peters, "Integral equation analysis of artificial media," *IEEE Trans. Antennas Propagat.*, vol. 42, no. 5, pp. 727-731, May 1994.

[18] A. Cucini, S. Maci, and G. Vecchi, "Macro-scale modulation of local synthetic functions for large finite arrays and FSS," *28th ESA Antenna Workshop on Space Antenna Systems and Technologies*, Noordwijk, The Netherlands, 31 May - 3 June, 2005.

Alessio Cucini was born in Poggibonsi, Italy, in 1973. He received the Laurea degree (cum laude) in telecommunications engineering and the Ph.D. degree in electromagnetic engineering from the University of Siena, Italy, in 1999 and 2003, respectively. He is currently a Research Associate at the Department of Information Engineering, University of Siena, Italy. He is also with WaveComm S.r.l., a company operating in the field of electromagnetic software, antennas, sensors, and RF and microwave systems.

His research interests are in the area of applied electromagnetics, focused on numerical and asymptotic methods for phased arrays, frequency selective surfaces, EBG structures, artificial surfaces and microstrip antennas. Since 1999, he has been involved in projects of the European Space Agency (ESA) and of the European Community regarding software for antenna simulation.

Stefano Maci was born in Rome, Italy, in 1961. He received the laurea degree (cum laude) in electronic engineering from the University of Florence, Italy, in 1987. From 1990 to 1998, he was with the Department of Electronic Engineering, University of Florence, as an Assistant Professor. Since 1998, he has been an Associate Professor at the University of Siena, Italy. In 2004 he won the national competition for Full Professor.

His research interests include electromagnetic engineering, mainly concerned with high-frequency and numerical methods for antennas and scattering problems. He was a co-author of an incremental theory of diffraction, for the description of a wide class of electromagnetic scattering phenomena at high frequency, and of a diffraction theory for the high-frequency and hybrid analysis of large truncated periodic structures.

He has been and presently is responsible for several research contracts and projects supported by the European Union, by the European Space Agency (ESA-ESTEC, Noordvjiik, The Netherlands), and by various industry and research centers. In the sixth EU framework program, he is responsible of the European School of Antennas in the Antenna Center of Excellence. He was an Associate Editor of IEEE TRANSACTIONS ON ELECTROMAGNETIC COMPATIBILITY. He is presently a member of the Technical Advisory Board of the URSI Commission B and a member of the advisory board of the Italian Ph.D. School of Electromagnetism. He organized and/or served as a chairman for several special sessions at international conferences and has been chairman of two international workshops. Dr. Maci is principal author or co-author of about 45 papers in IEEE Journals, 50 papers in other international journals, and more than 200 papers in proceedings of international conferences.

A Serial-Parallel FDTD Approach for Modeling the Coupling problem between Two Large Arrays

(*Invited Paper*)

Raj Mittra[1], Hany E. Abd-El-Raouf[2], and Neng-Tien Huang[1]
[1] Electromagnetic Communication Laboratory, 319 EE East
The Pennsylvania State University
University Park, PA 16802
[2] Department of Electrical & Computer Engineering,
College of Engineering, International Islamic University Malaysia
P.O. Box 10, 50728 Kuala Lumpur, Malaysia

***Abstract*–**Solution of large problems using a numerically rigorous approach is always challenging because of the heavy burden they impose on the CPU. In this paper we introduce a new serial-parallel FDTD approach to solve large electromagnetic problems, e.g., coupling between two arrays separated by a large distance, that is difficult to handle via a direct application of the FDTD algorithm because of large size. This technique is based on dividing the original problem into relatively small sub-regions, and evaluating the solution that are localized in each of these sub-regions. The excitation of the sub-regions can either be direct sources, as for instance in the aggressor array, or be derived from the fields propagating into domain–from adjacent regions through the interfaces. We show that the results obtained by using the proposed approach compare well with the direct FDTD solution for some test problems, involving coupling between two phased arrays. Of course, the advantage of using the serial-parallel approach is that it can handle very large problems, well beyond the scope of the direct methods.

I. INTRODUCTION

Historically, various asymptotic methods e.g., PO, GTD and PTD have been employed for the solution of electrically large electromagnetic problems. It is well known, however, that asymptotic techniques are not well suited for handling problems that involve inhomogeneous media, complex geometries and multiscale features, *e.g.*, phased arrays, and it is necessary to employ numerically rigorous techniques, such as the Finite Element (FE) method or the Finite Difference Time Domain (FDTD) technique. An obvious limitation of the numerically rigorous techniques, however, is their ability to solve large problems that place a heavy burden on the CPU memory and time. Although numerous attempts have been made by researchers to obviate this problem, it is still difficult, if not impossible, to use numerically rigorous methods to solve large problems with Degrees of Freedom (DOFs) that can fall in the range of 10^8 to 10^{10}, even with a large number of processors.

The domain decomposition method (DDM) is one approach [1, 2] to solving large electromagnetic problems by breaking them up into smaller and more manageable sizes. A DDM has been applied in conjunction with the Finite Difference Frequency Domain (FDFD), by solving the problem [3] in each of the individual subdomains, and then constructs the global solution via an iterative procedure. In [4], the FD method has been applied in conjunction with the PML and the impedance boundary condition for mesh truncation, and has been combined with the overlapping domain decomposition procedure to compute the capacitances of orthogonal interconnect configurations. This technique has been extended to handle interconnect structures that are not necessarily orthogonal, as for instance vias and crossovers oriented at arbitrary angles [5]. The Finite Volume Time Domain (FVTD) and the DDM also has been used to evaluate the current on a cable inside an airplane [6].

The purpose of this paper is to present a novel time domain approach, referred to herein as the Serial-Parallel FDTD (SPFDTD), for modeling the problem of coupling between two arrays that may be large and may also be separated by a large distance. An example problem is that of phased arrays mounted on masts of a ship, where the intervening space between the arrays may be covered by RAM materials and their separation distance may be large. A preliminary form of this method has been described in [7], in connection with the EMI problem of penetration of EM energy into a large room that present a challenge, because of its size, when one attempts to solve it using the FDTD approach

directly. The serial-parallel FDTD method for handling such problems takes a cue from the TDR approach to modeling microwave circuit problems that tracks the propagation of time domain waveforms through a device.

II. THE SERIAL-PARALLEL FDTD METHOD

In the SPFDTD method, we begin by subdividing the computational domain comprising of two arrays, for instance, into moderate-sized subdomains, with overlaps at the interfaces between the domains, as shown in Fig.1.

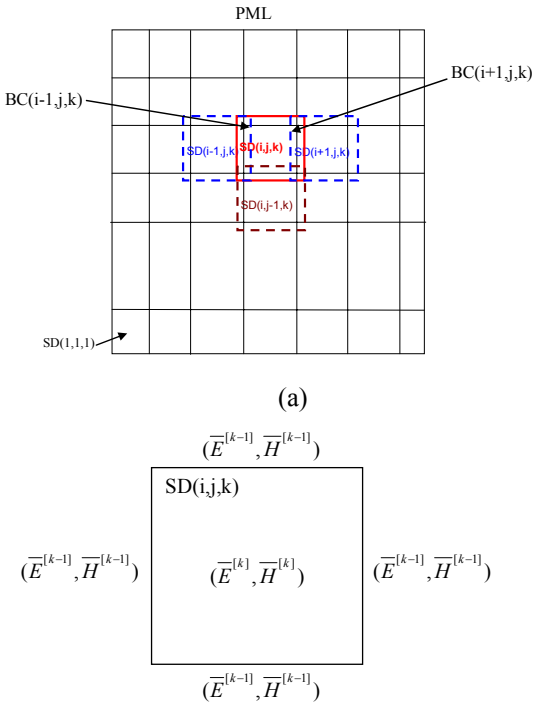

Fig. 1. Application of the CBFDTD. (a) decomposition of the computational domain; (b) deriving the k-th basis function.

The subdomain sizes are chosen such that they can be handled directly via the FDTD, using the available computer resources. Unlike the conventional domain decomposition approach, where spurious effects arise because of artificial truncation of the individual domains, the primary solutions in the present technique are generated by using PML terminations, which can be made to have a very low reflection. Furthermore, the approach is both physics-based and intuitive, because it is implemented in the time domain. For instance, referring to Fig. 1 (a), if we start with a source located in subdomain SD (1,1,1), the solution in that region would not be affected by the structures in the other subdomains until the signal from the above subdomain has had time to traverse these other subdomains, and has then backtracked into the original subdomain SD (1,1,1) at a later time. These reflections are physical as opposed to being spurious due to truncation effects and are dealt with later in a systematic way. It is also useful to note that all the other subdomains will have no primary excitations because there are no sources located in them.

Let us now turn to the task of generating the field solution in the region on the right (subdomain-2), which stems from the coupling into this region from the source region on the left (subdomain-1). In the example geometry shown in Fig. 2 (a), the field solution in the second region will only be due to the excitation originating from subdomain-1, and until the reflected waves appear in this subdomain from the region to its right at a later time. In addition, if the reflections are relatively small, this coupled field will also be the dominant one in subdomain-2.

To derive the coupled field in subdomain-2, we first compute and store the fields in the interface plane located in the overlapping region. This field is, of course, obtained from the solution in subdomain-1, with which we have dealt already. We may view these fields as the Huygens' sources that excite the subdomain-2, and, hence, in general, we need to store both the tangential E and H fields in space and time to derive the solution in subdomain-2.

For instance, in the subdomain SD (i,j,k) of Fig. 1 (a), we use the tangential electric field $\overline{E}^{[1]}$ in the plane BC(i-1,j,k) as an excitation, or implicitly as a boundary condition for the subdomain SD(i-1,j,k). Similarly, the fields on BC (i+1,j,k) are used as a boundary condition for the subdomain SD(i+1,j,k) to evaluate the secondary basis. In general, the solution $(\overline{E}^{[k]},\overline{H}^{[k]})$ in SD (i,j,k) is obtained by applying the FDTD associated with the (k-1)th basis functions which have been derived previously by solving the problem in the adjacent subdomain shown in Fig. 1 (b). Eventually, the field solutions are represented as linear combinations of the basis functions as follows:

$$\overline{E}(x,y,z)=\sum_{k=1}^{M}\overline{E}^{[k]}(x,y,z), \qquad (1a)$$

$$\overline{H}(x,y,z)=\sum_{k=1}^{M}\overline{H}^{[k]}(x,y,z). \qquad (1b)$$

Assuming a one-dimensional topology as shown in Fig. 2 (a), we update the FDTD equations in each of the subdomains in a sequential manner, starting with the excited one. The primary tangential electric basis

field $\overline{E}_t^{[1]}(\bar{r})$, $\bar{r} \in P_1$, is stored where P_1 is the interface plane. This field is then used as a boundary condition to generate the fields coupled into the adjacent subdomains. The tangential electric field is also stored and used as a boundary condition inside the PML layers in the plane P_1, to ensure that it decays correctly in the transverse directions. Referring to the subdomain (i) in Fig. 2(a), it includes an overlapping region at the interface plane P_i (Fig. 2(b)), and is terminated by PML layers to absorb the outgoing waves. The subdomain (i+1) is bounded by the plane P_i and the stored tangential electric field values in P_i are employed as boundary conditions for the region (i+1).

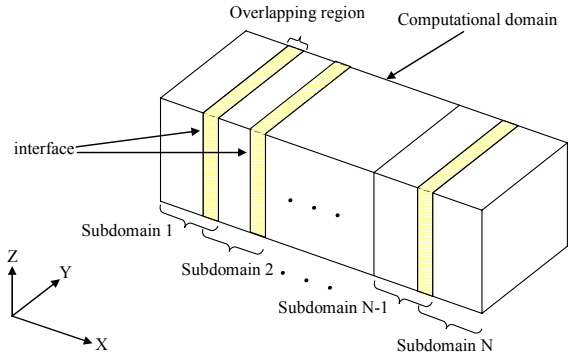

(a)

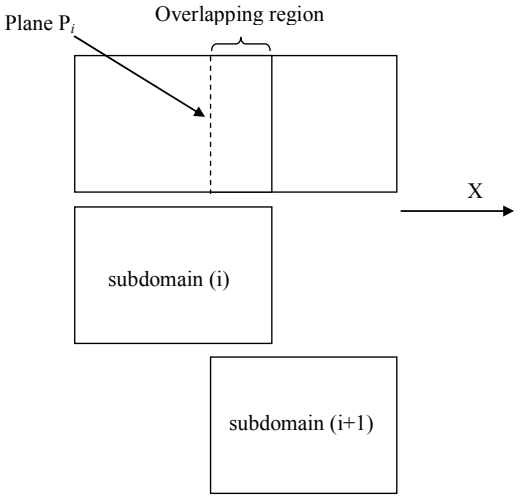

(b)

Fig. 2. Serial application of the SPFDTD with parallel processing along the y-direction. (a) dividing the computational domain into subdomains; (b) schematic diagram for subdomains (i) and (i+1).

III. APPLICATIONS TO THE PROBLEM OF COUPLING BETWEEN TWO ARRAYS

In this section we apply the SPFDTD to the problem of coupling between two patch arrays (see Fig. 3), for which the intervening medium may be inhomogeneous, and we use the total-field FDTD formulation for this problem. We assume that the array on the left is transmitting, while the one on the right is terminated. Our objective is to compute the level of coupling from the transmitter to the receiver, and we also investigate how the coupling is reduced when an absorbing material is introduced between the two arrays.

To analyze large arrays, we can divide the problem into sub-arrays along the longitudinal direction and apply the SPFDTD. In addition, we can also subdivide the intervening geometry into sub-regions with manageable sizes to tackle the coupling problem using the SPFDTD, even when the entire dimension of the problem (arrays + coupling region) is very large.

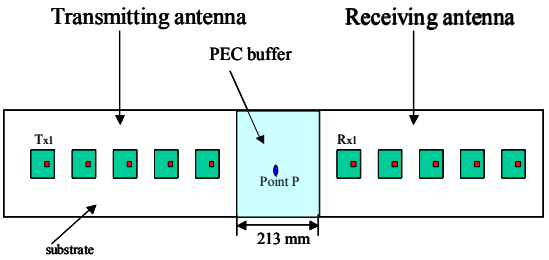

(a)

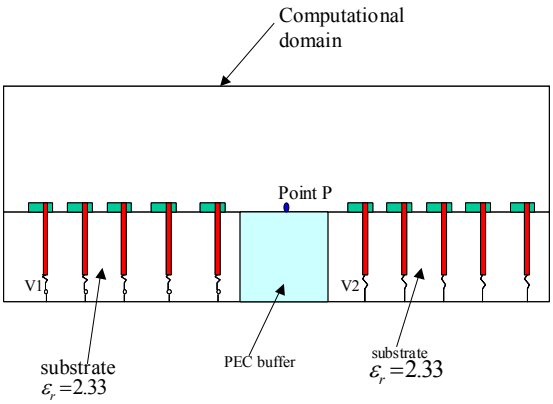

(b)

Fig. 3. Problem of coupling between two 5 x 1 arrays. (a) Top view; (b) Side view.

For the present problem we assume that the two patch arrays are printed on the same substrate, each one has 5 x 1 elements, and that the separation distance

between the arrays is $\sim 3\lambda$, (see Fig. 3). The details of the single element in this array are presented in Fig. 4.

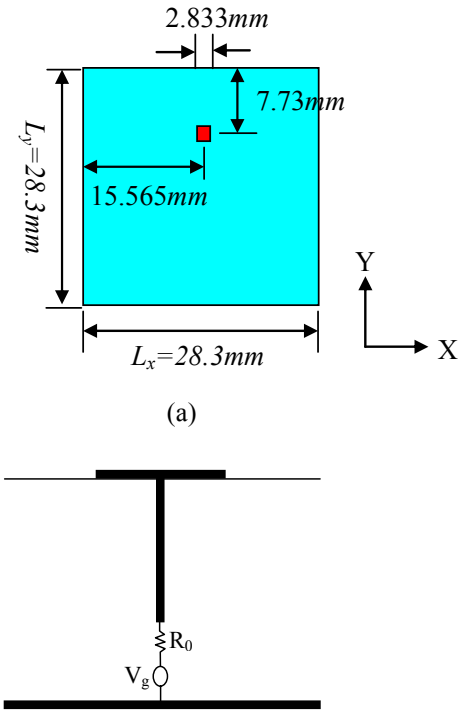

Fig. 4. (a) Top view of the single element patch, (b) Modeling of coaxial feeding line using a voltage source with internal resistor inside a feeding gap.

The resonant frequency of this patch antenna is 3.25 GHZ. All of the elements of the transmit array are excited with a voltage source whose internal resistance is 50 Ω, and all the receiver elements are also terminated by using 50 Ω resistors. The computational domain for this problem has the dimensions of 99mm x 803 mm x 237 mm, and we use the cell sizes of $\Delta x = \Delta y$ = 2.83 mm and Δz = 0.285 mm. We employ the SPFDTD after dividing the original problem region into two subdomains and using two processors along the horizontal direction. The dimensions of the first subdomain are 99 mm × 505 mm × 237 mm, while it is 99 mm × 494 mm × 237 mm for the second, with an overlapping length of 196mm. Figure 5 plots the voltage at the terminals of R_{x1}, and the field E_z at the point P (see Fig. 3), located on the receive array. Figure 6 shows the ratio of the voltage at R_{x1} to the voltage at T_{x1} in the frequency domain. The comparisons, presented in Figs. 5 and 6, show very good agreements between the SPFDTD results and those derived via a direct application of the FDTD.

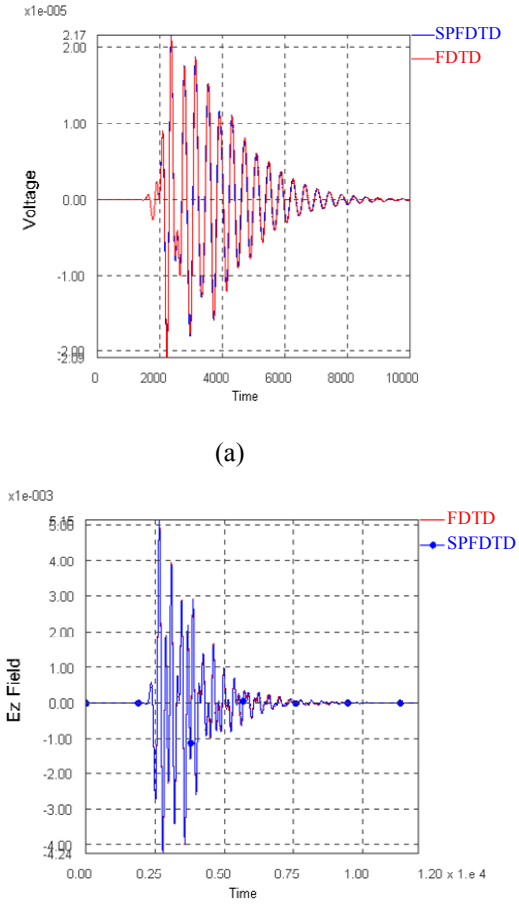

Fig. 5. Comparison of the results of the CBFDTD and the direct application of the FDTD: (a) Voltage V2(t) at Rx1; (b) electric field Ez (t) at the point P of Fig. 3.

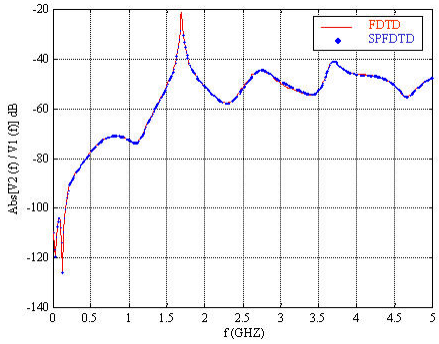

Fig. 6. Comparison of the results of the CBFDTD and the direct application of the FDTD for V2(f)/V1(f), where V2 is the voltage at Rx1, V1 is the voltage at T x 1.

For the second example we consider a larger and more complex problem, which is representative of antennas used for shipboard applications. It is

comprised of two arrays of folded dipoles, arranged in a spiral fashion, one of which is designed for the X-band while the other for the Ku-band. The elements are shown in Fig. 7 and the entire coupled system appears in Fig. 8. The relevant dimensions of the array are: Ku band array $8.64\lambda_0 \times 8.16\lambda_0$; X-band array $11.52\lambda_0 \times 11.04\lambda_0$; separation between these two arrays is $40\lambda_0$, where λ_0 is the free space wavelength at 14.2 GHz.

A direct solution of this large array coupling problem requires the solution of a problem involving 6.97×10^9 unknowns, and represents a formidable challenge. Typically, a CPU equipped with 2 GB of memory can handle a problem requiring up to about 8.3×10^7 unknowns. The direct FDTD simulation for the two-array coupling problem with ~7 billion unknowns requires at least 85 CPUs on a distributed processor, with 170 GB of memory, which is obviously quite burdensome. The number of DOFs is so large for this problem because the smallest cell size in the x-, and y-directions is on the order of $\lambda_0/208$ and the size is approximately double that in the z-direction. We should mention that such a fine discretization is needed to accurately represent the geometry in the feed region, and that we use a non-uniform mesh and gradually increase the cell size to ~ $\lambda_0/20$ in the region between the two arrays.

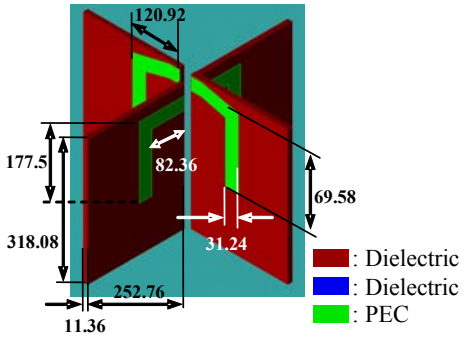

(a) X band array element

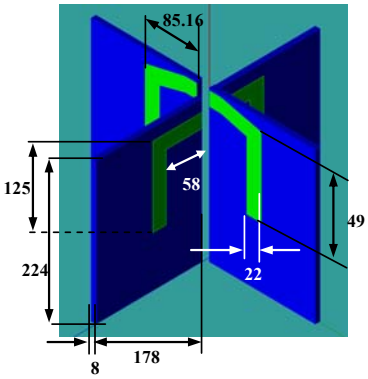

(b) Ku band array element

Fig. 7. Folded dipole elements of the Ku- and the X-band spiral arrays. The dimensions are in mils.

However, the use of the SPFDTD approach eases the system resource requirements mentioned above, renders the problem manageable, and yields the desired estimate of the signal coupled into the array in the right, when one on the left is transmitting. To handle this problem with the SPFDTD method, the above problem is divided into two sub-domains, shown in Fig. 9, and the number of unknown involved in each region is 3.6×10^9 and 3.81×10^9, respectively.

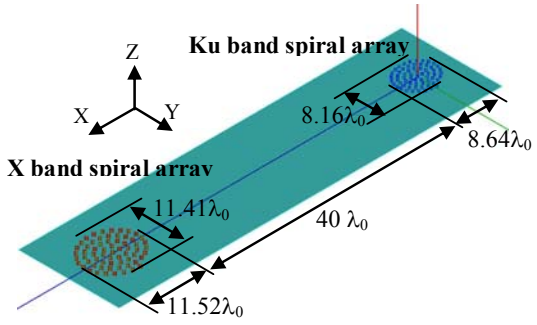

Fig. 8. Layout of the Ku- and the X- band spiral arrays.

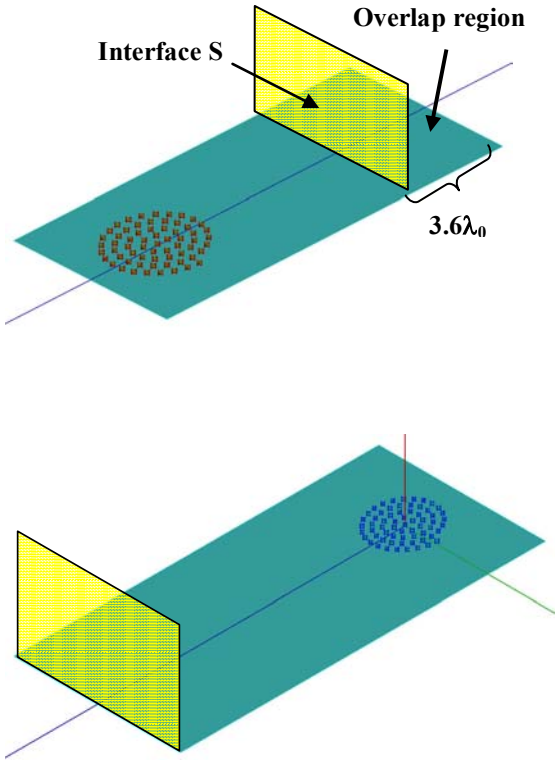

Fig. 9. Set-up for serial-parallel FDTD simulation.

Following the lines of the previous example, we again compute the tangential fields on the interface plane directly in the time domain, downsample it in the

time domain by approximately a factor of 10, and store these fields in external files that are to serve as excitations for the following stage. Downsampling is employed because the time step associated with the FDTD, which is dictated by the Courant condition, typically results in over-sampling and, hence, redundancy. This is because according to the Nyquist criterion, a sampling rate in the time domain that equals twice the highest frequency component in the incident pulse is sufficient to recover the original signal from the sampled data. Additionally, we employ the downsampling because it reduces the hard drive space required to store the tangential fields on the interface, needed for the computation step that follows, namely the field computation in the adjacent domain situated on the right of the interface.

To validate the SPFDTD approach for this problem, we initially downsize it to a smaller version that is more manageable for direct solution, *viz.,* the coupling between a Ku band and an X band spiral array of folded dipoles, both of which have 8-elements. The sizes of the Ku band and X band arrays are $2.27\lambda_0 \times 2.41\lambda_0$ and $3.17\lambda_0 \times 3.43\lambda_0$, respectively, and the separation distance between them is $11.52\lambda_0$, where λ_0 is the free space wavelength at 14.2 GHz. The size of the computational domain for the entire problem is $21.6\lambda_0 \times 6.96\lambda_0 \times 3.72\lambda_0$. For the serial parallel FDTD simulation, the problem domain is divided into 2 subdomains, whose dimensions are $11.4\lambda_0$ and $12.12\lambda_0$, along the x-direction, and there is an overlap of $1.92\lambda_0$ shared by the two regions. The number of unknowns involved in the entire problem is 6.33×10^8, while the corresponding number for two stages of the first the serial-parallel processes are 3.02×10^8 and 3.53×10^8, respectively. Both the direct and serial-parallel processes were simulated on a 16 CPU cluster, equipped with dual AMD Opteron CPUs and 8 GB of memory on each node. The total CPU time needed to run 8000 FDTD time steps were: 4:37 h for the direct, 2:02 h for the first stage and 2:35 h for the second. Figure 10 shows the comparison of the time domain signals (E-field components) generated from the direct FDTD as well as the SPFDTD at an observation point P located at $1.92\lambda_0$ from the left end of the computational domain boundary in the second region, which is also shown in this figure.

The agreement between these results is seen to be excellent. Fig. 11 shows the voltage and current measurements at the terminals of a folded dipole element AE (see Fig. 11) in the receiving array. Again, the agreement between the direct simulation result and that of the SPFDTD is seen to be very good. This example validates the application of the SPFDTD method to the problem of coupling between arrays that can be far apart.

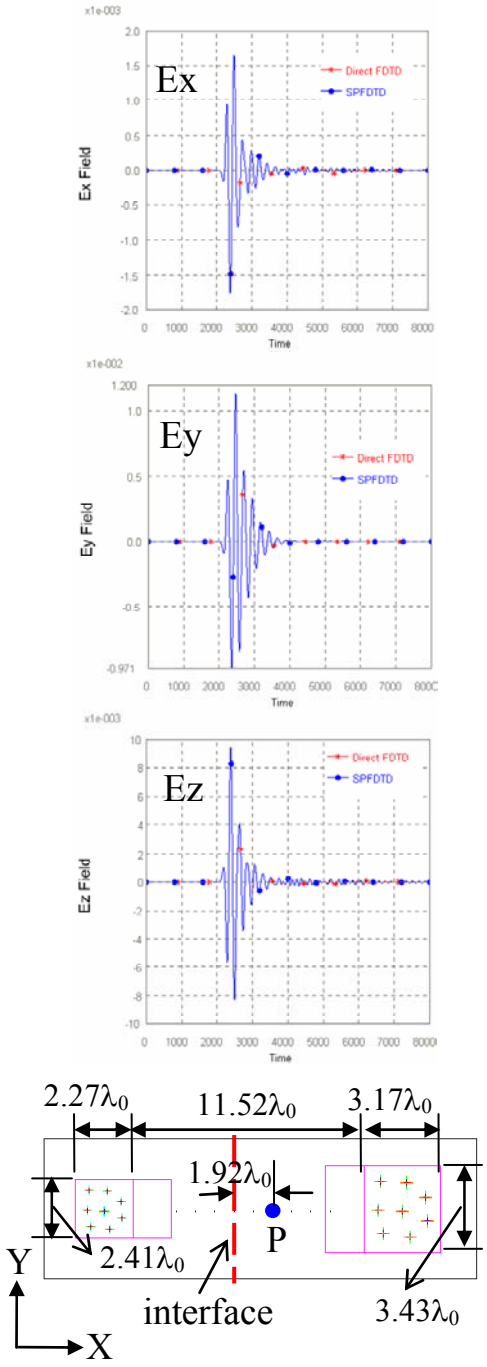

Fig. 10. E-field signals at an observation point P in the time domain.

Following this validation exercise, we return to the original problem of coupling between Ku and X band arrays shown in Fig. 8. Of course, the problem can be divided into more than two subdomains, if desired, so that the solution in each of these individual regions can be handled with fewer CPUs because of the reduction in the problem size in these sub-regions. For the present

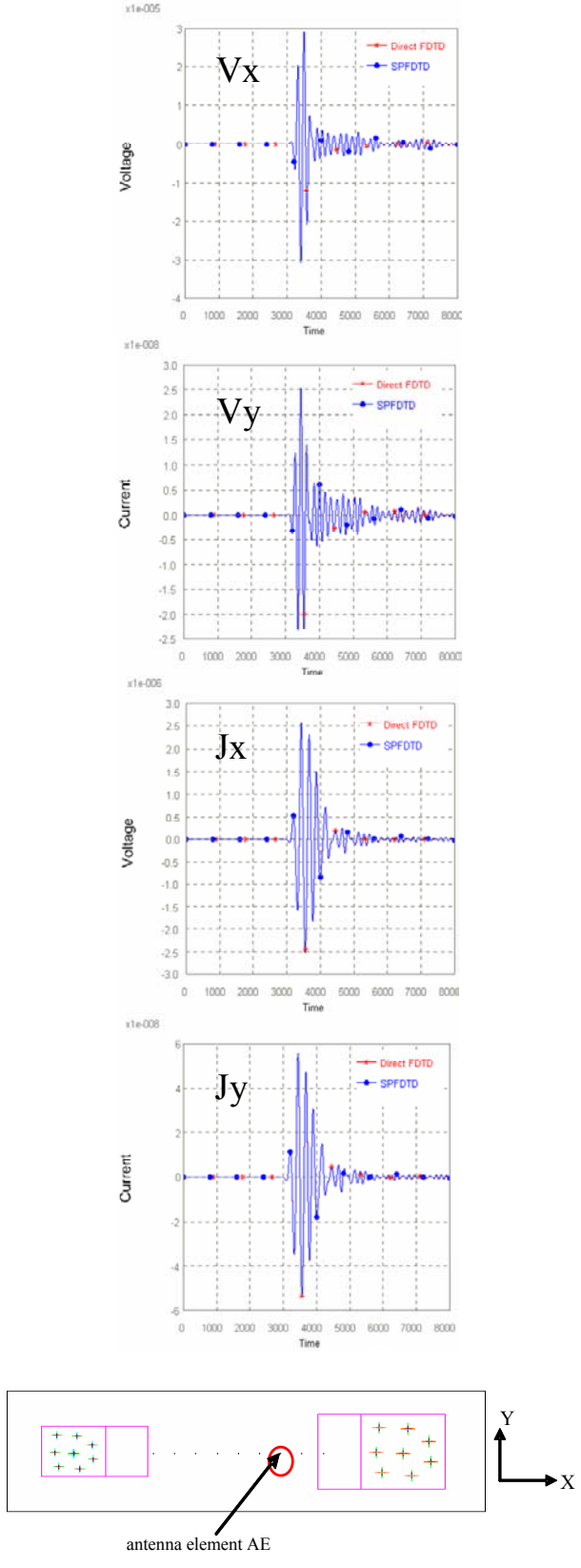

Fig. 11. Voltage and current signals at an antenna element AE in the time domain.

case, where we use two subdomains, we simulate them with 56 CPUs on a PC cluster, where each node is equipped with dual Intel Xeon 3.06 or 3.2 GHz CPUs and 4 GB of memory. The CPU time consumed are 33 hour 24 minutes for 22000 time steps associated with the first stage simulation, and 96 hours for 20000 time steps in the latter one. The extra CPU time consumed in the second stage accounts for the interpolation process used to recover the tangential field information on the interface at time steps where the tangential field information is not recorded during the first stage of the simulation. The simulation results are shown in Fig.12 for the induced current and voltage measurements at the antenna elements (AE1 and AE2) in the receiving array.

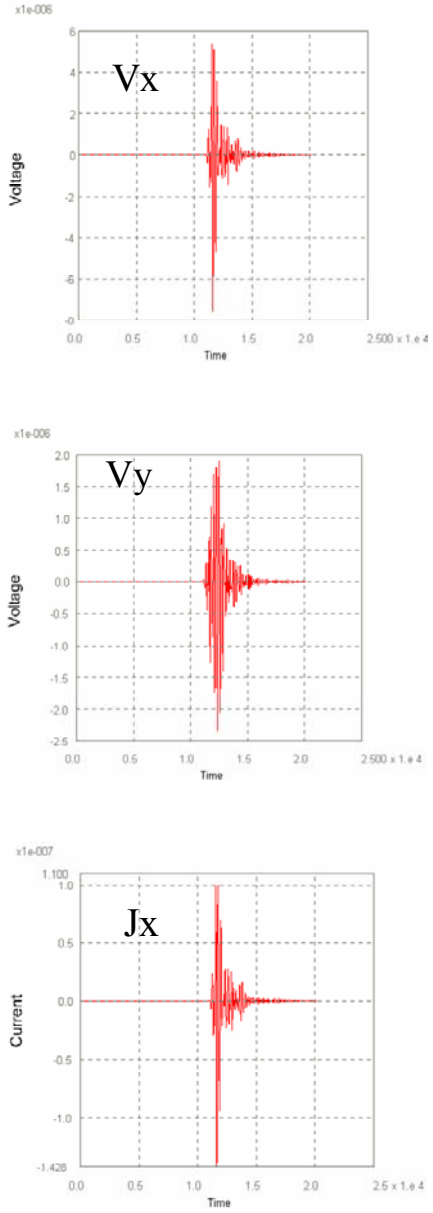

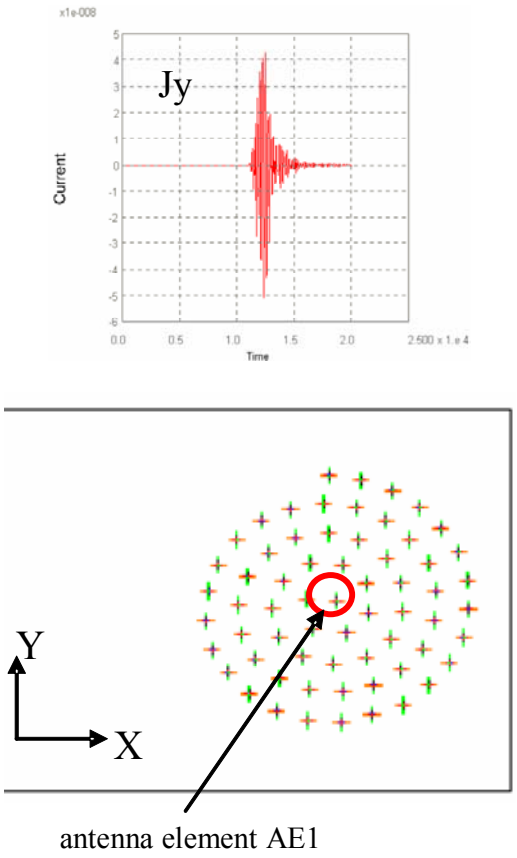

(a) Voltage and current signals at antenna element AE1.

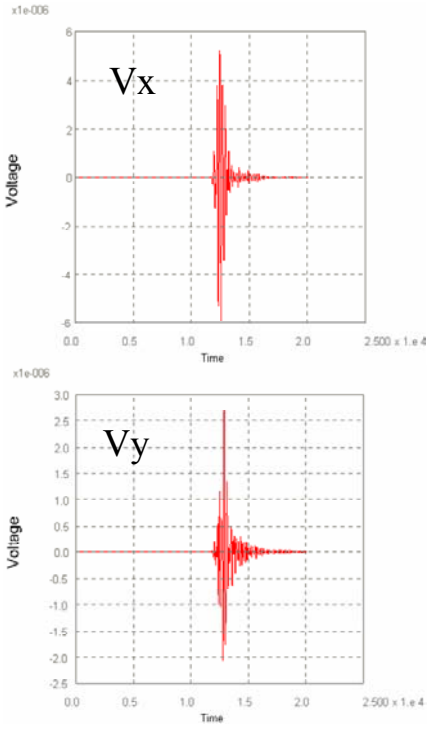

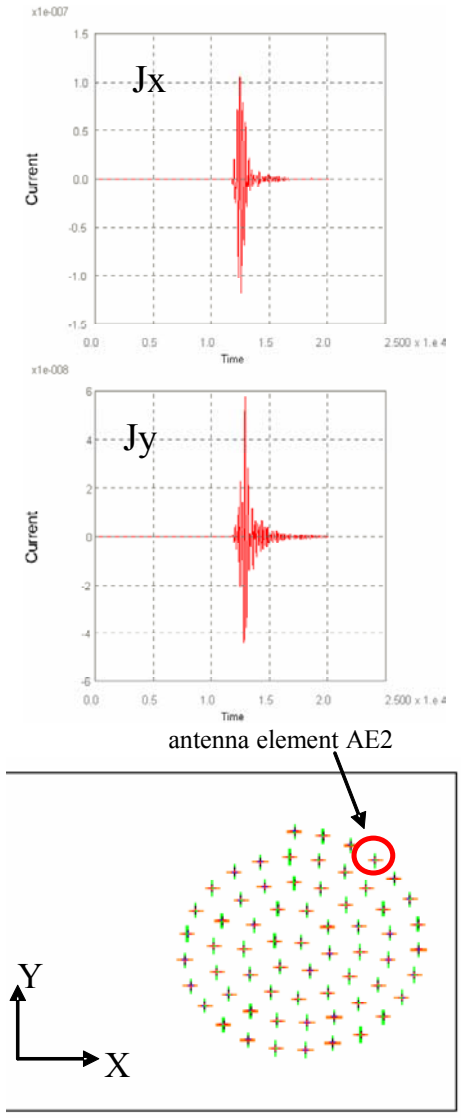

(b) Voltage and current signals at antenna element AE2.

Fig. 12. Voltage and current signals at antenna elements in time domain.

IV. CONCLUSIONS

In this paper we have developed a novel FDTD technique, referred to herein as the SPFDTD, designed to solve large electromagnetic radiation and scattering problems. The SPFDTD approach is capable of handling very large problems ($>10^9$ DOFs) that may not be amenable to analysis using a direct approach.

By following the same procedure as employed for the forward-going waves, this technique has also been extended [7] to the case where there are reflections from discontinuities in the second domain that introduce waves traveling in the reverse direction,

whether we are solving scattering or antenna coupling problems.

REFERENCES

[1] B. Stupfel and M. Mogonot, "A domain decomposition method for the vector wave equation," *IEEE Trans. Antennas Propagat.*, Vol.48 pp. 653-660, May 2000.

[2] C. T. Wolfe, U. Navariswala, and S. Gedney, " A parallel Finite-Element tearing and interconnecting algorithm for solution of the vector wave equation," *IEEE Trans. Antennas Propagat.*, Vol. 48, pp. 278-284, Feb. 2000.

[3] L. Yin, J. Wang, and W. Hong, "A novel algorithm based on the domain-decomposition method for the full-wave analysis of 3-D electromagnetic problems," *IEEE Trans. Antennas Propagat.*, Vol. 50, pp. 2011-2017, Aug. 2002.

[4] V. Veremey and R. Mittra, "Efficient computation of interconnect capacitances using the domain decomposition approach," *IEEE Trans. Antennas Propagat.*, Vol. 22, pp. 348-355, Aug. 1999.

[5] V. Veremey and R. Mittra, "Domain decomposition approach for capacitance computation of nonorthogonal interconnect structures," IEEE *Trans. Antennas Propagat*., Vol. 48, pp. 1428-1434, Sept. 2000.

[6] D. Lacour, X. Ferrieres, P. Bonnet, V. Gobin, and J. Alliot, "Application of multi-domain decomposition method to solve EMC problem on an aeroplane," *Electronics Letters*, Vol. 33, No. 23, pp. 1932-1933, 6th Nov. 1997.

[7] H. E. Abd El-Raouf and R. Mittra, "A Novel Longitudinal-section FDTD algorithm for Simulating Large-size Electromagnetic Compatibility and Interference (EMC/EMI) Problems," *IEEE Antennas & Propagation Society International Symposium/URSI*, Columbus, OH, June 2003.

Raj Mittra is Professor in the Electrical Engineering department of the Pennsylvania State University and the Director of the Electromagnetic Communication Laboratory.
He is also the President of RM Associates, which is a consulting organization that provides services to industrial and governmental organizations, both in the U. S. and abroad.

Hany E. Abd El-Raouf was born in Cairo, Egypt, in 1964. He received the B.S. degree in electronics and communication systems from Helwan University, Cairo, Egypt, in 1986 and the M.S. and Ph.D degrees in electrical engineering from Al-Azhar University, Cairo, Egypt, in 1994 and 2000, respectively. In 1989, he joined the Microwave Engineering Department, Electronic Research Institute, Cairo, Egypt, as a Research Assistant where he then became an Assistant Professor. He joined the Electrical Engineering Department, Pennsylvania State University, University Park 2001 to 2005, where he was a Postdoctoral Fellow and a Visiting Assistant Professor. Currently, he is an Assistant Professor in the Department of Electrical & Computer Engineering, College of Engineering, International Islamic University Malaysia. His research interests include electromagnetic modeling and simulation of microwave circuits, radar scattering, antenna design, electromagnetic compatibility and interference (EMC/EMI) problems, and parallel electromagnetic computation.

Neng-Tien Huang recently completed his Ph.D. program in Electrical Engineering at the Pennsylvania State University, and is currently serving as an intern at Intelligent Automation Incorporated (IAI) in Rockville, Maryland.

Preconditioned GIFFT: A Fast MoM Solver for Large Arrays of Printed Antennas

(*Invited Paper*)

[1,2] B. J. Fasenfest, [1,3] F. Capolino, and [1] D. R. Wilton
[1] Department of Electrical and Computer Engineering, University of Houston, Houston TX, USA
(e-mail: capolino@dii.unisi.it, wilton@uh.edu)
[2] Lawrence Livermore National Laboratory, Livermore, CA, USA
[3] Department of Information Engineering, University of Siena, 53100 Siena, Italy

***Abstract*—** A new type of fast method of moments (MoM) solution scheme using standard basis functions for large arrays with arbitrary contours and/or missing elements is applied to array antennas in a layered configuration. The efficiency of the method relies on use of the FFT along with approximating the Green's function as a separable sum of interpolation functions defined on a relatively sparse, uniform grid. The method is ideally suited for solving array problems, and its effectiveness is demonstrated here for planar arrays of printed antennas. Both fill and solve times, as well as memory requirements, are dramatically improved with respect to standard MoM solvers.

***Index Terms*—**Array antennas, fast solvers, method of moments, periodic structures.

I. INTRODUCTION

A straightforward numerical analysis of large arrays requires significant memory storage and long computation times. Several techniques are currently under development to reduce this cost. One such technique is the GIFFT (Green's function interpolation and FFT) method [1] that belongs to the class of fast solvers for large structures. This method uses a modification of the standard AIM approach [2] that takes into account the reusability properties of matrices that arise from identical array elements. Like the methods presented in [3]-[6], the GIFFT algorithm is an extension of the AIM method in that it uses basis-function projections onto a rectangular grid of Green's function samples that are interpolated with Lagrange interpolating polynomials. The use of a rectangular grid results in a matrix-vector product involving the Green's function samples that is convolutional in form and can thus be evaluated using FFTs. Although our method differs from [3]-[6] in various respects, the primary differences between the AIM approach [2] and the GIFFT method [1] is the latter's use of interpolation to represent the Green's function (GF) and its specialization to periodic structures by taking into account the reusability properties of matrices that arise from interactions between identical cell elements.

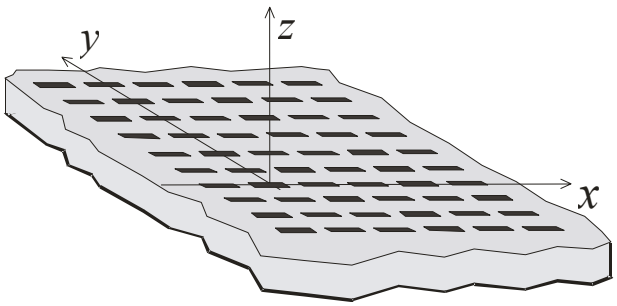

Fig. 1. Array of dipoles excited by delta gap voltage generators on an infinite grounded dielectric slab.

It should be mentioned that fast multipole methods (FMM) [7]-[9] have also been effectively applied to model large structures. In addition, a general numerical scheme has been introduced in [10] that use FMM to determine the coupling between periodic cells, with the interior of each cell being analyzed by the finite element method. To reduce the fill and solve time, other algorithms have been developed that use periodicity-induced physical properties. For example, the methods in [11], [12] use an a priori estimate of the fields scattered by truncated arrays, which behave as Floquet-modulated-diffracted fields [13], to construct global basis functions.

The present work reports performances of the GIFFT method for the cases of conducting dipole antennas in free space and printed on a dielectric grounded slab (Fig. 1), and for patch antennas fed by aperture slots excited by microstrip lines (Fig. 2). For these cases, the Lagrange interpolation scheme is applied to the layered material dyadic Green's function for the mixed potential integral equation [14]. Furthermore, a multi-region interaction is considered since magnetic current unknowns are located on both sides of a shorted screen separating the two regions on either side of the slot (Fig. 2). A block

preconditioning scheme is implemented to greatly reduce the number of iterations required for a solution. If the array consists of planar conducting bodies, the array elements are meshed using standard subdomain basis functions for triangles [15]; the same bases may be used in the apertures where magnetic unknowns are defined. The GIFFT algorithm has been implemented in the standard method of moments (MoM) code EIGER$_{TM}$ [16]. In our implementation, the array boundaries are not restricted to be rectangular, and the array excitation can be arbitrary.

The method greatly reduces solution time by speeding up the computation of matrix-vector products needed in iterative solutions. The GIFFT approach also reduces fill time and memory requirements since the sparse interpolation can be used for all but near element interactions.

II. FEED REGION AND RADIATION REGION: DEFINITION OF INTERPOLATION DOMAIN

The antenna structures analyzed in this paper are shown in Figs. 1 and 2. In Fig. 1 an array antenna of M conducting dipoles is printed on a grounded dielectric substrate. The dipoles are fed by delta gap generators and meshed with triangles that form the sub-domains of triangle surface patch basis functions. Voltage generators $V_g^{\mathbf{p}}$, with $\mathbf{p}=(p_1,p_2)$ a generic double index, are defined for all the dipoles.

In the second example, illustrated in Fig. 2, the region above the ground plane may include a multilayered substrate with M conducting patches fed by slots. Below each slot the microstrip line feeding each antenna is assumed not to interfere with the feed networks of other patches. Mutual coupling between the patches and the slots is considered in the region above the ground plane. Hence, the only model approximation is to neglect coupling between the microstrip lines and slots in the region below the ground plane.

The multiport analysis that one may obtain from this approach may subsequently be used as a multiport equivalent network for designing (or refining) the actual feed network. Array scan blindness, grating lobes and array edge effects are correctly taken into account since they are produced by the mutual coupling above the ground plane. In Fig. 2, voltage generators $V_g^{\mathbf{p}}$ are defined on the microstrip lines below every slot. Concerning notation, as shown in Figs. 1 and 2, the array is decomposed into blocks of elements with each element denoted by the two-component multi-index $\mathbf{p}$; a prime is added to distinguish source from observation element locations ($\mathbf{p}'=(p_1',p_2')$). Within each block representing an element, the electric and magnetic currents are expressed in terms of the usual divergence-conforming basis functions $\mathbf{\Lambda}_n^{\mathbf{p}'}$. The m-indexed test functions are denoted by $\mathbf{\Lambda}_m^{\mathbf{p}}$ (see [1] for more details).

In solving the system, the vanishing of the tangential electric field is imposed on every conducting patch in Fig. 1, leading to the discretized electric field integral equation (EFIE) defined in the standard way (see also [1])

$$\left[Z_{mn}^{\mathbf{p}\mathbf{p}'+} \right]\left[\mathrm{I}_n^{\mathbf{p}'} \right] = \left[V_{\mathrm{g},m}^{\mathbf{p}} \right] \tag{1}$$

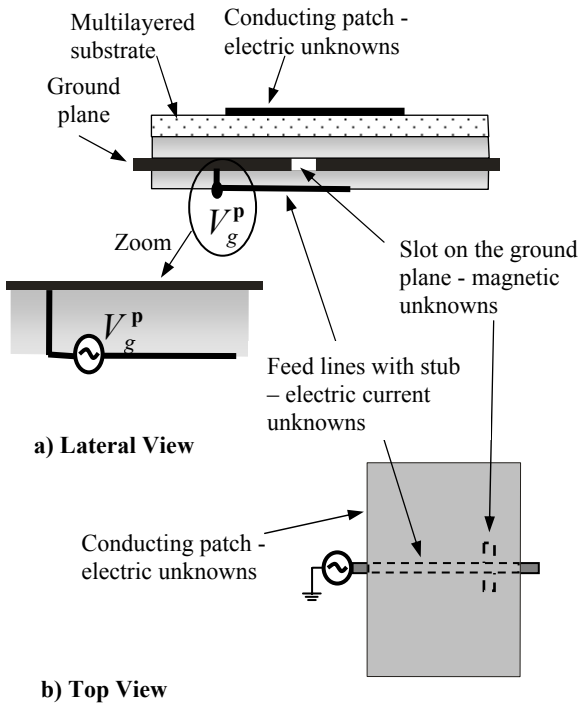

Fig. 2. Single array element of an array of printed antennas in a multilayered environment. (a) Lateral view; (b) Top view. The ***p***th element is fed by an independent microstrip line excited by a voltage $V_g^{\mathbf{p}}$ ($\mathbf{p}$=(p_1,p_2) is a double index). The array elements are coupled via the region above the ground plane. Identical feed lines for each array antenna are assumed uncoupled; hence the Green's function is interpolated only in the region above the ground plane.

where $\left[\mathrm{I}_n^{\mathbf{p}'} \right]$ are the weights of the electric unknowns defined on each $\mathbf{p}$ th dipole and $V_{g,m}^{\mathbf{p}}$ are the voltage generators. For the geometry in Fig. 2 the magnetic currents provide continuity of the electric field, and we impose continuity of the magnetic field (MFIE) on each of the M slots. Therefore, electric unknowns are defined on the patch ($\left[\mathrm{I}_n^{\mathbf{p}'} \right]$) and microstrip ($\left[\bar{\mathrm{I}}_n^{\mathbf{p}'} \right]$) while

magnetic unknowns $\left[V_n^{\mathbf{p}'}\right]$ are placed on the slots, resulting in the system equation

$$\begin{pmatrix} \left[Z_{mn}^{\mathbf{pp}'+}\right] & 0 & \left[-\beta_{mn}^{\mathbf{pp}'+}\right] \\ 0 & 0 & 0 \\ \left[\beta_{mn}^{\mathbf{pp}'+}\right] & 0 & \left[Y_{mn}^{\mathbf{pp}'+}\right] \end{pmatrix} \begin{pmatrix} \left[\mathrm{I}_n^{\mathbf{p}'}\right] \\ \left[\overline{\mathrm{I}}_n^{\mathbf{p}'}\right] \\ \left[V_n^{\mathbf{p}'}\right] \end{pmatrix} + \delta_{\mathbf{p},\mathbf{p}'} \begin{pmatrix} 0 & 0 & 0 \\ 0 & \left[Z_{mn}^{-}\right] & \left[-\beta_{mn}^{-}\right] \\ 0 & \left[\beta_{mn}^{-}\right] & \left[Y_{mn}^{-}\right] \end{pmatrix} \begin{pmatrix} \left[\mathrm{I}_n^{\mathbf{p}'}\right] \\ \left[\overline{\mathrm{I}}_n^{\mathbf{p}'}\right] \\ \left[V_n^{\mathbf{p}'}\right] \end{pmatrix} = \begin{pmatrix} 0 \\ \left[V_{\mathrm{g},m}^{\mathbf{p}}\right] \\ 0 \end{pmatrix}. \tag{2}$$

The + or – superscripts denote operators for regions above or below the ground plane. The matrix $Z_{mn}^{\mathbf{pp}'}$ is the EFIE operator connecting blocks $\mathbf{p}$ and $\mathbf{p}'$, and $Y_{mn}^{\mathbf{pp}'}$ is its dual, representing the magnetic field due to magnetic current sources; $\beta_{mn}^{\mathbf{pp}'}$ is the corresponding magnetic field integral equation (MFIE) operator. Subscripts m and n index testing and basis functions within cells $\mathbf{p}$ and $\mathbf{p}'$, respectively, and the matrix vector products in (1), (2) sum over the indices m

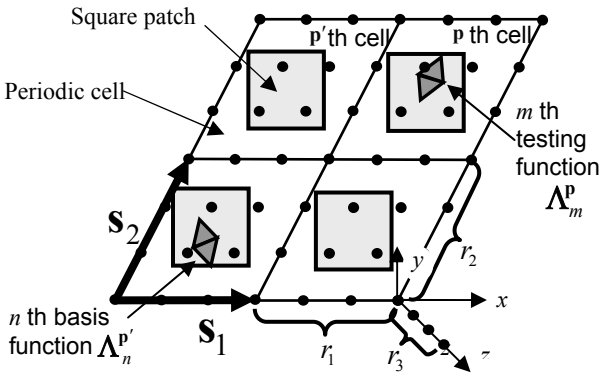

Fig. 3. Array cell index definitions and arbitrary skew lattice vectors $\mathbf{s}_1, \mathbf{s}_2$. The periodic grid on which the Green's function is evaluated and sampled is shown superimposed on the array cells. Within an array cell, the Green's function is evaluated at $r_1 \times r_2 \times r_3$ points. The square-shape darker regions represent conductors within the array cells.

and $\mathbf{p}' = (p_1', p_2')$. The corresponding matrices Z_{mn}^{-}, Y_{mn}^{-}, and β_{mn}^{-} that appear only on diagonal blocks represent the coupling to the structures below the ground plane for each array element; they affect only the $\mathbf{p} = \mathbf{p}'$ self blocks because the Kronecker delta $\delta_{\mathbf{p},\mathbf{p}'} = 1$ for $\mathbf{p} = \mathbf{p}'$, and $\delta_{\mathbf{p},\mathbf{p}'} = 0$ for $\mathbf{p} \neq \mathbf{p}'$. Note that the number of blocks in the first matrix in (2) grows as the square of the number of array elements while the size of the second matrix remains the same for any number of array elements.

Using standard MoM, the matrix in (1) or the first matrix in (2) has huge memory, fill, and solve time requirements for large arrays. This computational difficulty arises from the top region because of the coupling between even widely separated array elements that in most situations cannot be neglected. The numerical burden is reduced by applying GIFFT to this region. That is, the Green's function terms in this region are sampled and interpolated as shown below, and the matrix vector product for the majority of the system is accelerated by using the FFT.

III. THE GIFFT METHOD

For simplicity we show the basic idea of the GIFFT method only for the EFIE, i.e., the moment matrix-vector for the original discretized EFIE in (1). Analogous concepts apply to the other operators $\beta_{mn}^{\mathbf{pp}'+}$ and $Y_{mn}^{\mathbf{pp}'+}$ involved in (2). Thus, (1) or the first block product from the left matrix of (2), is written as [1]

$$\left[Z_{mn}^{\mathbf{pp}'}\right]\left[\mathrm{I}_n^{\mathbf{p}'}\right] = \left[\Delta Z_{mn}^{\mathbf{pp}'}\right]\left[\mathrm{I}_n^{\mathbf{p}'}\right] + \left[\tilde{Z}_{mn}^{\mathbf{pp}'}\right]\left[\mathrm{I}_n^{\mathbf{p}'}\right] \tag{3}$$

where $\tilde{Z}_{mn}^{\mathbf{pp}'}$ denotes matrix elements approximated via the interpolation scheme. The interpolation, however, is inaccurate for nearby cells, which require the correction matrix $\Delta Z_{mn}^{\mathbf{pp}'} = Z_{mn}^{\mathbf{pp}'} - \tilde{Z}_{mn}^{\mathbf{pp}'}$. The correction matrix is a block Toeplitz difference matrix that may be taken as zero for elements whose indices satisfy $|p_1 - p_1'| \geq c_1$ and $|p_2 - p_2'| \geq c_2$ for some constants (c_1, c_2); hence it is sparse. Furthermore, it is constructed from a single computation on a stencil of cells consisting of an observation cell and adjacent cells. The m-indexed test functions are denoted by $\Lambda_m^{\mathbf{p}}$ (see [1] for more details.) To evaluate the matrix/vector product, we note that $\left[\Delta Z_{mn}^{\mathbf{pp}'}\right]\left[\mathrm{I}_n^{\mathbf{p}'}\right]$ is quickly computed since $\Delta Z_{mn}^{\mathbf{pp}'}$ is sparse, whereas $\left[\tilde{Z}_{mn}^{\mathbf{pp}'}\right]\left[\mathrm{I}_n^{\mathbf{p}'}\right]$ is of convolutional form and can be evaluated using a 2D FFT as follows [1]:

$$\left[\tilde{Z}_{mn}^{\mathbf{pp}'}\right]\left[\mathrm{I}_n^{\mathbf{p}'}\right] = \sum_{\mathbf{i},j,j'} < \Lambda_m^{\mathbf{p}}, L_{\mathbf{i}} L_j > \cdot \mathsf{MASK}_{\mathbf{i}}\, \mathsf{FFT}_{\mathbf{i}}^{-1} \cdot \left[\left(\mathsf{FFT}_{\mathbf{i}}\, \overline{\overline{\mathcal{G}_{\mathbf{i},j,j'}^{\mathrm{E}}}} \right) \cdot \mathsf{FFT}_{\mathbf{i}} \left(\overline{\overline{\sum_{\mathbf{p}'} \sum_{n=1}^{N} < L_{\mathbf{i}} L_{j'}, \Lambda_n^{\mathbf{p}'} > \mathrm{I}_n^{\mathbf{p}'}}} \right) \right] \tag{4}$$

where $\mathbf{i}, j$ and $\mathbf{i}', j'$ denote periodic grid points for the Green's function evaluations (Fig. 3), and the double bars

over a quantity indicate that its length is extended so as to obtain a circular convolutional form and then zero-padded to obtain vectors of length 2^k for efficient application of the fast Fourier transform (FFT); FFT^{-1} denotes the inverse fast Fourier transform, and $\mathsf{MASK}_{\mathbf{i}}$ is the array mask restricting the result to array elements within the array boundary. $< \mathbf{\Lambda}^{\mathbf{p}}_m, L_{\mathbf{i}} L_j >$ is the projection of the mth basis function in the $\mathbf{p}$th array cell onto the Lagrange polynomial $L_{\mathbf{i}} L_j$ interpolating the $\mathbf{i}, j$ th point. $\mathcal{G}^{\mathrm{E}}_{\mathbf{i},j,j'}$ represents the sampled Green's electric field dyad (though in reality the field is calculated in mixed-potential form). Since vector basis functions are used, $< \mathbf{\Lambda}^{\mathbf{p}}_m, L_{\mathbf{i}} L_j >$ is a vector. For arrays made of nonplanar scatterers in free space the FFT algorithm is applied to the interpolation points along z, while for layered media the FFT is only applied along the two transverse directions $\mathbf{S}_1$ and $\mathbf{S}_2$ along the planar array.

In homogeneous media, the dyad can be expressed in terms of a single scalar potential. For layered material, however, the far interactions require the computation and storage of the five non-zero components of the magnetic vector potential Green's dyad and two scalar potentials for all possible interactions between interpolating points in at most two planes separated in the z dimension, and for all unique discrete separations in the transverse dimension. There is a very high cost of computing these seven Green's potentials compared to the homogeneous medium case, but this cost is dramatically reduced by first generating the potentials at a suitable set of sample points along radial lines in each source plane representing possible source/observation point separations in the transverse dimension. Potential values between sample points along the sampling line are accurately generated via a non-rational interpolation scheme. Along any other radial line, potentials having the same separation can be constructed from those along the sampling line simply by multiplying by factors involving at most cosines or sines of the angle from the sampling line. The Green's function values along the sampling line are thus used to generate values on the regular grid by interpolation; in turn, a second level of interpolation on the grid is employed in the GIFFT algorithm. The increased number of potential components increases memory requirements when layered media are present, but does not increase the number of FFT's that must be performed per iteration. Furthermore, the Green's potential samples themselves are transformed only once, before any iterations are performed. During each iteration, the updated current coefficients are projected onto the interpolating grid as usual. Once the projections are transformed into the spectral domain, then a single matrix vector multiplication for each dyadic component of the Green's function must be performed. The inverse transform is then computed to complete the iteration step. Assuming N interpolation points, the number of multiplications in the spectral domain is O(N) while the FFT operation is O($N \log N$). Hence, the presence of the extra Green's function terms does not greatly slow the iteration.

IV. BLOCK DIAGONAL PRECONDITIONER

When using an iterative solver such as BiCGStab on a very large matrix system, the solution may converge very slowly if conditioning is poor. For this reason, a preconditioner is needed to improve the solution time. Since many arrays are designed to minimize mutual coupling between array elements, a block diagonal preconditioner for an array seems a logical and simple choice. This preconditioner consists of the self-cell interaction terms of the impedance matrix only. The inverse of this matrix is also a block-diagonal matrix and contains the inverse of the self-array cell blocks $\left[Z^{\mathbf{pp}'}_{mn} \right]$, with $\mathbf{p} = \mathbf{p}'$. Physically, this preconditioner solves the original problem as if there were no interaction between array cells. For array designs with little mutual coupling this is a very good assumption and often only a handful of iterations are required. For arrays with strong coupling some deterioration in performance is to be expected. Because an accurate computation of the self block is needed for the near interaction corrections, this preconditioner does not require additional setup time. The cost of inverting a self block is also negligible since the number of unknowns involved is small compared to the overall array size. Thus after each matrix-vector product is computed during an iteration, the resulting vector is multiplied by the preconditioner, adding an O(MN^2) computation to the total time for the matrix vector product (M is the number of array elements and N is the number of degrees of freedom in each array cell.)

V. RESULTS

Four different test arrays geometries were simulated and the results of the GIFFT method, both with and without preconditioning, were compared to an "exact" MoM solution of these arrays. The "exact" solution does not use interpolation or fast multiplication, but does utilize the Toeplitz nature of the matrices to speed fill time and reduce storage.

A. Array of Dipoles

The first two arrays consist of 20×20 elements with a lattice spacing $S_1 = S_2 = 0.5\lambda_0$, where λ_0 is the free space wavelength, in both x and y directions. Each dipole is fed by a delta gap source at its center. Each dipole

contains 23 unknowns and is $0.39\lambda_0$ long and $0.01\lambda_0$ wide. In the first test case the dipoles are in free space, while in the second one the same dipoles are printed on a grounded dielectric slab as in Fig. 1. The height of the dielectric slab is $d = 0.19\lambda_0$ and its relative permittivity is $\varepsilon_r = 2.55$, as for the case treated in [17]. Both these cases used fourth order interpolation of the Green's Function in both transverse directions. The GF is thus sampled at five points in each direction, resulting in $r_1 \times r_2 = 5 \times 5 = 25$ points for each array cell. Interpolation points are also distributed along the border of an array cell and are thus shared by contiguous cells, so the computational burden is determined by the evaluation and storage of the various GF components for only 16 distinct points per array cell.

The third case analyzed consists of an array of 25×25 square conducting patches in free space illuminated by a plane wave at 6 GHz incident from a direction perpendicular to the array plane. The patches are 11.4 [mm] on a side with a separation of 3.8 [mm] between patches, and thus the lattice spacings are $S_1 = S_2$ =15.2 [mm]. Each patch was meshed using triangles, creating 65 unknowns per patch. This GIFFT method used fifth order (25 distinct points per cell) interpolating polynomials in both planar directions.

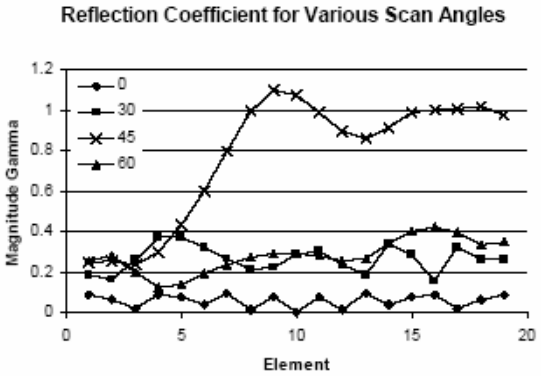

Fig. 4. Active reflection coefficients for various scan angles on the E-plane for an array of 19 x 19 dipoles on a grounded dielectric slab. Scan blindness occurs for $\theta = 45.8°$.

Table 1 shows the run times for the standard MoM and GIFFT solutions of the three arrays, as well as the error in the GIFFT solution compared to that of the standard MoM, which takes advantage of the Toeplitz storage that also reduces the fill time. It can be clearly seen that the GIFFT method offers a dramatic savings in both fill and solve times while maintaining a high level of accuracy that is evaluated as the average of the relative errors over all the unknowns. It can also be seen that use of the preconditioner dramatically reduces the number of BiCGstab iterations needed for a solution, further reducing solution time. The BiCGstab iterations are stopped when the solution error determined by the algorithm is lower than 10^{-4}. The GIFFT method also dramatically reduces the memory storage requirements. For example, for the 25×25 square patch array (M = 625 array cells), each patch was discretized using N=65 basis functions, requiring storage of $N \times N$ =4225 complex numbers for *each* $\mathbf{p}, \mathbf{p}'$ block $\left[Z_{mn}^{\mathbf{pp}'} \right]$ of the full impedance matrix. Instead, using GIFFT with a fifth order interpolation scheme, we need to store only 36 Green's function samples per array cell. Interpolation points are also distributed along the border of an array cell and are thus shared by contiguous cells resulting in 25 *distinct* sampling points per array cell. GIFFT's storage advantage is further amplified by the fact that if there are M = 625 array cells in a square array, there are M^2 matrix blocks in the complete matrix, while there are only about $4M$ blocks of sampled Green's function points. The factor four arises from extending the evaluation domain of the Green's function to consider all possible interactions on the actual array as shown in [1, Fig. 3]. For the 25×25 array, this means that the system matrix for a standard solution must contain about $N^2 \times M^2 = 1.65 \times 10^9$ complex entries (that reduce to $N^2 \times (2M - 1) = 5.28 \times 10^6$ when stored in the Toeplitz format), while there are only $25 \times 4 \times M = 62.5 \times 10^3$ entries in the sampled Green's function array in free space. As explained in Sec. III, for layered media, the number of the GIFFT complex samples must be multiplied by seven, the number of unique dyadic and scalar potential terms used in the mixed potential formulation.

The results in Fig. 4 are related to an array of 19×19 (to match the results in [17]) dipole elements on the same grounded dielectric slab considered before ($d = 0.19\lambda_0$, $\varepsilon_r = 2.55$) that exhibits scan blindness in the E-plane at $\theta = 45.8°$ [17], [18]. Therefore the dipoles are fed with a linear progressive phase along x so as to scan the array beam along the θ direction in the E-plane (the x-z plane in Fig. 1). The active reflection coefficients for the center row of array elements are shown for various scan angles. As pointed out in [17], the results show that for a broadside scan angle $\theta = 0°$ the reflection coefficients are symmetric with respect to the center element (the 10 th) that is well matched, i.e., the magnitude of the reflection coefficient is much less than unity. This verifies that the antenna elements have been matched to the input impedance of the center element at broadside. When the array is scanned to $\theta = 45°$, the reflection coefficient varies considerably across the center row of the array. The center element actually has a reflection coefficient greater than unity, which implies

that it absorbs power from some of the other elements. In other words, the left-hand dipoles in Fig. 4 radiate power, some of which is delivered to the right-hand array elements through the strongly-excited guided wave on the structure.For this particular scan angle, most of the elements are not matched, showing the scan blindness effect, yet a few near the array edges still have relatively low reflection coefficients. These results for the reflection coefficient show very good agreement with previously published results for this array [17, Fig. 4].

Table 1: Matrix setup (fill) and solve times for GIFFT and standard MoM for several structures.

	Fill Time [s]	Solve Time [s]	Number Iterations	Average % Error
Dipoles in Free Space	608.0	1591.2	309	---
GIFFT	4.2	232.0	263	0.20
GIFFT w/ preconditioner	4.2	7.2	7	0.19
Dipoles on Grounded Substrate	4698.6	4297.1	833	---
GIFFT	47.1	1132.7	911	0.15
GIFFT w/ preconditioner	47.6	23.2	17	0.15
Square Patches in Free Space	4391.8	53612.1	463	---
GIFFT	27.7	1100.5	340	0.96
GIFFT w/ preconditioner	27.0	32.0	9	0.97

B. Array of Patch Antennas Excited by Slots

The final case considered is an array of elements that are geometrically more complex, as shown in Fig.2, and the meshed patch, slot and microstrip are shown in Fig. 5. Two cases are considered: and array of 8×8 and a larger one of 25×25 element. The array elements are arranged on a rectangular lattice with periods $S_1 = S_2 = 30$ [mm]. The square conducting patches with dimensions $24.5\,[\text{mm}] \times 24.5\,[\text{mm}]$ are placed on a grounded dielectric substrate with $\varepsilon_r = 2.17$ and height =3 [mm]. The feeding slot has dimensions $10\,[\text{mm}] \times 1.5\,[\text{mm}]$ and is located 5.25 [mm] off the center of the patch. The microstrip under the ground plane has a width of 1.6 [mm], and a length of 17 [mm] that includes an open stub of length 10 [mm]. The microstrip substrate has $\varepsilon_r = 2.17$ and a thickness of 0.5 [mm]. The microstrip lines are excited by delta gap voltage generators and the operating frequency is 3.7 GHz. The design is not optimized to minimize the input impedance over a certain band, but is merely intended to illustrate the effectiveness of our new method. Each patch, slot and microstrip is meshed using quadrilaterals, creating 128 unknowns per array element as shown in Fig. 5. The GIFFT method used fourth-order interpolating polynomials in both planar directions.

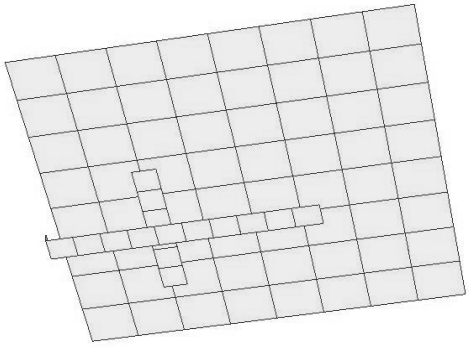

Fig. 5. Mesh of the square patch, slot and microstrip of one of the array elements. The ground plane surrounding the slot and the dielectric layers are not shown.

Table 1 shows the run times for the standard MoM and GIFFT solution of the array. It can be clearly seen that the GIFFT method offers a dramatic savings in both setup and solve times while maintaining a high level of accuracy. In this case the BiCGstab iterations are stopped when the algorithm's relative solution error falls below 0.5×10^{-4} to limit the overall simulation time. Also in this case it is seen that the use of the preconditioner dramatically reduces the number of BiCGstab iterations needed for a solution, further reducing solution time. For the larger 25x25elements array the iterations are stopped when the error falls below 10^{-2}.

As in the previous cases, the memory storage requirements are dramatically reduced by GIFFT. For example, for the $M = 625 = 25 \times 25$ square patch array, each element is discretized using N =128 basis functions (112 on the patch, 5 on the slot and 11 on the microstrip), requiring a storage of $N \times N$ =16384 complex numbers for *each* $\mathbf{p}, \mathbf{p}'$ block $\left[Z_{mn}^{\mathbf{pp}'} \right]$ of the impedance matrix. Instead, using GIFFT with a fourth-order interpolation scheme, requiring $r_1 \times r_2 = 5 \times 5 = 25$ sampling points per cell, only 16 distinct Green's function samples per cell are stored. For the layered medium considered here, this number must be multiplied by seven, the number of unique dyadic and scalar potential terms used in the mixed-potential formulation. The GIFFT storage advantage is further amplified by the fact that for $M = 625$ array elements in the square array, there are $M^2 = 390625$ matrix blocks in the complete matrix (which is why a Toeplitz fill was used instead), while there are only about $4M = 2500$ blocks of sampled Green's function points. For the 25×25 array, this means that the system matrix

for a standard MoM must contain about $117 \times 117 \times M^2 + 16 \times 16 \times M = 5.3 \times 10^2$ complex entries; this reduces to $117 \times 117 \times (2M - 1) + 16 \times 16 \times M = 17.1 \times 10^6$ when stored in the Toeplitz format. By contrast, there are only $7 \times 16 \times 4 \times M = 280 \times 10^3$ entries in the sampled Green's function array in addition to those relative to the self blocks and difference matrix (see (2)) that also grow as *M*.

Table 2: Matrix setup (fill) and solve times for GIFFT and standard MoM.

Array of patches with slots and microstrip lines (Fig.2)	Setup Time [s]	Solve Time [s]	Number Iterations	Average % Error
Array 8x8				
MoM w/ Toeplitz fill w/o precond.	1797	12551	2373	---
GIFFT w/o precond.	240	4627	2473	0.55
GIFFT w/ precond.	240	36	19	0.55
Array 25x25				
MoM w/ Toeplitz fill w/ precond.	≈ 9 hr	≈ 11 min per sing BiCGstab iteration	>100 program stopped before end	---
GIFFT w/ precond.	≈ 25 min	≈ 4 min (14s per iteration)	17	

VI. CONCLUSION

The GIFFT method for solving large array problems [1] is extended here to arbitrary arrays of printed elements in a layered material with the possible slot feeds. A block diagonal preconditioner has been tested and found to greatly improve the solution time by reducing the number of iterations required by the BiCGstab solver. The examples presented show the advantages of the method in reducing the memory requirements of the MoM matrix, as well as in reducing setup and solution times. A multiport analysis of such arrays can thus be performed in reasonable time even for large array structures. An extension of the GIFFT algorithm for arrays of cavity-backed patch antennas is currently under progress.

REFERENCES

[1] B. J. Fasenfest, F. Capolino, D. R. Wilton, D.R. Jackson, and N. Champagne, "A fast MoM solution for large arrays: Green's function interpolation with FFT," *IEEE Antennas and Wireless Propagation Letters,* Vol. 3, pp. 161-164, 2004.

[2] E. Bleszynski, M. Bleszynski, and T. Jaroszewicz, "AIM: Adaptive integral method for solving large scale electromagnetic scattering and radiation problems," *Radio Sci.*, Vol. 31, No. 5, pp. 1225-1251, 1996.

[3] S-Q Li, Y. Yu, C. H. Chan, K. F. Chan, and L. Tsang, "A sparse-matrix/canonical grid method for analyzing densely packed Interconnects," *IEEE Trans. Microwave Theory Tech.,* Vol. 49, No. 7, pp. 1221-1228, July 2001.

[4] L. Tsang; C. H. Chan, P. Kyung, and H. Sangani, "Monte-Carlo simulations of large-scale problems of random rough surface scattering and applications to grazing incidence with the BMIA/canonical grid method," *IEEE Trans. Antennas Propagat.,*, Vol. 43, No. 8, Aug. 1995.

[5] S. M. Seo, and J. F. Lee, "A fast IE-FFT algorithm for solving PEC scattering problems," *IEEE Trans. on Magnetics,* Vol. 41, No. 5, pp. 1476 – 1479, May 2005.

[6] A. Mori, F. De Vita, and A. Freni, "A modification of the canonical grid series expansion in order to increase the efficiency of the SMCG method," *IEEE Geoscience and Remote Sensing Letters,* Vol. 2, No. 1, pp. 87-89 Jan. 2005.

[7] R. Coifman, V. Rokhlin, and S. Wandzura, "The fast multipole method for the wave equation: A pedestrian prescription," *IEEE Antennas Propagat. Mag.*, Vol. 35, No. 3, pp. 7-12, June 1993.

[8] W. C. Chew, J.-M. Jin, C.-C. Lu, E. Michielssen, and J. M. Song, "Fast solution methods in electromagnetics," *IEEE Trans. Antennas Propagat.,* Vol. 45, No. 3, pp. 533 – 543, March 1997.

[9] J. Song, C.-C. Lu, and W. C. Chew, "Multilevel fast multipole algorithm for electromagnetic scattering by large complex objects", *IEEE Trans. Antennas Propagat.,* Vol. 45, No. 10, pp. 1488 – 1493, Oct. 1997.

[10] R. W. Kindt and J. L. Volakis, "Array decomposition-fast multipole method for finite array analysis," *Radio Sci.,* Vol. 39, RS2018, 2004.

[11] A. Neto, S. Maci, G. Vecchi, and M. Sabbadini, "Truncated Floquet wave diffraction method for the full wave analysis of large phased arrays. Part I and II," *IEEE Trans. Antennas Propagat.*, Vol. 48, No. 4, pp. 594-611, April 2000.

[12] O. A. Civi, P.H. Pathak, H-T. Chou, and P. Nepa, "A hybrid uniform geometrical theory of diffraction-moment method for efficient analysis of electromagnetic radiation/scattering from large finite planar arrays," *Radio Science*, Vol. 32, No. 2, pp. 607-620, March-April, 2000.

[13] F. Capolino, M. Albani, S. Maci, and L. B. Felsen, "Frequency-domain Green's function for a planar

periodic semi-infinite phased array. Part I and II," *IEEE Trans. Antennas and Prop.*, Vol. 48, No. 1, pp. 67 – 85, Jan. 2000.

[14] K. A. Michalski, and D. Zheng, "Electromagnetic scattering and radiation by surfaces of arbitrary shape in layered media. I. Theory," *IEEE Trans. Antennas Propagat.*, Vol. 38, No. 3, pp. 335-344, March 1990.

[16] S. M. Rao, D. R. Wilton, and A. W. Glisson, "Electromagnetic scattering by surfaces of arbitrary shape," *IEEE Transactions on Antennas and Propagation*, Vol. AP-30, No. 3, pp. 409-418, May 1982.

[17] W. A. Johnson, R. E. Jorgenson, L. K. Warne, J. D. Kotulski, J. B. Grant, R. M. Sharpe, N. J. Champagne, D. R. Wilton, and D.J. Jackson, "Our experiences with object-oriented design, FORTRAN 90, and massively parallel computations," *1998 Digest USNC/URSI National Radio Science Meeting*, p. 308, June 21-26, Atlanta, GA, 1998.

[18] D. M. Pozar, "Analysis of finite phased arrays of printed dipoles," *IEEE Trans. Antennas Propagat.*, Vol. 33, No. 10, pp. 1045-1053, Oct. 1985.

[19] D. M. Pozar, and D. H. Schaubert, "Analysis of an infinite array of rectangular microstrip patches with idealized probe feeds," *IEEE Trans. Antennas Propagat.*, Vol. 32, No. 10, pp. 1101-1107, Oct. 1984.

Bejamin. J. Fasenfest was born in Sacramento, CA, in 1980. He received the B.S. (summa cum laude) from the University of Houston in 2002, where an undergraduate research fellowship funded his research of dielectric resonator antennas. He was awarded a Tau Beta Pi fellowship, and continued on to a M.S. at the University of Houston in 2004, with a thesis on fast methods for large arrays. From 2004 to the present, he has worked at Lawrence Livermore National Laboratory, where his research interests include computational electromagnetics and electromagnetics modeling, from statics to terahertz.

Filippo Capolino was born in Florence, Italy, in 1967. He received the Laurea degree (cum laude) in electronic engineering and the Ph.D. degree, from the University of Florence, Italy, in 1993 and 1997, respectively. He has been a Research Associate until 2002 at the Dept. of Information Engineering, University of Siena, Italy, where he is presently an Assistant Professor. From 1997 to 1998, he was a Fulbright Research Visitor with the Dept. of Aerospace and Mech. Engineering, Boston University, MA, where he continued his research with a Grant from the Italian National Research Council (CNR), from 1998 to 1999. From 2000 to 2001 he was Research Assistant Visiting Professor with the Department of Electrical and Comp. Engineering, University of Houston, TX, where he is now an Adjunct Assistant Professor. In Nov.-Dec- 2003 he was an Invited Assistant Professor at the Institut Fresnel, France. His primary research interests include array antennas, periodic structures, numerical modeling, and metamaterials. He is the coordinator of the Siena Unit for the Network of Excellence "Metamorphose" on Metamaterials of the EU sixth framework program.

Dr. Capolino was awarded with a MMET'94 Student Paper Competition Award in 1994, the Raj Mittra Travel Grant for Young and Senior Scientists in 1996, and 2006, respectively, the "Barzilai" prize for the best paper at the National Italian Congress of Electromagnetism (XI RiNEm) in 1996, and a Young Scientist Award for participating at the URSI Int. Symp. Electromagn. Theory in 1998. He received the R.W. P. King Prize Paper Award from the IEEE Antennas and Propagation Society for the Best Paper of the Year 2000, by an author under 36. He is an Associate Editor for the IEEE Transactions on Antennas and Propagation.

Donald R. Wilton was born in Lawton, OK, October 25, 1942. He received the B.S., M.S., and Ph.D. degrees from the University of Illinois, Urbana-Champaign, in 1964, 1966, and 1970, respectively.

From 1965 to 1968 he was with Hughes Aircraft Co., Fullerton, CA, engaged in the analysis and design of phased array antennas. From 1970–1983 he was with the Department of Electrical Engineering, University of Mississippi, and since 1983 he has been Professor of Electrical Engineering at the University of Houston. From 1978–1979 he was a Visiting Professor at Syracuse University. During 2004-2005 he was a visiting professor at the Polytechnic of Turin, Italy, the Sandia National Laboratories, and the University of Washington. His primary research interest is in computational electromagnetics, and he has published, lectured, and consulted extensively in this area.

Dr. Wilton is a Fellow of the IEEE and received the IEEE Third Millenium Medal. He has served the IEEE Antennas and Propagation Society as an Associate Editor of the Transactions on Antennas and Propagation, as a Distinguished National Lecturer, and as a member of AdCom. Dr. Wilton is also a member of Commission B of URSI, in which he has held various offices including Chair of U. S. Commission B.

Generalized Scattering Matrix (GSM) Approach for Multilayer Finite Array Analysis

(*Invited Paper*)

Arun K. Bhattacharyya

Northrop Grumman Space Technology, Space Park, Redondo Beach, CA 90278

Email: arun.bhattacharyya@ngc.com

Abstract **—** The paper presents the Generalized Scattering Matrix (GSM) approach for analyzing multilayer printed array structures. The analysis involves computation of the overall GSM of an infinite array structure, Floquet modal based analysis of mutual coupling between array elements followed by estimation of finite array characteristics. A slot-fed patch array of 225 elements is used as an example for numerical results. It is found that the input match of the edge elements significantly differs from that of the elements in the center region of the array. The advantages and disadvantages of the approach are discussed at the end.

Index Terms—Finite Array, GSM Approach, Multilayer Array, Floquet Analysis, Mutual Coupling.

I. INTRODUCTION

The purpose of this paper is to provide a general overview of the GSM approach for analyzing multilayer finite printed array structures. Multilayer printed patch structures are used for enhancing the bandwidth performance [1,2] of a printed array. They are also used as a multiband frequency selective surface [3], wide band screen polarizers [4] and for realizing photonic band-gap materials [5]. The GSM approach is very convenient for analyzing such structures. The GSM approach essentially is a modular approach, where each layer of a multilayer structure is analyzed independently and then characterized in terms of a matrix. The matrix is called the GSM of the layer, because the reflection and transmission characteristics of the layer with respect to several incident modes are embedded within the matrix. The complete characterization of a multilayer structure is obtained by cascading the individual GSMs of the layers.

The GSM of an array essentially characterizes the periodic array that is extended to infinity in the transverse directions. In addition, the GSM is associated with an ideal Floquet excitation, defined by uniform amplitude and linear phase progression. For a finite array or a tapered excitation, the analysis involves few additional steps. In this paper, we outline the steps and illustrate their mathematical foundations. We demonstrate that the results of an infinite array can be utilized to predict the performances of a finite array with an arbitrary excitation. The predicted result would be *exact* if we define a "finite array" as *a physically infinite array with a finite number of excited elements*. The remaining elements are non-excited, though they *must be physically present*. Such a finite array is impractical. A real finite array, however, has only a finite number of physical elements. In many situations radiation characteristics of a real finite array can be approximated as that of a finite array defined above, because the non-excited elements generally do not contribute significantly to the radiated fields, particularly in the main lobe region.

Section II briefly outlines the GSM approach for an infinite multilayer array. Section III formulates the mutual coupling that plays the most important role in the performance of a finite array. Section IV presents the analytical procedure of a finite array employing the mutual coupling data. Numerical results of a multilayer slot-fed finite patch array antenna are shown in Section V and the important conclusions are made in Section VI.

II. THE GSM APPROACH

The GSM approach of a multilayer finite array involves the following steps:

- Computation of GSM of each layer,
- Combining GSMs of the individual layers to obtain overall GSM of the structure,
- Mutual coupling computation between the array elements using Floquet modal theory,
- Active element pattern computation,
- Computations of finite array pattern and return loss of the elements.

A typical multilayer array consists of four types of basic building blocks: printed elements layer, dielectric layer, dielectric interface and aperture (slot aperture, for instance) layer. The GSM of a printed element layer and slot aperture layer are usually obtained using Galerkin's MoM analysis [6]. The GSM of a dielectric layer and the interface are determined using Floquet modal analysis [7]. The GSMs of the individual layers are then combined to obtain the overall GSM of the multilayer structure. The

GSM analysis and the cascading formulas are outlined in the following Section.

A. The GSM

The GSM essentially represents the input-output characteristics of an infinite array structure with respect to a set of Floquet modes. For a multilayer array structure, the GSMs of individual layers are determined and then combined together to obtain the overall GSM of the structure, as typically done in a mode-matching analysis of waveguide horns or filters.

To illustrate the GSM approach pictorially, consider a three-layer periodic array structure (patch-dielectric-patch) as shown in Fig. 1(a). The three-layer-structure is equivalent to five modules connected in cascade as shown in Fig. 1(b).

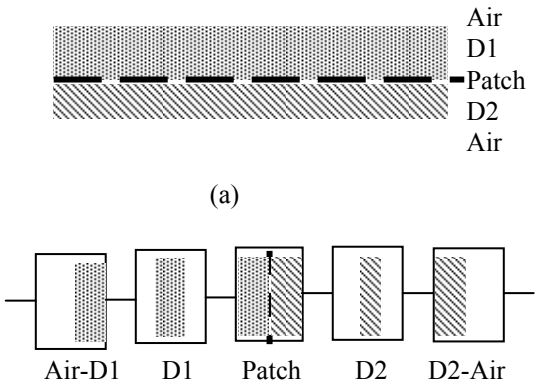

Fig. 1. (a) A three-layer array structure, (b) Modular representation of the array (D1 and D2 represent dielectric layers).

Identical cell-sizes and cell-orientations for the periodic arrays are assumed. Also, the structure is assumed to be infinite extent along x and y directions and is under Floquet excitation.

The GSM of a module is defined through the relation between incident and reflected voltages as below

$$\begin{bmatrix} a_1^- \\ a_2^- \end{bmatrix} = \begin{bmatrix} S_{11} & S_{12} \\ S_{21} & S_{22} \end{bmatrix} \begin{bmatrix} a_1^+ \\ a_2^+ \end{bmatrix} \quad . \tag{1}$$

In the above $[a_1^+]$ and $[a_2^+]$ are the incident voltage vectors with respect to the Floquet modes at the two sides (or ports) of the module and $[a_1^-]$ and $[a_2^-]$ are the corresponding reflected voltage vectors. The [S] matrix at the right-hand side of (1) is called the GSM of the layer. It consists of four sub-matrices, namely $[S_{11}]$, $[S_{12}]$, $[S_{21}]$, and $[S_{22}]$, respectively.

The overall GSM of the multilayer structure is obtained by combining the individual GSMs of the layers or modules. The cascading formula for two modules A and B is given by [7, p. 190]

$$[S_{11}^{AB}] = [S_{11}^{A}] + [S_{12}^{A}][I - S_{11}^{B}S_{22}^{A}]^{-1}[S_{11}^{B}][S_{21}^{A}], \tag{2a}$$

$$[S_{12}^{AB}] = [S_{12}^{A}][I - S_{11}^{B}S_{22}^{A}]^{-1}[S_{12}^{B}], \tag{2b}$$

$$[S_{21}^{AB}] = [S_{21}^{B}][I - S_{22}^{A}S_{11}^{B}]^{-1}[S_{21}^{A}], \tag{2c}$$

$$[S_{22}^{AB}] = [S_{22}^{B}] + [S_{21}^{B}][I - S_{22}^{A}S_{11}^{B}]^{-1}[S_{22}^{A}][S_{12}^{B}]. \tag{2d}$$

This formula can be applied repeatedly to obtain the overall GSM of a multilayer array. The GSM cascading formulas is applicable only if the layers have identical periodicities and have identical cell orientations. This insures that a Floquet modal vector function has an identical expression for all the layers. If the layers have different periodicities, then the process is more involved as detailed in [7, 8].

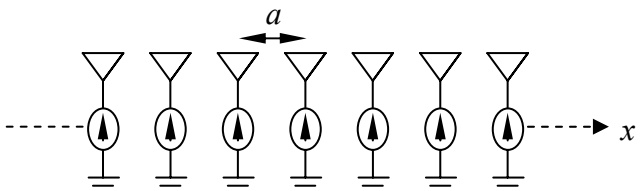

Fig. 2. Infinite linear array.

III. MUTUAL COUPLING FORMULATION

An accurate analysis of a finite array with an arbitrary excitation necessitates an estimation of the mutual coupling between the array-elements. The mutual coupling between the elements can be estimated by invoking the Floquet modal analysis of an infinite array [9].

The mutual coupling between the elements is generally quantified in terms of the following three measurable quantities:

(a) Mutual impedance,
(b) Mutual admittance,
(c) Scattering parameters.

The above three measurable quantities are related to each other by simple algebraic relations. In this Section we will first derive the mutual impedance from Floquet impedance of an infinite array [7,9]. We first consider a one-dimensional array. The result can be extended for a two-dimensional array.

A. Mutual Impedance

Consider the infinite array shown in Fig. 2. The elements are arranged along the x-direction with element spacing a. Suppose the elements are excited uniformly with linear phase progression, known as Floquet excitation. Suppose ψ is the phase difference between two adjacent elements. Then following the definition of mutual impedance, the input voltage for the 0-th element can be obtained as

$$V_0(\psi) = \sum_{n=-\infty}^{\infty} I_n Z_{0n} \,. \tag{3}$$

In the above V_0 is the input voltage for the element located at $x = 0$, I_n is the input current of the n-th element and Z_{0n} is the mutual impedance between the two elements that are located at $x = 0$ and at $x = na$, respectively. For Floquet excitations, the input currents can be expressed as

$$I_n = I_0 \exp(-jn\psi) \tag{4}$$

where I_0 is the input current for the element at $x = 0$. The input impedance seen by the $n=0$ element is

$$Z_0(\psi) = \frac{V_0(\psi)}{I_0} \,. \tag{5}$$

Substituting (3) and (4) in (5) we obtain

$$Z_0(\psi) = \sum_{n=-\infty}^{\infty} Z_{0n} \exp(-jn\psi) \,. \tag{6}$$

For a Floquet excitation, the above input impedance must be equal to the Floquet impedance $Z^{FL}(\psi)$. Therefore we obtain

$$Z^{FL}(\psi) = \sum_{n=-\infty}^{\infty} Z_{0n} \exp(-jn\psi) \,. \tag{7}$$

The right hand side of (7) is the Fourier series expansion of the Floquet impedance where the Fourier coefficients are equal to the mutual impedances. Thus, the mutual impedance Z_{0n} is readily obtained in terms of the Fourier integral as follows,

$$Z_{0n} = \frac{1}{2\pi} \int_{-\pi}^{\pi} Z^{FL}(\psi) \exp(jn\psi) d\psi \,. \tag{8}$$

If the two elements are located at $x = ma$ and $x = na$, respectively, then the mutual impedance between these two elements can be expressed as

$$Z_{mn} = \frac{1}{2\pi} \int_{-\pi}^{\pi} Z^{FL}(\psi) \exp\{-j(m-n)\psi\} d\psi \,. \tag{9}$$

Equation (9) establishes the relation between the Floquet impedance and the mutual impedance between the elements. It is important to observe that equation (9) yields the mutual impedance in the array environment. Also observe that Z_{mn} and Z_{nm} are identical because $Z^{FL}(\psi) = Z^{FL}(-\psi)$ [7, p. 130]. The symmetry property of $Z^{FL}(\psi)$ can be utilized to express Z_{mn} in the following convenient form from computational point of view:

$$Z_{mn} = \frac{1}{\pi} \int_{0}^{\pi} Z^{FL}(\psi) \cos\{(m-n)\psi\} d\psi \,. \tag{10}$$

The mutual impedance deduced in (10) includes the effects of scattering from the intermediate and surrounding elements that are open-circuited. The element-by-element approach [10] typically ignores the scattering effects; therefore the present formulation for mutual coupling is generally more accurate than the element-by-element approach.

It is worth pointing out that for some arrays the Floquet impedance Z^{FL} may have a finite number of singularities due to resonances of selective Floquet modes with the guided wave modes supported by the array structures. Under such a situation, a singularity extraction technique [11] must be employed to compute the integral near a singular point.

The mutual admittance between the two elements in array environment can be obtained as

$$Y_{mn} = \frac{1}{\pi} \int_{0}^{\pi} Y^{FL}(\psi) \cos\{(n-m)\psi\} d\psi \tag{11}$$

where $Y^{FL}(\psi)$ is the Floquet admittance, reciprocal to the Floquet impedance $Z^{FL}(\psi)$ and Y_{mn} is the mutual admittance between the m-th and the n-th elements. The distance between the two elements is $(m-n)a$. The scattering parameters between the elements also follow the similar relation. If S_{mn} represents the scattering parameter defined as the voltage received by the m-th element when the n-th element is excited with all other elements including the m-th element are matched terminated, then

$$S_{mn} = \frac{1}{\pi} \int_{0}^{\pi} \Gamma^{FL}(\psi) \cos\{(m-n)\psi\} d\psi \tag{12}$$

where $\Gamma^{FL}(\psi)$ is the reflection coefficient of an array element under Floquet excitation. Since $\Gamma^{FL}(\psi) = \Gamma^{FL}(-\psi)$, one can see that $S_{mn} = S_{nm}$. It should be noted that the integral for S_{mn} does not have any singularity because the magnitude of $\Gamma^{FL}(\psi)$ does not exceed beyond unity. Thus, from computational point of view, scattering matrix formulation is advantageous as compared with

impedance/admittance formulation for a finite array analysis.

The mutual coupling formulation can be extended for a two dimensional planar array. For a rectangular lattice structure, the mutual impedance involves a two-dimensional integral with variables ψ_x and ψ_y, where ψ_x and ψ_y represent the phase difference between the adjacent elements along x and y directions, respectively. For a triangular lattice, the formulation is slightly different (see [7, p.141]).

IV. Finite Array: Active Impedance and Radiation Patterns

The mutual coupling information between the elements is utilized to determine the active impedance or return loss of an element with respect to given amplitude and phase distributions. The active impedance of an element depends on the amplitude and phase distributions and the load-conditions of the non-excited elements [7, p.146]. In the present study we will assume that the non-excited elements of a "finite array" are match terminated. This assumption is somewhat justified because a matched element have a small scattered field, thus closely resembles the absence of an element.

Under such a situation the scattering matrix relation will yield the exact active input impedance solution. The relation in this situation is

$$[V^-] = [S][V^+] \tag{13}$$

where $[V^+]$ and $[V^-]$ are the incident and reflected voltage vectors. Elements of $[S]$ are obtained using (12). Equation (13) can be utilized to obtain the complex reflection coefficients of the elements with respect to a given amplitude distribution of a finite array.

The radiation pattern of the finite array for this particular situation can be obtained directly from superposition. The result becomes [7, p.150]

$$E^{array} = E^a[P][V^+] \tag{14}$$

where E^a is the active element pattern, which is defined as the radiation pattern of an element in array environment while other elements are match terminated. The vector form of the active element pattern can be obtained from Floquet analysis and the final expression becomes [7, p.109]

$$\vec{E}_a(\theta,\phi) = \hat{\theta}\{jV_{00}^{TM}\sqrt{ab/\lambda_0^2}\} - \hat{\phi}\{jV_{00}^{TE}\sqrt{ab/\lambda_0^2}\cos\theta\} \tag{15}$$

In the above V_{00}^{TM} and V_{00}^{TE} are the modal voltages at the array aperture for the TM_{00} and TE_{00} Floquet modes, respectively. The modal voltages are functions of scan direction (θ,ϕ). The gain can be determined by normalizing element and array structures.

V. Results

To illustrate the GSM approach, we consider a multilayer finite array of slot-fed patch elements. Figure 3 shows the element and array structure. The element numbering scheme is also shown pictorially. We computed the Floquet return loss (return loss under Floquet excitation) versus scan angle and plotted in Fig. 4. The return loss is generally good near the bore-sight scan, however a sharp resonant spike is observed near 39 degree scan angle along the E-plane. The resonant spike causes a complete mismatch and the array is ceased to radiate at this angle. This phenomenon is known as scan blindness. The TM_0 surface wave mode, supported by the grounded dielectric structure, is responsible for this blindness. At that scan angle, the surface wave mode has a perfect phase-match with the element phase causing a resonance[1]. The surface wave resonance for the D-plane scan is not present because the resonant condition is not satisfied for the square grid structure under consideration. For the H-plane scan, the resonance does not occur because the surface wave is not excited at the first place due to polarization mismatch between the patch mode and the surface wave mode.

Figure 5 shows the active element pattern cuts for the array. The patterns are normalized with respect to the incident power. The active element gain is about 6.39 dBi, which is 0.23 dB lower than that of a 100% aperture-efficient element. This gain loss is due to back side radiation of the feed slot. The E-plane pattern has a null (blind angle) near 39 degree which is consistent with the return loss behavior. For the E and H-plane patterns, the cross-polarization components do not exist because of symmetrical geometry. The cross-polarization level is substantial at the D-plane scan, particularly near 60-degree off-boresight.

Figure 6 shows the radiation pattern of a finite array of 15×15 elements. Two scan angles were considered in this case. The radiation patterns of the finite array were computed using (14). The amplitude taper (Gaussian) was 10 dB for both cases. For the bore-sight beam, the peak gain is about 28.95 dBi, which is about 1 dB lower than that of a uniform excitation. The scanned beam has a peak gain of 28.06 dBi. The side lobes are 25 dB below the beam peaks in both cases.

Equation (12) was utilized to compute the mutual coupling in terms of the array scattering parameters.

[1] As stated at the introduction, the present analysis assumes infinite array with a finite number of excited elements. For a real finite array, the effects of edge diffraction may be included approximately through complex reflection coefficient of the surface wave mode due to the ground plane and dielectric truncation [12].

Figure 7 shows the coupling level of the array elements with respect to the center elements. The E-plane elements are tightly coupled than the H-plane elements.

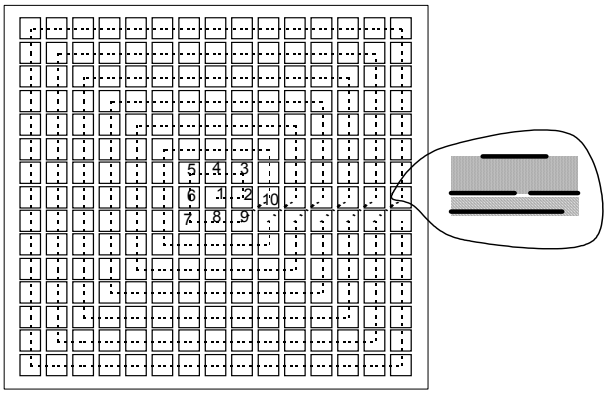

Fig. 3. A 15×15 element array of slot-fed patch elements. The element numbering scheme is also shown.

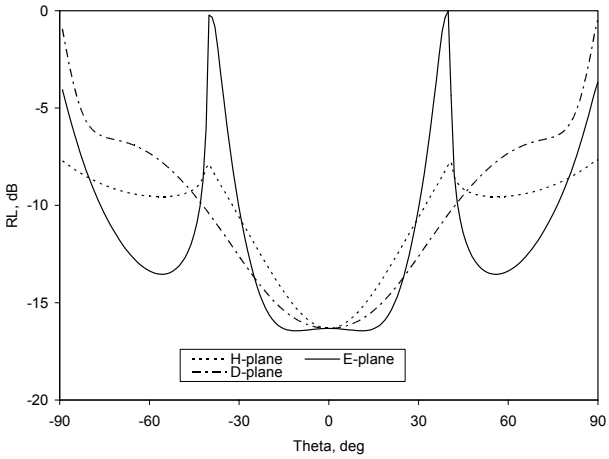

Fig. 4. Floquet return loss of a slot-fed patch array versus scan angle. Cell size =0.6 × 0.6, patch size=0.24 × 0.47, slot size =0.017 × 0.25, patch side ε_r =2.53, thickness=0.058, feed side ε_r =9.8, thickness=0.026, 50 Ohms feed line. All dimensions are in wavelength in free space.

Figure 8 shows the active return loss of the elements in the 15×15 elements patch array with uniform and tapered distributions, respectively. For the tapered array, Gaussian amplitude distributions with 10 dB taper for both planes were considered. For the plots, elements were numbered according to the numbering scheme depicted in Fig. 2. Four cases were considered as indicated at the inset of Fig. 8. The elements were designed to have about -16 dB bore-sight match under Floquet excitation. It is found that the active return loss varies from element to element. In particular, elements near the edge have noticeably different return losses than the rest. For the

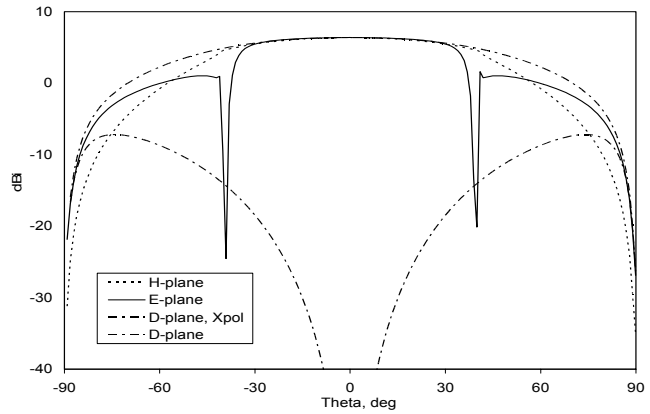

Fig. 5. Active element pattern cuts of the array. Element dimensions are sane as in Fig. 4.

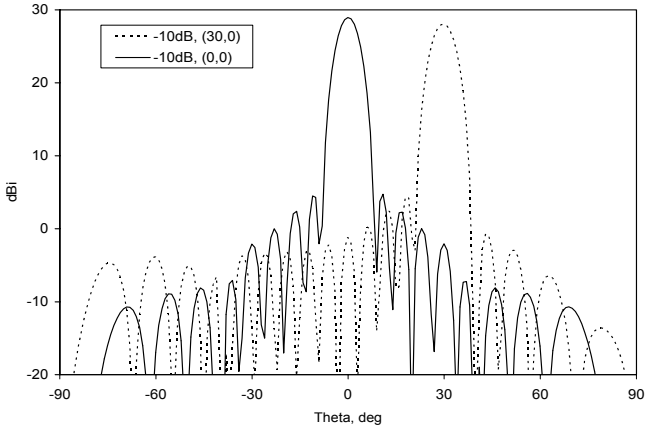

Fig. 6. Radiation pattern of 15 x 15 element patch array.

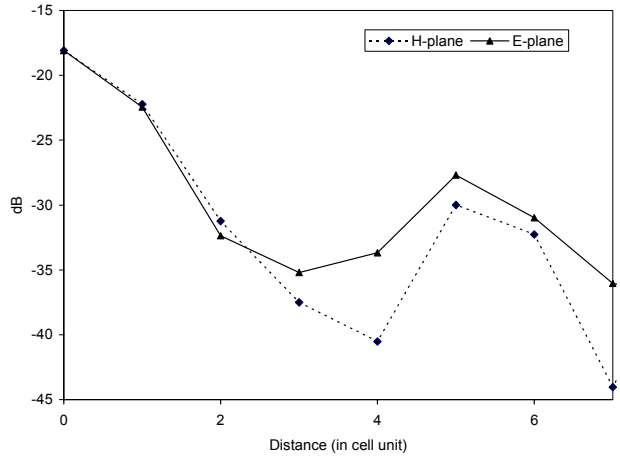

Fig. 7. Mutual coupling between patch elements in array environment. Patch dimensions are in Fig. 4.

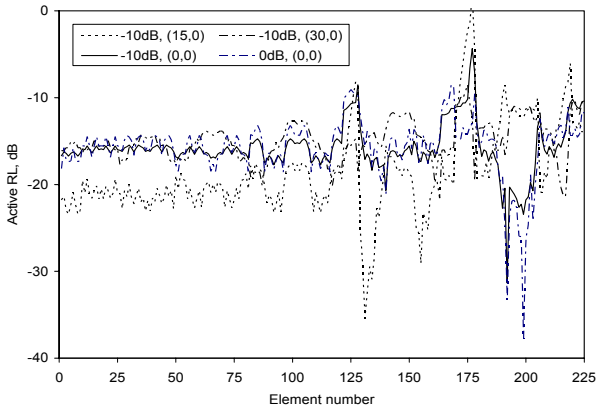

Fig. 8. Active return loss of the 15 x 15 element patch array in Fig. 3. The patch dimensions are in Fig. 4. The element numbering scheme is shown in Fig. 3.

bore-sight scan, the return loss for most of the elements lies below –15 dB. The return loss deteriorates for the off-bore-sight scans.

VI. CONCLUSIONS

In this paper we demonstrated the GSM approach for analyzing multilayer finite array. We considered a finite slot-fed patch array as an example. The mutual coupling between the elements, active element pattern, active return loss and array patterns were computed and results are shown. It is found that the mutual coupling is stronger between the E-plane elements than H-plane elements. The active return loss is substantially different for the elements near the edge, than the elements at the center region of the array.

The GSM approach is a modular approach as compared to an integrated approach. Computationally, the GSM approach for finite array analysis is much more efficient than FEM and FDTD approaches, because the problem size of a GSM is limited to a cell only. Furthermore, the matrix size of the MoM based GSM approach is much smaller as compared to a grid-based approach. However, a grid-based approach is more versatile because it can be applied to non-periodic geometries also without additional complexity.

REFERENCES

[1] Y. Lubin and A. Hessel, "Wide-band, wide-angle microstrip stacked-patch-element phased arrays," *IEEE Trans., Antennas Propagat*., Vol. 39, No. 8, pp. 1062-1070, Aug. 1991.

[2] A. K. Bhattacharyya, "A modular approach for probe-fed and capacitively coupled multilayered patch arrays," *IEEE Trans., Antennas Propagat*., Vol. 45, No. 2, pp. 193-202, Feb. 1997.

[3] T. K. Wu (Ed.), Frequency Selective Surface and Grid Array, Wiley, New York, 1995.

[4] R. S. Chu and K. M. Lee, "Analytical model of multilayered meander line polarizer plate with normal and oblique plane-wave incidence," *IEEE Trans., Antennas Propagat*., Vol. 35, No. 6, pp. 652-661, June 1987.

[5] H-Y. D. Yang, N. G. Alexopoulos and E. Yablonovitch, "Photonic band-gap materials for high-gain printed antennas," *IEEE Trans., Antennas Propagat*., Vol. 45, No. 1, pp. 185-187, Jan. 1997.

[6] A. K. Bhattacharyya, "A numerical model for multilayered microstrip phased-array antennas," *IEEE Trans., Antennas Propagat*., Vol. 44, No. 10, pp. 1386-1393, Oct. 1996.

[7] A. K. Bhattacharyya, Phased Array Antennas, Hoboken, Wiley, 2006.

[8] A. K. Bhattacharyya, "Analysis of multilayer infinite periodic array structures with different periodicities and axes orientations," *IEEE Trans., Antennas Propagat*., Vol. 48, No. 3, pp. 357-369, Mar. 2000.

[9] A. K. Bhattacharyya, "Floquet modal based analysis for mutual coupling between elements in an array environment," *IEE Proc*., MAP, Vol. 144, No. 6, pp. 491-497, Dec. 1997.

[10] D. M. Pozar,"Input impedance and mutual coypling of rectangular microstrip antennas," *IEEE Trans., Antennas Propagat*., Vol. 30, pp. 1191-1196, 1982.

[11] I. E. Rana and N. G. Alexopoulos, "Current distribution and input impedance of printed dipoles," *IEEE Trans., Antennas Propagat*., Vol. 29, No. 1, pp. 99-105, Jan. 1981.

[12] A. K. Bhattacharyya, "Effect of ground plane and dielectric truncation on the efficiency of a printed structure," *IEEE Trans., Antennas Propagat*, Vol. 39, No. 3, pp. 303-308, March 1991 (also see reply to comments on the paper appeared in January 2004 issue of the transaction for correction notes).

Arun K. Bhattacharyya was born in India in 1958. He received his B.Eng. degree in electronics and telecommunication engineering from Bengal Engineering College, University of Calcutta in 1980, and the M.Tech. and Ph.D. degrees from Indian Institute of Technology, Kharagpur, India, in 1982 and 1985, respectively.

From November 1985 to April 1987, he was with the University of Manitoba, Canada, as a Postdoctoral Fellow in the electrical engineering department. From May 1987 to October 1987, he worked for Til-Tek Limited, Kemptville, Ontario, Canada as a senior antenna engineer. In October 1987, he joined the University of Saskatchewan, Canada as an assistant professor of electrical engineering department. He was promoted to the associate professor rank in 1990. In July 1991 he joined Boeing Satellite Systems (formerly Hughes Space and Communications), Los Angeles as a senior staff engineer, and then promoted to scientist and senior scientist ranks in 1994 and 1998, respectively. Dr. Bhattacharyya became a Technical Fellow of Boeing in 2002. In September 2003 he joined Northrop Grumman Space Technology group as a staff scientist, senior grade. He is the author of "Electromagnetic Fields in Multilayered Structures-Theory and Applications", Artech House, Norwood, MA, 1994 and "Phased Array Antennas", Hoboken, Wiley, 2006. He authored over 80 technical papers and has 12 issued patents. His technical interests include applied electromagnetics, printed antennas, multilayered structures, active phased arrays and modeling of microwave components and circuits.

Dr. Bhattacharyya is a fellow of IEEE. He is a recipient of numerous awards including the 1996 Hughes Technical Excellence Award, 2002 Boeing Special Invention Award for his invention of high efficiency horns, 2003 Boeing Satellite Systems Patent Awards and 2005 Tim Hannemann Annual Quality Award, Northrop Grumman Space Technology.

Modeling the RF Performance of a Small Array

(Invited Paper)

P. R. Foster* and A. E. Wicks**
* MAAS, Malvern, UK
** QinetiQ, Malvern, UK

ABSTRACT - Large phased arrays can be reasonably accurately modelled in finite element programs, such as HFSS using an infinite array model of the embedded element. This approximation is not applicable to small arrays, where each element is in a different electromagnetic environment. Very small arrays of simple elements (of about 10 elements or less) can be modelled as a complete unit, but slightly larger or more complex arrays require additional techniques to be modelled accurately. The predicted performance of several versions of a small array has been compared using HFSS V9.5. The arrays contained either waveguide or printed dipole elements and, within the limits of available computing resources, solutions were generated for (1) complete array models, (2) half and quarter array models with symmetry planes, and (3) infinite array models.

I. INTRODUCTION

A Finite Element program, High Frequency Structure Simulator, HFSS, [1], has been used to compute the performance of an array of 23 elements (Figure 1) over a 5% bandwidth at 10 GHz. The array lattice geometry was determined from the requirements to scan +/- 35 degrees in the Y-direction and +/-15 degrees in the X-direction. These requirements for a small field of view led to the elements being spaced by approximately 1 wavelength at 10 GHz in the X-direction and 0.5 wavelength in the Y-direction.

The objective of the work was to compare the RF performance of two different kinds of antenna elements when used in this small array. The first element was a printed double dipole which had already been developed [2], [3] and the second element was a very simple waveguide element. The major objective of this work was to see if more gain could be obtained from an array of waveguide elements rather than an array of the printed elements.

Since problems might be encountered in the accurate determination of the behaviour of such an array with only 23 elements, the computation of the array behaviour was approached in 3 ways. Firstly the single element was treated as though embedded in an infinite array and the single element performance used to model the array through the use of the array factor. Secondly one quarter of the complete array was modelled using symmetry. Thirdly the array was modelled as a complete unit. The advantages and disadvantages of these methods are discussed as applied to two different radiating elements.

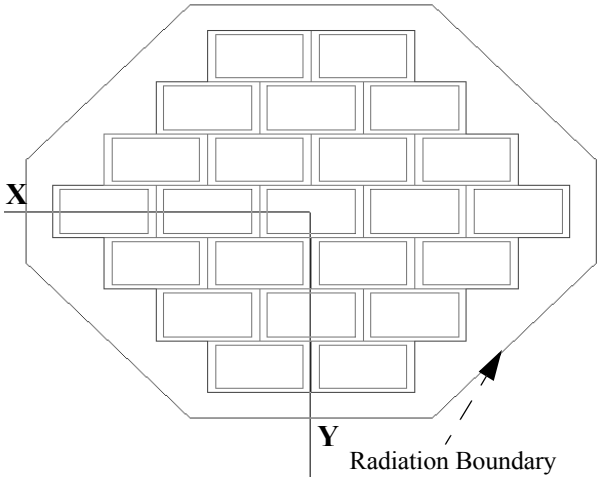

Figure 1. HFSS Geometry of array model showing the outer radiation boundary. The Z-axis is out of the plane of the paper. An Azimuth cut is in the XZ plane and an Elevation cut in the YZ plane.

II. ELEMENTS

Two elements were used. The first was a rectangular waveguide element fitted into the dimensions of the required array lattice (Figure 1). This was compared with a previously designed printed element [2], [3] formed of 2 half-wavelength dipoles plus a T-junction to make a double dipole element [4].

III. WAVEGUIDE ELEMENT

Although a waveguide element with a small aperture of 1 by 0.5 wavelengths is simple to design, there was a requirement for low coupling values. The maximum dimensions available for an element are 1 by 0.5 wavelengths at 10 GHz. A rectangular waveguide was fitted

into this area and its dimensions adjusted to get the lowest inter-element coupling between adjacent elements. The Finite Element Analysis, FEA, model for a single element (Figure 2) included the necessary radiation box and converged with 7,400 tetrahedra. The array was modelled in several ways which are described in the next section.

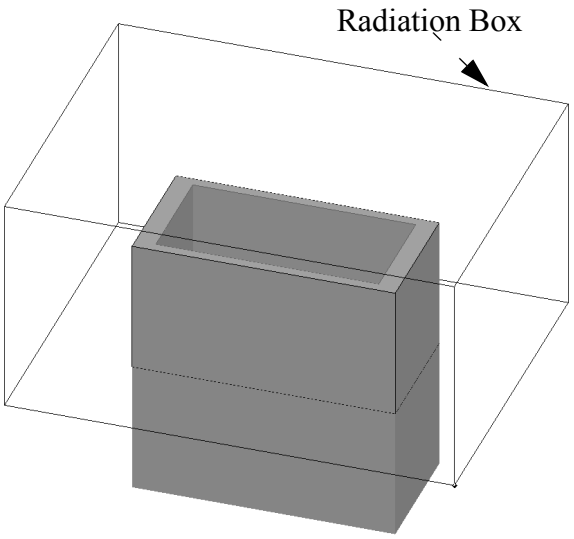

Figure 2. FEA model of final waveguide element in free space showing the surrounding radiation box. The outer dimensions of the element are 1 by 0.5 wavelength at 10 GHz.

A. Rectangular Infinite Array

The complete array of waveguide elements was modelled using the FEA program's inbuilt infinite array facility. Using this facility, a single array element can be modelled which has a boundary box of the same dimensions as the single element in the Z-direction but is cut to lie along the boundaries between adjacent array elements in the X and Y-directions (Figure 3). The array grid is therefore rectangular. The scan angle can be included in the computation. The array factor corresponding to Figure 1 was then applied. The problems with this approach are that:

- the use of an infinite array method for such a small array must be subject to errors,
- the element was modelled with opposing faces as pairs. This is immediately applicable to a rectangular array but is of doubtful validity for a triangular array.

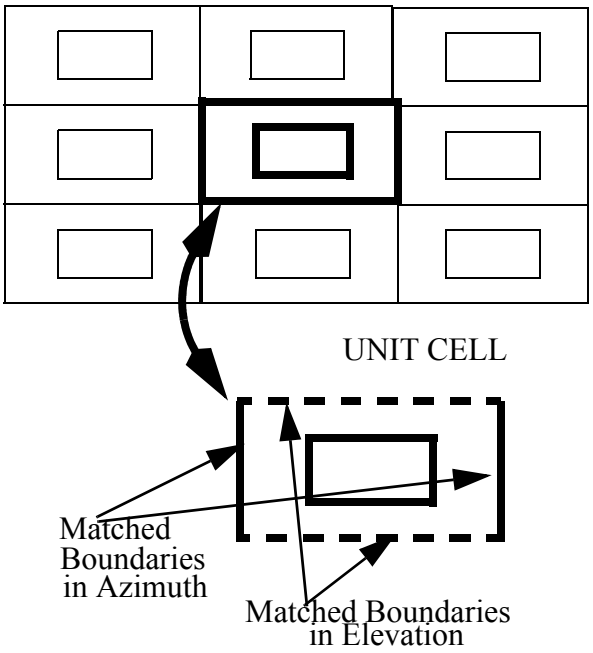

Figure 3. Geometry of infinite array, showing unit cell with matching boundaries to model an infinite array on a rectangular grid.

B. Triangular Infinite Array

The same waveguide element geometry was used as for the infinite rectangular array but the unit walls were set out differently so that the model tessellates exactly into a triangular array (Figure 4 and Figure 5). The array factor corresponding to Figure 1 was then applied.

C. Complete Array

Since the array element is very small in terms of wavelengths and is also simple in geometry, the array geometry was modelled exactly as shown in Figure 1 This avoided the necessity of including any definitions of the arrays. In addition to modelling the complete array, the array was modelled as a half array with E-plane symmetry and as a quarter array (Figure 6) with both E and H-plane symmetry since E and H-plane symmetry boundaries can be exploited within HFSS [1] to reduce the size of the problem. All three of these models gave the same radiation patterns and S-parameters.

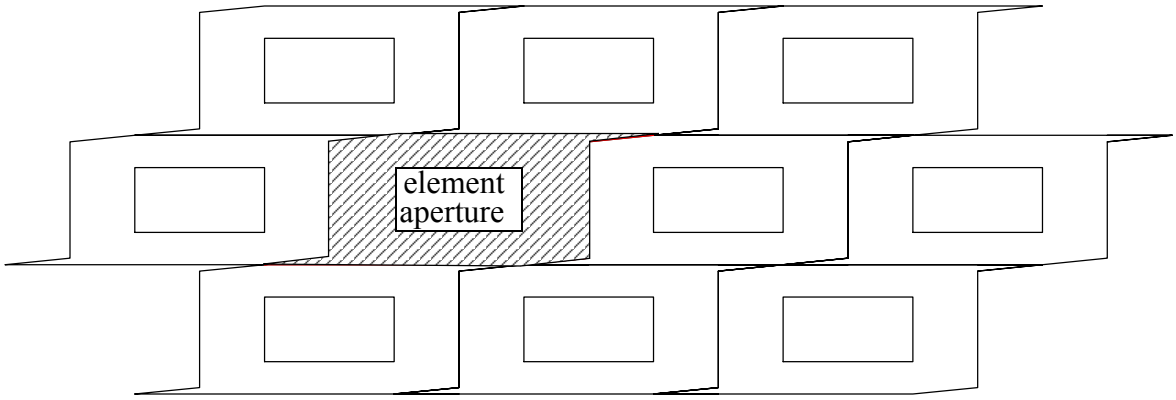

Figure 4. Geometry of triangular array, showing unit cell as hatched.

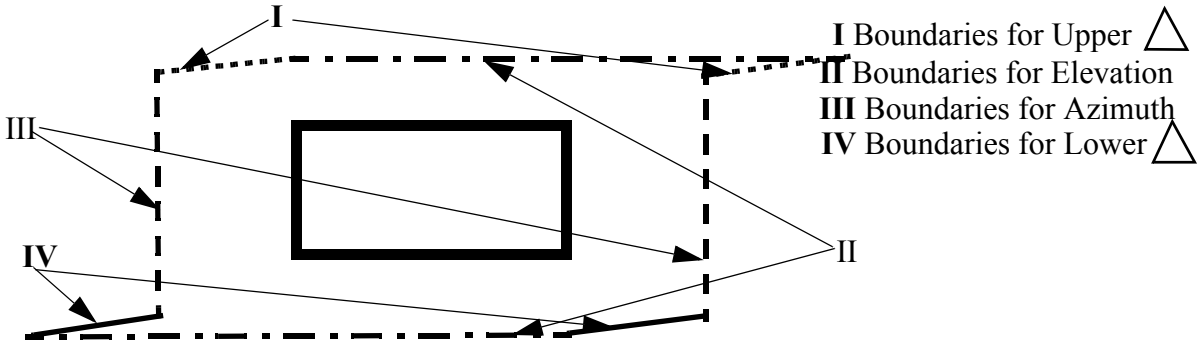

Figure 5. Unit Cell for triangular geometry of an infinite array (see Figure 4) showing matching boundaries.

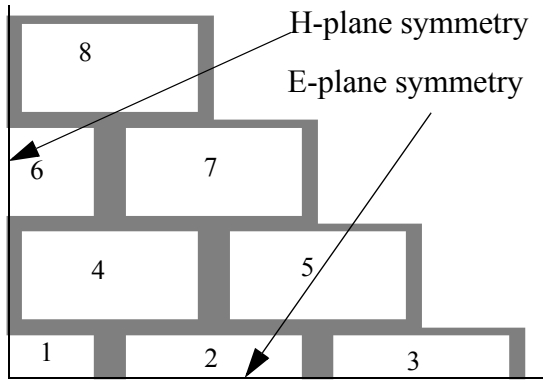

Figure 6. Geometry of one quarter of the complete array showing the use of both E and H-plane symmetry to reduce the model size by a factor of 4.

D. Comparison

The radiation pattern of an isolated waveguide element is shown in Figure 7 and for an embedded element using Methods 2 and 3 above. There is a difference in the backlobe which is greater by 15 dB in the isolated element. This is as expected because the isolated element will have currents running on the waveguide exterior which will contribute to the backlobe whereas the embedded element in Method 2 will have no currents on the exterior. Currents will run only on the array periphery in Method 3.

The crosspolar levels are a maximum in the diagonal plane, that is, Phi = 45.0 degrees. The peak crosspolar levels for these models (Figure 8) are high for the free space element and in the quarter array (-15.6 dB and -13 dB respectively) while that for the triangular infinite array is much lower at -24 dB. The radiation patterns of the complete array computed with different models are slightly different (Figure 9 and Figure 10). The differences in peak gain are less than 0.2 dB. The greatest difference is in the crosspolar levels which rise to -30 dB for the complete array but are less than -40 dB for the infinite array models.

The solution time and the number of tetrahedra used (and therefore computing memory required) for all the above models is shown in Table 1. The efficiency of the infinite array approximations is clearly shown. Use of symmetry gave a large improvement in runtime for the complete array model although extra time is required by HFSS to deal with the symmetry plane. The time quoted is that for convergence at 10 GHz and computation at 20 frequencies between 9 GHz and 11 GHz.

Table 1. Summary of HFSS Performance - Waveguide Element.

Array Model	No of Tetrahedra	Time (minutes)	Peak Gain	Azimuth 1st Sidelobe (dB)	Elevation 1st Sidelobe (dB)	Diagonal 1st Sidelobe (dB)
Infinite Array Method 1	3,046	8	21.52	-23.6	-23.4	-16.0
Infinite Array Method 2	2,750	8	21.33	-24.2	-23.6	-16.6
Complete Array	75,246	60	21.54	-24.5	-22.4	-15.9
Half Array	75,508	94	21.54	-24.5	-22.4	-15.9
Quarter Array	38,042	44	21.56	-24.5	-22.4	-15.9
Free Space Element	7,400	6	NR	NR	NR	NR

The number of tetrahedra and the runtime for the whole array and a half array using symmetry are very similar. The same criterion for convergence was used in all cases and this must be due to the size of the step used in moving from one mesh geometry, 62,923 tetrahedra, where convergence had not quite been achieved, to the next, 75,508 tetrahedra, where convergence was achieved.

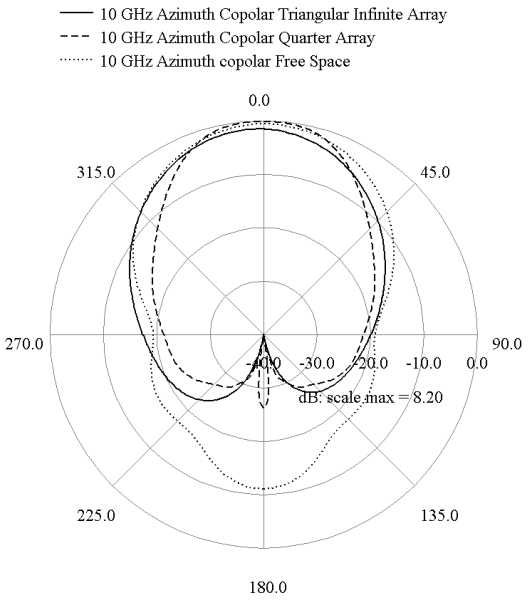

Figure 7. Comparison of Azimuth radiation patterns of a single waveguide element.

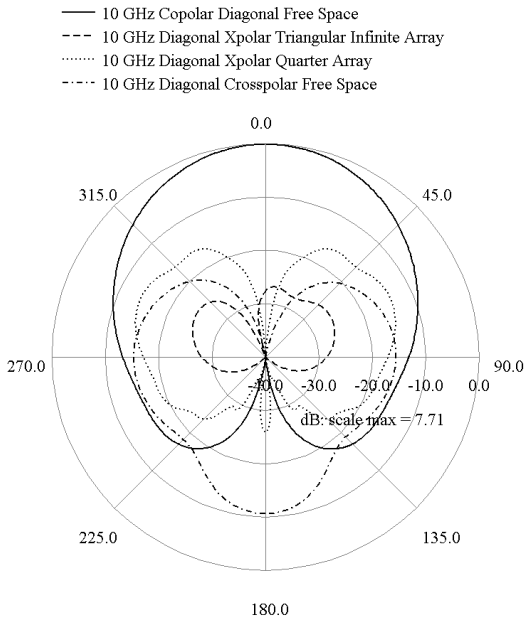

Figure 8. Comparison of diagonal (Phi= 45 degrees) crosspolar radiation patterns of a single waveguide element.

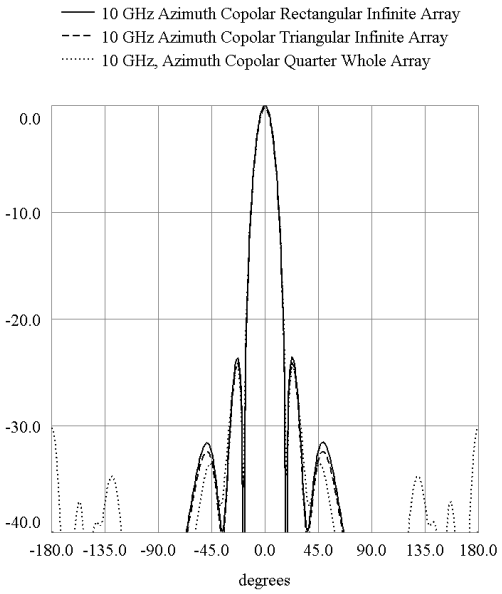

Figure 9. Comparison of array Azimuth copolar patterns with waveguide element. Gain normalised to 21.61 dBi.

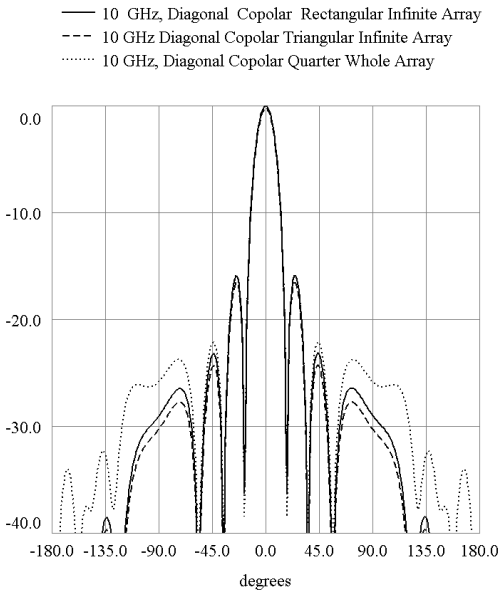

Figure 10. Comparison of array diagonal copolar patterns with waveguide element. Gain normalised to 21.56 dBi.

E. Scattering Parameters

Figure 11 shows that the Return Loss of an element in the two infinite arrays is very similar while that of the central element in the complete array is 4 dB higher and that of the single element is yet higher by 1 dB. This has important implications for the design procedure. To interface with the following electronics, the waveguide element must be terminated in a coaxial transition. An element with an integrated coaxial transition which had been optimised for a single element in free space would no longer be optimised when used in an array. Optimisation of the match in an infinite array will not be satisfactory for the array of 23 elements. Since a coaxial transition will increase the number of tetrahedra in the model, use of a half or quarter array would be beneficial but the transition must have symmetry for this to be possible. Given the close packing of the array, an end-launched transition will be needed and this can be made symmetrical.

The coupling between adjacent elements has been computed by placing 3 elements side by side in the X-direction or the Y-direction. The use of an infinite array (Array Methods 1 and 2) does not provide any coupling results. The use of a complete array does provide such information and this is plotted with the results from a three-element subarray in Figure 12 There is good agreement between the coupling values in the X-direction. In the Y-direction, the results for the row of elements are for 2 elements offset in the Y-direction only and are around -15 dB while the results for the complete array refer to 2 elements which are offset in the X-direction as well as the Y-direction. This triangular lattice improves the coupling by 7 dB so that the coupling between elements is better than -20 dB in the complete array.

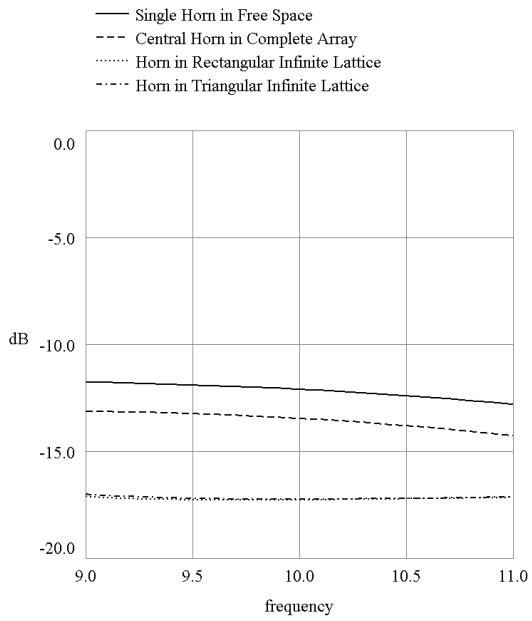

Figure 11. Comparison of predicted Return Loss for waveguide element.

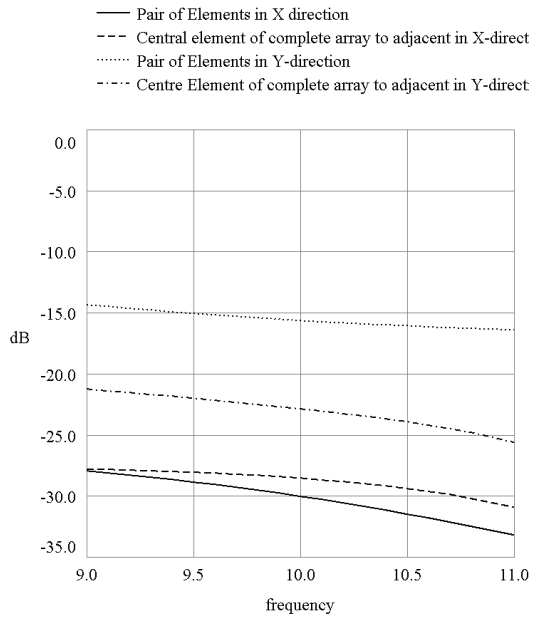

Figure 12. Coupling between adjacent waveguide elements.

IV. PRINTED ELEMENT

The second element that was investigated was a previously designed printed element [2], [3] formed of 2 half-wavelength dipoles plus a T-junction to make a double dipole element [4]. The FEA model of the element is shown in Figure 14 The meshing took 25,000 tetrahedra for a single element, compared to 7,400 for the waveguide element.

Modelling the array can be carried out using the infinite array techniques applied to the waveguide element and 24,910 tetrahedra were required for the model. A complete array of 23 elements would require about 575,000 tetrahedra. HFSS V9.5 is restricted on a Microsoft WINDOWS NT machine to a memory size of about 1.5 GBytes which can accommodate a maximum of about 125,000 tetrahedra. Therefore a complete array cannot be modelled with the available computing software and hardware. It is not possible to use 2 planes of symmetry either because the printed element is not symmetrical and one plane of symmetry (half the array) would still require too many tetrahedra.

When the radiation patterns of the printed element were computed using an infinite array method, they were very similar to the array of waveguide elements (Figure 13).

On the evidence from this work on arrays of waveguide elements with a boresight beam, the final radiation patterns of such a small array will not be very different from those computed for the printed element using an infinite array technique. While the work on the waveguide element showed that the array radiation patterns did not differ much with the modelling method used, the Return Loss did differ. This is also the case with the printed element (Figure 15) where the response in an infinite array is much narrower in bandwidth and shifted down in frequency. The coupling between adjacent printed elements has been modelled in two different configurations (Figure 16 and Figure 17). Compared with the coupling between adjacent waveguide elements (Figure 12) which is 15 dB in the X-direction and 30 dB in the Y-direction, the coupling between adjacent printed elements is poor at 17 dB and 19 dB at 10 GHz. On the basis of these coupling figures, one would expect the Return Loss, when the element is embedded in the array, to be quite different from that in free space.

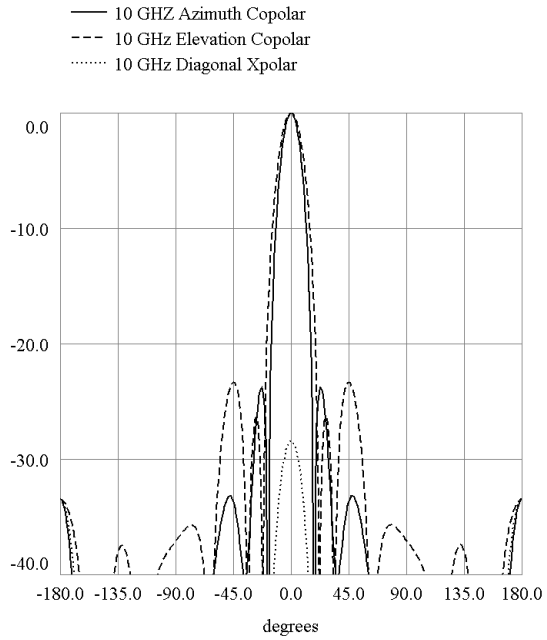

Figure 13. Radiation patterns of a complete array of printed elements - based on an element in an infinite array. Gain normalised to 21.61 dBi.

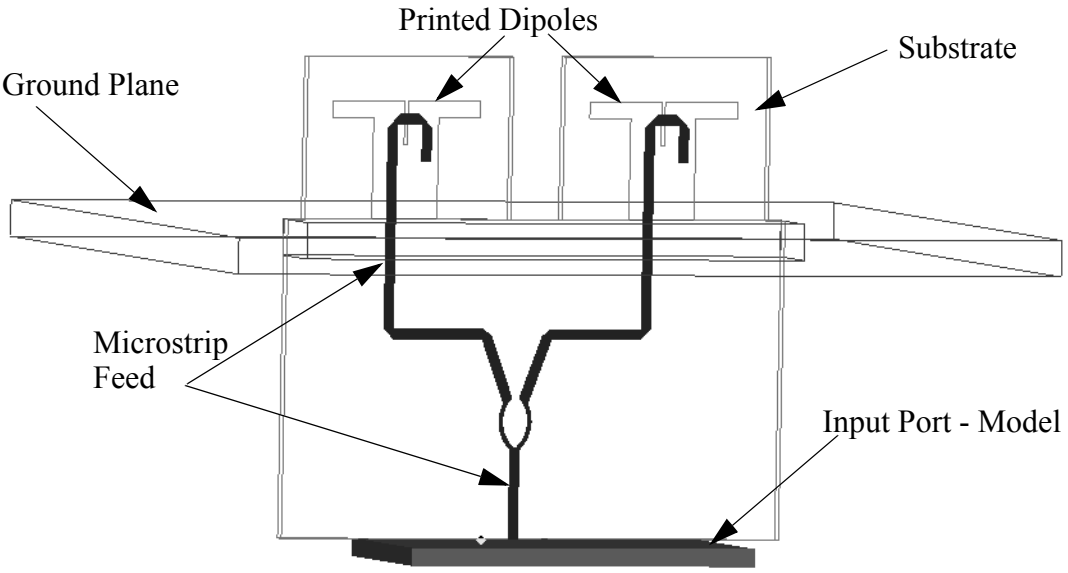

Figure 14. Model of Double Dipole. The centre-line of the dipole arms is 7.9 mm above the ground plane which is 0.263 wavelengths at 10 GHz. Other details may be found in [2].

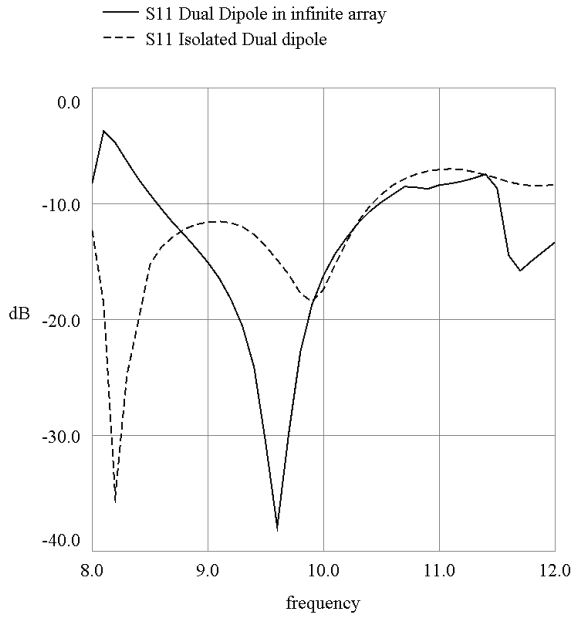

Figure 15. Return Loss for printed element in free space and in an infinite array.

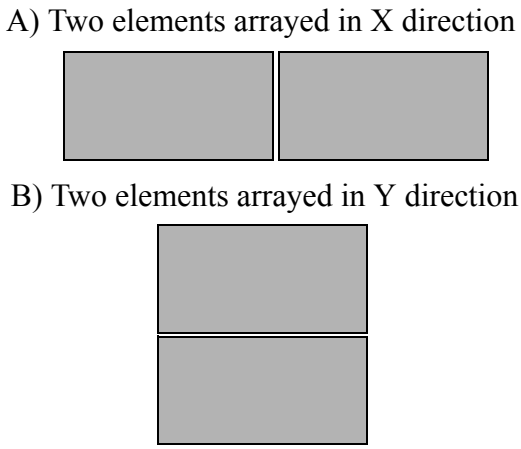

Figure 16. Geometry of two printed elements for coupling computation.

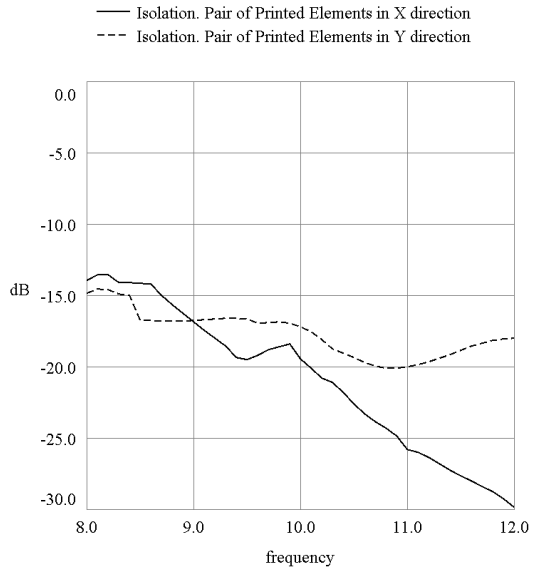

Figure 17. Coupling between two adjacent printed elements.

V. CONCLUSIONS

Two elements, a waveguide element and a printed double dipole, have been considered for use in an array of 23 elements in a triangular lattice. A commercial FEA program, HFSS V9.5, was used in all the computations.

When the waveguide element was modelled in the array using different methods (complete array, two geometries of infinite array), the gain and radiation patterns differed very little. The peak crosspolarisation did differ but values were less than -30 dB in all models. However the Return Loss of a single element varied a great deal according to the array model used. Since it was possible to use a complete array model, the Return Loss could be used to optimise a coaxial transition.

The printed element required far more tetrahedra in the mesh and it was impossible to run a complete array or use symmetry because of memory limitations. The results for the radiation patterns have to be based on the infinite array model but are probably indicative of what could be achieved. The Return Loss in free space and in the infinite array model were very different.

VI. ACKNOWLEDGMENTS

This work has been carried out with the support of the Weapon and Platform Effectors Domain of the UK MOD research programme.

REFERENCES

[1] I. Bradi and Z. J. Cendes, “New Directions in HFSS for Designing Microwave Devices”, Microwave J, pp. 22 - 36, August 1998.

[2] G. S. Hilton, C. J. Railton, G. J. Ball, M. Dean, A. L. Hume, “Finite-difference time-domain analysis of a printed dipole antenna”, 9th International Conference on Antennas and Propagation, Eindhoven, pp. 1062 - 1065, 1995.

[3] G. S. Hilton, C. J. Railton, G. J. Ball, M. Dean, A. L. Hume, “Modelling a three-element printed dipole antenna array using the FDTD technique”, 1997. IEEE AP-S International Symposium and URSI North American Radio Science Meeting, Montreal, Canada, pp. 72 - 75, July 13-18, 1997.

[4] A. Beckett, MBDA, Bristol, UK, Private communication, 2004.

Patricia Foster has a BSc in Physics from Edinburgh University and PhD in Radioastronomy from Cambridge. She has worked for Marconi Research Centre, Gt Baddow, ERA Technology, Leatherhead and British Aerospace, Filton. Since 1983, she has run Microwave and Antenna Systems which is an R&D house for antennas. Her special interests are computational electromagnetics particularly for installed performance of antennas.

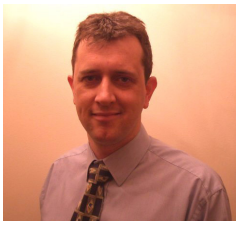

Andrew Wicks BSc MSc CEng MIEE graduated with a BSc in Physics from Exeter University in 1991 and an MSc in Microwave Solid State Physics from Portsmouth University in 1992. He joined QinetiQ, then the UK MoD's Defence Research Agency (DRA), in 1992. Initially designing and testing microwave circuits, his work included the integration of novel microwave heterojunction bipolar transistors in printed circuits. For the last ten years he has been principally involved with airborne active phased array radar programmes, leading activities on microwave transmit/receive module development. This work also included development of antenna elements for phased arrays and the design of antenna arrays. He is currently working on the antenna for Tarsier(r), QinetiQ's 94GHz runway debris monitoring radar.

A Critical Examination of Receive and Transmit Scan Element Pattern for Phased Arrays

(*Invited Paper*)

R. C. Hansen
P.O. Box 570215 Tarzana, CA 91357 818-345-0770, www.rchansen.com

***Abstract* —** The measurement of Scan Element Pattern by exciting only the center element is evaluated, both for gain at broadside and for behavior versus scan (normalized at broadside). A large dipole array of 50 × 50 elements is used in a 64 bit computer test bed, for calculations including mutual impedance. These results are compared with those where all elements are properly excited. A simple rigorous derivation of SEP including impedance mismatch is presented.

***Index Terms* —** Scan Element Pattern, phased arrays, array measurements.

I. INTRODUCTION

Scan Element Pattern, (SEP), (formerly active element pattern[1]) was developed circa 1960 in [1–4], to provide phased array gain behavior versus scan angles. Its utility for decades has been to give insight and results on the scan performance of various elements and lattices. A common but incorrect measurement procedure terminates all elements in the array, with the excited center element connected to a gain measurement setup. It was recognized in the Lincoln Lab reports [1] that the impedance seen in the measurement was not the *scan impedance* (SI), (impedance seen when all elements are excited with the proper amplitude and phase), due to the passive mutual couplings. The textbook definition of gain was used in the derivation provided in [1] where the scan impedance mismatch loss was not included. Hannan included this mismatch, but his formulas were based on "intuitive reasoning" [3].

Clearly his SEP which is proportional to $\cos\theta$ is only an approximation [3, 5], which fails for large scan angles and for some types of elements at all angles. The excited center element procedure does not include the correct *scan impedance*, Z_s and it does not accurately yield the correct SEP. It is useful to examine closely how the 1960 results were obtained. In [1, 6], all mutual impedances were set to zero, and a zero order inversion of the impedance matrix was used, resulting in the array gain equal to N times the SEP. Hannan used superposition to produce the same result [3]. Superposition, as defined by Silver in [7], states that when currents are added the fields produced by the currents are added. There are N sets of currents; each set includes a current at the driven element and currents at all the other elements. In each current set a different element is driven. Unfortunately in any current set, none of the currents are what they would be if all elements were excited. Thus superposition is not useful: each current set produces incorrect voltages, and the sum of sets of incorrect voltages is also incorrect. Phased array books [8, 9] also use this incorrect formulation.

This paper determines the utility and inaccuracy of the excited center element procedure, herein called transmit SEP, and compares it with results from receive SEP. Both are simulated in computer programs.

First a rigorous derivation of scan element pattern is presented. It is similar to Lincoln Labs circa 1960 derivations, except that impedance mismatch is included.

II. DERIVATION OF SCAN ELEMENT PATTERN

Consider a linear or planar array with N elements. The *scan element pattern* is the gain per element at the peak of the scanned beam. All phase factors are considered zero, thus the array gain is written as:

$$G(\theta,\phi)=\frac{4\pi r^2\left|E(\theta,\phi)\cdot H(\theta,\phi)\right|}{P} \tag{1}$$

where P is the radiant power and in terms of electric field only,

$$G(\theta,\phi)=\frac{r^2E(\theta,\phi)\cdot E^*(\theta,\phi)}{30P}. \tag{2}$$

For any wire or patch antenna element, E is a constant times current times isolated pattern, divided by r. In particular for dipoles,

[1] This terminology is deprecated as "active" carries electron device connotation.

$$E(\theta,\phi)=\frac{60F(\theta,\phi)}{r}\sum^{N} I_n \,. \tag{3}$$

Here the sum is over the elements of the array, and the pattern function F is,

$$F(\theta,\phi)=\frac{\cos kh-\cos(kh\cos\theta)}{\sin kh\sqrt{1-\cos^2\theta\cos^2\phi}}\,. \tag{4}$$

The dipoles are along the x-axis and in the x-y plane. Thus the array axis is for $\phi=0$. Dipole half-length is h, and k=$2\pi/\lambda$.

Power into the array, without matching or source impedance, is simply,

$$P=\sum^{N} I_n I_n^{*} R_{sn} \tag{5}$$

where R_{sn} is the *scan resistance* of the nth element. Gain equation now takes the form

$$G(\theta,\phi)=\frac{120F^2(\theta,\phi)\sum^{N} I_n \sum^{N} I_n^{*}}{\sum^{N} I_n I_n^{*} R_{sn}}\,. \tag{6}$$

Since the *scan element pattern* is gain per element, one gets

$$SEP=\frac{120F^2(\theta,\phi)\sum^{N} I_n \sum^{N} I_n^{*}}{N\sum^{N} I_n I_n^{*} R_{sn}}\,. \tag{7}$$

This can be written in terms of the isolated element gain g_{iso}, where

$$g_{iso}(\theta,\phi)=\frac{120F^2(\theta,\varphi)}{R_{iso}}\,. \tag{8}$$

Thus SEP becomes,

$$SEP(\theta,\phi)=\frac{R_{iso}g_{iso}(\theta,\phi)\sum^{N} I_n \sum^{N} I_n^{*}}{N\sum^{N} I_N I_N^{*} R_{sn}}\,. \tag{9}$$

For a large array most element impedances will be the same thus SEP reduces to,

$$SEP(\theta,\phi)=\frac{R_{iso}g_{iso}(\theta,\phi)\sum^{N} I_n \sum^{N} I_n^{*}}{NR_s\sum^{N} I_n I_n^{*}}\,. \tag{10}$$

For a large uniformly excited array the currents will also be nearly equal. Thus the infinite array SEP becomes,

$$SEP(\theta,\phi)=\frac{R_{iso}g_{iso}(\theta,\phi)}{R_s}\,. \tag{11}$$

Power transfer to, or from, each element is affected by the load impedance Z_l and matching impedance. For a complex load /match Z_l, and resistance R_l, the power transfer, compared to perfectly matched transfer, is,

$$\frac{P_l}{P_{noload}}=\frac{4R_sR_l}{(Z_s+Z_l)(Z_s+Z_l)^{*}}\,. \tag{12}$$

Again for large arrays the SEP reduces to

$$SEP(\theta,\phi)=\frac{4R_{iso}R_lg_{iso}(\theta,\phi)}{(Z_s+Z_l)(Z_s+Z_l)^{*}}\,. \tag{13}$$

The new factors represent power transfer with a reflection coefficient modified for complex load impedance,

$$\frac{4R_sR_l}{(Z_s+Z_l)(Z_s+Z_l)^{*}}=1-\left|\Gamma_{*}\right|^2 \tag{14}$$

where,

$$\Gamma_{*}=\frac{Z_s^{*}-Z_l}{Z_s+Z_l}\,. \tag{15}$$

Note that for all real values of load-match, these equations revert to the usual ones.

Going back to equation (10), an alternate from, appropriate for computer analysis is

$$SEP(\theta,\phi)=\frac{120R_{isom}F^2(\theta,\phi)\sum^{N} I_n \sum^{N} I_n^{*}}{R_s(\theta,\phi)\sum^{N} I_n I_n^{*}}\times\left[1-\left|\Gamma_{*}(\theta,\phi)\right|^2\right]. \tag{16}$$

where R_s is the *scan resistance*.

The only approximation in (16) is that all element *scan resistances* are equal, which affect the power sum and the mismatch factor. For arrays that are not large, the mismatch factor can be calculated for each element, and then averaged. The effectiveness of this will be shown in Section 4.

III. MODELLING TRANSMIT SEP MEASUREMENT

To determine exactly how the transmit SEP measurement process behaves with angle and frequency, a planar array code using thin dipoles on a square lattice, is employed. This code treats a finite square array, up to 100 on elements each axis, thereby replicating the measurement procedure. As the dipoles are thin, and the maximum length is half-wave, the current distribution is very closely sinusoidal, thus Moment Methods solution is not necessary. All elements were terminated with a resistance, and the center element was excited. Solution of the mutual impedance matrix equation gives the complex currents for all the array elements. Mutual impedances and matrix inversion were calculated in double precision. Far field pattern was calculated by summing the element currents times the appropriate steering phases times the elements pattern. Power was calculated from Real (VI) for the driven element. Gain is simply $12E^2/P^*(1-|\Gamma|^2)$, where Γ is the reflection coefficient. Two matching impedances were used: one for an infinite array of excited dipoles, and the other for only the center element excited. Calculations were performed on an HP 64 bit UNIX workstation.[2]

Results are given for a 50 × 50 element array (2500 unknowns) in Fig.1. The values of SEP (gain per element) are normalized to zero dB at broadside as the absolute values are incorrect due to the passive mutual impedances. Absolute values are as discussed in Section 5. The broadside array impedance of 63 + j23 Ohms is used for matching. In comparison with the well-known infinite array results [9], the transmit SEP values are roughly 2 dB higher in the range of θ from 40 to 80 degrees for the E-plane. H-plane results are slightly higher. The departure from absolute gain is much worse than would be indicated by the modest change in the centre element impedance. The mutual coupling significantly reduces the current magnitudes, thus decreasing the gain per element. Significant oscillations in the E-plane SEP are due to edge effects, even for such a large array [10]. Note that in fig. 1 the E-plane SEP is higher than the H-plane, which is contrary to the infinite array Floquet results [9].

With the ground screen added, at a spacing equal to half the dipole spacing, the transmit SEP is as shown in Fig. 2. The broadside array impedance of 70 + j58 ohms is again used as match impedance. The E-plane result departs markedly from the infinite array result; the H-plane values are higher than the infinite array results to about 60 degrees, and lower for large angles. Note the large change in embedded impedance from the infinite array value of 153 + j32.

[2] CPU chips optimized for floating point operations tend to be several times as fast as PC chips optimized for integer handling, all for the same clock rate.

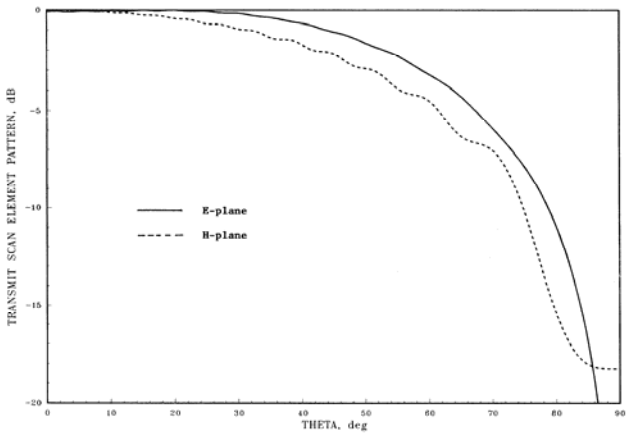

Fig. 1. A 50 × 50 dipole array, L = Dx = Dy = 0.5λ.

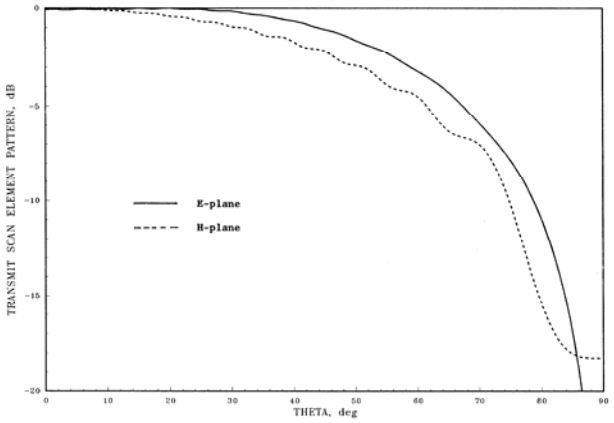

Fig. 2. A 50 × 50 dipole/screen array, L = Dx = Dy = 0.5λ, h = 0.25λ.

Not only is the absolute SEP at broadside is incorrect, but the scan performance, normalized to 0 dB at broadside, is not good predictor of array gain versus scan.

IV. MODELLING RECEIVE SEP MEASUREMENT

The same computer model was used to simulate the receive SEP measurement. All elements were excited by unit amplitude voltage and the proper scan phase. *Scan element pattern* was calculated again from $120E^2/P$ x $(1-|\Gamma|^2)$. Figure 3 shows SEP, in an absolute value.

A matched array would have an SEP of $2\pi A/N\lambda^2$, which is $\pi/2 = 1.97$ dB for the half wave case of Fig. 3. The E-plane curve is a fair fit (but slightly lower) to infinite array results out to about 70 degrees, but there are edge effect oscillations. The H-plane curve is slightly

higher for large angles. Calculations of 20 x 20 and 30 x 30 arrays (not shown) indicate that as the array size is larger, the match at large θ becomes better.

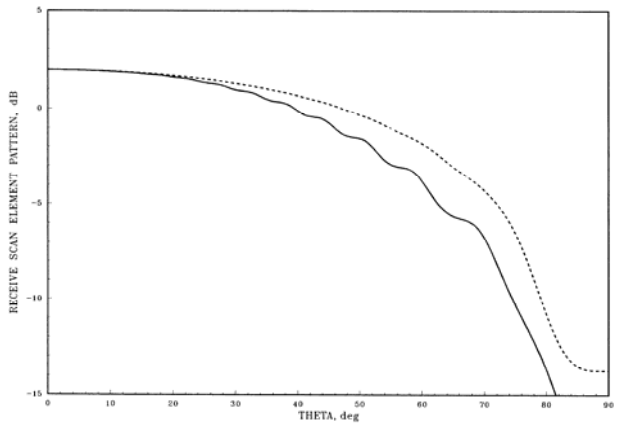

Fig. 3. A 50 × 50 dipole array, L = Dx = Dy = 0.5λ.

Figure 4 gives SEP with a ground screen, again spaced from the screen half the dipole spacing. The E-plane SEP contains large oscillations, building up as θ increases. These oscillations occur as the *scan impedance* of the center element oscillates about the infinite array value. An average curve through the oscillations matches well the infinite array data. H-plane data are roughly 1 dB high for angles larger than 50 deg.

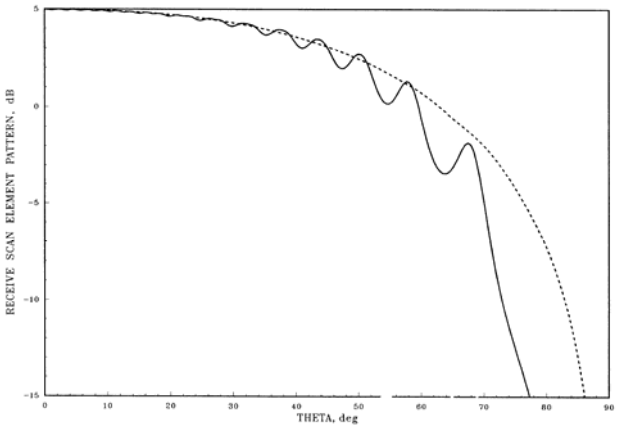

Fig. 4. A 50 × 50 dipole/screen array, L = Dx = Dy = 0.5λ, h = 0.25λ.

A better result comes from the average of the scan reflection coefficients of all elements. Figure 5 shows SEP for the half-wave dipole array, using the average reflection coefficient. The oscillations in Fig. 4 for the E-plane have been smoothed out and the H-plane SEP is higher, as it should be. Figure 6 is for the dipole with ground plane case with few oscillations. These two graphs compare well with the infinite array results of [9] but even for an array of 50 element wide, there are some edge effects at larger scan angles, thus Figs. 5 and 6 are slightly different from the infinite array results.

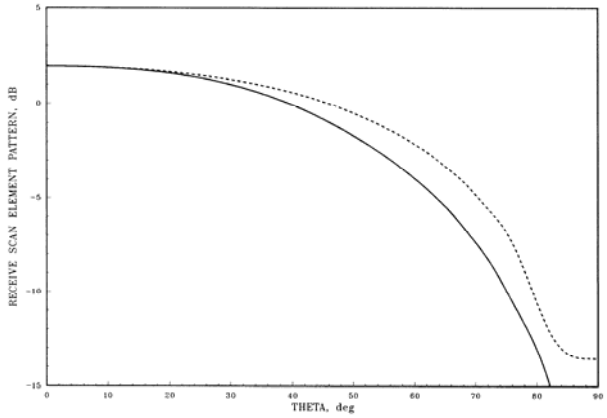

Fig. 5. A 50 × 50 dipole array, L = Dx = Dy = 0.5λ, average CGAM.

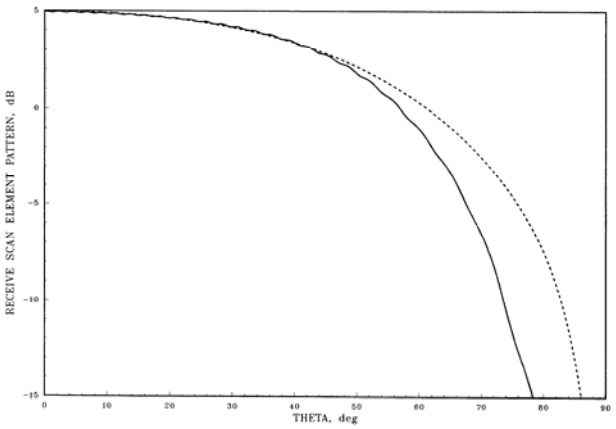

Fig. 6. A 50 × 50 dipole/screen array, L = Dx = Dy = 0.5λ, average CGAM.

V. COMPARISION OF BROADSIDE GAINS

The preceding transmit graphs were all normalized to 0 dB at broadside, to show scan behavior. Actual SEP, gain per element at broadside, is given in Table 1 for the 50 x 50 dipole array. For the (correct) receive case, with center element match, the SEP is $\pi/2$ =1.96 dB, as expected. The error in the (incorrect) transmit case is 6.2 dB. The passive mutual coupling reduces all currents but that of the center element, resulting in grossly incorrect gain.

Table 1. 50 x 50 Dipole Array at Broadside.

	SEP-T	SEP-R
Center Element Match	-4.26dB	+1.96 dB
Infinite Array Match	-5.00 dB	

The array over a ground plane gives the results in Table 2. Now the center element match case produces 4.97 dB as expected; the transmit case gives a gain of 11.4dB in error. When the infinite array impedances are used as a match, the results are nearly the same.

Table 2. 50 x 50 Dipole/Screen Array at Broadside.

	SEP-T	SEP-R
Center Element Match	-6.42 dB	+4.97 dB
Infinite Array Match	-8.71 dB	

VI. CONCLUSIONS

Measuring *scan element pattern* of an array with one element excited gives crude relative scan performance with significant errors, while the absolute values are grossly incorrect; due to only one element excitation leading to passive mutual coupling effects. SEP should be measured with the arrays in the receiving mode in a standard gain test facility. E-plane receive SEP may show oscillations for small arrays, which can be smoothed out by measuring or calculating SEP of several elements, and using averaging.

REFERENCES

[1] J. L. Allen et. al., Phased Array Radar Studies, July 1959 - July 1960, TR228, MIT Lincoln Lab., Aug.1960.

[2] A. A. Oliner and R. G. Malech, "Mutual Coupling in Infinite Scanning Arrays," *Chap. 3 in Microwave Scanning Antennas*, vol. 2, R. C. Hansen, ED., Academic Press, 1966.

[3] P. W. Hannan, "The Element-Gain Paradox for a Phased Array Antenna," *IEEE Transactions on Antennas and Propagations*, vol. AP-12, pp. 423-433, July 1964.

[4] L. Stark, "Radiation Impedance of a Dipole in an Infinite Planar Phased Array," *Radio Science*, vol. 3, pp. 461-375, March 1966.

[5] D. M. Pozar, "The Active Element Pattern," *IEEE Transactions on Antennas and Propagations*, vol. AP-42, pp. 1176-1178, Aug. 1994.

[6] J. L. Allen et. al., Phased Array Radar Studies, July 1960 - July 1961, TR236, MIT Lincoln Lab., Nov.1961.

[7] S. Silver, *Microwave Antenna Theory and Design,* vol. 12, Rad. Lab. Series, McGraw-Hill, pp. 66, 1949.

[8] R. J. Mailloux, *Phased Array Antenna Handbook*, Artech House, 1994.

[9] R. C. Hansen, *Phased Array Antennas*, John Wiley & Sons, Inc., 1998.

[10] R. C. Hansen, "A Gibbsian Model for Finite Scanned Arrays," *IEEE Transactions on Antennas and Propagations*, vol. AP-44, pp. 243-248, Feb. 1966.

Robert C. Hansen was born in 1926 in St. Louis, Missouri. He received a BSEE degree from the Missouri School of Mines, Rolla in 1949 and a PhD degree from the University of Illinois, Urbana in 1995.

He was an electronic technician in the U.S. Navy in 1945-46. From 1949-55 Dr. Hansen worked in the University of Illinois Antenna Laboratory. At Huges Aircraft Co. he was section head in the Microwave Laboratory working on antennas. In 1960 Dr. Hansen became a senior staff member in the Telecommunication Laboratory of STL, Inc. (now TRW). At Aerospace Corp. (1961-67), he was associate Director of Satellite Control, then director of the Test Mission Analysis Office, and finally Operations Group director of the Manned Orbiting Laboratory Systems Engineering Office. During 1967-70 he was with KMS Industries in Ann Arbor, Michigan. Since 1971 he has been a consulting engineer for antennas and systems related problems.

Dr. Hansen was perhaps the first to simulate antennas on a main frame computer (asymmetric spherical harmonics on ILLIAC, circa 1953). His work on antennas has been eclectic: he published first papers on low noise antennas, near-field power densities, reduced RCS measurements, minimum spot size of focused aperture, inductive loading of short monopoles, segmented aperture SAR, one-parameter circular aperture distributions, GTD analysis of compact ranges, S/N performance of aperiodic monopoles, focal region characteristics of focused arrays, superconducting antenna matching loss, measurement distance effects on Bayliss difference patterns, Gibbsian models for edge effects in scanning arrays, sub-array

quantization lobe decollimation, and analysis of the countrawound toroidal helix antenna.

Dr.Hansen is a Life Fellow of IEEE, a Fellow of IEE and was President of the Antennas and Propagation Society (1964 and 1980), and Director IEEE (1975). He was chair of U.S. Commission B of URSI (1967-69), and is a registered Professional Engineer in California and England. He is a member of the American Physical Society, Tau Beta Pi, Sigma Xi, Eta Kappa Nu, and Phi kappa Phi. He was awarded an honorary Doctor of Engineering degree by the University of Missouri-Rolla in 1975. The University of Illinois Electrical Engineering Department gave him a Distinguished Alumnus award in 1981, and the College of Engineering awarded a Distinguished Alumnus Service Medal in 1986. The IEEE AESS Barry Carlton best paper prize was awarded in 1991. He received the 2002 IEEE Electromagnetics Award. He was elected to the National Academy of Engineering in 1992.

Dr. Hansen has written over 100 papers on electromagnetics (most recently in 2006), has been Associate Editor of Microwave Journal (1960-95), was Associate Editor or Radio Science (1967-69), and Associate Editor of Microwave Engineer's Handbook(1970). His books are: Microwave Scanning Antennas(1964); Significant Phased Array Papers(1973); Geomentric Theory of Diffraction(1981); Moment Methods in Antennas and Scattering (1990); Phased Array Antennas (1998); and Electrically Small, Superdirective, and Superconducting Antennas(2006).

Modeling Conformal Array Antennas of Various Shapes Using Uniform Theory of Diffraction (UTD)

(Invited paper)

Patrik Persson
Royal Institute of Technology, Division of Electromagnetic Engineering,
SE-100 44 Stockholm, Sweden; E-mail: patrik.persson@ee.kth.se

Abstract - Traditionally, antennas have been designed as separate components, mounted on e.g. masts, buildings, and vehicles. Modern systems, however, require antennas to be integrated with existing structures. This paper discusses the analysis of conformally integrated array antennas using the hybrid UTD-MoM method, in particular arrays on doubly curved surfaces. Computed results are shown including singly and doubly curved surfaces. Most of the results are verified by measured results and calculated results obtained with a modal solution.

I. INTRODUCTION

The rapid growth in wireless communications, especially mobile communications, has caused the requirements on antenna systems to be more and more demanding. For future antenna systems a typical requirement is to integrate the antennas in the surface of different vehicles or platforms. For example, a modern aircraft has today many antennas protruding from the structure, for navigation, various communication systems, instrument landing systems, radar altimeter and so on. Integrating these antennas into the aircraft skin is highly desirable [1]. Antennas can also be integrated in various structures such as lampposts, chimneys, even trees, etcetera, in order to be more easily accepted by the public, as shown in Figure 1.

The need for such antennas, *conformal antennas*, is even more pronounced for the large apertures that are necessary in *e.g.* satellite communication and military airborne surveillance radars. In order to ensure proper operation of these systems, it is important to be able to determine the characteristics of the antennas. Thus, efficient (numerical) methods suitable for the analysis of conformal antennas are needed.

This paper will discuss modeling of conformal array antennas, in particular, antennas on electrically large, doubly curved surfaces. The emphasis is on the numerical implementation. The results are verified with measured data, but also with a modal solution. The layout of the paper is as follows; first, methods of analysis are discussed in general, but the main focus will be on the hybrid UTD-MoM method. This includes a discussion about geodesic ray tracing on surfaces with varying curvature. Finally, results are given to illustrate the accuracy of the hybrid method for singly and doubly curved PEC surfaces. The antenna element used through out this paper is the waveguide-fed aperture antenna, both with rectangular and circular cross-sections.

Figure 1. Possible location for base station antennas [2].

II. METHODS OF ANALYSIS

Important steps in the analysis of conformal array antennas are to find the mutual coupling among the radiating elements and the (isolated and/or embedded) radiation patterns of the individual elements. A critical step in the analysis is therefore to find the electromagnetic fields on the surface and in the far-field in the presence of a complex and arbitrarily shaped body. This is, in general, a difficult problem since the surface is often large (in terms of wavelength) and it may be convex or concave or both. Furthermore, the surface can have edges and other discontinuities, and a dielectric layer can cover the antenna aperture.

The available methods are often divided into two categories; frequency domain methods and time domain methods. Frequency domain methods are probably the most commonly used methods for analysis of antennas, including conformal antennas. Thus, our focus will be on these methods -- the interested reader can find an overview of time domain methods (mainly FDTD and techniques to avoid staircase approximation errors) in [3].

The classical way of analyzing conformal antennas is to use a modal solution. Such a solution is possible to obtain only for some special cases like a perfectly conducting circular cylinder, elliptic cylinder, cone, or sphere [4]. However, if the geometry is more complex, *e.g.* a rotationally symmetric surface of arbitrary cross section, a modal solution is very difficult, if at all possible, to obtain. The analysis is also typically highly complex and suffers convergence problems when the size of the geometry is increased (in terms of wavelengths). Hence, the process of extracting numerical results can be difficult and very time-consuming. A simplification of the modal solution for structures with rotational symmetry is to reduce the 3D problem to a spectrum of 2D problems by applying a Fourier transformation with respect to the symmetry axis as described by R. F. Harrington [5].

For arbitrarily shaped (3-D) bodies no exact analytical solutions exist. In the low frequency range, several reliable numerical procedures, *e.g.* method of moments (MoM) [6] and the finite element methods (FEM) [7], are available for solving the radiation/scattering problem. However, for higher frequencies, these numerical techniques become impractical since the associated matrix becomes very large.

One way of avoiding these problems is to use a high frequency approach. The term high frequency means that the fields are being considered in a system where the properties and size parameters of the geometry vary slowly with the frequency. This is not a serious limitation in many cases since the minimum radius of curvature of the surface can be quite small. A commonly used requirement is $kR \geq 2-5$ (k is the wave number, R is the radius of the cylinder) for accurate results [8]. From an engineering point of view these conditions are often fulfilled for large bodies when the frequency is in the microwave frequency band or higher.

There are a number of different high frequency techniques, or asymptotic techniques, available. The reason is that an asymptotic technique is often specialized for a certain problem and cannot be generalized easily. However, a general formulation is very desirable for efficient analysis of various realistic conformal antennas. A well known formulation is the ray-based uniform theory of diffraction (UTD) [9-11]. This approach has been successful and the solution is useful for different types of convex PEC surfaces, including doubly curved surfaces. Note, however, that UTD also has disadvantages as will be discussed later.

If coated surfaces are considered there is no general tool for electrically large surfaces. For the special case of circular cylinders an efficient high frequency method is described in [12-13], valid in the non-paraxial region. For coated circular cylinders and spheres of moderate sizes, an efficient modal solution is described in [14].

An overview of different frequency domain methods suitable for conformal antennas, including a comparison of different methods, can be found in [3].

III. THE HYBRID UTD-MOM APPROACH

As indicated in the previous section all methods have their advantages and disadvantages. To overcome the disadvantages a hybrid approach (a combination of different methods) is often used in practice. A commonly used method when analyzing conformal antennas is the hybrid UTD-MoM method, an alternative is the FE-BI method [15]. In the following, we will discuss the UTD-MoM method applied to waveguide-fed aperture antenna arrays on curved PEC surfaces. We will first present the general approach and then some aspects of the UTD formulation. Finally, the issue of finding ray paths (geodesics) on curved surfaces is described.

A. General formulation

The approach is based on the integral equation formulation, solved by the MoM. As will become clear, the general analysis is not any different from the planar case. However, it is more difficult to find the field representation outside a curved surface.

Figure 2 shows the waveguide-fed aperture problem for aperture m with the computational domain divided into two regions, the interior and exterior regions. By using the field equivalence theorem [5, page 106] an equivalent (exterior) problem is obtained by covering the apertures with a perfectly conducting surface and introducing unknown equivalent magnetic current moments on the surface. These infinitesimal magnetic current moments then radiate in the presence of the curved perfectly conducting surface.

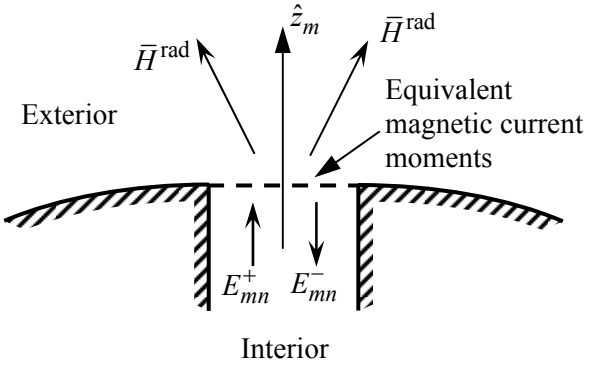

Figure 2. The interior and exterior domains at aperture m with the n^{th} waveguide mode for a PEC surface.

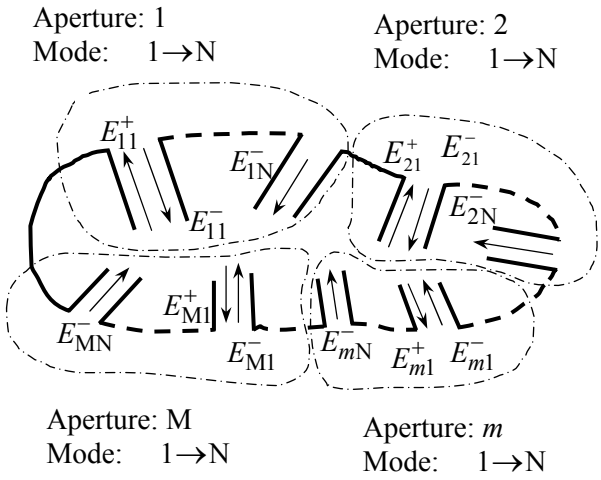

Figure 3. A symbolic picture of the physical and electrical ports in the antenna array.

Applying the boundary condition for the tangential magnetic field results in the following integral equation;

$$\bar{H}^{\text{ext}}_{\tan}\Big|_{\bar{r}\in S^+_{ap}} = \bar{H}^{\text{int}}_{\tan}\Big|_{\bar{r}\in S^-_{ap}} \tag{1}$$

where S_{ap} is the set of all apertures, $\bar{H}^{\text{ext}}_{\tan}$ is the external surface field caused by the equivalent magnetic current moments, and $\bar{H}^{\text{int}}_{\tan}$ is the magnetic field in the interior region.

Let us now consider an array with M apertures and N modes in each aperture. The antenna array can be treated as a $\text{M}\times\text{N}$ port circuit according to Figure 3. Hence, the aperture magnetic field in the internal region is given as

$$\bar{H}^{\text{int}}_{\tan}\Big|_{\bar{r}\in S^-_{ap}} \approx \sum_{m=1}^{M}\sum_{n=1}^{N}\left[Y^n_g E^+_{mn}\left(\hat{z}_m\times\bar{e}^n_m\right) - Y^n_g E^-_{mn}\left(\hat{z}_m\times\bar{e}^n_m\right)\right]. \tag{2}$$

Equation (2) expresses the field expanded into a series of basis functions. Here, we have used the waveguide modes $\left(\bar{e}^n_m\right)$ in the waveguide as basis functions with unknown amplitudes E^+_{mn} and E^-_{mn} (Y^n_g is the modal admittance). The plus sign indicates a wave propagating towards the aperture and the minus sign a wave propagating away from the aperture Note that we have used a single mode index n to represent the triple mode index i, j, TE/TM where i, j are the usual mode indices and TE/TM is an index that indicate TE- or TM-mode.

It should be noted that throughout this paper the transmitting apertures are fed by the dominant waveguide mode only. However, at the different waveguide openings, see Figure 2, infinitely many reflected evanescent modes are generated. Also at the receiving apertures infinitely many modes are generated from the external field. A single/dominant mode approximation is often used, but for a more accurate analysis higher order modes are needed as will be discussed later.

To solve for the unknown modal amplitudes, (2) is inserted into (1). The discretized integral equation is then transferred to a matrix equation by using Galerkin's method (*i.e.* weighting functions = basis functions) with the inner product defined as $\left\langle \bar{f},\bar{g}\right\rangle = \iint\left(\bar{f}\cdot\bar{g}\right)dS$. We get

$$\sum_{m=1}^{M}\sum_{n=1}^{N}\left[E^+_{mn}\underbrace{\left\langle \bar{H}^{\text{ext}}_{\tan}\left(\bar{e}^n_m\right),\hat{z}_p\times\bar{e}^q_p\right\rangle}_{Y^{qn}_{pm}} + E^-_{mn}\underbrace{\left\langle \bar{H}^{\text{ext}}_{\tan}\left(\bar{e}^n_m\right),\hat{z}_p\times\bar{e}^q_p\right\rangle}_{Y^{qn}_{pm}}\right]\Bigg|_{\bar{r}\in S^+_{ap}} =$$

$$\sum_{m=1}^{M}\sum_{n=1}^{N}\left[Y^n_g E^+_{mn}\underbrace{\left\langle \hat{z}_m\times\bar{e}^n_m,\hat{z}_p\times\bar{e}^q_p\right\rangle}_{\delta^{qn}_{pm}} - Y^n_g E^-_{mn}\underbrace{\left\langle \hat{z}_m\times\bar{e}^n_m,\hat{z}_p\times\bar{e}^q_p\right\rangle}_{\delta^{qn}_{pm}}\right] \forall p,q \tag{3}$$

As seen, the mutual admittance $\left(Y^{qn}_{pm}\right)$ between modes $n\to q$ in the apertures $m\to p$ is directly identified in

equation (3). Hence, both the mutual admittance and the unknown modal amplitudes $\left(E_{mn}^{+}, E_{mn}^{-}\right)$ can be found if $\bar{H}_{\tan}^{\text{ext}}\left(\bar{e}_m^n\right)$ is known. From the modal amplitudes the far-field radiation pattern can be calculated.

A very important parameter in the analysis of (conformal) array antennas is the mutual coupling among the elements. Of interest is the scattering matrix which can be found easily since the mutual admittances are directly identified in (3). The scattering matrix is given by the following formula

$$\mathbf{S} = \left(\mathbf{I} - \mathbf{Y}\right)\left(\mathbf{I} + \mathbf{Y}\right)^{-1}. \tag{4}$$

Note that two cases can be distinguished. The first is the mutual coupling between two elements only, referred to as the isolated coupling since no other elements are involved. The other elements of the array are assumed to be absent (short circuited in case of apertures). For this case, $\mathbf{Y}$ is a 2×2 element matrix calculated as a function of the spacing or any other parameter of interest. With all elements present we use the term array mutual coupling. The array mutual coupling is obtained by considering all elements in the array, thus $\mathbf{Y}$ is an $\mathrm{M}\times\mathrm{M}$ element matrix where M is the number of elements in the array. If higher order waveguide modes are used in the analysis the matrix is of the size $\mathrm{MN}\times\mathrm{MN}$ where N is the number of modes used (see equation (3)).

An important observation is that the integral equation is referred to the curved aperture plane. However, the basis functions $\left(\bar{e}_m^n\right)$ are valid in a planar surface in a cross section of the waveguide. See Figure 4 where the planar surface in the waveguide is shadowed. Despite this fact, the fields at the convex surface are often assumed to be the same as in the waveguide and the gap in Figure 4 is disregarded.

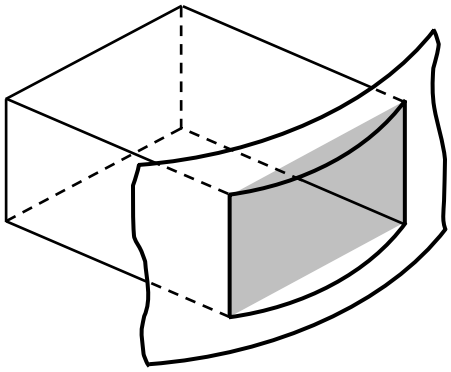

Figure 4. The geometry at the aperture.

In many applications this approximation may be tolerable, especially if the radius of curvature is large in the "wide" plane of the aperture. But, if the radius of curvature becomes smaller, the error may become too large. One way of reducing the error is to add a phase to the aperture field at the planar surface to include the small distance to the curved surface. This is done in the simulations presented in this paper.

B. The Uniform Theory of Diffraction (UTD)

The uniform theory of diffraction was developed to retain all the advantages of GTD and overcome the failure of GTD in the shadow boundary transition region. Assuming that the principal radius of curvature of the surface is large in terms of wavelength, and slowly varying along the surface, it was possible to obtain uniform asymptotic solutions to the canonical problems of diffraction by perfectly conducting circular cylinders and spheres [9-11]. These solutions can then be generalized to arbitrary convex surfaces with the aid of the local properties of high frequency wave propagation.

In this section, we limit the discussion to the surface field only, since it is needed in order to solve the integral equation for the unknown modal amplitudes (and the mutual coupling)[#]. The formulas will, however, not be repeated here, and the reader is referred to the papers indicated above for all details. The focus will be on a couple of complications that exist in the UTD solution.

It is well known that the UTD solution experiences problems when the ray path approaches the axial direction of the cylindrical geometry. The reason is that the approximation used for the fields in terms of Fock type Airy functions cannot be completely justified in the paraxial region. However, limiting forms for the components of the surface dyadic Green's function can be obtained for the PEC surface. This approach seems to give results accurate enough, and is used throughout this paper. But there is also an alternative, more accurate, solution available for the paraxial region. It is obtained by including higher order terms in the asymptotic evaluation of the exact solution and was presented by Boersma and Lee [16].

Another disadvantage with UTD is that small details cannot be included. Due to the approximations used in the derivation, the distance between the source and field points must be larger than circa 0.5λ. This is a problem, especially when calculating the self admittance since the dyadic for the surface magnetic

[#] The radiation pattern can be found using the formulas in [10] once the modal amplitudes are found.

field has a s^{-3} singularity as $s \to 0$ (s is the distance between the source and field points). For the circular cylinder Yung et al. [17] has shown that it is possible to rewrite the dyadic for the surface magnetic field with the help of the planar Green's function. Thus, a regularization can be obtained if the surface dyadic Green's function $\bar{\bar{G}}$ is rewritten as

$$\bar{\bar{G}} = \bar{\bar{G}}^{\text{pl.}} + \underbrace{\bar{\bar{G}}^{\text{cyl.}}_{\text{asympt.}} - \bar{\bar{G}}^{\text{pl.}}_{\text{asympt.}}}_{\bar{\bar{G}}^{\text{pert.}}} \tag{5}$$

The second term in (5) can be viewed as a perturbation due to the curvature of the circular cylinder. Furthermore, note that the asymptotic cylindrical dyadic is still used in (5). This is possible, at least when calculating the self admittance of the dominant TE_{10} mode as shown in [18]. The only requirement is that the cylinder radius exceeds about two wavelengths. This requirement is often fulfilled in most practical applications. An explicit expression for the self admittance of the dominant TE_{10} mode, based on the above approach, is found in [19]. The outlined approach can also be used for arbitrarily shaped singly curved surfaces by approximating the surface at the aperture location with a circular cylinder. The radius of the circular cylinder then equals the local radius of curvature at the element position.

Another possible approximation for handling small separations between source and field points is to use a planar solution.. Comparison of the planar approach and the above mentioned regularization process has shown that the planar approximation gives satisfactory results for the geometries of practical interest. A rigorous study for doubly curved surfaces has, to the author's knowledge, not been performed. But, it can be assumed that the planar approximation is accurate enough for most applications. Hence, in the calculations made in this paper the planar approximation is used both for singly and doubly curved surfaces. The result is satisfactory as will be seen later.

C. Geodesics

Before UTD can be applied to curved surfaces it is important to find the proper ray(s) that connect(s) arbitrarily located points on a smooth surface. For a correct solution, the rays must obey certain conditions in order to be valid geodesics on the surface. A complete treatment of this problem is beyond the scope of this paper, the interested reader is referred to textbooks on differential geometry (see e.g. [20]), but some highlights will be discussed with emphasis on doubly curved surfaces.

In its most general form, the geodesics are given by a second order differential equation, which satisfies the generalized Fermat's principle. Unfortunately, the solution to the differential equation is often difficult to find explicitly; instead some kind of numerical (ray tracing) procedure has to be used. Anyhow, every solution (it may be more than one!) that fulfills the geodesic equation is called a geodesic, whether it is an arc of shortest distance or not. Thus, geodesics may be regarded as *stationary* curves rather than strictly shortest distances on the surface. Hence, a general definition of a geodesic is that "along the geodesic the principal normal ($\hat{n}$) coincides with the surface normal ($\hat{N}$)". Figure 5 illustrates a situation when a curve along the surface is not a geodesic.

Fortunately, the ray tracing procedure can be simplified for certain geometries. This considerably reduces the numerical computations. The class of surfaces that can be analyzed in this way belongs to the geodesic coordinate system (GCS) [20], *i.e.* the parameter lines of the surface are orthogonal to each other. In these cases the geodesic equation is reduced to a first order differential equation. Examples of surfaces that belong to the GCS are any of the eleven surfaces defined by the Eisenhart coordinate system. Actually, the analysis presented here can also be extended to non-Eisenhart surfaces. The only requirement is that the surface can be defined in the GCS. One example of a non-Eisenhart surface is the ogive, which is of great interest in aerospace engineering since it can describe many of the shapes encountered in the area. The ogive is not a coordinate surface of an Eisenhart coordinate system but can be identified as the coordinate surface of the bispherical coordinate system [21], which fulfills the requirements. Thus, a straight forward analysis can be performed for many geometries of interest within the conformal antenna area.

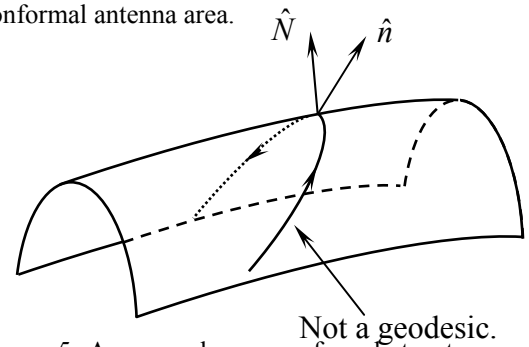

Figure 5. A curve along a surface, but not a geodesic surface ray.

Assume that the parametric equation of the surface is $x_i = X_i(u,v),\ i = 1...3$ where u and v are the curvilinear coordinates, within a certain closed interval.

Then, the geodesic equation for the surfaces belonging to the GCS is given as

$$v(u)=\underbrace{\int \frac{\pm\alpha\sqrt{E}}{\sqrt{G}\sqrt{G-\alpha^2}}du}_{\Im(u,\alpha)}+\beta \tag{6}$$

where E and G are two out of three so called first fundamental coefficients [20]. α is a constant of integration, known as the first geodesic constant. The $\pm$ sign in front of α depends on whether v is monotonically increasing or decreasing with u. β is the second geodesic constant. The physical significance of α and β is that they uniquely characterize a geodesic.

The solution to (6) provides the general solution for the specific geometry. To find the particular solution that connects two points on a surface the geodesic constants α and β have to be found. Since the positions of the different antenna elements are known, as well as the field or diffraction points, α and β can be found by solving the following system of equations

$$\begin{aligned} v_{\text{start}} &= \Im(u_{\text{start}},\alpha)+\beta, \\ v_{\text{stop}} &= \Im(u_{\text{stop}},\alpha)+\beta. \end{aligned} \tag{7}$$

The analysis is facilitated since the integral in (6) can be solved in closed form for the surfaces defined by the Eisenhart coordinate system! Furthermore, both the ray parameters of the differential type as well as the integral type in the UTD formulation can be found directly for the geometries discussed here with the aid of differential geometry. In fact, the only unknown in these expressions is the first geodesic constant α. Hence, the accuracy of the results obtained with UTD depends exclusively on the accuracy of the first geodesic constant α. As a consequence some authors have called the method the geodesic constant method (GCM) [22].

Analyzing singly curved surfaces is straightforward since they are developable surfaces. Thus, they can be unfolded and analyzed as flat surfaces and the key parameters in the UTD formulation are obtained from a two-dimensional analysis. Hence, they can be studied directly without solving the geodesic equation.

More interesting is the solution of the geodesic equation for doubly curved surfaces. Any rotational symmetric, doubly curved surface can be described, in parametric form, as

$$x=f(u)\cos v,\ y=f(u)\sin v,\ z=g(u) \tag{8}$$

and the solution to the geodesic equation (6) becomes

$$v(u)=\int \frac{\pm\alpha\sqrt{\left(f'(u)\right)^2+\left(g'(u)\right)^2}}{f(u)\sqrt{\left(f(u)\right)^2-\alpha^2}}du+\beta\,. \tag{9}$$

For the case of a sphere $\left(x=a\sin\theta\cos\varphi,\ y=a\sin\theta\sin\varphi,\ z=a\cos\theta\right)$ the geodesics are given by:

$$\varphi=-\tan^{-1}\left[\frac{\alpha\cos\theta}{\sqrt{a^2\sin^2\theta-\alpha^2}}\right]+\beta\,. \tag{10}$$

The paraboloid of revolution $\left(x=au\cos\varphi,\ y=au\sin\varphi,\ z=-u^2\right)$ has the following solution to the geodesic equation:

$$\begin{aligned} \varphi=\frac{\alpha}{a^2}\ln\frac{a\sqrt{a^2+4u^2}+2\sqrt{a^2u^2-\alpha^2}}{a\sqrt{a^2+4u^2}-2\sqrt{a^2u^2-\alpha^2}}+ \\ \sin^{-1}\left[\frac{a\sqrt{a^2u^2-\alpha^2}}{u\sqrt{a^4+4\alpha^2}}\right]+\beta. \end{aligned} \tag{11}$$

Additional explicit formulas for geodesics on singly and doubly curved surfaces are found in [3].

One important factor, as already indicated, is that the accuracy of the field solution depends on the accuracy of α. It has been stated that α must be computed accurately with up to eight decimal places for a given arbitrary set of source and observation points [23]. By changing the value of α from the correct result the angular distance will change resulting in a shorter or longer geodesic. In the analysis of conformal antennas some surface-ray parameters will then change and in the worst case give unsatisfactory results. To keep the angular distance within one tenth of a degree (assuming the field and observation points are at the same z-value of a paraboloid) α has to be computed accurately up to four decimal places for this example. If eight decimals are correct the angular difference will change no more than about 0.000005^{o} in this case. Another example is shown in Figure 6 where a paraboloid is considered with: $a=1.0$, $u_{\text{start}}=0.5$, $u_{\text{stop}}=2.5$ and $\left|\varphi_{\text{stop}}-\varphi_{\text{start}}\right|=130^{\text{o}}$. In this example the correct geodesic is shown together with two geodesics when

the correct value of α is increased and decreased, respectively, with 1%. The result is an angular difference of circa 3 degrees. Hence, as shown here, it is probably not necessary to compute α with up to eight decimal places in the practical analysis of conformal antennas.

Another important factor when analyzing doubly curved surfaces is the geodesic splitting phenomenon. It appears for certain combinations of source and observation coordinates for which the geodesic equation can result in two distinct values for α, thereby resulting in two distinct geodesics for a given direction and order. This may be surprising since it is well known that between any two arbitrarily located points on a cone or a cylinder, there exists primary and higher-order (of multiple encirclements) geodesics in both anticlockwise and clockwise directions. However, the number of geodesics of a given order and direction never exceeds one. In contrast, for doubly curved surfaces the geodesic of a given order and direction can be split into two! For the paraboloid this phenomenon appears when the start and stop positions have the same z-value, but with an angular distance $\geq 180^{\mathrm{o}}$. Figure 7 shows an example of the splitting phenomena for a paraboloid with $a = 1.6$, $u_{\mathrm{start}} = u_{\mathrm{stop}} = 2$, and $\left|\varphi_{\mathrm{stop}} - \varphi_{\mathrm{start}}\right| = 220^{\mathrm{o}}$.

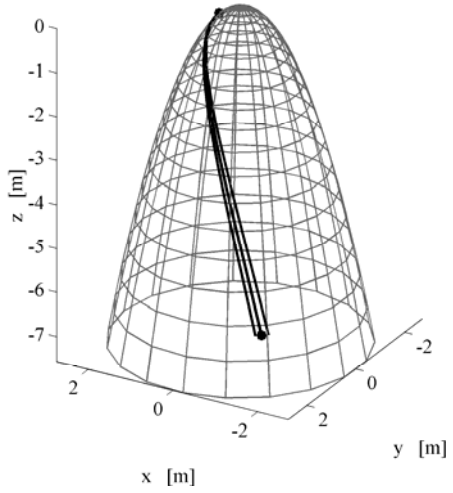

Figure 6. One example where the angular difference has changed with 3 degrees when α was changed ±1%.

Unfortunately, there is no a priori method of identifying which geodesics are the dominant contributors to the total surface ray field. Thus, the splitting phenomenon gives, in general, an unavoidable doubling of the computations. However, in most cases the arc length

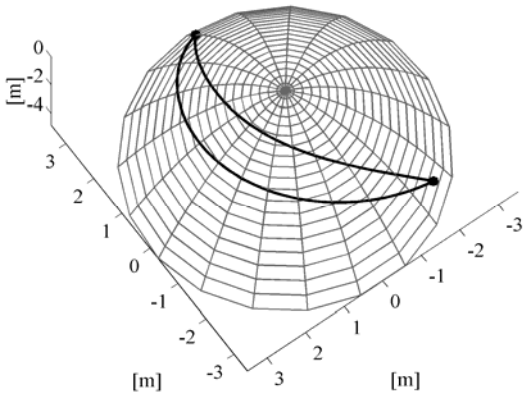

Figure 7. An example of geodesic splitting.

gives a hint about which geodesic is the dominant one since the surface ray field is decaying as a function of the arc length. Hence, the situation in Figure 7 is not critical since the geodesic traveling in the opposite direction around the surface is the shortest one. But for a more general surface there can be situations when two (or more) geodesics have about equal lengths. In such cases the arc length is no longer a useful parameter for finding the dominant surface ray path. One option is then to consider the radius of curvature since the loss of energy is also due to diffraction from the surface ray. If this does not give information enough all geodesics have to be included in the analysis.

IV. NUMERICAL RESULTS

This section discusses several examples to illustrate the accuracy and usability of the UTD-MoM method. Both singly and doubly curved PEC surfaces are considered. If a coating is present the problem becomes more difficult, especially for electrically large surfaces as discussed earlier. The results shown are in many cases verified with measured results, but the modal solution is also used to study circular cylinders with small radii.

A. Singly curved surfaces

Antennas mounted on singly curved surfaces are an important class of conformal arrays for applications where a large (azimuthal) angular coverage is required. These types of antennas have been used in many experimental radar and communication systems. An overview of different types of antennas is found in *e.g.* [3, 24].

The first example to be considered is a PEC circular cylinder with radius $R = 0.3$ m. The array consists of 54 rectangular aperture radiators with circumferential polarization. The size of the apertures is 0.016 m × 0.039 m and they are located in three rows with 18

elements in each row. Each row corresponds to an angular interval of approximately 120 degrees and the frequency is chosen to be 4.3 GHz (the cutoff frequency for the dominant TE_{10} mode is ≈ 3.8 GHz). These data correspond to an experimental antenna built by Ericsson Microwave Systems AB in Mölndal, Sweden in 1998. The antenna is shown in Figure 8.

As may be seen, the cylinder is truncated at the rear due to practical reasons. Hence, no surface rays encircling the cylinder were taken into account in the calculations (*i.e.* only a single surface ray was accounted for in the simulations). Furthermore, during the measurements, absorbers were placed on the edges to minimize edge effects. Note that the aperture in the lower left corner is aperture number 1, and aperture number 54 is located in the upper right corner.

The results shown here is the array mutual coupling, *i.e.* the coupling among the elements in the array environment with all elements present and terminated in matched loads. Additional results (other frequencies, *H*-plane coupling, radiation patterns and so on) can be found in [3, 25]. Figure 9 shows the amplitude and phase of the mutual coupling along the center row of the array, *i.e. E*-plane array coupling. In the calculations only a single waveguide mode is used.

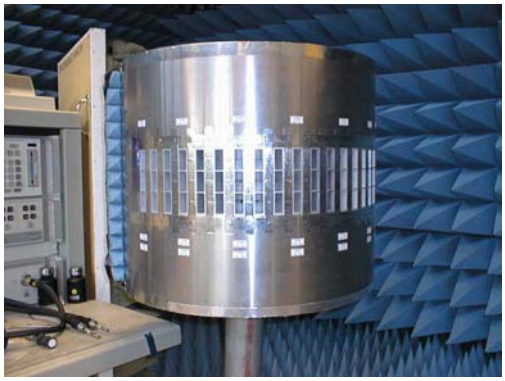

Figure 8. The experimental antenna. Courtesy of Ericsson Microwave Systems AB.

Even with a single mode approximation, the mutual coupling diagram shows good agreement between the calculated and measured results (including the self term), at least down to about -50 dB. For elements far away the agreement is not so good but here the coupling levels are very low.

In order to improve the accuracy even further, higher order waveguide modes were included in the analysis. With the four lowest TE-modes (in increasing cutoff order, *i.e.* TE_{10}, TE_{20}, TE_{01}, and TE_{11}) only small differences were observed. But when taking also the TM_{11} mode into account a significant improvement was obtained, see Figure 10. Now the simulated results show good agreement with measurements down to coupling levels as low as –80 dB. The agreement of the phase is also improved. Using even more modes (up to 20 modes were tried) improved the results very little [25]. Hence, the results are certainly sufficient for array design purposes. The importance of the TM_{11} mode is probably explained by the fact that this mode is the first mode with an electric field component parallel with the direction of propagation in the waveguide.

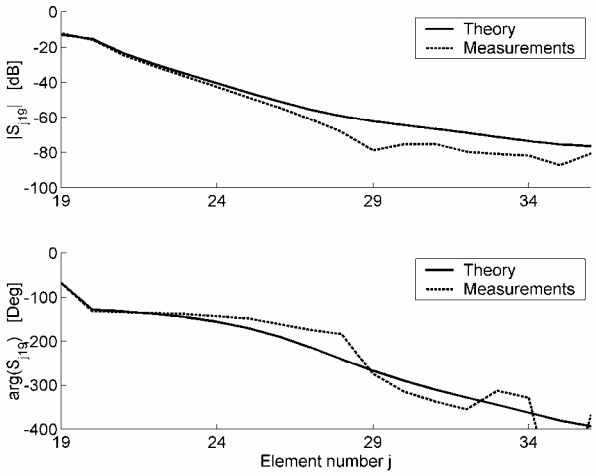

Figure 9. The array mutual coupling (including the self term $S_{19,19}$) along the center row of the array (*E* plane). Single mode approximation, $f = 4.3$ GHz.

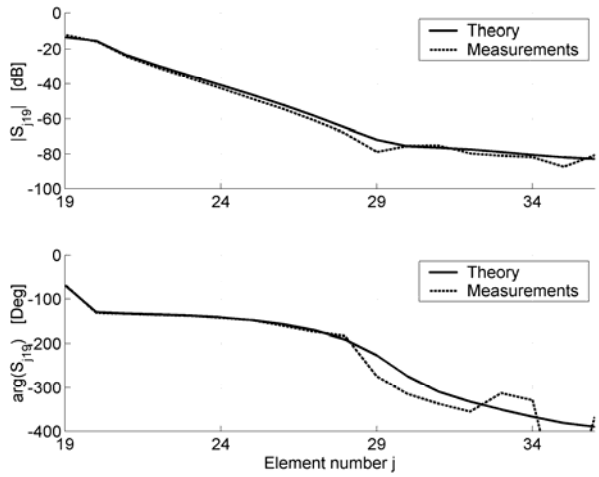

Figure 10. The array mutual coupling (including the self term $S_{19,19}$) along the center row of the array (*E* plane). 5 modes approximation, $f = 4.3$ GHz.

To investigate the ability of the UTD-MoM solution to handle electrically small surfaces, we will now consider a circular cylinder with a very small radius. The same elements as above (and frequency) is used, but the radius is reduced to 0.06 m (0.86λ). This is less than the commonly accepted limit for the UTD formulation where a radius of curvature as small as 1λ is expected to be very close to the limit. Figure 11 (a) shows the amplitude and phase of the isolated coupling between two elements as a function of the angular distance along the circumferential direction (*i.e.* *E*-plane coupling). Figure 11 (b) shows the case when the axial distance between the apertures is changed and equals 0.041 m (0.59λ). The angular extent in the circumferential direction is 180 degrees in both cases, and a single mode approximation is used. It has been shown [3] that the inclusion of higher order modes does not increase the accuracy in the case of isolated mutual coupling. Furthermore, two rays are included in the UTD-MoM solution – one in each direction around the circular cylinder. To be able to verify the solution a modal solution is used [4]. Generally speaking, the agreement is good and it appears as if the UTD-MoM solution recovers the canonical cylindrical solution even for small cylinders. The disagreement seen in Figure 11 (a) appears when the angular distance is less than 20 degrees. However, this equals an arc length of 0.3λ, and, as mentioned earlier, the UTD solution is supposed to be valid for distances larger than about 0.5λ.

Considered next is the PEC elliptic cylinder. By changing the ellipticity different kind of surfaces can be studied. We show the isolated mutual coupling in the *E* plane as a function of the ellipticity, *i.e.* the ratio between the major and minor axes (a/b). The

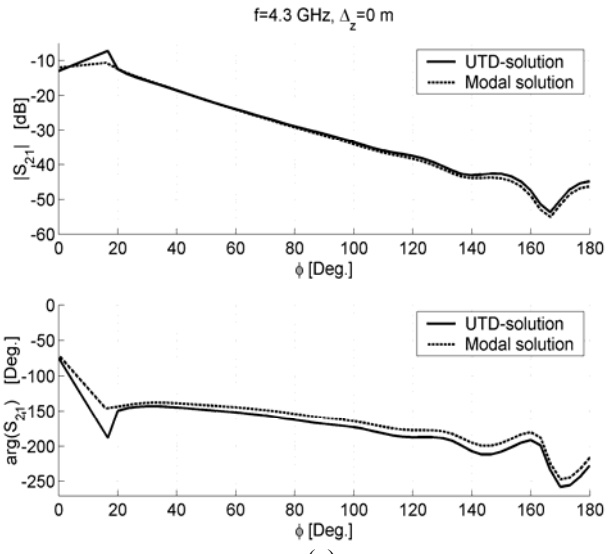

(a)

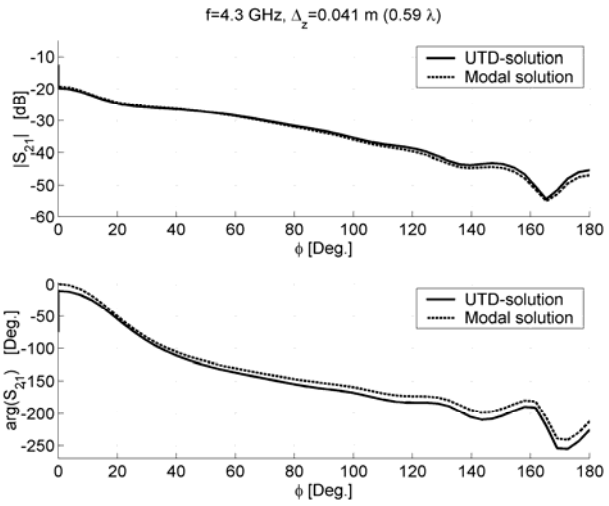

(b)

Figure 11. The isolated mutual coupling between two apertures located on a circular cylinder, $R \approx 0.86\lambda$. (a) Along the circumferential direction, *i.e.* *E*-plane coupling. (b) Along the circumferential direction when the two elements are 0.59λ apart in the axial direction.

transmitting element (indicated by a cross in Figure 12) is fixed, but the receiving element is moved along the surface in the counter clockwise direction. Its final position is indicated by a ring in Figure 12. The same type of rectangular waveguide-fed aperture is used as in the experimental antenna, but the frequency is changed to 5 GHz. Furthermore, only a single mode approximation is used here and two surface rays are included in the simulations, one in each direction around the elliptic cylinder. Figure 13 shows the isolated coupling vs. the shape of the elliptic surfaces. Due to space limitations only the amplitude is shown.

As expected, the decay of the isolated mutual coupling is reduced when the surface gets flat but increases again when passing through the sharpest part of the surface. The ripple at large separations is caused by the interference of the two waves traveling in opposite directions around the elliptic cylinder. In this example, the UTD-MoM solution is once again pushed to its limit for some of the surfaces with very sharp edges. In the results shown here the local radii of curvature at the sharpest point are (starting with the circular cylinder) $r = 5\lambda$, 3.47λ, 1.25λ, and 0.14λ. And, as seen, the results have a reasonable behavior. However, the accuracy cannot be ascertained since no reference results have been found. The most important conclusion is, however, that the UTD solution gives satisfactory

results for many surfaces that are interesting from a practical engineering point of view.

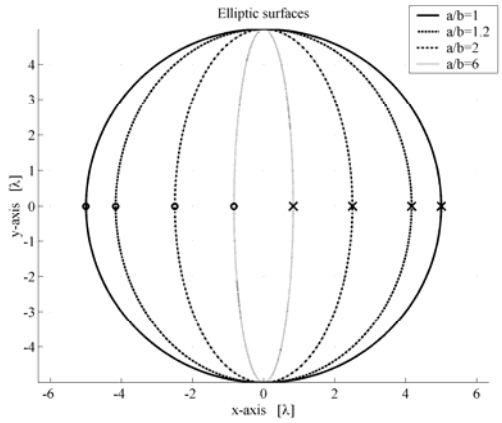

Figure 12. The different elliptic cylinders considered. A cross indicates the fixed position of the transmitting aperture, and a circle shows the final position of the second aperture. The circular cylinder is also shown for comparison.

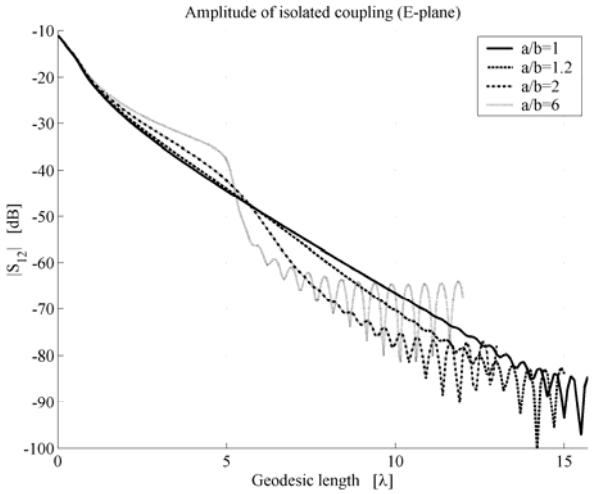

Figure 13. The amplitude of the isolated mutual coupling in the circumferential direction (*E* plane) for apertures at elliptic cylinders.

B. Doubly Curved Surfaces

The extension to doubly curved PEC surfaces is challenging and interesting. Unfortunately, the literature references in this area are not many and much remains to be investigated.

Shown here are some results for a doubly curved array, both mutual coupling results and radiation patterns are considered. The doubly curved experimental antenna

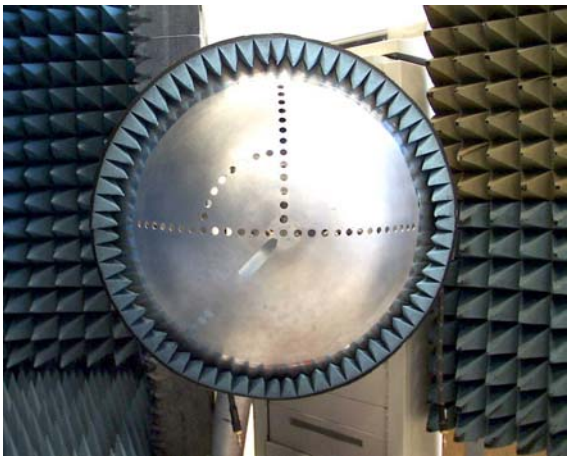

Figure 14. The geometry of the experimental doubly curved antenna. Courtesy of Ericsson Microwave Systems AB.

shown in Figure 14 was built at Ericsson Microwave Systems AB in Mölndal, Sweden, in 2000. The experimental antenna is shaped as a paraboloid of revolution with $f/d \approx 0.22$, and the diameter of the surface is approximately 600 mm with a depth of approximately 175 mm. Absorbers were placed on the edge to minimize edge effects. In this example circular waveguide-fed apertures are used, with a diameter of 14.40 mm. For practical reasons they are filled with Rexolite ($\varepsilon_r = 2.53$). The cutoff frequency for the dominant TE_{11}-mode is 7.65 GHz.

The surface has 48 circular apertures with the layout shown in Figure 14. The positions have been chosen to cover most element positions of interest in a doubly curved array, without covering the surface completely. In order to study polarization effects one of two orthogonal polarizations can be selected. This is achieved by rotating the waveguides by 90 degrees.

Figure 15 shows the isolated coupling along the principal plane of the paraboloid. The fed element is the element farthest away from vertex. Shown here is the *E*-plane coupling when using the dominant TE_{11}-mode only. Furthermore, only a single ray is accounted for in the simulations, but the first geodesic constant α is obtained with high accuracy (at least eight decimals). Measured results are also included here and the agreement is good. If the surface had been more pointed a slope change could have been observed when passing the vertex point $(s = 0\lambda)$.

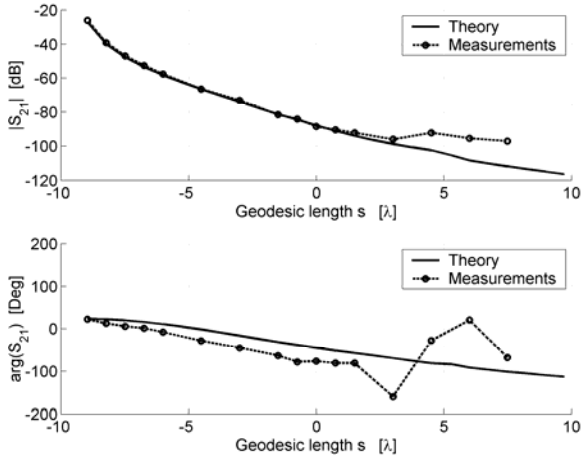

Figure 15. Isolated coupling along the principle direction of the paraboloid, *H* plane. Single mode approximation, $f = 8.975$ GHz.

The next example shows the isolated power pattern. If the element at vertex is element number 1, the pattern is shown for element number 7. Assume that the origin is at vertex and that the *z*-axis is pointing out of Figure 14, then the pattern is shown in a plane containing the symmetry axis of the paraboloid. The element is polarized in such a way that we get an *E*-plane pattern, and the result is shown in Figure 16 including measured data. Once again, only a single mode is used as well as a single ray. Note, however, that Kaifas et al. [26] shows that a ray caustic appears for certain element positions versus the shape of the surfaces. In these cases the single ray splits into three rays and has to be treated separately, but this does not appear for the cases considered here.

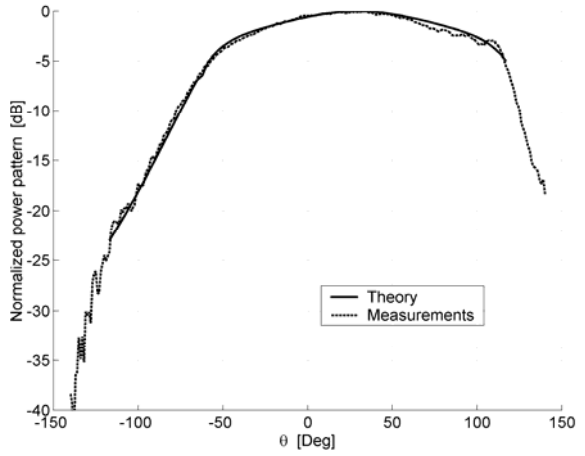

Figure 16. Calculated and measured power pattern (*E* plane) from a circular waveguide-fed aperture at the paraboloid. Single mode approximation, $f = 8.9$ GHz.

The results presented here are, to our knowledge, one of few where a UTD based method has been experimentally verified for a doubly curved surface. As seen, the agreement is good and it is possible to use UTD also for analyzing and designing doubly curved conformal array antennas.

Additional results (different polarization combinations, single element patterns, array patterns etcetera) can be found in [3, 27].

V. CONCLUSIONS

This paper presents an overview of the analysis of conformal array antennas. The focus is on the hybrid UTD-MoM method, and both singly and doubly curved PEC surfaces are considered. An important factor for accurate results is the problem of finding the geodesics. The reason is that it is possible to formulate the UTD-MoM solution in a single parameter form for certain types of surfaces. The solution then becomes directly related to the geodesics through the first geodesic constant α. Hence, the accuracy of the results depends exclusively on the accuracy of α. In this paper α is determined with an accuracy of at least eight decimal places.

The types of surfaces considered here belong to the geodesic coordinate system. This means that the parameter lines of the surface are orthogonal to each other, and any rotational symmetric doubly curved surface belongs to this class. For these cases the geodesics are found by quadrature, and in many cases the integral can be solved in closed form. This facilitates the analysis a lot.

As shown here, it is possible to generate very accurate results for different singly and doubly curved PEC surfaces by using the UTD-MoM approach. Both mutual coupling and radiation patterns have been considered. The results are verified by measured data obtained from two experimental antennas built at Ericsson Microwave Systems AB in Mölndal, Sweden. Furthermore, the limitation of the UTD formulation has been studied by comparing the results with results obtained from a modal solution. In conclusion, the hybrid UTD-MoM approach is surprisingly accurate both for electrically large and small PEC surfaces. Hence, the method is accurate enough to be used when designing conformal array antennas. However, more research is needed to be able to include coated surfaces. Some special cases can be handled, as indicated in this paper. But, there is today no verified tool for electrically large coated surfaces in general.

ACKNOWLEDGEMENT

Prof. Lars Josefsson at Chalmers University of Technology, Gothenburg, Sweden, is gratefully acknowledged for his valuable comments on this paper.

REFERENCES

[1] D. A. Wingert and B. M. Howard, "Potential Impact of Smart Electromagnetic Antennas on Aircraft Performace and Design," *NATO Workshop on Smart electromagnetic Antenna Structures*, Brussels, pp. 1.1-1.10, November 1996.

[2] Website: http://www.stealthsite.com/index.htm, 2005-09-13.

[3] L. Josefsson and P. Persson, *Conformal Array Antenna Theory and Design*, Wiley-IEEE Press, February 2006.

[4] J. R. Wait, *Electromagnetic Radiation from Cylindrical Structures*, Pergamon Press, 1959.

[5] R. F. Harrington, *Time Harmonic Electromagnetic Fields*, Prentice-Hall, 1961.

[6] J. J. H. Wang, *Generalized Moment Methods in Electromagnetics*, John Wiley & Sons, 1991.

[7] J. Jin, *The Finite Element Method in Electromagnetics*, John Wiley & Sons, 1993.

[8] D. A. McNamara, C. W. I. Pistorius, and J. A. G. Malherbe, *Introduction to The Uniform Geometrical Theory of Diffraction*, Artech House, 1990.

[9] P. H. Pathak, W. D. Burnside, and R. J. Marhefka, "A Uniform GTD Analysis of the Diffraction of Electromagnetic Waves by a Smooth Convex Surface," *IEEE Trans. on Antennas and Propagation*, Vol. AP-28, No. 5, pp. 631-642, September 1980.

[10] P. H. Pathak, N. Wang, W. D. Burnside, and R. G. Kouyoumjian, "A Uniform GTD Solution for the Radiation from Sources on a Convex Surface," *IEEE Trans. on Antennas and Propagation*, Vol. AP-29, No. 4, pp. 609-622, July 1981.

[11] P. H. Pathak and N. Wang, "Ray analysis of Mutual Coupling Between Antennas on a Convex Surface," *IEEE Trans. on Antennas and Propagation*, Vol. AP-29, No. 6, pp. 911-922, November 1981.

[12] P. Persson and R. G. Rojas, "High-frequency Approximation for Mutual Coupling Calculations Between Apertures on a Perfect Electric Conductor Circular Cylinder Covered with a Dielectric Layer: Nonparaxial Region," *Radio Science*, Vol. 38, No. 4, 2003.

[13] B. Thors and R. G. Rojas, "Uniform Asymptotic Solution for the Radiation from a Magnetic Source on a Large Dielectric Coated Circular Cylinder: Non-paraxial Region," *Radio Science*, Vol. 38, No. 5, 2003.

[14] Z. Sipus, P.-S. Kildal, R. Leijon, and M. Johansson, "An Algorithm for Calculating Green's Function of Planar, Cylindrical and Spherical Multilayer Substrates," *ACES Journal*, Vol. 13, No.3, pp. 243-254, Nov. 1998.

[15] C. A. Macon, L. C. Kempel, and S. W. Schneider, "Modeling Cavity-Backed Apertures Conformal to Prolate Spheroids Using the Finite Element-Boundary Integral Technique," *IEEE AP-S Intern. Symp.*, pp. 550-553, 2002.

[16] J. Boersma and S. W. Lee, "Surface Field due to a Magnetic Dipole on a Cylinder: Asymptotic Expansion of Exact Solution," Electromagnetics Laboratory, Technical Report No. 78-17, University of Illinois, December 1978.

[17] E. K. Yung, S. W. Lee, and R. Mittra, "GTD Solution of the Input Admittance of a Slot on a Cone," *IEEE AP-S. Intern. Symp.*, Vol. 17, pp. 667-670, 1979.

[18] T. S. Bird, "Accurate Asymptotic Solution for the Surface Field due to Apertures in a Conducting Cylinder," *IEEE Trans. on Antennas and Propagation*, Vol. AP-33, pp. 1108-1117, October 1985.

[19] G.-X. Fan and J. M. Jin, "Scattering from a Cylindrically Conformal Slotted Wavegudie Array Antenna," *IEEE Trans. on Antennas and Propagation*, Vol. 45, pp. 1150-1159, July 1997.

[20] D. J. Struik, *Lectures on Classical Differential Geometry*, Second edit., Dover Publications, Inc., 1988.

[21] R. M. Jha, S. A. Bokhari, V. Sudhakar, and P. R. Mahapatra, "Closed Form Surface Ray Tracing on Ogival Surfaces," *1989 IEEE AP-S Intern. Symp*., pp. 1294-1297, June 26-30, 1989.

[22] R. M. Jha and W. Wiesbeck, "The Geodesic Constant Method: A Novel Approach to Analytical Surface-Ray Tracing on Convex Conducting Bodies," *IEEE Antennas and Propagation Magazine*, Vol. 37, No. 2, pp. 28-38, April 1995.

[23] R. M. Jha, S. A. Bokhari, V. Sudhakar, and P. R. Mahapatra, "Geodesic Splitting on General Paraboloid of Revolution and its Implications to the Surface Ray Analysis," *1989 IEEE AP-S Intern. Symp*., pp. 223-226, June 26-30, 1989.

[24] R. C. Hansen, *Phased Array Antennas*, John Wiley & Sons, 1998.

[25] P. Persson and L. Josefsson, "Calculating The Mutual Coupling Between Apertures on a Convex Circular Cylinder Using a Hybrid UTD-MoM Method," *IEEE Trans. on Antennas and*

Propagation, Vol. AP-49, No. 4, pp. 672-677, April 2001.

[26] T. N. Kaifas, T. Samaras, K. Siakavara, and J. N. Sahalos, "A UTD-OM Technique to Design Slot Arrays on a Perfectly Conducting Paraboloid," *IEEE Trans. on Antennas and Propagation*, Vol. 53, No. 5, pp. 1688-1698, May 2005.

[27] P. Persson, L. Josefsson, and M. Lanne, "Investigation of the Mutual Coupling between Apertures on Doubly Curved Convex Surfaces: Theory and Measurements," *IEEE Trans. on Antennas and Propagation*, Vol. AP-51, No. 4, pp. 682-692, April 2003.

Patrik Persson was born in Stockholm, Sweden, in 1973. He received the M.Sc. Eng. and Ph.D. degrees in electromagnetic theory from the Royal Institute of Technology, Stockholm, in 1997 and 2002, respectively. He is currently employed as a research associate in the division of Electromagnetic Engineering, Royal Institute of Technology. His main research interests include conformal antennas, high-frequency techniques, and broad-band array antennas. Dr. Persson is the author of more than 40 journals and conference publications. He is also the coauthor of the book Conformal Array Antenna Theory & Design, published by Wiley-IEEE Press.

He spent 6 months of the academic year 2000-2001 at the ElectroScience Laboratory, Ohio State University, Columbus, Ohio as a visiting scholar, working on the development of high-frequency models for conformal antennas. He has also been a visiting scientist (part time, Feb. 2002-Apr. 2004) at the department of Physics and Measurements Technology, Division of Theoretical Physics, Linköping University in Sweden. During this period, he was involved with work on faceted conformal antennas. Patrik Persson has been involved in the organization of several European Workshops on Conformal Antennas (EWCA).

Dr. Persson received the 2002 R. W. P. King Prize Paper Award given by IEEE.

Efficient Wideband Power Divider for Planar Antenna Arrays

(*Invited Paper*)

Veysel Demir, Dalia A. Elsherbeni, Darko Kajfez, and Atef Z. Elsherbeni
Center for Applied Electromagnetic Systems Research (CAESR),
Department of Electrical Engineering
The University of Mississippi, University, MS, 38677, USA

Abstract — Power dividers with a good match over a wideband of frequencies are designed using Klopfenstein impedance taper for use with wideband antenna arrays. To validate the proposed design procedure a 2-way stripline, and a 2-way microstrip power divider are designed, fabricated, and measured. The measured return loss reveals better than –24 dB (from 4.3 GHz to 19.5 GHz) match for the 2-way stripline, and –27 dB (from 2.2 GHz to 12 GHz) match for the 2-way microstrip. Then a single Klopfenstein taper is used in the design of a 4-way stripline power divider. Measurements reveal return loss better than –22 dB (from 2.3 GHz to 19 GHz) for the 4-way stripline power divider. Furthermore, use of a single taper resulted in a shorter feed network compared to the traditional 4-way feed network using 2-way power dividers at two stages.

I. INTRODUCTION

Power dividers are passive RF components that are commonly used to split and distribute power in various proportions to different components of networks. Two major areas for power divider applications are (1) distribution of input signal to amplifiers and (2) distribution of RF signal to antenna arrays. Various types of power divider configurations have been introduced to support planar circuit applications. An overview of these configurations can be found in [1].

A branch-line type power divider, in combination with a quarter-wavelength transformer or a stepped transmission line transformer [2], is frequently employed in the feeding networks of planar antenna arrays. This kind of power divider supports narrow band operations due to limited bandwidth of the quarter-wave transformer. When it becomes necessary to feed a wideband antenna array, the corresponding power dividers should be capable to operate in a much wider bandwidth. For a good match, a return loss of -20 dB is desirable. Some configurations of branch-line circuits described in [1] have only a narrow frequency range (less than 10 %) in which the return loss is better than -20 dB. Others never reach this level of matching.

Various techniques have been proposed for the realization of wideband branch-line type power dividers. One of the methods is to employ wideband matching circuits to match the input line impedance to that of the junction. In [3] a 5-way wideband planar power divider is developed using a 4-section quarter wavelength transformer and shunt resistances for the wideband matching. In [4], 3 and 4 section quarter wavelength transformers are used to realize wideband characteristics. This paper demonstrates the use of Klopfenstein taper [5] for the design of wideband matching circuits and power dividers for printed antenna array applications. Typical length of the Klopfenstein impedance taper is about one-half wavelength at the lowest frequency, and the upper frequency limit is theoretically infinite. In comparison, a two-section quarter wavelength binomial impedance transformer [6, p. 313] can provide the return loss of -30 dB only in a 1.5:1 frequency ratio. As will be shown here, much wider frequency ratios are easily achievable in practice. Therefore, for a good match, the tapered impedance transformer is vastly superior to a multi-section quarter-wavelength transformer. This kind of taper was utilized in the design of 2-way finline power combiners in [7].

Section II gives the Klopfenstein equations used to design the tapers presented in this paper. Section III describes a 2-way power divider in stripline realization. Section IV describes a 2-way power divider in microstrip configuration. In Section V, a 4-way stripline power divider is proposed to reduce the feeding network length. Measurements show that it operates in about 8:1 frequency range. All designs have been first optimized by simulation software, and then fabricated and measured. In all three designs, the tapered section is designed for a -30 dB ripple, with the hope that the branching and 90-degree bend sections will not degrade the overall ripple significantly.

The effect of dispersion of microstrip lines on the bandwidth of the matching circuit is discussed. Sonnet[1] software package and a FDTD program developed by our group are used as electromagnetic simulation tools in the design process. Issues that are vital in accurate simulation and measurement of planar circuits are discussed, and guidelines are given as well. The extension of the proposed power divider design to

[1] Sonnet Software, Inc., 100 Elwood Davis Road, North Syracuse, NY 13212.

applications with larger number of elements for antenna array systems is straightforward.

II. KLOPFENSTEIN EQUATIONS

For largest possible bandwidth with a fixed maximum magnitude of reflection coefficient, the input reflection coefficient ρ for a continuous taper takes the form [5]

$$\rho = \rho_0 \frac{\cos\left[\sqrt{(\beta l)^2 - A^2}\right]}{\cosh(A)} e^{-j\beta l} \qquad (1)$$

where β is the wave number, and l is the taper length. The specification of the parameter A determines the maximum magnitude of reflection coefficient in the pass band which consists of all frequencies such that $\beta l \geq A$. The reflection coefficient magnitude takes on its maximum value $|\rho_0|$ at zero frequency, and it oscillates in the pass band with constant amplitude equal to $\rho_0/\cosh(A)$, which has been set to –30 dB for the current applications. The value of ρ_0 is calculated using $\rho_0 = 0.5 \times \ln(Z_2/Z_1)$, where Z_1 and Z_2 are the characteristic impedances at the ends of the taper. In [8] the variation of the characteristic impedance along the taper section is given by

$$\ln(Z_0(x)) = \frac{1}{2}\ln(Z_1 Z_2) + \frac{1}{2}\frac{\ln(Z_2/Z_1)}{\cosh(A)} \times \left[A^2 \phi\left(\frac{2x}{l}, A\right) + U\left(x - \frac{l}{2}\right) + U\left(x + \frac{l}{2}\right) - 1\right] \qquad (2)$$

where U is the unit step function, and ϕ is a function defined as

$$\phi(z, A) = \int_0^z \frac{I_1\left(A\sqrt{1-y^2}\right)}{A\sqrt{1-y^2}} dy, \qquad |z| \leq 1 \qquad (3)$$

and I_1 is the first kind modified Bessel function of the first order.

III. 2-WAY STRIPLINE POWER DIVIDER DESIGN

In this section, the design of a wideband 2-way stripline power divider is demonstrated. The design mainly consists of two steps: the first is the design of a taper that will provide wideband matching between the 50 Ohms (Z_2) input line and 25 Ohms (Z_1) junction of output branches and the second is the design of the junction with very low return loss over a frequency band as wide as possible.

The Klopfenstein taper is ideally a smooth continuous transition; however for simulation purposes a 21 section stepped impedance transition of length $l \approx \pi/\beta$ is analyzed. For a desired return loss less than -30 dB the maximum reflection coefficient in the pass band is

$$\max(\rho) = 10^{-30/20} = 0.0316227 . \qquad (4)$$

For impedance transition from 50 Ohms to 25 Ohms $\rho_0 = 0.3466$. Since the pass band starts at $\beta l = A$, one can use this condition to calculate A from (1) along with the defined values of max(ρ) and ρ_0. The corresponding value of A is 3.0853 which is then used in (2) to compute the characteristic impedance of each section of the tapered line as listed in Table I. Rogers RT5880 laminate with dielectric constant 2.2, loss tangent 9×10^{-4}, and thickness 1.575 mm is used for the physical design. The physical dimensions of the sections of the taper that are matching to the impedances in Table I are determined by simulations using Sonnet and the line widths are listed in Table I. The lengths of individual sections are equal to 1 mm. Figure 1 shows the simulated taper while Fig. 2 shows simulation results compared to the theoretically expected curve which is calculated using (1).

Table I. Stripline taper design parameters for 50 Ω to 25 Ω transition with maximum –30 dB return loss.

Section	Z_0 (Ω)	Width (mm)	Section	Z_0 (Ω)	Width (mm)
input	50	2.60	11	35.355	4.25
1	48.383	2.75	12	33.930	4.50
2	47.565	2.80	13	32.582	4.75
3	46.589	2.90	14	31.337	5.00
4	45.465	3.00	15	30.198	5.25
5	44.209	3.15	16	29.167	5.45
6	42.834	3.30	17	28.275	5.70
7	41.393	3.45	18	27.493	5.90
8	39.889	3.65	19	26.830	6.05
9	38.361	3.80	20	26.280	6.20
10	36.841	4.05	21	25.836	6.35
			output	25	6.6

The observed very good match between the simulation results and the theory suggests that this taper can support a high pass operation above 4.9 GHz with a return loss better than –30 dB.

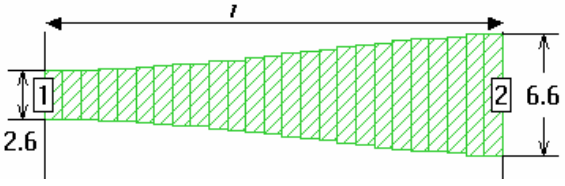

Fig. 1. Impedance taper as simulated in Sonnet.

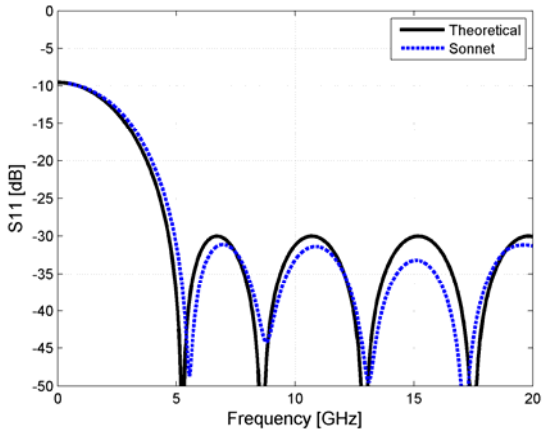

Fig. 2. Simulated return loss compared to theoretical curve.

Once the taper is designed, the next step is to design the junction branching from 25 Ω line to two 50 Ω lines. After a series of simulations the optimum dimensions for minimum return loss over a possible maximum bandwidth are determined. At this point an optimization technique could be employed to achieve an optimum design. The optimized dimensions are given in Fig. 3.

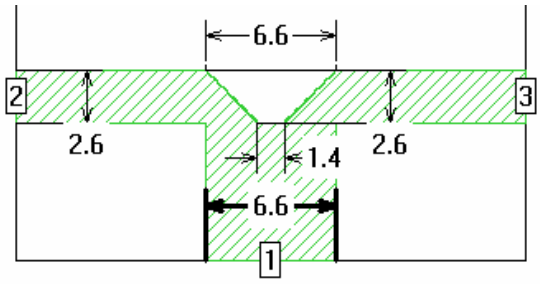

Fig. 3. Optimized junction from 25 Ω to two 50 Ω striplines (Dimensions are in millimeters).

The circuits in Figs. 1 and 3 are cascaded to form a stripline power splitter. The final design is manufactured as shown in Fig. 4. Figure 5 shows the measurements compared to simulation of the final design in Sonnet. The simulation result from Fig. 2 is also displayed in this figure in order to show the effect of the branching junction. Measured results demonstrate that the manufactured circuit is a good wideband power divider with a return loss better than –24 dB over a frequency band from 4.3 GHz to 19.5 GHz.

An accurate determination of return loss is a difficult task to achieve both in simulations and measurements. In the network analyzer measurement set up, time gating is used in order to eliminate the effect of the coaxial-to-stripline launchers from the circuit response. However, it has been realized that the input line was not long enough to eliminate the second reflection between the branching discontinuity and the input port. Thus, it can be inferred that if the input line was made longer, the actual response of the measured circuit may become even better than the one shown in Fig. 5.

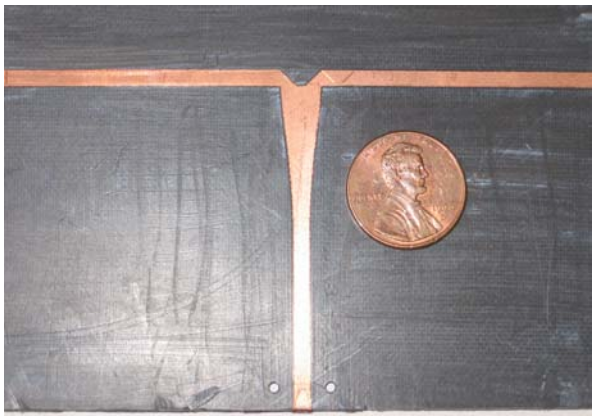

Fig. 4. Manufactured stripline power divider.

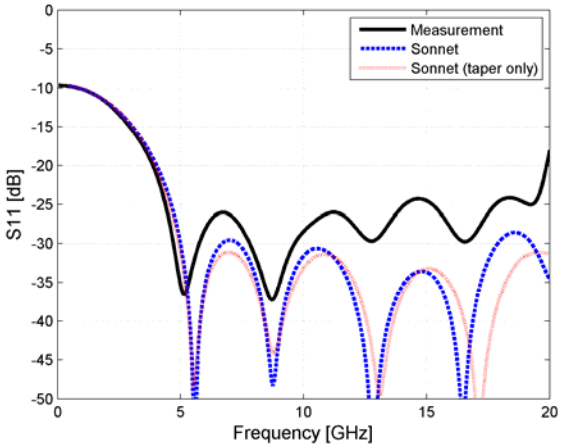

Fig. 5. Stripline power divider measurement compared to simulated return losses.

It is worth mentioning that the effect of conductor thickness also must be modeled for an accurate simulation [9]. As much as 1 Ω difference in the characteristic impedance of a line can be observed when the conductor thickness is taken into account.

IV. 2-WAY MICROSTRIP POWER DIVIDER DESIGN

In this section, a wideband power divider design is realized as a microstrip circuit. Microstrip lines are dispersive unlike striplines, and the frequency dependence of the characteristic impedances of microstrip lines imposes additional challenge on the design of a wideband taper. Since it is not possible to maintain constant impedance values over a very wide band, a taper would work the best around the

frequencies where the impedance values in Table II are maintained. Therefore, the physical dimensions of the taper sections shall be calculated at the frequencies of interest. In the current design the section widths are calculated to satisfy characteristic impedances at frequencies around 8-10 GHz as given in Table II, and each section is 2 mm long.

Table II. Microstrip taper design parameters for 50 Ω to 25 Ω transition with maximum –30 dB return loss.

Section	Z_0 (Ω)	Width (mm)	Section	Z_0 (Ω)	Width (mm)
input	50	1.80	11	35.355	3.00
1	48.383	1.88	12	33.930	3.20
2	47.565	1.96	13	32.582	3.36
3	46.589	2.04	14	31.337	3.56
4	45.465	2.08	15	30.198	3.72
5	44.209	2.20	16	29.167	3.96
6	42.834	2.28	17	28.275	4.08
7	41.393	2.40	18	27.493	4.24
8	39.889	2.52	19	26.830	4.36
9	38.361	2.68	20	26.280	4.48
10	36.841	2.84	21	25.836	4.56
			output	25	4.80

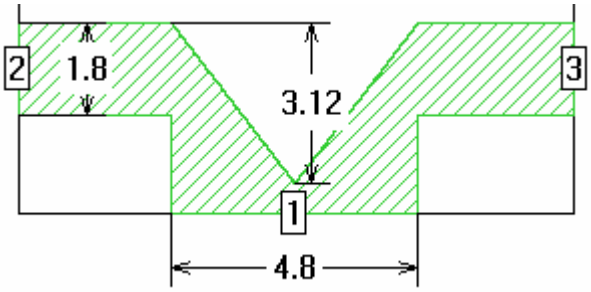

Fig. 6. Optimized junction from 25 Ω to two 50 Ω microstrip lines. (Dimensions are in millimeters)

The Gil GML1000 laminate of relative dielectric constant 3.2, loss tangent 4×10^{-3}, and thickness 0.762 mm is used for the physical design. After a series of simulations the optimum dimensions for minimum return loss over a possible maximum bandwidth are determined. The optimized dimensions are given in Fig. 6. The taper and the junction circuit in Fig. 6 are cascaded to form a microstrip power divider. The final design is manufactured as shown in Fig. 7. As can be noticed from the picture, the input line length is kept long in order to perform a more accurate time-gated measurement. The measured return loss is compared to those obtained using Sonnet and FDTD simulations in Fig. 8. The measurement shows that a wideband 2-way microstrip power divider is realized with a return loss better than –27 dB from 2.2 GHz up to at least 12 GHz.

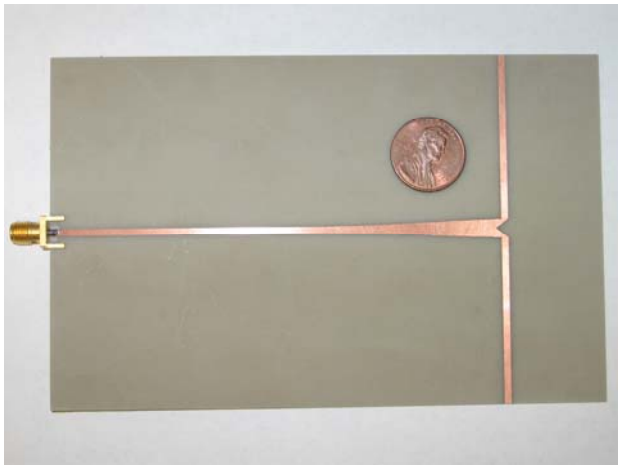

Fig. 7. Manufactured microstrip power divider.

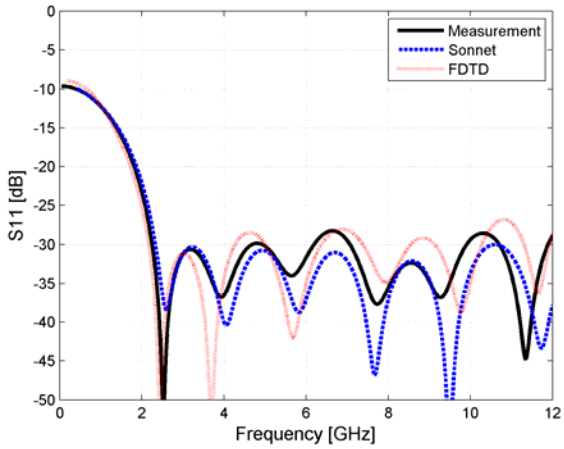

Fig. 8. Microstrip power divider measurement compared to simulated return losses.

V. 4-WAY STRIPLINE POWER DIVIDER DESIGN

The Klopfenstein taper can also be used to match impedances of junctions having more than two branches. In this section, the design of a 4-way stripline power divider is discussed. In the case of 4 output lines the 50 Ω input line impedance shall be matched to 12.5 Ω. The impedance values for a 21 section taper are listed in Table III. These impedances are determined such that a transition from 50 Ω to 12.5 Ω will have –30 dB return loss for the frequencies above which the taper length is 0.579 wavelength long. The widths of the sections, computed for a stripline using Gil GML1000 laminates with 0.762 mm thickness, are listed in Table III. After the taper design and simulation are completed, the junction with 12.5 Ω line input and two 25 Ω lines output is designed for minimum reflection for a frequency band as wide as possible. Then, the junction with 25 Ω line input and two 50 Ω lines output such as in Fig. 3 is added on each side. The final circuit is formed with the inclusion of optimally designed mitered

bends. The fabricated circuit is displayed in Fig. 9, and the measurement and simulation results are shown in Fig. 10 together with the simulation of the taper alone. Comparing simulations it can be observed that although the taper provides a high pass operation, the branching sections slightly degrade the overall performance. The measurement still has a good agreement with simulation and shows a wideband performance with a return loss better than –22 dB between 2.3 GHz and 19 GHz.

Table III. Stripline taper design parameters for 50 Ω to 12.5 Ω transition with maximum –30 dB return loss.

Section	Z_0 (Ω)	Width (mm)	Section	Z_0 (Ω)	Width (mm)
input	50	0.90	11	25.000	2.45
1	48.206	0.95	12	22.784	2.80
2	46.862	1.00	13	20.809	3.10
3	45.157	1.05	14	19.082	3.45
4	43.112	1.15	15	17.602	3.80
5	40.773	1.25	16	16.357	4.15
6	38.210	1.40	17	15.329	4.50
7	35.507	1.55	18	14.497	4.80
8	32.753	1.75	19	13.841	5.05
9	30.036	1.95	20	13.337	5.30
10	27.431	2.20	21	12.965	5.45
			output	12.5	5.70

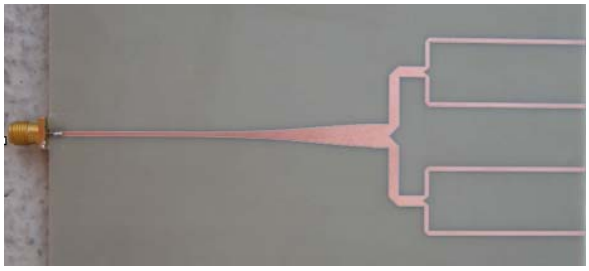

Fig. 9. Fabricated wideband 4-way stripline power divider.

One of the advantages of this 4-way power divider design is that only one taper is used to achieve power division to four outputs. Therefore, the length of the network is shorter than a conventional power divider that uses 2-way power dividers at two stages to achieve four outputs. The network path being short provides compactness as well as less attenuation while feeding the antenna arrays. The return loss achieved by this design is higher than those obtained from 2-way power dividers designed in previous sections. This difference is acceptable since the 4-way power divider is a more complicated design, and the return loss includes the combined effect of two power-dividing stages, mitered bends and the taper. Therefore it is feasible to use this approach for designing power division networks with higher number of ports with a return loss better than -20 dB.

V. CONCLUSION

Wideband planar power dividers have been designed using Klopfenstein taper and their performances were verified through simulations and measurements. The presented designs exhibit two main advantages; wideband characteristics and reduced size-feeding network.

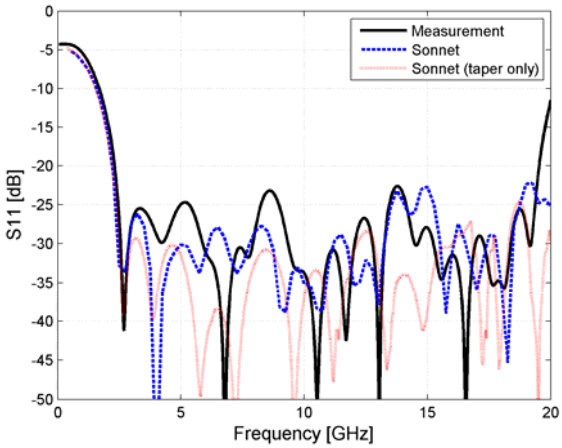

Fig. 10. Return loss of a 4-way stripline power divider.

ACKNOWLEDGEMENT

The authors wish to thank Dr. James Rautio of Sonnet Software Inc., North Syracuse, NY for providing the electromagnetic simulator Sonnet, which has been extensively used in this work. The supply of laminate material from Rogers and Gil corporations is also appreciated.

REFERENCES

[1] M. D. Abouzahra and K. C. Gupta, *Hybrids and power dividers/combiners, Analysis and Design of Planar Microwave Components*, IEEE Press, New York, 1994.

[2] M. A. Hamid and M. M. Yunik, "On the Design of Stepped Transmission-Line Transformers," *IEEE Transactions on Microwave Theory and Techniques*, vol. 15, no. 9, pp. 528–529, September 1967.

[3] W. Yau, J. M. Schellenberg, and Y. C. Shih, "A new n-way broadband planar power combiner/divider," *1986 IEEE MTT-S International Microwave Symposium Digest*, vol. 86, issue 1, pp. 147–149, June 1986.

[4] M. Kishihara, K. Yamane, I. Ohta, and T. Kawai, "A design of multi-stage, multi-way microstrip power dividers with broadband properties," *IEEE MTT-S International Microwave Symposium Digest*, vol. 1, pp. 69–72, June 2004.

[5] R. W. Klopfenstein, "A transmission-line taper of improved design," *Proc. IRE*, vol. 44, pp. 31–35, January 1956.
[6] D. M. Pozar, Microwave Engineering, 3rd edition, John Wiley & Sons, New York, 2004.
[7] P. Jia, L.-Y. Chen, N.-S. Cheng and R. A. York, "Design of waveguide finline arrays for spatial power combining," *IEEE Transactions on Microwave Theory and Techniques*, vol. 49, no. 4, pp. 609–614, April 2001.
[8] D. Kajfez and J. Prewitt, "Correction to a transmission line taper of improved design," *IEEE Transactions on Microwave Theory and Techniques*, vol. MTT-21, p. 364, May 1973.
[9] J. C. Rautio and V. Demir, "Microstrip conductor loss models for electromagnetic analysis," *IEEE Transactions on Microwave Theory and Techniques*, vol. 51, no. 3, pp. 915–921, March 2003.

Veysel Demir was born in Batman, Turkey, in 1974. He received the B.S.E.E. degree from the Middle East Technical University, Ankara, Turkey, in 1997, and received MSEE and Ph.D. degrees from Syracuse University, Syracuse, NY, in 2002 and 2004, respectively. He had been working in Sonnet Software Inc., Liverpool, NY from 2000 to 2004. He is currently working as a visiting research scholar at The Electrical Engineering Department of The University of Mississippi. His research interests include numerical analysis techniques (FDTD, FDFD, MoM), and microwaves and RF circuits analysis and design.

Dalia Elsherbeni received the B.S. degree in electrical engineering from The University of Mississippi, Oxford, MS, in 2004. She is currently working toward the M.S. degree in electromagnetics at the University of Mississippi. Since 2004 she has been employed full time by Radiance Technologies, Inc. working in the research and development department. Ms. Elsherbeni is a member of IEEE. She was the recipient of the Mississippi Academy of Sciences (MAS) Third Place Oral Presentation Award in Vicksburg, MS in 2006.

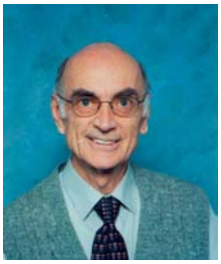

Darko Kajfez is Emeritus Professor of Electrical Engineering at the University of Mississippi. He obtained the electrical engineer's degree (Dipl. Ing.) from University of Ljubljana, Slovenia, in 1953, and the PhD degree from U.C. Berkeley in 1967. His research interests include rf and microwave measurement and analysis. He can be reached at eedarko@olemiss.edu.

Atef Z. Elsherbeni received an honor B.Sc. degree in Electronics and Communications, an honor B.Sc. degree in Applied Physics, and a M.Eng. degree in Electrical Engineering, all from Cairo University, Cairo, Egypt, in 1976, 1979, and 1982, respectively, and a Ph.D. degree in Electrical Engineering from Manitoba University, Winnipeg, Manitoba, Canada, in 1987. He was a Research Assistant with the Faculty of Engineering at Cairo University from 1976 to 1982, and from 1983 to 1986 at the Electrical Engineering Department, Manitoba University. He was a part time Software and System Design Engineer from March 1980 to December 1982 at the Automated Data System Center, Cairo, Egypt. From January to August 1987, he was a Post Doctoral Fellow at Manitoba University. Dr. Elsherbeni joined the faculty at the University of Mississippi in August 1987 as an Assistant Professor of Electrical Engineering. He advanced to the rank of Associate Professor on July 1991, and to the rank of Professor on July 1997. He became the director of The School of Engineering CAD Lab at the University of Mississippi on August 2002, and the associate director of The Center for Applied Electromagnetic Systems Research (CAESR) at The University of Mississippi on August 2002. He was appointed as Adjunct Professor, at The Department of Electrical Engineering and Computer Science of the L.C. Smith College of Engineering and Computer Science at Syracuse University on January 2004. He spent a sabbatical term in 1996 at the Electrical Engineering Department, University of California at Los Angeles (UCLA) and was a visiting Professor at Magdeburg University during the summer of 2004.

Dr. Elsherbeni received the 2005 School of Engineering Faculty Service Award for Outstanding Performance in Service, the Mississippi Academy of Science 2003 Outstanding Contribution to Science Award, the 2002 IEEE Region 3 Outstanding Engineering Educator Award, the 2002 School of Engineering Outstanding Engineering Faculty Member of the Year Award, the 2001 Applied Computational Electromagnetic Society (ACES) Exemplary Service Award for leadership and contributions as Electronic Publishing Managing Editor 1999-2001, the 2001 Researcher/Scholar of the year award in the Department of Electrical Engineering, The University of Mississippi, and the 1996 Outstanding Engineering Educator of the IEEE Memphis Section.

Dr. Elsherbeni has conducted research in several areas such as: scattering and diffraction by dielectric and metal objects, inverse scattering, finite difference time domain analysis of passive and active microwave devices, field visualization and software development for EM education, dielectric resonators, interactions of electromagnetic waves with human body, and development of sensors for soil moisture and for monitoring of airports noise levels, air quality including haze and humidity, reflector antennas and antenna arrays, and analysis and design of printed antennas for radars and communication systems. His recent research has been on the application of numerical techniques to microstrip and planar transmission lines, antenna measurements, and antenna design for radar and personal communication systems. He has published 88 technical journal articles and 21 book chapters on applied electromagnetics, antenna design, and microwave subjects, and contributed to 250 professional presentations and offered 16 short courses and 18 invited seminars. He is the coauthor of the book entitled "MATLAB Simulations for Radar Systems Design", CRC Press, 2003, the coauthor of the "Antenna Design and Visualization using Matlab" book published by Scitech in 2005, and the main author of the chapters "*Handheld Antennas*" and "*The Finite Difference Time Domain Technique for Microstrip Antennas"* in Handbook of Antennas in Wireless Communications, CRC Press, 2001.

Dr. Elsherbeni is a senior member of the Institute of Electrical and Electronics Engineers (IEEE). He is the Editor-in-Chief for the Applied Computational Electromagnetic Society (ACES) Journal, an Associate Editor to the Radio Science Journal, and the electronic publishing managing editor of ACES. He serves on the editorial board of the Book Series on Progress in Electromagnetic Research, the Electromagnetic Waves and Applications Journal, and the Computer Applications in Engineering Education Journal. He was the Chair of the Engineering and Physics Division of the Mississippi Academy of Science and the Chair of the Educational Activity Committee for the IEEE Region 3 Section. Dr. Elsherbeni's home page can be found at http://www.ee.olemiss.edu/atef and his email address is Elsherbeni@ieee.org

Genetic Algorithm Applications for Phased Arrays

(*Invited Paper*)

Randy L. Haupt

Applied Research Laboratory, The Pennsylvania State University, State College, PA

Abstract—Analytical approaches to phased array optimization started in the mid 1940s and transitioned to numerical techniques that can find a local minimum. Computers spurred the development of many different local optimization algorithms that worked well for a few variables and a cost function with a single minimum. In the 1990s, the genetic algorithm (GA) emerged as a competent optimization algorithm for a wide range of complex cost functions. This paper reviews phased array optimization and lays the foundation for the use of the GA. An extensive reference list is provided and some future research areas are discussed.

Index Terms—Phased arrays, genetic algorithms, arrays, optimization

I. INTRODUCTION

The introduction of genetic algorithms (GAs) to engineering produced a revolution in the design of complex systems. Over the past ten years, GAs moved from arcane toys of computer scientists to mainstay numerical optimization algorithms. Their popularity in phased array antenna design is apparent by the large number of papers published in this area as of the submission of this paper (see [1] to [139]).

This paper begins with a historical development of phased array optimization and a demonstration of a few cost functions. Next, some GA details are presented with a list of advantages over traditional optimization techniques. Finally, a review of GA applications to phased arrays is given and wrapped up with some ideas of where the future lies. A major contribution of this paper is the extensive reference list and categorizing of the references.

II. PHASED ARRAY OPTIMIZATION

The cost function for most phased array optimization is based on the array factor that includes the relative position and weightings of all the elements. An arbitrary array of N elements in three-dimensional space has an array factor given by

$$AF = \sum_{n=1}^{N} w_n e^{jk[x_n \sin\theta\cos\phi + y_n \sin\theta\sin\phi + z_n \cos\theta]} \quad (1)$$

where

$w_n = a_n e^{j\delta_n} =$ complex weight at element n

$a_n =$ amplitude weight at element n

$\delta_n =$ phase weight at element n

$(x_n, y_n, z_n) =$ location of element n

$\theta =$ elevation angle

$\phi =$ azimuth angle

The array designer controls the array factor via the amplitude weights, the phase weights, and/or the element locations in order to meet performance specifications, such as sidelobe levels, beamwidth, nulls, and bandwidth.

Initially, analytical optimization methods were used to find low sidelobe array amplitude weights. The first optimum antenna array distribution was the binomial distribution proposed by Stone [140]. As is now well known, the amplitude weights of the elements in the array correspond to the binomial coefficients, and the resulting array factor has no sidelobes. Dolph mapped the Chebychev polynomial onto the array factor polynomial to get all the sidelobes at an equal level [141]. The Dolph-Chebychev amplitude distribution is optimum in that specifying the maximum sidelobe level results in the smallest beam width, or specifying the beam width, results in the lowest possible maximum sidelobe level. Nine years later, Taylor developed a method to optimize the sidelobe levels and beam width of a line source [142]. Bayliss used a method similar to Taylor's amplitude taper but applied to a monopulse difference pattern [143]. The Taylor and Bayliss tapers are routinely used for low sidelobe arrays. Elliot extended Taylor's work to new horizons including Taylor based tapers with asymmetric sidelobe levels, arbitrary sidelobe level designs, and null free patterns [144].

Analytical approaches to finding optimum array amplitude weights are still used today. They work well, because the unknown array weights are coefficients of a

complex Fourier series. If the unknowns are the element spacings or element phases, then they appear in the complex exponent and are not easily found. Checking all combinations of values of the array variables is not realistic unless the number of variables is small. Optimizing one variable at a time does not work nearly as well as following the gradient vector downhill. The steepest descent method, invented in the 1800's, is based on this concept and is still widely used today. Newton's method uses second derivative information in the form of the Hessian matrix to find the minimum. Although more powerful than steepest descent, calculating the second derivative of the cost function may be too difficult.

In order to avoid the calculation of derivatives, Nelder and Mead introduced the downhill simplex method in 1965 [145]. This technique has become widely used by commercial computing software. A simplex has $n+1$ sides in n-dimensional space. Each iteration generates a new vertex for the simplex. If the new point is better than the worst vertex, then the new point replaces the worst vertex. In this way, the diameter of the simplex gets smaller until it reaches a specified tolerance.

Also during the mid 1960s, successive line minimization methods were developed. A successive line minimization algorithm begins at a random point, chooses a direction to move, then moves in that direction until the cost function begins to increase. The procedure is then repeated in a new direction. A conjugate direction is a new direction that does not interfere with the minimization of the prior direction. The conjugate directions are chosen so that the change in the gradient of the cost function remains perpendicular to the previous direction. Powell devised an efficient way to specify the conjugate directions [146]. If there is additional information on the gradient of the cost function, the conjugate gradient method can be applied. This method simply uses this gradient information to choose the conjugate directions. An even better set of directions can be chosen if the matrix of second partial derivatives, the Hessian matrix, is known. The BFGS algorithm [146]. finds a way to approximate this matrix and employs it in determining the appropriate directions of movement. This algorithm is "quasi-Newton" in that it is equivalent to Newton's method for prescribing the next best point to use for the iteration, yet it doesn't use an exact Hessian matrix. Quadratic programming assumes the cost function is quadratic (variables are squared) and the constraints are linear. This technique is based upon Lagrange multipliers and requires derivatives or approximations to derivatives [147].

Numerical optimization has been used to find nonuniform element spacings, complex weights, and phase tapers that resulted in desired antenna patterns. Some examples of nonuniform spacing synthesis include dynamic programming [148], Nelder Mead downhill simplex algorithm [149], steepest descent [150], and simulated annealing [151]. Numerical methods were used to iteratively shape the main beam while constraining sidelobe levels for planar arrays [152], [153], and [154]. Linear programming [155] and the Fletcher-Powell method [156] were applied to optimizing the footprint pattern of a satellite planar array antenna. Quadratic programming was used to optimize aperture tapers for various planar array configurations [157] and [158]. Numerical optimization was used to find phase tapers that maximized the array directivity [159], and a steepest descent algorithm used to find the optimum phase taper to minimize sidelobe levels [160].

The numerical optimization algorithms mentioned so far find a minimum in a valley of the cost function closest to the starting point. In other words, the convergence of the algorithm assumes the cost function is quadratic or bowl shaped with a single minimum. The next section gives a few examples of phased array cost functions that need non-local optimization techniques to find the best minimum.

III. PHASED ARRAY COST FUNCTIONS

The cost function for a phased array antenna can be quite complex, so the array factor is often optimized rather than a full wave computational electromagnetics model. Using point sources allows for the modeling of a large number of elements but ignores polarization, mutual coupling, environmental scattering, and other effects. Often, optimizing the array factor provides sufficient design information.

As an example, consider finding the minimum maximum sidelobe level by either adjusting the amplitude weights, element spacing, or phase weights of a linear array that lies along the x-axis and has dipoles parallel to the y-axis (Fig. 1). The spacing, amplitude weights, and phase weights are symmetric with respect to the center of the array. In order to visualize the cost surface, only two variables can be used. Figure 2 is the cost function when the amplitude weights are the optimization variables with limits $0.1 \le a_{2,3} \le 1.0$, and $\delta_{1,2}$ and $x_1 = 0.25\ \lambda$, $x_2 = 0.75\ \lambda$, and $x_2 = 1.25\ \lambda$. The cost surfaces for the dipole model and array factor look very similar implying that element location is more important than coupling. Fig. 3 is the cost function when $a_{2,3} = 1.0$ and $\delta_{1,2} = 0$, and the element spacings are bound by $x_1 = 0.25\ \lambda$, $x_2 = 0.25\ \lambda + \Delta_2$, and $x_3 = 0.25\ \lambda + \Delta_2 + \Delta_3$. As with the amplitude weights, the cost surfaces for the dipole model and array

factor look very similar. Fig. 4 is the cost function when $a_{2,3} = 1.0$, $0 \le \delta_{1,2} \le \pi$, and $x_1 = 0.25\ \lambda$, $x_2 = 0.75\ \lambda$, and $x_3 = 1.25\ \lambda$. Again, the cost functions for the dipoles and point sources are similar.

All the cost functions in these figures have ridges, narrow valleys, and dramatic variations in slope. The cost surface variations will slow the convergence of most minimization algorithms. Speed of convergence is highly dependent upon the starting point on the cost surface. For the six element case, the minimization algorithms mentioned so far will find the true minimum most of the time. On the other hand, adding more array variables dramatically increases the complexity of the cost surface and renders many "local" optimizers powerless to find a good minimum.

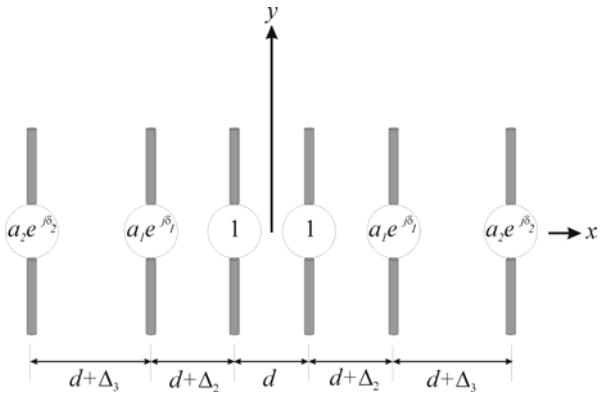

Fig. 1. Diagram of the array that generates the cost functions.

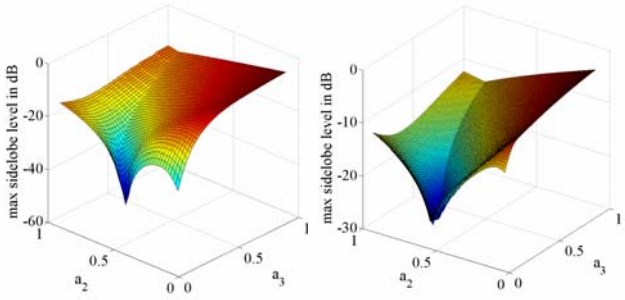

a. Dipoles b. Point sources

Fig. 2. Cost surface associated with varying the amplitude weights of the six element array.

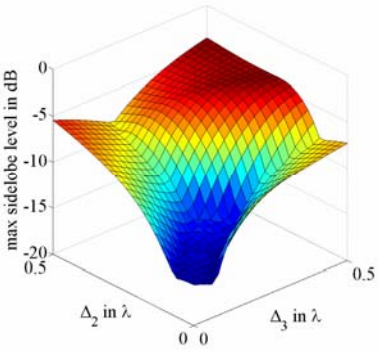

a. Dipoles

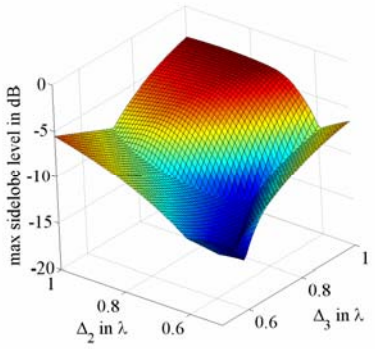

b. Point sources

Fig. 3. Cost surface associated with varying the spacing of the six element array.

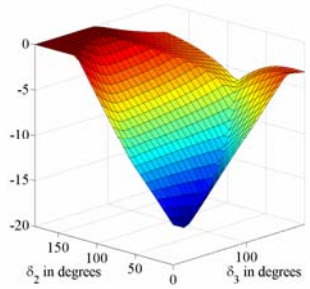

a. Dipoles

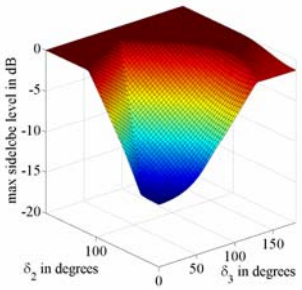

b. Point sources

Fig. 4. Cost surface associated with varying the phase weights of the six element array.

The next example is too difficult for local optimizers to find the global minimum. Fig. 5 is a graph of the maximum sidelobe level in dB versus the thinning configuration for a 32 element array. Elements in the array are either turned on with an amplitude of 1 or turned off with an amplitude of 0. The end elements are always on and the array is assumed to be symmetric. Values along the x-axis are the decimal versions of the 15 bit binary thinning configuration. As an example, one of the thinned array configurations is

$$1011110100110101\underbrace{0101100101111}_{=22110}01 \tag{2}$$

There are a total of 2^{15} possible thinning configurations. Not only is the cost surface riddled with local minima, but the variable values are discrete. This type of cost function is ideal for optimization by a GA as described in the next section.

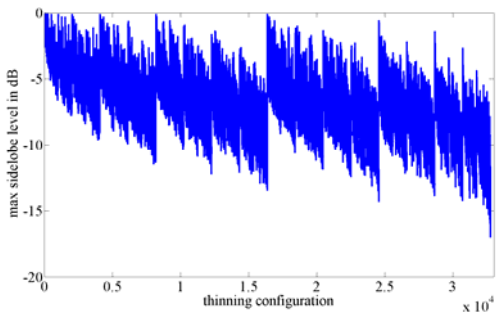

Fig. 5. Cost function for thinned array.

IV. GA BASICS

The GA begins with a random set of starting points on the cost surface called chromosomes. Each chromosome is evaluated by the cost function. Chromosomes may consist of binary or continuous values. Chromosomes with high costs are discarded, while chromosomes with low costs form a mating pool. Two parents are randomly selected from the mating pool. Selection is inversely proportional to the cost. Offspring are created through some combination of the parents. The offspring replace the discarded chromosomes. Next, random chromosomes in the population are randomly modified or mutated. Finally, the new and modified chromosomes are evaluated the process repeated. A flowchart of a GA is shown in Fig. 6.

Since its introduction, the GA has become a dominant numerical optimization algorithm in many disciplines. Holland started the GA [164] while Goldberg demonstrated its usefulness [165]. Details on implementing a GA can be found in [166] and a variety of applications to electromagnetics are reported in [167]. Some of the advantages of a GA include that it

- Optimizes continuous or discrete variables,
- Does not calculate derivatives,
- Works with a large number of variables,
- Is suited for parallel computers,
- Can jump out of a local minimum,
- Provides a list of optimum variables, not just a single solution,
- May encode the variables so that the optimization is done with the encoded variables, and
- Works with numerically generated data, experimental data, or analytical functions.

These advantages have been capitalized by many phased array researchers.

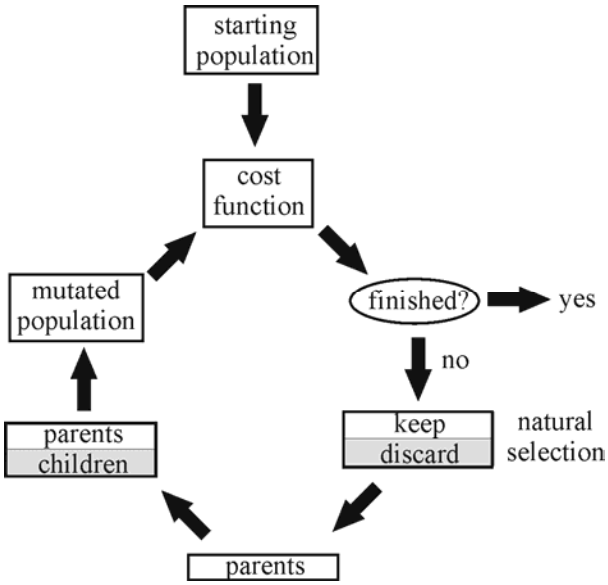

Fig. 6. Flow chart of a GA.

V. REVIEW OF GA APPLICATIONS TO PHASED ARRAYS

At this point, you should suspect that the GA outperforms traditional optimization approaches for many practical phased array designs. The GA has been applied to the cost functions in Section III but with many more variables. In addition, a wide range of other phased array optimization topics have been investigated. Attempt to categorize the literature into 19 topics. Most of these topics deal with phased array design. The adaptive/smart antenna topic involves using a GA in real time. The references are listed in

chronological order from [1] to [139]. The author tried to include all papers dealing with GA applications to phased arrays. Apologies are made to those authors whose papers were missed. Rather than trying to summarize the research done, readers can look at the references listed under a given topic.

Table 1. References to GA applications for phased arrays are categorized.

Topic	Reference
Array synthesis	**[4][11][14][18][21][24][25][26][27][30][37][44][52][53][56] [70][71][74][84][85][87][101][109][114][123][126][128][138]**
Nulling	**[3][19][23]**
adaptive/smart arrays	**[10][20][22][34][35][40][42][46][50][57][66][75] [86][96][105][106][112][117][127][130][134]**
Subarray	**[7][76][98][118]**
Element failures	**[38][48][68][115][116]**
Mutual coupling	**[41][47][51][54][63][64][65][72][80][81][83][94][102][111][124][136]**
Multiple beams	**[9][49]**
Shaped beam synthesis	**[28][29][36][39][60][93][103][113][133]**
Phase taper	**[8][78]**
GA combined and other methods	**[12][15][16][73][88][89][100][107][115][121][122][129]**
Conformal arrays	**[42][81][95][98]**
GA parameters	**[45][55][58][61][90][99][108][132]**
Ring arrays	**[33][43][125]**
Aperiodic arrays	**[6][31][32][59][79][92][110][119][120][137]**
Direction of arrival arrays	**[69][102]**
Beam scanning	**[97][104][135]**
Planar arryas	**[62][90][130][131]**
Multiple objective optimization	**[17][77][98]**
Thinned arrays	**[1][2][5][13][67][72][81][139]**

VI. GA FRONTIERS

The biggest hurdle for GAs is the time needed to find a good optimum solution. At this point, we have a powerful optimization algorithm that can create new designs, but computers and software models that are too slow for the cost function evaluations. Evaluating the cost function quickly and accurately can be done in three ways:

1. *Faster GAs.* Finding the optimum parameters such as population size and mutation rate can make orders of magnitude difference in the number of function calls needed to find an acceptable solution. Adaptively changing the parameters may be very helpful. Hybrid approaches that combine the GA and other approaches, especially local optimizers need more exploration. GAs can produce better and faster results with human input during the operation of the algorithm. Humans can even be used to create a subjective cost associated with a phased array design. Operator bias in the cost function may be as valuable as the mathematical equations in the model.
2. *Faster cost functions.* Using fast, approximate function evaluations in early generations and converting to slow, more exact function evaluations in later generations has some promise. Efficient hybrid methods can make large problems tractable. Eliminating unimportant variables helps optimization algorithms converge faster. Some costs are more sensitive than others. Some costs require a finer grid for sufficient accuracy than toher costs. Adaptively adjusting the grid size can result in significant time savings.
3. *Faster computers.* Clock speed and memory are bottlenecks for large complex optimization problems. GAs are ideally suited for parallel processing, since the cost function for each chromosome can be evaluated simultaneously.

A phased array consists of more than just the antenna elements. Optimization of the feed structure, the active components, the component costs, etc. are possible with a GA. The design of wideband feed networks to match wideband elements is an important step in developing wideband phased arrays. The GA has certainly advanced the design of complex phased arrays. As can be seen in the references, GAs are becoming more accepted as a design tool.

REFERENCES

[1] R. L. Haupt, J. J. Menozzi, and C. J. McCormack, "Thinned arrays using genetic algorithms," *IEEE AP-S Int'l Symp.*, pp. 712-715, Jun 1993.

[2] R. L. Haupt, "Thinned arrays using genetic algorithms," *IEEE AP-S Trans.*, vol. 42, pp. 993-999, Jul. 1994.

[3] A. Tennant, M. M. Dawoud, and A. P. Anderson, "Array pattern nulling by element position perturbations using a genetic algorithm," *Electronics Letters*, vol. 30, pp. 174-176, 3 Feb. 1994.

[4] M. Shimizu, "Determining the excitation coefficients of an array using genetic algorithms," *IEEE AP-S Int'l Symp*., pp. 530-533, Jun. 1994.

[5] D. J. O'Neill, "Element placement in thinned arrays using genetic algorithms," OCEANS 94, pp. 301-306, Sep. 1994.

[6] R. L. Haupt, "An introduction to genetic algorithms for electromagnetics," *IEEE AP-S Mag.* vol. 37, pp. 7-15, Apr. 1995.

[7] R. Haupt, "Optimization of subarray amplitude tapers," *IEEE AP-S Int'l Symp.*, pp. 1830 – 1833, Jun. 1995.

[8] R. L. Haupt, "Optimum quantised low sidelobe phase tapers for arrays," *Electronics Letters*, vol. 31, pp. 1117-1118, 6 Jul. 1995.

[9] D. Marcano, F. Duran, and O. Chang, "Synthesis of multiple beam linear antenna arrays using genetic algorithms," *IEEE AP-S Int'l Symp.*, pp. 328-332, Jul. 1995.

[10] B. Chambers, A. P. Anderson, and R. J. Mitchell, "Application of genetic algorithms to the optimization of adaptive antenna arrays and radar absorbers," *First Int'l Conf. Genetic Algorithms in Engineering Systems: Innovations and Applications*, pp. 94-99, Sep. 1995.

[11] D. Marcano, M. Jimenez, F. Duran, and O. Chang, "Synthesis of antenna arrays using genetic algorithms," *IEEE Int'l Caracus Conf.* on Devices, Circuits, and Systems, pp. 328-332, Dec 1995.

[12] F. Ares, et.al., "Application of genetic algorithms and simulated annealing technique in optimising the aperture distributions of antenna array patterns," *Electronics Letters*, vol. 32, pp. 148-149, 1 Feb. 1996.

[13] R. L. Haupt, "Genetic algorithm design of antenna arrays," *IEEE Aerospace Applications Conf.*, pp. 103-109, Feb. 1996.

[14] D. Marcano, M. Jiminez, and O. Chang, "Synthesis of linear array using Schelkunoff's method and genetic algorithms," *IEEE AP-S Int'l Symp.*, pp. 814-817, Jul. 1996.

[15] F. Ares, et.al., "Application of genetic algorithms and simulated annealing technique in optimizing the aperture distributions of antenna arrays," *IEEE AP-S Int'l Symp.*, pp. 806-809, Jul. 1996.

[16] M. J. Buckley, "Linear array synthesis using a hybrid genetic algorithm," *IEEE AP-S Int'l Symp.*, pp. 584-587, Jul. 1996.

[17] D. S. Weile and E. Michielssen, "Integer coded Pareto genetic algorithm design of constrained antenna arrays," *Electronics Letters*, vol. 32, pp. 1744-1745, 12 Sep. 1996.

[18] R. J. Mitchell, B. Chambers, and A. P. Anderson, "Array pattern synthesis in the complex plane optimised by a genetic algorithm," *Electronics Letters*, vol. 32, pp. 1843-1845, 26 Sep. 1996.

[19] A. Alphones and V. Passoupathi, "Null steering in phased arrays by positional perturbations: a genetic algorithm approach," *3rd Int'l Conf. High Performance Computing*, pp. 4-9, Dec. 1996.

[20] R. L. Haupt and S. E. Haupt, "Phase-only adaptive nulling with a genetic algorithm," *IEEE Aerospace Applications Conf.*, pp. 151-160, Feb. 1997.

[21] R. J. Mitchell, B. Chambers, and A. P. Anderson, "Array pattern control in the complex plane optimised by a genetic algorithm," *10th Int'l Conf. Antennas and Propagation*, pp. 330-333, Apr. 1997.

[22] R. L. Haupt, "Phase-only adaptive nulling with a genetic algorithm," *IEEE AP-S Trans.*, vol. 45, pp. 1009-1015, Jun. 1997.

[23] W. P. Liao and F. L. Chu, "Array pattern nulling by phase and position perturbations with the use of the genetic algorithm," *Microwave and Optical Technology Letters*, vol. 15, pp. 251-256, Jul. 1997.

[24] Y. Keen-Keong and L. Yilong, "Sidelobe reduction in array-pattern synthesis using genetic algorithm," *IEEE AP-S Trans.*, vol. 45, pp. 1117-1122, Jul. 1997.

[25] D. Marcano, "Synthesis of linear and planar antenna arrays using genetic algorithms," *IEEE AP-S Int'l Symp.*, pp. 1688-1691, Jul. 1997.

[26] F. Ares, et.al., "Application of genetic algorithms in the design and optimization of array patterns," *IEEE AP-S Int'l Symp.*, pp. 1684-1687, Jul. 1997.

[27] D. Marcano, L. Gomez, and O. Sosa, "Planar array antenna synthesis using genetic algorithms with a penalty function," *IEEE Int'l Microwave*

and Optoelectronics Conf., pp. 285-290, Aug. 1997.

[28] J. M. Johnson and Y. Rahmat-Samii, "Genetic algorithms in engineering electromagnetics," *IEEE AP-S Mag.* vol. 39, pp. 7 – 21, Aug. 1997.

[29] N. V. S. N. Sarma and R. Chandrasekharam, "Shaped beam radiation pattern synthesis using genetic algorithm," *Int'l Conf. Electromagnetic Interference and Compatibility*, pp.171 – 174, Dec. 1997.

[30] K. Markus and L. Vaskelainen, "Optimisation of synthesised array excitations using array polynome complex root swapping and genetic algorithms," *IEE Proceedings Microwaves, Antennas and Propagation,* vol. 145, pp. 460-464, Dec. 1998.

[31] P. Kozakowski, M. Mrozowski, and W. Zieniutycz, "Synthesis of nonuniformly spaced arrays using genetic algorithm," *12th Int'l Conf. Microwaves and Radar*, pp. 340-344, May 1998.

[32] G. P. Junker, S. S. Kuo, and C. H. Chen, "Genetic algorithm optimization of antenna arrays with variable interelement spacings," *IEEE AP-S Int'l Symp.*, pp. 50-53, Jun. 1998.

[33] C. W. Brann and K. L. Virga, "Generation of optimal distribution sets for single-ring cylindrical arc arrays," *IEEE AP-S Int'l Symp.*, pp. 732 – 735, Jun. 1998.

[34] R. L. Haupt and H. L. Southall, "Experimental adaptive nulling with a genetic algorithm," Microwave Journal, vol. 42, no. 1, pp. 78-89, Jan. 1999.

[35] R. L. Haupt and H. Southall, "Experimental adaptive cylindrical array," *IEEE Aerospace Applications Conf.*, pp. 291 – 296, Mar. 1999.

[36] J. M. Johnson, "Genetic algorithm design of a switchable shaped beam linear array with phase-only control," *IEEE Aerospace Applications Conf.*, pp. 297-303, Mar. 1999.

[37] F. J. Ares-Pena, J. A. Rodriguez-Gonzalez, E. Villanueva-Lopez, and S. R. Rengarajan, "Genetic algorithms in the design and optimization of antenna array patterns," *IEEE AP-S Trans.*, vol. 47, pp. 506-510, Mar. 1999.

[38] Y. Beng-Kiong and L. Yilong, "Array failure correction with a genetic algorithm," *IEEE AP-S Trans.*, vol. 47, pp. 823-828, May 1999.

[39] R. L. Haupt and J. M. Johnson, "Dynamic phase-only array beam control using a genetic algorithm," First NASA/DoD Workshop on Evolvable Hardware, pp. 217 – 224, Jul. 1999.

[40] Y. C. Chung and R. L. Haupt, "Optimum amplitude and phase control for an adaptive linear array using a genetic algorithm," *IEEE AP-S Int'l Symp.*, pp. 1424-1427, Jul. 1999.

[41] K. F. Sabet, et. al., "Efficient printed antenna array synthesis including coupling effects using evolutionary genetic algorithms," *IEEE AP-S Int'l Symp.*, pp. 2084-2087, Jul. 1999.

[42] C. You Chung and R. L. Haupt, "Adaptive nulling with spherical arrays using a genetic algorithm," *IEEE AP-S Int'l Symp.*, pp. 2000-2003, Jul. 1999.

[43] B. P. Kumar and G. R. Branner, "Design of low sidelobe circular ring arrays by element radius optimization," *IEEE AP-S Int'l Symp.*, pp. 2032-2035, Jul. 1999.

[44] A. Udina, N. M. Martin, and L. C. Jain, "Linear antenna array optimisation by genetic means," *Third Int'l Conf. Knowledge-Based Intelligent Information Engineering Systems,* pp. 505 – 508, Aug. 1999.

[45] Y. H. Lee, A. C. Marvin, and S. J. Porter, "Genetic algorithm using real parameters for array antenna design optimisation," *High Frequency Postgraduate Student Colloquium*, pp. 8-13, Sep. 1999.

[46] T. Fukusako, et.al., "Microstrip adaptive array antenna using semiconductor plasma and genetic algorithm," *Asia Pacific Microwave Conf.*, pp. 76-79, Dec. 1999.

[47] L. Landesa, F. Obelleiro, and J. L. Rodríguez, "Practical improvement of array antennas in the presence of environmental objects using genetic algorithms," *Microwave and Optical Technology Letters*, vol. 23, pp. 324-326, 5 Dec. 1999.

[48] J. A. Rodriguez, et.al., "Genetic algorithm procedure for linear array failure correction," *Electronics Letters*, vol. 36, pp. 196-198, 3 Feb. 2000.

[49] K. N. Sherman, "Phased array shaped multi-beam optimization for LEO satellite communications using a genetic algorithm," *IEEE Int'l Conf. Phased Array Systems and Technology*, pp. 501-504, May 2000.

[50] Y. Lu and B.K. Yeo, "Adaptive wide null steering for digital beamforming array with the complex coded genetic algorithm," *IEEE International Conference Phased Array Systems and Technology*, pp. 557-560, May 2000.

[51] H. Cheng-Nan, et.al., "Design of the cross-dipole antenna with near-hemispherical coverage in finite-element phased array by using genetic algorithms," *IEEE International Conference Phased Array Systems and Technology*, pp. 303-306, May 2000.

[52] E. A. Jones and W. T. Joines, "Genetic design of linear antenna arrays," *IEEE AP-S Mag.*, vol. 42, pp. 92-100, Jun. 2000.

[53] D. Marcano and F. Duran, "Synthesis of antenna arrays using genetic algorithms," *IEEE AP-S Mag.*, vol. 42, pp. 12-20, Jun. 2000.

[54] A. Armogida, et.al., "Synthesis of point-to-multipoint patch antenna arrays by using genetic algorithms*," IEEE AP-S Int'l Symp.*, pp. 1038-1041, Jul. 2000.

[55] C. You Chung and R. L. Haupt, "GAs using varied and fixed binary chromosome lengths and real chromosomes for low sidelobe spherical-circular array pattern synthesis," *IEEE AP-S Int'l Symp.*, pp. 1030-1033, Jul. 2000.

[56] R. Shavit and S. Levy, "Improved Orchard-Elliott pattern synthesis algorithm by pseudo-inverse technique and genetic algorithm," *IEEE AP-S Int'l Symp.*, pp. 1042-1045, Jul. 2000.

[57] Y. Kimura and K. Hirasawa, "A CMA adaptive array with digital phase shifters by a genetic algorithm and a steepest descent method*," IEEE AP-S Int'l Symp*., pp. 914-917, Jul. 2000.

[58] R. L. Haupt, "Optimum population size and mutation rate for a simple real genetic algorithm that optimizes array factors," *IEEE AP-S Int'l Symp.*, pp. 1034-1037, Jul. 2000.

[59] B. J. Barbisch D. H. Werner, and P. L. Werner "A genetic algorithm optimization procedure for the design of uniformly excited and nonuniformly spaced broadband low sidelobe arrays," *Applied Computational Electromagnetics Society Journal*, vol. 15, no. 2, pp. 34-42, Jul. 2000.

[60] N. N. Jackson and P. S. Excell, "Genetic-algorithm optimization of an array for near-field plane wave generation," *Applied Computational Electromagnetics Society Journal*, vol. 15, no. 2, pp. 61-74, Jul. 2000.

[61] R. L. Haupt and S. E. Haupt, "Optimum population size and mutation rate for a simple real genetic algorithm that optimizes array factors," *Applied Computational Electromagnetics Society Journal*, vol. 15, no. 2, pp. 94-102, Jul. 2000.

[62] D. F. Li and Z. L. Gong, "Design of hexagonal planar arrays using genetic algorithms for performance improvement," *2nd International Conference Microwave and Millimeter Wave Technology*, pp. 455 - 460, Sep. 2000.

[63] K. C. Lee, "Optimization of a finite dipole array with genetic algorithm including mutual coupling effects," *International Journal of RF and Microwave Computer-Aided Engineering*, vol. 10, no. 6, pp. 379-382, Nov. 2000.

[64] A. Petosa and S. Thirakoune, "Linear array of dielectric resonator antennas optimized using a genetic algorithm for low-sidelobe applications," *Asia-Pacific Microwave Conf.*, pp. 21-24, Dec. 2000.

[65] A. Miura and M. Tanaks, "A study of array pattern tuning method using hybrid genetic algorithms for figure-8 satellites's earth station antenna," *Asia-Pacific Microwave Conf.*, pp. 325-329, Dec. 2000.

[66] Y. Yashchyshyn and M. Piasecki, "Improved model of smart antenna controlled by genetic algorithm," *6th Int'l Conf. CAD Systems in Microelectronics*, pp. 147 - 150, Feb. 2001.

[67] S. E. El-Khamy, et.al., "Thinned multi-ring arrays using genetic algorithms," *18th National Radio Science Conf.*, pp. 113-121, Mar. 2001.

[68] H. M. Elkamchouchi and M. M. Wagib, "Failure restoration and array synthesis using genetic algorithms," *18th National Radio Science Conf.*, pp. 123-130, Mar. 2001.

[69] P. Karamalis, et.al., "Direction of arrival estimation using genetic algorithms," *Vehicular Technology Conference*, pp. 162 - 166, May 2001.

[70] C. Chien-Hung and C. Chien-Ching, "Novel radiation pattern by genetic algorithms," *Vehicular Technology Conference*, pp. 8 - 12, May 2000.

[71] D. W. Boeringer, D. W. Machuga, and D. H. Werner, "Synthesis of phased array amplitude weights for stationary sidelobe envelopes using genetic algorithms," *IEEE AP-S Int'l Symp.*, pp. 684-687, Jul. 2001.

[72] M. G. Bray, et.al., "Thinned aperiodic linear phased array optimization for reduced grating lobes during scanning with input impedance bounds," *IEEE AP-S Int'l Symp.*, pp. 688-691, Jul. 2001.

[73] A. Miura and M. Tanaka, "An apply of hybrid GA for array pattern control of quasi-zenithal satellite's Earth station antenna," *IEEE AP-S Int'l Symp*., pp. 230-233, Jul. 2001.

[74] V. R. Mognon, W. A. Artuzi, Jr., and J. R. Descardeci, "Tilt angle and sidelobe level control of array antennas by using genetic algorithm," *SBMO/IEEE MTT-S Int'l Microwave and Optoelectronics Conf.*, pp. 299-301, Aug. 2001.

[75] D. S. Weile and E. Michielssen, "The control of adaptive antenna arrays with genetic algorithms using dominance and diploidy," *Antennas and*

Propagation, IEEE Transactions on, vol. 49, pp. 1424-1433, Oct. 2001.

[76] P. Lopez, et.al., "Subarray weighting for the difference patterns of monopulse antennas: joint optimization of subarray configurations and weights," *IEEE AP-S Trans.,* vol. 49, pp. 1606-1608, Nov. 2001.

[77] D. Ansell and E. J. Hughes, "Use of multi-objective genetic algorithms to optimise the excitation and subarray division of multifunction radar antennas," *IEE Multifunction Radar and Sonar Sensor Management Techniques* (Ref. No. 2001/173), pp. 8/1 - 8/4, Nov. 2001.

[78] P. Lopez, et.al., "Low-sidelobe patterns from linear and planar arrays with uniform excitations except for phases of a small number of elements," *Electronics Letters*, vol. 37, pp. 1495-1497, 6 Dec. 2001.

[79] A. Lommi, et.al., "Sidelobe reduction in sparse linear arrays by genetic algorithms," *Microwave and Optical Technology Letters,* vol. 32, no. 3, pp. 194-196, 5 Feb. 2002.

[80] S. Misra, et.al. "Design and optimization of a nonplanar multidipole array using genetic algorithms for mobile communications," *Microwave and Optical Technology Letters*, vol. 32, no. 4, pp. 301-304, 20 Feb. 2002.

[81] Y. C. Chung and R.L. Haupt, "Low-sidelobe pattern synthesis of spherical arrays using a genetic algorithm," *Microwave and Optical Technology Letters*, vol. 32, pp. 412-414, 2002, 20 Mar. 2002.

[82] M. G. Bray, et.al., "Matching network design using genetic algorithms for impedance constrained thinned arrays," *IEEE AP-S Int'l Symp*., pp. 528 - 531, Jun. 2002.

[83] S. Mummareddy, D. H. Werner, and P. L. Werner, "Genetic optimization of fractal dipole antenna arrays for compact size and improved impedance performance over scan angle," *IEEE AP-S Int'l Symp.*, pp. 98 - 101, Jun. 2002.

[84] A. A. Varahram and J. Rashed-Mohassel, "Sidelobe level optimization using modified genetic algorithm," *IEEE AP-S Int'l Symp*., pp. 742 - 745, Jun. 2002.

[85] T. Dong, Y.-y. Li, and X.-w. Xu, "Genetic algorithm in the synthesis of low sidelobe antenna array," *3rd International Conference on Microwave and Millimeter Wave Technology*, pp. 751 – 754, Aug. 2002.

[86] M. Vitale, et.al., "Genetic algorithm assisted adaptive beamforming," *IEEE 56th Vehicular Technology Conference*, pp. 601 - 605, Sep. 2002.

[87] T. Dong, Y.-y. Li, and X.-w. Xu, "Genetic algorithm in the synthesis of low sidelobe antenna array," *5th International Symposium Wireless Personal Multimedia Communications*, pp. 757 - 761, Oct. 2002.

[88] W. Yan and L. Yilong, "The combination of neural networks and genetic algorithm for fast and flexible wide ing in digital beamforming," *9th International Conf . Neural Information Processing*, pp. 782 - 786, Nov. 2002.

[89] M. G. Bray, et.al., "Optimization of thinned aperiodic linear phased arrays using genetic algorithms to reduce grating lobes during scanning," *IEEE AP-S Trans.*, vol. 50, pp. 1732-1742, Dec. 2002.

[90] D. W. Boeringer and D. H. Werner, "Adaptive mutation parameter toggling genetic algorithm for phase-only array synthesis," *Electronics Letters*, vol. 38, pp. 1618-1619, 5 Dec. 2002.

[91] S. Caorsi, et.al., "Planar antenna array design with a multi-purpose GA-based procedure," *Microwave and Optical Technology Letters*, vol. 35, no. 6, pp. 428-430, 20 Dec. 2002.

[92] D.G. Kurup, M. Himdi, and A. Rydberg, "Design of an unequally spaced reflectarray," *Antennas and Wireless Propagation Letters*, vol. 2, pp. 33- 35, 2003.

[93] R. Haupt, "Generating a plane wave with a linear array of line sources," *IEEE AP-S Trans.*, vol. 51, pp. 273-278, Feb. 2003.

[94] K. C. Lee, "Genetic algorithms based analyses of nonlinearly loaded antenna arrays including mutual coupling effects," *IEEE AP-S Trans.*, vol. 51, pp. 776-781, Apr. 2003.

[95] R. J. Allard, D. H. Werner, and P. L. Werner, "Radiation pattern synthesis for arrays of conformal antennas mounted on arbitrarily-shaped three-dimensional platforms using genetic algorithms," *IEEE AP-S Trans.*, vol. 51, pp. 1054-1062, May 2003.

[96] C. Salvatore, et.al., "A real-time approach to array control based on a learned genetic algorithm," *Microwave and Optical Technology Letters*, vol. 36, pp. 235-238, 20 Feb. 2003.

[97] M. A. Mangoud, M. Aboul-Dahab, and M. Sabry, "Optimum steering techniques for linear and planar antenna arrays using genetic algorithm," *20th National Radio Science Conference*, pp. B7-1-8, Mar. 2003.

[98] D. W. Ansell and E. J. Hughes, "Using multi-objective genetic algorithms to optimise the

subarray partitions of conformal array antennas," *20th Int'l Conf. Antennas and Propagation*, pp. 151-155, Mar. 2003.

[99] H. M. Elkamchouchi and M. M. Wagih, "Genetic algorithm operators effect in optimizing the antenna array pattern synthesis," *Twentieth National Radio Science Conference*, pp. B12 - 1-7, Mar. 2003.

[100] L. L. Wang, D. G. Fang, and W. X. Sheng, "Combination of genetic algorithm (GA) and fast fourier transform (FFT) for synthesis of arrays," *Microwave and Optical Technology Letters*, vol. 37, pp. 56-59, 5 Apr. 2003.

[101] F. H. Kashni, F. Arazm, and M. Asgari, "The synthesis of super-resolution array through genetic algorithm using CRB," *5th European Personal Mobile Communications Conf.*, pp. 60-64, Apr. 2003.

[102] T. Huang and A.S. Mohan, "Effects of array mutual coupling on near-field DOA estimation," *IEEE Canadian Conference Electrical and Computer Engineering*, pp. 1881- 1884, May 2003.

[103] R. Haupt, "Synthesis of a plane wave in the near field with a planar phased array," *IEEE AP-S Int'l Symp*., pp. 792-795, Jun. 2003.

[104] T. Koleck, "Active antenna coverage synthesis for GEO satellite using genetic algorithm," *IEEE AP-S Int'l Symp*., pp. 142-144, Jun. 2003.

[105] C. H. Hsu, et.al., "Optimizing broadside array antenna with adaptive interference cancellation using amplitude-position perturbations in a linear array," *IEEE AP-S Int'l Symp.*, pp. 69-72, Jun. 2003.

[106] A. T. Bu, et.al., "Design of the sector array antenna based on genetic algorithm for smart antenna system front end," *IEEE AP-S Int'l Symp*., pp. 686-689, Jun. 2003.

[107] D. W. Boeringer and D. H. Werner, "A comparison of particle swarm optimization and genetic algorithms for a phased array synthesis problem," *IEEE AP-S Int'l Symp*., pp. 181-184, Jun. 2003.

[108] D. W. Boeringer and D. H. Werner, "Genetic algorithms with adaptive parameters for phased array synthesis," *IEEE AP-S Int'l Symp*., pp. 169-172, Jun. 2003.

[109] Y.H. Liu, et.al., "Modeling antenna array elements and bandwidth enhanced by genetic algorithm," *IEEE AP-S Int'l Symp*., pp. 884-887, Jun. 2003.

[110] M. Wang, et.al., "The synthesis and optimization of arbitrarily distributed array with circular sparse array," *IEEE AP-S Int'l Symp*., pp. 812-815, Jun. 2003.

[111] S. Xiao, et.al., "Reconfigurable microstrip antenna design based on genetic algorithm," *IEEE AP-S Int'l Symp*., pp. 407- 410, Jun. 2003.

[112] C. H. Hsu, J. S. Row, and K. H. Kuo, "Downlink optimal radiation pattern design of smart antennas by phase-amplitude perturbations in a linear array," *IEEE AP-S Int'l Symp*., pp. 80- 83, Jun. 2003.

[113] R. Haupt, "Generating a plane wave in the near field with a planar array antenna," *Microwave Journal*, Aug. 2003.

[114] F. H. Wen-Chia Lue, "Use of B-spline curves and genetic algorithms to reduce the sidelobe level in array-patterns," *Microwave and Optical Technology Letters*, vol. 38, pp. 308-311, 20 Aug. 2003.

[115] W. Ling-Ling and F. Da-Gang, "Combination of genetic algorithm and fast Fourier transform for array failure correction," *6th Int'l Symp. Antennas, Propagation and EM Theory*, pp. 234 - 237, Oct. 2003.

[116] A. Taskin and C. S. Gurel, "Antenna array pattern optimisation in the case of array element failure," *33rd European Microwave Conference*, pp. 1083- 1085, Oct. 2003.

[117] W. Qi and G. Zhong Lin, "On the performance of genetic algorithm based adaptive beamforming," *6th Int'l Symp. Antennas, Propagation and EM Theory*, pp. 339 - 343, Oct. 2003.

[118] G. Golino, "A genetic algorithm for optimizing the segmentation in subarrays of planar array antenna radars with adaptive digital beamforming," *IEEE Int'l Symp. Phased Array Systems and Technology*, pp. 211-216, 2003.

[119] R. G. Hohlfeld and N. Cohen, "Genetic optimization of sparse, frequency invariant arrays using the HCR principle," *IEEE Int'l Symp. Phased Array Systems and Technology*, pp. 588 - 593, Oct. 2003.

[120] W. Ling-Ling and F. Da-Gang, "Synthesis of nonuniformly spaced arrays using genetic algorithm," *Asia-Pacific Conf. Environmental Electromagnetics*, pp. 302-305, Nov. 2003.

[121] D. W. Boeringer and D. H. Werner, "Particle swarm optimization versus genetic algorithms for phased array synthesis," *IEEE AP-S Trans.*, vol. 52, pp. 771-779, Mar. 2004.

[122] S. Caorsi, et.al., "Peak sidelobe level reduction with a hybrid approach based on GAs and difference sets," *IEEE AP-S Trans.*, vol. 52, pp. 1116- 1121, Apr. 2004.

[123] S. H. Son, et.al., "Mobile phased array antenna design with low sidelobe pattern by genetic algorithm," *IEEE AP-S Int'l Symp*., pp. 4112-4115, Jun. 2004.

[124] S. E. El-Khamy, "Fractal multiband antennas using GA/MOM optimized log periodic dipole arrays," *IEEE AP-S Int'l Symp*., pp. 3433- 3436, Jun. 2004.

[125] A. Erentok and K. L. Melde, "Comparison of MATLAB and GA optimization for three-dimensional pattern synthesis of circular arc arrays," *IEEE AP-S Int'l Symp*., pp. 2683-2686, Jun 2004.

[126] D. A. Tonn and R. Bansal, "Sidelobe minimization in interrrupted phased arrays by mean of a genetic algorithm," *IEEE AP-S Int'l Symp.*, pp. 531 – 534, Jun. 2004.

[127] C. Sacchi, et.al., "Adaptive antenna array control in the presence of interfering signals with stochastic arrivals: assessment of a GA-based procedure," *IEEE Trans. Wireless Communications*, vol. 3, pp. 1031- 1036, Jul. 2004.

[128] F. Soltankarimi, J. Nourinia, and C. Ghobadi, "Side lobe level optimization in phased array antennas using genetic algorithm," *IEEE Eighth Int'l Symp. Spread Spectrum Techniques and Applications*, pp. 389- 394, Aug. 2004.

[129] F. Yu, et.al., "Pattern synthesis of linear arrays using a hybrid optimization algorithm," *7th International Conf Signal Processing*, pp. 428-430, Aug. 2004.

[130] A. Massa, et.al., "Planar antenna array control with genetic algorithms and adaptive array theory," *IEEE AP-S Trans.*, vol. 52, pp. 2919-2924, Nov. 2004.

[131] M. Donelli, et.al., "A versatile enhanced genetic algorithm for planar array design," *Journal of Electromagnetic Waves and Applications*, vol. 18, no. 11, pp. 1533-1548, 2004.

[132] D. W. Boeringer, D. H. Werner, and D. W. Machuga, "A simultaneous parameter adaptation scheme for genetic algorithms with application to phased array synthesis," *IEEE AP-S Trans.*, vol. 53, pp. 356- 371, Jan. 2005.

[133] S. H. Zainud-Deen, et.al., "Synthesis of linear arrays with shaped pattern using genetic algorithm and an orthogonal method," *Twenty-Second National Radio Science Conference*, pp. 89- 96, Mar. 2005.

[134] S. H. Zainud-Deen, et.al., "Adaptive arrays of smart antennas using genetic algorithm," Twenty-*Second National Radio Science Conference*, pp. 145- 154, Mar. 2005.

[135] J. N. Bogard and D. H. Werner, "Optimization of peano-gosper fractile arrays using genetic algorithms to reduce grating lobes during scanning," *IEEE Int'l Radar Conf.*, pp. 905- 909, May 2005.

[136] S. Tao and H. Ling, "Array beamforming in the presence of a mounting tower using genetic algorithms," *IEEE AP-S Trans.*, vol. 53, pp. 2011- 2019, Jun. 2005.

[137] Y.B. Tian and J. Qian, "Improve the performance of a linear array by changing the spaces among array elements in terms of genetic algorithm," *IEEE AP-S Trans.*, vol. 53, pp. 2226- 2230, Jul. 2005.

[138] S. Yang, et.al., "Design of a uniform amplitude time modulated linear array with optimized time sequences," *IEEE AP-S Trans.*, vol. 53, pp. 2337- 2339, Jul. 2005.

[139] R. L. Haupt, "Interleaved Thinned Linear Arrays," *IEEE AP-S Trans.*, vol. 53, pp. 2858-2864, Sep. 2005.

[140] J. S. Stone, US Patents 1,643,323 and 1,715,433.

[141] C. L. Dolph, "A current distribution for broadside arrays which optimizes the relationship between bream width and side-lobe level," Jun. 1946.

[142] T. T. Taylor, "Design of line source antennas for narrow beamwidth and low side lobes," *IRE AP Trans., AP-7*, pp. 16-28, 1955.

[143] E. T. Bayliss, "Design of monopulse antenna difference patterns with low sidelobes," The Bell System Tech. J., vol. 47, pp.623-650, May-Jun. 1968.

[144] R. S. Elliott, *Antenna Theory and Design*, New York: Prentice-Hall, 1981.

[145] J. A. Nelder and R. Mead, Computer Journal, vol. 7, pp. 308-313, 1965.

[146] W. H. Press, et. al., *Numerical Recipes in FORTRAN*, New York: Cambridge University Press, 1992.

[147] D. G. Luenberger, *Linear and Nonlinear Programming*, Reading, MA: Addison-Wesley, 1984.

[148] M. I. Skolnik, G. Nemhauser, and J. W. Sherman, III "Dynamic programming applied to unequally spaced arrays," *IEEE AP-S Trans.*, vol. 12, pp. 35-43, Jan. 1964.

[149] N. Balakrishnan, P. K. Murthy, and S. Ramakrishna, "Synthesis of antenna arrays with spatial and excitation constraints," *IEEE AP-S Trans.*, vol. 27, no. 5, pp. 690-696, Sep. 1979.

[150] J. Perini, "Note on antenna pattern synthesis using numerical iterative methods," *IEEE AP-S Trans*., vol. 12, pp. 791-792, Jul. 1976.

[151] C. S. Ruf, "Numerical annealing of low-redundancy linear arrays," *IEEE AP-S Trans*., vol. 41, no.1, Jan. 1993.

[152] W. L. Stutzman, and E. L. Coffey, "Radiation pattern synthesis of planar antennas using the iterative sampling method," *IEEE AP-S Trans*., vol. AP-23, no. 6, pp.764 - 769, Nov. 1975.

[153] H. J. Orchard, R. S. Elliot, and G. J. Stern, "Optimizing the synthesis of shaped beam antenna patterns," *IEE Proceedings*, vol. 132, no.1, pp. 63 - 68, Feb. 1985.

[154] R. S. Elliot and G. J. Stearn, "Shaped patterns from a continuous planar aperture distribution," *IEEE Proceedings*, vol. 135, no. 6, pp. 366 - 370, Dec. 1988.

[155] J. E. Richie and H. N. Kritikos, "Linear program synthesis for direct broadcast satellite phased arrays," *IEEE AP-S Trans.*, vol. 36, no. 3, pp. 345-348, Mar. 1988.

[156] F. Ares, R. S. Elliott, and E. Moreno, "Design of planar arrays to obtain efficient footprint patterns with an arbitrary footprint boundary," *IEEE AP-S Trans.*, vol. 42, no. 11, pp. 1509-1514, Nov. 1994.

[157] O. Einarsson, "Optimization of planar arrays," *IEEE AP-S Trans.*, vol. AP-27, no.1, pp.86 - 92, Jan. 1979.

[158] T. S. Ng, J. Yoo Chong Cheah, and F. J. Paoloni, "Optimization with controlled null placement in antenna array pattern synthesis," *IEEE AP-S Trans.*, vol. 33, no. 2, pp. 215 - 217, Feb. 1985.

[159] D. K. Cheng, "Optimization techniques for antenna arrays," *Proc. of IEEE*, vol. 59, no. 12, pp. 1664-1674, Dec. 1971.

[160] J. F. DeFord and O. P. Gandhi, "Phase-only synthesis of minimum peak sidelobe patterns for linear and planar arrays," *IEEE AP-S Trans.*, vol. 36, no.2, pp. 191-201, Feb. 1988.

[161] R. L. Haupt, "Thinned arrays using genetic algorithms," *IEEE AP-S Trans*, vol. 42, no. 7, pp 993-999, July 1994.

[162] S. Kirkpatrick, C. D. Gelatt, and M. P. Vecchi, "Optimization by Simulated Annealing," Science, vol. 220, no. 4598, pp. 671-680, 13 May 1983.

[163] N. Metropolis, A. Rosenbluth, and M. Rosenbluth, J. Chemical Physics, vol. 21, pp. 1087-1092, 1953.

[164] J. H. Holland, *Adaptation in Natural and Artificial Systems*, Ann Arbor: The University of Michigan Press, 1975.

[165] D. E. Goldberg, *Genetic Algorithms in Search, Optimization, and Machine Learning*, New York: Addison-Wesley, 1989.

[166] R. L. Haupt and S. E. Haupt, *Practical Genetic Algorithms*, 2nd edition, New York: John Wiley & Sons, 2004.

[167] Y. Rahmat-Samii and E. Michielssen, eds., *Electromagnetic Optimization by Genetic Algorithms*, New York: John Wiley & Sons, 1999.

Randy L. Haupt received his Ph.D. in Electrical Engineering from the University of Michigan, MS in Electrical Engineering from Northeastern University, MS in Engineering Management from Western New England College, and BS in Electrical Engineering from the USAF Academy.

He is Department Head of Computational Electromagnetics and Senior Scientist at the Penn State Applied Research Laboratory. He was Professor and Department Head of Electrical and Computer Engineering at Utah State University from 1999-2003. He was a Professor of Electrical Engineering at the USAF Academy and Professor and Chair of Electrical Engineering at the University of Nevada Reno. In 1997, he retired as a Lt. Col. in the USAF. Dr. Haupt was a project engineer for the OTH-B radar and a research antenna engineer for Rome Air Development Center. He has many journal articles, conference publications, and book chapters on antennas, radar cross section and numerical methods and is co-author of the book *Practical Genetic Algorithms*, 2 ed., John Wiley & Sons, 2004. Dr. Haupt has eight patents in antenna technology.

Dr. Haupt is a Fellow in the IEEE, was the Federal Engineer of the Year in 1993, and is a member of ACES, Tau Beta Pi, Eta Kappa Nu, URSI Commission B, and Electromagnetics Academy.

Genetic Algorithm Optimization of a Traveling Wave Array of Longitudinal Slots in a Rectangular Waveguide

(*Invited Paper*)

Anders Jensen[1] and Sembiam R. Rengarajan[2]
[1] Cushcraft Corporation, Carlsbad, CA 92010
[2] Department of Electrical and Computer Engineering, California State University, Northridge, CA 91330
e-mail: [1]anders.jensen@ieee.org, [2]srengarajan@csun.edu

Abstract **—** Genetic Algorithm is used to optimize the performance characteristics of a traveling wave array consisting of longitudinal slots cut in the broad wall of a rectangular waveguide. An analysis method employing a loaded transmission line to model the slot arrays is employed. External mutual coupling is considered. The self admittance of the radiating slots is computed using the method-of-moments technique applied to the pertinent integral equations. Numerical results indicate typical performance improvements possible using the genetic algorithm optimization.

I. INTRODUCTION

Longitudinal slots cut in the broadwall of a rectangular waveguide have been employed as radiating elements in linear and planar arrays for numerous radar and communication applications. The design of a traveling wave linear array of longitudinal slots was presented by Elliott circa 1977 [1]. A design procedure developed by Elliott is applicable to both traveling wave and standing wave arrays [2]. That procedure uses an iterative technique to design the array at the center frequency of the desired bandwidth. Usually the array performance is optimum at the design frequency and it degrades away from the center frequency. Optimizing an array with respect to any performance parameter is a multi-dimensional problem. Due to the presence of many extrema, local optimization techniques such as conjugate gradient and Fletcher-Powell minimization techniques may not be well-suited to this work. Genetic Algorithms (GA) has the ability to search hyperplanes extensively and they are less susceptible to get stuck at local maxima [3]. In this work we investigated the optimization of different performance parameters of a traveling wave array of longitudinal slots using GA. Many case studies are shown for the 21-element array discussed by Elliot in [1]. The purpose of this work is to show typical performance improvements possible in traveling wave arrays designed using the genetic algorithm optimization.

II. THE METHOD OF ANALYSIS

A. Self Admittance

The analysis employs a moment method solution to the pertinent integral equation for the aperture electric field of a single slot when excited by an incident TE_{10} wave. From the aperture electric field the TE_{10} mode scattered wave coefficients in the forward and backward directions are determined. Since the slot scattering is very nearly symmetric, a shunt admittance model is found to be an excellent assumption. The self admittance of the slot is determined as a function of slot offset and length from the scattered wave coefficients. The basic equations of the method of moments analysis are shown here leaving all the details since the method is very similar to that presented in [4].

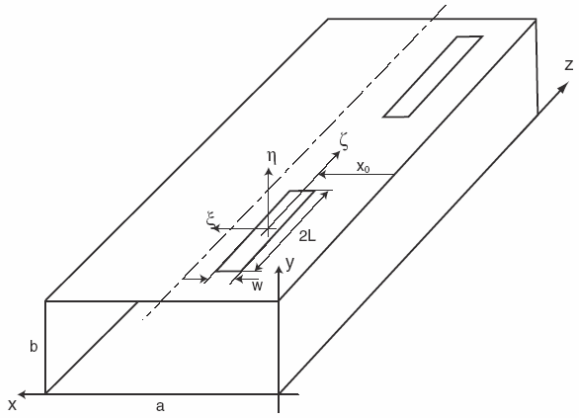

Fig. 1. Longitudinal slots cut in the waveguide broadwall.

The continuity of the tangential component of the aperture electric field is implicitly satisfied. The boundary condition for the dominant component of the magnetic field in each aperture of the thick slot is enforced as follows,

$$H_z^{ext}(P) - H_z^{\text{int}}(P) = H_z^{inc}(P), \quad (1)$$

$$H_z(P) = j\omega\varepsilon \int_{slot} G(P,P')\left[-\hat{n}xE_x\hat{x}\right]ds'. \quad (2)$$

Equation (1) satisfies the continuity of the magnetic field across the slot aperture. For simplicity only one equation is shown. For a thick slot two equations are used so as to satisfy the boundary conditions at the interior as well as the exterior aperture. The Green's function inside the integral in (2) is that of the rectangular waveguide, a cavity formed by the thick slot with both openings shorted by thin conducting sheets, or the exterior half space respectively for each of the three regions. The complete expressions for all the Green's functions are found in [4]. Global sinusoidal expansion functions describe the longitudinal variation of the electric field across the slot in (3). A uniform transverse distribution is assumed in (3). The weighting functions have similar longitudinal variation but exhibit a delta function in the transverse direction as shown in (4),

$$E_x(P') = \sum_{q=1}^{N} E_q \sin\left[\frac{q\pi}{2L}(\varsigma'+L)\right], \quad (3)$$

$$w_p(P) = \sin\left[\frac{p\pi}{2L}(\varsigma+L)\right]\delta(\xi). \quad (4)$$

The primed coordinates (ζ',ξ') along and across the slot are used for the source region and unprimed coordinates (ζ,ξ) in Fig. 2 denote the field region. The integral equations are reduced to matrix equations and their solution yields the coefficients of expansion of the aperture electric field. It is then possible to obtain the back scattering coefficient, Γ and the normalized self admittance as shown below [4],

$$\frac{Y}{Y_0} = \frac{-2\Gamma}{1+\Gamma}. \quad (5)$$

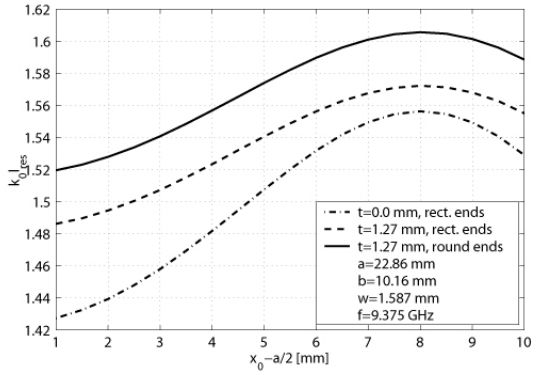

Fig. 2. Normalized resonant length versus slot offset.

The normalized self admittance computed in (5) is an important parameter in the design optimization. First, the normalized resonant length $k_0 l_{res}$ versus slot offset from the centerline of the broadwall is found as shown in Fig. 2 for a range of values of slot offsets. Fig. 2 shows that the resonant length is dependent on the slot thickness and hence the data need to be computed for the specific wall thickness of interest. The value of slot length, $2l_{res}$, that makes the phase of the back scattered TE_{10} mode wave equal to 180^o with respect to the incident wave electric field, both referenced to a plane passing through the center of the slot, is said to be the resonant length [4]. The real and imaginary parts of the self admittance as a function of the slot offset and the normalized length of the slot with respect to free space wavelength are then obtained. These data are shown in Figs. 3 and 4, respectively, over a range of values of slot offsets and lengths normalized to resonant lengths. The computed MoM data for the slot admittance as a function of the slot offset and normalized length shown in Figs. 2 through 4 are cast in the form of Stegen normalization [5]. The data are then curve-fitted as fourth order polynomials using the least mean square error criterion. The polynomial representations are easy to work with in the GA optimizations.

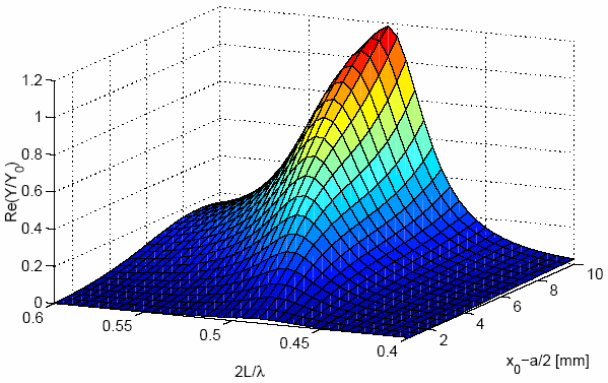

Fig. 3. Equivalent slot conductance versus slot offset and length.

B. Array Analysis Procedure

Elliott's design equations were rearranged by Hamadallah [6] to facilitate the analysis of a slot array. The direct method of analysis discussed in [6] is used in the GA optimization process. The basic analysis equations alone are reproduced here for ready reference and the details are omitted. The complete equations and the definitions of all symbols are found in [2, 6]. The slot voltages found in the column matrix on the left side of (6) are computed directly from the solution of the matrix equation (6).

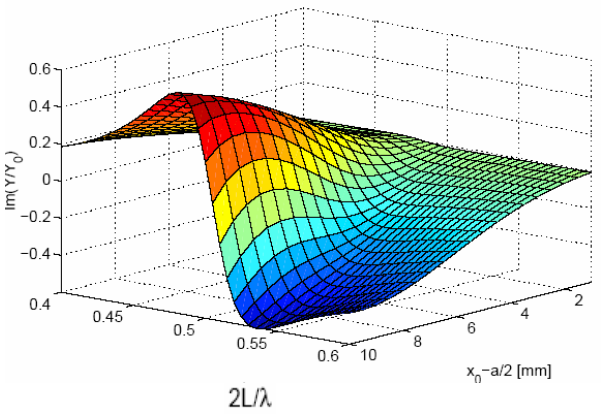

Fig. 4. Equivalent slot susceptance versus slot offset and length.

C. Array Analysis Procedure

Elliott's design equations were rearranged by Hamadallah [6] to facilitate the analysis of a slot array. The direct method of analysis discussed in [6] is used in the GA optimization process. The basic analysis equations alone are reproduced here for ready reference and the details are omitted. The complete equations and the definitions of all symbols are found in [2, 6]. The slot voltages found in the column matrix on the left side of (6) are computed directly from the solution of the matrix equation (6),

$$\begin{bmatrix} g_{11} & g_{12} & \cdots & g_{1N} \\ g'_{21} & g_{22} & & g_{2N} \\ \vdots & & \ddots & \\ g'_{N1} & g'_{N2} & & g_{NN} \end{bmatrix} \begin{bmatrix} V_1^s \\ V_2^s \\ \vdots \\ V_N^s \end{bmatrix} = \left(\frac{k_2}{k_1}\right) V_1 \begin{bmatrix} f_1 \cdot E_1 \\ f_2 \cdot E_2 \\ \vdots \\ f_N \cdot E_N \end{bmatrix} \tag{6}$$

where

$$g'_{mn} = g_{mn} \quad if \quad m \geq n,$$
$$g'_{mn} = g_{mn} - jk_2 f_m f_n \sin(n-m)\phi \quad if \quad m < n. \tag{7}$$

The mutual coupling terms g_{mn} are given by

$$g_{mn} = \int_{-L_m}^{L_m} \int_{-L_n}^{L_n} \cos\left(\frac{\pi\zeta_m}{2L_m}\right) \cos\left(\frac{\pi\zeta'_n}{2L_n}\right) \frac{e^{-jkR}}{R^5} \cdot$$
$$\left[k^2R^4 + (2 + 2jkR - k^2R^2) \cdot \right. \tag{8}$$
$$\left. (z_c + \zeta'_n - \zeta_m)^2 - (1 + jkR)x_c^2 \right] d\zeta'_n \, d\zeta_m.$$

The analysis procedure discussed in [6] provides the expression for the input admittance, not shown here, from which the input VSWR is also determined.

D. Genetic Algorithms

GA is one of the most popular global optimization techniques. GA optimizes the trade-off between exploring new evaluations and exploiting information computed previously. It has an implicit parallelism, wherein extensive search of hyperplanes is carried out without directly testing all hyperplanes. Its ability to maintain multiple solutions concurrently makes it less susceptible to problems of local maxima.

The length and offset of each slot are quantized into 64 values or 6 genes each. Thus for the 21-element slot array each set of input values of slot lengths and offsets may be represented by a chromosome of 252 genes. The population or family size used for these GA optimizations was 50, the cross over probability was 0.5 and the mutation probability was 0.02. A Fortran computer program developed by Carroll was used with the array analysis program [7]. During search a figure of merit is assigned to each array design (organism) according to the performance function (*pf*) as shown below,

$$pf = D^{\alpha}\left(1 - \frac{P_{load}}{P_{in}}\right)^{\beta} \frac{1}{VSWR^{\gamma}} \frac{1}{SLL^{\tau}} \tag{9}$$

where D is the directivity, SLL is the sidelobe level, and P_{load}/P_{in} is the ratio of power dissipated in the load to the input power. The directivity is calculated easily from the power radiated which is $P_{in} - P_{ref} - P_{load}$ and the power density at the maximum far field direction. The population size was kept at 50. The values of α, β, γ and τ were varied depending on the parameters that were optimized. When the bandwidth was optimized the performance function was computed over five frequencies within the band.

III. NUMERICAL RESULTS AND DISCUSSION

The results presented here are for the 21-element traveling wave array investigated by Elliott [1]. The slots are cut in a standard X-band waveguide (a = 0.9 in, b = 0.4 in., wall thickness = 0.05 in.) using round ended slots of width 1/16 in. The design frequency is 9.375 GHz and the slot spacing is 0.685 in. for a beam peak at 45°. The slots are all offset on the same side of the centerline to provide the correct phase of excitation. The results obtained in this work are typical of the improvements in performance achievable using GA optimization for a slot array. Initially we used the analysis equations [6] with MoM data for the above-mentioned traveling wave array and obtained the following results:

VSWR=1.05, P_{load}/P_{in}= 16.7%, SLL = -20.1 dB. These results compare well with the experimental results shown in Elliott's paper, VSWR=1.05 and SLL = -22 dB. The slight discrepancy in the SLL may be attributed to the edge diffraction effects of the finite ground plane, especially in the E plane. The value of P_{load}/P_{in} could not be measured but it was computed to be 12.3 % [1]. We believe that our computed results are more accurate than Elliott's since our results are closer to the experimental ones. In subsequent optimizations we nominally kept the slot data close to the original design data [1] and varied the values of slot lengths and offsets to optimize certain performance functions.

Figure 5 shows the GA optimized design where the VSWR and P_{load}/P_{in} are minimized with values of 1.011 and 2.1%, respectively. The SLL improved to -22.1 dB. Subsequently we optimized the sidelobe level to a low value of -25.2 dB. VSWR became 1.016 and P_{load}/P_{in} was 4.6%. The resulting radiation pattern is shown in Fig. 6. When the design was optimized for 5% bandwidth, the SLL is better than -21.9 dB and P_{load}/P_{in} is lower than 6.2% within the band. The radiation pattern at 9.375 GHz is shown in Fig. 7 and the computed input VSWR as a function of frequency is shown in Fig. 8. In the bandwidth optimization exercises performance parameters were computed at five frequency points within the bandwidth and minimized.

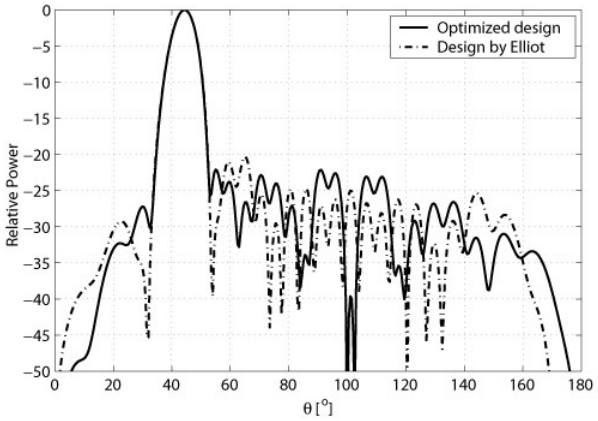

Fig. 5. Radiation pattern at 9.375 GHz (design optimized for VSWR and P_{load}).

The VSWR is better than 1.02 in the frequency range of interest in Fig. 8. When the design was optimized for 10% bandwidth, SLL was found to be better than -20.9 dB and P_{load}/P_{in} is lower than 7.1%. A typical radiation pattern is similar to that shown in Fig. 7. The computed input VSWR plot is shown in Fig. 9. Clearly the VSWR values are higher than those for the 5% bandwidth case but still the array is found to be well-matched.

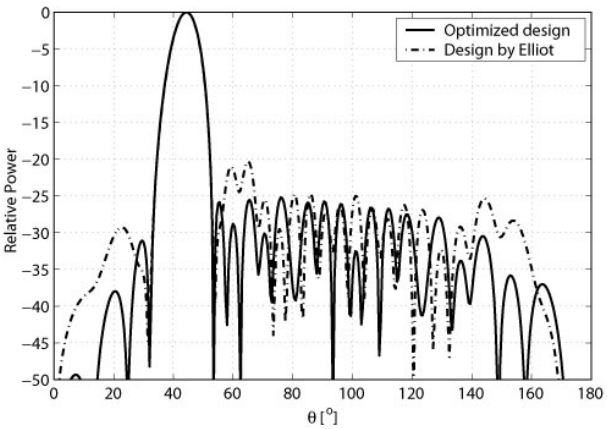

Fig. 6. Radiation pattern at 9.375 GHz (design optimized for sidelobe level).

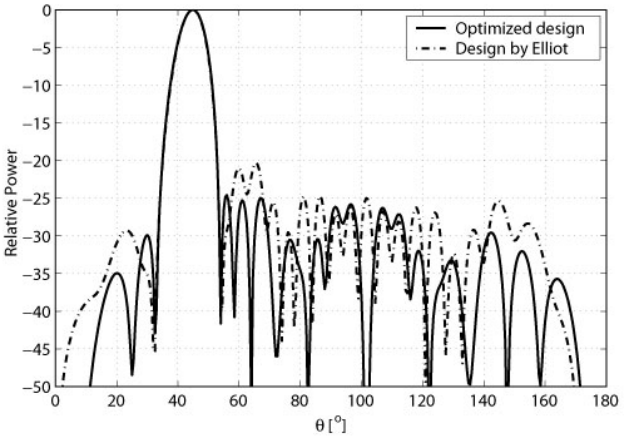

Fig. 7. Radiation pattern at 9.375 GHz (design optimized for 5% bandwidth).

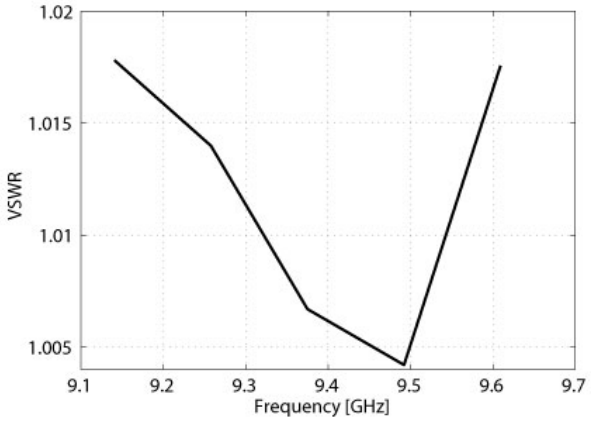

Fig. 8. VSWR versus frequency.

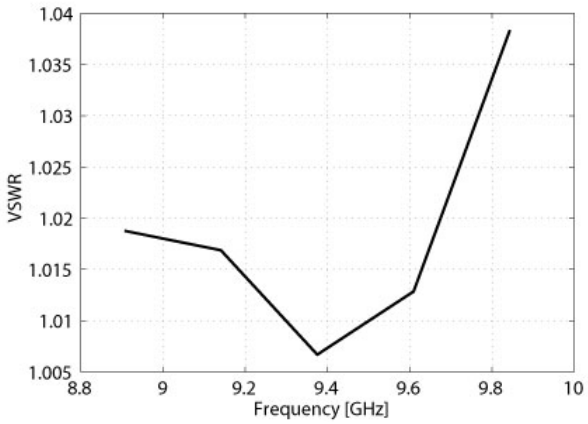

Fig. 9. VSWR versus frequency.

IV. CONCLUSIONS

We have presented the results of a genetic algorithm optimization of a traveling wave array of longitudinal slots cut in a rectangular waveguide. The input parameters, lengths, and offsets of slots were varied to optimize the performance functions such as directivity, SLL, input VSWR, power dissipated in the load, and bandwidth. GA optimizations produced significant improvement in performance over the conventional design.

REFERENCES

[1] R. S. Elliott, "On the design of traveling-wave-fed longitudinal shunt slot arrays," *IEEE Transactions on Antennas and Propagation*, vol. AP-25, no. 5, pp. 717-720, Sep. 1977.

[2] R. S. Elliott, "An improved design procedure for small arrays of shunt slots," *IEEE Transactions on Antennas and Propagation*, vol. AP-31, no. 1, pp. 48-53, Jan. 1983.

[3] D. Goldberg, Genetic Algorithms in Search, Optimization and Machine Learning, Addison-Wesley, 1989.

[4] L. G. Josefsson, "Analysis of longitudinal slots in rectangular waveguides," *IEEE Transactions on Antennas and Propagation*, vol. AP-35, pp. 1351-1357, 1987.

[5] R. S. Elliott, Antenna Theory and Design, Prentice Hall, Englewood Cliffs, NJ, 1981.

[6] M. Hamadallah, "Frequency limitations on broad-band performance of shunt slot arrays," *IEEE Transactions on Antennas and Propagation*, vol. 37, no. 7, pp. 817-823, July 1989.

[7] D. Carroll, University of Illinois, GA Driver.

Anders Jensen was born in Denmark in Feb 1975. He received his M.S.E.E. in 2000 from the Technical University of Denmark. He became a Member of IEEE in 2001. He was a visiting scholar at California State University, Northridge in 1999.

He has held positions at Saab Erricson Space in Sweden and Remec Inc in California. He is currently employed by Cushcraft Corporation as a Senior Designer Engineer in Carlsbad, California.

Sembiam Rengarajan received the Ph.D. degree in Electrical Engineering from the University of New Brunswick, Canada in 1980.

Since 1980 he has been with the department of Electrical and Computer Engineering, California State University, Northridge, CA, presently serving as a Professor. His experience includes periods at Bharat Electronics Ltd., India, NASA/JPL, UCLA, Chalmers University of Technology, Sweden, Universidad de Santiago de Compostela, Spain, Rome Laboratory of the US Air Force, the University of Pretoria, South Africa, Naval Researc Lab., Washington, D.C., and the Technical University of Denmark. He has served as a consultant to JPL, Lockheed Martin, Hughes Aircraft Company, Rantec, Saab Ericsson Space, Sweden, and the United Nations Development Program in India. His research interests include analytical and numerical techniques in electromagnetics with applications to antennas, scattering, and passive microwave components.

Dr. Rengarajan has authored/co-authored about 175 journal and conference papers. He is a Fellow of IEEE (1994), a member of USNC/URSI Commission B, and the Electromagnetics Academy. He served as the chair of the LA Chapter of IEEE Antennas and Propagation Society (1983-84), Chair of the San Fernando Valley Section of IEEE (1995), and as an Associate Editor of the IEEE Transactions on Antennas and Propagation (2000-2003). He was the chair of the Education Committee of the IEEE Antennas and Propagation Society and was an Associate Editor of the IEEE Antennas and Propagation Magazine. He has received several awards for his innovative research and technical contributions to NASA. He also received the Preeminent Scholarly publication Award from the California State University, Northridge in 2005 and a Distinguished Engineering Educator of the Year Award from the Engineers' Council of California in 1995. He serves as the secretary of the Commission B of the United States National Committee of the International Union of Radio Science (2002-present). He is an Adjunct Professor at the Electromagnetics Academy at Zhejiang University in China.

Approximate Compensation for Mutual Coupling in a Direct Data Domain Least Squares Approach using the In-situ Measured Element Patterns

(Invited Paper)

Wonsuk Choi and Tapan K. Sarkar
Department of Electrical Engineering and Computer Science, Syracuse University
Syracuse, NY 13244-1240, USA. Tel: (315) 443-3775
Email: wchoi01@syr.edu, tksarkar@mailbox.syr.edu

Oliver E. Allen and John S. Asvestas
NAVAIR, Radar and Antenna Systems Division,Code 4.5.5
B2187, S3140-A4, Unit 5
48110 Shaw Rd, Patuxent River, MD 20670. Tel (301) 342-0053
Email: oliver.allen@navy.mil, john.asvestas@navy.mil

Abstract —This paper presents a new technique for an approximate compensation of the effects of mutual coupling among the elements of an array using the measured in-situ element patterns in a direct data domain least squares algorithm. In this paper, we consider the antenna elements in the phased array to have finite dimensions, i.e., they are not omni-directional radiators. Hence, the antenna elements sample and re-radiate the incident fields resulting in mutual coupling between the antenna elements. Mutual coupling not only destroys the linear wavefront assumption for the signal of interest but also for all the interferers impinging on the array. Thus, we propose a new direct data domain approach that partly compensates for effect of mutual coupling, specifically when the jammer strengths are comparable to that of the signal. For strong interferers, a more accurate compensation for the mutual coupling is necessary using the transformation matrix through the formation of a uniform liner virtual array.

Key Words: Adaptive Processing**,** Direct Data Domain Approach, Element pattern, Mutual Coupling, Least Squares

I. INTRODUCTION

The principal advantage of an adaptive array is the ability to electronically steer the mainlobe of the antenna to any desired direction while also automatically placing deep pattern nulls along the specific directions of interferences. Recently, a direct data domain least squares (D3LS) algorithm has been proposed [1-3]. A D3LS approach [3] has certain advantages related to the computational issues associated with the adaptive array processing problem as it analyzes the data for each snapshot as opposed to forming a covariance matrix of the data using multiple snapshots, and then solving for the weights utilizing that information. A single snapshot in this context is defined as the array of complex voltages measured at the feed point of the antenna elements. Another advantage of the D3LS approach is that when the direction of arrival of the signal is not known precisely, additional constraints can be applied to fix the mainlobe beam width of the receiving array a priori and thereby reduce the signal cancellation problem.

Most adaptive algorithms assume that the elements of the receiving array are independent isotropic point sensors that sample, but do not reradiate, the incident fields. They further assume that the array is isolated from its surroundings. In a real system, however, each array element has physical dimensions. Therefore, the elements spatially sample and reradiate the incident fields. The reradiated fields interact with the other antenna elements causing the sensors to be mutually coupled. The effect of mutual coupling may provide erroneous results for the estimated strength of the signal of interest (SOI) and direction of arrival (DOA) of the signal. So several authors have proposed different algorithms to eliminate the effects of mutual coupling in adaptive processing.

Gupta and Ksienski [4] analyzed and compensated for the effects of mutual coupling using a statistical adaptive algorithm. Adve and Sarkar [5-7] illustrated degradation in the capabilities of the D3LS algorithms if the mutual couplings are not accounted for. Adve [7] used a transformation matrix to correct the voltages induced at the antenna elements to compensate for mutual coupling.

In this paper we propose a new technique for an approximate compensation for the effect of mutual coupling between the elements of an array using D3LS algorithms. In this algorithm we use the measured voltages across the loads connected to the antenna elements in the array without using such a transformation, as in [7]. This is equivalent to using the reciprocity theorem to link the measured in-situ far field element pattern to the voltage we are now measuring at the element terminals. We test the new algorithm using an array of dipoles. The mutual coupling among the dipole elements is computed using WIPL-D [8].

This article is organized as follows. In section II we formulate the problem. In section III we present simulation results illustrating the performance of the proposed method. Finally, in section IV we present our conclusions.

II. FORMULATION OF THE NEW DIRECT DATA DOMAIN APPROACH APPROXIMATELY COMPENSATING FOR THE EFFECTS OF MUTUAL COUPLING USING THE IN-SITU ELEMENT PATTERNS

A. Forward Method

Using the complex envelope representation for a uniform linear array where all the antenna elements are equally spaced, the $N \times 1$ complex vectors of phasor voltages $[V(t)]$ received by the antenna elements at a single time instance t can be expressed by

$$[V(t)] = \begin{bmatrix} V_1(t) \\ V_2(t) \\ \vdots \\ V_N(t) \end{bmatrix} = \sum_{m=1}^{M} [a(\theta_m)] s_m(t) + [n(t)] \quad (1)$$

where s_m and θ_m are the amplitude and DOA, respectively, of the m^{th} source incident on the array at the instance t, while $[a(\theta_m)]$ is the steering vector of the array toward direction θ_m and $[n(t)]$ is the noise vector at each of the antenna elements. We now analyze the data using a single snapshot of the voltages measured at the antenna terminals.

Let us assume that the signal is coming from the angular direction θ_s and our objective is to estimate its amplitude while simultaneously rejecting all other interferences. The signal arrives at each sensor at different times dependent on the DOA of the target and the geometry of the array. At each of the N antennas, the received signal is the sum of the SOI, interference, clutter and thermal noise. The interference may consist of coherent multipaths of the SOI along with clutter and thermal noise. Therefore, by suppressing the time dependence in phasor notation, we can reformulate (1) as

$$[V] = \begin{bmatrix} V_1 \\ V_2 \\ \vdots \\ V_N \end{bmatrix} = \alpha_s \begin{bmatrix} a_1(\theta_s) \\ a_2(\theta_s) \\ \vdots \\ a_N(\theta_s) \end{bmatrix} + \sum_{m=1}^{M-1} s_m \begin{bmatrix} a_1(\theta_m) \\ a_2(\theta_m) \\ \vdots \\ a_N(\theta_m) \end{bmatrix} + [n] \quad (2)$$

where α_s is the complex amplitude of the SOI, to be determined. The column vectors in this equation explicitly show the various components of the signal induced in each of the N antenna elements. In (2), a_n represents the voltage induced at the n^{th} antenna element due to a 1-Volt signal arriving from the particular direction θ. There are $M - 1$ undesired signal components in addition to the SOI. For the conventional adaptive array system, using each of K weights W_k, we can estimate the SOI through the following weighted sum

$$y = \sum_{k=1}^{K} W_k V_k \quad (3)$$

or in compact matrix form as

$$y = [W]^T [V] \quad (4)$$

where the superscript T denotes the transpose of a matrix and K is equal to number of weights. In the present method, $K = (N + 1)/2$ [3]. Also K has to be greater than the number of interferers $M - 1$, i.e. $K \geq M$.

Let us define another matrix $[S]$

$$[S] = \begin{bmatrix} S_1 \\ S_2 \\ \vdots \\ S_N \end{bmatrix} = \begin{bmatrix} a_1(\theta_s) \\ a_2(\theta_s) \\ \vdots \\ a_N(\theta_s) \end{bmatrix} \quad (5)$$

where a_n represents the voltage induced at the n^{th} antenna element due to the SOI only, with an assumed amplitude of 1V. However, the actual complex amplitude of the SOI is not 1V but α_s which is to be determined. This SOI is arriving from the particular direction θ_s. So the value of S_n in the absence of mutual coupling is

$$S_n = \exp\left[j2\pi \frac{nd}{\lambda} \cos\theta_s \right], \quad n = 1, 2, ..., N. \quad (6)$$

Then, $V_2/S_2 - V_1/S_1$ will have no components of the SOI, moreover, there are only undesired signal components left in it [6]. In a real environment, however, there is mutual coupling among the antenna elements. In this case the elements of the vector $[S]$

should be the measured voltages due to the SOI in the antenna array with an assumed amplitude of 1V. So, if we use the actual voltages from the real antenna array for the vector [*S*] and [*V*], then $V_2/S_2 - V_1/S_1$ contains undesired signal components and mutual coupling due to both the SOI and the undesired signals.

Therefore one can form a reduced rank matrix $[T]_{(K-1)\times K}$, generated from the vector [*V*] and [*S*], such that

$$\begin{bmatrix} \frac{V_2}{S_2}-\frac{V_1}{S_1} & \frac{V_3}{S_3}-\frac{V_2}{S_2} & \cdots & \frac{V_{K+1}}{S_{K+1}}-\frac{V_K}{S_K} \\ \frac{V_3}{S_3}-\frac{V_2}{S_2} & \frac{V_4}{S_4}-\frac{V_3}{S_3} & \cdots & \frac{V_{K+2}}{S_{K+2}}-\frac{V_{K+1}}{S_{K+1}} \\ \vdots & \vdots & \vdots & \vdots \\ \frac{V_K}{S_K}-\frac{V_{K-1}}{S_{K-1}} & \frac{V_{K+1}}{S_{K+1}}-\frac{V_K}{S_K} & \cdots & \frac{V_N}{S_N}-\frac{V_{N-1}}{S_{N-1}} \end{bmatrix}_{(K-1)\times K} \times \begin{bmatrix} W_1 \\ W_2 \\ \vdots \\ W_K \end{bmatrix}_{K\times 1} = \begin{bmatrix} 0 \\ 0 \\ \vdots \\ 0 \end{bmatrix}_{(K-1)\times 1} \tag{7}$$

So if we find the weighting vectors which satisfy above matrix equation, we can then eliminate all the undesired signals. Mutual coupling due to the undesired signals is also partially compensated for when we use the actual measured voltage from the real antenna array for the elements of vector [*V*] and [*S*]. To achieve a perfect compensation we have to use a transformation matrix [3] that transforms the measured voltages [*V*] to an equivalent set of voltages that is induced in a uniform linear virtual array consisting of isotropic point radiators radiating in free space. This transformation takes care of the effect of the dissimilarity in the values in the self terms of the port admittance matrix of the array which is reduced to an identity matrix when dealing with isotropic point radiators operating in free space.

In order to make the matrix full rank, we fix the gain of the array to be *C* along the direction of θ_s. This provides an additional equation resulting in

$$\begin{bmatrix} 1 & 1 & \cdots & 1 \\ \frac{V_2}{S_2}-\frac{V_1}{S_1} & \frac{V_3}{S_3}-\frac{V_2}{S_2} & \cdots & \frac{V_{K+1}}{S_{K+1}}-\frac{V_K}{S_K} \\ \frac{V_3}{S_3}-\frac{V_2}{S_2} & \frac{V_4}{S_4}-\frac{V_3}{S_3} & \cdots & \frac{V_{K+2}}{S_{K+2}}-\frac{V_{K+1}}{S_{K+1}} \\ \vdots & \vdots & \vdots & \vdots \\ \frac{V_K}{S_K}-\frac{V_{K-1}}{S_{K-1}} & \frac{V_{K+1}}{S_{K+1}}-\frac{V_K}{S_K} & \cdots & \frac{V_N}{S_N}-\frac{V_{N-1}}{S_{N-1}} \end{bmatrix}_{K\times K} \times \begin{bmatrix} W_1 \\ W_2 \\ \vdots \\ W_K \end{bmatrix}_{K\times 1} = \begin{bmatrix} C \\ 0 \\ \vdots \\ 0 \end{bmatrix}_{K\times 1} \tag{8}$$

or, in short,

$$[F][W] = [Y]. \tag{9}$$

Once the weights are solved by using (9), the complex amplitude of SOI α_s may be estimated from

$$\alpha_s = \frac{1}{C}\sum_{k=1}^{K}\frac{V_k}{S_k}W_k \,. \tag{10}$$

For the solution of [*F*][*W*]=[*Y*] in (9), the conjugate gradient method starts with an initial guess $[W]_0$ for the solution and continues with the calculation of the following [1-3]

$$[P]_0 = -b_{-1}[F]^H[R]_0 = -b_{-1}[F]^H\{[F][W]_0 - [Y]\} \tag{11}$$

where superscript *H* denotes the conjugate transpose of a matrix. At the k^{th} iteration the conjugate gradient method develops the following:

$$c_k = \frac{1}{\left\| [F][P]_k \right\|^2} \,, \tag{12}$$

$$[W]_{k+1} = [W]_k + c_k[P]_k \,, \tag{13}$$

$$[R]_{k+1} = [R]_k + c_k[F][P]_k \,, \tag{14}$$

$$b_k = \frac{1}{\left\| [F]^H[R]_{k+1} \right\|^2} \,, \tag{15}$$

$$[P]_{k+1} = [P]_k - b_k[F]^H[R]_{k+1} \,. \tag{16}$$

The norm is defined by

$$\left\| [F][P]_k \right\|^2 = [P]_k^H[F]^H[F][P]_k \,. \tag{17}$$

The above equations are applied in an iterative fashion till the desired error criterion for the residuals $\|[R]_k\|$, is satisfied, where $[R]_k = [F][W]_k - [Y]$. In our case, the error criterion is defined by

$$\frac{\|[R]_k\|}{\|[Y]\|} = \frac{\|[F][W]_k - [Y]\|}{\|[Y]\|} \leq 10^{-6}. \quad (18)$$

B. Backward Method

Next we reformulate the problem using the same data to obtain a second independent estimate for the solution. This is achieved by reversing the data sequence and then complex conjugating each term of that sequence. It is well-known in the parametric spectral estimation literature that a sampled sequence which can be represented by a sum of exponentials with purely imaginary argument can be used either in the forward or in the reverse direction resulting in the same value for the exponent. From physical considerations we know that if we solve a polynomial equation with the weights W_i as the coefficients then its roots provide the DOA for all the unwanted signals including the interferers. Therefore whether we look at the snapshot as a forward sequence as presented in the last section or by a reverse conjugate of the same sequence the final results for W_i must be the same. Hence for these classes of problems we can observe the data either in the forward direction or in the reverse direction. This is equivalent to creating a virtual array of the same size but located along a mirror symmetry line. Therefore, if we now conjugate the data and form the reverse sequence, then one gets an independent set of equations similar to (8) for the solution of the weights [W]. This is represented by

$$\begin{bmatrix} 1 & 1 & \cdots & 1 \\ \frac{V^*_N}{S^*_N} - \frac{V^*_{N-1}}{S^*_{N-1}} & \frac{V^*_{N-1}}{S^*_{N-1}} - \frac{V^*_{N-2}}{S^*_{N-2}} & \cdots & \frac{V^*_K}{S^*_K} - \frac{V^*_{K-1}}{S^*_{K-1}} \\ \frac{V^*_{N-1}}{S^*_{N-1}} - \frac{V^*_{N-2}}{S^*_{N-3}} & \frac{V^*_{N-2}}{S^*_{N-2}} - \frac{V^*_{N-3}}{S^*_{N-3}} & \cdots & \frac{V^*_{K-1}}{S^*_{K-1}} - \frac{V^*_{K-2}}{S^*_{K-2}} \\ \vdots & \vdots & \vdots & \vdots \\ \frac{V^*_{K+1}}{S^*_{K+1}} - \frac{V^*_K}{S^*_K} & \frac{V^*_K}{S^*_K} - \frac{V^*_{K-1}}{S^*_{K-1}} & \cdots & \frac{V^*_2}{S^*_2} - \frac{V^*_1}{S^*_1} \end{bmatrix}_{K\times K} \times \begin{bmatrix} W_1 \\ W_2 \\ \vdots \\ W_K \end{bmatrix}_{K\times 1} = \begin{bmatrix} C' \\ 0 \\ \vdots \\ 0 \end{bmatrix}_{K\times 1} \quad (19)$$

or in a matrix form as

$$[B][W] = [Y] \quad (20)$$

and the complex amplitude of signal α_s can again be determined by

$$\alpha_s = \left[\frac{1}{C'} \sum_{k=1}^{K} W_k \frac{V^*_{K-k+1}}{S^*_{K-k+1}} \right]^*. \quad (21)$$

Note that for both the forward and the backward methods described in Sections II.A and II.B, we have $K = (N + 1)/2$. Hence the degrees of freedom are the same for both the Forward and the Backward method. However, we have two independent solutions for the same adaptive problem. In a real situation when the solution is unknown two different estimates for the same solution may provide a level of confidence on the quality of the solution.

C. Forward-Backward Method

Finally, in this section we combine both the forward and the backward method to double the given data and thereby increase the number of weights or the degrees of freedom significantly over that of either the forward or the backward method. This provides a third independent solution. In the forward-backward model we double the amount of data by not only considering the data in the forward direction but also conjugating it and reversing the direction of increment of the independent variable. This type of processing can be done as long as the series to be approximated can be fit by exponential functions of purely imaginary arguments. This is always true for the adaptive array case. So by considering the data set V_n and V^*_{-n} we have essentially doubled the amount of data without any penalty, as these two data sets for our problem are linearly independent.

An additional benefit accrues in this case. For both the forward and the backward method, the maximum number of weights we can consider is given by $(N + 1)/2$, where N is the number of the antenna elements. Hence, even though all the antenna elements are being utilized in the processing, the number of degrees of freedom available for this approach is essentially $(N + 1)/2$. For the forward-backward method, the number of degrees of freedom can be significantly increased without increasing the number of antenna elements. This is accomplished by considering the forward and backward versions of the array data. For this case, the number of degrees of freedom Q, can reach $(N + 0.5)/1.5$. This, Q, is approximately equal to 50% more weights or number of degrees of freedom than the two previous cases of K. The equation that needs to be solved for the

weights is given by combining (8) and (19), with C′ = C, into

$$\begin{bmatrix} 1 & 1 & \cdots & 1 \\ \frac{V_2}{S_2}-\frac{V_1}{S_1} & \frac{V_3}{S_3}-\frac{V_2}{S_2} & \cdots & \frac{V_{Q+1}}{S_{Q+1}}-\frac{V_Q}{S_Q} \\ \frac{V_3}{S_3}-\frac{V_2}{S_2} & \frac{V_4}{S_4}-\frac{V_3}{S_3} & \cdots & \frac{V_{Q+2}}{S_{Q+2}}-\frac{V_{Q+1}}{S_{Q+1}} \\ \vdots & \vdots & \vdots & \vdots \\ \frac{V_Q}{S_Q}-\frac{V_{Q-1}}{S_{Q-1}} & \frac{V_{Q+1}}{S_{Q+1}}-\frac{V_Q}{S_Q} & \cdots & \frac{V_N}{S_N}-\frac{V_{N-1}}{S_{N-1}} \\ \frac{V_N^*}{S_N^*}-\frac{V_{N-1}^*}{S_{N-1}^*} & \frac{V_{N-1}^*}{S_{N-1}^*}-\frac{V_{N-2}^*}{S_{N-2}^*} & \cdots & \frac{V_Q^*}{S_Q^*}-\frac{V_{Q-1}^*}{S_{Q-1}^*} \\ \frac{V_{N-1}^*}{S_{N-1}^*}-\frac{V_{N-2}^*}{S_{N-3}^*} & \frac{V_{N-2}^*}{S_{N-2}^*}-\frac{V_{N-3}^*}{S_{N-3}^*} & \cdots & \frac{V_{Q-1}^*}{S_{Q-1}^*}-\frac{V_{Q-2}^*}{S_{K-2}^*} \\ \vdots & \vdots & \vdots & \vdots \\ \frac{V_{Q+1}^*}{S_{Q+1}^*}-\frac{V_Q^*}{S_Q^*} & \frac{V_Q^*}{S_Q^*}-\frac{V_{Q-1}^*}{S_{Q-1}^*} & \cdots & \frac{V_2^*}{S_2^*}-\frac{V_1^*}{S_1^*} \end{bmatrix} \times \begin{bmatrix} W_1 \\ W_2 \\ \vdots \\ W_Q \end{bmatrix}_{Q\times 1} = \begin{bmatrix} C \\ 0 \\ \vdots \\ 0 \end{bmatrix}_{(2Q-1)\times 1} \tag{22}$$

or in matrix form as

$$[FB]\,[W] = [Y]. \tag{23}$$

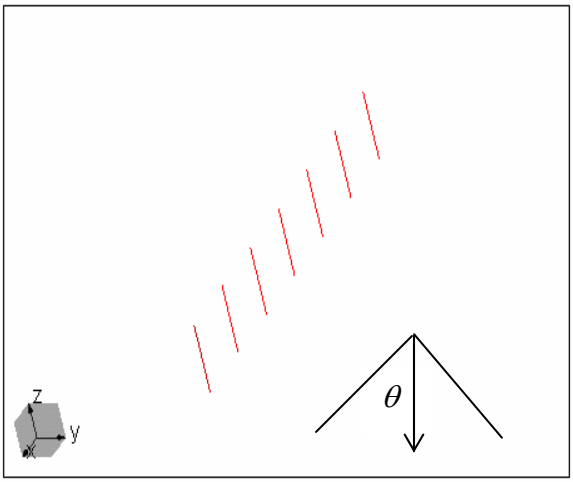

Fig. 1. A uniform linear array of dipoles.

III. SIMULATION RESULTS

As a first example, we consider a signal of unit amplitude arriving from θ_s = 95°. We form a 7-element dipole array of half wavelengths long and centrally loaded with 50 Ω as shown in Figure 1. The parameters for the dipole antenna array are given in Table I. We consider the mutual coupling in this array of dipoles and analyze the antenna array using WIPL-D [8]. The goal is to recover the complex amplitude of the SOI using the proposed method, in the presence of mutual coupling using the insitu measured element patterns. However, for numerical simulation we use the voltages measured at the loads of the antenna elements as the insitu element patterns are related to these voltages through reciprocity. The proposed algorithm tries to maintain the gain of the array along the direction of SOI while automatically placing nulls along the directions of the interferences. In this simulation we take the SOI of unit amplitude to be arriving from θ_s = 95°. Two jammers are present at 80° and 110°. The intensities of these jammers are varied from 1 to 30 [V/m]. We assume that we know the DOA of the signal but we need to estimate its complex amplitude. In addition, we do not know the complex amplitudes or the DOA of the interferers nor do we have any probabilistic description of the thermal noise. We assume that we have 20 dB of signal-to-noise ratio at the antenna elements. The output signal-to-interference-plus-noise ratio (Output SINR) is shown in Figure 2. The output SINR is an indicator of the accuracy of our estimate. It is defined as

$$\mathrm{SINR}_{\mathrm{out}} = 20\log\left|\frac{\alpha_s}{\alpha_s - \alpha_{est}}\right| \tag{25}$$

where, the numerator α_s provides the true value for the complex amplitude of the desired signal and α_{est} is the output providing the estimated complex amplitude. The denominator term $\alpha_s - \alpha_{est}$ then provides the residual interference plus noise error, which resulted from the processing. Results are shown for the three different methods (Forward method, Backward method and Forward-Backward method) in Figure 2. It is seen from Figure 2 that as the intensity of the interferer increases the results become inaccurate if we do not correct for the mutual coupling.

Table I. Parameters defining the elements of the dipole array.

Number of elements in array	7
Length of z-directed wires	$\lambda/2$
Radius of wires	$\lambda/200$
Spacing between wires	$\lambda/2$
Loading at the center	50 Ω

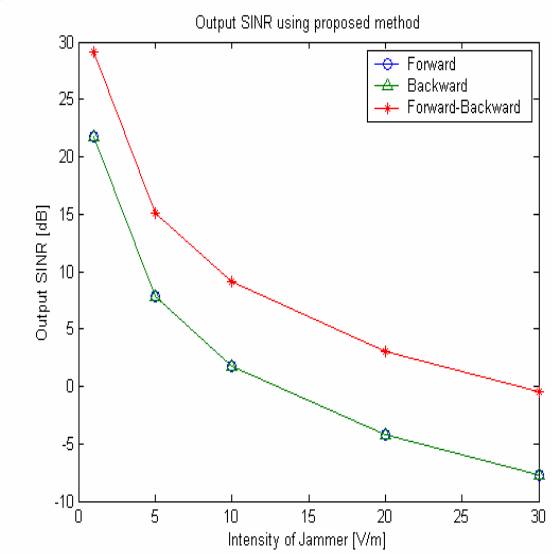

Fig. 2. Output SINR as a function of the intensity of the jammer for a 7-element ULA of half-wave dipoles without correcting for the mutual coupling.

Figure 3a presents the results for the D3LS method which does account for the mutual coupling between the antenna elements using the transformation matrix and forming a uniform linear virtual array as illustrated in [3]. Figure 3a shows the improvement in the performance of the output SINR for the Forward method and Figure 3b for the Forward-Backward method. As seen in Figures 3, the proposed method deteriorates gracefully as the intensity of the jammers increase and a more accurate analysis, through the use of a uniform linear virtual array to compensate for the mutual coupling between the antenna elements.

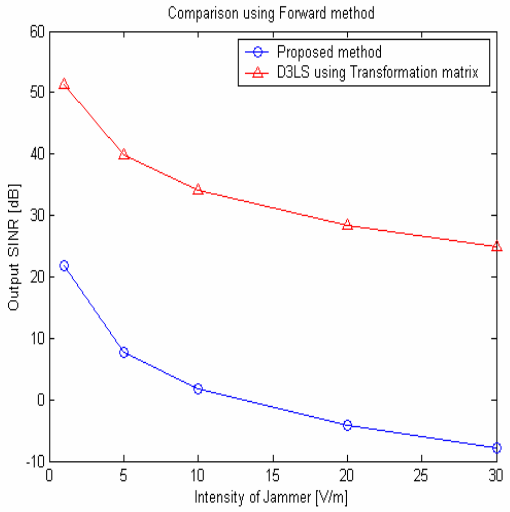

Fig. 3(a). Comparison of the output SINR using the Forward processor between the proposed method and the use of a more accurate treatment of mutual coupling through the transformation matrix.

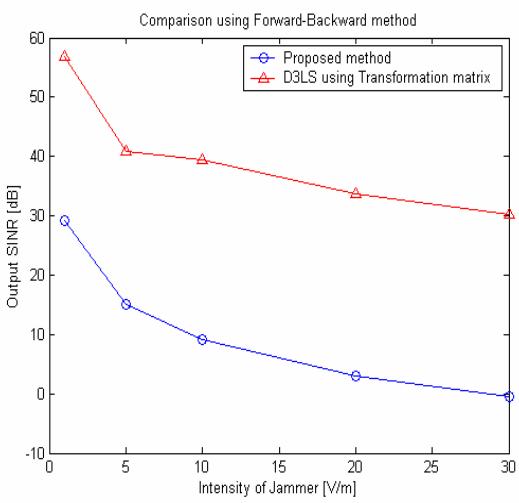

Fig. 3(b). Comparison of the output SINR using the Forward-Backward processor between the proposed method and the use of a more accurate treatment of mutual coupling through the transformation matrix.

For the second example, we study the performance of the proposed method as we increase the number of antenna elements both with and without an accurate compensation for the mutual coupling between the elements of the array. In this simulation we use the same geometry of the antenna array as in the first simulation. The DOA of the SOI and the jammers are also the same. The intensities of the jammers are 30 [V/m]. The number of antenna elements in the array is increased from 7 to 31. In Figure 4 we present the output SINR as a function of the number of antenna elements using the proposed method. It is seen that if we significantly increase the number of antenna elements then it is not necessary to perform an accurate compensation for the mutual coupling.

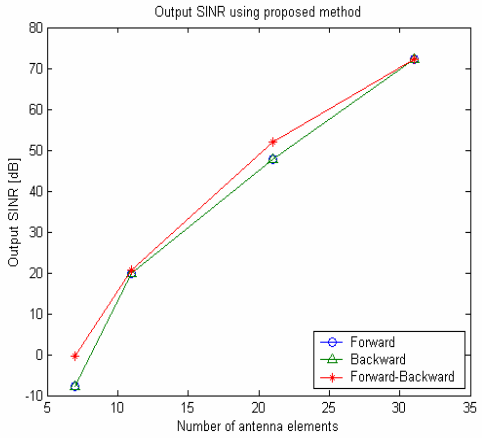

Fig. 4. Output SINR as a function of the number of antenna elements in the array using the proposed methods.

Figures 5a and 5b present the output SINR when we do and do not perform an accurate compensation for the mutual coupling between the elements in the array. It is seen that accurately compensating for the mutual coupling provides a more accurate estimate for the SOI.

For the third example, we simulate the same array but put some additional dummy antenna elements at the ends of the antenna array. In this case, the measured element pattern will be approximately the same for all the elements of the array including the ones at the end. We receive the same signaland the interferers using this modified array, which has dummy elements at the end, and apply the proposed adaptive algorithm to the voltages received by this modified array. In this simulation we take the SOI of unit amplitude to be arriving from $\theta_s = 90°$. Two jammers are present at 70° and 120°. And the intensity of the SOI is 1 [V/m] and the intensity of the interferers is varied from 30 [V/m] to 1000 [V/m]. Simulation results are shown in Tables II through V.

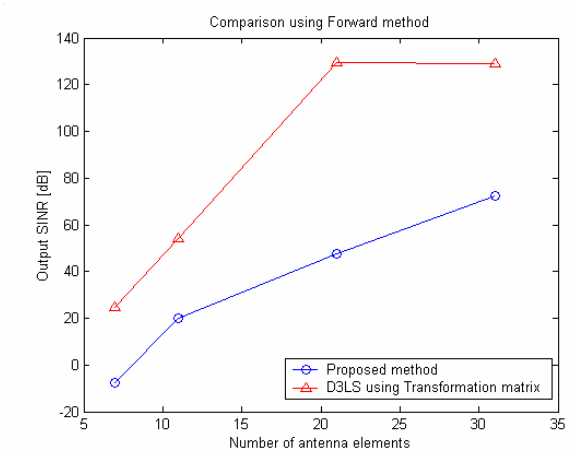

Fig. 5(a). Comparison of the output SINR between the proposed method and a more accurate compensation for mutual coupling using the Forward processor.

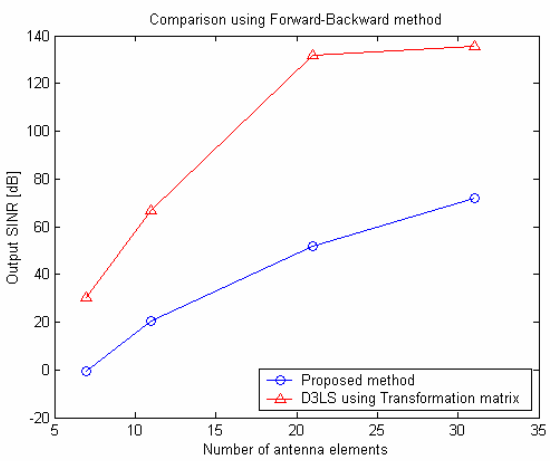

Fig. 5(b). Comparison of the output SINR between the proposed method and a more accurate compensation for mutual coupling using the Forward-Backward processor.

Table II. Output SINR as a function of the number of dummy elements at the two ends of the array (Intensity of SOI: 1 [V/m], Intensity of jammers: 30[V/m])

# of elements		Number of dummy elements (each side)			
		0	1	2	3
7	α ($SINR_{out}$)	1.8105 – 1.1179i (–2.8029 dB)	1.2645 – 0.2704i (8.4445 dB)	0.8695 + 0.2312i (11.5191 dB)	1.0054 + 0.0340i (29.2558 dB)
11		1.0565 + 0.3828i (8.2464 dB)	1.0416 + 0.0528i (23.4450 dB)	0.9950 – 0.0132i (37.0187 dB)	1.0120 + 0.0078i (36.8500 dB)
21		0.9976 + 0.0009i (51.9185 dB)	0.9983 + 0.0005i (55.2192 dB)	0.9986 + 0.0005i (56.5733 dB)	1.0000 – 0.0006i (64.9739 dB)

Table III. Output SINR as a function of the number of dummy elements at the two ends of the array (Intensity of SOI: 1 [V/m], Intensity of jammers: 100 [V/m])

# of elements		Number of dummy elements (each side)			
		0	1	2	3
7	α ($SINR_{out}$)	3.7017 – 3.7265i (–13.2605 dB)	1.8816 – 0.9013i (–2.0131 dB)	0.5649 + 0.7706i (1.0616 dB)	1.0181 + 0.1134i (18.7982 dB)
11		1.1882 + 1.2761i (–2.2112 dB)	1.1388 + 0.1760i (12.9874 dB)	0.9834 - 0.0439i (26.5611 dB)	1.0401 + 0.0262i (26.3925 dB)
21		0.9920 + 0.0029i (41.4609 dB)	0.9945 + 0.0017i (44.7613 dB)	0.9953 + 0.0017i (46.1159 dB)	1.0000 – 0.0019i (54.5161 dB)

Table IV. Output SINR as a function of the number of dummy elements at the two ends of the array (Intensity of SOI: 1 [V/m], Intensity of jammers: 500 [V/m])

# of elements		Number of dummy elements (each side)			
		0	1	2	3
7	α ($SINR_{out}$)	14.5086 –8.6324i (–27.2399 dB)	5.4082 – 4.5066i (–15.9925 dB)	–1.1753 + 3.8532i (–12.9178 dB)	1.0905 + 0.5670i (4.8188dB)
11		1.9409 + 6.3806i (–16.1906 dB)	1.6941 + 0.8802i (–0.9920 dB)	0.9168 - 0.2197i (12.5817 dB)	0.9168 – 0.2197i (12.4131 dB)
21		0.9602 + 0.0143i (27.4818 dB)	0.9724 + 0.0086i (30.7822 dB)	0.9767 + 0.0084i (32.1365 dB)	1.0001 – 0.0094i (40.5368 dB)

As shown in the tables the estimation for the SOI can be improved significantly when we use additional dummy elements at the end of the array.

For the final example, we consider a semi-circular array (SCA). The SCA is analyzed using WIPL-D. The signal intensity is then recovered using the proposed method, by using the voltages induced in the elements of the array. The antenna elements have the same dimension as presented in Table I. In this simulation we consider the SOI of unit amplitude is arriving from θ_s = 100°. And there are two jammers which are coming from 60° and 120°. The signal intensity is set to 1 [V/m] and the intensities of these jammers are varied from 1 to 50 [V/m]. In this case we observe the performance of this method as a function of the number of antenna elements in the circular array. As the number of elements increases the array dimension also increase as shown in Table VI. Table VII provides the output SINR for the circular array as a function of the number of antenna elements. Again, it is clear that a more accurate compensation for the mutual coupling is necessary when the intensity of the jammer increases.

Again the performance of the adaptive algorithm improves as the number of elements in the array is increased. In addition, when the jammers are much stronger than the signal a more accurate method for treating mutual coupling between the antenna elements presented in [3] should be employed.

IV. REASON FOR A DECLINE IN THE PERFORMANCE OF THE ALGORITHM WHEN THE INTENSITY OF THE JAMMER IS INCREASED

The performance of the proposed method deteriorates when one increases the intensity of the jammers with respect to the SOI, is because when one is using the embedded element pattern, it is equivalent to use of the measured voltages at the loads of the

Table V. Output SINR as a function of the number of dummy elements at the two ends of the array (Intensity of SOI: 1 [V/m], Intensity of jammers: 1000 [V/m])

# of elements		Number of dummy elements (each side)			
		0	1	2	3
7	α ($SINR_{out}$)	28.0172 –7.2649i (–33.2605 dB)	9.8164 – 9.0133i (–22.0131 dB)	–3.3505 + 7.7064i (–18.9384 dB)	1.1809 + 1.1341i (-1.2018 dB)
11		2.8818 +12.7611i (–22.2112 dB)	2.3883 + 1.7604i (–7.0126 dB)	0.8335 – 0.4394i (6.5611 dB)	1.4013 + 0.2616i (6.3925 dB)
21		0.9204 + 0.0285i (21.4612 dB)	0.9448 + 0.0171i (24.7616 dB)	0.9535 + 0.0168i (26.1159 dB)	1.0003 – 0.0188i (34.5164 dB)

Table VI. Radius of the SCA

# of elements	Radius
7	1.115 m
11	1.752 m
21	3.344 m
31	4.936 m

Table VII. Output SINR as a function of the number of antenna elements in the SCA using the Forward method. (Intensity of signal: 1 [V/m])

# of elements		Intensities of the two Jammers		
		1 [V/m]	30 [V/m]	50 [V/m]
7	α ($SINR_{out}$)	1.6755 + 0.1147i (3.2846 dB)	21.2636 + 3.4414i (-26.2578 dB)	34.7727 + 5.7356i (-30.6948 dB)
11		1.3045 - 0.1666i (9.1918 dB)	10.1335 - 4.9987i (-20.3506 dB)	16.2226 - 8.3311i (-24.7876 dB)
21		0.9242 - 0.0528i (20.6891 dB)	-1.2743 - 1.5834i (-8.8534 dB)	-2.7905 - 2.6389i (-13.2903 dB)
31		0.9894 - 0.0284i (30.3767 dB)	0.6820 - 0.8509i (0.8342 dB)	0.4700 - 1.4182i (-3.6027 dB)

antenna elements due to the SOI only. This value is affected by the port admittance matrix of the array. Since when mutual coupling is present, the port admittance matrix is not diagonal. Because of these additional terms the equations used in (8), (19) and (22) does not exactly cancel the signal when we take the difference between the two ratios in the elements of the matrix. That is why when the jammer intensity increases it is necessary to introduce a more accurate compensation methodology using the transformation matrix. The use of a SCA provides worse results than a linear array as the influence of the port admittance matrix is more dominant in the circular array as the influence from neighboring elements are increased in a SCA over that of a linear array.

V. CONCLUSION

We have presented a new technique that compensates for the effect of mutual coupling among the elements of an array based on a direct data domain least squares algorithms using the embedded element patterns only. Since no statistical methodology is employed in the proposed adaptive algorithm, there is no need to compute a covariance matrix. Therefore, this procedure can be implemented on a general-purpose digital signal processor for real time implementations. As shown in the numerical examples, the proposed method provides a good estimate for the complex amplitude of the signal of interest when the jammer intensities are not high. We also investigated the relationship between the number of antenna elements in the array and the estimate of the signal estimation, both in the presence and absence of dummy elements at end of the array. When we increase the number of elements of the array we can get a higher output signal-to-interference plus noise ratio (output SINR), even for a non-linear array like a semi-circular array.

REFERENCES

[1] T. K. Sarkar, S. Park, J. Koh and R. A. Schneible, "A Deterministic Least Squares Approach to Adaptive Antennas," *Digital Signal Processing - A Review Journal*, Vol. 6, pp. 185-194, 1996.

[2] T. K. Sarkar, S. Nagaraja and M. C. Wicks, "A Deterministic Direct Data Domain Approach to Signal Estimation Utilizing Nonuniform and Uniform 2-D Arrays," *Digital Signal Processing – A review Journal,* Vol. 8, pp. 114-125, 1998.

[3] T. K. Sarkar, M. Wicks, M. Salazar-Palma and R. Bonneau, *Smart Antennas*, John Wiley & Sons, 2003.

[4] I. J. Gupta and A. A. Ksienski, "Effect of mutual coupling on the performance of adaptive arrays," *IEEE Trans. Antennas and Propagation*, vol. AP-31, pp. 785–791, Sept. 1983.

[5] R. S. Adve and T. K. Sarkar, "Compensation for the Effects of Mutual Coupling in Adaptive Algorithms", *IEEE Trans. Antennas and Propag.*, Vol. 48, No. 1, pp. 86–94, Jan 2000.

[6] W. S. Choi and T. K. Sarkar, "Phase-Only Adaptive Processing Based on a Direct Data Domain Least Squares Approach Using the Conjugate Gradient Method", *IEEE Trans. Antennas and Propag.*, Vol. 52, No. 12, pp. 3265–3272, Dec. 2004.

[7] K. Kim, T. K. Sarkar, and M. Salazar Palma, " Adaptive Processing Using a Single Snapshot for a Nonuniformly Spaced Array in the Presence of Mutual Coupling and Near-Field Scatterers," *IEEE Transactions on Antennas & Propagation*, Vol. 50, No. 5, pp. 582-590, May 2002.

[8] B. M. Kolundzija, J. S. Ognjanovic and T. K. Sarkar, *WIPL-D* (for Windows manual), Artech House, Norwood, Mass., 2000.

[9] D. H. Johnson and D. E. Dudgeon, *Array Signal Processing*, Prentice Hall, Englewood Cliffs, NJ, 1993.

[10] S. Haykin, *Adaptive Filter Theory,* Prentice Hall, Englewood, Cliffs, NJ, 1986.

[11] T. K. Sarkar, S. Park, R. Adve, J. Koh, K. Kim, Y. Zhang, M. C. Wicks and R. D. Brown, "A Deterministic Least-Squares Approach to Space-Time Adaptive Procession (STAP)," *IEEE Transactions on Antennas & Propagation*, Vol. 49, No. 1, pp. 91-103, Jan. 2001.

[12] K. Kim, T. K. Sarkar, H. Wang and M. Salazar Palma, "Direction of Arrival Estimation Based on Temporal and Spatial Processing Using a Direct Data Domain Approach, " *IEEE Transactions on Antennas and Propagation*, Vol. 52, Issue: 2, , pp. 533-541, Feb. 2004.

Wonsuk Choi was born in Seoul, Korea. He received the B.S. degree from Dankook University, Korea, in 1997 and the M.S. degree from Syracuse University, Syracuse, NY. He is currently working toward the Ph.D. degree in the Department of Electrical Engineering at Syracuse University.

He is a Research Assistant at Syracuse University. His current research interests include digital signal processing related to adaptive antenna problems and space-time adaptive signal processing.

Tapan K. Sarkar received the B.Tech. degree from the Indian Institute of Technology, Kharagpur, in 1969, the M.Sc.E. degree from the University of New Brunswick, Fredericton, NB, Canada, in 1971, and the M.S. and Ph.D. degrees from Syracuse University, Syracuse, NY, in 1975.

From 1975 to 1976, he was with the TACO Division of the General Instruments Corporation. He was with the Rochester Institute of Technology, Rochester, NY, from 1976 to 1985. He was a Research Fellow at the Gordon McKay Laboratory, Harvard University,

Cambridge, MA, from 1977 to 1978. He is now a Professor in the Department of Electrical and Computer Engineering, Syracuse University. His current research interests deal with numerical solutions of operator equations arising in electromagnetics and signal processing with application to system design. He obtained one of the "best solution" awards in May 1977 at the Rome Air Development Center (RADC) Spectral Estimation Workshop. He received the Best Paper Award of the IEEE Transactions on Electromagnetic Compatibility in 1979 and in the 1997 National Radar Conference. He has authored or coauthored more than 280 journal articles and numerous conference papers and 32 chapters in books and fifteen books, including his most recent ones, *Iterative and Self Adaptive Finite-Elements in Electromagnetic Modeling* (Boston, MA: Artech House, 1998), *Wavelet Applications in Electromagnetics and Signal Processing* (Boston, MA: Artech House, 2002), *Smart Antennas* (John Wiley & Sons, 2003), and *History of Wireless* (John Wiley & Sons, 2005).

Dr. Sarkar is a Registered Professional Engineer in the State of New York. He received the College of Engineering Research Award in 1996 and the Chancellor's Citation for Excellence in Research in 1998 at Syracuse University. He was an Associate Editor for feature articles of the IEEE Antennas and Propagation Society Newsletter (1986-1988), Associate Editor for the IEEE Transactions on Electromagnetic Compatibility (1986-1989), Chairman of the Inter-commission Working Group of International URSI on Time Domain Metrology (1990–1996), distinguished lecturer for the Antennas and Propagation Society from (2000-2003) and on the board of directors of ACES (2000-2006) and vice president of the Applied Computational Electromagnetics Society (ACES). He is currently a member of the IEEE Electromagnetics Award board and an associate editor for the IEEE Transactions on Antennas and Propagation. He is on the editorial board of Digital Signal Processing – A Review Journal, Journal of Electromagnetic Waves and Applications and Microwave and Optical Technology Letters. He is a member of Sigma Xi and International Union of Radio Science Commissions A and B.

He received Docteur Honoris Causa both from Universite Blaise Pascal, Clermont Ferrand, France in 1998 and from Politechnic University of Madrid, Madrid, Spain in 2004. He received the medal of the *friend of the city of Clermont Ferrand*, France, in 2000.

John S. Asvestas was born in Athens, Greece. He received the B.S.E., M.S.E., and Ph.D. degrees in Electrical Engineering from The University of Michigan, Ann Arbor, in '63, '65, and '68, respectively. He has worked at The University of Michigan Radiation Laboratory, the Technical University of Denmark Applied Mathematical Physics Laboratory, the University of Delaware Mathematics Department, the Radar Systems Group of Hughes Aircraft Company (currently Raytheon), and the Corporate Research Center of Grumman Corporation (currently Northrop/Grumman). He presently works for NAVAIR in the Radar and Antenna Systems Division. His main interest is in analytical and computational electromagnetics.

Oliver Eric Allen received the B.S.I.E. degree from the University of Wisconsin-Madison in 1982, the B.E.E. degree from the Johns Hopkins University, Baltimore, MD in 1989, the M.S.E.E. degree from the University of Colorado-Boulder in 1992 and the D.Sc. degree in Electrical Engineering from the George Washington University, Washington DC in 2004.

From 1982 to 1985, Dr. Allen was detailed to the Fleet Analysis Center in Corona, California; the Naval Air Rework Facility in Norfolk, Virginia; and the Naval Electronics Systems Engineering Activity in St. Inigoes, Maryland while he was assigned to the Naval Material Command, Washington, D.C. From 1985 to 1987, he was with the Naval Air Test Center, Anti-Submarine Aircraft Test Directorate in Patuxent River, Maryland. In 1987 he transferred to the Electromagnetic Environmental Effects Division of the Naval Air Warfare Center. During the 1989-1990 academic-year he conducted research at the National Institute of Standards and Technology in Boulder, Colorado while attending the University of Colorado. In 1997 he served a two-year assignment as the Science and Technology Advisor to the Commander U.S. Seventh Fleet in Yokosuka, Japan. From 1999 to 2003 he was detailed to the Office of Naval Research, Ocean, Atmosphere and Space Department in Arlington, Virginia directing research in non-acoustic anti-submarine warfare. He is currently the Chief Radar Systems Engineer at the Naval Air Systems Command in Patuxent River, MD.

Multiple Beam Antenna Technology for Satellite Communications Payloads

(Invited Paper)

Sudhakar Rao, Minh Tang, and Chih-Chien Hsu
Lockheed Martin Commercial Space Systems
100 Campus Drive, Newtown, PA 18940
Email: sudhakar.rao@lmco.com

***Abstract*—**This paper reviews multiple beam antenna (MBA) technologies that are applicable for satellite communications payloads. It provides design, performance analysis, and hardware implementation aspects of various types of MBAs that include reflector MBAs, phased array MBAs, and lens MBAs. Parametric design of these MBAs and RF analysis for coverage gain and inter-beam isolation are given. Recent advances and trends in MBA technologies for space applications are discussed.

***Index Terms*—**Antenna arrays, lens antennas, multiple beam antennas, reflector antennas

I. INTRODUCTION

THERE has been a tremendous growth in the use of multiple beam antenna (MBA) payloads for both commercial and military communications satellites over the last decade [1-6]. MBAs are currently being used for direct broadcast satellites (DBS) such as EchoStar-X, DirecTV-4S, DirecTV-7S etc., personal communication satellites (PCS) such as Anik-F2, SpaceWay, CIEL-2, etc., mobile communications satellites such as ACeS, Thuraya, MSV, TerraStar, ONDAS, etc., military communications satellites such as WGS, MUOS, TSAT etc., and navigation satellites such as GPS-2, GPS-3, etc. These antenna systems for most cases provide a contiguous coverage of a geographical region as seen by the satellite by using high-gain multiple spot beams that provide downlink (satellite-to-ground) and uplink (ground-to-satellite) signals. Main advantages of the MBAs when compared to conventional contoured beam antennas are:

- Significantly higher antenna gain due to smaller size of the beam, resulting in improved effective isotropic radiated power (EIRP) for the downlink and improved gain-to-noise temperature (G/T) for the uplink,
- Increase in effective spectral bandwidth by several folds due to re-use of the frequency channels over several spot beams,
- Allows the use of much smaller ground terminals.

Fig. 1 illustrates typical contoured beam coverage and multiple beam coverage of the continental United States (CONUS) from a geo-stationary satellite. Contoured beam antenna shown in Fig. 1a has typical edge-of-coverage (EOC) gain of 30 dBi and has no frequency re-use (frequency re-use factor FRF is 1.0). The MBA shown in Fig. 1b has 68 overlapping spot beams arranged in a hexagonal grid lattice with an adjacent beam spacing of 0.52 degrees and beam diameter of 0.6 degrees at the triple-beam crossover point. The EOC gain is about 45 dBi (15 dB more than the contoured beam antenna) and has FRF of 17 with a 4-cell frequency re-use scheme. FRF is defined as the ratio of the number of beams to the number of frequency cells (typically 3, 4 or 7) per polarization. The multiple beams can be formed using either a single aperture or multiple aperture antennas and could use different frequency cell re-use schemes. Fig. 2 illustrates the

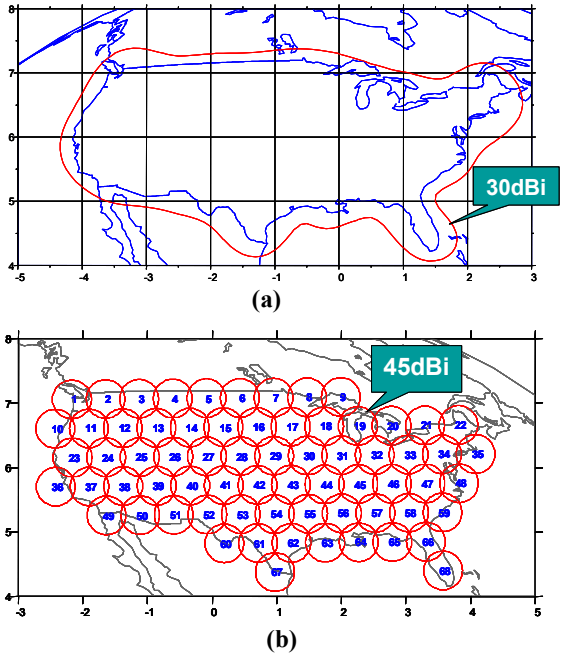

Fig. 1. Comparison of CONUS coverage beams with (a) conventional contoured beam antenna, and (b) multiple beam antennas (X-axis: Azimuth & Y-axis: Elevation).

aperture and frequency re-use concepts for MBAs. The aperture concepts include single, three, or four antenna apertures (reflectors or lenses), whereby adjacent beams are generated by different apertures and form an inter-leaved spot beam coverage on ground. The advantage of multiple aperture MBA is that it allows increasing the spacing between beams produced by the same aperture by a factor of 1.73 for a 3-aperture MBA and by a factor of 2.0 for a 4-aperture MBA.

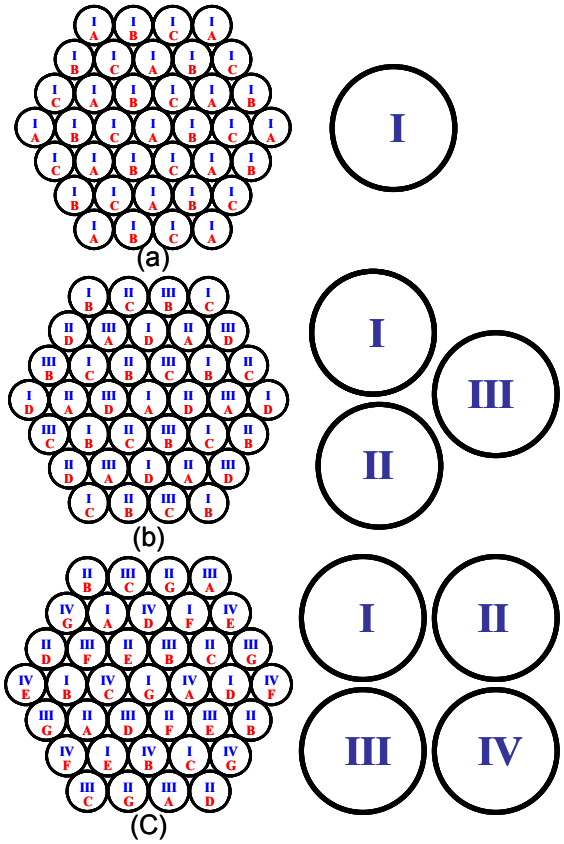

Fig. 2. Aperture and frequency re-use concepts for MBAs: (a) single-aperture MBA with 3-cell re-use scheme, (b) three-aperture MBA with 4-cell re-use, and (c) four-aperture MBA with 7-cell re-use.

The larger beam spacing allows increase in the feed horn size such that it optimally illuminates the reflector with increased beam EOC gain and reduced side lobe levels. Fig. 3 shows typical plot applicable to reflector or lens MBAs showing the impact of feed horn size (assuming single feed per beam without beam-forming networks) on the MBA performance. Single aperture MBAs have typical feed sizes of less than 1 wavelength and therefore have low efficiency values of around 45% and high sidelobes. On the other hand, a 4-aperture MBA has typical feed size of more than 2 wavelengths, resulting in antenna efficiency values of more than 75% and sidelobe levels of –25 dB. An increase in antenna gain of more than 2.2 dB and sidelobe improvement of about 8 dB are achieved with a 4-aperture reflector/lens

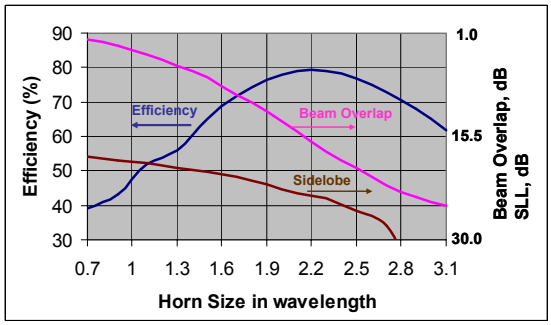

Fig. 3. MBA performance as a function of feed horn size.

MBA when compared to a single-aperture MBA (both employ single feed per beam). The main objectives of the MBA design are:

- Maximize the minimum coverage gain of each beam including pointing error,
- Minimize the gain loss due to beam scan effects,
- Maximize the aggregate co-polar isolation (C/I) among beams that re-use the same frequency,
- Maximize the cross-polar isolation (C/X) for each beam, and
- Maximize the beam congruency among uplink and downlink beams (for PCS, MSS applications).

The coverage region for most applications needs to be contiguously covered by the satellite with multiple spot beams. A hexagonal grid layout is usually preferred due to tight packing of the beams. The optimum beam diameter for circular coverage with uniform beams, total number beams, and adjacent beam spacing are given approximately as

$$\theta_0 = 0.6155\theta_c / N\,, \tag{1}$$

$$N_T = 1 + 3N(N+1)\,, \tag{2}$$

$$\theta_s = 0.866\theta_0 \tag{3}$$

where θ_0 is the beam diameter at triple-beam crossover level, N is the number of rings of the hexagonal layout excluding the central beam, N_T is the total number of beams, θ_c is the coverage diameter, and θ_s is the spacing between adjacent beams.

The typical beam layout of an MBA for global coverage from a geo-stationary satellite is shown in Fig. 4. It employs 91 overlapping spot beams with a hexagonal grid layout. The spacing between adjacent beams is 1.732 degrees and the beam diameter at triple beam cross-over is 2.0 degrees. Table 1 shows the

design variables for a global coverage with 17.6 degrees diameter.

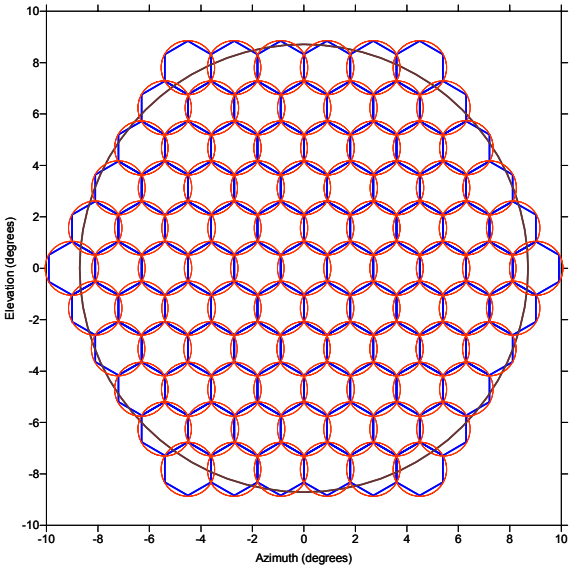

Fig. 4. Global coverage of an MBA with 91 over-lapping spot beams.

Table 1. Beam size versus number of beams for global coverage.

Beam Diameter	Beam Spacing	No. of Rings	Total No. of Beams
($?_0$)	($?_s$)	(M)	(M_T)
0.7	0.606	15	721
0.8	0.693	14	631
0.9	0.779	12	469
1.0	0.866	11	397
1.1	0.953	10	331
1.2	1.039	9	271
1.4	1.212	8	217
1.8	1.559	6	127
2.0	1.732	5	91
2.4	2.078	5	91
2.8	2.425	4	61

For national coverage with non-circular shape, the number of beams is obtained using the equation

$$N_T = 1.27 A_C / (\theta_s)^2 \qquad (4)$$

where A_C is the area of the coverage region in square degrees. Multiple beam antennas for satellite communications can be broadly classified into three categories: a) reflector MBAs, b) lens MBAs, and c) phased array MBAs. These three types of MBAs have been employed in the past for satellite communications. Both reflector and lens MBAs require feed arrays, where each beam is generated with single or multiple feeds. The phased array MBA employs the complete array to generate each beam. Waveguide lens MBAs have been used on DSCS III satellite [7, 8], but suffer from the disadvantages of limited bandwidth due to zoning of the lens to reduce mass, high mutual coupling among waveguide elements of the lens, and poor return loss. Dielectric lens MBAs are not preferred for space applications, especially for the transmit downlink, because of the electro-static discharge (ESD) and out-gassing associated with dielectric materials in vacuum. Reflector MBAs are most frequently used in the space industry due to their superior RF performance reduced mass, reduced cost, and mature technology. Multiple aperture reflector MBAs, where adjacent beams are generated from different apertures, are preferred over single reflector MBAs at higher frequencies such as Ku, Ka, and EHF bands where multiple reflectors (3 or 4) can be accommodated on the spacecraft. However, for mobile satellites at L-band and S-band frequencies, a single reflector MBA with beam-forming network is more commonly used due to spacecraft accommodation issues associated with large unfurlable mesh reflectors. Phased array MBAs have been developed mostly for military communications, where extensive on-orbit beam re-configurability is required. Details of these MBAs are given in the following sections.

II. REFLECTOR MBAS

Reflector MBAs are most commonly used for satellite communications due to better RF performance in terms of coverage gain and C/I, payload simplicity, reduced cost, and mature technology. These MBAs are classified into the following types: (a) single reflector with a single feed per beam, (b) single reflector with over-lapping feed clusters, and (c) multiple reflectors with single element per beam. The reflectors are typically offset-fed parabolic reflectors and the feed elements are usually horns. Type (a) requires electrically small feed horns of about one wavelength in diameter in order to achieve high adjacent beam overlaps, which result in gain values that are 2 dB to 3 dB lower than what could be achieved using optimal horn size as shown in Fig. 3 [1]. Type (b) design requires low-level beam-forming networks (LLBFNs where beams are formed before the high power amplifiers for transmit and after the low-noise amplifiers for receive) to provide element sharing among beams (typically shared among 7 beams) and beam combining functions (typically 7 elements used to form a beam). An advantage of LLBFN is that the network losses do not impact EIRP or G/T performance of the MBA. Type (b) MBA is typically used for mobile satellites at low frequencies such as L-band and S-band due to large physical sizes of the reflectors (larger than 5 meter) and feed arrays. These applications employ typically one large deployable mesh reflector and a feed array due to limitations of the spacecraft bus to accommodate multiple large reflectors. Type (c) employs multiple reflectors, each being illuminated with its own feed array, with three or four independent apertures. Each beam is generated

with a single feed horn of more than 2 wavelengths in diameter that provides optimal illumination on the reflector. Type (c) MBAs are used at Ku-band, Ka-band, and EHF, where smaller physical size of the reflector (typically less than 100 in. diameter) allows accommodation of multiple reflectors on the spacecraft.

a) Design and Analysis

Design and analysis of reflector MBAs are addressed in this section. Closed form equations are presented for the design of MBAs and their performance analysis, based on Gaussian beam representation of primary and secondary patterns. The beam parameters and the reflector parameters are shown in Fig. 5. Typical beam layout of a four-reflector MBA with 4-cell re-use scheme is shown in Fig. 5(a). The two "A" beams come from the same reflector in this example. It is to be noted that the feed horn size depends on the number of

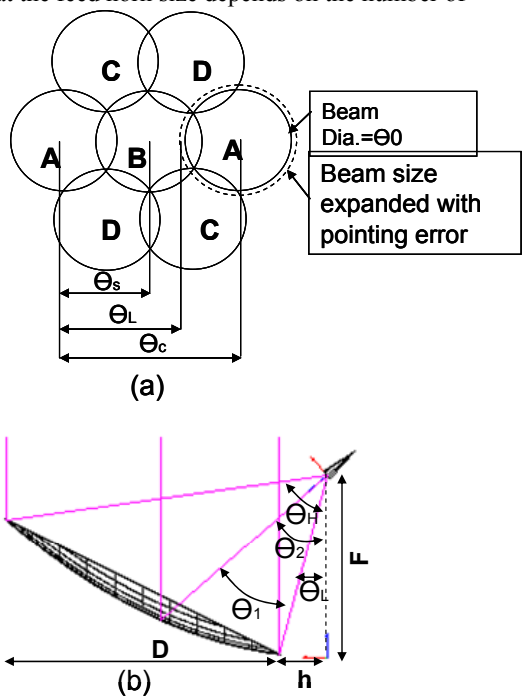

Fig. 5. (a) Beam Parameters with 4-aperture MBA with 4-cell re-use, and (b) Reflector Parameters.

reflectors used for the MBA and is independent of the frequency re-use scheme. The spacing between adjacent beam centers coming from the same reflector for a single reflector, 3-reflector, 4-reflector, and 7-reflector MBAs is given as

$$\theta_C^{1,3,4,7} = G^{1,3,4,7}\theta_s \ . \tag{5}$$

The constant G in the above equation is 1.0, 1.732, 2.0, and 2.646 for a single-reflector, 3-reflector, 4-reflector, and 7-reflector MBAs, respectively. The beam diameters shown in Fig. 5(a) need to be expanded with the satellite pointing error in order to evaluate the coverage gain and isolation into the re-use beams. The closest distance of the re-use beams from the beam peak is given by

$$\theta_L = \theta_C - 0.5\theta_0 - \Delta\theta^P \ . \tag{6}$$

The design of the MBA starts with the beam size requirements or the number of beams over a desired coverage region, and the frequency re-use plan. The beam size is defined as the diameter of the beam at the triple-beam crossover point, and is X dB below the beam peak (a typical value for X is about 4 dB). For a four-aperture MBA, the reflector size can be determined using the following equation

$$\theta_0^X = 65\left[\frac{X}{3}\right]^{0.5}\left(\frac{\lambda_L}{D}\right) \tag{7}$$

where θ_0^X is the full beam-width at X dB below beam peak, λ_L is the wavelength at the lowest frequency of the band, and D is the reflector diameter. The constants relating the beam-width to the normalized reflector size are 65.0, 75.0, and 83.9 for X=3, 4, and 5, respectively.

The focal-length to reflector diameter ration (F/D) depends on the coverage size and the maximum number of beam-widths scanned from the bore-sight direction. It also depends on the mechanical packaging issues on the spacecraft. For large scans (more than 4 beam-widths), a larger F/D ratio is desired to minimize the beam distortions caused by the coma lobes and to minimize gain loss due to scan. Typical F/D ratio for satellite antennas is in the range 1.0 to 1.6. The offset clearance h is selected such that the blockage-free condition is maintained for the maximum scanned beam, and is given approximately using the equation

$$h \geq 2F\tan\theta_{sm} \tag{8}$$

where θ_{sm} is the maximum scan angle towards the reflector offset from the bore-sight direction. The feed size and type of feed are the key design parameters for the MBAs. The feed diameter d_m depends on the beam spacing, number of apertures, and the reflector geometry, and is given as

$$d_m^{1,3,4,7} = G^{1,3,4,7}\theta_s / S_F \tag{9}$$

where S_F is the scan factor that depends on the reflector geometry and is given by:

$$S_F = \frac{1+X\left(\frac{D}{4F}\right)^2}{1+\left(\frac{D}{4F}\right)^2}\left[\frac{1+\cos\theta_2}{2F}\right] \tag{10}$$

and X = 0.30 for T < 6, and X = 0.36 for T > 6, and T is the feed illumination taper (positive dB) on the edge of

the reflector. The angular parameters θ_{l2} of the reflector geometry are given in [2].

The feed size and type of feed are critical to MBA design. For multiple-reflector MBA, the types of feeds applicable are Potter horns, high-efficiency horns, and corrugated horns. Corrugated horns are rarely used due to the thick walls required that make the electrical aperture smaller. Potter horns have broader beams and lower efficiency of about 70%. High-efficiency horns employ TE_{11}, TE_{12}, TE_{13}, etc. modes that make the aperture illumination uniform in both E-plane and H-planes and provide high efficiency values of up to 93% [5, 10]. The feed horn pattern can be modeled using a Gaussian beam representation which is given by

$$E(\theta) = \exp[-A(\theta/\theta_b)^2] \tag{11}$$

where θ_b is the half angle of the 3 dB beamwidth and is expressed as a function of efficiency as

$$\theta_b = [31 - 0.0041(93-\eta)^2 + 0.341(93-\eta)](\lambda/d_m) \tag{12}$$

where η is the efficiency of the feed horn. The feed illumination taper on the edge of the reflector T is given as

$$T = -20\log_{10}[\exp\{-0.3467(\theta_1/\theta_b)^2\}]. \tag{13}$$

The minimum coverage area directivity, taking into effect the scan loss, peak to edge gain variation of the beam, and the satellite pointing error is given as

$$D_C = 10\log_{10}\left[\left(\frac{\pi D}{\lambda_L}\right)^2 \eta_i\right] - GL(\delta_m) - B(\delta_m) - 10\log_{10}\left(\frac{0.5\theta_0^X + \Delta\theta^P}{0.5\theta_0^X}\right)^2 \tag{14}$$

where δ_m is the maximum number of beamwidths scanned from boresight, GL is the gain loss due to scan, and η_i is the antenna efficiency. GL and η_i are given as

$$GL(\delta) = \frac{0.0015\delta^2}{\left[(F/D_P)^2 + 0.02\right]^2} + \frac{0.011\delta}{\left[(F/D_P)^2 + 0.02\right]} \tag{15}$$

$$\eta_i = 4\cot^2(\theta_1/2)\left[1-\cos^n(\theta_1/2)\right]^2\left\{\frac{n+1}{n^2}\right\}\left[1.025 + 0.5119(\eta_f - 0.74) - 7.542(\eta_f - 0.74)^2\right] \tag{16}$$

and n is related to the feed taper as

$$n = \frac{-0.05T}{\log_{10}(\cos(\theta_1/2))}. \tag{17}$$

The 3 dB beamwidth of the reflector MBA at boresight and as a function of scan is given by

$$\theta_0^3 = (0.058T^2 + 0.171T + 58.44)(\lambda/D)$$

$$\theta_0^3(\delta) = \theta_0^3 10^{0.05GL(\delta)} \tag{18}$$

$$B(\delta_m) = X\left[\frac{\theta_0^X}{\theta_0^X(\delta_m)}\right]^2. \tag{19}$$

The copolar isolation (C/I) can be calculated by the power addition of all the J interfering beams that re-use the same frequency as the beam of interest and comparing with the directivity of the beam at any angular location of the coverage beam and is given as

$$C/I = D_C - 10\log_{10}\left[\left(\frac{\pi D}{\lambda}\right)^2 \eta_f\right] + \sum_{j=1}^{J}\left\{GL(\delta_j) + B_j\left(\frac{\theta_{js} + 0.5\theta_j - \Delta\theta^P}{0.5\theta_j}\right)^2\right\} \tag{20}$$

where θ_j is the diameter of jth interferer, and θ_{js} is the distance from the closest edge of the jth interferer to the beam of interest.

The C/I values are typically 10 dB, 13 dB, and 18 dB for a 3-cell, 4-cell, and 7-cell re-use schemes of the MBA.

b) Advanced Reflector MBA Technologies

This section describes some of the recent advances in reflector MBA technology. Fig. 6 illustrates evolution of reflector MBA technology. Configuration "A" is a conventional MBA employing separate set of reflectors for uplink and downlink frequency bands. The uplink reflectors are typically 1.5 times smaller than the downlink reflectors. Configuration "B" employs dual-band reflector antennas being fed with corrugated horns in order to reduce the number of apertures from 8 to 4. It suffers from reduced EOC gain and inferior C/I due to reduced efficiency of the feed (about 54% efficiency) caused by thick walls. The dual-band MBA (DMBA) configuration "C" overcomes the above limitations by employing smooth-walled dual-band high efficiency horns [5, 9, 10]. A novel MBA employing "stepped-reflector antenna" (SRA) technology, as illustrated in configuration "D" in Fig. 6, has been developed and patented by Lockheed Martin Commercial Space Systems (LMCSS) [4, 11]. It combines feed horn advancements with improved reflector technology in order to achieve significant performance improvements for future DMBAs. The high efficiency horns have been developed earlier for single narrow band applications, where desired higher order modes are generated with step discontinuities. In order to achieve

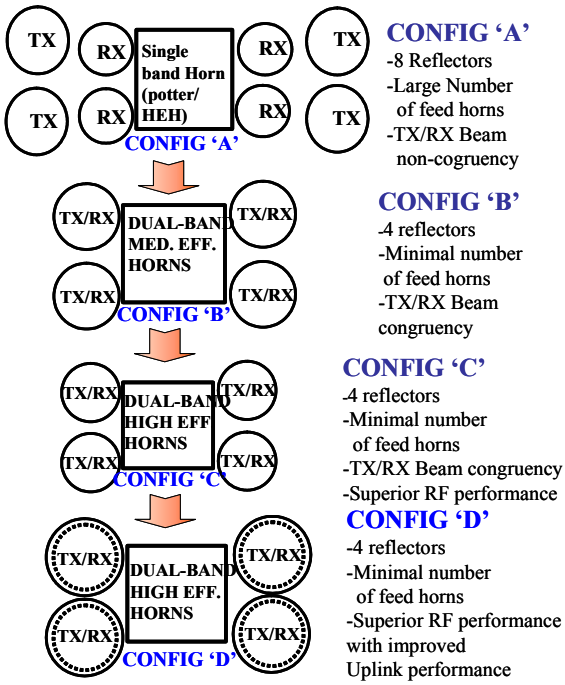

Fig. 6. Evolution of Reflector MBA Technology.

high efficiency values over both Tx and Rx bands of the DMBAs, a number of slope-discontinuities have been used to generate higher order $TE_{1,n}$ modes [10]. The horn geometry is synthesized using iterative analysis that employs mode-matching technique combined with a generalized scattering matrix (GSM) to evaluate the performance of the horn. Desired requirements for efficiency return loss, and cross-polar levels can be specified over both Tx and Rx frequencies and the synthesis method can be implemented by minimizing the cost function using mini-max optimization. Fig. 7 shows performance of a 2.27 in. diameter high-efficiency horn compared with a conventional corrugated horn. Both horns were used to evaluate detailed performance of a dual-band reflector with 80 in. reflector diameter, 116 in. focal length, and a 26 in. offset clearance. The reflector surface is shaped to broaden the Rx beam in both cases. Table 2 summarizes performance comparison of the DMBA with both types of horns. The DBHEH, when compared to a corrugated horn, improves EOC gain by about 0.9 dB at Tx and by about 2.0 dB at Rx, and improves C/I by about 3.0 dB.

DMBA configuration "D" developed by LMCSS includes use of the stepped-reflector antenna (SRA) technology to further improve the DMBA performance. The concept of SRA is illustrated in Fig. 8, where it employs outer annular region that are stepped and attached to the central portion of the reflector. Both central and annular stepped regions can be shaped to improve the RF performance and the transition region can be blended into the reflector to avoid abrupt discontinuities. The height h of the step is designed in conjunction with the DBHEH feed phase characteristics at the Rx frequencies in order to provide a 180-degree "phase reversal" at the step resulting a "flat-topped" Rx beams with significantly improved G/T.

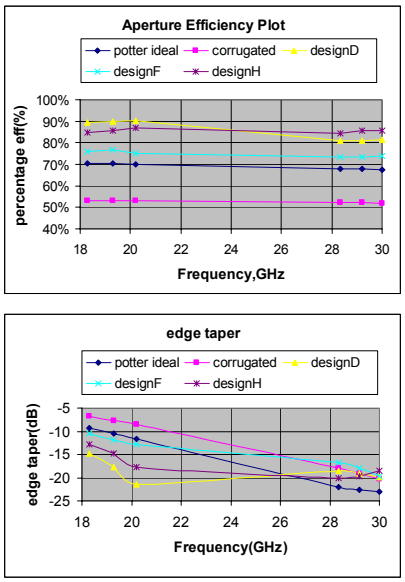

Fig. 7. Aperture efficiency and edge illumination taper comparison of various MBA horns.

Table 2. Performance Comparison of DMBAs "B" & "C" using conventional corrugated horns and DBHEH.

Performanc Paramete	CONVENTIONA HORN	HIGH EFF. DESIGN
	TX/RX	TX/RX
Efficiency, %	54 / 52	85 / 85
Edge Taper,	7/18	13 / 17
Primary C/X, dB	33 / 33	20 / 23
EOC Directivity, dBi	43.8 / 41.7	44.7 / 43.7
C/I, 3-cell (dB)	11.1 / 13.0	14.2 / 11.6
C/I, 4-cell (dB)	12.0 / 15.8	15.7 / 14.5
C/I, 7-cell (dB)	18.2 / 19.5	22.7 / 21.9
C/X, dB	30.0 / 28.0	21.0 / 20.0

The near-field phase distribution of the SRA is plotted in Fig. 9 and shows the desired 180-degree phase reversal near the transition region of the step. As a result, the Rx beam patterns of the SRA shown in Figure 10 have flat-topped patterns with increased EOC gain. Rx beam EOC gain improvement is about 1.2 dB when compared with Configuration "C". By combining the feed phase quadratic variation and the phase variation due to the step, the step size can be minimized and the step can be blended with the reflector shape. The SRA concept works well for wide angle coverage regions and shows significant improvements in Rx gain, Rx C/I, Tx C/I and moderate improvement of Tx gain when compared to a reflector without the step(s).

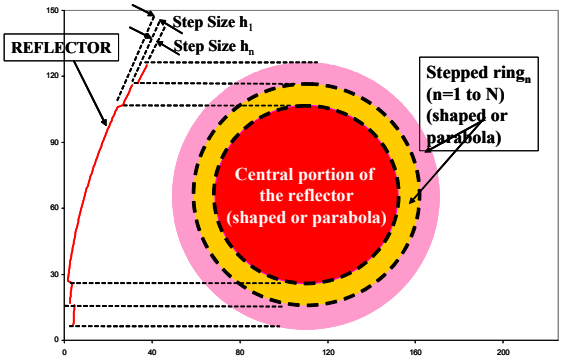

Fig. 8. Concept of "Stepped-Reflector Antenna".

c) DBS Antennas

LMCSS has developed advanced antenna payloads for direct broadcast satellites for local channel broadcast over the CONUS. These include multi-aperture reflectors with high efficiency feeds. Figure 11 shows typical coverage using multiple spot beams covering

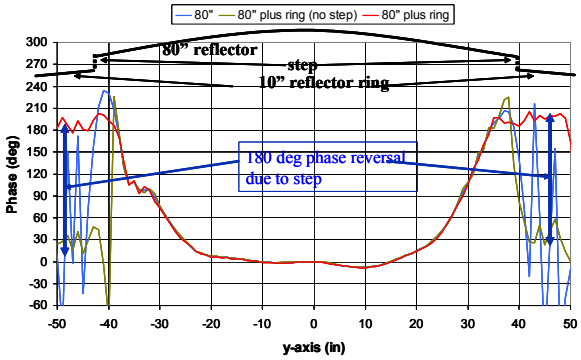

Fig. 9. Near-Field Phase Distribution of SRA.

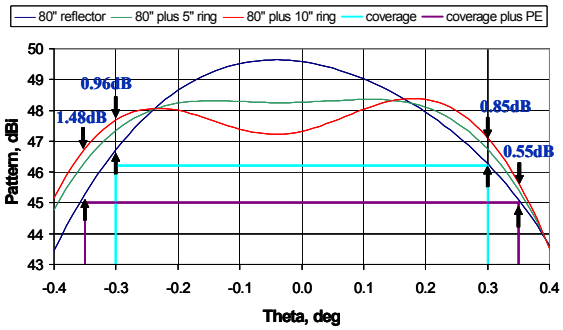

Fig. 10. Computed DMBA patterns of SRA showing "flat-topped" main beam with increased EOC gain.

designated market areas (DMAs). Key limitation for these systems is the downlink C/I performance that has significant impact on the link availability. Use of high efficiency horns and selective shaping approach to the reflectors alleviate this limitation by providing improved C/I compared to conventional antennas. Typical EIRP and aggregate C/I performance for a specific channel are shown in Figs. 12 and 13. These beams reuse the frequency channel. The aggregate C/I has improved by

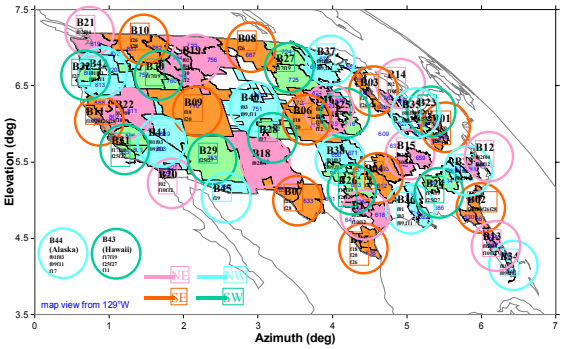

Fig. 11. DMA Coverage for a DBS Satellite.

more than 4.0 dB by employing high efficiency horns. The worst C/I performance is better than 15 dB.

d) Reconfigurable Antennas

LMCSS has been developing reconfigurable payloads for HIEO and GEO satellites using "non-focused reflector" (NFR) antennas being fed with a small active feed array [12]. Main advantages are that it minimizes the number of feed array elements required for a given coverage, and has better scan performance due to the fact that the feed array location relative to the reflector is unchanged.

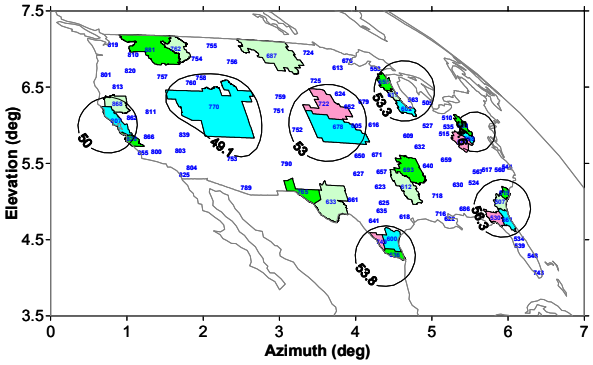

Fig. 12. EIRP Plots for the DMA Coverage of a channel.

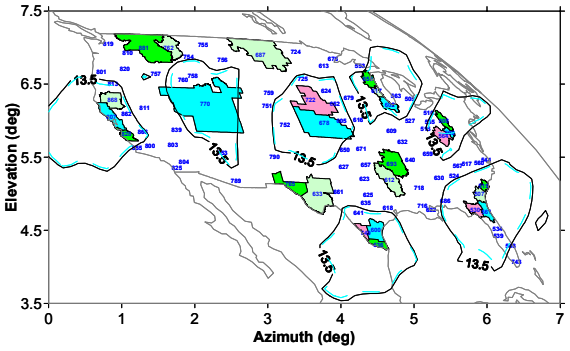

Fig. 13: Aggregate C/I Performance of the DMAs reusing the same frequency.

A quadratic phase distribution is generated by "opening-up" or "closing-in" the parent paraboloidal reflector. The NFR broadens the element beams significantly that allows reducing the number of feed array elements, when compared to a conventional parabolic reflector with de-focused feed array used for mobile satellites. The concept of NFR is illustrated in Fig. 14. Design examples of a HIEO satellite using a 37 element feed array are discussed. All the feed array elements are excited uniformly in amplitude and the relative phase excitations are varied through variable phase shifters to electronically reconfigure the beam as the satellite goes through the highly elliptical orbit. Fig. 15 shows the element beams covering CONUS and synthesized beams for different yaw angles are shown in Fig. 16. The NFR technology is applicable to both HIEO and GEO satellites and has the advantages of reconfiguring the beam for different orbital locations of the satellite and provides continuous reconfiguration of the beam at different times of the HIEO satellite.

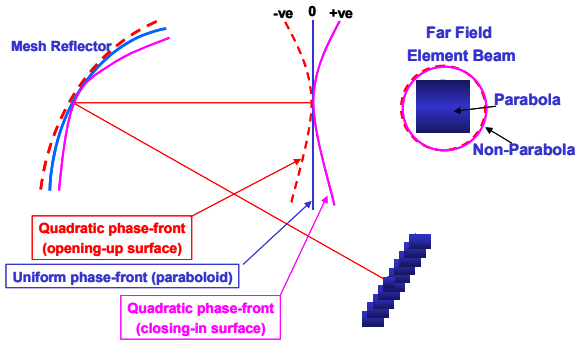

Fig. 14. NFR Concept for Reconfigurable Beam Antennas.

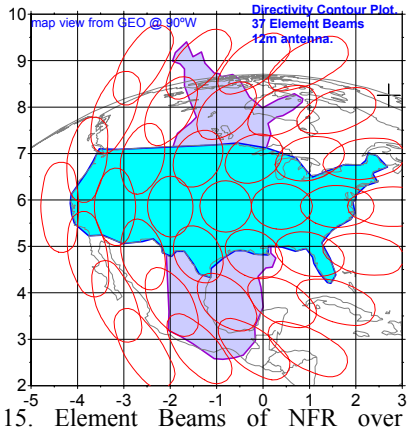

Fig. 15. Element Beams of NFR over CONUS Coverage.

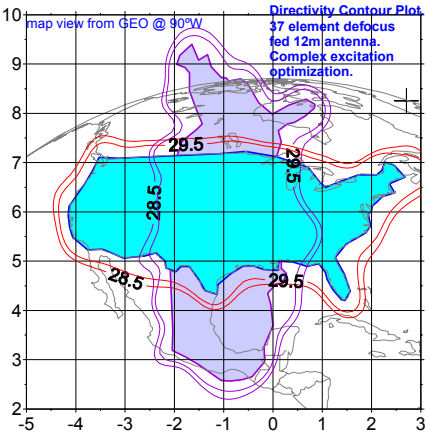

Fig. 16. Synthesized CONUS Beam of a HIEO Satellite for different Yaw angles of the satellite.

III. LENS MBAs

The lens MBAs are similar to reflector MBAs with the exception that they work on the transmission of RF signals through the lens material instead of reflection from the surface of the reflector. Because of this, lens MBAs have symmetrical geometries and are located typically on nadir deck of the spacecraft. Lenses have more degrees of freedom than reflector MBAS, but are rarely used for satellite communications due to limited bandwidth, accommodation issues on spacecraft, increased mass, and susceptibility to electro-static discharge in the case of dielectric lenses. Lens MBAs are classified into dielectric lens MBAs and waveguide lens MBAs.

a) Dielectric Lens MBAs

It was demonstrated that a thin spherical lens satisfying the Abbe sine condition, has virtually no coma lobes and therefore has wide scan properties [13, 14]. The radiated beams from such a lens are virtually invariant with scan resulting in maximum coverage gain and better sidelobe isolation among frequency re-use beams. Advantages of spherical lens are that it has very

low scan loss (< 0.7 dB over +/ 10 beamwidths of scan), ease of fabrication, and significant mass reduction (about 75%) achievable through zoning of the lens using finite steps. Surface matching of the lens is usually realized by means of circumferential slots on both surfaces of the lens. A triangular ray-tube analysis method for accurate prediction of lens antennas has been developed by Chan et al [15]. Fig. 17 shows the zoned dielectric lens using Rexolite material and designed with 5 zones. Measured radiation patterns of the lens MBA are shown in Fig. 18.

Fig. 17. Zoned Dielectric Lens Antenna at EHF.

b) Waveguide Lens MBAs

Waveguide lenses for MBA applications have been used for the DSCS program. It is very similar to the dielectric lens, except it is made up of large number of waveguide elements (circular or rectangular) with varied lengths in order to compensate for the phase variation across the lens. The waveguide lens needs to be zoned in order to minimize the mass. Because of the zoning, the bandwidth of the waveguide lens is narrow and is typically of the order 5% or less. It also suffers from gain loss due to high mutual coupling among the waveguide elements and poor return loss, but is preferred over dielectric lens MBAs for space applications. Details of the waveguide lens are given earlier [7, see Fig. 3.139 for a photograph of an X-band waveguide lens MBA].

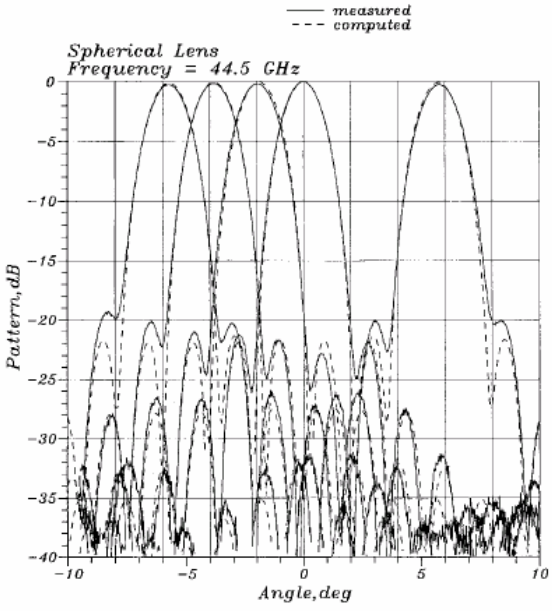

Fig. 18. Radiation Patterns of an EHF Dielectric Lens MBA.

IV. PHASED ARRAY MBAs

The phased array MBAs have been employed in the past for satellite communications requiring multiple beams. The advantage with phased array MBA is that it requires a single aperture to generate all the beams. Because of the limited bandwidth capability of phased arrays, it requires separate antennas, one for Tx and the other for Rx. These phased arrays typically employ horns as radiating elements. Array elements are arranged in either a square lattice or a hexagonal lattice. Maximum size of the element is determined by the grating lobe criteria and is given as

$$\frac{d^{S,H}}{\lambda_H} \le \frac{1.0,1.1547}{\sin\theta_G + \sin\theta_{sm}} \tag{21}$$

where θ_{sm} is the maximum scan angle over the coverage region of MBA, θ_G is the closest location of the grating lobe, λ_H is the wavelength at highest frequency of operation, and $d^{S,H}$ are the maximum size of the horn element for square and hexagonal array lattices of the array. For example, the feed horn size is about 3 wavelengths with θ_{sm} as 9 degrees and θ_G as 13 degree The element directivity is a function of the element size and the efficiency, and is given in by

$$D_e = 10\log_{10}\left[\frac{4\pi A_e}{\lambda^2}\eta_e\right] \quad \text{dBi} \tag{22}$$

where A_e is the element area, and η_e is the element efficiency which is a function of the type of the radiating element. In order to size the phased array in terms of number of elements, the scan loss of the array needs to be calculated. The scan loss is a function of element roll-off and is given in dB as

$$SL = 3\left[\frac{\theta_{sm}}{0.5\theta_3}\right]^2 \tag{23}$$

where θ_{sm} is the maximum scan angle of the coverage region and θ_3 is the half-power beam-width of the element which is given by

$$\theta_3 = A\lambda / d_e \tag{24}$$

where the constant A varies with the type of the horn and is 63, 70, 55, and 52 for high-efficiency circular horn, Potter horn, dominant-mode square or rectangular horn, and high-efficiency square/rectangular horns, respectively. The number of elements required for the array is given as

$$N = 10^{0.1(D_A - D_e)} \tag{25}$$

where D_A is the required antenna directivity to meet the desired edge-of-coverage gain of the MBA and is given as

$$D_A = G_m + X + L_S + SL + T_L + I_m \tag{26}$$

where G_m is the minimum coverage gain, X is the triple beam overlap of the MBA (typically 3 dB to 5 dB), SL is the scan loss, L_S is the antenna loss, T_L is the illumination taper loss of the array, and I_m is the implementation margin to account for gain degradation due to amplifier failures, amplitude and phase excitation errors, and thermal effects.

Fig. 19 shows typical block diagram of the phased array transmit MBA. Each of the M beams are synthesized independently using phase only synthesis with fixed amplitude distribution of the array. The desired amplitude distribution can be achieved by using SSPAs with varying RF power. The beam forming network is realized at low-level (before amplifiers) in order to minimize output losses.

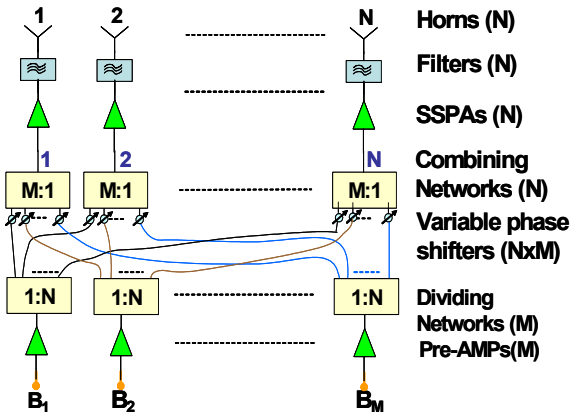

Fig. 19. Block Diagram of the Phased Array MBA.

There are a number of ways that beamforming for phased array MBAs can be realized. The block-diagram shown in Fig. 19 employs corporate BFN using couplers. This is considered suitable for most of the commercial satellite applications requiring moderate bandwidths of less than 15%. However, for wide bandwidth and multi-band applications Rotman lens BFN (Fig. 20) is widely used. The advantage of the Rotman lens BFN is that the beam locations are invariant with frequency, since it produces true-time delay response over the array. A three-dimensional

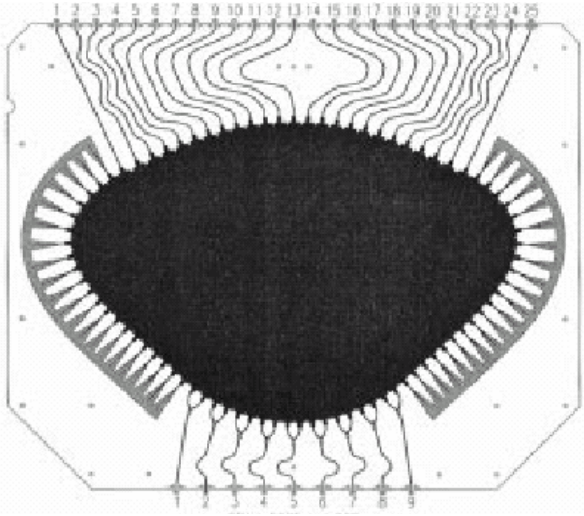

Fig. 20. Trace of a single Rotman lens with 9 beam ports and 25 array ports.

stack of row and column Rotman lenses feeding an array with hexagonal grid has been presented [16]. The number of Rotman lenses required is the maximum number of elements in a row of the array plus the maximum number of beams in a row of the coverage region. Rotman lenses can be implemented in either strip-line or microstrip medium. Dual-port excitation method for the beam ports is often employed in order to minimize the spill-over losses of the lens. Figure 20 shows the trace of a single Rotman lens with 9 beam ports and 25 array ports. The three-dimensional stack of 34 Rotman lenses feeding an array of 489 elements is shown in Fig. 21. Fig. 22 shows radiation patterns of a prototype array with Rotman lens feed network.

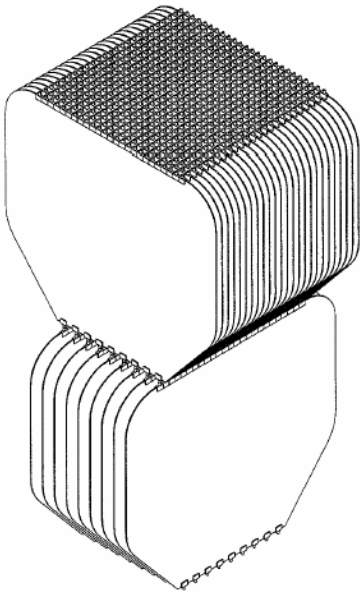

Fig. 21. Rotman Lens BFN with row and column boards.

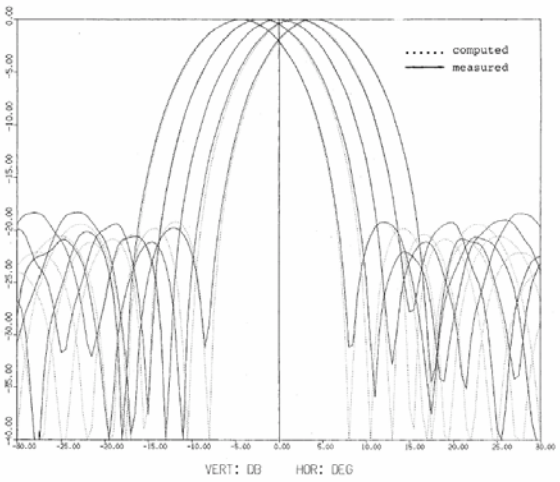

Fig. 22. Radiation Patterns of an Array Antenna with Rotman Lens BFN.

V. CONCLUSIONS

A review of multiple beam antenna technology applicable for satellite communication payloads is presented. It includes reflector MBAs, lens MBAs, and phased array MBAs. Design of MBAs, performance analysis, and hardware implementation aspects are discussed. The reflector MBAs are widely used for satellite applications due to mature technology, reduced cost, and improved performance.

REFERENCES

[1] S. Rao, G. Morin, M. Tang, and K.K. Chan, "Development of a 45 GHz Multiple-Beam Antenna for Military Satellite Communications," IEEE Trans. Antennas Propagat., Vol. 43, pp. 1036-1047, October 1995.

[2] S. Rao, "Design and Analysis of Multiple-Beam Reflector Antennas," IEEE Antennas Propagat. Magazine, Vol. 41, pp. 53-59, August 1999.

[3] S. Rao, "Parametric Design and Analysis of Multiple-Beam Reflector Antennas for Satellite Communications," IEEE Antennas Propagat. Magazine, Vol. 45, pp. 26-34, August 2003.

[4] S. Rao and Minh Tang, "Stepped-Reflector Antenna for Dual-Band Multiple Beam Satellite Communications Payloads," IEEE Trans. Antennas Propagat., Vol. 54, pp. 801-811, March 2006.

[5] S. Rao, K.K. Chan, and M. Tang, "Dual-band multiple beam antenna system for satellite communications," IEEE AP-S Symposium, Washington, DC, July 2005.

[6] O. Sotoudeh et al., "Dual-band hard horn for use in cluster-fed multi-beam antennas in Ka-band", IEEE AP-S Symposium, Washington, DC, July 2005.

[7] A. W. Rudge et al., "The Handbook of Antenna Design," Peter Peregrinus Ltd, IEE, pp. 466-505, 1986

[8] L. J. Ricardi et al., "Radiation pattern calculations for a waveguide lens multiple-beam antenna operating in the AJ mode," MIT Lincoln Laboratory Technical Note 1975-25, 1976.

[9] S. Rao et al., "Multiple beam antenna using reflective and partially-reflective surfaces," US Patent # 6,759,994 B2, July 06, 2004.

[10] S. Rao and M. Tang, "Multiple-beam antenna system using high-efficiency dual-band feed horns," US Patent Application 60/622785, October 29, 2004.

[11] S. Rao and M.Tang, "Stepped-reflector antenna system for dual-band multiple beam satellite payloads," US Patent Application 60/693832, June 27, 2005.

[12] S. Rao et al., "Reconfigurable payload using non-focused reflector antenna for HIO and GEO satellites," US Patent Application 60/758684, January 13, 2006.

[13] W. Rotman and R.F. Turner, "Wide angle microwave lens for line source applications," IEEE Antennas & Propagat., vol. 11, pp. 623-632, Novemnber 1963.

[14] D. Archer, "Lens-fed multiple beam arrays," Microwave Journal, vol. 18, pp. 37-42, 1975.

[15] K. K. Chan et al., "Triangular ray-tube analysis of dielectric lens antennas," IEEE Trans. Antennas Propagat., vol. 45, pp. 1277-1285, August 1997.

[16] K.K. Chan and S. Rao, "Design of a Rotman lens feed network to generate a hexagonal lattice of multiple beams," IEEE Trans. Antennas Propagat., vol. 50, pp. 1099-1108, August 2002.

Sudhakar K. Rao (M'83–SM'97–F'06) was born in Tenali, Andhra Pradesh, India. He received the B.Tech degree from REC Warangal, India, in 1974, the M. Tech degree from the Indian Institute of Technology, Kharagpur, in 1976, and the Ph. D degree from the Indian Institute of Technology, Madras, in 1980, all in electrical engineering. From 1976 to 1977, he worked as a Technical Officer at the Electronics Corporation of India Limited (ECIL), Hyderabd, and was involved with the design and test of LOS and TROPO communications antennas. From 1980 to 1981, he worked as a Senior Scientific Officer at the Electronics and Radar Development Establishment (LRDE), Bangalore, and worked on phased array radar antennas. During 1981 to 1982, he worked at the University of Trondheim, Norway, on a post-doctoral fellowship from the Royal Norwegian Council for Scientific and Industrial Research (NTNF). He was a Research Associate at the University of Manitoba, Winnipeg, Canada, from 1982 to 1983, where he worked on low-sidelobe antennas. From 1983 to 1996, he worked as a Staff Scientist at the Spar Aerospace Limited, Ste-Anne-de-Bellevue, Quebec, Canada on several satellite communications payloads for fixed and broadcast satellite services, mobile satellites, agile beam payloads at EHF, and led the IRAD team that developed several advanced antenna components and sub-systems that include cup-dipole arrays, lens antennas, helical antennas, phased arrays, and dual-gridded shaped reflectors. From 1996 to 2003, he worked at Hughes Satellite Communications (that later became Boeing Satellite Systems), El Segundo, CA as a Chief Scientist and developed advanced multiple beam and reconfigurable beam payloads for several commercial and military communications satellites that include Wideband Gapfiller, Anik-F2, NewSkies-8, GOES, DTV-4S, Thuraya, and GPS-2. He is currently working at Lockheed Martin Commercial Space Systems, Newtown, PA, as a Division Fellow in the payload engineering directorate. He has published over 90 technical papers in various journals and conferences in the areas of microwave antennas and satellite communications payloads and has 30 U.S. patents issued/pending. His current research interests include reconfigurable payloads, multiple beam payloads, feed assemblies, high power payload test methods, and reflector antennas.

Dr. Rao received several awards including Boeing's Technical Fellow award in 2001, Boeing's Special Invention award in 2002, BSS' Technical/Patent Excellence award in 2003, Lockheed Martin's Inventor of New Technology award in 2005, LMCSS' Special Recognition awards in 2004 & 2005, and LMCSS's Technical Excellence award in 2006. In 2006, Dr. Rao received IEEE Benjamin Franklin Key award in Philadelphia in recognition of his original contributions and innovations in the field of satellite communications. His work on modeling of satellite antenna patterns was adopted by the CCIR in 19992. Dr. Rao is an IEEE Fellow and served as the member of technical program committee for several IEEE AP-S/URSI conferences, chaired numerous technical sessions, served as the IEEE A&A Committee for Senior Member selection for Region 2, and has been serving as a reviewer for the IEEE Transactions on Antennas and Propagation since 1985.

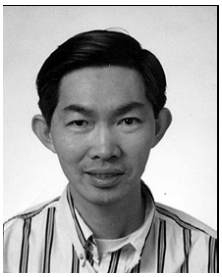

Minh Q. Tang was born in Saigon, Vietnam. He studied physics and mathematics at the University of Winnipeg, Manitoba, Canada, from 1976 to 1978. He received the B.S. degree in electrical engineering from the University of Manitoba, Manitoba, in 1981, where, from 1981 to 1982, he engaged in graduate studies. From 1983 to 1996, he worked at Spar Aerospace Limited, Ste-Anne-de-Bellevue, Quebec, Canada, as a Specialist Engineer and was involved with antenna designs for contoured beam and multiple beam payloads for both commercial and military satellites. From 1996 to 2004, he worked at Space Systems Loral, Palo Alto, CA, where he served as a Technical Consultant for the satellite antenna division. He has been with Lockheed Martin Commercial Space Systems, Newtown, PA, since 2004, where he is currently a Principal Engineer working with new business group of the Payload Engineering Division. He has published about 14 papers in technical conferences and journals and has five U.S. patents that are issued and pending. His current research interests include contoured beam antennas, reconfigurable antennas and multiple beam antennas. Mr. Tang received Lockheed Martin's Technology Award in 2005 and LMCSS' Special Recognition Award in 2005 and in 2006.

Chih-Chien Hsu was born in Taipei, Taiwan, in 1965. He received the B.S. degree in Electronics Engineering from the National Chiao-Tung University, Taiwan in 1987, and M.S. & PH.D. from Massachusetts Institute of Technology in 1992 and 1996, respectively. He has been working on antenna systems for communication and radar applications at Boeing Satellite System and Lockheed Martin Corporation for the past 10 years. Currently he is with Lockheed Martin Commercial Space System, Newtown, PA, as a Senior Staff Engineer working with new business group of the Payload Engineering Division. His current research interests are in the areas of multi-beam antenna design and phased array technology. He has four U.S. patents on antenna and communication system.

A Survey of Phased Arrays for Medical Applications

(*Invited Paper*)

Cynthia Furse
Electrical and Computer Engineering, University of Utah, 50 S Campus Drive 3280 MEB
Salt Lake City, Utah 84112
cfurse@ece.utah.edu, www.ece.utah.edu/~cfurse
Phone: (801) 585-7234
Fax: (801) 581-5281

***Abstract*—** This paper presents a survey of phased arrays for a wide variety of medical applications. Medical imaging modalities including tomography, confocal imaging, thermography, and MRI are covered, as well as hyperthermia for treatment of cancer. Arrays include planar, cylindrical, and conformal configurations of many types of antennas including monopoles, dipoles, microstrips, horns, bowties, loops, etc.

***Keywords*—** Antenna Arrays, Medical Imaging, Breast Cancer, Hyperthermia, Magnetic Resonance Imaging (MRI)

I. INTRODUCTION

Antenna arrays have been used for a wide variety of medical applications, most notably imaging and hyperthermia treatment of cancer. These arrays may be phased electronically; however more often the received signals are phased after detection. The arrays can be built of multiple antennas or can be produced synthetically by scanning a single antenna or pair of antennas over the object of interest. Medical applications for phased arrays have borrowed heavily on radar applications such as ground penetrating radar, ultrawideband radar, and synthetic aperture radar. This paper surveys the medical imaging and hyperthermia applications of phased array antennas. Microwave tomography, confocal imaging, thermography, and magnetic resonance imaging are covered in section II. Hyperthermia is covered in section III. Some numerical methods for simulating antenna arrays are surveyed in section IV.

II. ANTENNA ARRAYS FOR MEDICAL IMAGING

One of the most promising uses of antenna arrays in medical applications is for imaging the location of leukemia 0, breast tumours [1] - [25], and cardiac anomalies [26] - [27]. Microwave imaging methods rely on the fact that the electrical properties of normal and malignant tissue are significantly different [28] - [35] and that there is significant variation from tissue to tissue. Location of breast cancer shows particular promise, because the relatively low loss of fatty tissue allows electromagnetic fields to propagate to the tumor and back, and the proximity of the tumor to the outer surface of the body means that the signal does not have more than a few inches to propagate. Two major microwave imaging methods utilize antenna arrays. Tomography [2] - [9] attempts to map a complete electrical profile of the breast, and confocal imaging [10] - [25] maps only the location of significant scatterers. Both of these methods have used antenna arrays made up of wideband elements to send and receive the test signals. Microwave thermography picks up the passive electromagnetic fields from the body [36] - [52]. Magnetic Resonance Imaging (MRI) uses a strong magnetic field to cause the magnetic dipoles in the body to align and precess, gradient fields to control and tip the dipoles and then uses an array of receiving loops to pick up the fields when they relax back to their normal state [59] -[74].

A. Tomography for Breast Cancer Detection

Microwave tomography is used to provide a complete spatial mapping of the electrical properties in the region of interest. During the acquisition phase, an array of antennas surrounds the region of interest. One of the antennas in the array is used to transmit a signal, normally a sine wave [2], set of sine waves [3] -[4], or a broadband signal [5], and all of the other antennas are used to receive the reflected signal. The array is scanned so that each antenna transmits each frequency, and those signals are received by each of the other antennas. After all of the data has been acquired, it is processed by comparing the received data with what would be expected from a simulated model of the region. A numerical "forward model" is used to predict how much power is transmitted from the transmit antenna, passes into and reflects from the breast/tumor model, and is received by the receive antenna. Originally the simulated model is just a good guess for

what might be present, generally a generic breast model with no tumor. The differences between the measured and expected received data are used to modify the original guess to obtain an ideal model that best matches the measured data. This "inversion" is used to predict what model would have produced the measured data.

Microwave tomography for breast cancer has been demonstrated by several groups [2] - [9]. In the Dartmouth system, [2] for instance, sine waves from 300-1000 MHz (being expanded to 3 GHz) are transmitted from a circular array of 16 transmit/receive monopole antennas to produce 2D reconstructed images of the breast. Quarter wave monopole antennas (in the fluid) were built by extending the inner conductor of semi-rigid coax used for this application. Monopoles were chosen, because they are easy to model as a line source in a 2D reconstruction algorithm with high accuracy [2]. Water-filled waveguide apertures have also been used for tomography, however the monopole antennas were found to be as accurate, and easier to build [6]. The accuracy of the tomography approach depends on being able to accurately predict the expected received fields from a given transmit antenna / breast model. The antennas and their locations must be accurately modeled in both the transmit and receive case, as any inaccuracy in the antenna models affect the forward model not once, but twice and has a significant impact on the accuracy of the final solution. Monopole antennas can be very accurately modeled and are a good choice for this application. In addition, monopoles have been found to be excellent radiators when resistively loaded by lossy material, having a return loss of about -10 dB from 100 to 1100 MHz when immersed in saline [6]. Thus, for applications such as medical imaging where it is imbedded in a lossy conducting fluid surrounding the object of interest, simple monopoles demonstrate good radiation properties [2]. One of the key factors in obtaining accurate models of the antenna array is to model each of the inactive array elements as a microwave sink, so that the signal is not re-radiated [7] -[8]. This was accomplished in the numerical model by imposing an impedance boundary condition on a finite diameter around each inactive element. The forward model uses a hybrid boundary element (BEM) and finite element method (FEM). In the hardware, a matched switch was the last element in the switching matrix, so that when the antenna is not radiating, any coupled signal is terminated at the switch. The 32 channel data acquisition system allows each antenna (16 transmit and 16 receive) to act as only a transmitter or receiver, which provides a dynamic range of 130 dB and channel-to-channel isolation of greater than 120 dB.

Since the goal is to identify tumours that have significant dielectric discontinuity from the surrounding tissue, best results will be obtained if they are the primary scatterers in the environment. Blood vessels are also significant scatterers, but these cannot be controlled. They will also show up on a tomographic image. The other major scattering source is the air-skin interface, and this can be controlled. This reflection can be minimized by immersing the antennas and breast in a fluid medium that is electrically similar to breast/skin. Originally saline was used, which is a better match than air, inexpensive and safe, however its relative permittivity is significantly higher than that of fatty breast tissue, and a better matched fluid material is recommended. The monopole antennas are designed to be used in the liquid medium, rather than air, with the conductive fluid providing the resistive loading of the monopoles. The feed system also needs to be designed so that it can be used in fluid. The sealing of the antenna feed system along with the ability to raise and lower the array in parallel with the fluid level was a significant challenge in the system prepared for clinical trials in [6] .

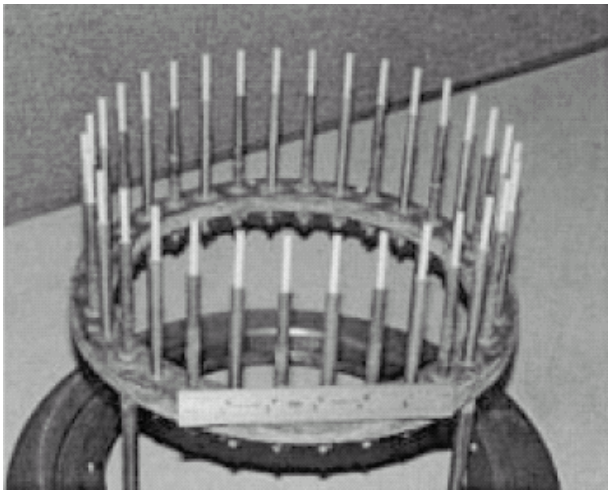

Fig. 1. 2D Monopole array used for tomographic imaging of the breast (from [2] © 2000 IEEE).

For a microwave tomography breast exam, the woman lies with the breast pendant through a hole in the examination table and immersed in the tank of matching fluid. The circuit antenna array of monopoles is also immersed in this fluid and radially surrounds the breast. For each 2D breast scan, signals are transmitted from each antenna and individually received in parallel at the remaining antennas. This is repeated for 12 frequencies over the 300-1000 MHz band. This is repeated for seven vertical array positions on the order of 1cm. The total acquisition time for the 3D image of both breasts is about 15 min. A complete set of seven images at a single frequency can be reconstructed in less than 5 min using a Compaq AlphaServer ES40 68/833.

Microwave tomography has been validated experimentally [9]. The presence of 1.1 or 2.5 cm saline tubes (representing tumours) in excised breast tissue are seen to be clearly visible [8]. Objects as small as 4 mm in diameter have been imaged at 900 MHz [9].

B. Confocal Imaging for Breast Cancer Detection

Confocal imaging for breast cancer detection is another exciting application of antenna arrays in medical imaging. Confocal imaging is similar to ground penetrating radar. Unlike microwave tomographic imaging, this method does not provide a complete electrical mapping of the region of interest. Instead it identifies locations of significant scattering. This method typically uses a single antenna scanned in a flat array pattern above the breast or in a cylindrical pattern around the breast [10]. For planar imaging, the patient lies face up, and the antenna is physically scanned in a plane above the breast [11] - [13]. For cylindrical imaging, the patient lies face down, with the breast extending into a cylindrical tank containing the antenna through a hole in the table [14] - [15]. Matching fluid surrounding the breast, similar to that used for microwave tomography, is suggested in this case. Both methods provide similar results [15]. The confocal imaging process is shown in Fig. 2. One antenna in the array transmits an ultrawideband pulse, which propagates into the breast, where it is reflected off significant electrical discontinuities, and is received in parallel by the other antennas in the array. Knowing the physical spacing between the array elements, the different delays between the transmit antenna, scattering point, and receiving antenna can be calculated geometrically. The received pulses representing a specific point in space can then be time delayed appropriately for each antenna, added up and integrated to indicate the magnitude of the scattered energy from that point in space. This is effectively correlating the signals received from that point at all antennas.

The antennas used for confocal imaging must be ultrawideband and small enough to fit within the relatively small array area. Resolution of less than 1 cm requires a bandwidth of at least 5 GHz. The lossy nature of tissue attenuates high frequency signals, limiting the upper frequency to about 10 GHz. Initially, resistively loaded bowtie were suggested for the planar configuration, [11]-[13], [17], [19], while dipole antennas were suggested for the cylindrical system [14]-[15]. Resistively loaded Vee dipoles have also been proposed [18]. In the cylindrical configuration, and the planar system, a single antenna is scanned over the surface, creating a synthetic antenna aperture. In order to overcome the inherent inefficiency of resistively loaded antennas, a modified ridged horn antenna operating from 1 to 11 GHz has been introduced [20]. Most of the antennas are designed to observe co-polarized reflections from the breast, however using two resistively loaded bowtie antennas in the shape of a Maltese cross has also been proposed to pick up the cross polarized reflections[12]. Cross-polarized reflections from simple tumor models were also examined in [16].

The antenna shown in Fig. 3 [16] consists of two cross polarized bowtie antenna elements, an octagonal cavity behind the bowtie elements, and a metal flange attached to the cavity. The broadband bowties have flare angles of 45°. They are 1.67 cm long, which is a half-wavelength at 3 GHz in fat (similar to breast). The octagonal cavity blocks waves radiated away from the breast.

The cavity is approximated as a circular waveguide filled with fat material for matching and size reduction. The first cutoff frequency is set to be 2 GHz for 2-4 GHz operation. The cavity length is a quarter-wavelength, which is 11 mm at 3 GHz. The flange consists of an inner and outer component, and is designed to block unwanted waves such as surface waves. The antenna performance does not change significantly when the flange size is varied between 10–6.25 cm, therefore, the width of the outer flange is set to be 6.25 cm. The inner flange is designed to prevent possible electric field overshoot at the inner corners of the opening of the octagonal cavity or at the ends of the bowtie elements.

A slotline bowtie antenna shown in Fig. 4 has also been proposed in [22]. The slotline was produced on a high dielectric substrate (Rogers RT-Duroid 6010.2LM, Rogers Corporation, Rogers, CT, USA). The substrate has an ε_r of 10.2 at 10 GHz with a low-loss factor tan δ of 0.0023 and a thickness of 635 μm. The ultra-wideband balun uses a via as a short. The holes for the vias in the balun are drilled and electroplated. The balun and the profile of the antenna are then milled. The bowtie plates are designed to be cut from a 508 μm-thick sheet of copper. To obtain the correct contour of the plates accurately without damaging the fragile antenna board, a steel jig was made by tracing the contour of the antenna board. The bowtie plates were bent along this jig, and then carefully soldered on to the antenna board at right angles. The antenna plates were encased in a dielectric epoxy (Eccostock Hi K Cement, Emerson & Cuming Microwave Products, Randolph, MA, USA) with ε_r =10 for structural support and improved matching.

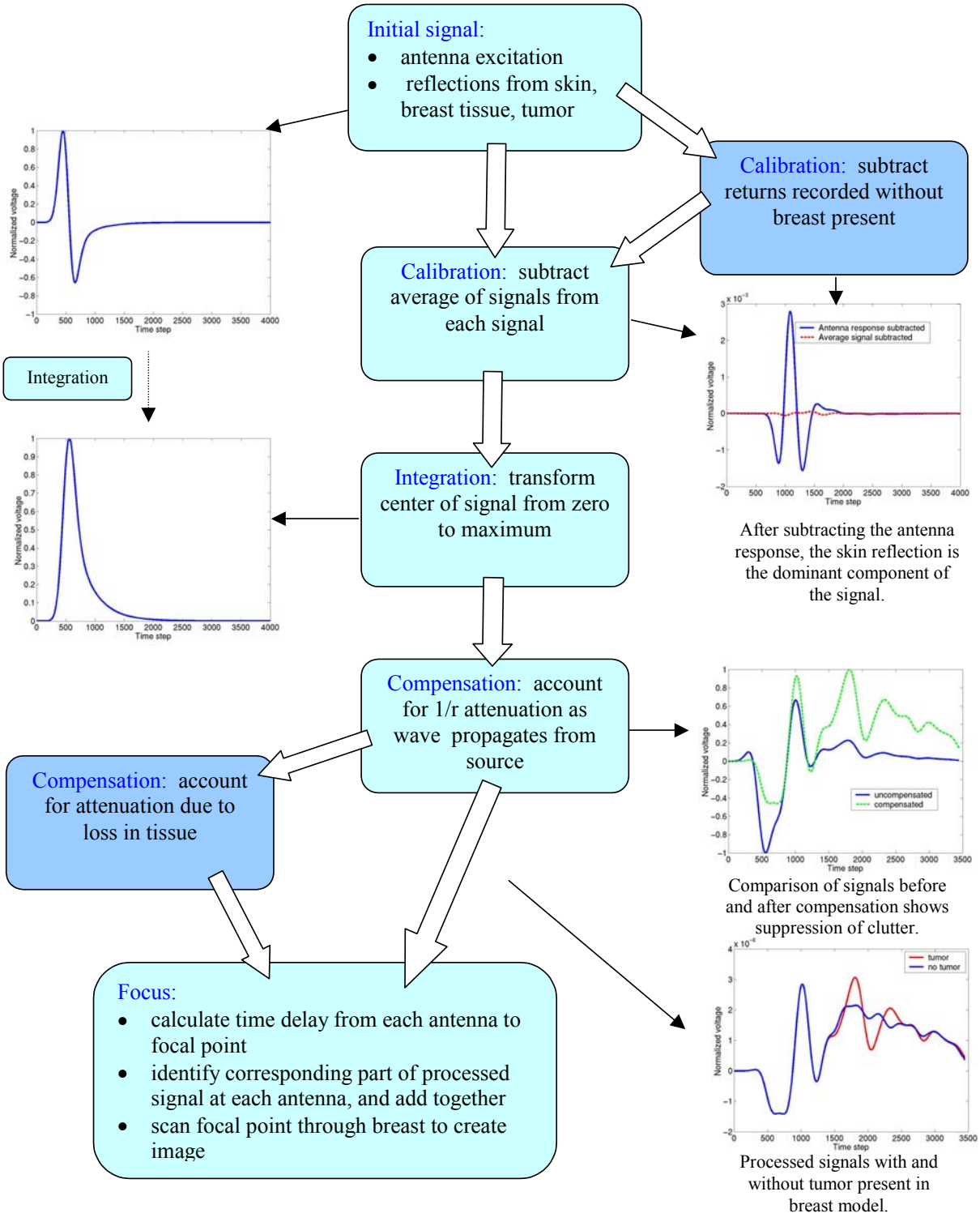

Fig. 2. Confocal Microwave Imaging Process. (From [10] © 2002 IEEE)

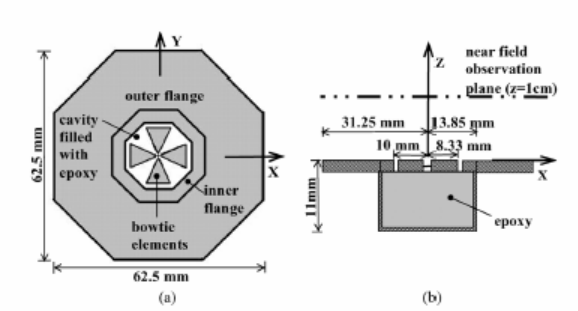

Fig. 3. Cross polarized antenna for confocal imaging. The properties of the substance inside the cavity and the medium outside the antenna are similar to fat (ε_r = 9; σ = 0:2 S/m). (From [16] © 2005 IEEE)

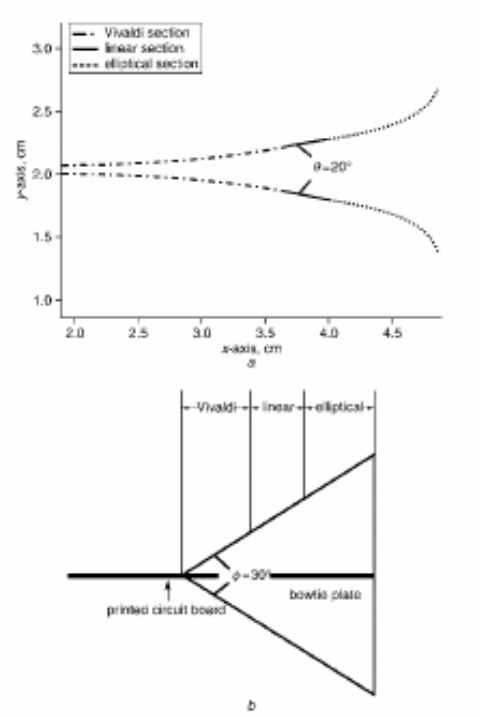

Fig. 4. Slotline Antenna and a Top view with Vivaldi, linear and elliptical sections indicated b Side view with Vivaldi, linear and elliptical sections and bowtie plates. (From [22] © 2005 IEEE)

A resistively loaded monopole antenna shown in Fig. 5 suitable for use in the cylindrical system was proposed in [25]. Based on the Wu–King design [75] - [76] this antenna was designed to be useable from 1to10 GHz immersed in canola oil (ε_r = 3.0) for matching to breast tissue. The antenna is fabricated using high-frequency chip resistors (Vishay 0603HF) (Malvern, PA) soldered to a high-frequency substrate (Rogers RO3203 series) (Rogers Corporation, Chandler, AZ). The substrate (ε_r = 3.02 and σ= 0.001 S/m) has electrical properties similar to those of the canola oil. The antenna is soldered to a subminiature A (SMA) connector and attached to a metal plug for connection into the oil-filled test canister.

The cylindrical confocal imaging system has been experimentally tested [77], [23], [25]. Simulated tumours of diameter 1 cm have been detected using a system that represents the skin as 2D and the tumor model as 3D.

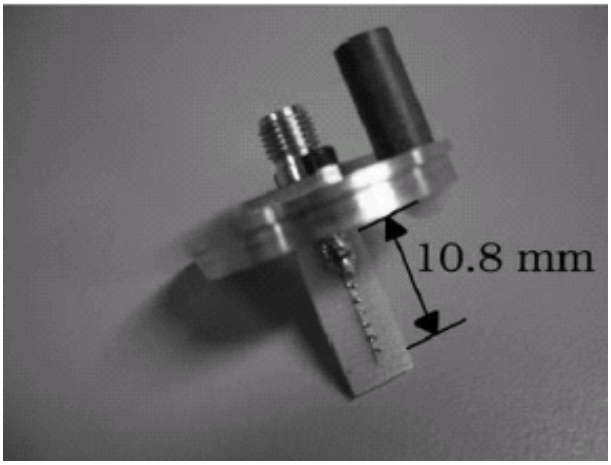

Fig. 5. Fabricated resistively loaded monopole antenna soldered to an SMA connector and attached to a metal plug. (From [25] © 2005 IEEE)

C. Microwave Radiometry

Microwave radiometry is a passive method where the natural electromagnetic radiation or emission from the body is measured to allow detection or diagnosis of pathogenic conditions in which there are disease-related potentials [36] -[37]. This method has been proposed for detection of breast cancer [40], [50], [51] and brain cancer [41], in which the metabolism of cancer cells increases the localized temperature 1-3°C. This method has also been used for fluid and blood warming [37], detection or rheumatology [39], and for monitoring of temperature rise during hyperthermia treatment [38].

Typical antennas include open ended rectangular waveguides [42]-[45], small-loop antennas [47], or a horn antenna with a dielectric lens [48]. Working around 3 GHz, all of these antennas have radiation patterns that have minimal penetration into the body, thus strongly weighting them to monitoring of surface temperatures. [49], [52] Increased focus and therefore better spatial accuracy was obtained with an array of six rectangular aperture antennas filled with low loss dielectric (ε_r = 25), which were scanned over the object of interest in an overlapping pattern. Preliminary results indicated promise for location of breast tumours [50] - [51].

D. Magnetic Resonance Imaging

Magnetic Resonance Imaging (MRI) uses a very strong magnetic field (0.5T, 1.5T, 3T, 4T, 7T, perhaps in the future 8T) to make the magnetic dipoles in the body precess (line up). When they are released, a set of receiver coils picks up the magnetic field created when these dipoles return to their normal orientations (position may change a lot as in blood imaging, diffusion etc.). The relaxation properties of the different tissues effects the relative received signal intensities and a 3D map of the body can be produce. There are two basic types of receiver coils used for MRI. Volume coils, such as the quadrature birdcage head coil shown in Fig. 6 [53] and whole body coils [54] are used for imaging large sand deep anatomic structures volume of the body and provide homogeneous field profiles.. For high resolution applications that are more localized, such as angiographic imaging, hypocampus imaging, and functional imaging, in which the object features are very small, volume coils pick up less signal and more noise, thus having a lower signal to noise ratio and poor quality images. Modifications of the birdcage, such as the use of an RF reflector or "endcap" [53], and modified shapes such as the elliptical [55], or "dome" [56], [57] coils, have been developed. Smaller volume surface coils [58] have been shown to improve image quality, particularly when combined into phased arrays [59]-[67] such as the one shown in Fig. 7. Phased array coils are closer to the area of interest so pick up larger signal strength and are smaller so pick up less noise, thus having higher signal to noise ratio (SNR). Adjacent elements are overlapped so that the mutual inductance between coils is zero. The coupling between non-adjacent elements is greatly decreased using, very low input impedance preamplifiers. Coil to coil interactions are minimized for optimal SNR [59]. Part of the price for this improved image quality is the complexity of the receiver and data acquisition system, as each antenna element requires a separate receiver channel. The image processing is also more computationally expensive, as the signal from each antenna is weighted depending on its proximity to the target region (and hence expected relative SNR), phase shifted, and combined with the other similarly processed signals. Among the practical considerations that are challenging with phased array coils are the expense of additional receiver channels (or the limited number of channels on existing scanners), data acquisition time and the limited field of view, particularly for applications where the region of interest (an arterial occlusion, for instance) may not be precisely known and is therefore easy to miss. Phased-array coils have been used for numerous magnetic resonance angiography (MRA) applications including peripheral [68], [69] abdominal, intracranial and carotid imaging [70] - [72]. Recent coil designs have started to integrate phased-array elements into volume-like coils with the ability to control how the image is constructed to achieve maximum image quality [73], [74]. For these applications, the coil array functions much like the phased array in a synthetic aperture radar application. The image quality for the different coil types and configurations depends strongly on the application. The optimal image construction algorithm depends strongly on the application and region of interest, making the flexibility of being able to synthetically develop large or small subarrays very attractive.

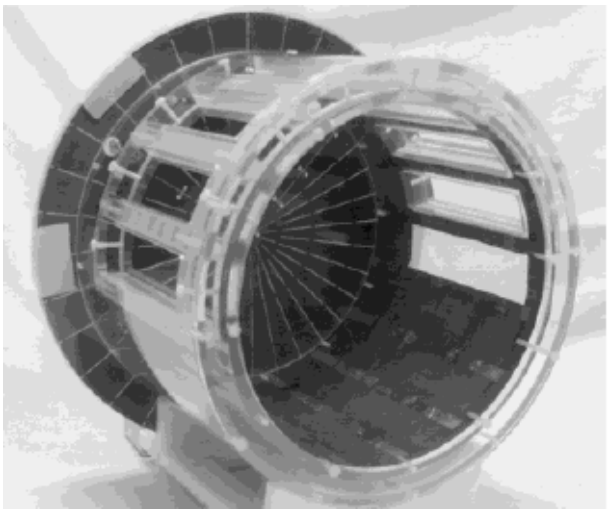

Fig. 6. Quadrature birdcage coil with endcap used for whole-volume head imaging. (Reprinted with permission from [53])

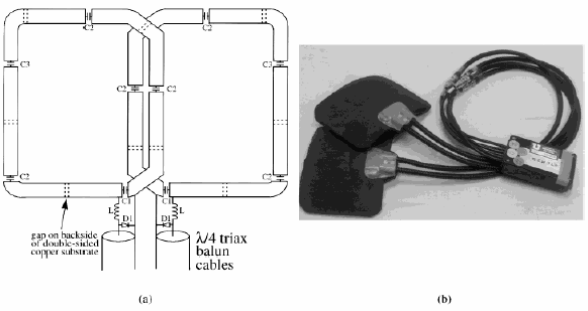

Fig. 7. (a) Two element phased-array coil design. Dashed lines indicate the breaks in the underside of the double-sided copper section of the coil. (b) Image of finished phased array coils (enclosed in foam) with triax balun cables and phased-array port connector box. (Reprinted with permission from [53])

III. ANTENNA ARRAYS FOR HYPERTHERMIA CANCER TREATMENT

Hyperthermia (HT) [78], [79] is a method of treating cancer by heating the body. The tissue is typically heated to 41-45°C for 30-60 min. Often, this involves focusing the energy on the tumor region, relying on the tumor to be more sensitive to heat than the surrounding healthy tissues. HT has also been shown to increase the effectiveness of radiation or chemotherapy [80] - [81]. The most commonly used frequencies for hyperthermia are 433, 915, and 2450 MHz. The type of antenna or antenna array used for HT depends on if it is to be administered superficially, interstitially, or deep-body.

Superficial HT applicators include microstrip [82], waveguide [83], current sheets [84], and the dual concentric conductor antenna, or DCC shown in Fig. 8 [85] -[87]. The DCC is particularly attractive, because it can be easily fabricated on flexible printed circuit board material, which makes it easy to conform to virtually any part of the human body. The DCC aperture is a ring-slot configuration fed simultaneously on all four sides. Prediction and optimization of the heating is normally done by analyzing the near fields of the antenna (the heating region) with numerical methods [86].

Interstitial applicators for HT are typically monopole antennas made from coaxial cables with the center conductor extending beyond the outer ground shield of the cable [88]. These antennas have a tear-drop shaped radiation pattern, so the majority of the heating is near the feedpoint of the antenna (where the ground shield stops), leaving the tip of the antenna extended beyond the useable heating range. The heating distribution can be made more uniform by varying the width of the conductor [89], [90] or adding a choke to the antenna [91]. The heating pattern can be adjusted within the array by phasing the antenna elements [89], [90] or by using nonuniform insulation [92]. Several interstitial applicators were simulated in [93].

Deep body HT applicators are generally based on annular phased arrays (APA) of waveguides [79], coaxial TEM apertures [94], printed antennas [88],[95] and induction systems[96]. Originally, APA systems contained only one ring of 2-D applicators surrounding the patient [97]. The ring could be scanned vertically. Significant improvement with a true 3-D HT system with the applicators vertically offset has been observed [88]. The first clinically used 3-D-type applicator is the SIGMA-Eye applicator (BSD Medical Corp., SLC, UT [98]). A detailed description of this applicator and different numerical antenna feed models can be found in [98],[99].

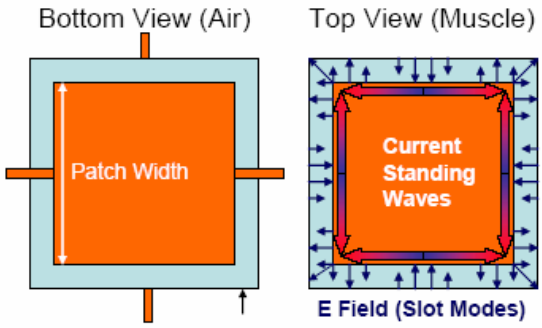

Fig. 8. DCC antenna geometry, E fields in the ring slot and edge currents. (From [85] © 2003 IEEE)

Among the ongoing antenna design challenges in this area is the design of antennas that can be used to also monitor temperature and administer radiation therapy [87], [95], [100]. One prototype combination device is shown in Fig. 9 and another in Fig. 10. Another research area is the use of optimization approaches to predict and control the heating pattern [101], [102]

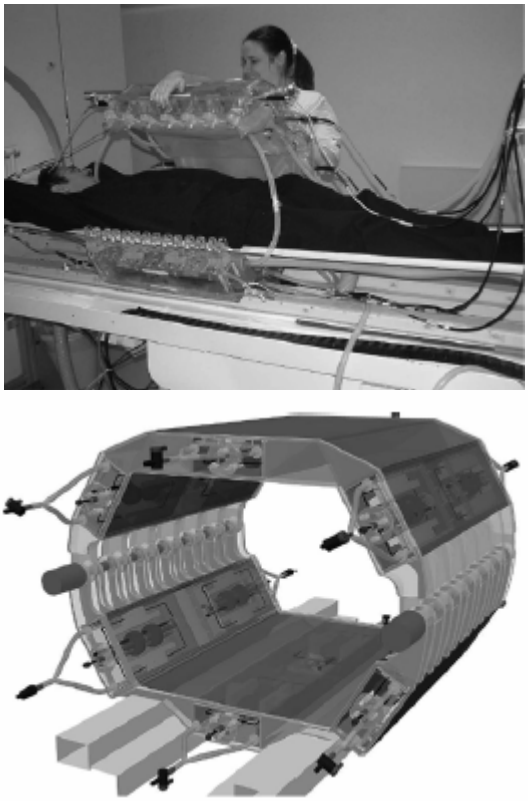

Fig. 9. A prototype of the new Berlin MR-compatible Water-Coated Antenna Applicator (WACOA). (From [100] © 2005 IEEE)

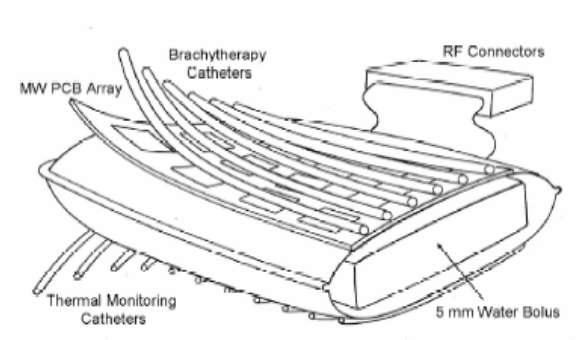

Fig. 10. Schematic of combination applicator showing component parts: parallel catheter arrays for brachytherapy sources and thermal mapping sensors, PCB antenna array, and water coupling bolus. (From [95] © 2004 IEEE)

IV. NUMERICAL SIMULATION METHODS FOR BIOMEDICAL ARRAYS

Several methods for analyzing antenna arrays for medical applications exist. For simple cases where the biological structure can be approximated as uniform or by very simple models such as layers or cylinders, classical methods such as analytical analysis [53], [103] or method of moments [104]-[105] can be used. If the structure of the body varies so much that anatomically-precise modeling is rendered imprecise by variation between individuals, these simple analyses can be used to determine an optimal array design for the range of expected variation between individuals. An example of this was done in [106] for design of coils for vascular MRI. Another example when the body can be modeled as near-uniform is in the case of arrays for hyperthermia of the brain. In [89] stepped-impedance dipoles were modeled using method of moments in an homogenous brain with a localized (non-homogenous) tumor. Method of moments with a simple pulsed basis function (which is the most numerically efficient form) has limitations for heterogeneous models, however, due to artificial charge build up on the dielectric interfaces. [107] Higher order basis functions can overcome this limitation, although the computational complexity is significantly increased [108] - [109]. In addition, the method of moments is very computationally expensive when heterogenous models are evaluated. It requires N logN computations, where N is the number of cells in the model, including those making up the heterogeneous object.

A more efficient method for calculation of heterogeneous objects is the finite difference time domain (FDTD) method, which has lead to its tremendous popularity for numerical bioelectromagnetic calculations. For example, the interstitial array of hyperthermia applicators simulated using method of moments in [89] was simulated with a fraction of the computational resources using FDTD in [90]. Several individual hyperthermia applicators have been simulated using FDTD in [93]. FDTD requires N^2 computations, where N is a cell in the (normally cubical) FDTD grid. Unlike method of moments, every cell in space (including at least a minimal amount of air surrounding the model) must be included in the discrete model, so the total number of cells, N, is likely to be larger. However the significant improvement in computational efficiency generally makes this tradeoff favor FDTD for bioelectromagnetic simulations. Complete detailed analysis of breast cancer imaging modalities was also done with FDTD [2]-[25], as well as hyperthermia systems [97], and evaluation of cell phones (including those with dual antennas) near the human head. [110],[111] Antennas for implantation in the body (mostly microstrip or PIFA types) have been simulated with FDTD and in some cases optimized with genetic algorithms [112]. Deep hyperthermia applicators (annular phased arrays) have been simulated extensively with FDTD [113] -[115].

Several FDTD developments have been important for bioelectromagnetic simulations including the development of frequency-dependent methods $(FD)^2TD$, [116] low frequency FDTD methods, [117] efficient FDTD computation, [118] and evaluation of temperature using the bioheat equation [115].

Model development is one of the significant challenges of numerical bioelectromagnetics. Models have progressed from the prolate spheroidal models of the human used during the 1970s [119] to roughly 1cm models based on anatomical cross sections used during the 1980s [120] to a new class of millimeter-resolution MRI-based models of the body that have been the hallmarks of research since the 1990s [121]-[124]. Today probably the most widely used models are derived from the Visible Man Project [125].

Once a tissue-segmented model has been chosen, the electrical properties of the tissues are defined. The properties of human tissue change significantly with frequency, so it is essential to use data accurately measured at the frequency of interest. There is a wide range of published data on measured tissue properties [28] -[35], [119], [126]-[129], and work is still underway to measure and verify these properties. These and other references are electronically searchable at [130].

Periodic boundary conditions are available for method of moments [131], [132] and the FDTD method [133] - [138] for predicting array behavior from

evaluation of a single antenna in the array. These may have application in antenna arrays for medical applications; however they have not been used in this application space yet. This is no doubt due at least in part to the fact that the nearby human body is neither uniform nor periodic in shape.

VI. CONCLUSIONS

The applications for phased arrays in medicine have borrowed strongly from other applications of phased arrays, particularly those seen in radar. Imaging methods including tomography, confocal imaging, thermography, and MRI provide enhanced medical imaging. Hyperthermia treatments often improve the outcome of radiation and chemotherapy for cancer treatment. A wide variety of antennas have been used in these arrays, and the arrays have been produced either physically or synthetically by scanning a single antenna or pair of antennas over the region of interest. The arrays have been phased either electronically, or (more commonly) by time delaying the received signals during recombination. Design challenges for these applications include making the antennas small enough to be physically useable, coupling the signal to the body with minimal reflection, using low enough frequency to penetrate lossy biological material yet high enough frequency to obtain good resolution. Among the current research challenges are optimized design of the arrays for a variety of configurations and integration of other technologies (radiation therapy and temperature monitoring, for instance) with the antenna design. Applications for phased array antennas promise continued growth in the medical arena.

ACKNOWLEDGEMENTS

The author gratefully acknowledges the assistance of Dr. Rock Hadley for contributions to the MRI section of this paper.

REFERENCES

[1] D. Colton and P. Monk, “A new approach to detecting leukemia: Using computational electromagnetics,” *IEEE Trans. Comput. Sci. Eng.*, vol.2, pp. 46–52, winter 1995.

[2] P. M. Meaney, M. W. Fanning, D. Li, S. P. Poplack, and K. D. Paulsen, “A clinical prototype for active microwave imaging of the breast,” *IEEE Trans. Microwave Theory Tech.*, vol. 48, pp. 1841-1853, Nov. 2000.

[3] W. C. Chew and J. H. Lin, “A frequency-hopping approach for microwave imaging of large inhomogeneous bodies,” *IEEE Microwave Guided Wave Lett.*, vol. 5, pp. 439–441, Dec. 1995.

[4] O. S. Haddadin and E. S. Ebbini, “Imaging strongly scattering media using a multiple frequency distorted Born iterative method,” *IEEE Trans. Ultrason., Ferroelect., Freq. Contr.*, vol. 45, pp. 1485–1496,Nov. 1998.

[5] Q. Fang, P. M. Meaney, and K. D. Paulsen, “Microwave image reconstruction of tissue property dispersion characteristics utilizing multiple-frequency information,” *IEEE Trans. Microwave Theory Tech.*, vol. 52, pp. 1866-1875, Aug. 2004.

[6] P. M. Meaney, K. D. Paulsen, A. Hartov, and R. C. Crane, “An active microwave imaging system for reconstruction of 2-D electrical property distributions,” *IEEE Trans. Biomed. Imag.*, vol. 42, pp. 1017–1026, Oct. 1995.

[7] K. D. Paulsen and P. M. Meaney, “Compensation for nonactive array element effects in a microwave imaging system: Part I—Forward solution vs. measured data comparison,” *IEEE Trans. Med. Imag.*, vol. 18, pp. 496–507, June 1999.

[8] P. M. Meaney, K. D. Paulsen, M. W. Fanning, and A. Hartov, “Nonactive antenna compensation for fixed-array microwave imaging: Part II—Imaging results,” *IEEE Trans. Med. Imag.*, vol. 18, pp. 508-518, Jun. 1999.

[9] P. M. Meaney, K. D. Paulsen, A. Hartov, and R. K. Crane, “Microwave imaging for tissue assessment: Initial evaluation in multitarget tissue-equivalent phantoms,” *IEEE Trans. Biomed. Eng.*, vol. 43, pp. 878-890, Sept. 1996.

[10] E. C. Fear, S. C. Hagness, P. M. Meaney, M. Okieniewski, and M. Stuchly, “Enhancing breast cancer detection using near field imaging,” *IEEE Microwave Magazine,* pp. 48-56, March 2002.

[11] S. C. Hagness, A. Taflove, and J. E. Bridges, “Two-dimensional FDTD analysis of a pulsed microwave confocal system for breast cancer detection: Fixed-focus and antenna-array sensors,” *IEEE Trans. Biomed. Eng.*, vol. 45, pp. 1470–1479, Dec. 1998.

[12] S. C. Hagness, A. Taflove, and J. E. Bridges, “Three-dimensional FDTD analysis of a pulsed microwave confocal system for breast cancer detection: Design of an antenna-array element,” *IEEE Trans. Antennas Propagat.*, vol. 47, pp. 783–791, May 1999.

[13] X. Li and S. C. Hagness, “A confocal microwave imaging algorithm for breast cancer detection,” *IEEE Microwave Wireless Comp. Lett.*, vol. 11, pp. 130–132, Mar. 2001.

[14] E. Fear and M. Stuchly, “Microwave system for breast tumor detection,” *IEEE Microwave Guided Wave Lett.*, vol. 9, pp. 470–472, Nov. 1999.

[15] E. C. Fear and M. A. Stuchly, "Microwave detection of breast cancer," *IEEE Trans. Microwave Theory Tech.*, vol. 48, pp. 1854–1863, Nov. 2000.

[16] X. Yun, E. C. Fear, and R. H. Johnston, "Compact Antenna for Radar-Based Breast Cancer Detection," *IEEE Trans. Antennas and Propagation,* vol. 53, no. 8, pp. 2374 -2380, Aug. 2005.

[17] S. C. Hagness, A. Taflove, and J. E. Bridges, "Wideband ultralow reverberation antenna for biological sensing," *Electronic Lett.*, vol. 33, no. 19, pp. 1594–1595, Sep. 1997.

[18] M. A. Hernandez-Lopez, M. Pantoja, M. Fernandez, S. Garcia, A. Bretones, R. Martin, and R. Gomez, "Design of an ultra-broadband V antenna for microwave detection of breast tumors," *Microw. Opt. Tech. Lett.*, vol. 34, no. 3, pp. 164–166, Aug. 2002.

[19] E. C. Fear and M. A. Stuchly, "Microwave breast tumor detection: Antenna design and characterization," *IEEE Antennas Propag. Symp. Dig.*, vol. 2, pp. 1076–1079, 2000.

[20] X. Li, S. C. Hagness, M. K. Choi, and D. W. W. Choi, "Numerical and experimental investigation of an ultrawideband ridged pyramidal horn antenna with curved launching plane for pulse radiation," *IEEE Antennas Wireless Propag. Lett*., vol. 2, pp. 259–262, 2003.

[21] X. Yun, E. C. Fear, and R. H. Johnston, "Radar-based microwave imaging for breast cancer detection: Tumor sensing with cross-polarized reflections," *IEEE Antennas Propag. Society Symp. Dig*., vol. 3, pp. 2432–2435, 2004.

[22] C. J. Shannon, E. C. Fear, and M. Okoniewski, "Dielectric-filled slotline bowtie antenna for breast cancer detection," *Electronics Letters*, vol. 41, no. 7, March 2005.

[23] J. M. Sill and E. C. Fear, "Tissue sensing adaptive radar for breast cancer detection: A study of immersion liquid," *Electronics Letters*, vol. 41, no. 3, pp. 113–115, Feb. 2005.

[24] J. M. Sill and E. C. Fear, "Tissue sensing adaptive radar for breast cancer detection: Preliminary experimental results," *IEEE MTT-S Int. Microwave Symp. Dig*., Long Beach, CA, June 2005.

[25] J. M. Sill and E. C. Fear, "Tissue Sensing Adaptive Radar for Breast Cancer Detection—Experimental Investigation of Simple Tumor Models," *IEEE Trans. Microwave Theory Tech.*, vol. 53, no. 11, pp. 3312-3319, Nov. 2005.

[26] S. Y. Semenov, A. E. Bulyshev, A. E. Souvorov, R. H. Svenson, Y. E. Sizov, V. Y. Borisov, V. G. Posukh, I. M. Kozlov, A. G. Nazarov, and G. P. Tatsis, "Microwave tomography: Theoretical and experimental investigation of the iteration reconstruction algorithm," *IEEE Trans. Micr. Theory Tech.*, vol. 46, pp. 133–141, Feb. 1998.

[27] S. Y. Semenov, R. H. Svenson, A. E. Bulyshev, A. E. Souvorov, A.G. Nazarov, Y. E. Sizov, V. G. Posukh, and A. Pavlovsky, "Three-dimensional microwave tomography: Initial experimental imaging of animals," *IEEE Trans. Biomed. Eng*., vol. 49, pp. 55–63, Jan. 2002.

[28] C. Gabriel, S. Gabriel, and E. Corthout, "The dielectric properties of biological tissues: I. Literature survey," *Phys. Med. Biol*., vol. 41, pp. 2231-2249, 1996.

[29] S. Gabriel, R. W. Lau, and C. Gabriel, "The dielectric properties of biological tissues: II. Measurements on the frequency range 10 Hz to 20 GHz," *Phys. Med. Biol*., vol. 41, pp. 2251-2269, 1996.

[30] S. Gabriel, R. W. Lau, and C. Gabriel. "The dielectric properties of biological tissues: III. Parametric models for the dielectric spectrum of tissues," *Phys. Med. Biol*., vol. 41, pp. 2271-2293, 1996.

[31] K. R. Foster and H. P. Schwan, "Dielectric properties of tissues and biological materials: A critical review," *Crit. Rev. Biomed. Eng*., vol. 17, pp. 25-104, 1989.

[32] S. S. Chaudhary, R. K. Mishra, A. Swarup, and J. M. Thomas, "Dielectric properties of normal and malignant human breast tissues at radiowave and microwave frequencies," *Indian J. Biochem. Biophys*., vol. 21, pp. 76-79, 1984.

[33] A. J. Surowiec, S. S. Stuchly, J. R. Barr, and A. Swarup, "Dielectric properties of breast carcinoma and the surrounding tissues," *IEEE Trans. Biomed. Eng.*, vol. 35, pp. 257-263, Apr. 1988.

[34] W. T. Joines, Y. Z. Dhenxing, and R. L. Jirtle. "The measured electrical properties of normal and malignant human tissues from 50 to 900 MHz," *Med. Phys*., vol. 21, pp. 547-550, 1994.

[35] A. M. Campbell and D. V. Land, "Dielectric properties of female human breast tissue measured in vitro at 3.2 GHz," *Phys. Med. Biol*., vol. 37, pp. 193-210, 1992.

[36] K. L. Carr, "Microwave radiometry: Its importance to the detection of cancer," *IEEE Trans. Microwave Theory Tech.*, vol. 37, no. 12, pp. 1862-1869, Dec. 1989.

[37] K. L. Carr, "Radiometric sensing," *IEEE Potentials*, pp. 21-25, April/May 1997.

[38] L. Dubois, J. – P. Sozanski, V. Tessier, J. –C. Camart, J. –J. Fabre, J. Pribetich, and M. Chiv, " Temperature Control and Thermal Dosimetry by Microwave Radiometry in Hyperthermia," *IEEE*

Trans. Microwave Theory Tech., vol. 44, no. 10, pp. 1755-1761, Oct. 1996.

[39] S. M. Fraser, D. V. Land, and R. D. Sturrock, "Microwave Thermography - an Index of Inflammatory Disease," *Br. J. Rheumatology*, vol. 26, pp. 37-39, 1987.

[40] B. Bocquet, J. C. Van de Velde, A. Mamouni, and Y. Leroy, "Microwave radiometric imaging at 3 GHz for the exploration of breast tumours," *IEEE Trans. Microwave Theory Tech*., vol. 38, pp. 791-793, 1990.

[41] J. Robert, J. Edrich, P. Thouvenot, M. Gautherie, and J. M. Escanye, "Millimeter wave thermography: Preliminary clinical finding on head and neck diseases," *J. Microwave Power*, vol. 14, 1979.

[42] K. L. Carr, A. M. ElMahdi, and J. Schaeffer, "Dual mode microwave system to enhance early detection of cancer," *IEEE Trans. Microwave Theory Tech*., vol. 29, pp. 256-260, 1980.

[43] E. A. Cheever, J. B. Leonard, and K. R. Foster, "Depth of penetration of fields from rectangular apertures into lossy media," *IEEE Trans. Microwave Theory Tech*., vol. 35, pp. 865-867, 1987.

[44] J. Audet, J. C. Bolomey, C. Pichot, D. D. n'Guyen, M. Robillard, M. Chive, and Y. Leroy, "Electrical characteristics of waveguide applicators for medical applications," *J. Microwave Power*, vol. 15, pp. 177-186, 1980.

[45] A. W. Guy, "Electromagnetic fields and relative heating patterns due to a rectangular aperture source in direct contact with bilayered biological tissue," *IEEE Trans. Microwave Theory Tech*., vol. 29, pp. 214-223, 1971.

[46] D. V. Land, "Medical microwave radiometry and its clinical applications," *IEE Colloquium Application of Microwaves in Medicine*, pp. 2/1 - 2/5, 28 Feb 1995.

[47] B. Enander and G. Larson, "Microwave radiometry measurements of the temperature inside a body," *Electronic Letters*, vol. 10, pp. 317, 1974.

[48] J. Edrich and P. C. Hardee, "Thermography at millimeter wavelengths," *Proc. IEEE*, vol. 62, pp. 1391-1392, 1974.

[49] E. A. Cheever and K. R. Foster, "Microwave radiometry in living tissue: What does it measure?" *IEEE Trans. Biomedical Engineering*, vol. 39, no .6, pp. 563-568, June 1992.

[50] B. Bocquet, J. C. van de Velde, A. Mamouni, Y. Leroy, G. Giauz, J. Delannoy, and D. Delvalee, "Microwave Radiometric Imaging at 3 GHz for the Exploration of Breast Tumors," *IEEE Trans. Microwave Theory Tech.*, vol. 38, no.6, pp. 791-793, June 1990.

[51] L. Enel, Y. Leroy, J. C. Van de Velde, and A. Mamouni, "Improved recognition of thermal structures by microwave radiometry," *Electronics Letters*, vol. 20, pp. 293-294, 1984.

[52] Y. Leroy, A. Mamouni, J. C. Van de Velde, B. Bocquet, and B. Dujardin, "Microwave radiometry for non invasive thermometry," *Automedica (Special Issue on Noninvasive Thermometry)*, vol. 8, pp. 181-201, 1987.

[53] J. R. Hadley, B. E. Chapman, J. A. Roberts, D. C. Chapman, K. C. Goodrich, H. R. Buswell, A. L. Alexander, J. S. Tsuruda, and D. L. Parker, "A Three-Coil Comparison for MR Angiography," *Journal of Magnetic Resonance Imaging*, 11 pp. 458–468, 2000.

[54] C. E. Hayes, W. A. Edelstein, and J. F. Schenck, et al., "An efficient, highly homogeneous radiofrequency coil for whole-body NMR imaging at 1.5 T," *J. Magn. Reson. Imaging*, vol. 63, pp. 622–628, 1985.

[55] M. C. Leifer, "Theory of the quadrature elliptic birdcage coil," *Magn. Reson. Med.*, vol. 38 pp. 726–732, 1997.

[56] S. Li, C. M. Collins, and B. J. Dardzinski, et al., "A method to create an optimum current distribution and homogeneous B1 field for elliptical birdcage coils," *Magn. Reson. Med*., vol. 37, pp. 600–608,1997.

[57] J. R. Fitzsimmons, J. C. Scott, and D. M. Peterson, et al., "Integrated RF coil with stabilization for FMRI human cortex," *Magn. Reson. Med*., vol. 38, pp. 15–18, 1997.

[58] L. E. Hendrix, J. A. Strandt, and D. L. Daniels, et al., "Three-dimensional time-of-flight MR angiography with a surface coil: evaluation in 12 subjects," *American Journal Radiology*, vol. 159, pp. 103–106, 1992.

[59] P. B. Roemer, W. A. Edelstein, C. E. Hayes, S.P.Souza, and O.M.Mueller, "The NMR phased array, " *Magn. Reson. Med.*, 16(2), pp. 192-225, 1996.

[60] C. E. Hayes, N. Hattes, and P. B. Roemer, "Volume imaging with MR phased arrays," *Magn. Reson. Med*., vol. 18, no. 2, pp. 309-319,1991.

[61] C. E. Hayes and P. B. Roemer, "Noise correlations in data simultaneously acquired from multiple surface coil arrays," *Magn. Reson. Med.* , vol. 16, no. 2, pp. 181-191, 1991.

[62] S. M. Wright, R. L. Magin, and J. R. Kelton, "Arrays of mutually coupled receiver coils: theory and application," *Magn. Reson. Med.*, vol. 17, no. 1, pp. 252-268, 1991.

[63] S. M. Wright and L. L. Wald, "Theory and application of array coils in MR spectroscopy," *NMR Biomed.*, vol. 10, no. 8, pp. 394-410, 1997.

[64] G. R. Duensing, H. R. Brooker, and J. R. Fitzsimmons, "Maximizing signal-to-noise ratio in the presence of coil coupling," *Magn. Reson*. B, vol. 111, no. 3, pp. 230-235, 1996.

[65] D. K. Sodickson and W. J. Manning, "Simultaneous acquisition of spatial harmonics (SMASH): ultra-fast imaging with radiofrequency coil arrays," *Magn. Reson. Med.*, vol. 38, pp. 591-603, 1997.

[66] K. P. Pruessmann, M. Weiger, M. B. Scheidegger, and P. Boesiger, "SENSE: Sensitivity encoding for fast MRI," *Magn. Reson. Med.*, vol. 42, pp. 952-962, 1999.

[67] Y. Zhu, "Parallel excitation with an array of transmit coils," *Magn. Reson. Med.*, vol. 51, no. 4, pp. 775-784, 2004.

[68] K. Y. Kojima, J. Szumowski, and R. C. Sheley, et al., "Lower extremities: MRangiography with a unilateral telescopic phased-array coil," *Radiology*, 196, pp. 871–875, 1995.

[69] J. W. Monroe, P. Schmalbrock, and D. G. Spigos, "Phased array coils for upper extremity MRA," *Magn. Reson. Med.*, vol. 33, pp. 224–229, 1995.

[70] C. E. Hayes, C. M. Mathis, and C. Yuan, "Surface coil phased arrays for high-resolution imaging of the carotid arteries," *Magn. Reson. Imaging*, vol. 1, pp. 109–112, 1996.

[71] C. Yuan, J. W. Murakami, and C. E. Hayes, et al, "Phased-array magnetic resonance imaging of the carotid artery bifurcation: preliminary results in healthy volunteers and a patient with atherosclerotic disease," *Magn. Reson. Imaging*, vol. 5, pp. 561–565 1995.

[72] S. H. Faro, S. Vinitski, and H. V. Ortega, et al, "Carotid magnetic resonance angiography: improved image quality with dual 3-inch surface coils," *Neuroradiology*, vol. 38, pp. 403–408, 1996.

[73] H. A. Stark and E. M. Haacke, "Helmet and cylindrical shaped CP array coils for brain imaging: a comparison of signal-to-noise characteristics," *Proceedings of the International Society for Magnetic Resonance in Medicine*, pp. 1412, 1996.

[74] J. R. Porter, S. M. Wright, and A. Reykowski, "A 16-element phased-array head coil," *Magn. Reson. Med.*, vol. 40, pp. 272–279, 1998.

[75] T. Wu and R. King, "The cylindrical antenna with nonreflecting resistive loading," *IEEE Trans. Antennas Propag.*, vol. AP-13, no. 3, pp. 369–373, May 1965.

[76] T. Wu and R. King, "Corrections to 'The cylindrical antenna with nonreflecting resistive loading'," *IEEE Trans. Antennas Propag*., vol. AP-13, no. 11, p.998, Nov. 1965.

[77] E. C. Fear, J. Sill, and M. A. Stuchly, "Experimental Feasibility Study of Confocal Microwave Imaging for Breast Tumor Detection ," *IEEE Trans. Microwave Theory Tech*., vol. 51, no. 3, pp. 887-892, March 2003.

[78] *Special Issue of IEEE Trans. Microwave Theory Tech*., MTT-34, 1986.

[79] C. H. Durney and M. F. Iskander, *Antenna Handbook*. Eds. Y.T. Lo & S.W. Lee, 1993.

[80] P. K. Sneed and T. L. Phillips, "Combining hyperthermia and radiation: How beneficial?," *Oncology*, vol. 5, pp. 99-108, 1991.

[81] C. C. Vernon, J. W. Hand, and S. B. Field, et al., "Radiotherapy with or without hyperthermia in the treatment of superficial localized breast cancer: Results from five randomized controlled trials," *Int. J. Radiat. Oncol. Biol. Phys*., vol. 35, pp. 731-44, 1996.

[82] F. Monteccia, "Microstrip antenna design for hyperthermia treatment of superficial tumors," *IEEE Trans. BME*, vol. 39, no. 6, pp. 580-588, June 1992,

[83] J. Vba, C. Franconi, F. Montecchia, and I. Vannucci, "Evanescent-Mode Applicators (EMA) for superficial and subcutaneous hyperthermia," *IEEE Trans. Biomed. Eng*., vol. 40, no.5, pp. 397-407, May 1993.

[84] M. V. Prior, M. L. D. Lumori, J. W. H, G. Lamaitre, C. J. Schneider, and J. D. P. van Dijk, "The Use of a Current Sheet Applicator Array for Superficial Hyperthermia: Incoherent Versus Coherent Operation," *IEEE Trans. Biomed. Eng*., vol. 43, no. 7, pp. 694-698, July 1995.

[85] P. R. Stauffer, M. Leoncini, and V. Manfrini, et al., "Dual concentric conductor radiator for microwave hyperthermia with improved field uniformity to periphery of aperture," *IEICE Trans. on Communicat.*, vol. E78-B, pp. 826-35, 1995.

[86] P. F. Maccarini, H. Rolfsnes, D. Neuman and P. Stauffer, "Optimization of a Dual Concentric Conductor Antenna for Superficial Hyperthermia Applications," *Proceedings of the 26th Annual International conference of the IEEE EMBS*, San Francisco, CA, USA , September 1-5, 2004.

[87] S. Jacobsen, P. R. Stauffer, and D. G. Neuman, "Dual-mode antenna design for microwave heating and noninvasive thermometry of superficial tissue disease," *IEEE Trans. Biomed. Eng*., vol. 47, 2000.

[88] P. F. Turner, "Interstitial Equal-Phased Arrays for EM Hyperthermia," *IEEE Trans. Microwave Theory and Tech*., vol. 34, no.5, pp. 572 - 578, May 1986.

[89] C. M. Furse and M. F. Iskander, "Three-dimensional Electromagnetic Power Deposition in Tumors using Interstitial Antenna Arrays,"

IEEE Trans. on Biomedical Engineering, vol. 36, pp. 977-986, Oct. 1989.

[90] P. Cherry and M. F. Iskander, "FDTD analysis of power deposition patterns of an array of interstitial antennas for use in microwave hyperthermia," *IEEE Trans. Microwave Theory and Tech,* vol. 40, no. 8, pp. 1692-1700, Aug 1992.

[91] R. D. Nevels, G. D. Arndt, G. W. Raffoul, J. R. Carl, and A. Pacifico, "Microwave catheter design," *IEEE Trans. on Biomedical Engineering*, vol. 45, pp.885–890, July 1998.

[92] C. Manry, S. L. Broschat, C.-K. Chou, and J. A. McDougall, "An eccentrically coated asymmetric antenna applicator for intracavity hyperthermia treatment of cancer," *IEEE Trans. on Biomedical Engineering*, vol. 39, no. 9, pp. 935-942, Sept. 1992.

[93] J. C. Camart, D. Despretz, M. Chive, and J. Pribetich, "Modeling of various kinds of applicators used for microwave hyperthermia based on the FDTD method," *IEEE Trans. Microwave Theory and Tech*., vol. 44, no. 10, pp. 1811-1818, Oct. 1996.

[94] P. F. Turner, "Hyperthermia and Inhomogeneous Tissue Effects Using an Annular Phased Array," *IEEE Trans. Microwave Theory and Tech*., vol. 32, no. 8, pp. 874 - 875, Aug. 1984.

[95] P. Stauffer, J. Schlorff, R. Taschereau, T. Juang, D. Neuman, P. Maccarini, J. Pouliot and J. Hsu, "Combination Applicator for Simultaneous Heat and Radiation," *Proceedings of the 26th Annual International Conference of the IEEE EMBS*, San Francisco, CA, September 1-5, 2004.

[96] Y. Kotsuka, E. Hankui, and Y. Shigematsu, "Development of Ferrite Core Applicator System for Deep-Induction Hyperthermia," *IEEE Trans. Microwave Theory and Tech*., vol. 44, no. 10, pp. 1803-1810, Oct. 1996.

[97] D. M. Sullivan, "Three-dimensional computer simulation in deep regional hyperthermia using the FDTD Method," *IEEE Trans. Microwave Theory and Tech*., vol. 38, no. 2, pp. 201-211, Feb. 1990.

[98] P. F. Turner, "Sigma 60–24 Prototype Test Results," *BSD Medical Corporation*, Salt Lake City, UT, Internal Rep., 1992.

[99] J. Nadobny, H. Fähling, M. Hagmann, P. Turner, W. Wlodarczyk, J.Gellermann, P. Deuflhard, and P. Wust, "Experimental and numerical investigations of feed-point parameters in a 3-D hyperthermia applicator using different models of feed networks*," IEEE Trans. Biomed. Eng*., vol. 49, no. 11, pp. 1348–1359, Nov. 2002.

[100] J. Nadobny, W. Wlodarczyk, L. Westhoff, J. Gellermann, R. Felix, and P. Wust, "A Clinical Water-Coated Antenna Applicator for MR-Controlled Deep-Body Hyperthermia: A Comparison of Calculated and Measured 3-D Temperature Data Sets," *IEEE Trans. on Biomedical Engineering*, vol. 52, no. 3, pp. 505-519, March 2005.

[101] K. S. Nikita and N. K. Uzunoglu, "Coupling Phenomena in Concentric Multi-Applicator Phased Array Hyperthermia Systems," *IEEE Trans. Microwave Theory and Tech*., vol. 44, no. 1, pp. 65-74, Jan 1996.

[102] F. Bardati, A. Borrani, A. Gerardino, and G. A. Lovisolo, "SAR Optimization in a Phased Array Radiofrequency Hyperthermia System," *IEEE Trans. on Biomedical Engineering*, vol. 42, no. 12, pp. 1201-1207, Dec. 1995.

[103] R. W. P. King, G. J. Fikioris, and R. B. Mack, *Cylindrical Antennas and Arrays*, Cambirdge, U.K.: Cambridge Univ. Press, 2002.

[104] S. Ebihara and T. Yamamoto, "Resonance analysis of a circular dipole array antenna in cylindrically layered media for directional borehole radar," *IEEE Trans. Geosci. Remote Sensing*, vol. 44, no.1, pp. 22-31, Jan. 2006.

[105] K. Holliger and T. Bergmann, "Numerical modeling of borehole geo-radar data," *Geophysics*, vol. 67, no. 4, pp. 1249-1257, July/Aug. 2002.

[106] J. R. Hadley, "Design of Radio Frequency Coil Arrays for Optimal Signal to Noise Ratio for Magnetic Resonance Angiography," PhD Dissertation, University of Utah Electrical and Computer Engineering Department, 2005.

[107] H. Massoudi, C. H. Durney, and M. F. Iskander, "Limitations of the cubical block model of man in calculating SAR distribution," *IEEE Trans. Microwave Theory and Tech.*, vol. 32, pp. 746-752, 1984.

[108] C. T. Tsai, H. Massoudi, C. H. Durney, and M. F. Iskander, "A procedure for calculating fields inside arbitrarily-shaped, inhomogeneous dielectric bodies using linear basis functions with the moment method," *IEEE Trans. Microwave Theory and Tech*., vol. 34, pp. 1131-1139, 1986.

[109] O. H. Schaubert, D. R. Wilton, and A. W. Glisson, "A tetrahedral modeling method of electromagnetic scattering by arbitrarily shaped inhomogeneous objects," *IEEE. Trans. Antennas and Propagation*, vol. 32, pp. 75-82, 1984.

[110] B. M. Green and M. A. Jensen, "Diversity performance of dual-antenna handsets near operator tissue," *IEEE. Trans. Antennas and Propagation*, vol. 48, no. 7, pp. 1017-1024, July 2000.

[111] O. Gandhi, G. Lazzi, and C. Furse, "Electromagnetic Absorption in the Human Head

and Neck for Mobile Telephones at 835 and 1900 MHz," *IEEE Trans. on Microwave Theory and Tech*., vol. 44, pp. 1884 -1897, 1996.

[112] P. Soontornpipit, C. M. Furse, and Y. C. Chung , "Design of Implantable Microstrip Antenna for Communication with Medical Implants*," Special Issue of IEEE Trans. on Microwave Theory and Tech. on Medical Applications and Biological Effects of RF/Microwaves* , Sept. 2004.

[113] C. E. Reuter, A. Taflove, V. Sathiaseelan, M. Piket-May, and B. B. Mittral, "Unexpected physical phenomena indicated by FDTD modeling of the Sigma-60 deep hyperthermia applicator," *IEEE Trans. Microwave Theory and Tech*., vol. 46, no.4, pp. 313-319, April 1998.

[114] C.-Q. Wang and O. P. Gandhi, "Numerical simulation of annular phased arrays for anatomically based models using the FDTD method," *IEEE Trans. Microwave Theory and Tech*., vol. 37, no.1, pp. 118-126, Jan, 1989.

[115] D. Sullivan, D. Buechler, and F. A. Gibbs, "Comparison of measured and simulated data in an annular phased array using an inhomogeneous phantom," *IEEE Trans. Microwave Theory and Tech*., vol. 40, no.3, pp. 600-604, Mar. 1992.

[116] C. M. Furse, J.-Y. Chen, and O. P. Gandhi, "Use of the Frequency-Dependent Finite-Difference Time-Domain Method for Induced Current and SAR Calculations for a Heterogeneous Model of the Human Body," *IEEE Trans. on Electromagnetic Compatibility*, pp.128-133, May 1994.

[117] C. Furse and O. P. Gandhi, "Calculation of Electric Fields and Currents Induced in a Millimeter-Resolution Human Model at 60 Hz Using the FDTD Method," *Bioelectromagnetics*, 19 (5), pp.293-299, 1998.

[118] C. M. Furse and O. P. Gandhi, "A Memory Efficient Method of Computing Specific Absorption Rate in CW FDTD Simulations," *IEEE Transactions on Biomedical Engineering*, vol. 43, no. 5, pp. 558-560, May 1996.

[119] C. H. Durney, C. C. Johnson, P. W. Barber, H. Massoudi, M. F. Iskander, J. L. Lords, D. K. Ryser, S. J. Allen, and J. C. Mitchell, *Radiofrequency Radiation Dosimetry Handbook*, 2nd ed., USAF School of Medicine, Brooks AFB, TX, 1978.

[120] O. P. Gandhi, , Y. G. Gu, J. Y. Chen, and H. I. Bassen, "Specific absorption rates and induced current distributions in an anatomically based human model for plane-wave exposures," *Health Physics*, 63(3), pp. 281-290, 1992.

[121] O. P. Gandhi and C. M. Furse, "Millimeter-resolution MRI-based models of the human body for electromagnetic dosimetry from ELF to microwave frequencies," *Voxel Phantom Development: Proceedings of an International Workshop held at the National Radiological Protection Board*, Chilton, UK, July 6-7, 1995, Peter J. Dimbylow, editor.

[122] P. J. Dimbylow, "The development of realistic voxel phantoms for electromagnetic field dosimetry," *Voxel Phantom Development: Proceedings of an International Workshop held at the National Radiological Protection Board*, Chilton, UK, July 6-7, 1995, Peter J. Dimbylow, editor.

[123] P. Olley and P. S. Excell, "Classification of high resolution voxel image of a human head," *Voxel Phantom Development: Proceedings of an International Workshop held at the National Radiological Protection Board*, Chilton, UK, July 6-7, 1995, Peter J. Dimbylow, editor.

[124] M. A. Stuchly, K. Caputa, A. van Wensen, and A. El-Sayed, "Models of human and animal bodies in electromagnetics," *Voxel Phantom Development: Proceedings of an International Workshop held at the National Radiological Protection Board*, Chilton, UK, July 6-7, 1995, Peter J. Dimbylow, editor.

[125] National Library of Medicine, Visible Man Project, MRI scans, CT scans, and photographs available on CD through Research Systems, Inc., 2995 Wilderness Place, Boulder, CO 80301.

[126] C. Gabriel, "Compilation of the dielectric properties of body tissues at RF and microwave frequencies," *Final Report AL/OE-TR-1996-0037 submitted to Occupational and Environmental Health Directorate, RFR Division*, 2503 Gillingham Dr., Brooks AFB, TX, June 1996.

[127] M. A. Stuchly and S. S. Stuchly, "Dielectric properties of biological substances – tabulated," *J. Microwave Power*, 15 (1), pp. 19-26, 1980.

[128] S. Rush, J. A. Abildskov, and R. McFee, "Resistivity of body tissues at low frequencies," *Circ. Research*, vol. XII, pp. 40-50, 1963.

[129] L. A. Geddes and L. E. Baker, "The specific resistance of biological material – a compendium of data for the biomedical engineer and physiologist," *Med. & Biol. Engng*., vol. 5, pp. 271-293, Pergamon Press., 1967.

[130] University of Utah Dielectric Database OnLine http://www.ece.utah.edu/dielectric/

[131] D. M. Pozar, "Microstrip antennas," *Proc. IEEE*, vol. 80, pp. 79-91, Jan 1992.

[132] A. Cucini, M. Albani, and S. Maci, "Truncated floquet wave full-wave analysis of large phased arrays of open-eneded waveguides with nonuniform amplitude excitation," *IEEE Trans. Antennas and Propagation*, vol. 51, no.6, pp. 1386-1394, June 2003.

[133] G. Turner and C. Christodoulou, "FDTD analysis of phased array antennas," *IEEE Trans. Antennas and Propagation*, vol. 47, no. 4, pp. 661-667, April 1999.

[134] J. Ren, O. P. Gandhi, L. R. Walker, J. Fraschilla, and C. R. Boerman, "Floquet-based FDTD analysis of two-dimensional phased array antennas," *IEEE Microwave and Guided Wave Letters*, vol. 4, no.4, pp. 109-111, April 1994.

[135] C. Railton and G. S. Hilton, "The analysis of medium-sized arrays of complex elements using a combination of FDTD and reaction matching," *IEEE Trans. Antennas and Propagation*, vol. 47, no. 4, pp. 707-714, April 1999.

[136] J. Gomez-Tagle, P. Wahid, M. Chriyssomallis, and C. Christodoulou, "FDTD analysis of finite-sized phased array microstrip antennas," *IEEE Trans. Antennas and Propagation*, vol. 51, no. 8, pp. 2057-2062, Aug. 2003.

[137] H. Holter and H. Steyskal, "On the size requirement for finite phased-array models," *IEEE Trans. Antennas and Propagation*, vol. 50, no. 6, pp. 836-840, June 2002.

[138] T. Su, N.-T. Huang, Y. Lio, W. Yu, and R. Mittra, "Investigation of instability characteristics arising in the FDTD simulation of electrically large antenna arrays," *IEEE Antennas and Propagation Society International Symposium*, vol. 1, pp. 1014-1017, June 2004.

Dr. Cynthia Furse is the Director of the Center of Excellence for Smart Sensors at the University of Utah and Professor in the Electrical and Computer Engineering Department. The Center focuses on imbedded antennas and sensors in complex environments, such as telemetry systems in the human body, and sensors for location of faults on aging aircraft wiring. Dr. Furse has directed the Utah "Smart Wiring" program, sponsored by NAVAIR and USAF, since 1998. She is Head of Research for LiveWire Test Labs, Inc., a spin off company commercializing devices to locate intermittent faults on live wires. Dr. Furse teaches electromagnetics, wireless communication, computational electromagnetics, microwave engineering, and antenna design. Dr. Furse was the Professor of the Year in the College of Engineering at Utah State University for the year 2000, and Faculty Employee of the year 2002. She is the chair of the IEEE Antennas and Propagation Society Education Committee, and associate editor of the IEEE Transactions on Antennas and Propagation.

2006 INSTITUTIONAL MEMBERS

AUSTRALIAN DEFENCE LIBRARY
Northcott Drive
Campbell, A.C.T. 2600 Australia

BAE SYSTEMS
W. Hanningfield Road
Technology Center Library
Great Baddow, Chelmsford
UK CM2 8HN

BEIJING BOOK COMPANY, INC
701 E Lindon Ave.
Linden, NJ 07036-2495

GOODRICH PUMP & ENGINE SYS.
533 HULLS HILL ROAD
Southbury, CT 06488

DARMSTADT U. OF TECHNOLOGY
Schlossgartenstrasse 8
Darmstadt, Hessen
Germany D-64289

DARTMOUTH COLL-FELDBERG LIB
6193 Murdough Center
Hanover, NH 03755-3560

DSTO-DSTORL EDINBURGH
Jets AU/33851-99, PO Box 562
Milsons Point, NSW
Australia 1565

DTIC-OCP/LIBRARY
8725 John J. Kingman Rd. Ste 0944
Ft. Belvoir, VA 22060-6218

ELLEDIEMME SRL
Via Baccina 30
Roma, Italy 00184

ELSEVIER
Bibliographic Databases
PO Box 2227
Amsterdam, Netherlands 1000 CE

ENGINEERING INFORMATION, INC
PO Box 543
Amsterdam, Netherlands 1000 Am

ETSE TELECOMUNICACION
Biblioteca, Campus Lagoas
Vigo, 36200 Spain

FGAN-FHR
Neuenahrerstrasse 20
Wachtberg, Germany 53343

FLORIDA INTERNATIONAL UNIV
10555 W. Flagler Street
Miami, FL 33174

GEORGIA TECH LIBRARY
225 North Avenue, NW
Atlanta, GA 30332-0001

HANYANG UNIVERSITY
Paiknam Academic Info. Ctr Library
17 Haengdang-Dong
Seongdong-Ku
Seoul, South Korea 133-791

HARIRI CANADIAN UNIVERSITY
PO BOX 10
Damour, Chouf, Lebanon 2010

HRL LABS, RESEARCH LIBRARY
3011 Malibu Canyon
Malibu, CA 90265

IEE INSPEC/Acquisitions Section
Michael Faraday House
6 Hills Way
Stevenage, Herts UK SG1 2AY

IND CANTABRIA
PO Box 830470
Birmingham, AL 35283

INSTITUTE FOR SCIENTIFIC INFO.
Publication Processing Dept.
3501 Market St.
Philadelphia, PA 19104-3302

ISRAEL AIRCRAFT INDUSTRIES
ATTN: Shmuel Averbuch, Dept 4416
Ben Gurion Airport, Israel 70100

LIBRARY of CONGRESS
Reg. Of Copyrights
Attn: 40T Deposits
Washington DC, 20559

LINDA HALL LIBRARY
5109 Cherry Street
Kansas City, MO 64110-2498

MISSISSIPPI STATE UNIV LIBRARY
PO Box 9570Mississippi State, MS
39762

MIT LINCOLN LABORATORY
Periodicals Library
244 Wood Street
Lexington, MA 02420

NAVAL POSTGRADUATE SCHOOL
Attn:J. Rozdal/411 Dyer Rd./ Rm 111
Monterey, CA 93943-5101

NAVAL RESEARCH LABORATORY
Code 3516
4555 Overlook Avenue SW
Washington, DC 20375-5334

NDL KAGAKU
C/0 KWE-ACCESS
PO Box 300613 (JFK A/P)
Jamaica, NY 11430-0613

OHIO STATE UNIVERSITY
1320 Kinnear Road
Columbus, OH 43212

OVIEDO LIBRARY
PO BOX 830679
Birmingham, AL 35283

PENN STATE UNIVERSITY
126 Paterno Library
University Park, PA 16802-1808

PHILIPS RESEARCH LABORATORY
Cross Oak Lane, Stella Cox
Salfords, Redhill
UK RH1 5HA

RENTON TECH LIBRARY/BOEING
PO BOX 3707
SEATTLE, WA 98124-2207

SWETS INFORMATION SERVICES
160 Ninth Avenue, Suite A
Runnemede, NJ 08078

TU DARMSTADT
Schlossgartenstrasse 8
Darmstadt, Hessen
Germany D-64289

TECHNISCHE UNIV. DELFT
Mekelweg 4, Delft, Holland, 2628 CD
Netherlands

TELSTRA
TRL/M2/770 Blackburn Road
Clayton, Victoria, Australia 3168

TIB & UNIV. BIB. HANNOVER
DE/5100/G1/0001
Welfengarten 1B
Hannover, Germany 30167

TOKYO KOKA UNIVERSITY
C/O KWE-ACCESS
PO BOX 300613 (JFK A/P)
Jamaica, NY 11430-0613

UNIV OF CENTRAL FLORIDA LIB.
4000 Central Florida Boulevard
Orlando, FL 32816-8005

UNIV OF COLORADO LIBRARY
Campus Box 184
Boulder, CO 80309-0184

UNIVERSITY OF MISSISSIPPI
John Davis Williams Library
PO Box 1848
University, MS 38677-1848

UNIV OF MISSOURI-ROLLA LIB.
1870 Miner Circle
Rolla, MO 65409-0001

USAE ENG. RES. & DEV. CENTER
Attn: Library/Journals
72 Lyme Road
Hanover, NH 03755-1290

USP POLI
AV. Elmira Martins Moreira, #455
Jardim Altos De Santata
Jacarei, Sao Paolo, BRAZIL
12306-730

ACES COPYRIGHT FORM

This form is intended for original, previously unpublished manuscripts submitted to ACES periodicals and conference publications. The signed form, appropriately completed, MUST ACCOMPANY any paper in order to be published by ACES. PLEASE READ REVERSE SIDE OF THIS FORM FOR FURTHER DETAILS.

TITLE OF PAPER:

AUTHORS(S)

PUBLICATION TITLE/DATE:

RETURN FORM TO:

Dr. Atef Z. Elsherbeni
University of Mississippi
Dept. of Electrical Engineering
Anderson Hall Box 13
University, MS 38677 USA

PART A - COPYRIGHT TRANSFER FORM

(NOTE: Company or other forms may not be substituted for this form. U.S. Government employees whose work is not subject to copyright may so certify by signing Part B below. Authors whose work is subject to Crown Copyright may sign Part C overleaf).

The undersigned, desiring to publish the above paper in a publication of ACES, hereby transfer their copyrights in the above paper to The Applied Computational Electromagnetics Society (ACES). The undersigned hereby represents and warrants that the paper is original and that he/she is the author of the paper or otherwise has the power and authority to make and execute this assignment.

Returned Rights: In return for these rights, ACES hereby grants to the above authors, and the employers for whom the work was performed, royalty-free permission to:

1. Retain all proprietary rights other than copyright, such as patent rights.
2. Reuse all or portions of the above paper in other works.
3. Reproduce, or have reproduced, the above paper for the author's personal use or for internal company use provided that (a) the source and ACES copyright are indicated, (b) the copies are not used in a way that implies ACES endorsement of a product or service of an employer, and (c) the copies per se are not offered for sale.
4. Make limited distribution of all or portions of the above paper prior to publication.
5. In the case of work performed under U.S. Government contract, ACES grants the U.S. Government royalty-free permission to reproduce all or portions of the above paper, and to authorize others to do so, for U.S. Government purposes only.

ACES Obligations: In exercising its rights under copyright, ACES will make all reasonable efforts to act in the interests of the authors and employers as well as in its own interest. In particular, ACES REQUIRES that:

1. The consent of the first-named author be sought as a condition in granting re-publication permission to others.
2. The consent of the undersigned employer be obtained as a condition in granting permission to others to reuse all or portions of the paper for promotion or marketing purposes.

In the event the above paper is not accepted and published by ACES or is withdrawn by the author(s) before acceptance by ACES, this agreement becomes null and void.

AUTHORIZED SIGNATURE — TITLE (IF NOT AUTHOR)

EMPLOYER FOR WHOM WORK WAS PERFORMED — DATE FORM SIGNED

Part B - U.S. GOVERNMENT EMPLOYEE CERTIFICATION

(NOTE: if your work was performed under Government contract but you are not a Government employee, sign transfer form above and see item 5 under Returned Rights).

This certifies that all authors of the above paper are employees of the U.S. Government and performed this work as part of their employment and that the paper is therefor not subject to U.S. copyright protection.

AUTHORIZED SIGNATURE — TITLE (IF NOT AUTHOR)

NAME OF GOVERNMENT ORGANIZATION — DATE FORM SIGNED

PART C - CROWN COPYRIGHT

(NOTE: ACES recognizes and will honor Crown Copyright as it does U.S. Copyright. It is understood that, in asserting Crown Copyright, ACES in no way diminishes its rights as publisher. Sign only if *ALL* authors are subject to Crown Copyright).

This certifies that all authors of the above Paper are subject to Crown Copyright. (Appropriate documentation and instructions regarding form of Crown Copyright notice may be attached).

AUTHORIZED SIGNATURE TITLE OF SIGNEE

NAME OF GOVERNMENT BRANCH DATE FORM SIGNED

Information to Authors

ACES POLICY

ACES distributes its technical publications throughout the world, and it may be necessary to translate and abstract its publications, and articles contained therein, for inclusion in various compendiums and similar publications, etc. When an article is submitted for publication by ACES, acceptance of the article implies that ACES has the rights to do all of the things it normally does with such an article.

In connection with its publishing activities, it is the policy of ACES to own the copyrights in its technical publications, and to the contributions contained therein, in order to protect the interests of ACES, its authors and their employers, and at the same time to facilitate the appropriate re-use of this material by others.

The new United States copyright law requires that the transfer of copyrights in each contribution from the author to ACES be confirmed in writing. It is therefore necessary that you execute either Part A-Copyright Transfer Form or Part B-U.S. Government Employee Certification or Part C-Crown Copyright on this sheet and return it to the Managing Editor (or person who supplied this sheet) as promptly as possible.

CLEARANCE OF PAPERS

ACES must of necessity assume that materials presented at its meetings or submitted to its publications is properly available for general dissemination to the audiences these activities are organized to serve. It is the responsibility of the authors, not ACES, to determine whether disclosure of their material requires the prior consent of other parties and if so, to obtain it. Furthermore, ACES must assume that, if an author uses within his/her article previously published and/or copyrighted material that permission has been obtained for such use and that any required credit lines, copyright notices, etc. are duly noted.

AUTHOR/COMPANY RIGHTS

If you are employed and you prepared your paper as a part of your job, the rights to your paper initially rest with your employer. In that case, when you sign the copyright form, we assume you are authorized to do so by your employer and that your employer has consented to all of the terms and conditions of this form. If not, it should be signed by someone so authorized.

NOTE RE RETURNED RIGHTS: Just as ACES now requires a signed copyright transfer form in order to do "business as usual", it is the intent of this form to return rights to the author and employer so that they too may do "business as usual". If further clarification is required, please contact: The Managing Editor, R. W. Adler, Naval Postgraduate School, Code EC/AB, Monterey, CA, 93943, USA (408)656-2352.

Please note that, although authors are permitted to re-use all or portions of their ACES copyrighted material in other works, this does not include granting third party requests for reprinting, republishing, or other types of re-use.

JOINT AUTHORSHIP

For jointly authored papers, only one signature is required, but we assume all authors have been advised and have consented to the terms of this form.

U.S. GOVERNMENT EMPLOYEES

Authors who are U.S. Government employees are not required to sign the Copyright Transfer Form (Part A), but any co-authors outside the Government are.

Part B of the form is to be used instead of Part A only if all authors are U.S. Government employees and prepared the paper as part of their job.

NOTE RE GOVERNMENT CONTRACT WORK: Authors whose work was performed under a U.S. Government contract but who are not Government employees are required so sign Part A-Copyright Transfer Form. However, item 5 of the form returns reproduction rights to the U. S. Government when required, even though ACES copyright policy is in effect with respect to the reuse of material by the general public.

APPLIED COMPUTATIONAL ELECTROMAGNETICS SOCIETY JOURNAL
http://aces.ee.olemiss.edu

INFORMATION FOR AUTHORS

PUBLICATION CRITERIA

Each paper is required to manifest some relation to applied computational electromagnetics. **Papers may address general issues in applied computational electromagnetics, or they may focus on specific applications, techniques, codes, or computational issues.** While the following list is not exhaustive, each paper will generally relate to at least one of these areas:

1. **Code validation.** This is done using internal checks or experimental, analytical or other computational data. Measured data of potential utility to code validation efforts will also be considered for publication.

2. **Code performance analysis.** This usually involves identification of numerical accuracy or other limitations, solution convergence, numerical and physical modeling error, and parameter tradeoffs. However, it is also permissible to address issues such as ease-of-use, set-up time, run time, special outputs, or other special features.

3. **Computational studies of basic physics.** This involves using a code, algorithm, or computational technique to simulate reality in such a way that better, or new physical insight or understanding, is achieved.

4. **New computational techniques**, or new applications for existing computational techniques or codes.

5. **"Tricks of the trade"** in selecting and applying codes and techniques.

6. **New codes, algorithms, code enhancement, and code fixes.** This category is self-explanatory, but includes significant changes to existing codes, such as applicability extensions, algorithm optimization, problem correction, limitation removal, or other performance improvement. **Note: Code (or algorithm) capability descriptions are not acceptable, unless they contain sufficient technical material to justify consideration.**

7. **Code input/output issues.** This normally involves innovations in input (such as input geometry standardization, automatic mesh generation, or computer-aided design) or in output (whether it be tabular, graphical, statistical, Fourier-transformed, or otherwise signal-processed). Material dealing with input/output database management, output interpretation, or other input/output issues will also be considered for publication.

8. **Computer hardware issues.** This is the category for analysis of hardware capabilities and limitations of various types of electromagnetics computational requirements. Vector and parallel computational techniques and implementation are of particular interest.

Applications of interest include, but are not limited to, antennas (and their electromagnetic environments), networks, static fields, radar cross section, shielding, radiation hazards, biological effects, electromagnetic pulse (EMP), electromagnetic interference (EMI), electromagnetic compatibility (EMC), power transmission, charge transport, dielectric, magnetic and nonlinear materials, microwave components, MEMS technology, MMIC technology, remote sensing and geometrical and physical optics, radar and communications systems, fiber optics, plasmas, particle accelerators, generators and motors, electromagnetic wave propagation, non-destructive evaluation, eddy currents, and inverse scattering.

Techniques of interest include frequency-domain and time-domain techniques, integral equation and differential equation techniques, diffraction theories, physical optics, moment methods, finite differences and finite element techniques, modal expansions, perturbation methods, and hybrid methods. This list is not exhaustive.

A unique feature of the Journal is the publication of unsuccessful efforts in applied computational electromagnetics. Publication of such material provides a means to discuss problem areas in electromagnetic modeling. Material representing an unsuccessful application or negative results in computational electromgnetics will be considered for publication only if a reasonable expectation of success (and a reasonable effort) are reflected. Moreover, such material must represent a problem area of potential interest to the ACES membership.

Where possible and appropriate, authors are required to provide statements of quantitative accuracy for measured and/or computed data. This issue is discussed in "Accuracy & Publication: Requiring, quantitative accuracy statements to accompany data," by E. K. Miller, *ACES Newsletter*, Vol. 9, No. 3, pp. 23-29, 1994, ISBN 1056-9170.

EDITORIAL REVIEW

In order to ensure an appropriate level of quality control, papers are peer reviewed. They are reviewed both for technical correctness and for adherence to the listed guidelines regarding information content.

JOURNAL CAMERA-READY SUBMISSION DATES

March issue	deadline 8 January
July issue	deadline 20 May
November issue	deadline 20 September

Uploading an acceptable camera-ready article after the deadlines will result in a delay in publishing this article.

STYLE FOR CAMERA-READY COPY

The ACES Journal is flexible, within reason, in regard to style. However, certain requirements are in effect:

1. The paper title should NOT be placed on a separate page. The title, author(s), abstract, and (space permitting) beginning of the paper itself should all be on the first page. The title, author(s), and author affiliations should be centered (center-justified) on the first page.

2. An abstract is REQUIRED. The abstract should be a brief summary of the work described in the paper. It should state the computer codes, computational techniques, and applications discussed in the paper (as applicable) and should otherwise be usable by technical abstracting and indexing services.

3. Either British English or American English spellings may be used, provided that each word is spelled consistently throughout the paper.

4. Any commonly-accepted format for referencing is permitted, provided that internal consistency of format is maintained. As a guideline for authors who have no other preference, we recommend that references be given by author(s) name and year in the body of the paper (with alphabetical listing of all references at the end of the paper). Titles of Journals, monographs, and similar publications should be in italic font or should be underlined. Titles of papers or articles should be in quotation marks.

5. Internal consistency shall also be maintained for other elements of style, such as equation numbering. As a guideline for authors who have no other preference, we suggest that equation numbers be placed in parentheses at the right column margin.

6. The intent and meaning of all text must be clear. For authors who are NOT masters of the English language, the ACES Editorial Staff will provide assistance with grammar (subject to clarity of intent and meaning).

7. Unused space should be minimized. Sections and subsections should not normally begin on a new page.

PAPER FORMAT

The preferred format for initial submission and camera-ready manuscripts is 12 point Times Roman font, single line spacing and double column format, similar to that used here, with top, bottom, left, and right 1 inch margins. Manuscripts should be prepared on standard 8.5x11 inch paper.

Only camera-ready electronic files are accepted for publication. The term **"camera-ready" means that the material is neat, legible, and reproducible.** Full details can be found on ACES site, Journal section.

ACES reserves the right to edit any uploaded material, however, this is not generally done. It is the author(s) responsibility to provide acceptable camera-ready pdf files. Incompatible or incomplete pdf files will not be processed, and authors will be requested to re-upload a revised acceptable version.

SUBMITTAL PROCEDURE

All submissions should be uploaded to ACES server through ACES web site (http://aces.ee.olemiss.edu) by using the upload button, journal section. Only pdf files are accepted for submission. The file size should not be larger than 5MB, otherwise permission from the Editor-in-Chief should be obtained first. The Editor-in-Chief will acknowledge the electronic submission after the upload process is successfully completed.

COPYRIGHTS AND RELEASES

Each primary author must sign a copyright form and obtain a release from his/her organization vesting the copyright with ACES. Copyright forms are available at ACES, web site (http://aces.ee.olemiss.edu). To shorten the review process time, the executed copyright form should be forwarded to the Editor-in-Chief immediately after the completion of the upload (electronic submission) process. Both the author and his/her organization are allowed to use the copyrighted material freely for their own private purposes.

Permission is granted to quote short passages and reproduce figures and tables from and ACES Journal issue provided the source is cited. Copies of ACES Journal articles may be made in accordance with usage permitted by Sections 107 or 108 of the U.S. Copyright Law. This consent does not extend to other kinds of copying, such as for general distribution, for advertising or promotional purposes, for creating new collective works, or for resale. The reproduction of multiple copies and the use of articles or extracts for commercial purposes require the consent of the author and specific permission from ACES. Institutional members are allowed to copy any ACES Journal issue for their internal distribution only.

PUBLICATION CHARGES

ACES members are allowed 12 printed pages per paper without charge; non-members are allowed 8 printed pages per paper without charge. Mandatory page charges of $75 a page apply to all pages in excess of 12 for members or 8 for non-members. Voluntary page charges are requested for the free (12 or 8) pages, but are NOT mandatory or required for publication. A priority courtesy guideline, which favors members, applies to paper backlogs. Authors are entitled to 15 free reprints of their articles and must request these from the Managing Editor. Additional reprints are available to authors, and reprints available to non-authors, for a nominal fee.

ACES Journal is abstracted in INSPEC, in Engineering Index, and in DTIC.